EFFECTIVELY GOING BEYOND THE STANDARD MODEL

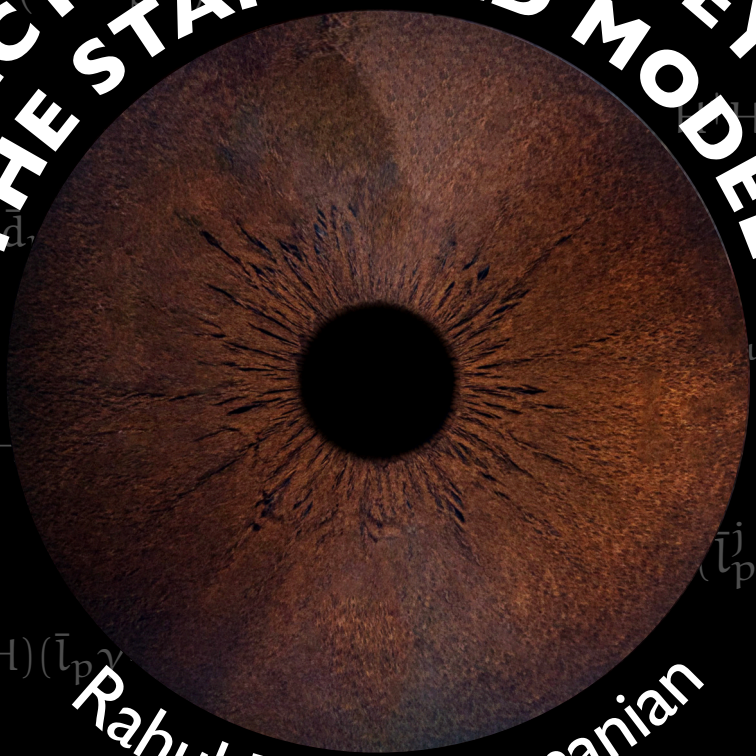

Rahul Balasubramanian

Combined interpretations of
Higgs boson and electroweak measurements
with the ATLAS experiment

Effectively going beyond the Standard Model

Combined interpretations of Higgs boson and electroweak measurements with the ATLAS experiment

Rahul Balasubramanian

ISBN: 978-94-6473-438-6

Effectively going beyond the Standard Model - Combined interpretations of Higgs boson and electroweak measurements with the ATLAS experiment

Thesis, Universiteit van Amsterdam (UvA), Amsterdam

Cover designed by Anastasiia Skurativska and Rahul Balasubramanian

Printed in the Netherlands by Ipskamp printing


This work has been funded by the Marie Skłodowska-Curie ITN Horizon 2020-funded project INSIGHTS (call H2020-MSCA-ITN-2017, grant agreement n.765710) and originates as part of the research programme of the Foundation for Fundamental Research on Matter (FOM), and falls as of April 1, 2017 under the responsibility of Foundation for Nederlandse Wetenschappelijk Onderzoek Instituten (NWO-I), which is part of the Dutch Research Council (NWO). The work has been performed at the National Institute for Subatomic Physics (Nikhef).

Effectively going beyond the Standard Model

Combined interpretations of Higgs boson and electroweak measurements with the ATLAS experiment

ACADEMISCH PROEFSCHRIFT

ter verkrijging van de graad van doctor
aan de Universiteit van Amsterdam
op gezag van de Rector Magnificus
prof. dr. ir. P.P.C.C. Verbeek
ten overstaan van een door het College voor Promoties ingestelde commissie,
in het openbaar te verdedigen in de Agnietenkapel
op woensdag 10 april 2024, te 13.00 uur

door

Rahul Balasubramanian

geboren te Bangalore, Karnataka

PROMOTIECOMMISSIE:

PROMOTOR:	prof. dr. W. Verkerke	Universiteit van Amsterdam
COPROMOTOR:	prof. dr. P. Ferrari	Radboud Universiteit
OVERIGE LEDEN:	prof. dr. P.J.G. Mulders	Vrije Universiteit Amsterdam
	dr. N.J.P Berger	LAPP Annecy
	dr. T.R. Pollmann	Universiteit van Amsterdam
	prof. dr. E.L.M.P. Laenen	Universiteit van Amsterdam
	prof. dr. M. Vreeswijk	Universiteit van Amsterdam
	prof. dr. H.G. Raven	Vrije Universiteit Amsterdam
	dr. F. de Almeida Dias	Universiteit van Amsterdam

Faculteit der Natuurwetenschappen, Wiskunde en Informatica

To my parents and all my teachers,

Contents

1

Introduction

What constitutes the universe, and how does it work? This profound inquiry has existed throughout human history, spanning diverse cultures and civilizations, and has propelled an extraordinary voyage toward a growing knowledge of the fundamental laws of Nature. An important milestone in the current theory, given by the Standard Model of Particle Physics, is the discovery of the Higgs boson in 2012 by the ATLAS [1] and CMS collaborations [2]. The presence of the Higgs boson explains the origin of the mass of other fundamental particles in the Standard Model. Nevertheless, even as the Standard Model stands as one of the most remarkable high-precision prediction models, it has limitations and leaves important phenomena unexplained, such as the matter-antimatter asymmetry in the universe and the nature of dark matter, still leaving many questions unanswered. Thus, it is imperative to continue scrutinizing Nature at the most fundamental scale experimentally.

The Large Hadron Collider (LHC) at CERN is the world's largest and most powerful particle collider. It allows the study of the fundamental constituents of Nature in a highly controlled environment. It covers the search for new particles that may be produced in high-energy collisions and precision measurements of the properties of known Standard Model particles. The large center-of-mass energy of the LHC, corresponding to 13 TeV, allows to test the Standard Model at the highest energies ever achieved in a laboratory.

The Standard Model is widely regarded as an approximation to a fundamental theory. While the fundamental theory operating at scales smaller than those described by the Standard Model remains unknown, it can be systematically examined within an Effective Field Theory (EFT) framework. An EFT approximates the fundamental theory in terms of known particles and symmetries, able to capture signatures arising from the fundamental theory.

While direct searches of new physics at high-energy colliders are potent in uncovering signatures of specific extensions to the Standard Model, it relies on specific hypotheses on the properties of the unknown fundamental theory. An EFT, on the other hand, provides a prescription that is agnostic to the specific type of new particles that extend the Standard Model and serves as a basis for capturing potential signatures of a wide range of fundamental theories.

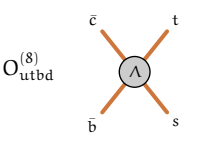

The data collected between 2015-2018 by ATLAS experiment during Run-2 of the LHC corresponding to an integrated luminosity of 139 fb^{-1} at a center-of-mass energy of 13 TeV provides a unique opportunity to test the Standard Model in unexplored kinematic regions. This large dataset enables precision measurements that are crucial to test the Standard Model within the EFT framework.

This thesis presents novel interpretations of the data collected by the ATLAS experiment in the context of the Standard Model Effective Field Theory (SMEFT) [3]. In SMEFT, many parameters are introduced to describe the effects of new physics that result in modifications to the total cross-sections and the shape of kinematic distributions. Due to the large number of parameters in SMEFT, in order to extract meaningful constraints, a dedicated sensitivity study is required to identify the subset of SMEFT parameters measurable with current experimental sensitivity. The kinematic properties of the production of Higgs boson are measured within the Simplified Template cross-section (STXS) framework. The interpretation of the combined Higgs boson STXS measurements from the $H \to \gamma\gamma$, $H \to ZZ^* \to 4l$, and $VH, H \to b\bar{b}$ channels provided a first opportunity to constrain the Higgs sector of the SMEFT. The SMEFT interpretation of the Higgs boson measurements is expanded with additional leading Higgs boson decay channels, including $H \to \tau\tau$ and $H \to WW^* \to l\nu l\nu$ and as well as rare Higgs boson decay channels such as $H \to \mu^+\mu^-$ and $H \to Z\gamma$.

The SMEFT is a framework that incorporates beyond the Standard Model effects consistently in measurements from other physics sectors across different experiments. Thus, a global approach is beneficial to obtain a comprehensive picture of SMEFT. The unified SMEFT model for Higgs boson production in the $H \to WW^* \to l\nu l\nu$ channel and electroweak production of a pair of W bosons sets the stage for a coherent joint interpretation of the Higgs and the electroweak sector. The SMEFT interpretation of combined Higgs boson measurements with the electroweak sector measurements from ATLAS and LEP/SLD demonstrates the utility of SMEFT as a global framework for uncovering deviations across different physics sectors within an experiment. Finally, SMEFT serves as an interface to specific UV-complete theories by mapping SMEFT to specific theories, known as matching. The accuracy of SMEFT is examined in the context of matching its predictions to that of the Two Higgs Doublet model.

1.1 Outline of the thesis and personal contributions

Chapter 2 describes the theory of the Standard Model and discusses its limitations. The Effective Field theory formalism is described, and an overview of the Higgs boson production mechanism and decay channels is discussed.

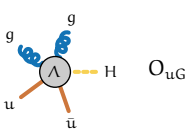

Chapter 3 introduces the LHC and the ATLAS experiment. A study based on using strain gauges to characterize the mechanical behavior of the structure for the ATLAS Inner tracker upgrade is also presented. I designed and tested the apparatus used to perform strain measurements and used it to characterize the build-up of strain when the structure is cooled.

Chapter 4 outlines the algorithms used by the ATLAS collaboration to reconstruct physics objects from raw detector information.

Chapter 5 provides an overview of the statistical modeling of data collected by the ATLAS collaboration to perform statistical inference on physics theories. The observable modeling in SMEFT is also described. Additionally, a nuisance parameter pruning algorithm is described. I devised and implemented the pruning technique to reduce the number of nuisance parameters involved in statistical profiling, allowing to speed up computationally expensive fits. The chapter also presents the Effective Lagrangian morphing method. I was responsible for implementing, documenting, and providing tutorials on the `RooLagrangianMorphFunc` class within the `RooFit` package in the `ROOT` software. I was a co-author of the class description in that is provided in [4].

Chapter 6 explains the SMEFT interpretation of the STXS measurements of three Higgs boson decay channels of $H \to \gamma\gamma$, $H \to 4l$, and $VH, H \to b\bar{b}$. I collaborated with two analyzers for this effort, and it is the first combined SMEFT interpretation performed by the ATLAS collaboration. I prepared the SMEFT prediction for the gluon-gluon fusion Higgs boson production mode. I validated the derivation of the parametrization and the sensitivity study that identifies sensitive directions in SMEFT. I was responsible for preparing the statistical model that combined the three analyses. I also performed the fits to obtain the profile likelihood scans for the linear and linear+quadratic models. The results are published in [5].

Chapter 7 presents the SMEFT interpretation of the ATLAS Run-2 combined Higgs boson measurements consisting of measurements of Higgs boson kinematic properties from all the main decay channels including $H \to WW^* \to l\nu l\nu$ and $H \to \tau^+\tau^-$ and also the inclusive signal strength of rare decay channels such as $H \to \mu\mu$ and $H \to Z\gamma$. It is the most comprehensive study of SMEFT in the Higgs sector by the ATLAS collaboration. As one of two analysis contacts, I led a team of ten analyzers towards achieving the results published in [6].

Chapter 8 describes the SMEFT interpretation of the inclusive production cross-section of ggF and VBF measured in $H \to WW^* \to l\nu l\nu$, probing the Higgs sector alongside the measurement of WW production probing the electroweak sector. This effort, published in [7], is the first step in the ATLAS collaboration towards combining measurements from different physics sectors. I worked with two analyzers and was responsible for preparing the combined statistical model, sensitivity

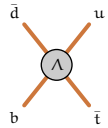

study, and performed the statistical inference to constrain the sensitive parameters.

Chapter 9 presents the SMEFT interpretation of the combined Higgs boson and electroweak measurements based on ATLAS data with Electroweak precision observables (EWPO) measured at LEP and SLD. I was the main analyzer and collaborated with seven analyzers. I was responsible for executing the statistical models, the sensitivity study, and obtaining the statistical constraints for the ATLAS-only and ATLAS+EWPO scenarios. It is the first global combination by the ATLAS collaboration and is published in [8].

Chapter 10 presents the SMEFT matching to the Two Higgs Doublet Model. I collaborated with an analyzer to obtain the first SMEFT matching result prepared by the ATLAS collaboration. The results are published in [6].

Chapter 11 provides the conclusions and the outlook of the thesis.

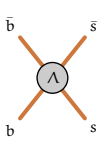

$O_{Qd}^{(8)}$

2

Theory of the Standard Model and Beyond

The Standard Model of particle physics - The Standard Model, in short - is the theory that describes Nature at the smallest distances and correspondingly at the highest energies. It provides a consistent description of three out of the four fundamental forces - electromagnetic, weak, and strong - except gravity which is described by General Relativity [9]. In this chapter, the theoretical framework of the Standard Model is outlined, followed by a discussion of the limitations of the Standard Model, which indicates the existence of a more fundamental theory beyond the Standard Model. The Standard Model Effective Field Theory is then introduced as a framework to parametrize the effects of physics beyond the Standard Model. Finally, the phenomenology of the Higgs boson production and decay at the Large Hadron Collider is discussed.

2.1 The Standard Model

The Standard Model is a relativistic quantum field theory that describes the dynamics of its constituents and is determined by its particle content and symmetries - the Poincaré symmetry corresponding to space-time symmetry and three internal gauge symmetries corresponding to rotations within symmetry groups that describe the three fundamental forces. A brief overview of the Standard Model is presented in this section. For a detailed introduction to the Standard Model, the reader is referred to [10–13] for well-known textbooks on the topic.

2.1.1 Particle Content

The constituents of the Standard Model correspond to particles with unique quantum numbers and charges, as illustrated in Figure 2.1. All particles can be classified based on their quantum numbers and charge within the Standard Model. Quantum numbers, which include properties such as electric charge, spin, and flavor, serve as fundamental attributes defining the distinct identities of particles within the Standard Model.

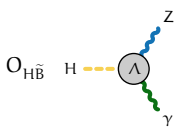

First, there are spin-1/2 fermions, which can be further divided into two categories: quarks and leptons. Quarks are distinctive for being charged under the strong nuclear force, while leptons do not experience the strong nuclear force. It is important to note that the precise nature of neutrinos, a subset of leptons, remains an open question. Neutrinos are under investigation to determine if they are *Dirac* fermions [14] or *Majorana* fermions [15]. The remaining fermions in the Standard Model are classified as Dirac fermions.

Leptons and quarks occur in three generations, where the different generations behave identically under the strong and the electromagnetic force. They differ in their masses and the interaction strength of mass eigenstates under the weak force. On the other hand, the bosonic content of the Standard Model consists of spin-1 gauge bosons, which act as carriers of the fundamental forces, and the spin-0 Higgs boson. The spin-1 gauge bosons are the photon, the gluon, the $W^{\pm}$ and Z bosons and mediate the interactions between the fermions. The Higgs boson is a spin-0 particle that is responsible for the mass of Standard Model particles through the electroweak symmetry breaking mechanism (EWSB) as described in Section 2.1.7.

2.1.2 Symmetries

The Standard Model is a Yang-Mills gauge theory [17] based on the gauge group $SU(3)_C \times SU(2)_L \times U(1)_Y$ where $SU(3)_C$ is the symmetry group of the strong interaction, $SU(2)_L$ is the symmetry group of the weak interaction, and $U(1)_Y$ is the symmetry group of the hypercharge. These symmetries lead to the conservation of electric, weak isospin, and color charge, respectively, following Noether's theorem [18]. For a gauge theory, the corresponding gauge bosons are spin-1 fields with the field strength tensor

$$F^a_{\mu\nu} = \partial_\mu A^a_\nu - \partial_\nu A^a_\mu - g f^{abc} A^b_\mu A^c_\nu, \tag{2.1}$$

where A^a_μ denotes the gauge field component indexed with a, g is the coupling strength, and f^{abc} are the structure constants of the gauge group given by the commutative relations of the gauge group generators

$$[t_a, t_b] = i f^{abc} t_c, \tag{2.2}$$

where t_i are the generators of the gauge group. The corresponding Lagrangian of the different interactions are described in the following sections.

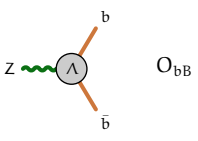

O_{bB}

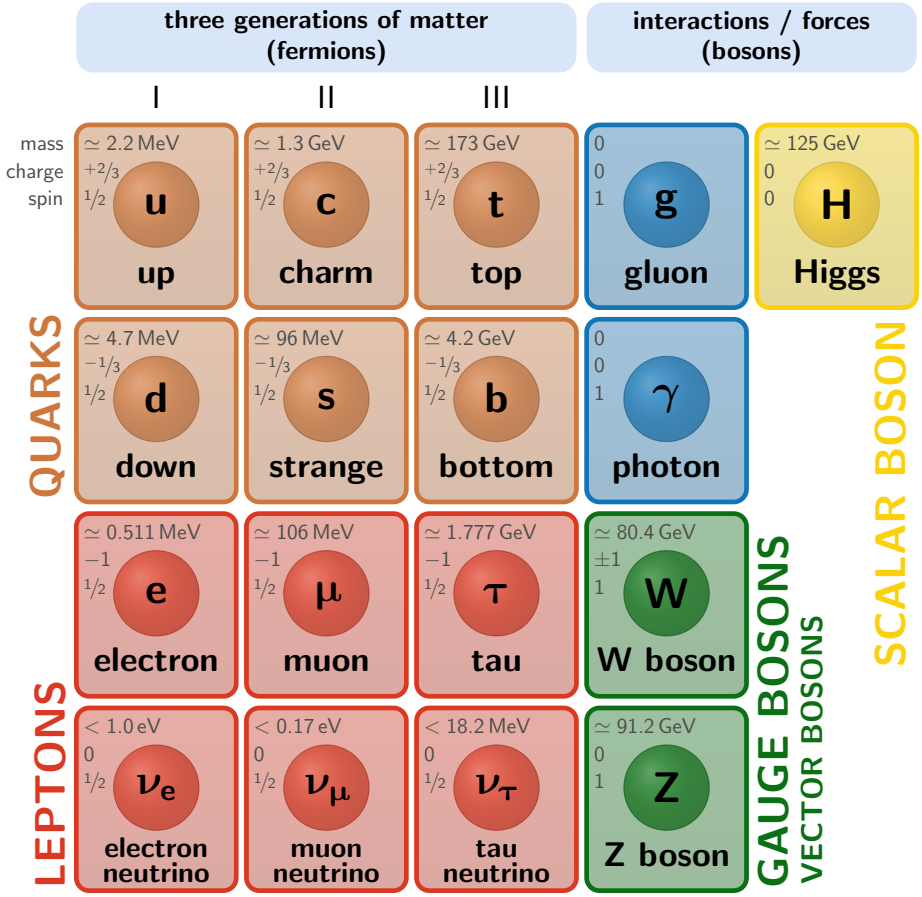

Figure 2.1: Overview of the contents of the Standard Model grouped by fermions and bosons. Taken from [16].

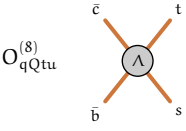

2.1.3 Quantum Electrodynamics

Quantum Electrodynamics (QED) [19–21] is the relativistic quantum field theory that describes the electromagnetic interaction of light with matter. The theory is based on the $U(1)$ gauge symmetry, which requires a massless vector field A_μ, consistent with the photon field. The photon field couples with fermions with a coupling strength that is characterized by their electric charge. The QED Lagrangian can be written out as the sum of the free photon term, the free fermion term, and the interaction term between the fermions and the photon. The QED Lagrangian is written as

$$\mathcal{L}_{QED} = -\frac{1}{4}F^{\mu\nu}F_{\mu\nu} + \sum_f \overline{\psi}_f \left(i\gamma^\mu \partial_\mu - m_f\right)\psi_f - q_f\overline{\psi}_f\gamma^\mu\psi_f A_\mu, \tag{2.3}$$

where the sum over f runs over all the electrically charged fermions with mass m_f and electric charge q_f. ψ_f is the Dirac spinor and the electromagnetic tensor $F_{\mu\nu}$ is given by $\partial_\mu A_\nu - \partial_\nu A_\mu$. The structure constant described in Equations 2.1-2.2 vanishes as the U(1) gauge group is commutative. The QED Lagrangian in Equation 2.3 can further be simplified by introducing the QED gauge covariant derivative, $D_\mu = \partial_\mu - iq_f A_\mu$, which describes the kinetic term of the fermion that is invariant under the U(1) transformation. The QED Lagrangian from Equation 2.3 can be expressed in the contracted form as

$$\mathcal{L}_{QED} = -\frac{1}{4}F^{\mu\nu}F_{\mu\nu} + \sum_f \overline{\psi}_f \left(i\gamma^\mu D_\mu - m_f\right)\psi_f. \tag{2.4}$$

2.1.4 Quantum Chromodynamics

Quantum Chromodynamics (QCD) [22, 23] is the quantum field theory that describes the strong nuclear force responsible for the interaction between quarks and gluons, providing a fundamental description of the interactions of hadrons. Hadrons are composite particles that are bound states of quarks. The QCD charge is denoted as color, and each quark carries one of the three colors (red, blue, green), whereas antiquark carries one of the three colors (antired, antiblue, antigreen). All three colors mixed, or any of these colors and its complement, is *colorless* and has a net color charge of zero. Only hadrons without color are found in Nature and belong to a color singlet; this is known as color confinement. The $SU(3)$ gauge group satisfies these requirements and is the symmetry group of QCD. The gluon fields that correspond to the generators of the symmetry group are

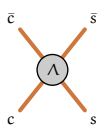

$O_{qq}^{(1,8)}$

given by $\lambda_i/2$ where $\lambda_i, i = \{1\text{–}8\}$ denote the eight Gell-Mann matrices. The QCD Lagrangian is expressed as

$$\mathcal{L}_{QCD} = -\frac{1}{4} G^{\mu\nu}_a G^a_{\mu\nu} + \sum_q \sum_{i,j} \overline{\psi}^i_q \left(i\gamma^\mu D^{ij}_\mu - m_q \delta^{ij} \right) \psi^j_q, \tag{2.5}$$

where the summation q runs over the six quark flavors from Figure 2.1 with mass m_q and the Dirac spinor ψ^i_q for each color, whereas the summations i, j run over the color indices from 1 to 3. The chromomagnetic tensor $G^{\mu\nu}_a$ is given according to Equation 2.1 as

$$G^{\mu\nu}_a = \partial^\mu G^\nu_a - \partial^\nu G^\mu_a - g_s f^{abc} G^\mu_b G^\nu_c, \tag{2.6}$$

where g_s or equivalently $\alpha_s = \frac{g_s^2}{4\pi}$ is the strong coupling constant, f^{abc} are the structure constants of $SU(3)$ and G^μ_a correspond to the gluon fields with the color gauge index a.

2.1.4.1 Asymptotic Freedom

Quarks interact strongly at low energies, leading to the confinement of quarks and gluons within composite hadrons that can be modeled only using non-perturbative techniques, such as lattice QCD. Although gluons are massless, the confinement property of QCD ensures that QCD is a short-range force. The strong force in the non-perturbative domain can be modeled by performing lattice QCD calculations, wherein the space-time continuum is discretized into a finite number of points where solutions to the QCD equations are computed. Lattice QCD has proved to be an essential tool for making QCD predictions: the coupling constant can be estimated, the masses of the quarks can be extracted, and the mass spectrum of most hadrons can be predicted.

The strong interaction also exhibits asymptotic freedom, which means that at higher energies, quarks interact weakly, subsequently allowing the system to be solved with perturbative methods. Thus, the strong force is characterized by a running coupling constant, which becomes small at high energies as shown in as shown in Figure 2.2.

In the framework of perturbative QCD, the strong coupling constant α_s is a function of the energy scale, satisfies the renormalization group equation (RGE),

$$\mu^2 \frac{d\alpha_s}{d\mu^2} = \beta(\alpha_s) = -\left(b_0 \alpha_s^2 + b_1 \alpha_s^3 + b_2 \alpha_s^4 + \ldots \right), \tag{2.7}$$

where the b_i corresponding to (i+1)-th loop contribution to the β function. The negative sign in Equation 2.7 is the origin of asymptotic freedom by ensuring that

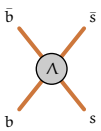

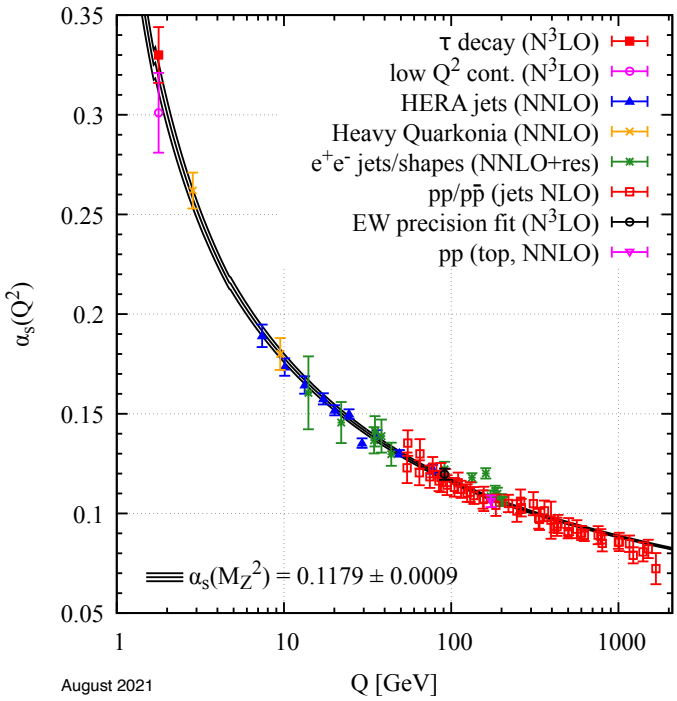

Figure 2.2: Running of the strong coupling constant α_s as summarized in [24].

the strong coupling becomes weak for a higher energy scale. Considering the first-loop correction as an approximation, the running coupling constant at an energy scale Q^2 is written as

$$\alpha_s(Q^2) = \frac{\alpha_s(\mu^2)}{1 + \frac{\alpha_s(\mu^2)}{12\pi}(11N_c - 2N_f)\ln(Q^2/\mu^2)}. \tag{2.8}$$

where N_c is the number of colors, N_f is the number of quark flavors, $\alpha_s(\mu^2)$ is the strong coupling constant at scale μ^2. Given that $11N_c > 2N_f$, the strength of the strong interaction decreases at high energies, as seen in Figure 2.2, reflecting the asymptotic freedom property of QCD. The above equation can also be re-written in terms of a parameter Λ_{QCD} as follows

$$\alpha(Q^2) = \frac{12\pi}{(11N_c - 2N_f)\ln(Q^2/\Lambda^2_{QCD})} + O\left(\frac{1}{(\ln(Q^2/\Lambda^2_{QCD}))^2}\right). \tag{2.9}$$

where Λ_{QCD} corresponds to the scale at which the perturbative expansion diverges. Its value indicates the energy range in which non-perturbative effects start to dominate. The value of Λ_{QCD} depends on the renormalization scheme.

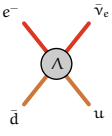

O_{1e}

For $N_f = 6$, Λ_{QCD} in the modified minimal subtraction $\overline{MS}$ scheme is (89 ± 6) MeV [25], where $\overline{MS}$-scheme [26] is the most widely used renormalization scheme in QCD.

2.1.5 QCD for proton-proton collisions

QCD plays an important role for proton-proton collisions and is essential for different aspects for obtaining predictions for the cross-section of the physics processes. The following section discusses the factorization in proton-proton collisions and the parton distribution functions, which are essential ingredients in obtaining predictions of processes.

Factorization in proton-proton interactions

The Large Hadron Collider (LHC) does not collide free quarks but collides protons that are composite particles composed of three valence quarks (uud), gluons, and sea quarks ($q\overline{q}$ pairs). Each of these constituents carries a fraction of the proton's total momentum, denoted as x_i. As mentioned in the previous section, the internal structure of hadrons is characterized by the confinement scale Λ_{QCD}. This scale marks the point at which the strong coupling constant in perturbative QCD would diverge and is dominated by non-perturbative QCD effects. In contrast, hard-scatter processes typically occur at high energies above the QCD scale and can be computed using perturbative QCD.

The factorization theorem [27] plays a crucial role in describing the cross-section of a general hadron-hadron process, denoted as $h_1 + h_2 \to f$. According to this theorem, the cross-section can be expressed as the convolution of a non-perturbative but universal parton distribution function (PDF) denoted as $f_{i/h}(x_i, Q^2)$ where Q^2 is the squared energy scale. This function describes the probability of finding a parton of type i with a longitudinal momentum fraction x_i within a hadron h at a specific energy scale Q.

The cross-section of a general hadron-hadron process, $h_1 + h_2 \to f$, is determined by the partonic cross-section of the hard-scatter process, denoted as $\hat{\sigma}_{i+j\to f}$, which is calculated perturbatively for partons i, j, and its convolution with the PDFs of the colliding partons. The cross-section of the general hadron-hadron process can be expressed as:

$$\sigma_{h_1+h_2\to f} \approx \sum_{i,j} \int dx_1\, dx_2 f_{i/h_1}(x_1, \mu_F^2) f_{j/h_2}(x_2, \mu_F^2) \hat{\sigma}_{i+j\to f}. \tag{2.10}$$

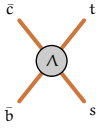

The factorization scale, denoted as μ_F, is introduced as part of the regularization of infrared (IR) effects in the integral. The factorization scale serves to distinguish between the effects of high-energy and low-energy processes.

Parton distribution functions

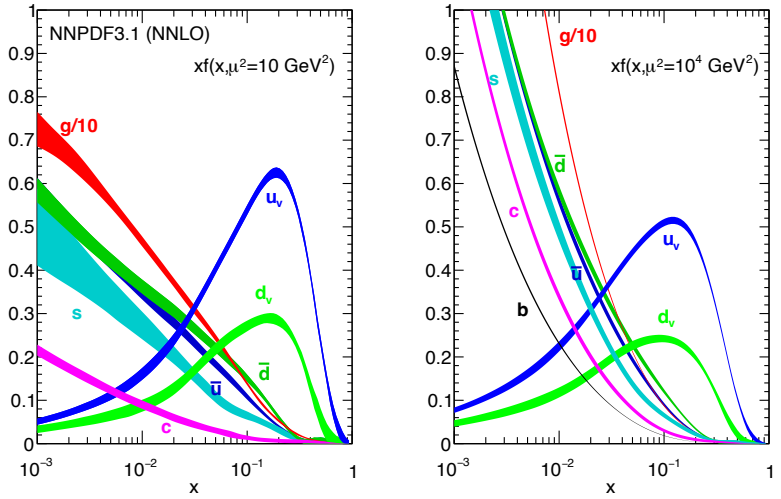

Figure 2.3: Parton distribution functions of the different components of the proton provided by the NNPDF collaboration. The distributions are shown as a function of the momentum fraction x for two scales μ^2. The x-dependence is obtained from a combined fit to data, and the scale dependence is calculated using DGLAP evolution. Taken from [28].

PDFs are not a priori calculable in QCD. However, they can be measured at an arbitrary scale μ_0 in well-understood processes, such as deep inelastic scattering (DIS) [29], Drell-Yan [30] and $pp \to$ jets [31], and, owing to their universality, extrapolated to other scales as a function of the factorization scale. The renormalization group equation is given by the Dokshitzer-Gribov-Lipatov-Altarelli-Parisi (DGLAP) equation [32–34],

$$\mu_F^2 \frac{df_{i/h}(x_i, \mu_F^2)}{d\mu_F^2} = \frac{\alpha_s(\mu_F^2)}{2\pi} \sum_j \int_{x_i}^1 \frac{dx_j}{x_j} P_{i\leftarrow j}\left(\frac{x_i}{x_j}\right) f_{j/h}(x_j, \mu_F^2), \tag{2.11}$$

where $P_{i\leftarrow j}$ describes the splitting of parton j into parton i in the collinear limit. Figure 2.3 shows the RGE evolution of the NNPDF3.1 PDFs set [28] as a function of the partonic momentum for the first two generation quarks and the gluon for a factorization scale of 3.16 GeV and 100 GeV.

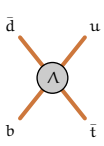

$O^{(1)}_{qQbd}$

2.1.6 Electroweak Theory

The electroweak theory of the Standard Model [35–37] provides an unified description of the electromagnetic force with the weak nuclear force. The weak nuclear force is, among others, responsible for β-decays and neutrino interactions. The electroweak theory is based on the $SU(2)_L \times U(1)_Y$ gauge symmetry proposed by Glashow, Weinberg, and Salam, which unifies electromagnetism with weak interaction described by the V-A theory proposed by Marshak and Sudarshan [38].

The generators of $SU(2)_L$ and $U(1)_Y$ are the weak isospin (labeled T) and weak hypercharge (labeled Y) respectively. The generators of the gauge groups give rise to the gauge field that mediates the electroweak interactions – the three W fields of weak isospin (W_1, W_2, and W_3) and the B field of weak hypercharge. The kinetic term of the gauge bosons is expressed in terms of their field strength tensor according to Equation 2.1 as

$$\mathcal{L}_{EW,gauge} = -\frac{1}{4} W_a^{\mu\nu} W_{\mu\nu}^a - \frac{1}{4} B^{\mu\nu} B_{\mu\nu}, \tag{2.12}$$

where the summation a runs over the three weak isospin indices. It is convenient to introduce the left-handed and right-handed projection operators, P_L and P_R, to discuss the weak interaction. The projection operators split the Dirac spinor into left-handed and right-handed chiral components as

$$\psi = \psi_L + \psi_R = P_L\psi + P_R\psi = \frac{1}{2}\left(1-\gamma^5\right)\psi + \frac{1}{2}\left(1+\gamma^5\right)\psi. \tag{2.13}$$

The left- and right-handed chiral components transform differently under the $SU(2)_L$ symmetry, where the left-handed components transform as doublets ($T_3 = \pm 1/2$) and the right-handed components transform as singlets ($T_3 = 0$). The kinetic term of the fermions in terms of the left- and right-handed components is given by

$$\begin{aligned}\mathcal{L}_{EW,fermion} = \sum_j & \overline{\boldsymbol{Q}}_{L,j} i\gamma^\mu D_\mu \boldsymbol{Q}_{L,j} + \overline{\boldsymbol{u}}_{R,j} i\gamma^\mu D_\mu \boldsymbol{u}_{R,j} \\ & + \overline{\boldsymbol{d}}_{R,j} i\gamma^\mu D_\mu \boldsymbol{d}_{R,j} + \overline{\boldsymbol{L}}_{L,j} i\gamma^\mu D_\mu \boldsymbol{L}_{L,j} + \overline{e}_{R,j} i\gamma^\mu D_\mu e_{R,j},\end{aligned} \tag{2.14}$$

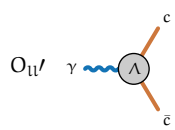

where j runs over the three generations of fermions. The notation for the fermions and their electroweak quantum numbers are given in Table 2.1. The quarks are denoted by

$$\boldsymbol{Q}_L = \left(\begin{pmatrix} u_L \\ d_L \end{pmatrix}, \begin{pmatrix} c_L \\ s_L \end{pmatrix}, \begin{pmatrix} t_L \\ b_L \end{pmatrix} \right), \tag{2.15}$$

$$\boldsymbol{u}_R = (u_R, c_R, t_R), \tag{2.16}$$

$$\boldsymbol{d}_R = (d_R, s_R, b_R), \tag{2.17}$$

where the left-handed doublet is given by $\boldsymbol{Q}_L$ and $\boldsymbol{u}_R$ and $\boldsymbol{d}_R$ represent the right-handed singlet of up- and down-type quarks. The leptons are denoted by

$$\boldsymbol{L}_L = \left(\begin{pmatrix} e_L \\ \nu_{eL} \end{pmatrix}, \begin{pmatrix} \mu_L \\ \nu_{\mu L} \end{pmatrix}, \begin{pmatrix} \tau_L \\ \nu_{\tau L} \end{pmatrix} \right), \tag{2.18}$$

$$\boldsymbol{\ell}_R = (e_R, \mu_R, \tau_R), \tag{2.19}$$

where $\boldsymbol{L}_L$ and $\boldsymbol{\ell}_R$ are the left-handed doublet and the right-handed singlet fields. The covariant derivative in Equation 2.14 is expressed as

$$D_\mu = \partial_\mu - i\frac{g_1}{2} T_a W_\mu^a - i\frac{g_2}{2} Y B_\mu. \tag{2.20}$$

Here, g_1 and g_2 are the coupling strength of the $SU(2)_L$ and $U(1)_Y$ gauge groups respectively. The T_a are the components of the weak isospin and Y is the weak hypercharge. The weak hypercharge is related to the electric charge Q by the Gell-Mann-Nishijima relation [39, 40] given by

$$Q = T_3 + \frac{1}{2} Y. \tag{2.21}$$

A hypothetical mass term for fermions of the form $m\overline{\psi}\psi = m\overline{\psi}_L\psi_R + m\overline{\psi}_R\psi_L$ would mix components with different weak isospin and weak hypercharge and would not conserve T_3 and Y and can therefore not exist. Additionally, as seen earlier for QED and QCD, the mass term for gauge bosons is forbidden since they are not invariant under gauge transformations.

2.1.7 Electroweak Symmetry Breaking

The Brout-Englert-Higgs (BEH) mechanism [41–46], commonly referred to as the Higgs mechanism, generates the mass of bosons and fermions by electroweak sym-

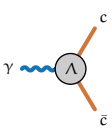

O_{uB}

	Generation (i)			Electrical Charge	Weak Isospin	Weak Hypercharge
	1	2	3	Q	T_3	Y
$\boldsymbol{L}_L$	(e_L, ν_{eL})	$(\mu_L, \nu_{\mu L})$	$(\tau_L, \nu_{\tau L})$	(-1, 0)	(-1/2, 1/2)	(-1, -1)
$\boldsymbol{l}_R$	e_R	μ_R	τ_R	-1	0	-2
$\boldsymbol{Q}_L$	(u_L, d_L)	(c_L, s_L)	(t_L, b_L)	(2/3, -1/3)	(1/2, -1/2)	(1/3, 1/3)
$\boldsymbol{u}_R$	u_R	c_R	t_R	2/3	0	4/3
$\boldsymbol{d}_R$	d_R	s_R	b_R	-1/3	0	-2/3

Table 2.1: Electric Charge (Q), third-component of the Weak Isospin (T_3), and Weak Hypercharge (Y) for fermion fields. For quarks, the left-handed doublet is denoted as $\boldsymbol{Q}_L$ and $\boldsymbol{u}_R$ and $\boldsymbol{d}_R$ denote the represent the right-handed singlet of up and down type quarks. For fermions, $\boldsymbol{L}_L$ and $\boldsymbol{\ell}_R$ denote the left-handed doublet and the right-handed singlet fields, respectively. Right-handed neutrinos do not exist in the Standard Model.

metry breaking (EWSB). It posits the existence of a scalar doublet - the Higgs field denoted H with a non-zero vacuum expectation value. The scalar $SU(2)$ doublet, which is a complex scalar field with four degrees of freedom (h_1, h_2, h_3, h_4) can be written as

$$H = \begin{pmatrix} h^+ \\ h^0 \end{pmatrix} = \begin{pmatrix} h_1 + ih_2 \\ h_3 + ih_4 \end{pmatrix}. \tag{2.22}$$

The most general renormalizable Lagrangian for the Higgs field is represented by

$$\mathcal{L} = (D_\mu H)^\dagger (D^\mu H) - \underbrace{\mu^2 H^\dagger H + \lambda \left(H^\dagger H\right)^2}_{V(H)}. \tag{2.23}$$

where the gauge covariant derivative in the first term is given by Equation 2.20. The last two terms correspond to the Higgs potential $V(H)$, which has two free parameters μ^2 and λ, which must be positive to ensure the potential is bounded from below. These two conditions give the Higgs potential a Mexican-hat shape, as shown in Figure 2.4.

The ground state of the Higgs potential is given by the minimum of the potential, which is determined by the condition

$$\partial V(H) = 0 \implies h_1^2 + h_2^2 + h_3^2 + h_4^2 = \frac{\mu^2}{\lambda}. \tag{2.24}$$

O_{ll}

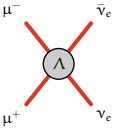

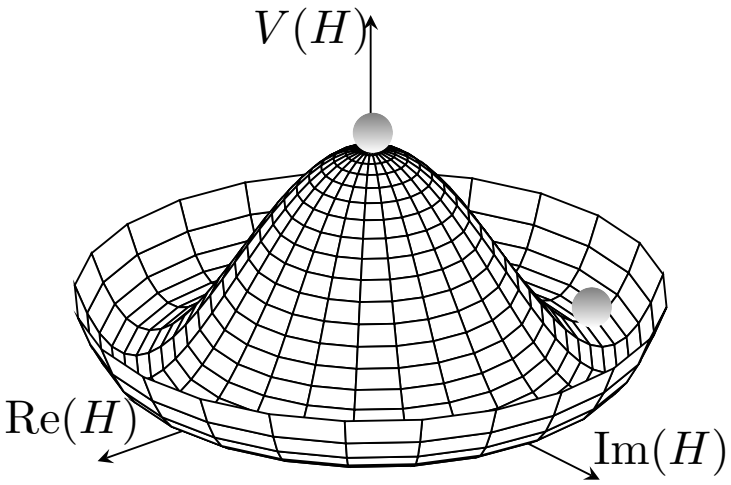

Figure 2.4: Plot of the Higgs potential V(H) as a function of the Higgs field H.

The ground state of the Higgs potential is not unique and is chosen as

$$\langle H \rangle = \frac{1}{\sqrt{2}} \begin{pmatrix} 0 \\ v \end{pmatrix} \tag{2.25}$$

where $v = \sqrt{2\mu^2/\lambda}$ is the vacuum expectation value.

The Higgs field can be expanded around the ground state in terms of small deviations in the field $\{\theta_1, \theta_2, h, \theta_4\}$ as,

$$H = \frac{1}{\sqrt{2}} \begin{pmatrix} \theta_1 + i\theta_2 \\ v + h + i\theta_4 \end{pmatrix} \approx \frac{1}{\sqrt{2}} \begin{pmatrix} 0 \\ v + h \end{pmatrix} e^{i \frac{\sigma^j}{2} \frac{\theta_j}{v}}, \tag{2.26}$$

where the Goldstone fields $(\theta_1, \theta_2, \theta_3)$ are absorbed into an overall phase factor that can be gauged away. The remaining excitation of the Higgs field is the physical Higgs boson h.

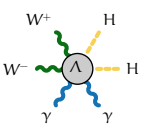

O_{HW}

2.1.7.1 Gauge boson masses

After the spontaneous symmetry breaking, the mass term for the gauge bosons can be obtained from Equation 2.23 which requires the covariant derivative from Equation 2.20

$$D_\mu H = \frac{1}{2\sqrt{2}} \begin{pmatrix} 2\partial_\mu + ig_1 W_\mu^{(3)} + ig_2 B_\mu & ig_1 \left(W_\mu^{(1)} - iW_\mu^{(2)}\right) \\ ig_1 \left(W_\mu^{(1)} + iW_\mu^{(2)}\right) & 2\partial_\mu - ig_1 W_\mu^{(3)} + ig_2 B_\mu \end{pmatrix} \begin{pmatrix} 0 \\ v + h \end{pmatrix} \tag{2.27}$$

$$= \frac{1}{2\sqrt{2}} \begin{pmatrix} ig_1 (v + h) \left(W_\mu^{(1)} - iW_\mu^{(2)}\right) \\ (v + h) \left(2\partial_\mu - ig_1 (W_\mu^{(3)} + ig_2 B_\mu)\right) \end{pmatrix}. \tag{2.28}$$

Taking the Hermitian conjugate $(D_\mu H)^\dagger$ and inserting Equation 2.23 gives,

$$\begin{aligned}(D_\mu H)^\dagger (D^\mu H) = \frac{1}{2}(\partial_\mu h)(\partial^\mu h) + \frac{1}{8}(v + h)^2 g_1^2 (W_\mu^{(1)} + iW_\mu^{(2)})(W^{(1)\mu} - W^{(2)\mu}) \\ + \frac{1}{8}(v + h)^2 (g_1 W_\mu^{(3)} - g_2 B_\mu)(g_1 W^{(3)\mu} - g_2 B^\mu).\end{aligned} \tag{2.29}$$

The mass terms for the gauge bosons are realized in the terms in $(D_\mu H)^\dagger (D^\mu H)$, which are quadratic in the gauge boson fields and can be obtained by expanding Equation 2.29 which results in the following terms:

$$\frac{v^2}{8} g_1^2 (W_\mu^{(1)} W^{\mu(1)} + W_\mu^{(2)} W^{\mu(2)}) + \frac{v^2}{8} (g_1 W_\mu^{(3)} - g_2 B_\mu)(g_1 W^{(3)\mu} - g_2 B^\mu). \tag{2.30}$$

The mass terms for the $W^{(1)}$ and $W^{(2)}$ bosons,

$$m_W = \frac{v g_1}{2} \tag{2.31}$$

are found to be identical and determined by the coupling constant of the $SU(2)_L$ gauge interaction g_1 and the vacuum expectation value of the Higgs field v. The quadratic term in $W^{(3)}$ and B fields in Equation 2.30 are

$$\begin{aligned}\frac{v^2}{8}(g_1 W_\mu^{(3)} - g_2 B_\mu)(g_1 W^{(3)\mu} - g_2 B^\mu) = \\ \frac{v^2}{8} \begin{pmatrix} W_\mu^{(3)} & B_\mu \end{pmatrix} \begin{pmatrix} g_1^2 & -g_1 g_2 \\ -g_1 g_2 & g_2^2 \end{pmatrix} \begin{pmatrix} W^{(3)\mu} \\ B^\mu \end{pmatrix},\end{aligned} \tag{2.32}$$

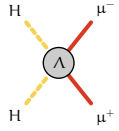

O_{eH}

where the non-diagonal mass matrix is given by M:

$$M = \begin{pmatrix} g_1^2 & -g_1 g_2 \\ -g_1 g_2 & g_2^2 \end{pmatrix}. \tag{2.33}$$

The Z boson and the photon are the physical boson fields corresponding to the mass eigenstates of Equation 2.32. The masses correspond to the eigenvalues (λ) obtained by $det(M - \lambda I) = 0$, where *det* denotes the determinant and I is the identity matrix, gives,

$$(g_1^2 - \lambda)(g_2^2 - \lambda) - g_1^2 g_2^2 = 0 \implies \lambda = 0 \quad \text{or} \quad \lambda = g_1^2 + g_2^2. \tag{2.34}$$

In the mass eigenstate basis, the mass terms in Equation 2.32 can be written in terms of the mass eigenvectors as

$$\frac{v^2}{8} \begin{pmatrix} A_\mu & Z_\mu \end{pmatrix} \begin{pmatrix} 0 & 0 \\ 0 & g_1^2 + g_2^2 \end{pmatrix} \begin{pmatrix} A^\mu \\ Z^\mu \end{pmatrix}, \tag{2.35}$$

$$\tag{2.36}$$

where A_μ and Z_μ are the physical fields corresponding to the photon and the Z boson, respectively. The mass of the photon and the Z boson is as follows

$$\begin{aligned} m_A &= 0 \\ m_Z &= \frac{v}{2}\sqrt{g_1^2 + g_2^2}. \end{aligned} \tag{2.37}$$

The corresponding physical fields of the photon and the Z boson are a mixture of the $W^{(3)}$ and B fields and are written as

$$\begin{pmatrix} A_\mu \\ Z_\mu \end{pmatrix} = \frac{1}{\sqrt{g_1^2 + g_2^2}} \begin{pmatrix} g_2 W_\mu^{(3)} + g_1 B_\mu \\ g_1 W_\mu^{(3)} - g_2 B_\mu \end{pmatrix} = \begin{pmatrix} \sin\theta_W W_\mu^{(3)} + \cos\theta_W B_\mu \\ \cos\theta_W W_\mu^{(3)} - \sin\theta_W B_\mu \end{pmatrix}. \tag{2.38}$$

The weak mixing angle θ_W in Equation 2.38 is defined as

$$\cos\theta_W = \frac{g_1}{\sqrt{g_1^2 + g_2^2}} = \frac{m_W}{m_Z} \tag{2.39}$$

and provides a measure of the relative strength of the $SU(2)_L$ and $U(1)_Y$ gauge interactions.

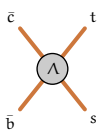

$O_{utbd}^{(1)}$

2.1.7.2 Fermion masses

As discussed earlier, a hypothetical fermion mass term $m\overline{\psi}\psi$ does not respect the $SU(2)_L \times U(1)_Y$ gauge symmetry. Instead, the mass term corresponds to a Yukawa interaction term with the Higgs (H) and the left- and right-handed components of the fermion fields as

$$\mathcal{L}_{Yukawa} = -\sum_f \left(\lambda_f^l \overline{L}_{L,f} H e_{R,f} + \lambda_f^u \overline{Q}_{L,f} H u_{R,f} + \lambda_f^d \overline{Q}_{L,f} \sigma_2 H d_{R,f} + h.c.\right), \tag{2.40}$$

where λ_f is the Yukawa coupling strength and f runs over the fermion generations. Unlike the hypothetical fermion mass term $m\overline{\psi}\psi$, the Yukawa interaction term is invariant under the $SU(2)_L \times U(1)_Y$ gauge symmetry. It gives rise to the fermion masses after the spontaneous symmetry breaking. This can be seen by expanding the Yukawa interaction term around the ground state of the Higgs potential $H = \frac{1}{\sqrt{2}}\begin{pmatrix} 0 \\ v+h \end{pmatrix}$ as

$$\mathcal{L}_{Yukawa} = -\sum_f \left(\lambda_f \frac{v}{\sqrt{2}} \overline{\psi}_{f,L} \psi_{f,R} + h.c.\right) - \sum_f \left(\lambda_f \frac{h}{\sqrt{2}} \overline{\psi}_{f,L} \psi_{f,R} + h.c.\right). \tag{2.41}$$

The first term in the above equation is the mass term for the fermions and the second term is the interaction term between the fermions and the Higgs boson. The fermion mass term generated by the Higgs mechanism can be expressed in terms of the Yukawa coupling strength λ_f and the vacuum expectation value of the Higgs field v as

$$m_f = \frac{\lambda_f v}{\sqrt{2}}. \tag{2.42}$$

2.2 Open questions in the Standard Model

While the Standard Model of particle physics has been incredibly successful in describing the behavior of fundamental particles and forces, it does have several limitations and shortcomings. Some open questions in the Standard Model are listed below.

- Gravity: The Standard Model does not incorporate the force of gravity into its framework. Gravity is described by the General Theory of Relativity [9] and attempts to unify gravity with the other forces have not yet been successful [47].

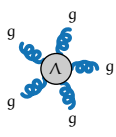

- Dark Matter: The Standard Model does not account for dark matter, which has been detected in astrophysical and cosmological observations [48–50]. From these observations, dark matter is expected to interact gravitationally but not with light, hence the name *dark matter*. The Standard Model does not provide a candidate for dark matter.
- Dark Energy: Supernovae measurements have established that the universe is expanding with an accelerating expansion [51, 52]. The accelerating expansion is explained with the Standard Model of cosmology, the ΛCDM model, by an unknown form of energy. The measured energy density causing the expansion is many orders of magnitude smaller than those estimated by accounting for the vacuum expectation value of the Standard Model [53].
- Neutrino Masses: While the Standard Model originally assumed that neutrinos were massless, neutrino oscillation experiments [54, 55] prove that they do have small but non-zero masses. This requires an extension of the Standard Model known as the seesaw mechanism [56] to explain the origin of neutrino masses.
- CP Violation and Matter-Antimatter Asymmetry: The Standard Model's explanation for the observed matter-antimatter asymmetry in the universe, known as baryogenesis, is not sufficient to explain the observed imbalance in the universe [57].
- Hierarchy Problem: The Higgs boson's mass is sensitive to quantum corrections that are many orders of magnitude larger than its observed value, and involves a delicate cancellation that is unnatural.
- Unification of Forces: While the Standard Model successfully unifies the electromagnetic and weak nuclear forces at high energies, it does not include the strong nuclear force in this unification.
- Higgs boson: The Higgs boson is the only known scalar field in the Standard Model. The Higgs mechanism assumed the Higgs field to be a double of complex scalar fields. While this is the simplest choice, it is not the only possibility. For instance, extensions of the Standard Model can include additional Higgs bosons.

Despite such shortcomings and open questions, the Standard Model has been incredibly successful in explaining and predicting a wide range of experimental results. However, addressing these open issues requires physics beyond the Standard Model and the development of theoretical extensions to overcome these challenges.

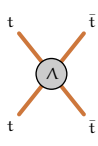

$O_{QQ}^{(1)}$

2.3 Effective field theory approach

Many theoretical extensions of the Standard Model have been proposed to address the shortcomings of the Standard Model. Typically, they introduce new particles that might be produced at the LHC and can be searched in experimental data. As seen from Figure 2.5, the current direct searches allow to search and exclude new particles proposed in various New Physics models up to a mass scale of a few TeV.

There are two ways to search for new particles: model-driven and data-driven. Given that there are many possible models in the model-driven approach, it is demanding to search for all of them. In the model-driven approach, the search for the resonant production of new particles with a distinct experimental signature as shown in Figure 2.5 - has largely been exhausted. A relatively unexplored area is the search for non-resonant effects of new physics, which could manifest themselves through a wide range of subtle deviations rather than a few localized deviations. Looking for these subtle deviations that would consistently affect many measurements requires a model-agnostic framework that can consistently capture the effects across different measurements. This framework can then be used to study the properties of possible new physics models and to guide the experimental searches for new physics.

An effective field theory (EFT) approach is a systematic and largely model-agnostic approach to describe the effects of heavy new physics. An EFT results from the Appelquist-Carrazone decoupling theorem [59], which ensures that the physics at a given energy scale can be described by the relevant particles at that scale and the heavier particles can be omitted up to corrections whose magnitude are of the order of inverse powers of the heavy mass scale.

There are two distinct approaches to constructing an EFT. The first is the top-down approach, where the high-energy theory is known and is reduced to a low-energy EFT by integrating out the heavy degrees of freedom. A top-down EFT approach simplifies the theory and obtains predictions for the low-energy observables. Some examples of a top-down EFT are the Fermi theory of weak interactions [60], Soft collinear Effective Theory (SCET) [61–65], and Heavy Quark Effective Theory (HQET) [66].

The second approach is known as bottom-up, where the underlying fundamental description at a heavy mass scale Λ is unknown. The EFT is constructed by considering all possible terms based on known fields that respect known symmetries. In a similar matter, before the discovery of the weak bosons, Fermi theory was the effective theory of the to-be-discovered fundamental electroweak theory. The Standard Model contains information from its constituents up to the electroweak scale. and does not contain any information about physics at a more fundamental scale. Thus, the Standard Model is likely to be a low-energy approximation of a

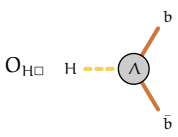

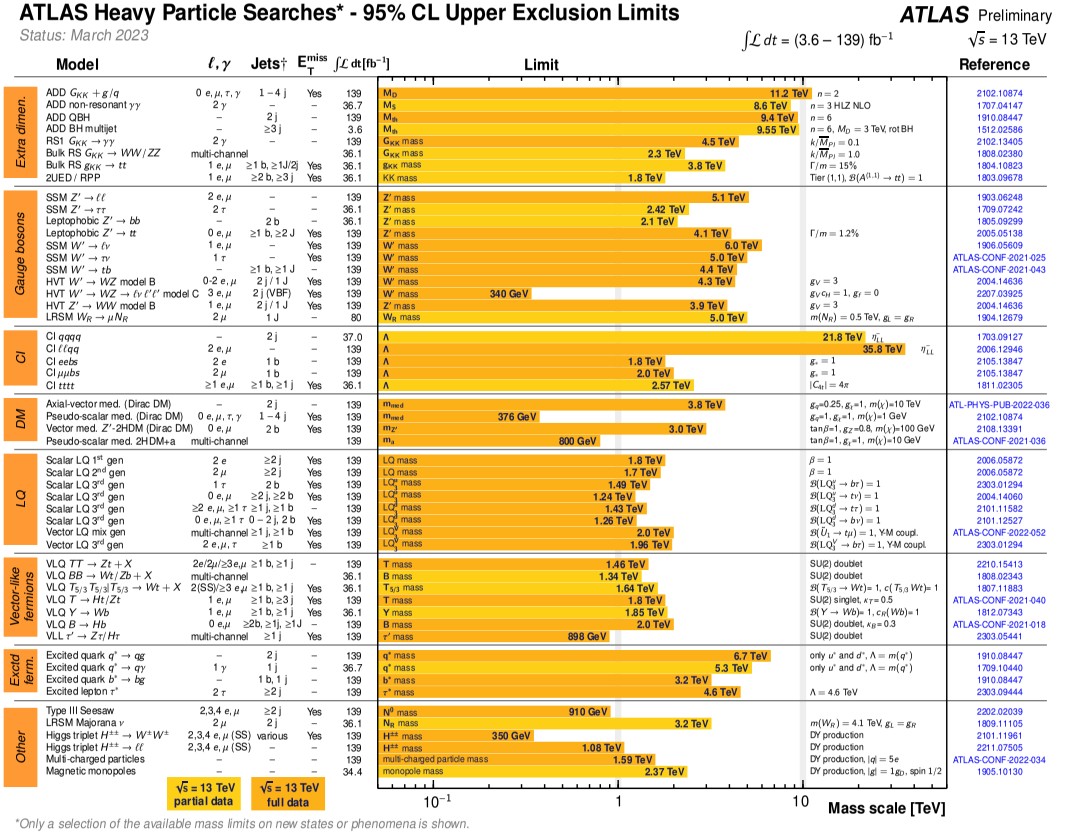

Figure 2.5: Summary of the limits from the ATLAS experiment on the mass of new particles obtained from searches for direct production of new particles. Taken from [58].

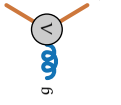

more fundamental theory at a higher energy scale and needs to be studied within an effective field framework to identify the effects of heavy new physics. A bottom-up EFT can be constructed for the Standard Model to examine effects of physics at a more unknown fundamental energy scale.

2.3.1 The Standard Model Effective Field Theory

The SM Lagrangian can be extended by considering a general Lagrangian consisting of Standard Model terms and a series of higher-order terms suppressed order-by-order by the scale of new physics. The energy scale of new physics Λ should be much higher than the Higgs vacuum expectation value v. The extended Lagrangian can be written as

$$\mathcal{L} = \frac{1}{\Lambda^0}\mathcal{L}_{SM} + \frac{1}{\Lambda^1}\mathcal{L}^{(d=5)} + \frac{1}{\Lambda^2}\mathcal{L}^{(d=6)} \ldots, \tag{2.43}$$

where the first term does not contain any information of Λ. The additional terms are suppressed by the energy scale of new physics, thus for energy scales far away from Λ, the contribution of these additional terms are suppressed. The terms are ordered by their energy dimensions d, and are suppressed by a factor Λ^{4-d}. All terms are constructed only using the SM fields, derivatives, and Pauli matrices. The energy dimension of the SM fields and the derivative operator in four-dimensional space-time are given by,

$$[H] = 1,\ [\psi] = \frac{3}{2}, [X] = 2, [D] = 1, \tag{2.44}$$

where H denotes the Higgs doublet, ψ is the fermion field, X denotes the field tensor and D denotes the derivative. All possible terms allowed from known experimentally verified symmetries corresponding to the Poincaré symmetry and the gauge symmetry $SU(3)_C \times SU(2)_L \times U(1)_Y$ are considered. Each term in Equation 2.43 is characterized by a set of Wilson operators $\{\mathcal{O}_i^{(d)}\}$ which are scaled by couplings $\{c_i\}$, known as the Wilson coefficients, and can be written as

$$\mathcal{L}^{(d)} = \sum_i c_i^{(d)} \mathcal{O}_i^{(d)}. \tag{2.45}$$

These Wilson coefficients can be measured in experimental data to test for the presence of higher-dimensional operators. Operators with non-zero values of Wilson coefficients are signs of new physics.

In the SMEFT, similar to the Standard Model, the Higgs field H is considered as a doublet of $SU(2)_L$, and the observed Higgs field is obtained from EWSB as described earlier in Section 2.1.7. Alternatively, the Higgs Effective Field Theory

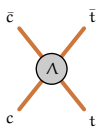

(HEFT) allows for a more general Higgs field and instead uses a singlet scalar state h with free couplings to the other SM states. While HEFT is more general in terms of the realization of EWSB, SMEFT, which assumes the doublet structure for H, is a good approximation for the Higgs boson couplings to the SM state. In this thesis, all measurements are interpreted within SMEFT.

The leading correction to the Standard Model is at dimension-5, and there is only one single-term at this order and is known as the Weinberg operator [67]. The Weinberg operator corresponds to the Majorana neutrino mass term and new physics scale from this term corresponds to

$$\Lambda \simeq \frac{v^2}{m_\nu} = 10^{13}\,\mathrm{GeV}, \tag{2.46}$$

where $m_\nu \sim 1$ eV corresponds to the neutrino mass scale. This operator also violates lepton number and baryon number conservation.

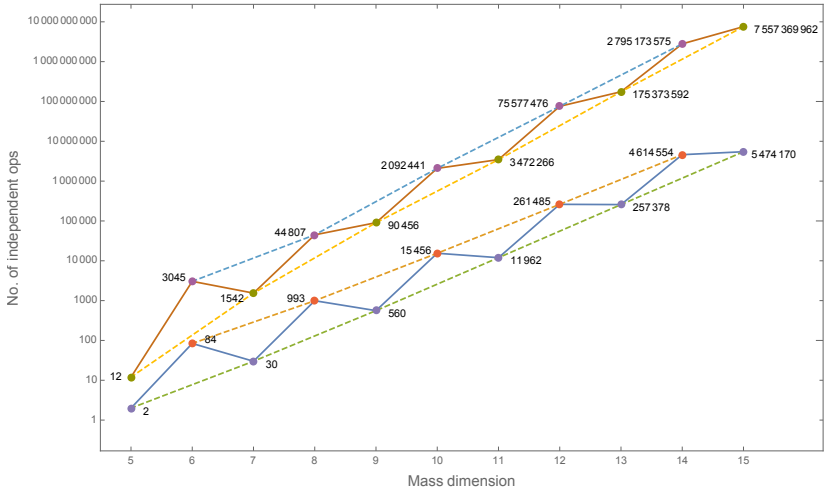

Figure 2.6: Number of independent operators (include baryon number violating operators) in SMEFT from dimension 5 to 15. Points joined by the lower solid line are for one fermion generation; those joined by the upper solid line are for three generations. Dashed lines show the growth of the even and odd mass dimension operators in both cases. Plot taken from [68].

The next leading contribution is the ensemble of dimension-6 terms. The scale of new physics from operators that violate baryon and lepton numbers are constrained to 10^{16} GeV from proton decay experiments. There are 2499 operators that preserve lepton and baryon numbers with no additional flavor consideration. The next order of operators that preserve lepton and baryon is at dimension-8, all

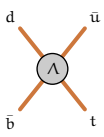

$O^{(1)}_{Qtqd}$

operators with odd-numbered dimensions violate lepton or baryon numbers. The total number of operators, including those that violate baryon number conservation, is shown in Figure 2.6.

To summarize, the core considerations for SMEFT are:

- **QFT** - The physics beyond the scale of the vacuum expectation value at much higher energies can still be described by a local quantum field theory that respects Poincaré symmetry. It allows making predictions for observables order-by-order which can systematically be improved.
- **Mass gap** - The mass scale of the new physics Λ is much larger than the electroweak scale $\Lambda \gg v$.
- **Gauge symmetry** - The SMEFT is based on the fact that the action is invariant under the $SU(3)_C \times SU(2)_L \times U(1)_Y$ gauge symmetry. If desired, an alternative approach via HEFT, which imposes only $SU(3)_C \times U(1)_{em}$ and the generator of $SU(3)_C \times SU(2)_L \times U(1)_Y$ that do not belong in the $SU(3)_C \times U(1)_{em}$ group are generated via a non-linear transformation of the scalar Goldstone bosons eaten by the W and Z fields.

2.3.2 SMEFT operators at dimension-6

SMEFT operators capture the effect of new physics at the energy scale Λ and are ordered by their energy dimension. The Warsaw basis [69] is a full set of independent operators at dimension-5 and -6, with the latter the most interesting to consider given that they are the first leading correction to lepton and baryon number preserving processes. The different classes of operators that conserve lepton and baryon numbers at dimension-6 are listed in Table 2.2 and their experimental relevance are introduced in the following section. The discussion on the dimension-6 operators is based [3, 70–72] where operators are grouped based on their field contents. The following notation (q,l,u,d,e) is used in SMEFT with

$$q = \begin{pmatrix} u_L \\ d_L \end{pmatrix}, l = \begin{pmatrix} \nu_L \\ e_L \end{pmatrix}, u = u_R, d = d_R, e = e_R. \tag{2.47}$$

Here, q corresponds to the left-handed quark doublet, l corresponds to the left-handed lepton doublet, u and d correspond to the right-handed up-type and down-type quarks, and e corresponds to the right-handed charged leptons.

Boson self-interaction (X^3, H^6) - These operators correspond to the boson self-interaction, and upon expanding give rise to interactions that contain three or more bosons. The gluon self-interaction and its CP-odd counterpart are represented by the operators O_G and $O_{\widetilde{G}}$, respectively. The operator corresponding to the boson self-interaction of the electroweak boson is denoted by O_W and the

$O^{(8)}_{quQb}$

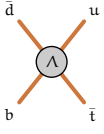

X^3		$\psi^2 XH$		$(\bar{R}R)(\bar{R}R)$	
O_G	$f^{abc}G^{a\nu}_{\mu}G^{b\rho}_{\nu}G^{c\mu}_{\rho}$	O_{eW}	$(\bar{l}_p\sigma^{\mu\nu}e_r)\sigma^i H W^i_{\mu\nu}$	O_{ee}	$(\bar{e}_p\gamma_\mu e_r)(\bar{e}_s\gamma^\mu e_t)$
$O_{\widetilde{G}}$	$f^{abc}\widetilde{G}^{a\nu}_{\mu}G^{b\rho}_{\nu}G^{c\mu}_{\rho}$	O_{eB}	$(\bar{l}_p\sigma^{\mu\nu}e_r)HB_{\mu\nu}$	O_{uu}	$(\bar{u}_p\gamma_\mu u_r)(\bar{u}_s\gamma^\mu u_t)$
O_W	$\varepsilon^{ijk}W^{i\nu}_{\mu}W^{j\rho}_{\nu}W^{k\mu}_{\rho}$	O_{uG}	$(\bar{q}_p\sigma^{\mu\nu}T^a u_r)\widetilde{H}G^a_{\mu\nu}$	O_{dd}	$(\bar{d}_p\gamma_\mu d_r)(\bar{d}_s\gamma^\mu d_t)$
$O_{\widetilde{W}}$	$\varepsilon^{ijk}\widetilde{W}^{i\nu}_{\mu}W^{j\rho}_{\nu}W^{k\mu}_{\rho}$	O_{uW}	$(\bar{q}_p\sigma^{\mu\nu}u_r)\sigma^i\widetilde{H}W^i_{\mu\nu}$	O_{eu}	$(\bar{e}_p\gamma_\mu e_r)(\bar{u}_s\gamma^\mu u_t)$
H^6		O_{uB}	$(\bar{q}_p\sigma^{\mu\nu}u_r)\widetilde{H}B_{\mu\nu}$	O_{ed}	$(\bar{e}_p\gamma_\mu e_r)(\bar{d}_s\gamma^\mu d_t)$
O_H	$(H^\dagger H)^3$	O_{dG}	$(\bar{q}_p\sigma^{\mu\nu}T^a d_r)H G^a_{\mu\nu}$	$O^{(1)}_{ud}$	$(\bar{u}_p\gamma_\mu u_r)(\bar{d}_s\gamma^\mu d_t)$
H^4D^2		O_{dW}	$(\bar{q}_p\sigma^{\mu\nu}d_r)\sigma^i H W^i_{\mu\nu}$	$O^{(8)}_{ud}$	$(\bar{u}_p\gamma_\mu T^a u_r)(\bar{d}_s\gamma^\mu T^a d_t)$
$O_{H\Box}$	$(H^\dagger H)\Box(H^\dagger H)$	O_{dB}	$(\bar{q}_p\sigma^{\mu\nu}d_r)H B_{\mu\nu}$		
O_{HD}	$(D^\mu H^\dagger H)\,(H^\dagger D_\mu H)$				
X^2H^2		ψ^2H^2D		$(\bar{L}L)(\bar{R}R)$	
O_{HG}	$H^\dagger H G^a_{\mu\nu}G^{a\mu\nu}$	$O^{(1)}_{Hl}$	$(H^\dagger i\overleftrightarrow{D}_\mu H)(\bar{l}_p\gamma^\mu l_r)$	O_{le}	$(\bar{l}_p\gamma_\mu l_r)(\bar{e}_s\gamma^\mu e_t)$
$O_{H\widetilde{G}}$	$H^\dagger H \widetilde{G}^a_{\mu\nu}G^{a\mu\nu}$	$O^{(3)}_{Hl}$	$(H^\dagger i\overleftrightarrow{D}^i_\mu H)(\bar{l}_p\sigma^i\gamma^\mu l_r)$	O_{lu}	$(\bar{l}_p\gamma_\mu l_r)(\bar{u}_s\gamma^\mu u_t)$
O_{HW}	$H^\dagger H W^i_{\mu\nu}W^{I\mu\nu}$	O_{He}	$(H^\dagger i\overleftrightarrow{D}_\mu H)(\bar{e}_p\gamma^\mu e_r)$	O_{ld}	$(\bar{l}_p\gamma_\mu l_r)(\bar{d}_s\gamma^\mu d_t)$
$O_{H\widetilde{W}}$	$H^\dagger H \widetilde{W}^i_{\mu\nu}W^{i\mu\nu}$	$O^{(1)}_{Hq}$	$(H^\dagger i\overleftrightarrow{D}_\mu H)(\bar{q}_p\gamma^\mu q_r)$	O_{qe}	$(\bar{q}_p\gamma_\mu q_r)(\bar{e}_s\gamma^\mu e_t)$
O_{HB}	$H^\dagger H B_{\mu\nu}B^{\mu\nu}$	$O^{(3)}_{Hq}$	$(H^\dagger i\overleftrightarrow{D}^i_\mu H)(\bar{q}_p\sigma^i\gamma^\mu q_r)$	$O^{(1)}_{qu}$	$(\bar{q}_p\gamma_\mu q_r)(\bar{u}_s\gamma^\mu u_t)$
$O_{H\widetilde{B}}$	$H^\dagger H \widetilde{B}_{\mu\nu}B^{\mu\nu}$	O_{Hu}	$(H^\dagger i\overleftrightarrow{D}_\mu H)(\bar{u}_p\gamma^\mu u_r)$	$O^{(8)}_{qu}$	$(\bar{q}_p\gamma_\mu T^a q_r)(\bar{u}_s\gamma^\mu T^a u_t)$
O_{HWB}	$H^\dagger\sigma^i H W^i_{\mu\nu}B^{\mu\nu}$	O_{Hd}	$(H^\dagger i\overleftrightarrow{D}_\mu H)(\bar{d}_p\gamma^\mu d_r)$	$O^{(1)}_{qd}$	$(\bar{q}_p\gamma_\mu q_r)(\bar{d}_s\gamma^\mu d_t)$
$O_{H\widetilde{W}B}$	$H^\dagger\sigma^i H \widetilde{W}^i_{\mu\nu}B^{\mu\nu}$	$O_{Hud}+\text{h.c.}$	$i(\widetilde{H}^\dagger D_\mu H)(\bar{u}_p\gamma^\mu d_r)$	$O^{(8)}_{qd}$	$(\bar{q}_p\gamma_\mu T^a q_r)(\bar{d}_s\gamma^\mu T^a d_t)$
ψ^2H^3		$(\bar{L}L)(\bar{L}L)$		$(\bar{L}R)(\bar{R}L)$, $(\bar{L}R)(\bar{L}R)$	
O_{eH}	$(H^\dagger H)(\bar{l}_p e_r H)$	O_{ll}	$(\bar{l}_p\gamma_\mu l_r)(\bar{l}_s\gamma^\mu l_t)$	O_{ledq}	$(\bar{l}^j_p e_r)(\bar{d}_s q_{tj})$
O_{uH}	$(H^\dagger H)(\bar{q}_p u_r\widetilde{H})$	$O^{(1)}_{qq}$	$(\bar{q}_p\gamma_\mu q_r)(\bar{q}_s\gamma^\mu q_t)$	$O^{(1)}_{quqd}$	$(\bar{q}^j_p u_r)\varepsilon_{jk}(\bar{q}^k_s d_t)$
O_{dH}	$(H^\dagger H)(\bar{q}_p d_r H)$	$O^{(3)}_{qq}$	$(\bar{q}_p\gamma_\mu\sigma^i q_r)(\bar{q}_s\gamma^\mu\sigma^i q_t)$	$O^{(8)}_{quqd}$	$(\bar{q}^j_p T^a u_r)\varepsilon_{jk}(\bar{q}^k_s T^a d_t)$
		$O^{(1)}_{lq}$	$(\bar{l}_p\gamma_\mu l_r)(\bar{q}_s\gamma^\mu q_t)$	$O^{(1)}_{lequ}$	$(\bar{l}^j_p e_r)\varepsilon_{jk}(\bar{q}^k_s u_t)$
		$O^{(3)}_{lq}$	$(\bar{l}_p\gamma_\mu\sigma^i l_r)(\bar{q}_s\gamma^\mu\sigma^i q_t)$	$O^{(3)}_{lequ}$	$(\bar{l}^j_p\sigma_{\mu\nu}e_r)\varepsilon_{jk}(\bar{q}^k_s\sigma^{\mu\nu}u_t)$

Table 2.2: Baryon number-conserving $\mathcal{L}_6$ operators in the Warsaw basis [69]. Taken from [70].

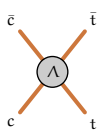

$O^{(8)}_{tu}$

CP-odd counterpart by $O_{\widetilde{W}}$. The Higgs boson self-coupling operator is O_H. The O_H operator affects the minimum of the Higgs potential, written as

$$V(H) = \lambda\left(H^\dagger H - \frac{1}{2}v^2\right)^2 - \frac{c_H}{\Lambda^2}\left(H^\dagger H\right)^3. \tag{2.48}$$

The minimum of the Higgs potential is

$$\langle H^\dagger H\rangle = \frac{v^2}{2}\left(1 + \frac{3c_H v^2}{4\lambda\Lambda^2}\right) \equiv v_T^2, \tag{2.49}$$

where v_T denotes the modified vacuum expectation value of the Higgs field in SMEFT.

Higgs boson kinetic terms (H^4D^2) - There are two operators in this class that are built using the Higgs field and the derivative operators. The operators affect the kinetic term of the Higgs field. They result in an overall rescaling to the Higgs field of the form $h \to (1 + c_{H,kin})h$ where h denotes the scalar Higgs field as introduced in Equation 2.26. The shift $c_{H,kin}$ is

$$c_{H,kin} = c_{H\Box} - \frac{1}{4}c_{HDD}. \tag{2.50}$$

The operator $O_{H\Box}$ affects only the Higgs boson kinetic term and thus affects all Higgs boson processes only via a constant rescaling. The operator O_{HDD} affects the Higgs boson kinetic term and the Z boson mass. The operator O_{HDD} corresponds to the T term in the Peskin-Takeuchi terms [73] that propose three terms (S, T, U) to parametrize new physics contributions to electroweak radiative corrections.

Higgs-gauge (X^2H^2) - These operators upon EWSB give rise to terms that are corrections to the kinetic term of the gauge bosons. These corrections lead to an overall rescaling of the kinetic term of the gauge bosons, i.e

$$\mathcal{L}_{gauge} \to -\frac{1}{4}B_{\mu\nu}B^{\mu\nu}\left(1 - \frac{2v^2}{\Lambda^2}c_{HB}\right) - \frac{1}{4}W^a_{\mu\nu}W^{\mu\nu}_a\left(1 - \frac{2v^2}{\Lambda^2}c_{HW}\right) \tag{2.51}$$

$$- \frac{1}{2}G^a_{\mu\nu}G^{\mu\nu}_a\left(1 - \frac{2v^2}{\Lambda^2}c_{HG}\right). \tag{2.52}$$

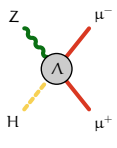

The operator O_{HWB} after EWSB introduces a kinetic mixing term between the B and third-component of the W field, $W^{(3)}$ corresponding to

$$-\frac{v^2}{2}\frac{c_{HWB}}{\Lambda^2}W^{(3)}_{\mu\nu}B^{\mu\nu}. \tag{2.53}$$

The operators O_{HG}, O_{HW}, and O_{HB} are fully absorbed into the definition of the fields and gauge couplings and affect only the Higgs gauge couplings and leave the pure gauge sector unaffected. The operator O_{HWB}, on the other hand, modifies all γ and Z couplings. This operator corresponds to the S term from the Peskin-Takeuchi terms.

Yukawa (ψ^2H^3) - These operators after EWSB modify the fermion masses and the Yukawa interaction with the Higgs boson. The fermion mass matrix in SMEFT is

$$[M_\psi]_{rs} = \frac{v_T}{\sqrt{2}}\left([Y_\psi]_{rs} - \frac{1}{2}v^2\frac{c^*_{\psi H_{sr}}}{\Lambda^2}\right). \tag{2.54}$$

The coupling to the Higgs boson is determined by the term $yh\psi_{f,L}\psi_{f,R}$ which provides the coupling strength of the Yukawa interaction. The Yukawa coupling matrix is expressed as

$$[Y_\psi]_{rs} = \frac{1}{v_T}[M_\psi]_{rs}(1 + c_{H,kin}) - \frac{1}{\sqrt{2}}v^2\frac{c^*_{\psi H_{sr}}}{\Lambda^2}. \tag{2.55}$$

The fermion couplings to the Higgs boson are not just proportional to the fermion masses like in the SM but also depend on the Wilson coefficients.

Higgs-gauge-fermions (ψ^2H^2D) - After EWSB, these operators introduce additional terms that modify the $hhVff$, $hVff$, and Vff couplings. These operators introduce systematic modifications in the Higgs boson and the electroweak sector.

Dipole moment (ψ^2XH) - The operators belonging to this group contribute primarily to anomalous magnetic and electric dipole moments of fundamental particles.

Four-fermion (ψ^4) - The four-fermion operators affect different possible quartets of fermions. In addition to the large number of operators that are accessible based on the underlying flavor symmetry, there are also different operators allowed depending on the helicity of the fermion current.

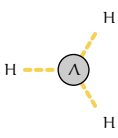

O_{HD}

	$U(3)^5$		topU3l		top		general	
	all	$\not{CP}$	all	$\not{CP}$	all	$\not{CP}$	all	$\not{CP}$
X^3	4	2	4	2	4	2	4	2
H^6	1	-	1	-	1	-	1	-
H^4D^2	2	-	2	-	2	-	2	-
X^2H^2	8	4	8	4	8	4	8	4
ψ^2H^3	6	3	10	5	14	7	54	27
ψ^2XH	16	8	28	14	36	18	144	72
ψ^2H^2D	9	1	15	2	21	2	81	30
$(\bar{L}L)(\bar{L}L)$	8	-	16	-	31	-	297	126
$(\bar{R}R)(\bar{R}R)$	9	-	27	2	40	2	450	195
$(\bar{L}L)(\bar{R}R)$	8	-	31	4	54	4	648	288
$(\bar{L}R)(\bar{R}L), (\bar{L}R)(\bar{L}R)$	14	7	40	20	64	32	810	405
tot	85	25	182	53	275	71	2499	1149

Table 2.3: Number of independent real parameters in each class of baryon number conserving dimension-6 operators, for the $U(3)^5$, `topU3l`, `top` scheme. $\not{CP}$ denotes the number of CP-violating parameters and the number of operators without any flavor assumptions is denoted as the general scheme. Taken from [70].

2.3.3 Flavor symmetry

From the 2499 operators that preserve baryon and lepton numbers at dimension-6, many of the operators can be merged by invoking additional flavor symmetries. These flavor symmetries reflect experimental considerations where it is not possible to distinguish the flavor of the underlying light quarks involved in the high-energy process. The flavor symmetries can also help optimize sensitivity to specific theories that match the corresponding flavor structure.

Some classes of operators, such as those in the classes - X^3, H^6, H^4D^2, X^2H^2 - corresponding to 15 parameters in total, are unaffected by flavor. Thus, most of the operators in the SMEFT are sensitive to flavor-specific signatures of New Physics.

Under a flavor symmetry, operators do not distinguish certain flavors of particles. As the most massive fundamental particle with O(1) Yukawa coupling, the top quark is treated separately in many EFT flavor symmetry schemes. More discussion on the flavor symmetry can be found in [70, 74]. The three flavor symmetries that are considered in the interpretations performed in this thesis are

- $\mathbf{U(3)^5}$: This flavor symmetry corresponds to an unbroken global flavor symmetry in the SM Lagrangian, valid in the limit where the Yukawa couplings are small ($Y_{u,d,e} \to 0$). The symmetry group is given by $U(3)_q \times U(3)_u \times U(3)_d \times$

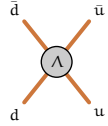

$U(3)_l \times U(3)_e$ and introduces common operators affecting the up-type quarks, down-type quarks, and leptons.

- **`topU3l`**: This flavor symmetry relaxes the assumption on the third quark generation, given that the top and bottom quarks are distinguishable experimentally at high-energy experiments by their unique signatures. This symmetry scheme is based on $U(2)_q \times U(2)_u \times U(2)_d \times U(3)_l \times U(3)_e$ and allows for separate modeling of operators involving top-quarks and bottom-quarks.
- **`top`**: This is the least restrictive scheme of the three, where the symmetry on the leptons is relaxed in addition to the dedicated operators for top and bottom quarks. The symmetry group for the `top` scheme is based on $U(2)_q \times U(2)_u \times U(2)_d \times U(3)_l \times U(3)_e$ $U(2)_q \times U(2)_u \times U(1)_e \times U(1)_\mu \times U(1)_\tau$

The total number of real-valued components of Wilson coefficients in the three symmetry scenarios for the different classes of operators are given in Table 2.3.

2.3.4 Global approach for SMEFT interpretation

Many operators affect multiple physics processes, and the measurement of any given process may be affected by multiple operators. For instance, the interplay of operators affecting Higgs, electroweak, and top measurements in Figure 2.7 shows a large overlap of operators between these physics sectors. Therefore, it is essential to take a global approach by considering different physics measurements and the effect of the relevant SMEFT operators. A global fit will allow to maximize sensitivity to the SMEFT parameter space and look for patterns of deviation across different measurements.

While most measurements are sensitive to many operators, individual measurements can typically only constrain a few linear combinations of operators and the others are degenerate. Combining measurements is thus essential to lifting these degeneracies, and the considerations for measurements to enter such combinations should thus not only take into account single-parameter sensitivities but also their ability to decorrelate measured coefficients.

SMEFT also serves as a framework to interpret measurements performed at different energy scales. For instance, the measurements performed at the LHC can be analyzed alongside low-energy precision measurements of electric dipole moment [76, 77], muon magnetic moment [78], and flavor physics [79, 80]. It is to be noted that the EFT interpretations of measurements at lower energy scales are typically performed within other effective field theory frameworks such as the Low-Energy EFT (LEFT) corresponding to the Fermi theory of weak interactions [60]. Including the low-energy measurements in the global fit requires a dedicated treatment of the LEFT operators in the SMEFT. The Wilson coefficients from the low-

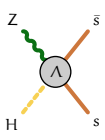

$O_{Hq}^{(1)}$

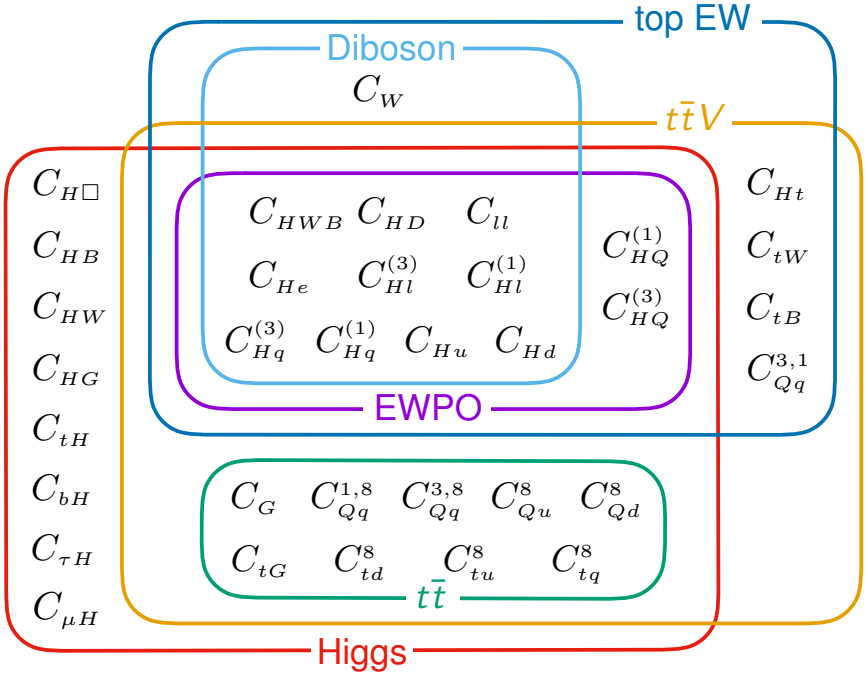

Figure 2.7: Schematic overview of interplay of affecting Higgs, electroweak, and top sector. EWPO denotes the electroweak precision observables, top EW denotes top electroweak processes, and $t\bar{t}V$ denotes the production of top-anti-top quark pair with vector bosons. The operators shown here consider a top-specific flavor symmetry. is Taken from [75].

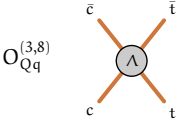

energy scale of the LEFT need to be matched to operators at a higher-energy scale in the SMEFT [81].

2.3.5 SMEFT matching to Ultraviolet-complete models

The main purpose of the SMEFT is to serve as a basis for capturing deviations from the Standard Model to uncover signatures of possible new physics models. The new physics signature can appear as a pattern of deviations across several operators. The constraints obtained on operators in the SMEFT can be used to probe the feasibility of new physics models, particularly those with heavy new particle(s). The process of mapping the SMEFT to a specific physics theory at high energy, the Ultraviolet-complete model, is known as *UV matching*. This procedure begins with obtaining the matching relation, which involves integrating out the heavy particle(s) in the new physics model Lagrangian and subsequently allows to obtain the relationship of the UV model with the corresponding terms in the SMEFT Lagrangian. Once the matching relations are available, the constraints on the SMEFT operators can be used to constrain the model parameters of the new physics theory.

Typically, specific new physics theories map to multiple SMEFT operators. In practice, the set of operators that map to a specific new physics theory cannot be measured in isolation. Their measurement is experimentally correlated with that of many other SMEFT operators that are irrelevant to the new physics theory under consideration but weaken the inference on the relevant parameters. The sensitivity to a specific new physics theory from a general SMEFT measurement is thus weaker than that of a dedicated measurement. The sensitivity of a SMEFT measurement to a specific theory could be enhanced by fixing all SMEFT operators irrelevant to the theory to zero, albeit at the cost of a possible loss of generality. In the following section, the two Higgs doublet model is introduced, and the corresponding matching to the SMEFT is discussed in Chapter 10.

2.3.6 Two Higgs doublet models

In two-Higgs-doublet (2HDM) models, the SM Higgs sector with one doublet of scalar complex fields Φ_1 is extended by introducing a second doublet Φ_2 [82–84]. The models considered here assume CP conservation and a softly-broken Z_2 discrete symmetry that forbids quartic terms of the scalar field potential $V(\Phi_1, \Phi_2)$ that contain odd powers of either Φ_1 or Φ_2. The most general gauge-invariant scalar Higgs potential, under the Paschos-Glashow-Weinberg condition [85, 86], formed by the two doublets Φ_1 and Φ_2 is given by:

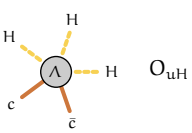

$$V(\Phi_1,\Phi_2) = m_{11}^2\Phi_1^\dagger\Phi_1 + m_{22}^2\Phi_2^\dagger\Phi_2 - \left[m_{12}^2\Phi_1^\dagger\Phi_2 + \text{ h.c. }\right] + \frac{1}{2}\lambda_2\left(\Phi_2^\dagger\Phi_2\right)^2 + \lambda_3\left(\Phi_1^\dagger\Phi_1\right)\left(\Phi_2^\dagger\Phi_2\right) + \lambda_4\left(\Phi_1^\dagger\Phi_2\right)\left(\Phi_2^\dagger\Phi_1\right) + \left[\frac{1}{2}\left(\Phi_1^\dagger\Phi_2\right)^2 + \text{ h.c. }\right], \tag{2.56}$$

with all m and λ parameters real and related to the physical masses and mixing angles of the Higgs bosons. The two doublets Φ_1 and Φ_2 contain eight scalar fields as follows:

$$\Phi_a = \frac{1}{\sqrt{2}}\begin{pmatrix} \Phi_a^+ \\ v_a + \eta_a + i\chi_a \end{pmatrix} \text{ with } \langle\Phi_a\rangle = \frac{1}{\sqrt{2}}\begin{pmatrix} 0 \\ v_a \end{pmatrix}, \text{ and } a = 1,2. \tag{2.57}$$

Here, Φ^+, η, and χ correspond to the charged, pseudo-scalar, and scalar fields, respectively. The eight degrees of freedom in Equation 2.57 contain three massless Goldstone bosons, which become the longitudinal polarizations of the $W^\pm$ and Z bosons when under spontaneous symmetry breaking. The vacuum expectation values $v_{1,2}$ of the scalar doublets $\Phi_{1,2}$ that minimize V are related by the sum rule $v_1^2 + v_2^2 = v^2$. These can be assumed to be real and non-negative without loss of generality. Electroweak symmetry breaking leads to five physical scalar Higgs fields: two neutral CP-even Higgs bosons h and H, one neutral CP-odd Higgs boson A, and two charged Higgs bosons $H^\pm$.

The observed Higgs boson is typically identified with the light CP-even neutral scalar particle h. The Z_2 symmetry of the potential forbids tree-level flavor-changing neutral currents [86, 87], and implies that all fermions with the same quantum numbers couple to only one Higgs doublet. Depending on which Higgs doublets couple to the three groups of elementary fermions (up- and down-type quarks, and leptons), four types of 2HDM are defined:

- Type I: All fermions couple to the same Higgs doublet.
- Type II: One Higgs doublet couples to up-type quarks, while the other couples to down-type quarks and charged leptons.
- Lepton-specific: One Higgs doublet couples to leptons while the other couples to up- and down-type quarks.
- Flipped: One Higgs doublet couples to down-type quarks, while the other couples to up-type quarks and leptons.

The Higgs sector of these models contains seven free physical parameters: four Higgs boson masses (m_h, m_H, m_A and $m_{H^\pm}$), two mixing angles α and β, and the coefficient m_{12}^2 of the $(\Phi_1^\dagger\Phi_2 + \Phi_2^\dagger\Phi_1)$ term in the Higgs field potential that

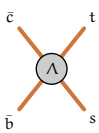

softly breaks the Z_2 symmetry. The angle β is defined as $\tan\beta = \frac{v_2}{v_1}$ and can be assumed to be in the first quadrant. The mixing angle α between the two neutral CP-even Higgs states is defined modulo a phase equal to π. The values of α and β determine the couplings of the Higgs fields to the vector bosons and fermions. The matching of the 2HDM to the SMEFT is discussed in Chapter 10.

2.4 Higgs boson production and decay modes at the LHC

The Higgs boson couples directly to all massive particles of the SM as discussed in 2.1.6. In the Standard Model, once the mass of the Higgs boson is determined, it is possible to calculate cross-sections for all processes that involve the Higgs boson. The total decay width of the Higgs boson in the Standard Model is predicted to be $\Gamma_H = 4.09 \pm 0.06$ MeV [88], which is much smaller than the Higgs boson mass itself. Therefore, the Narrow Width Approximation holds and the cross-section for any process involving the Higgs boson, $pp \to H \to X$ can be factorized separately into a production cross-section $\sigma(pp \to H)$ and a decay branching ratio $BR(H \to X)$ as

$$\sigma(pp \to H \to X) = \sigma(pp \to H) \times BR(H \to X) = \sigma(pp \to H) \times \frac{\Gamma_H^X}{\Gamma_H^{\text{total}}}. \tag{2.58}$$

This section describes the various Higgs boson production and decay modes and the specific SMEFT operators that affect these processes. The effect of SMEFT operators ranges from affecting a single Higgs boson decaymode (e.g., the Yukawa couplings) to all processes ($O_{H\Box}$, O_{HDD}). The section describes the operators that are not globally affecting the Higgs boson production and decay modes but are relevant to particular processes.

2.4.1 Higgs boson production modes

Multiple mechanisms exist at the Large Hadron Collider (LHC) to produce Higgs bosons. The main production modes: gluon-gluon fusion (ggF), vector boson fusion (VBF), associated production with a vector boson (VH), and production with top-anti-top quark pairs ($t\bar{t}H$) have all been discovered at the LHC. The rare production mode where the Higgs boson is produced in associated production with a top or anti-top quark ($tH/\bar{t}H$) is being searched. The Standard Model cross-section predictions for the different Higgs boson production modes for different center-of-mass energies are shown in Figure 2.8. Figure 2.9 shows Feynman diagrams for these processes.

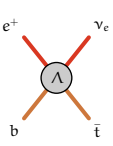

$O_{lQ}^{(3)}$

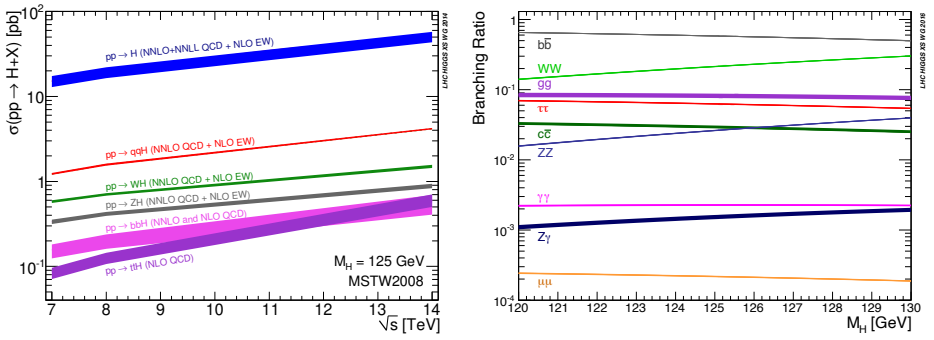

(a) (b)

Figure 2.8: The dependence of the cross-section of Higgs boson production modes with respect to the center-of-mass energy for proton-proton collisions (left) and the branching ratio of Higgs boson as a function of the Higgs boson mass between 120 GeV to 130 GeV (right). Taken from [89].

2.4.1.1 Gluon-gluon fusion

The gluon-gluon fusion (ggF) mode is the dominant Higgs boson production mode at high-energy proton-proton collisions, accounting for 87% of Higgs boson production, despite the absence of a Lagrangian term in the SM that couples gluons directly to the Higgs boson. In the SM, gluon-gluon fusion initiated Higgs boson production is mediated through a top-quark loop, as shown in Figure 2.9, with smaller contributions from b- and c-quarks, each suppressed by factors proportional to their mass. The large cross-section allows for precise measurements of Higgs boson properties.

In SMEFT, the ggF production mode allows to directly probe the tree-level gluon-gluon-Higgs operator O_{HG}. Additionally, given the primary role of the Higgs-top coupling in this process, it is also sensitive to modifications to the Higgs-top Yukawa operator O_{tH} and the operator affecting the top-quark chromomagnetic dipole moment O_{tG}. For gluon-gluon fusion events produced in association with jets, additional angular observables such as the jet opening angle $\Delta\phi_{jj}$ provide sensitivity to CP-odd operators such as $O_{H\tilde{G}}$.

2.4.1.2 Vector-boson fusion

A quark from each of the incoming LHC protons radiates a heavy vector boson. These bosons interact or “fuse” to produce a particle, such as a Higgs boson. The initial quarks that first radiated the vector bosons are deflected only slightly and travel roughly along their initial directions.

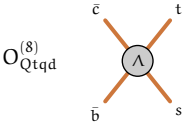

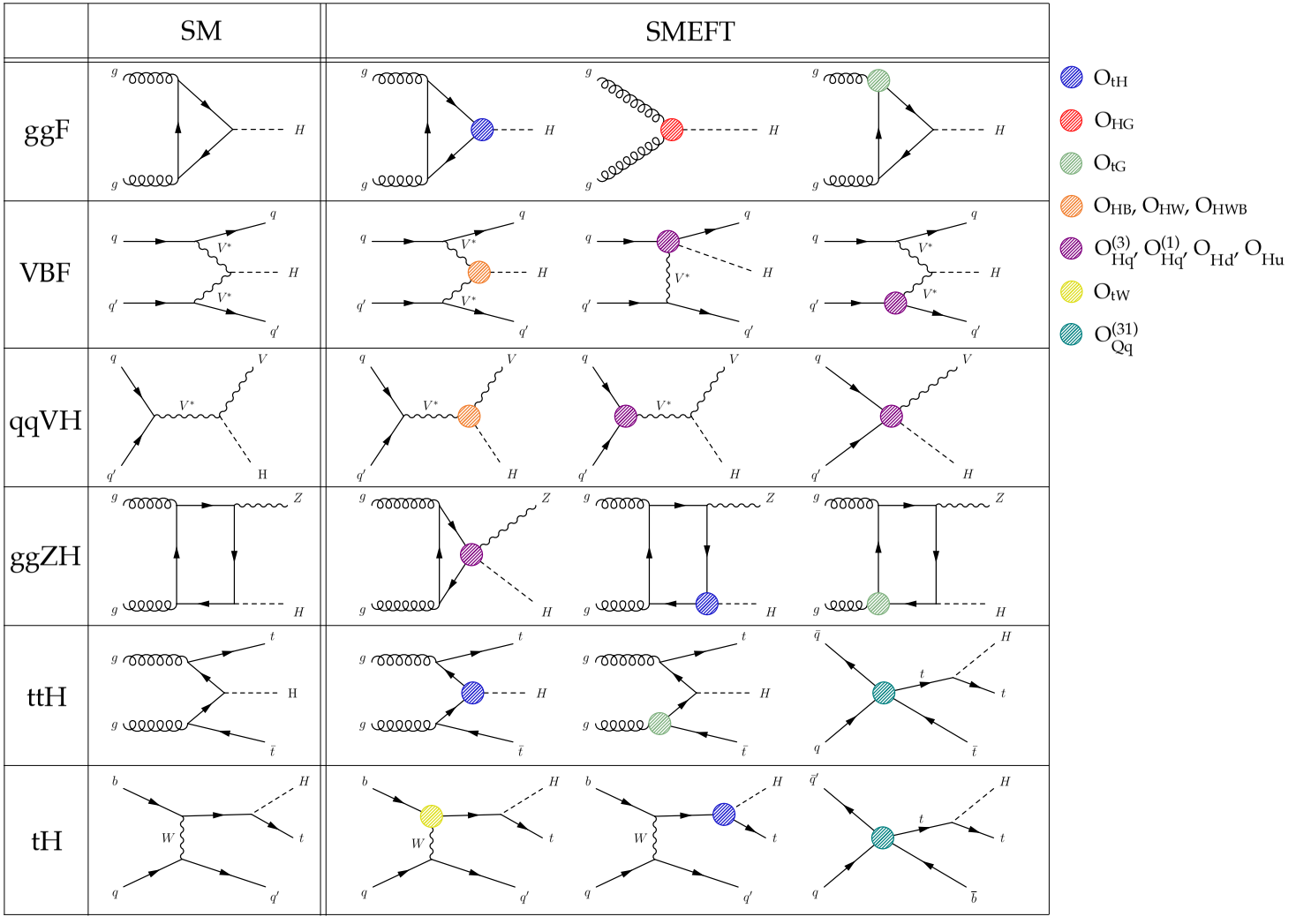

Figure 2.9: Representative Feynman diagram of the different Higgs boson production in the Standard Model and the SMEFT.

The second largest inclusive production mode is vector boson fusion (VBF), where two gauge bosons radiated from each of the protons interact to produce the Higgs boson. The quarks that radiate the vector bosons are deflected only slightly and have a large separation in rapidity. This kinematic feature is key in separating the VBF process from other production modes, such as gluon-gluon fusion in association with two jets, and Higgsstrahlung, where the associated weak boson decays hadronically.

Vector-boson fusion is sensitive to the HVV and VHqq couplings and is affected by operators such as O_{HWB}, O_{HW}, O_{HB}, $O_{Hq}^{(1)}$, $O_{Hq}^{(3)}$, O_{Hu}, and O_{Hd}. Similar to ggF production, angular observables such as $\Delta\phi_{jj}$ are sensitive to CP-odd operators such as $O_{HW\widetilde{B}}$, $O_{H\widetilde{B}}$, and $O_{H\widetilde{W}}$.

2.4.1.3 Associated production with a vector boson

This production mode, also known as Higgsstrahlung, is characterized by an associated weak boson that is produced alongside the Higgs boson. It has the third-largest inclusive production cross-section. The VH production modes can be further split into subsamples depending on the type of the associated vector boson (V=W, Z), as the processes involved in their production are different. The WH production is mediated by quark-initiated diagrams at leading order. For the ZH production mode, in addition to the quark-initiated diagrams, there is an additional contribution from the gluon-initiated process (ggZH), which is mediated by loop diagrams involving the top-quark.

The VH production mode is sensitive to the HVV coupling and through that to operators O_{HWB}, O_{HW}, and O_{HB}. Additionally, kinematic distributions such as the transverse momentum of the associated weak boson, p_T^V, are sensitive to operators that are expected to have enhanced sensitivity in the high-p_T tails such as $O_{Hq}^{(1)}$, $O_{Hq}^{(3)}$, O_{Hu}, and O_{Hd}. The ggZH production mode is sensitive to the gluon-gluon-Higgs operator O_{HG}, top chromomagnetic operator O_{tG}, the Higgs-top Yukawa operator O_{tH}, and the Higgs-gauge-fermion involving the top quark $O_{HQ}^{(3)}$ and O_{Ht}.

2.4.1.4 Higgs boson in association with top-anti-top quark pairs

This production mode is characterized by a Higgs boson produced alongside a top-anti-top quark pair. This process is sensitive to top-Higgs coupling modifiers that also affect ggF production such as, O_{tH} and O_{tG}, without being affected by O_{HG}, thereby allowing to disentangle the behavior of these operators. Furthermore, 4-fermion operators of the type O_{2q2t} affect the top-anti-top quark couplings with other quarks.

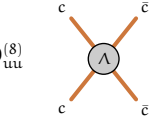

2.4.1.5 Higgs boson in association with a top/anti-top quark

Higgs boson production in association with a single top quark (tH) occurs via the t-channel process, where $qg \to tHq'b$, or through associated production with a W boson, denoted as $gb \to WtH$. In the Standard Model, the tH production cross-section is suppressed by almost fully destructive interference at the tree level between diagrams where the Higgs boson is radiated from a W boson, respectively. Consequently, the cross-section of tH production is extremely small, but due to the strong interference, it is still quite sensitive to several operators.

The tH process is sensitive to modification of the Higgs-top Yukawa operator O_{tH}, and operator O_{tW} that modify the top-W coupling. Additionally, the process is also sensitive to the four-fermion operator $O_{Qq}^{3,1}$.

2.4.2 Higgs boson decay modes

Given that the Higgs boson couples directly and indirectly to all Standard Model particles, once produced it can decay into all particles except the top quark, which is kinematically forbidden. Once the mass of the Higgs boson is determined, the Standard Model branching fraction can be calculated. The variation of the branching fraction of the Higgs boson for masses between 120 GeV to 130 GeV is shown in Figure 2.8. Representative Feynman diagrams of the different Higgs boson decays in the SM and SMEFT are shown in Figure 2.10.

Higgs to fermions

The Higgs boson decays to fermions are mediated by the Yukawa couplings in the Standard Model as described in Section 2.1.7.2. The Higgs boson decays to fermions are mediated by the Yukawa couplings and the partial width is proportional to the square of the fermion coupling. Additionally, for Higgs decays to quarks, there is a factor three enhancement to the branching ratio with respect to fermions due to the three color charges. Therefore, the Higgs boson decay to $b\bar{b}$ is the most common decay with a 58% branching fraction. This decay channel is followed by $\tau^+\tau^-$ (6.3%), $c\bar{c}$ (2.8%), and $\mu^-\mu^+$ (0.02%). The Higgs boson decays to fermions allow for a dedicated measurement of the effects of the operators that modify the Higgs-Yukawa coupling O_{fH}. Additionally, these operators are also affected by the CP-odd component of the Yukawa coupling, which can be measured by measuring angular observable as done in $H \to \tau\tau$ decays [90].

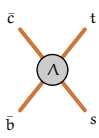

$O_{qtQd}^{(8)}$

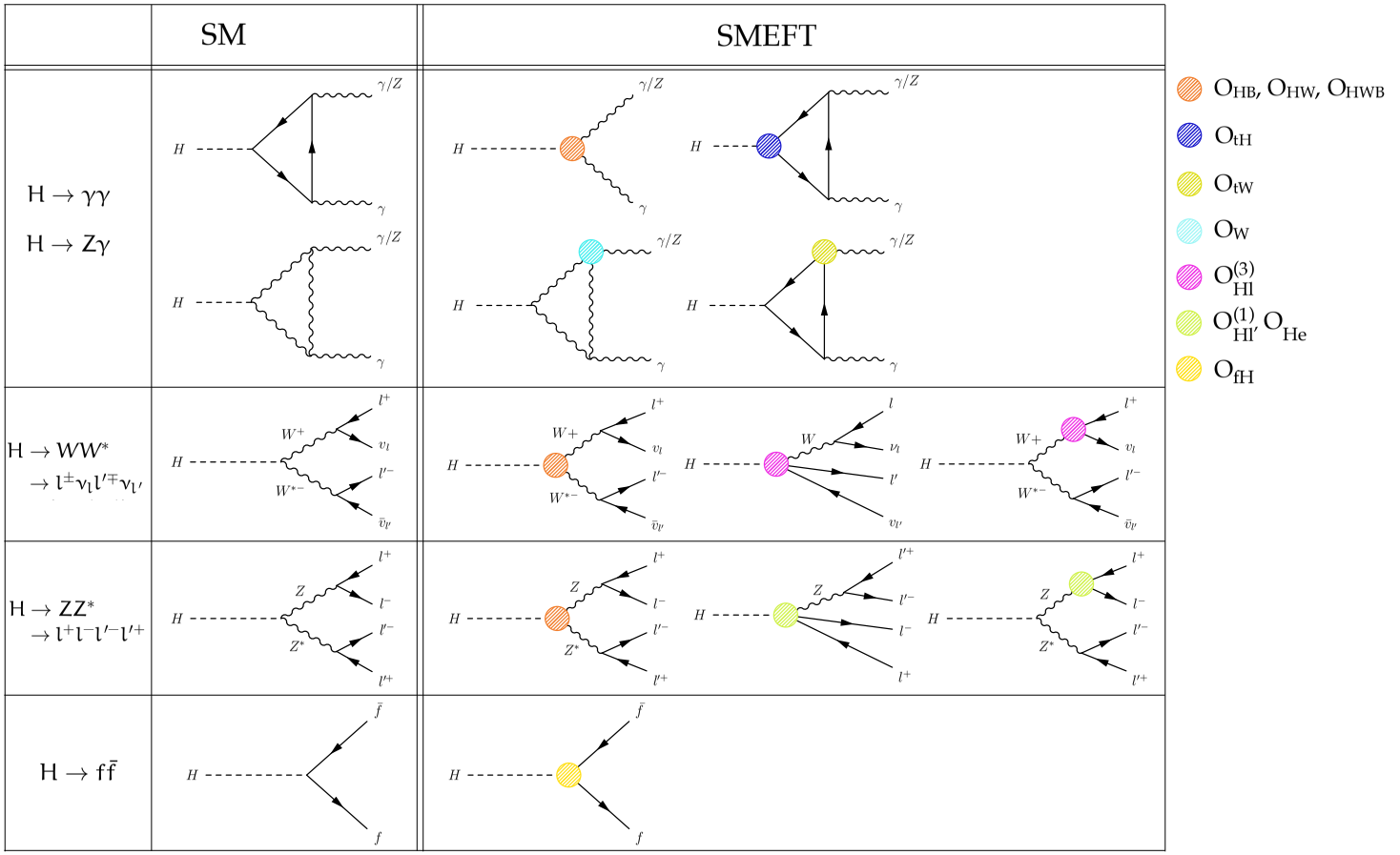

Figure 2.10: Representative Feynman diagram of the different Higgs boson decayin the Standard Model and the SMEFT. Note that the Higgs boson decays to fermions ($H \to f\bar{f}$) are grouped together.

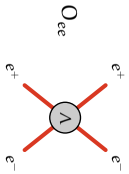

Higgs to bosons

The Higgs boson directly couples to the W and Z, and thus, the Higgs boson decays to bosons are dominated by the WW^* (22%) and ZZ^* (2.64%) channels, where one of the bosons is produced off-shell. In these channels, Higgs bosons are primarily measured in the corresponding leptonic decay modes $H \to WW^* \to l^{\pm}\nu_l l'^{\mp}\nu_{l'}$ and $H \to ZZ^* \to l^+l^-l'^-l'^+$, where $l, l' = \{e, \mu\}$.

The decays of $H \to \gamma\gamma$ (0.227%) and $H \to Z\gamma$ (0.15%) are loop-suppressed being mediated by the top-quark and W-boson in the loop. Given that these processes are loop-suppressed in the Standard Model, they have enhanced sensitivity in the SMEFT, where there are tree-level couplings introduced by operators O_{HW}, O_{HWB}, and O_{HB}. Additionally, they are also sensitive to SMEFT insertions within the loop that modifier Higgs-top couplings (O_{tH}), top-photon couplings (O_{tW}, O_{tB}), and self-coupling of weak bosons (O_W).

2.5 Simulation of the Standard Model Higgs boson signal

The analysis of Higgs boson relies strongly on accurate Monte-Carlo simulations of Higgs boson production in various production modes, in particular, to design analyses that aim to accurately measure Higgs boson kinematic distributions. For each Higgs boson decay mode, the branching fraction prediction corresponds to theoretical calculations at the highest available order [89]. The predictions for Higgs boson production are simulated using the Monte-Carlo generators listed in Table 2.4. The Monte-Carlo samples used to model the signal in this thesis are summarized in this section.

Process	Generator	Showering	PDF set	σ [pb] $\sqrt{s} = 13$ TeV	Order of σ calculation
ggH	NNLOPS	PYTHIA 8	PDF4LHC15	48.52	N^{3}LO(QCD)+NLO(EW)
VBF	POWHEG BOX	PYTHIA 8	PDF4LHC15	3.78	approximate-NNLO(QCD)+NLO(EW)
WH	POWHEG BOX	PYTHIA 8	PDF4LHC15	1.37	NNLO(QCD)+NLO(EW)
qq/qg→ZH	POWHEG BOX	PYTHIA 8	PDF4LHC15	0.76	NNLO(QCD)+NLO(EW)
gg→ZH	POWHEG BOX	PYTHIA 8	PDF4LHC15	0.12	NLO(QCD)
$t\bar{t}H$	POWHEG BOX	PYTHIA 8	PDF4LHC15	0.51	NLO(QCD)+NLO(EW)
$b\bar{b}H$	POWHEG BOX	PYTHIA 8	PDF4LHC15	0.49	NNLO(QCD)
tHqb	MG5_aMC@NLO	PYTHIA 8	NNPDF3.0nnlo	0.07	NLO(QCD)
tWH	MG5_aMC@NLO	PYTHIA 8	NNPDF3.0nnlo	0.02	NLO(QCD)

Table 2.4: Event generators and PDF sets used to model the signal process. The cross sections of Higgs production processes [88, 91–108] are reported for a center of mass energy of $\sqrt{s} = 13$ TeV and a SM Higgs with mass 125.09 GeV. The order of the calculated cross section is reported in each case. Table is taken from [109].

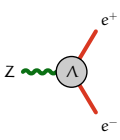

O_{He}

- **ggH**: Higgs boson production via gluon-gluon fusion (ggH) is simulated using the POWHEG BOX [110–113] NNLOPS implementation [114, 115]. The event generator uses HNNLO [116] to reweight the inclusive Higgs boson rapidity distribution produced by the next-to-leading order (NLO) generation of $pp \to H +$ parton, with the scale of each parton emission determined using the MiNLO procedure [117]. The PDF4LHC15 parton distribution functions are used for the central prediction and uncertainty. The sample is normalized such that it reproduces the total cross-section predicted by a next-to-next-to-next-to-leading-order (N^3LO) QCD calculation with NLO electroweak corrections applied [89, 91–94]. The NNLOPS generator reproduces the Higgs boson p_T distribution predicted by the NNLO plus next-to-next-to-leading logarithm (NNLL) calculation of HRES2.3 [118], which includes the effects of top- and bottom-quark masses and uses dynamical renormalization and factorization scales.
- **VBF, VH**: The VBF and VH production processes are simulated at NLO accuracy in QCD using the POWHEG BOX [119] generator with the PDF4LHC15 set of PDFs, where the simulation of VH relies on improved NLO calculations [120]. The VBF sample is normalized to an approximate-NNLO QCD cross-section with NLO electroweak corrections applied [89, 95–97]. The VH samples are normalized to cross-sections calculated at NNLO in QCD with NLO electroweak corrections [98, 100] and with additional NLO QCD corrections applied [99] for the $gg \to ZH$ subprocess [89].
- **ttH**: Higgs boson production in association with a top-antitop quark pair ($t\bar{t}H$), followed by an $H \to \gamma\gamma$ or $H \to ZZ^* \to 4\ell$ decay, is simulated at NLO accuracy in QCD using the POWHEG BOX generator with the PDF4LHC15 set of PDFs. For the generation of $t\bar{t}H$ events in the other Higgs boson decay channels, the MADGRAPH5_AMC@NLO [121] generator is used with the NNPDF3.0 [122] set of PDFs. In both cases, the sample is normalized to a calculation with NLO QCD and electroweakcorrections [88, 101–103, 123].

  tH: Higgs boson production in association with a single top quark and a W boson (tHW) and Higgs boson production with a single top quark in the t-channel (tHq) is generated at LO accuracy using MADGRAPH5_AMC@NLO. The tHq production is generated with CT10 [124] PDF sets. The tH samples are normalized to NLO QCD calculations [89, 108].

All parton-level events are input to PYTHIA8 [125] to model the Higgs boson decay, parton showering, hadronization, and multiple parton interactions (MPI). The generators are interfaced to PYTHIA8, using the AZNLO and A14 parameter sets [126].

Particle-level events are passed through a GEANT 4 [127] simulation of the ATLAS detector [128] and reconstructed using the same analysis software used for the data. Event pile-up is included in the simulation by overlaying inelastic pp collisions, such that the average number of interactions per bunch crossing reproduces

that observed in the data. The inelastic pp collisions were simulated with PYTHIA8 using the MSTW2008LO [129] set of PDFs with the A2 [130] set of tuned parameters or using the `NNPDF3.0lo` set of PDFs with the A3 [131] set of tuned parameters.

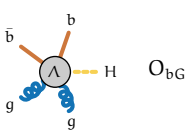

O_{bG}

3

The ATLAS Experiment at the Large Hadron Collider

To thoroughly investigate the Standard Model at high energies, it is essential to establish a comprehensive experimental program capable of precisely examining various physics processes. Such a program will aid in revealing any subtle deviations from the predictions of the Standard Model. Central to such a comprehensive experimental program is the Large Hadron Collider (LHC), a particle accelerator and collider located at CERN, the European Organization for Nuclear Research, on the border between Switzerland and France. The LHC operates at the forefront of scientific exploration, allowing to study physics at the most fundamental level.

This chapter summarizes the facilities at the Large Hadron Collider (LHC), the most energetic particle accelerator constructed to date. It hosts four primary detector facilities that study hadron collisions to address fundamental topics. The ALICE (A Large Ion Collider Experiment) experiment [132] studies the quark-gluon plasma. The LHCb (Large Hadron Collider beauty) experiment [133] is a forward spectrometer that studies flavor physics. There are two general-purpose experiments, the CMS (Compact Muon Solenoid) experiment [134] and the ATLAS (A Toroidal LHC Apparatus) experiment [135], which have complementary designs and independent programs to explore the energy frontier and study the properties of the heaviest constituents of the Standard Model, such as the top quark and the Higgs boson and perform searches for as-of-yet undiscovered particles.

The analyses in this thesis make use of the data collected at the ATLAS experiment during Run-2 of the LHC between 2015 and 2018. One of the goals of this thesis is to use this dataset to put the Standard Model to the test at the highest energy scales. This chapter contains an overview of the LHC and the ATLAS experiment. A detailed description of the LHC and the ATLAS experiment can be found in [135, 136].

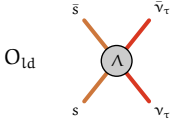

3.1 The Large Hadron Collider

3.1.1 The LHC Accelerator Complex

The LHC is a particle accelerator and collider at CERN used to study Nature at the most fundamental level. The LHC is housed in a 26.7 km circular tunnel - originally constructed for the Large Electron-Positron collider - and is situated between 45 m and 170 m below the surface.

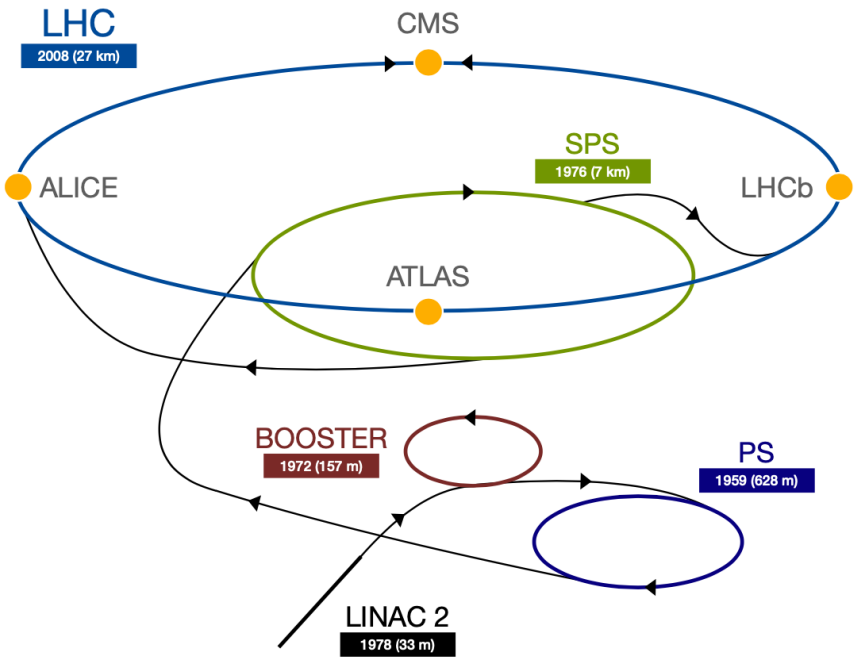

Figure 3.1: Figure depicting the LHC injector chain. Figure taken from [137].

In the LHC, two beams of protons travel in opposite directions within evacuated beam pipes. The path of the protons is guided by approximately 1200 dipole magnets located in the LHC arc sectors, which ensure the protons follow a closed trajectory. The superconducting dipole magnets have a field strength up to 8.3 T, over 100,000 times the Earth's magnetic field, and are constructed with niobium-titanium coils. They are cooled down to a temperature of 1.9 K using liquid helium, enabling them to operate in a superconducting state. The LHC is designed to accelerate protons to an energy of up to 7 TeV and heavy ions, such as lead, to up

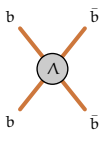

$O_{QQ}^{(1)}$

to 2.76 TeV per nucleon. Heavy ion collisions are used to study the properties of quark-gluon plasma and are not relevant to this thesis.

Before entering the LHC, protons undergo a series of pre-acceleration stages, utilizing the existing infrastructure at CERN. The injector chain, responsible for supplying protons to the LHC, is depicted in Figure 3.1. The process begins by ionizing hydrogen gas in a duoplasmatron to generate a continuous proton beam. Subsequently, a radio frequency quadrupole is employed to focus, bunch, and accelerate the protons before they enter a linear accelerator (LINAC 2). Following LINAC 2, the protons proceed through a sequence of synchrotrons, each increasing in size: the Booster, the Proton Synchrotron (PS), and the Super Proton Synchrotron (SPS).

Within the PS, the proton bunches are consolidated into a train, with a spacing of 25 ns between each bunch. As the proton bunch trains depart from the SPS and are injected into the LHC, they have a kinematic energy of 450 GeV. Various filling schemes are employed to target different instantaneous luminosity values. At its designated instantaneous luminosity of $L = 10^{34}\ cm^{-2}s^{-1}$, each proton beam comprises up to 2808 bunches, with approximately 10^{11} protons contained within each bunch.

3.2 The ATLAS detector

The ATLAS detector is designed to measure particles produced in the collisions of the LHC and this imposes a number of requirements on the design, such as to

- operate effectively in a high-rate and harsh environment, using fast and radiation-hard electronics and sensor elements. Moreover, a high level of detector granularity allows to handle dense particle fluxes and minimizes the impact of overlapping collisions in the same LHC bunch crossing.
- have a large angular coverage, i.e., full coverage of the azimuthal angle, and a large coverage of the polar angle.
- have an efficient resolution for reconstructing the trajectories of charged particles, with an excellent resolution for measuring their momentum, as measured from the curvature of the tracks in the transverse plane due to the magnetic field. Vertex detectors near the interaction region allow for observing secondary vertices to identify τ-leptons and b-jets.
- perform accurate electron and photon identification and energy measurements with a robust electromagnetic (EM) calorimeter. Furthermore, full-coverage hadronic calorimetry allows for precise energy measurements of jets and the total (missing) transverse energy.

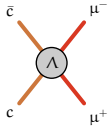

- have a reliable muon identification system with excellent momentum resolution resolution and charge identification across a wide momentum range.
- ensure a highly efficient triggering system that saves events of interest for offline processing with a total rate not exceeding 1 kHz. For the physics of interest, it is important that collision events featuring objects of interest, such as b-jets and leptons, at a moderate transverse momentum, around 20-30 GeV, can be selected with good efficiency.

The design targets for the polar coverage and energy/momentum resolution of the various ATLAS detector sub-systems are summarized in Table 3.1.

Detector component	Required resolution	η coverage	
		Measurement	Trigger
Tracking	$\sigma_{p_T}/p_T = 0.05\% p_T \oplus 1\%$	± 2.5	
EM calorimetry	$\sigma_E/E = 10\%/\sqrt{E} \oplus 0.7\%$	± 3.2	± 2.5
Hadronic calorimetry (jets)			
barrel and end-cap	$\sigma_E/E = 50\%/\sqrt{E} \oplus 3\%$	± 3.2	± 3.2
forward	$\sigma_E/E = 100\%/\sqrt{E} \oplus 10\%$	$3.1 < \lvert\eta\rvert < 4.9$	$3.1 < \lvert\eta\rvert < 4.9$
Muon spectrometer	$\sigma_E/E = 100\%/\sqrt{E} \oplus 10\%$	$3.1 < \lvert\eta\rvert < 4.9$	$3.1 < \lvert\eta\rvert < 4.9$

Table 3.1: Performance targets of the ATLAS detector where the required resolution is the resolution required to achieve the physics goals of the experiment. The η coverage is the coverage of the detector in the pseudo-rapidity space. Table taken from [135].

3.2.1 The ATLAS coordinate system

In the ATLAS experiment, the primary interaction point of a collision event defines the origin of the coordinate system. The beam direction defines the z-axis, and the $x-y$ plane is transverse to the beam direction. The positive x-axis is defined as the direction pointing from the interaction point to the center of the LHC ring, and the positive y-axis is defined as pointing upwards. The side-A and side-C of the detector are defined as those with positive and negative z, respectively. A cylindrical symmetric coordinate system (R,θ,ϕ) is also used where the azimuthal angle ϕ is measured as the angle around the beam axis in the $x-y$ plane, and the polar angle θ represents the angle with respect to the beam axis. The distance in the transverse plane is given by the radial distance R. The coordinate system is sketched in Figure 3.2.

The rapidity (y) of a particle is a Lorentz invariant quantity that is commonly used as a measure of relativistic velocity. It is defined as $y = \frac{1}{2}\ln\left(\frac{E+p_z}{E-p_z}\right)$ where E is the energy and p_z is the momentum component along the beam axis. In the ultra-relativistic limit, the rapidity is approximated by the pseudo-rapidity $\eta =$

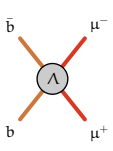

O_{lb}

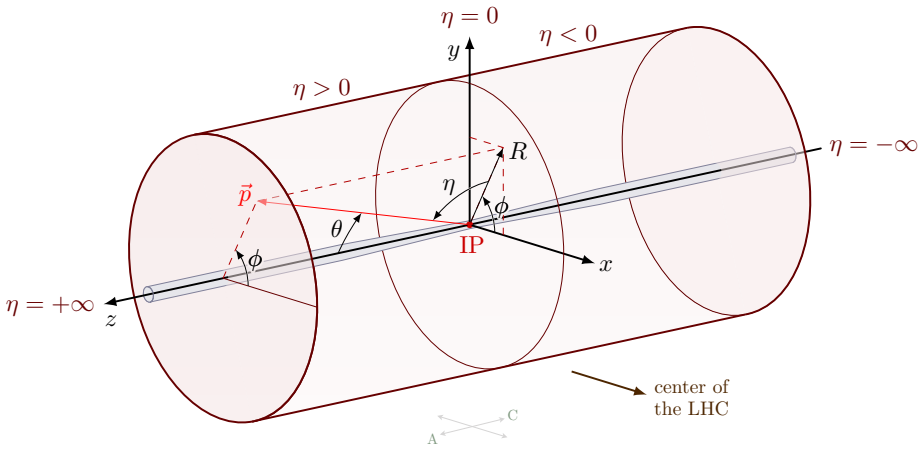

Figure 3.2: Schematic of the ATLAS coordinate system. Figure adapted from [138].

$-\ln\left(\tan\left(\frac{\theta}{2}\right)\right)$, where θ is the polar angle as described earlier. Pseudo-rapidity is a convenient coordinate in collider physics, as a Lorentz boost of a process along the beam axis results in a simple shift in the pseudo-rapidity of the resulting particle distributions. Transverse quantities such as transverse momentum (p_T), transverse energy (E_T), and missing transverse energy (E_T^{miss}) are defined as the component of the momentum or energy in the $x-y$ plane. The distance in the pseudo-rapidity and azimuthal angle space (η, ϕ) is known as angular distance. The angular distance is defined as $\Delta R = \sqrt{\Delta\eta^2 + \Delta\phi^2}$.

3.2.2 Particle identification with the ATLAS detector

The ATLAS detector aims to measure well the signature particles of physics processes of interest, primarily (stable) leptons and photons, as well as the remnants of outgoing quarks and gluons, which result in jets of particles that can also be reconstructed. Measurement of these objects, in turn, allows us to identify and measure the kinematics of unstable particles of interest, i.e., W and Z bosons, Higgs boson, and top quark.

Different detectors are utilized to measure the position of the vertex, the momentum and charge of charged particles, and the energy of the particles. These detectors are organized in layers, as shown in Figure 3.3. The vertex and tracking detectors are immersed in a solenoidal magnetic field that bends charged particles in the transverse plane. The vertex detector is closest to the beam pipe and aims to determine the origin of the high-energy interaction. Surrounding tracking layers measure the charge and the momentum of charged particles, whereas neutral

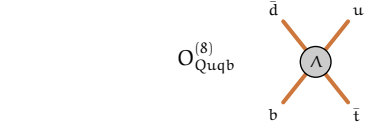

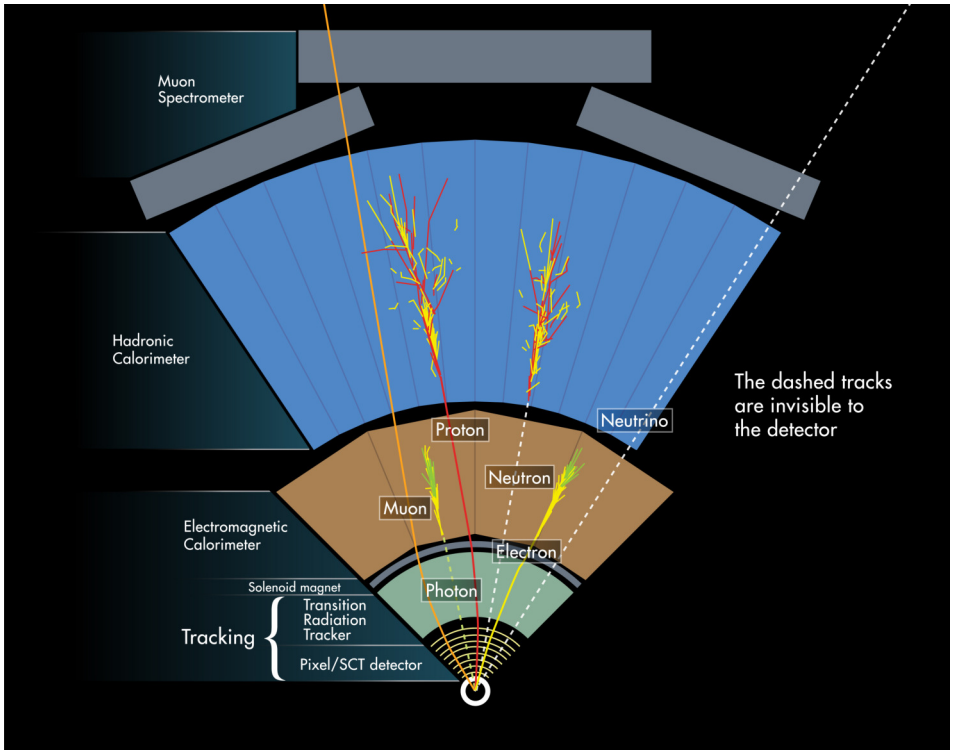

Figure 3.3: Sketch of the different layers of the ATLAS detector in the transverse plane with the illustration of the sensitivity to measure different particles. Figure taken from [139].

particles such as neutrons and photons pass through without interaction. The next layer, the electromagnetic calorimeter, precisely measures the energy of electrons and photons. The energy of all other particles, charged and neutral, is measured from the combined signals of the electromagnetic and hadronic calorimeter. A final layer of tracking detectors in a toroidal magnetic field performs precision measurements of muon momenta, the only charged particle that can traverse calorimeter layers. Each detector is discussed further in the following subsections.

3.2.3 Inner Detector

The ATLAS Inner Detector (ID) consists of three sub-detectors - the pixel detector, the semi-conductor tracker (SCT), and the transition radiation tracker (TRT) as shown in Figure 3.4. The ID is subject to a 2T axial magnetic field to bend the trajectory of charged particles to determine their momentum. Charged particles deposit energy as they traverse through the ID and are used to reconstruct the

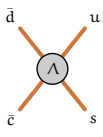

$O^{(8)\prime}_{quqd}$

trajectories of the particles and measure their momentum. The ID is also used to determine the origin of particle tracks, a procedure known as vertexing that allows identifying τ-leptons and the decay chain of heavy hadrons.

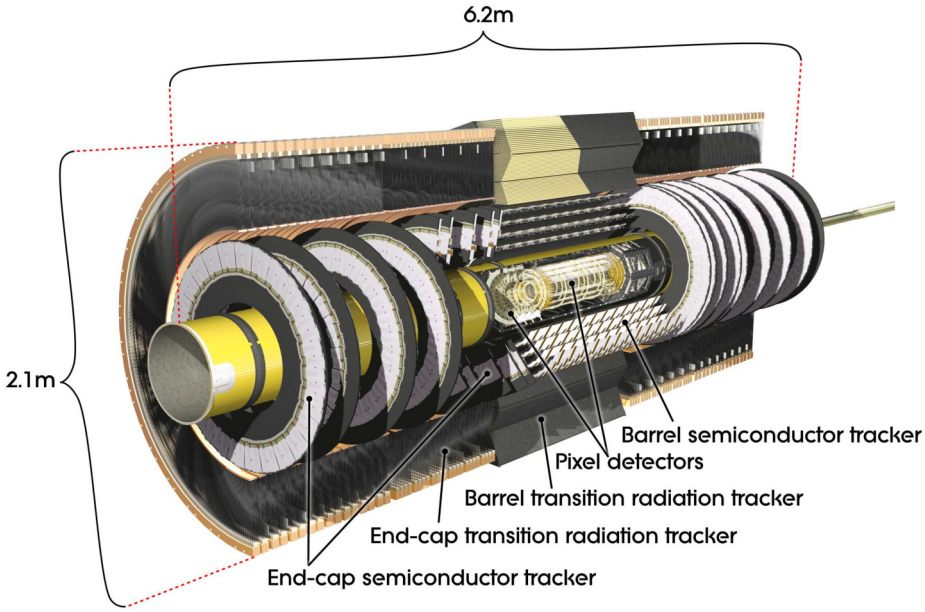

Figure 3.4: Cutaway view of the ATLAS Inner Detector. Figure taken from [135].

The ID is built around the beam pipe with cylindrical geometry. The ID consists of barrel layers centered around the interaction point and end-cap wheels or disks at either end of the barrel. Figure 3.4 shows a cut-away view of the ID. The ID is built using two technologies: silicon sensors and straw drift tubes. Silicon pixels are used in the Pixel detector, and silicon strips are used in the SCT. Straw drift tubes are used in the TRT. When charged particles cross the silicon sensors, they generate electron-hole pairs, which can be collected with an applied electric field. The sensor records this charge locally, identifying the particle's position. A similar process occurs in the straw drift tubes. Charged particles traversing the drift tubes ionize gas contained within the straw. The liberated electrons drift in the applied electron field to the wire at the center of the straw, where they are recorded.

Pixel detector: The Pixel detector is the sub-detector closest to the interaction point and provides the finest granularity. The innermost layer of the barrel is the Insertable B-Layer (IBL), which is positioned at a radius of 33 mm from the beam axis and consists of modules with a pixel size of 50 $\times$ 250 μm^2 in the R-ϕ and z

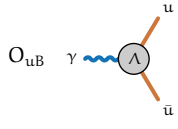

directions, respectively. The remaining layers of the pixel detector consist of over 80 million channels. The Pixel detector provides, on average, three measurements per charged particle and has a position resolution of 10 μm in the R-ϕ plane and 115 μm in the z direction. The Pixel detector provides full coverage in ϕ, and coverage up to 2.5 in $|\eta|$.

Semiconductor Tracker (SCT): The SCT surrounds the Pixel detectors. Each SCT layer is composed of a double layer of silicon strips, whose axes are tilted with respect to one another, which allows for a 2D hit reconstruction in the plane of the module. The pair of measurements at each SCT layer locates charged particles in R-ϕ, with an accuracy of 17 μm, and along z, with an accuracy of 580 μm. The SCT provides between four and nine measurements per particle, covering up to $|\eta| < 2.5$.

Transition radiation Tracker (TRT): The TRT is the largest sub-detectors in the ID. The TRT comprises of ~300k straw drift tubes that provide position measurements with an accuracy of 130 μm in the R-ϕ plane in the barrel. It provides coverage up to $|\eta| \leqslant 2.0$. In addition to being a tracking detector, the TRT provides particle identification by detecting transition radiation. Charged particles emit transition radiation (TR) photons when traversing the TRT. The probability of emitting a TR photon is a function of the Lorentz factor-γ. At the same momentum, electrons emit more transition radiation photons than charged hadrons. The number of TR photons detected in the TRT provides separation between electrons and charged hadrons. Combining precision trackers at small radii with the TRT at a large radius gives robust pattern recognition and high precision in the $R-\phi$ and z coordinates.

3.2.4 Calorimeter

The ATLAS calorimeter system consists of an electromagnetic calorimeter (ECAL) and a hadronic calorimeter (HCAL) to measure the energy of particles by making them deposit all of their energy primarily via the electromagnetic and the strong interaction, respectively. The calorimeters are sampling calorimeters and thus consist of layers of an absorbing high-density material that stops incoming particles, interleaved with layers of an active medium that measures their energy. Incident particles produce showers of energy in the calorimeter. Only a fraction of the energy produced by the particle is measured by active detector sensors and the energy of the full shower can be inferred from the observed energy. The calorimeter system measures the energy of hadrons, electrons, and photons. It provides coverage up to $|\eta| < 4.9$, using multiple technologies. The calorimeter system fully contains both electromagnetic and hadronic showers, stopping particles before they reach the muon system. An overview of the calorimeter system is shown in Figure 3.5.

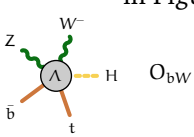

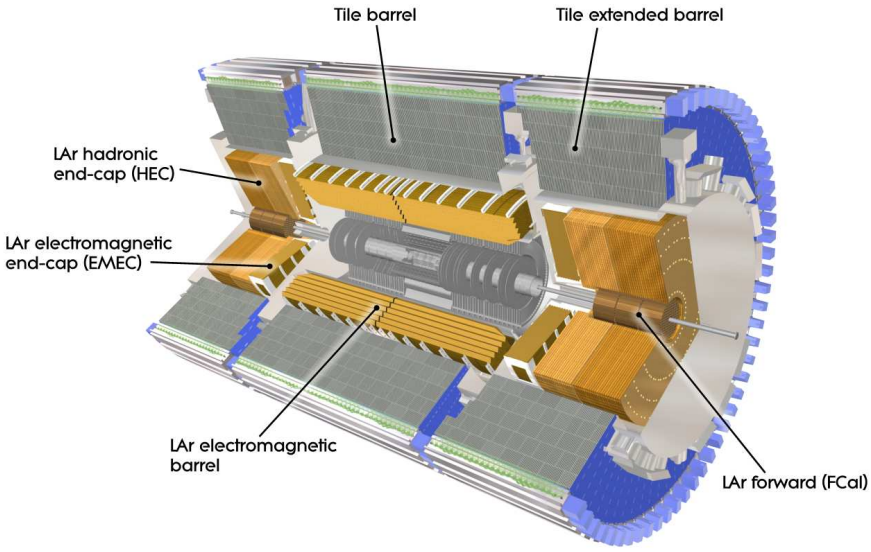

Figure 3.5: Cutaway view of the ATLAS calorimeter system. Figure taken from [135].

Electromagnetic Calorimeter: The energies of electrons and photons are measured by the liquid-argon (LAr) electromagnetic (EM) barrel and end-cap calorimeters. The LAr, together with kapton electrodes, act as active material, and lead plates act as absorbers. The ECAL geometry provides complete and symmetric ϕ coverage, with detectors providing high granularity measurements critical for particle identification in the range $|\eta| < 2.5$. The EM calorimeter is segmented into three radial sections with different η-ϕ granularities. Figure 3.5 shows a cutaway view of the different layers in the EM barrel calorimeter. The first layer, called strips, has excellent segmentation in η. The strips can separate between showers initiated by electrons or photons and showers initiated by neutral pions. The second sampling provides most of the energy measurement and provides segmentation in both η and ϕ. The third sampling is coarser and adds additional depth to the calorimeter. The EM calorimeters cover the pseudorapidity range $|\eta| < 3.2$. The Tile calorimeters and the LAr hadronic end-cap calorimeter are designed to measure the energy of hadrons. This range $|\eta| < 1.7$ is covered by the Tile calorimeter. The scintillator-tile calorimeter is separated into a barrel and two extended barrel cylinders. In the end-caps, $1.5 < |\eta| < 3.2$, high granularity liquid-argon (LAr)

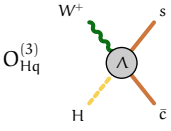

electromagnetic sampling calorimeters, with excellent performance in energy and position resolution, cover the pseudorapidity range of $|\eta| < 3.2$.

Hadronic Calorimeter: The HCAL is situated behind the ECAL and is relevant for energy measurements of hadronic particles. It consists of three sampling calorimeters that use different choices of active and passive materials. A tile calorimeter is used in region $|\eta| < 1.0$ and $0.8 < |\eta| < 1.7$. The tile calorimeter modules consist of layers of scintillating tiles as active material and steel plates as absorbers. It is separated into a large barrel and two extended barrel sectors. For the region $|\eta| > 1.5$, the LAr technology is also used for the hadronic calorimeter and matches the outer $|\eta|$ limits of the electromagnetic calorimeter. The LAr hadronic end-cap calorimeter offers coverage in $1.5 < |\eta| < 3.2$ and consists of planar modules with LAr as the active material and copper as the absorber. The LAr forward calorimeter covers the region of $3.1 < |\eta| < 4.9$ and consists of three modules. The first module uses copper as the absorber, and the other two modules use tungsten.

3.2.5 Muon Spectrometer

Located at the outermost layer of the detector, the Muon Spectrometer (MS) surrounds the calorimeters and operates within a large superconducting air core magnet system. A cutaway sketch of the MS is shown in Figure 3.6. The primary purpose of the MS is to detect and measure charged particles that traverse the calorimeters. The primary particles of interest are muons, which form the bulk of the particles that penetrate the calorimeters in the energy range of interest. The driving goal of the MS is to have an accuracy of 10% for muon tracks with $p_T = 1$ TeV, which translated to a sagitta of 500 μm with a resolution $\leqslant 50$ μm.

Dedicated toroidal magnetic systems are used to bend the trajectories of muons. The bending power of the magnets in the volume is estimated using $\int B\,dl$ where B is the magnetic field and dl is the path length of a muon in the limit of large momentum between the inner and outermost chamber planes. The central toroids provide a bending power of 1.5 to 5.5 Tm in the region $|\eta| < 1.4$. The end-cap toroid magnets consist of two toroid magnets that provide a bending power of 1 to 7.5 Tm in the region $1.6 < |\eta| < 2.7$. Muons traversing the transition region between the barrel and end-cap regions are subject to a lower bending power.

The MS comprises several subdetectors that work together to measure the trajectories and momenta of muons precisely. Three layers of high-precision tracking chambers, known as the Monitored Drift Tubes (MDTs) and Cathode Strip Chambers (CSCs), are used for detecting muons in the $R - z$ plane.

Monitored Drift Tubes: The MDT serves as the primary tracking detector, employing precision drift tubes filled with a gas mixture. As muons traverse these tubes, they ionize the gas, generating ionization electrons that drift toward an an-

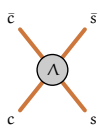

$O^{(1)}_{quqd}$

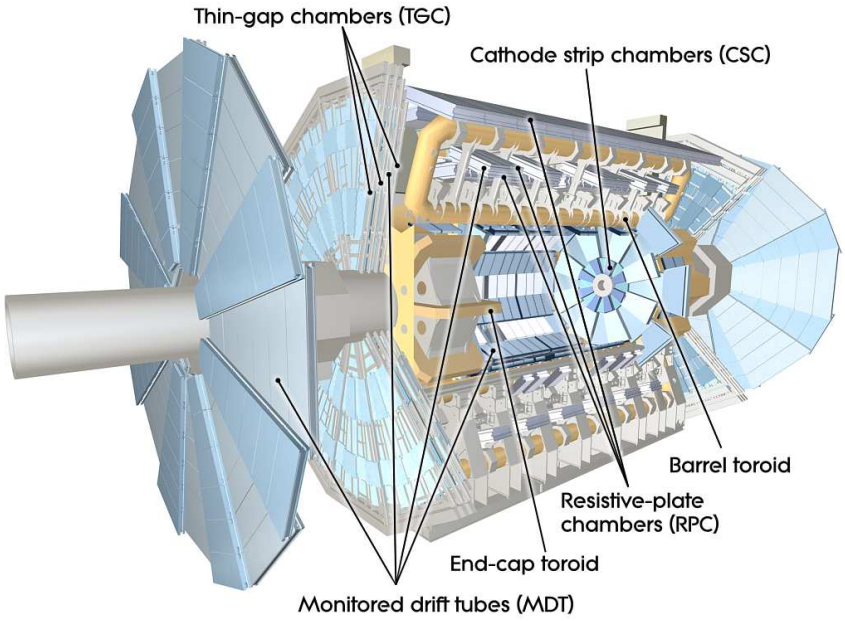

Figure 3.6: Cutaway view of the ATLAS muon system. Figure taken from [135].

ode wire. By analyzing the arrival times of these drifting electrons, the position of the muon's track can be accurately determined. The MDTs ensure high spatial resolution and are robust for precise muon tracking. The MDTs cover a region of $|\eta| < 2.7$, except for the innermost layer where CSCs are employed instead in the region of $2 < |\eta| < 2.7$. They are arranged in concentric cylinders approximately 5, 7.5, and 10 m from the beam axis. The overall layout of the MDTs is projective with respect to the interaction points, i.e., the layer dimensions and chamber sizes increase with an increasing distance from the interaction point.

Cathode Strip Chambers: In the forward region, given that the particle fluxes and muon-track density are highest, the MS incorporates CSCs in the innermost layer of the forward region between $2 < |\eta| < 2.7$. These multiwire proportional chambers utilize cathode strip readout to measure the position and timing of muon tracks. Designed to handle the high particle flux, the CSCs provide rapid response times for efficient muon detection and tracking.

It is required to know the location and characterize the deformation of the chambers with a precision better than 30 μm to achieve the high position resolution for the sagitta measurement. The position and the internal deformation of the MDT chambers are measured using a high-precision optical system.

O_{1e}

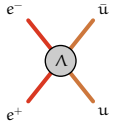

Trigger chambers: The precision tracking system is complemented by the trigger system, where fast subdetectors provide the capacity to trigger on muon tracks. The RPCs are gaseous detectors that supplement the precise tracking capabilities of the MDT and CSC. They offer fast response times and are particularly effective for triggering purposes. By utilizing resistive plates as electrodes, the RPCs provide accurate timing information for muon detection.

Completing the suite of subdetectors, the Thin Gap Chambers (TGC) cover the end-cap regions of the Muon Spectrometer. The TGCs are doublet (two wire planes) or triplet (three wire planes) chambers that excel in triggering and delivering swift response times. Through the implementation of a high electric field within a small gap, the TGCs achieve superior timing and spatial resolution.

Together, these subdetectors deliver precise measurements of muon tracks and their momenta. The MDT ensures exceptional spatial resolution for precise tracking, while the CSCs, RPCs, and TGCs provide complementary information for triggering and timing purposes. By integrating the data obtained from these subdetectors, the ATLAS Muon Spectrometer can effectively identify and accurately measure the trajectories and momenta of muons generated during high-energy collisions at the Large Hadron Collider (LHC).

3.2.6 Trigger and DAQ

LHC collisions occur every 25 ns, which corresponds to a rate of 40 MHz. Given that a typical event size is O(1.5) MB, storing all the data at a rate of O(60 TB/s) is not feasible. Therefore, a trigger is used to select events of interest. The ATLAS trigger and data acquisition (TDAQ) consists of three levels of selection: Level-1 (L1), Level-2 (L2), and Event Filter. The L2 and Event Filter are called the High-Level Trigger (HLT). The L1 trigger is implemented using custom-made electronics and is commonly referred to as a hardware trigger. The HLT, on the other hand, runs on a computing farm and is referred to as a software trigger. A diagram of the trigger and the data acquisition system employed by the ATLAS detector in Run-2 is shown in Figure 3.7.

Level-1 Trigger: The L1 trigger is designed to reduce the event rate from 40 MHz to 100 kHz and performs the initial event selection based on information from calorimeters and muon detectors. The L1 calorimeter trigger uses reduced granularity information from all the calorimeter sub-systems to identify high-p_T electrons, photons, jets, τ-leptons, and missing transverse energy. With precise timing accuracy, the L1 muon trigger uses information from finely segmented muon detectors - RPCs in the barrel region and TGCs in the end-cap region - to provide unambiguous identification of the bunch-crossing containing the muon candidate.

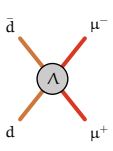

O_{ed}

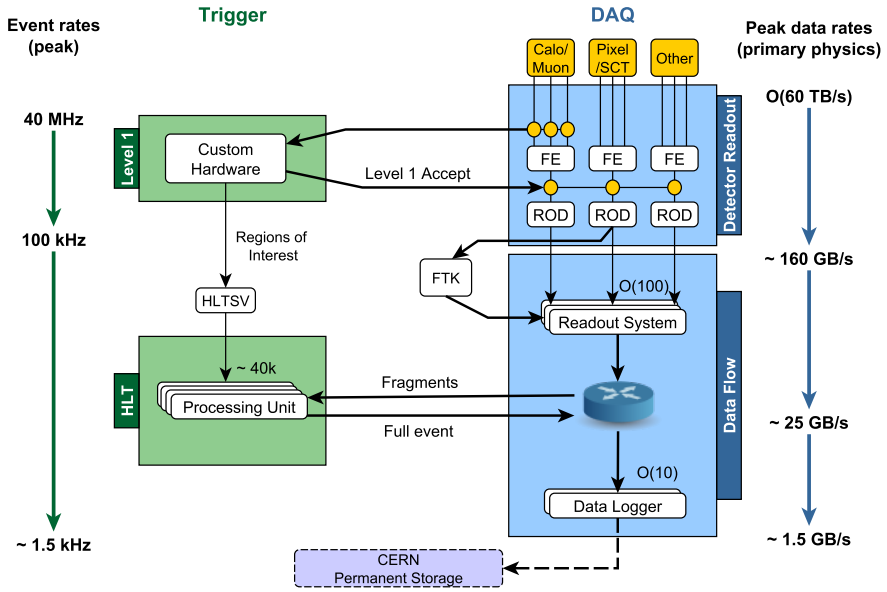

Figure 3.7: Diagram of the ATLAS Trigger and Data Acquisition system in Run-2 showing expected peak rates and bandwidths through each component [140].

The L1 muon trigger searches for patterns of hits consistent with high-p_T muons originating from the interaction region.

The L1 trigger decision consists primarily of multiplicities for electrons/photons, τ-leptons, jets, and muons, and flags indicating which thresholds were passed for total and missing transverse energy and the total jet transverse energy. The L1 Central Trigger Processor (CTP) uses this information to make the L1 accept decision. When the L1 trigger accepts the event, the geometric location information of the trigger objects that are retained in the calorimeter and muon trigger processors corresponds to Regions-of-Interest (RoI) that is used to seed the selection by the HLT.

High-Level Trigger: The L2 trigger uses the RoI information on coordinates, energy, and type of signatures to restrict the amount of data that must be transferred from the detector readout. The event filter uses offline analysis procedures on fully-built events to further select events down to a rate of approximately 1 kHz, which can be recorded for subsequent offline analysis. The HLT algorithms use the full granularity and precision of calorimeter and muon chamber data, as well as the data from the inner detector, to refine the selection of the earlier trigger layers.

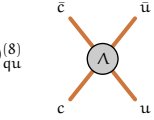

3.2.7 Luminosity and Pile-up during Run-2

The instantaneous luminosity of the LHC is defined as the ratio of the number of events per second to the cross-section of the process. The instantaneous luminosity is a property of the collider and depends on the beam parameters. For a collision of two identical beams and with a Gaussian beam distribution in the transverse plane, the instantaneous luminosity L is given by the following equation:

$$L = \frac{N_b^2 n_b \gamma_r f_{rev}}{4\pi\epsilon_n \beta^*} \underbrace{\left(1 + \left(\frac{\theta_c \sigma_z}{2\sigma^*}\right)^2\right)^{-\frac{1}{2}}}_{F} \tag{3.1}$$

where N_b is the number of particles per bunch, n_b is the number of bunches per beam, γ_r is the relativistic gamma factor, ϵ_n is the normalized transverse beam emittance, σ^* is the transverse root mean square beam size at the interaction point, β^* is the beta function at the collision point. f_{rev} is the revolution frequency of the beams. F is the geometric reduction factor due to the crossing angle at the collision point, which depends on σ^*, the RMS bunch length σ_z and the crossing angle at the interaction point θ_c. The instantaneous luminosity is measured in units of $cm^{-2}s^{-1}$. The cumulative luminosity delivered to ATLAS during stable beams for pp collisions is shown in Figure 3.8(a).

Multiple methods, subdetectors, and techniques are employed in the ATLAS experiment to measure the luminosity accurately [141]. The combination of multiple measurements helps ensure the precision and reliability of the luminosity determination, which is crucial for understanding the rate various physics processes in collision data. The luminosity is measured and calibrated using various methods, including but not limited to,

- LUCID 2 (LUminosity measurement using Cherenkov Integrating Detector): LUCID 2 [142] is a detector system designed to measure the luminosity by detecting Cherenkov radiation produced by particles passing through quartz detectors. The intensity of the Cherenkov light is related to the number of particles, allowing for determining luminosity. LUCID 2 consists of 40 quartz tubes arranged in four layers surrounding the beam pipe of the ATLAS detector. These quartz tubes detect the Cherenkov light emitted when charged particles pass through them. The intensity of the Cherenkov light is directly proportional to the number of charged particles, allowing LUCID 2 to measure the luminosity.
- ATLAS Zero-Degree Calorimeter (ZDC): The ZDC [143] measures the energy deposited by neutral particles emitted at very small angles relative to the beamline. By analyzing the energy deposition, the luminosity can be estimated.

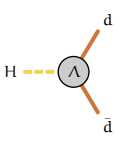

$O_{H\square}$

- Beam Conditions Monitor (BCM): The BCM [144] is a system of radiation-hard detectors placed around the beam pipe. It measures the rate of particles hitting the detectors, which is directly proportional to the luminosity.
- Van der Meer Scans: The luminosity can be calibrated by performing dedicated Van der Meer scans [145]. This involves deliberately offsetting the beams in the horizontal and vertical directions and scanning the beams across each other to measure the resulting beam size and overlap. The luminosity can be extracted by analyzing the beam profiles and the rate of events detected.

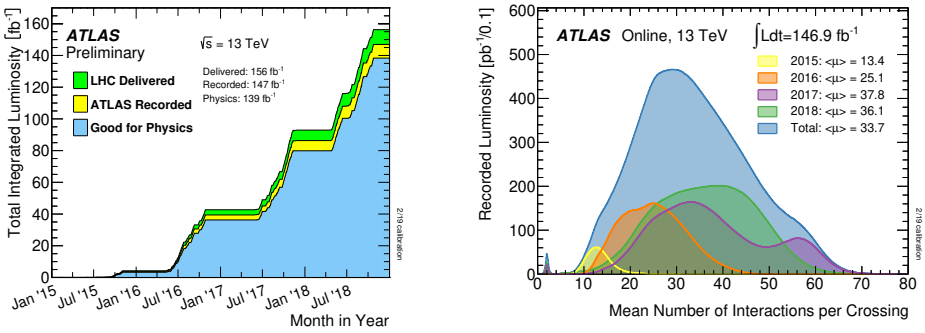

(a) (b)

Figure 3.8: Cumulative luminosity (left) delivered to ATLAS during stable beams for pp collisions at $\sqrt{s} = 13$ TeV during LHC Run-2. The luminosity is shown for the entire data-taking period (green) and for the periods where the data quality requirements for physics analyses were met (blue). The peak luminosity is 2.1×10^{34} cm^{-2}s^{-1}. The average number of interactions per bunch is denoted by $\langle\mu\rangle$ and is approximately 30 during Run-2. An indication for the pile-up distribution is shown in Figure 3.8(b).

3.3 Strain characterization for Inner Tracker Upgrade for High-Luminosity LHC

The High Luminosity phase of the LHC (HL-LHC) will push the instantaneous luminosity from 1-2 $\times 10^{-34}$ to 5-7.5 $\times 10^{-34}$cm^{-2}s^{-1} [146], allowing to enlarge the data set ATLAS can gather to study rare processes. This increase in instantaneous luminosity comes at the price of a strongly increased rate of pile-up events, with up to 200 overlapping collisions per bunch crossing at the HL-LHC. This harsh environment requires upgrading the existing tracking detector to maintain physics performance. A full silicon-based detector called the Inner tracker (ITk) will replace the current ATLAS Inner Detector and its layout is shown in Figure 3.9. The

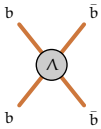

ITk will consist of a new pixel detector at a small radius close to the beamline, surrounded by a large-area strip tracking detector.

The construction of this detector requires a reliable mechanical structure to position the detector precisely and ensure minimal variation of the position of the active detector elements and its support with temperature variations. The mechanical support structure is thus a vital part of the detector, accurately holding up detector components to ensure correct track reconstruction of the detected particles. The following sections describe the characterization of the mechanical strain in the end-cap support structure and its variation with temperature.

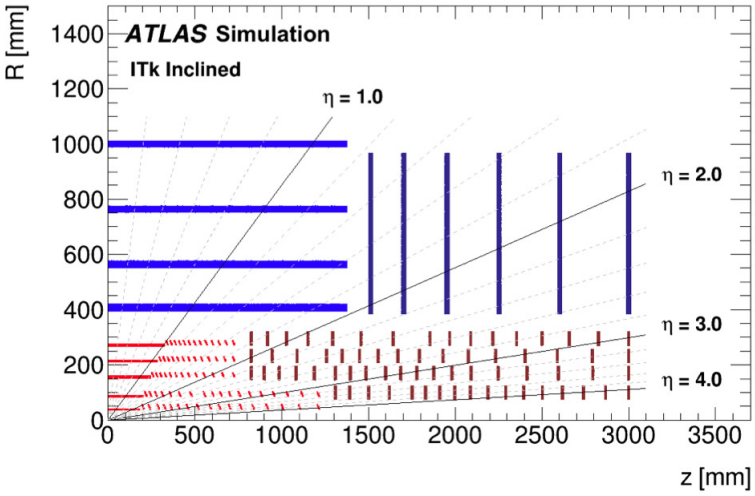

Figure 3.9: A schematic layout of the ITk for the HL-LHC phase of ATLAS. The violet planes represent the end-cap strip trackers that will be part of the upgrade [147].

3.3.1 ITk end-cap global structure

The mechanical structure for the end cap is made of carbon fiber – an ideal material that is light, sturdy, with a minimal material budget, and exhibits small variations with temperature. The coefficient of thermal expansion (CTE) of carbon fiber is between -1 to 8 $\mu m/m/^{\circ}C$. The frame consists of the carbon fiber weaves held together in the glue matrix, where the carbon fibers are embedded in the glue.

The ITk end-cap global structure is a cylindrical frame that supports the detectors, cooling pipes, and the electronics readout for the strip sensors. The strip sensors and their readouts are encased in basic mechanical building blocks of the detectors in a petal-like formation. The petals are mounted on the disks with a required positional accuracy of 100 μm in position. The inner and outer rings in the same

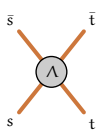

$O_{td}^{(8)}$

XY-plane are connected by blades as shown in Figure 3.10, which provide rigidity to the wheel, similar to the structure of a bicycle wheel where spokes establish the rigidity of the rim.

Each set of inner and outer rings, along with the eight interconnecting blades, form a wheel. At the outer ring, the disks are connected with rods and service elements in the z-direction. The blades are joined to the rims of the wheels using an adhesive and have been designed with two square profile tubes along the sides of unidirectional carbon fiber. The volume is filled with a carbon-fiber honeycomb or carbon foam sandwich and is covered with a carbon-fiber skin. Several holes of increasing size with the blade width are cut out in the sandwich to stay below the specified target of 0.2 X_0 of material budget. The six disks are supported by an inner cylinder tube, providing space for the ITk pixel detector. A stiffening disk is situated just outside the active tracking volume at the end of the detector to provide stiffness along the z-axis direction.

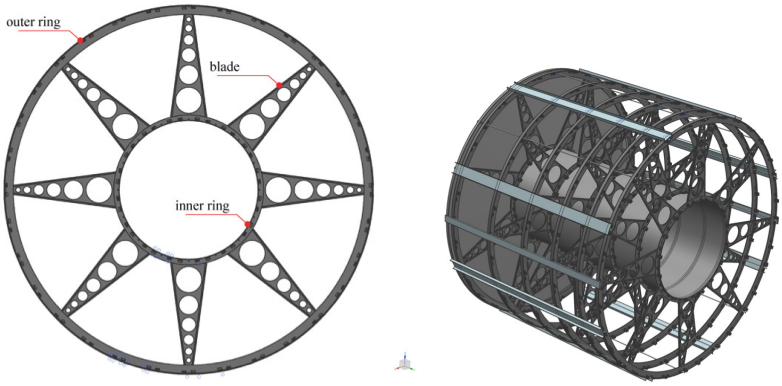

(a) (b)

Figure 3.10: A diagram of the wheel and its constituent components on the left and a diagram of the end-cap support structure, including the stiffener disk, which is situated in the back. Schematic is taken from [147].

The wheels hold the petals in a precisely controlled position and absorb mechanical stresses that may affect the petals in the plane. There are sixteen carbon fiber spacer rods between the rings, which provide further mechanical strength to the support structure. Outside the outer rings, eight service trays are distributed across the ring where cables and cooling tubes are placed. Two rails then mount the whole structure to the outer cylinder. More information regarding the end-cap structure, including the composition and the assembly, is available in [147].

The detector environment is controlled by a CO_2 evaporative cooling system and is subject to various physical conditions during operation and shut-down. In particular, thermal stress can occur once the detector is in operation, where the silicon

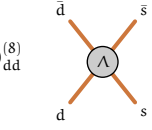

detector elements are cooled to temperatures below -35 °C. However, the remainder of the structure is exposed to an ambient temperature of around 20°C. In certain fault conditions, the cooling temperature may be lowered down to -55°C in the worst-case scenario [147].

3.3.1.1 Strain measurements

Strain definition: Mechanical strain is defined by the deformation of an object relative to its nominal configuration. Various ambient influences, such as changes in temperature, moisture, chemical composition, or external or internal forces, can cause the deformation. The Cauchy strain of an object is defined as the ratio of total deformation to the initial dimension of the object as

$$\varepsilon = \frac{l_f - l_i}{l_i} = \frac{\Delta l}{l_i}, \tag{3.2}$$

where l_i is the initial length of the object and l_f is the final length of the object. A strain gauge is a device that is used to measure the strain on an object and consists of either a metal foil strip, a length of flat metal wire, or a strip of semi-conductor material that can be stuck onto surfaces of materials like a postal stamp, as shown in Figure 3.11. When the foil, wire, or semi-conductor is stretched or compressed, it changes the element's resistance (R). The resistance is given in terms of the resistivity (ρ), length (l), and cross-sectional area (A) of the element as

$$R = \frac{\rho l}{A}. \tag{3.3}$$

The gauge factor (G_f) is defined as the ratio of fractional change in the resistance ($\Delta R/R$) to the fractional change in length ($\Delta l/l$) and is given by

$$G_f = \frac{\Delta R/R}{\Delta l/l}. \tag{3.4}$$

The gauge factor can be derived from the resistance of the strain gauge using Equation 3.3 as

$$\frac{\Delta R}{R} = \frac{\Delta l}{l} - \frac{\Delta A}{A} + \frac{\Delta \rho}{\rho} \tag{3.5}$$

$$G_f = \frac{\Delta R/R}{\Delta l/l} = 1 + 2\nu + \frac{\Delta \rho/\rho}{\Delta l/l} \tag{3.6}$$

where ν is the Poisson ratio of the strain gauge that characterizes the mechanical response, and where $\frac{\Delta \rho/\rho}{\Delta l/l}$ is accounting for the piezoresistive effect characterizes the change in the resistivity of the strain gauge. For constant temperature, neglect-

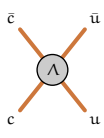

$O_{qq}^{(3,1)}$

ing the change in the resistivity, metallic strain gauges have a nominal gauge factor of 2.

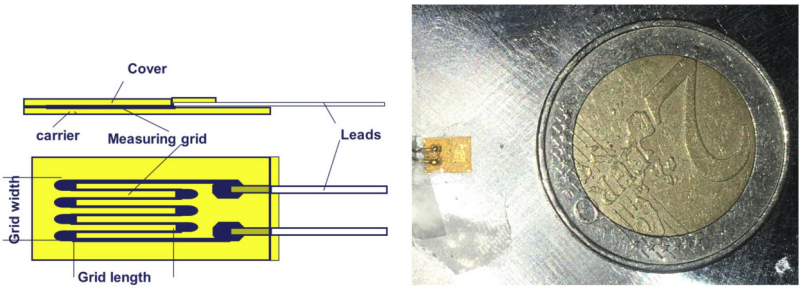

(a) (b)

Figure 3.11: An illustration of a single axial strain gauge on the left and a picture of one of the used strain gauges with a 2-euro coin for comparison.

In addition to the change due to external strain, there is a change in resistance of the strain gauge with a temperature change. This inherent change in resistance is accounted for by the technique of self-temperature compensation [148], which requires selecting a particular alloy matched to exhibit the thermal behavior of a well-known material. The strain gauges used and tested have been temperature-compensated to ferretic steel.

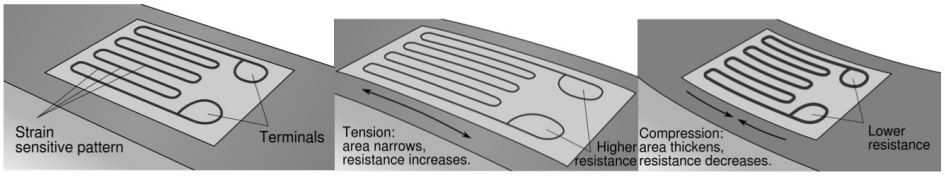

Figure 3.12: An illustration depicting the change in the shape of the strain gauge due to the deformation of the reference material along the axis of the strain gauge. On the left, we have the nominal position of the strain gauge. The middle image depicts the scenario wherein the gauge is under positive strain, which leads to a build-up of tension in the strain gauge strip. On the right, the strain gauge is under negative strain along the axis of the strain gauge, which compresses the strain gauge strip.

Strain characterization: The strain gauge is installed on the material of interest such that there is a complete transfer of the strain build-up to the strain gauge. A change in the shape of the strain gauge surface leads to a change in the resistance of the strain gauge, as illustrated in Figure 3.12. The strain gauge is sensitive to strain along the axis of the gauge. Other gauges, such as rosette strain gauges, typically involve two to three gauges per rosette oriented along different directions

that can be used to shed more light on the tensorial nature of the local strain build-up in the material. In the following study, only mono-axial strain gauges, which are sensitive to strain along a single direction, are used. The strain along different directions is measured by orienting multiple mono-axial strain gauges along the directions of interest. Given the cylindrical symmetry of the end-cap support, the strain gauges are oriented along the radial and azimuthal directions.

Temperature response: The resistance change due to temperature change is an important effect to consider given our scenario, where we cool down the material to which the strain gauges are attached. The strain gauges we use are manufactured to match the temperature behavior of a reference material. Therefore, the deformation in the material due to a change in temperature is made to this relative reference and can be written as

$$\frac{\Delta l}{l} = \frac{1}{G_f} \cdot \frac{\Delta R}{R} = (\alpha_{moi} - \alpha_{SG})\Delta T, \tag{3.7}$$

where α_{moi} and α_{SG} represent the coefficient of thermal expansion (CTE) of the material of interest and the strain gauge, respectively. The mechanical strain due to structural deformation will be measured along with the strain induced due to temperature variation.

3.3.2 Setup

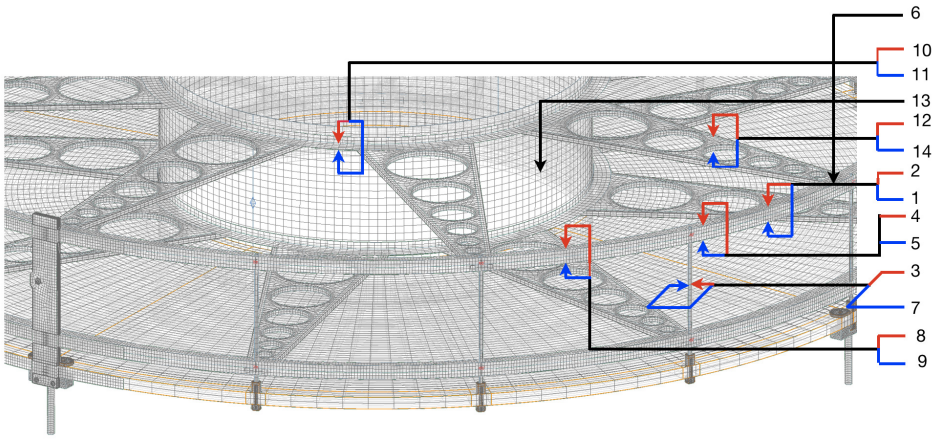

Figure 3.13: A map of the strain gauges installed on the mock-up.

The setup used to characterize the strain build-up in the mock-up of the end-cap support structure is described below. Fourteen strain gauges are installed on the mock-up to measure the thermal behavior. A large fraction of the gauges are glued on the upper outer ring, and the gauges are distributed on the inner ring, inner

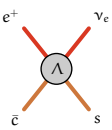

$O_{lq}^{(3)}$

cylinder, blade, and spacer rod. The strain gauges installed on the rings are oriented along the ϕ direction, i.e., along the carbon fibers' weave. The gauge on the inner cylinder and the pair of gauges on the spacer rod are oriented in the z-direction. The pair on the blade are oriented along the radial direction. In addition to those installed on the mock-up, one gauge was installed on reference samples of aluminium, borofloat 33, and an unconstrained carbon fiber spacer rod. The reference materials are placed near the strain gauges during the cooling, and their measurements help calibrate the thermal behavior of the gauges. A schematic of the position of the installed strain gauges is shown in Figure 3.13.

The resistance change across the strain gauge is measured using a four-wire resistance technique. The four-wire resistance technique [149] compensates for the lead resistance of the connecting wire by using a separate current source, as shown in Figure 3.14. The change in voltage due to the connecting wires is not measured by the volt meter. Although a small amount of current can flow through the connecting wires that measure the voltage, this is a much smaller current than the current flowing through the strain gauge, usually in the order of a pico Ampere, and can be ignored for all practical purposes.

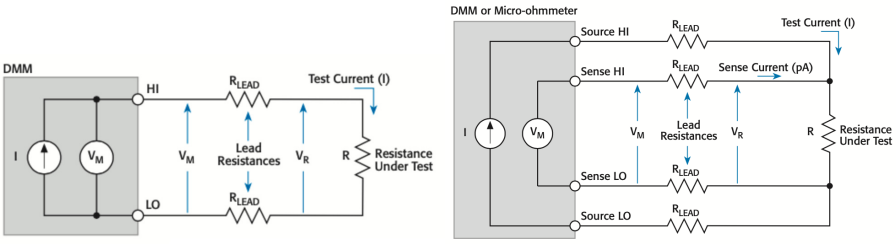

(a) (b)

Figure 3.14: A schematic of the two-wire (left) and the four-wire (right) technique used to measure resistance. Schematic taken from [149].

As shown in Figure 3.15, the mock-up consists of the stiffening disk and two wheels attached to it using the stiffening rods. The cooling test was performed by enclosing the mock-up in a thermally insulated box using insulating foam. Around 25 kg of dry ice was evenly distributed across the enclosure to cool the environment inside the box. The temperature across the mock-up was monitored at multiple points using thermo-resistive sensors.

Readout: The resistance across the different gauges is measured by a setup sketched in Figure 3.16. The gauges are connected to a Keithley 7708 differential multiplexer capable of measuring 20 channels of four-wire resistances at a given time. The multiplexer is connected to the Keithley 2701 system [150], which performs the data acquisition and logging. The system is connected via ethernet to a PC, pro-

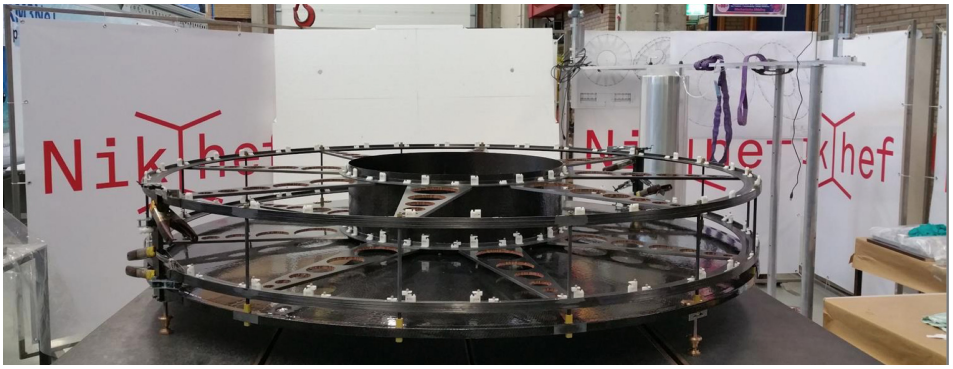

Figure 3.15: Image of the mock-up of the global structure placed on top of an anti-vibration table. The mock-up consists of the stiffening disk and two wheels connected using the stiffening rods.

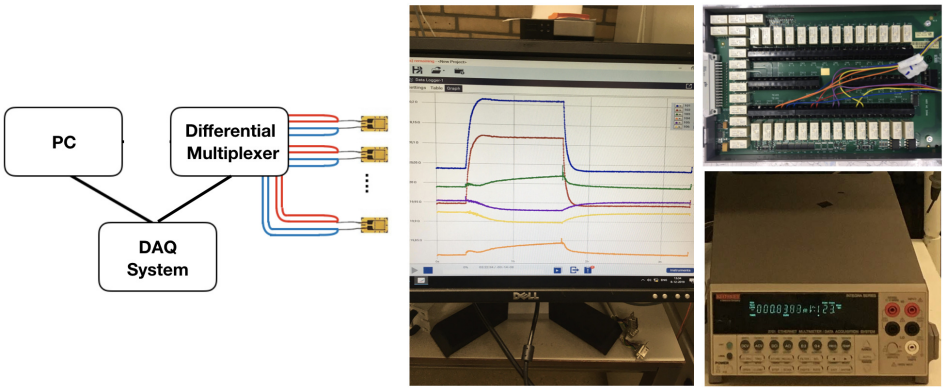

Figure 3.16: A schematic of the system used to measure the resistances of the installed strain gauges and a picture of the system that was used.

viding a logging and visualization platform. The KickStart software communicates to the DAQ system via a simple and clear interface.

3.3.3 Measurements

The cooling test was carried out for two hours, and a uniform temperature of $-30°C$ was reached and maintained for one hour and a half. The room temperature was $21°C$ before and after the cooling test. The temperature distribution can be affected due to non-uniform circulation. However, the temperature sensors that were distributed across the mock-up showed uniformity in measured temperature up to $1°C$. The variation in the temperature distribution is not probed, and the global temperature is assumed to be the temperature in the vicinity of the strain

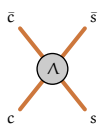

$O_{qu}^{(1)}$

gauge. The microstrain can be measured by using the relative change of resistance with respect to the nominal resistance value and scaling it with a gauge factor. For metallic strain gauges, this gauge factor is typically around two.

A selection of the resistance measurements for the cooling test is shown in Figure 3.17. The stable flat region corresponding to t = 1h and t = 2h was used for the average strain during the cooling phase. Before the gauges enter the stable region, there is a period with build-up of strain. Small perturbations in closing and taping the thermal insulating enclosure are observed as spikes in the behavior. The cooling was stopped roughly after two hours, which involved opening the lid and removing the remaining dry ice. The strain build-up drops sharply after the cooling is stopped. Most strain gauges have also captured the perturbations as spikes around t = 2 hrs when the cooling was stopped by opening the thermal enclosure.

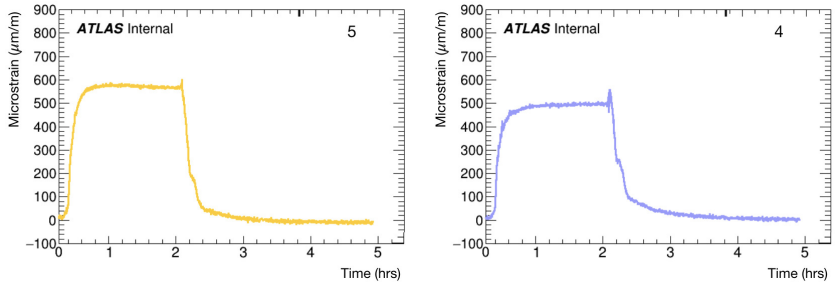

(a)

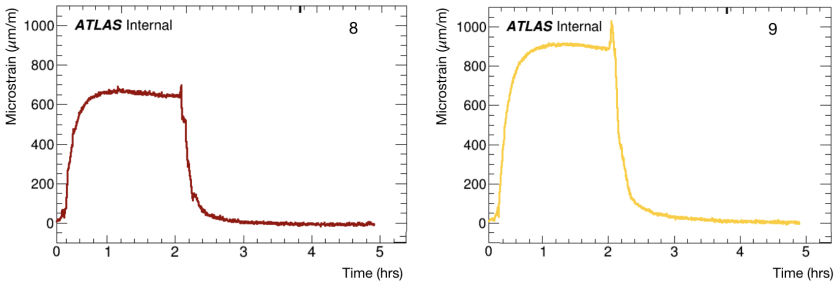

(b)

Figure 3.17: The measured strain during the cooling test for a selection of the strain gauge pairs installed in the parallel configuration. The left and right plots correspond to a pair each. The strain gauges are numbered according to the map in Figure 3.13.

The average strain build-up is calculated as the average over the set of measurements during the stable temperature period. The mean values of the micro strains measured are shown in the map in Figure 3.18.

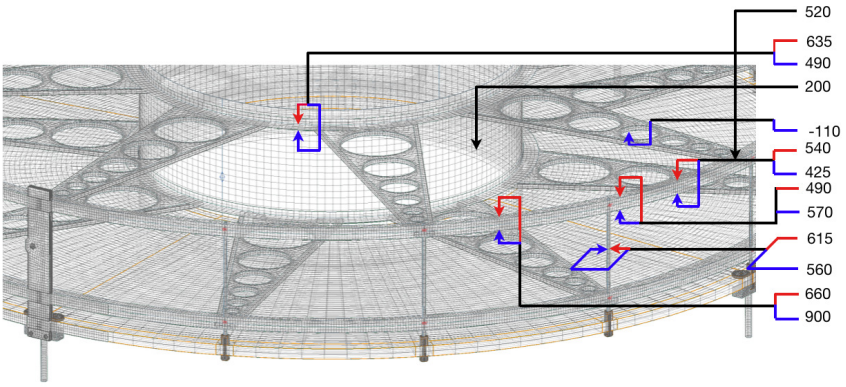

Figure 3.18: The total strain buildup (in μm/m) measured across the gauges during the cooling test. The strain includes the thermal response of the gauge and the strain transferred at the point of installation. The blue and red lines indicate strain gauge pairs. The numbers quoted have been rounded off to a 10 μm/m accuracy.

3.3.4 Coefficient of Thermal Expansion estimation

The coefficient of thermal expansion (CTE) is a measure of the fractional change in the size of a material for a given change in temperature. To estimate the CTE of the different points of the mock-up, it is required to know the CTE of the strain gauges. The strain gauges are compensated to ferretic steel, which exhibits a CTE of $\alpha_{SG} = 9$ (μm/m)/°C. The linear CTE for other materials is estimated using Equation 3.7 as

$$\alpha = \alpha_{SG} + \frac{1}{G_f \Delta T} \cdot \frac{\Delta R}{R}, \tag{3.8}$$

where G_f is the gauge factor, ΔT is the temperature change, and $\Delta R/R$ is the measured fractional change in resistance. Figure 3.19 presents the CTE estimates for various points in the mock-up. The strain gauge pairs installed in the parallel configuration are listed in Table 3.2.

The bending strain can be inferred from the difference in the CTE of the two parallel gauges (Table 3.2). The largest bending strain component is observed in the strain gauge pair installed on the outer ring between the stiffener rods. For the remaining strain gauge pairs, the bending strain component is relatively small, corresponding to 20-40% of the transverse strain component.

The measured strain at different points across the mock-up end-cap structure is a local property of the structure. It measures both the effect of the thermal behavior of the underlying material and the structural strain of the system. The CTE esti-

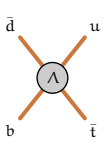

$O^{(1)}_{quQb}$

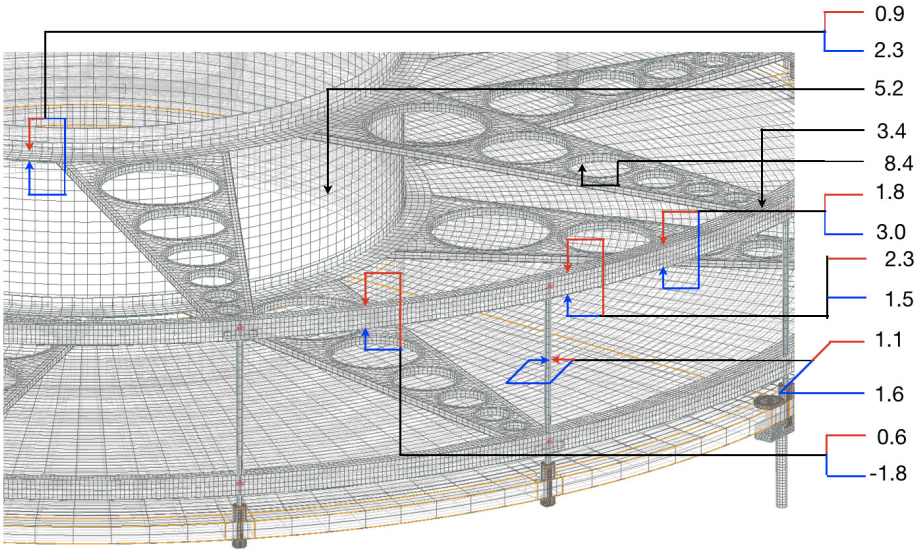

Figure 3.19: The linear CTE values at various points of the mock-up measured from the build-up of strain due to cooling down, the central values are rounded up to the 1σ uncertainty.

Pair	Installed on	location	Axial component	Bending component
(10,11)	Inner ring	In between blade support	1.6	0.7
(2,1)	Outer ring	between stiffener rods	2.4	0.6
(4,5)	Outer ring	in-between blades support	1.9	0.4
(3,7)	Stiffener rod	in-between blades support	1.3	0.2
(8,9)	Outer ring	In between stiffener rods	0.6	1.2

Table 3.2: The strain gauge pairs installed in the parallel configuration. The pair are denoted by the number shown in Figure 3.13. The axial component is the average of the two CTE estimates of the pair and the bending component is the absolute difference between the two CTE estimates divided by two. The CTE estimates are given in ($\mu m/m/^{\circ}C$).

mates enable us to understand the temperature behavior of the mock-up structure and its contribution to the bending strain. The linear CTE measured at various points, including the bending strain, is ~ 1 $\mu m/m^{\circ}C$. These numbers lie within the expected range for carbon fiber of -1 to 8 $\mu m/m^{\circ}C$.

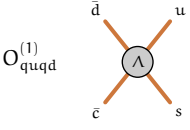

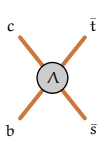

$O_{qtQd}^{(1)}$

4

Reconstruction of physics objects

Hits collected in the detectors must be reconstructed as physics objects to measure different physics processes from the data collected. This step aims to extract from the detector the four-momentum of particles and identify particles as electrons, photons, muons, jets, τ—leptons, and in the case of invisible signatures - the missing transverse momentum and transverse energy. Particle identification is achieved by making use of individual ATLAS subsystems as well as their combination in identifying and measuring electrons, photons, muons, taus and b-jets. The reconstructed objects are subsequently calibrated to ensure the accuracy and reliability of the reconstructed physics objects. The calibration procedure aims to correct instrumental effects and variations in detector response and improve particle energy or momentum measurements. This chapter summarizes the reconstruction algorithms used to obtain physics objects that enter the different measurements used for the SMEFT interpretation in this thesis.

Each particle has a dedicated reconstruction algorithm making use of different parts of the detector. An overview of the different reconstructed physics objects is summarized below and later described in more detail in further sections.

- Electrons are reconstructed by combining the energy deposits in the ECAL with the associated charged particle tracks from the ID.
- Photons are reconstructed based on energy clusters in the electromagnetic calorimeter.
- Muons are reconstructed using the tracking detectors and the muon spectrometer, allowing to determine their trajectories and momenta precisely. The calorimeter is also required as the energy loss in the calorimeter is measured and taken into account when necessary.
- The reconstruction of jets involves clustering algorithms that combine energy deposits from the calorimeters. It also combines track information and information regarding the primary vertex, which can be used to identify the flavor of the jet.
- The decay products of the τ-lepton are reconstructed using information from the tracking detectors and calorimeters. The tracking detectors provide informa-

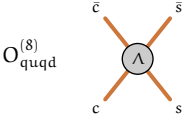

tion about the trajectory and charge of charged particles, while the calorimeters measure the energy deposited by decay products.

- Missing transverse energy is determined by summing the energies of all reconstructed objects and accounting for momentum conservation.

Throughout the reconstruction process, various calibration techniques are applied. Given the complex nature of particle identification in the ATLAS detector, most identification algorithms are designed to work at multiple operating points, implementing various trade-offs between purity and efficiency. Analysis workflows subsequently select the operating points that best match the challenges of the final state targeted.

4.1 Tracks and vertices

The reconstruction of tracks allows for tracing the trajectory of charged particles. It is an important input to different reconstruction steps such as lepton identification, pile-up removal, and jet flavor tagging. The essential steps and components are summarized in [151, 152]. Charged particles traversing the Inner Detector (ID) deposit energy when interacting with the tracking sensors, leaving a hit. The hits serve as the building block for track reconstruction. In the initial stage, hits in the pixel detector and Semi-conductor Tracker (SCT) are used to form clusters, and the timing information from the SCT is used to calibrated drift circles. A set of three space points in the silicon layers is used to form a track seed. The track reconstruction algorithm uses these seeds and proceeds in three steps: a loose pattern recognition that reconstructs track candidates and an ambiguity-solver that ensures that each hit is ultimately only associated with a single track candidate. The final step involves a track re-fit extended to account for hits in the Transition Radiation Tracker (TRT). The ID track reconstruction consists of two algorithms, the main *inside-out* track reconstruction and a consecutive *outside-in* reconstruction.

The inside-out algorithm starts with creating seeds formed in the first three layers of the pixel detector and extends them into the first layer of the SCT. Seeds are then further extended into the SCT, removing outlier clusters and resolving ambiguities amongst track seed candidates. A complimentary outside-in algorithm is used to look for tracks not found by the inside-out algorithm, such as ambiguous hits that are not associated with any track seed and tracks from secondary vertices that are not originating in the pixel detector. The outside-in algorithm is a pattern recognition sequence starting in the TRT, where the segments are formed based on a Hough transform. An association tool is used to prevent hits that have already been assigned to tracks in the inside-out procedure to be reused here in the

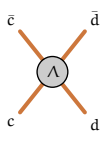

$O_{qq}^{(1)}$

outside-in procedure. The TRT track segments are followed back inwards to find track segments that are missed by the inside-out procedure.

The reconstruction of vertices is important to find the origin of the hard scatter interaction and reject pile-up collisions. The reconstruction algorithm and its performance are described in [153, 154]. The input to the vertex finding algorithm is tracks with a minimum transverse momentum of 400 MeV within the ID coverage ($|\eta| < 2.5$). Further requirements are imposed on the number of hits associated with the track in the ID. The vertex finding algorithm is based on an iterative procedure consisting of vertex finding and vertex fitting. It starts with a seed position for the first position and fits the tracks to find the best vertex position. Tracks are then assigned a weight based on their compatibility with the vertex, and the vertex fit is re-performed. Tracks incompatible with the resulting vertex are reused for identifying other vertices. The procedure is repeated until no further vertices are found.

4.2 Electrons

Electrons are reconstructed using energy deposits in the ECAL and matching tracks in the ID. Given their small mass, electrons produced in high-energy collisions are susceptible to radiating a significant amount of energy through Bremsstrahlung when they traverse the detector. This radiation can result in additional electrons, positrons, and photons, which need to be accounted for when reconstructing the four-momentum of the electron.

The algorithms used in electron reconstruction and identification are described in detail in [155]. The electron reconstruction algorithm identifies localized clusters of energy deposits found within the ECAL, charged-particle tracks identified in the inner detector, and matches these signatures to form the final electron candidates, as illustrated in Figure 4.1. Electrons are not considered in the forward region $|\eta| > 2.47$, where the ECAL coverage is limited.

First, topological clusters in the ECAL are reconstructed using a sliding-window algorithm, using dynamic, variable-size clusters, called superclusters, on the elements of the ECAL that are calibrated at the EM scale. The algorithm is executed iteratively until all elements in the calorimeter are covered. For overlapping candidates, the candidate with the highest transverse energy is retained, and the duplicate clusters are discarded.

Next, electron track reconstruction matches track clusters from the ID with dedicated algorithms to account for energy loss due to Bremsstrahlung. The pattern recognition algorithm assumes the pion hypothesis to model the energy loss from particle and detector interactions. If this does not result in a positive match between the EM cluster and a full track consisting of at least seven hits silicons

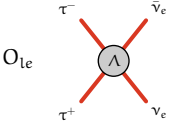

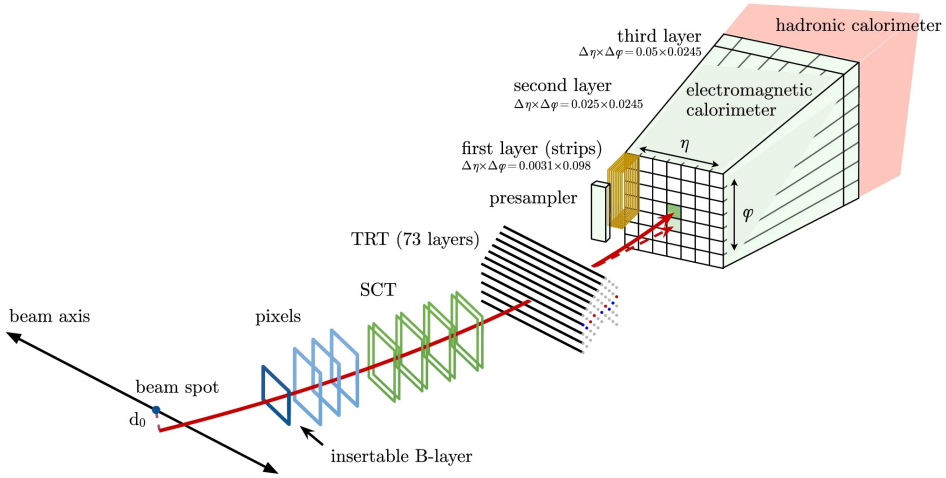

Figure 4.1: Illustration depicting the trajectory of an electron through the detector. Illustration taken from [155].

per candidate, the energy loss model is updated to match tracks with significant Bremsstrahlung. Subsequently, an optimized Gaussian-sum Filter (GSF) designed to better account for the energy loss of charged particles in material is applied. The GSF allows a better description of energy loss caused by interactions with material and introduces new track parameters. The additional track parameters capture the increased curvature in the electron's trajectory caused by Bremsstrahlung and, as a consequence, also improve all track parameters related to the bending plane, such as the transverse impact parameter (d_0). Finally, the GSF-track candidates are matched to the candidate calorimeter seed cluster.

Dedicated identification and isolation algorithms differentiate the prompt production of electrons from backgrounds such as semileptonic decays of heavy quarks and misidentified hadrons and photons converting into electron–positron pairs upstream of the electromagnetic calorimeter. The identification uses a likelihood-based (LH) technique based on probability density functions constructed from simulated events. The LH identification uses input quantities from the tracker and calorimeter and also quantities that combine tracker and calorimeter information. Isolation algorithms identify the activity near the candidate object based on both activity in the calorimeter and the tracker. Different operating points are defined for both the identification and isolation algorithms, with the tightest operating point providing the best background rejection at the cost of lower signal efficiency. The identification and isolation algorithms and their working points are described in detail in [155].

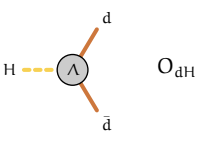

4.3 Photons

Photons are reconstructed from electromagnetic showers in the ECAL. They do not leave any hits in the ID as they do not carry any charge. However, photons can convert into electron-positron pairs in the material upstream of the ECAL and are called *converted photons*. They can thus have tracks associated within the ID originating from the conversion vertex. *Unconverted photons* do not have any tracks associated with them. Unconverted and converted photons each have dedicated reconstruction algorithms. The reconstruction and identification of both are described in detail in [156].

A converted photon is a cluster matched to a conversion vertex (or vertices), and an unconverted photon is a cluster matched to neither an electron track nor a conversion vertex. About 20% of photons at low $|\eta|$ convert in the ID, and up to about 65% convert at $|\eta| \approx 2.3$. To reconstruct converted photons, tracks loosely matched to fixed-size clusters serve as input to the reconstruction of the conversion vertex, using tracks with silicon hits and tracks reconstructed in the TRT. Clusters to which neither a conversion vertex candidate nor any track has been matched during the electron reconstruction are considered unconverted photon candidates.

The photon energy measurement is performed using information from the calorimeter. To calibrate for the non-linear response of the calorimeter, the energy of the electromagnetic clusters associated with the photon candidates is corrected in subsequent steps using a combination of simulation-based and data-driven correction factors, where the calibration is separately optimized for converted and unconverted photons.

Since most reconstructed photon candidates arise from non-prompt background photons from hadron decays in jets, photon identification and isolation algorithms can be used to reduce the background of non-prompt photons.

4.4 Muons

The main signature of muons is their minimal ionizing interaction with matter, resulting in regular ID and Muon Spectrometer (MS) tracks, and in most cases, only a minimal energy deposit in the calorimeter. Information from the calorimeters is nevertheless used and allows to reconstruct the sporadic cases where a large energy loss is measured in the calorimeters. The reconstruction and identification efficiency of muons with the ATLAS detector is described in detail in [157].

The reconstruction of generic charged particles in the ID is described in Section 4.1. Track reconstruction in the MS starts with identifying short straight-line local track segments in a station using a Hough transform [158]. Segments are subsequently

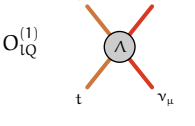

combined with trigger information, and an approximate track fit to create track candidates is performed. The track candidates are used in an iterative global χ^2 fit to account for material interactions and misalignment issues and to remove outlier hits. The final set of tracks is re-fitted with a loose interaction point constraint accounting for the energy loss in the calorimeters and is extrapolated back to the beam line.

Global muon reconstruction is based on using information from the ID and MS detectors as well as the calorimeters. There are five main reconstruction strategies corresponding to the following muon types: *combined* (CB), *inside-out* (IO), *muon-spectrometer extrapolated* (ME), *segment-tagged* (ST), and *calorimeter-tagged* (CT). Combined muons are identified with an outside-in algorithm by matching MS tracks to ID tracks, performing a combined track fit based on the ID and MS hits, and accounting for energy loss in the calorimeters. IO muons, on the other hand, are reconstructed using an inside-out algorithm and do not rely on an independently reconstructed MS track. ME muons correspond to an MS track that cannot be matched to an ID track. ST muons correspond to an ID track that extrapolates to the MS and satisfies angular matching requirements to at least one reconstructed MS segment. Finally, CT muons are identified by extrapolating ID tracks through the calorimeters to search for energy deposits consistent with a minimum ionizing particle.

Muon candidates are classified at different working points based on the number of hits in the various ID subdetectors and MS stations, on the track fit properties, and on variables that test the compatibility of the measurements in the two detector systems. Isolation criteria are applied to suppress non-prompt muons, such as those arising from the decay of heavy-flavor hadrons. Reconstruction and identification efficiencies are mainly measured using the tag-and-probe method applied to $Z \to \mu\mu$ data, where one leg of the decay, known as the tag, is required to satisfy stringent identification criteria and the second muon candidate in the pair, the probe, is used to measure the efficiency.

4.5 Jets

Quarks and gluons produced in high-energy collisions are characterized by their detector signature of *jets*, which are collimated sprays of charged and neutral particles. Jets are reconstructed using clustering algorithms that combine energy deposits in the calorimeters and tracks in the ID.

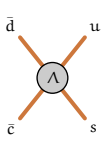

$O^{(1)\prime}_{quqd}$

The most common jet energy clustering algorithm used is the anti-k_t algorithm [159, 160] that groups energy clusters based on the distance between them (d_{ij}) and the transverse energy (k_t). The distance for a pair of objects (d_{ij}) is defined as

$$d_{ij} = \min\left(\frac{1}{p_{T,i}^2}, \frac{1}{p_{T,j}^2}\right) \times \frac{\Delta y_{ij}^2 + \Delta\phi_{ij}^2}{R^2}, \tag{4.1}$$

where p_T is the transverse momentum, and Δy_{ij} and $\Delta\phi_{ij}$ correspond to the difference in rapidity and azimuthal angle between particle i and j, respectively. Inputs to the clustering algorithm are individual 4-vectors of objects representing calorimeter clusters or tracks. The distance d_{ij} is calculated for all available clusters and the closest clusters are combined. The procedure is then repeated for every cluster until the distance between the two clusters is larger than the distance to the beamline. At this point, the procedure is stopped and the resulting object is referred to as a jet with a cone of radius R.

Small-R jets are anti-k_t jets using a radius parameter of R = 0.4, and large-R jets correspond to jets with a radius parameter of R=1.0. Dedicated calibration algorithms are applied to the small-R jets [161] and large-R jets [162], which allow to correct for experimental effects such as pile-up contamination, different calorimeter responses for electromagnetic and hadronic interactions and energy leakage. For large-R jets, a grooming algorithm is used to remove regions of the jet that only result in a small contribution to the transverse momentum of the jet. This procedure reduces the impact of energy deposits from pile-up and the underlying event, improving the energy and mass resolution of the reconstructed jet.

A flavor tagging algorithm is used to identify jets containing b-hadrons described in [163]. The algorithm uses multivariate techniques that exploit the properties of b-hadrons, such as long lifetime, high mass, and properties of the hadronic decay and fragmentation.

4.6 τ leptons

The reconstruction of the τ-lepton involves information from the tracker, calorimeter, and measurements of missing transverse momentum. The τ-lepton has a mass of 1.777 GeV and a proper decay length (lifetime) of 87 μm (290 fs) and typically decays before reaching the active regions of the ATLAS detector. Given its large mass, it can decay either leptonically (35%) ($\tau \to l\nu_l\nu_\tau, l = e, \mu$) or hadronically (65%) ($\tau \to$ hadrons ν_τ) and these decay modes are denoted by τ_{lep} and τ_{had}, respectively. Leptonic τ decays are almost indistinguishable from the prompt electrons or muons produced in the ATLAS detector with the main difference being

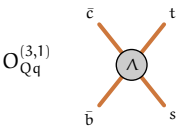

that the lifetime of the tau leads to a displacement in the production vertex of the electrons and muons, resulting in a different impact parameter distribution. The τ_{had} decay products comprise a neutrino and a set of visible decay products. These are most commonly one or three charged pions and up to two neutral pions and are referred to as $\tau_{had\text{-}vis}$ component.

The main background to hadronic tau lepton decays is jets originating from quarks and gluons. Dedicated multivariate algorithms [164] using discriminating variables based on the shower shape in the calorimeter, the number of tracks and the displaced τ-lepton decay vertex are used to distinguish $\tau_{had\text{-}vis}$ candidates from jets.

The performance of τ-lepton identification and energy scale calibration is measured using a tag-and-probe method applied to events enriched in the $Z \to \tau\tau$ process, with one τ-lepton decaying to muon and neutrinos, τ_μ (tag), and the other decaying to hadrons and neutrino, τ_{had} (probe). Additional correction factors for the identification and energy scale measurements are derived from performance on the algorithms on data and simulation [164].

4.7 Missing transverse energy

The ATLAS detector cannot directly measure missing transverse energy from particles such as neutrinos in the Standard Model or potential new particles introduced by physics beyond the Standard Model that do not interact with the detector. Instead, it is inferred from the components of the momentum imbalance in the transverse plane. Momentum conservation in the plane transverse to the beam axis implies that the transverse momenta of all particles in the final state should add up to effectively zero. Given that there is no missing coverage from the detector in the transverse plane, any momentum imbalance may indicate that particles invisible to the detector systems were produced in the collision. This momentum imbalance is known as missing transverse momentum (E_T^{miss}).

The E_T^{miss} reconstruction estimates the amount of missing transverse momentum in the detector using calibrated detector signals corresponding to the objects discussed earlier. The missing transverse momentum vector $\boldsymbol{E}_T^{miss}$ is calculated using the missing transverse momentum components muons (μ), electrons (e), photons (γ), hadronically decaying τ-leptons, and jets along the x and y axes as

$$E_{x(y)}^{miss} = E_{x(y)}^{miss,\mu} + E_{x(y)}^{miss,e} + E_{x(y)}^{miss,\gamma} + E_{x(y)}^{miss,\tau} + E_{x(y)}^{miss,jets} + E_{x(y)}^{miss,soft}, \tag{4.2}$$

where each term is calculated as the negative vectorial sum of transverse momenta of energy deposits or trajectories of charged particles. Energy deposits in the calorimeters and tracks are matched to reconstructed objects in an order cho-

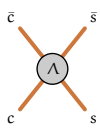

$O_{quqd}^{(1)\prime}$

sen to minimize double-counting of detector signals. The signals not associated with reconstructed objects form the soft term, whereas those associated with the reconstructed objects are collectively called the hard term. The soft term contains contributions from the underlying event and pile-up interactions and may contain contributions from the hard scatter. The vector $\boldsymbol{E_T}^{\text{miss}}$ provides the amount of the missing transverse momentum via its magnitude, E_T^{miss}, and its direction in the transverse plane in terms of the azimuthal angle ϕ_{miss}.

The resolution of missing transverse energy is affected by particle identification, energy scale and resolution of the reconstructed and calibrated physics objects. Object momentum measurement, calibration, and particles going through non-instrumented regions of the detector also impact $\boldsymbol{E_T}^{\text{miss}}$ reconstruction. Momentum contributions from pile-up interactions can enter into the $\boldsymbol{E_T}^{\text{miss}}$ calculation, contaminating the estimate of the $\boldsymbol{E_T}^{\text{miss}}$ of the hard scatter interaction of interest. These considerations are all taken into account in the $\boldsymbol{E_T}^{\text{miss}}$ reconstruction and calibration algorithms. The $\boldsymbol{E_T}^{\text{miss}}$ reconstruction algorithm is described in detail in [165].

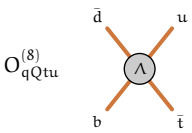

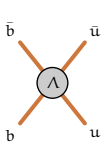

$O_{Qu}^{(8)}$

5

Statistical modeling

This chapter describes the methodology of using SMEFT described previously in Section 2.3.1 to derive predictions and perform statistical tests with data. The primary focus of this chapter is on the construction of the statistical model for physics observables, based on SMEFT predictions.

The observables are generally cross-sections defined at the fiducial or reconstruction level. Cross-sections can be treated inclusively for low-statistics processes or differentially for high-statistics processes, in which case they are modeled as coarsely binned differential distributions of an observable.

Fiducial cross-sections have the advantage of being largely independent of reconstruction effects. However, they must be explicitly constructed by applying the inverse procedure of the reconstruction to the data, using an estimate from simulation. This procedure is schematically shown in Figure 5.2(a) and is commonly known as *unfolding*. Fiducial cross-sections, expressed as regions of phase space defined in terms of particle-level quantities, allow to define measurable cross-sections that do not need to be extrapolated into the inclusive phase space and thus have potentially reduced systematic uncertainties.

Alternatively, it is possible to directly obtain constraints on SMEFT parameters by using the information at the reconstructed level in the detector where the SMEFT predictions are needed at the detector level. These cover different ways in which physics analyses can be performed and allow to define the interface between data and theory.

To perform statistical tests in SMEFT, reliable predictions of the physical observables in terms of all the relevant SMEFT parameters is crucial. The SMEFT dependence of observables relies on Monte Carlo simulations carried out at many SMEFT configurations. Due to the large number of operators, the dimensionality of the SMEFT parameter space is large compared to other theoretical models. This large complexity makes it challenging to construct a probability model for observables at the reconstruction level that is continuous in the model parameters, as a brute-force empirical sampling and interpolation strategy will not scale. However, due to the structure of SMEFT, it is instead possible to construct a probability model that is continuous in all model parameters by mirroring the structure of SMEFT. All differential distributions corresponding to single amplitude-squared terms are

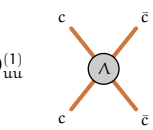

parameter-free in SMEFT. Parameters only enter via the Wilson coefficients that multiply each term in the sum that represents the full SMEFT prediction for any observable.

A statistical model for observables from Higgs data, constructed in this fashion from SMEFT predictions, can be used to estimate the model parameters from the observed data. Systematic uncertainties are captured in this inference, as their effects are included in the statistical model and expressed through additional nuisance parameters that carry uncertainties defined by auxiliary terms.

5.1 Observables used in measuring Higgs boson properties

Measurements in the Higgs sector have rapidly evolved since the Standard Model Higgs boson discovery in 2012. The discovery of the Standard Model was driven by optimizing the expected overall signal strength of Higgs boson production at the LHC. With a significant increase in the volume of the dataset, it is now possible to measure the kinematic properties of the Higgs boson rather than relying on the assumption of SM distributions.

The large dataset collected during LHC Run-2 gives access to perform a diverse range of observables. This section describes the possible observables that have been employed in measuring Higgs boson properties.

The relevant observables for studying the Higgs boson have steadily evolved from inclusive observables such as total production cross-sections and branching ratios. The state-of-the-art measurements provide detailed kinematic information extracted in fiducial cross-sections, differential cross-sections, and simplified template cross-sections. Detailed descriptions of these observables are available in [166].

5.1.1 Inclusive Higgs boson production cross-sections and branching ratios

The measurement of inclusive production cross-sections and branching ratios constitute the first step towards studying the properties of the observed Higgs boson and examining their compatibility with Standard Model prediction. The experimental analyses were designed to measure the Higgs boson production in different decay channels employing multiple event categories and multivariate techniques to optimize the sensitivity to the signal strength in each of the production modes. The ensemble of measured production and decay rates has been collectively interpreted using the Run-1 style coupling framework, commonly known as the κ-

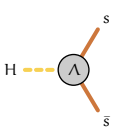

O_{dH}

framework [167]. The inclusive measurements of the signal strength of the Higgs boson production in various decay channels are depicted in Figure 5.1.

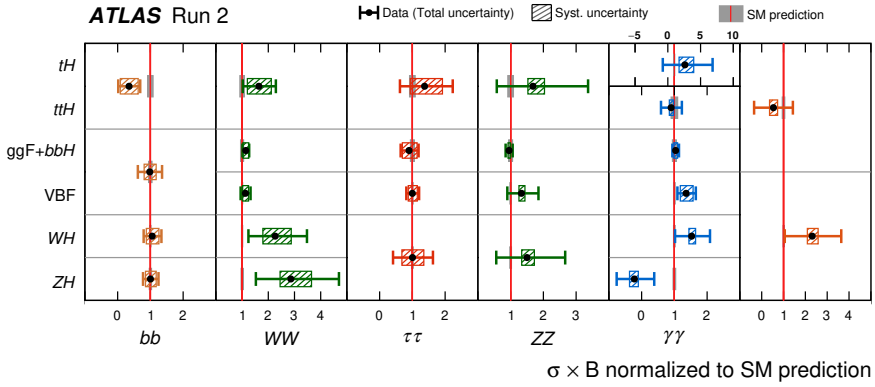

Figure 5.1: Ratio of observed rate to predicted SM event rate for different combinations of Higgs boson production and decay processes. The horizontal bar on each point denotes the 68% confidence interval. The narrow gray bands indicate the theory uncertainties in the SM cross-section times the branching fraction predictions. Figure taken from [168].

The inclusive measurements allow quantifying the compatibility of the coupling strength of various SM particles to the Higgs boson with the predictions of the SM. In the κ-framework, there is a direct relationship between the κ parameters, the inclusive production cross-sections, and the branching ratios. Analyses designed to optimize the statistical significance of inclusive observables ensure that the most sensitive values of the κ parameters can be extracted. Such inclusive cross-section measurements are not optimally sensitive to SMEFT as modification of SMEFT parameters may result in modified differential distributions with only small changes in the corresponding inclusive cross-section.

5.1.2 Higgs boson differential cross-sections

The size of the dataset recorded in Run-2 of the LHC is sufficiently large to enable measurements of kinematic distributions of the Higgs boson. In this regard, differential cross-section measurements performed in Higgs analyses allow extracting the Higgs boson's kinematic and event-level information. Differential cross-sections can be either measured in a fiducial manner matching the phase space of the analysis or can be extrapolated to the total phase space. The former is termed a fiducial differential cross-section, and the latter is termed a differential cross-section.

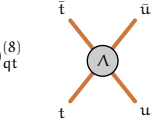

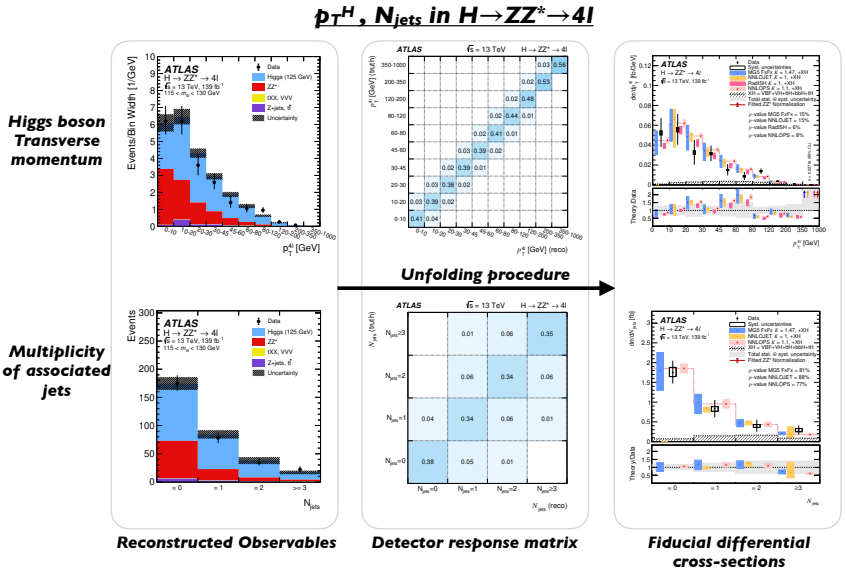

(a)

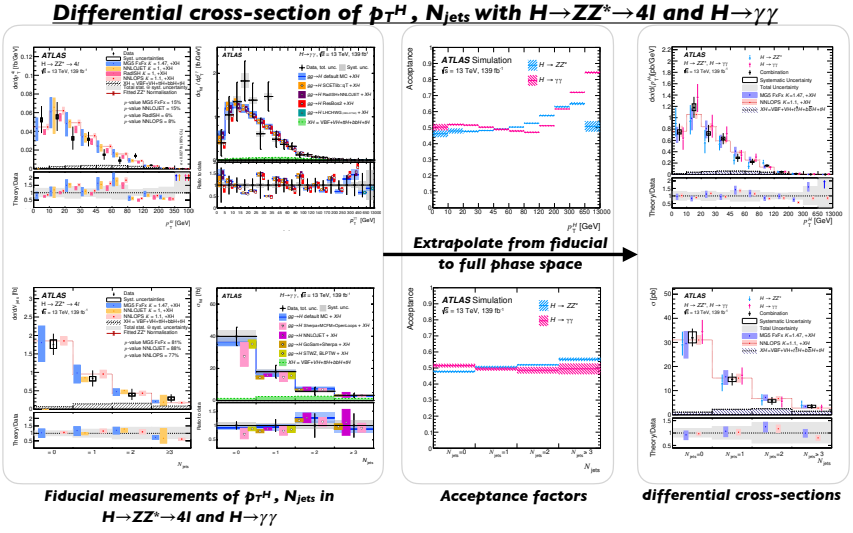

(b)

Figure 5.2: Figure 5.2(a) shows an example of the reconstructed observables, detector response functions and the unfolded fiducial measurements of the Higgs boson transverse momentum, p_T^H, and the associated jet multiplicity, N_{jets}, taken from [169]. Figure 5.2(b) shows the unfolded fiducial differential cross-sections from [169, 170] that are extrapolated to the total phase space shown on the right, taken from [171].

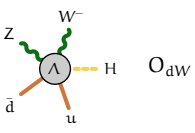

Fiducial cross-sections are defined on the particle level within a fiducial volume of the detector acceptance. Figure 5.2(a) shows, as an example, the fiducial measurement of the Higgs boson transverse momentum (p_T^H) and the number of associated jets (N_{jets}) performed in the $H \to ZZ^* \to 4l$ channel. Fiducial measurements avoid model-dependent extrapolations into kinematic regions that are much larger than the fiducial volume.

If desired, fiducial cross-sections can be extrapolated to the total kinematic phase space, and these measurements are termed differential cross-sections. The extrapolations usually consider Standard Model acceptance factors. These measurements are useful to combine observable data from different channels. An example of the extrapolated differential cross-sections is depicted in Figure 5.2(b), which shows the combined differential cross-sections of the Higgs boson transverse momentum (p_T^H) and the number of associated jets (N_{jets}). The differential cross-sections can be compared with state-of-the-art theoretical predictions for which the full chain of MC simulation is not yet available. However, such differential measurements are expected to depend on SM assumptions in the extrapolation and may be less precise to the additional systematic uncertainties arising in this extrapolation. For SMEFT interpretations, using measurements at the fiducial level is valuable instead of extrapolated distributions.

The choice of differential observables is based on those that can be reconstructed with sufficient experimental precision, especially in channels where the Higgs boson decay products can be reconstructed fully. In addition to kinematic observables related to the Higgs boson, such as the transverse momentum of the Higgs boson, p_T^H, and the Higgs boson rapidity, y_H, information on the associated jets can also be used. Jet-related observable distributions such as the number of jets N_{jet}, transverse momentum of leading and sub-leading jets, p_T^{j1}, p_T^{j2}, and invariant mass of the di-jet system, m_{jj}, are also used to study Higgs boson production. Angular observables such as the angle between Higgs boson decay products and the beam axis or the azimuthal angle between the leading jets in the case of events containing two or more jets, $\Delta\phi_{jj}$, are sensitive to spin, charge conjugation, and parity properties of the Higgs boson. The effect of experimental reconstruction efficiencies and resolution effects, and migrations at the boundaries of the fiducial region in a differential measurement are accounted for by the unfolding procedure as discussed in [172].

While fiducial measurements for a small set of observables can be performed, these are usually limited to decay channels where the Higgs boson decay products are reconstructed precisely, such as the $H \to \gamma\gamma$ and $H \to ZZ^* \to 4l$ channels. The observables defined for these precision channels are not well-attuned to other Higgs boson decay channels, where better sensitivity may be obtained in other observables. Fiducial cross-sections are explicitly optimized for minimal theory depen-

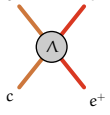

dence, and acceptance corrections in measurements are minimized by using only simple selection cuts.

With the current data volume, unfolding is usually performed only in a single observable distribution at a time. The same data may, however, be unfolded multiple times for different observables. However, these unfolded datasets do not represent independent measurements and cannot be trivially combined in a single measurement. Nevertheless, such combinations can be made using the bootstrapping technique to estimate and account for the degree of correlation between unfolded distributions. An example of this approach is given [170], where the correlation between the cross-section measurements in bins of the observables $p_T^{\gamma\gamma}$, N_{jets}, m_{jj}, $\Delta\phi_{jj}$, and p_T^{j1} is given. For example, the $\Delta\phi_{jj}$ observable provides sensitivity to CP-odd operators, whereas the remaining distributions allow probing CP-even operators.

5.1.3 Simplified Template Cross-Sections

An alternative to the computing-intensive unfolding procedure used for some of the precision channels is the Simplified Template Cross Section (STXS) [173] approach. In this method, binned distributions of observables at the reconstruction level are measured in terms of contributions from Higgs boson production processes that are kinematically sliced at the particle level in regions that are chosen to be close to the reconstruction-level regions. In general, multiple particle-level Higgs STXS cross-section bins will contribute to each reconstruction-level region, as smearing occurs between the particle level and reconstruction level. By measuring the sum of all particle-level contributions to each reconstructed region, the smearing effect of detector reconstruction is effectively modeled at the course granularity of the particle-level binning of the STXS regions. In effect, the STXS approach amounts to an *unfolding-by-fit* of Higgs boson production cross-sections.

It is desirable to split out the production of the Higgs boson to maximize sensitivity to SMEFT operators specific to a particular production mode. For instance, the gluon-gluon fusion for Higgs boson production in association with two jets radiating from the initial state has the same objects as the vector-boson fusion production of the Higgs boson. Given that the Higgs boson has a rich decay phenomenology, choosing observables that can be combined using individual channel measurements is vital.

The STXS framework is designed to perform detailed kinematic measurements of different Higgs boson production modes to maximize sensitivity within each production Higgs boson production mode while minimizing theoretical dependence. The sensitivity is achieved by extending the analysis techniques used for extracting the inclusive production modes to optimize sensitivity to different parts of the

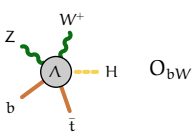

O_{bW}

phase space. The optimization is achieved by incorporating selections at the reconstruction level that match the selection of the kinematic regions defined within the STXS framework. The latter is achieved in a manner similar to the fiducial differential measurements by ensuring that the STXS regions are close to the actual phase space probed by the analyses and require minimal extrapolation. The STXS framework provides a common definition to measure Higgs boson production across different Higgs boson decay channels, which can be subsequently re-interpreted in theoretical models as shown in the schematic in Figure 5.3.

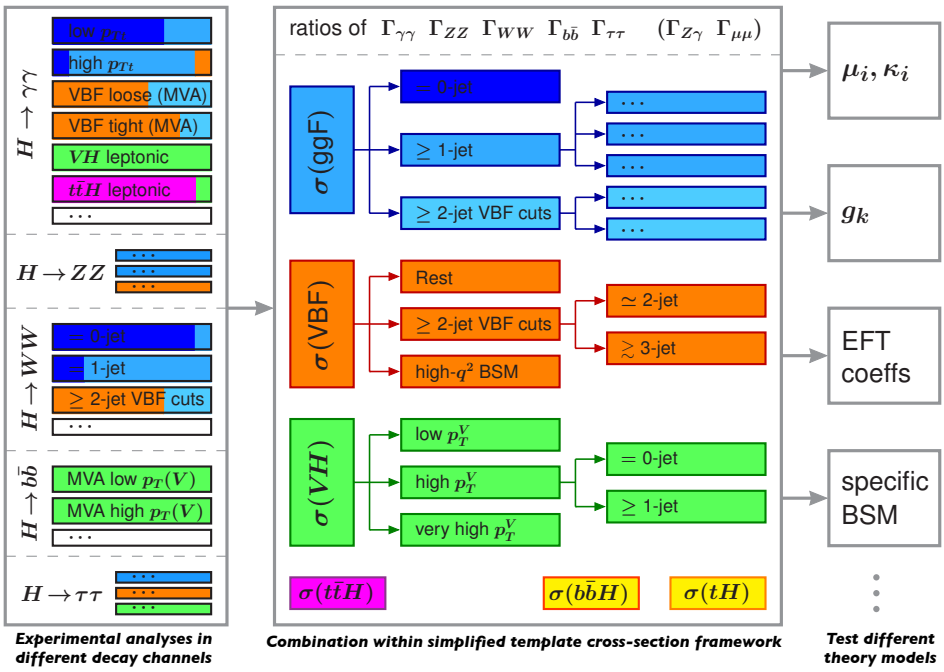

Figure 5.3: A schematic overview of the role of the simplified template cross-section taken from [88]. Different Higgs boson analyses are designed to measure parts of the phase space stated by the simplified template cross-section framework. The simplified template cross-section measurements can then be further interpreted in different theoretical models.

An important feature of the STXS framework is that it evolves with more data, allowing for finer splits in the kinematic observables. The current STXS binning, known as Stage 1.2, is described in detail in [174]. The major Higgs boson production modes are separated into the following regions,

- $gg \to H$: The kinematic bins for the $gg \to H$ mode are shown in Figure 5.4. These bins include both the virtual and real electroweak corrections, for instance, from the $gg \to Z(\to q\bar{q})H$ process. The cross-section is first split into a

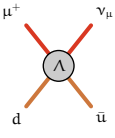

low-p_T^H region, $p_T^H < 200$ GeV, and a high-p_T^H region, $p_T^H > 200$ GeV, which is sparsely populated but sensitive to SMEFT effects from high-momentum transfer. The low-p_T^H region contains most of the inclusive cross-section and is further divided into regions with different jet multiplicities, i.e., 0-jet, 1-jet, and $\geqslant$ 2-jet regions.

- $qq \to Hqq$**:** The $qq \to Hqq$ kinematic bins are shown in Figure 5.4. These bins include the vector boson fusion mode in the t-channel and the $pp \to V(\to q\bar{q})H$ process known as the VH-hadronic mode in the s-channel. These modes are distinguished by employing a kinematic selection relying mainly on the invariant mass of the di-jet system, m_{jj}. Events are first separated by jet multiplicity, where a jet is expected to have a transverse momentum of at least $p_T{}^{jet} \geqslant 30$ GeV. The $\geqslant 2$ jet region can be studied well experimentally and is divided further into regions with into $m_{jj} > 350$ GeV and $m_{jj} < 350$ GeV. The $m_{jj} < 350$ GeV region is further split into finer bins in m_{jj}. The 60 GeV$< m_{jj} <$ 120 GeV targets the VH-hadronic mode. The remaining bins within this region are expected to contain many events from the ggF+2jet production mode. Measurements of the $m_{jj} > 350$ GeV allow the separation of the VBF contribution. Furthermore, the split at $p_T^H = 200$ GeV and the binning in m_{jj} allow isolating BSM effects. Selection criteria for the $\geqslant 2$ jet region in this process are aligned with those for the ggH+2-jets STXS bin to decorrelate the measurement of the two regions better and handle theoretical due to signal acceptance.
- $V(\mathrm{leptonic})H$**:** For the V(leptonic)H-production mode, the Higgs boson is produced in association with a vector boson that decays leptonically. The STXS binning for this shown in Figure 5.5, where it is split into three processes, $q\prime\bar{q} \to W(\to l\nu)H$, $q\bar{q} \to Z(\to l^+l^-)H$, and $gg \to Z(\to l^+l^-)H$. The hadronic decays of the weak boson are covered by the $qq \to Hqq$ and the $gg \to H$ STXS region. There is a further separation depending on the leptonic channel, which allows the separation of the WH and ZH production modes. Within these bins, the kinematic splitting in the transverse momentum of the associated vector boson, p_T^W or p_T^Z, provides a proxy for the transverse momentum of the recoiling Higgs boson. This observable is sensitive to momentum-dependent deviations from the Standard Model. There are further splits within the p_T^V regions into different jet multiplicities.
- $t\bar{t}H$**:** The Higgs boson production in association with a top-anti-top quark pair, ($t\bar{t}H$), is split into kinematic bins of the transverse momentum of the Higgs boson and is shown in Figure 5.5. This observable is a good proxy to the energy transfer of the $t\bar{t}H$ system and does not rely on top quark reconstruction.

The remaining rare production modes are either probed inclusively or merged into previously defined STXS categories. The Higgs boson production associated with a single top or anti-top quark (tH) is a separate inclusive bin. The contribution of

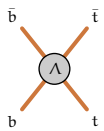

$O_{tb}^{(8)}$

the Higgs boson production in association with bottom-anti-bottom quarks, $b\bar{b}H$, is merged into the $gg \to H$ bins.

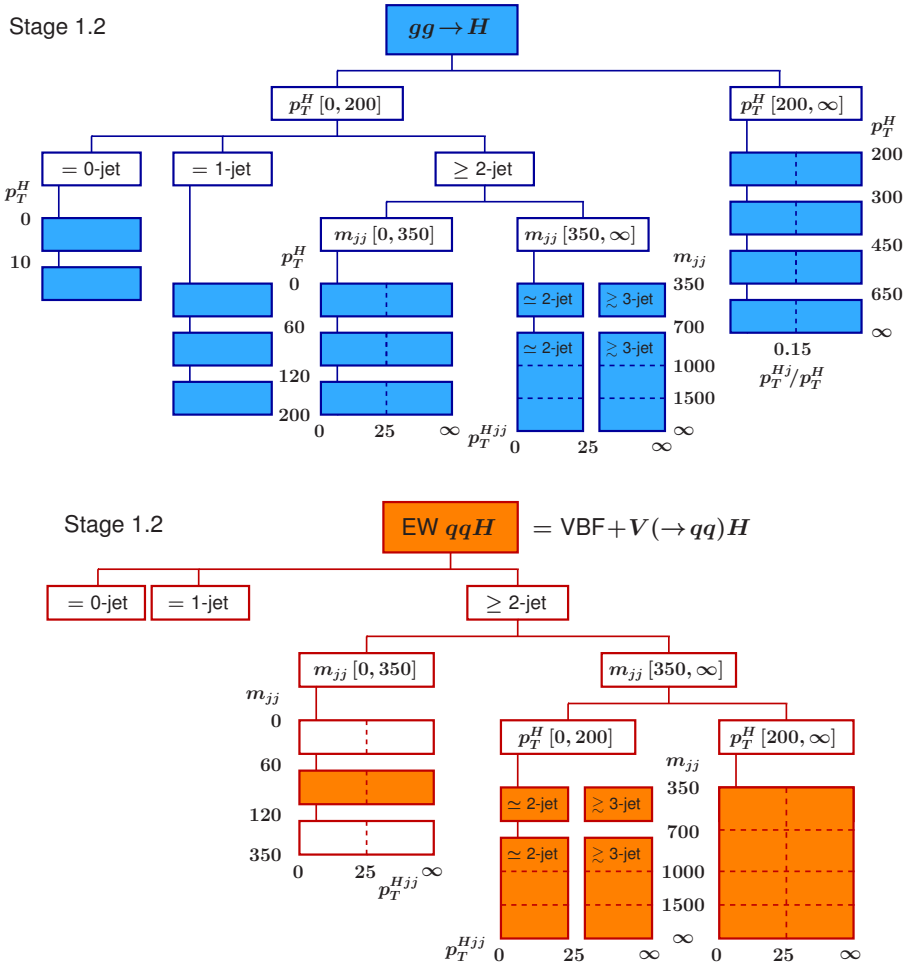

Figure 5.4: A schematic overview of the role of the simplified template cross-section taken from [88]. Different Higgs boson analyses are designed to measure parts of the phase space stated by the simplified template cross-section framework. The simplified template cross-section measurements can then be further interpreted in different theoretical models.

All kinematic splits are chosen carefully with experimental considerations in mind and are expected to capture multiple modifications arising in the SMEFT framework. Many of the chosen observables, e.g., p_T^H, p_T^V, m_{jj}, provide access to momentum transfer of the process and their distributions are thus sensitive to deviations from beyond the Standard Model in the highly energetic regime. However, these

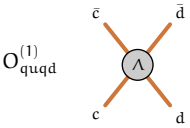

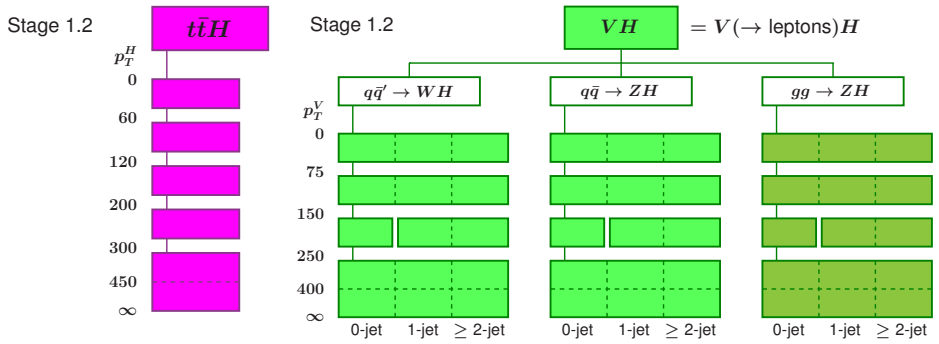

Figure 5.5: A schema of the kinematic bins in the STXS framework for the ttH and the VH production mode.

considerations are not necessarily expected to be fully optimized for measuring SMEFT parameters. For instance, the STXS framework contains only kinematic splitting and event properties pertaining to Higgs boson production. There is no information on the decay, only the possibility to measure the branching ratios of the Higgs boson decays.

In the STXS framework, it is generally assumed that the acceptance and the event reconstruction efficiency are not affected by SMEFT operators. However, Higgs boson decay kinematics can also be strongly modified by SMEFT operators and can result in sizeable changes in the acceptance, in particular for 4-body decays, such as $H \rightarrow ZZ^* \rightarrow 4l$. These effects are discussed later in Section 5.3.3. All STXS cross-sections are CP-even observables and hence do not have sensitivity to the interference of CP-odd operators with the Standard Model.

5.2 SMEFT prediction for observables

SMEFT provides a theoretically elegant language to consistently interpret a large class of new physics effects across different observables. The cross-section dependence of all relevant Wilson coefficients affecting the observables must be known to set constraints on SMEFT. The observable distributions at different configurations of Wilson coefficient parameters are estimated through Monte Carlo simulations. SMEFT Universal FeynRules Output (UFO) models such as `SMEFTsim 3.0` [175, 176], `SMEFTatNLO` [177] can be interfaced with Monte-Carlo generators such as MadGraph5_aMC@NLO [178] for the hard-scatter process and subsequently with Pythia [179] for showering to obtain the particle-level events of the observables for a particular configuration of the Wilson coefficients. If needed, these

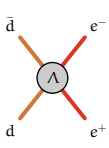

$O_{lq}^{(3)}$

events can be passed through detector simulation to obtain the observable distribution at the detector level.

The Wilson coefficients are coupling strengths accompanying each operator in an effective Lagrangian. The SMEFT Lagrangian from Equation 2.43 consists of an expansion in terms of the inverse of the new physics scale, Λ where terms are ordered in powers of $1/\Lambda$. From the matrix element relation, the square of the matrix element amplitude ($\mathcal{A}$) gives the cross-section in terms of the Wilson coefficients. Considering only dimension-6 operators, the cross-section can be written as

$$\begin{aligned}\sigma_{\text{SMEFT}} \propto |\mathcal{A}_{\text{SMEFT}}|^2 &= |\mathcal{A}_{\text{SM}} + \sum_i \mathcal{A}_i^{(6)}|^2 \\ &= |\mathcal{A}_{\text{SM}}|^2 \\ &\quad + \sum_i \frac{c_i^{(6)}}{\Lambda^2} 2\text{Re}\left(\mathcal{A}_i^{(6)} \mathcal{A}_{\text{SM}}^*\right) \\ &\quad + \sum_i \frac{\left(c_i^{(6)}\right)^2}{\Lambda^4} |\mathcal{A}_i^{(6)}|^2 + \sum_{i<j} \frac{c_i^{(6)} c_j^{(6)}}{\Lambda^4} 2\text{Re}\left(\mathcal{A}_i^{(6)} \mathcal{A}_j^{(6)*}\right).\end{aligned} \tag{5.1}$$

Thus, the observables' cross-sections are parametric functions of the Wilson coefficients. The cross-section predictions for any process in SMEFT can be broken down into three separate parts:

$$\sigma_{\text{SMEFT}} = \sigma_{\text{SM}} + \sigma_{\text{int}} + \sigma_{\text{BSM}}, \tag{5.2}$$

where σ_{SM} is the SM cross-section, σ_{int} describes the interference between the SMEFT operators and SM operators and is linear in the Wilson coefficients. The σ_{BSM} term involves cross-section contributions of SMEFT operators that is quadratic in the Wilson coefficients.

To reduce the perturbative QCD uncertainty on the extraction of the SMEFT Wilson coefficients, the parametrization of the predicted cross-section of Equation 5.2 is computed as a relative correction to the SM prediction computed at the highest available order for each process:

$$\sigma_{\text{SMEFT}} = \sigma_{\text{SM}}^{(\text{(N)N)NLO}} \times \left(1 + \frac{\sigma_{\text{int}}^{\text{(N)LO}}}{\sigma_{\text{SM}}^{\text{(N)LO}}} + \frac{\sigma_{\text{BSM}}^{\text{(N)LO}}}{\sigma_{\text{SM}}^{\text{(N)LO}}}\right). \tag{5.3}$$

This calculation strategy assumes that higher-order terms have the same relative effect on σ_{int} and σ_{BSM} as on σ_{SM} [180].

When considering only dimension-6 operators, it follows from Equation 5.2 that σ_{int} consists of terms involving the interference of the dimension-6 operator with

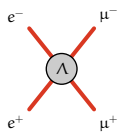

Standard Model, suppressing each term by a factor Λ^{-2}. The σ_{BSM} terms involve interference of dimension-6 operators with each other, resulting in a suppression by a factor Λ^{-4}. The lowest-order cross-section terms generated by dimension-8 operators that involve interference between SM and dimension-8 SMEFT operators are also suppressed by a factor Λ^{-4}. As no complete calculations are available yet for dimension-8 operators, it is not considered in the analyses presented in the thesis.

From Equation 5.1, any observable O_b, for example, the cross-section of a given process in a measurement bin b, can be expressed as

$$O_b = O_b^{SM}\left(1 + \sum_i A_{bi}c_i + \sum_i B_{bi}c_i^2 + \sum_{i<j} C_{bij}c_ic_j\right), \tag{5.4}$$

where O_b^{SM} is the SM value and A_{bi}, B_{bi}, and C_{bij} correspond to the linear, quadratic, and cross-term weights of the polynomial relative to the SM value. Once the values of A_{bi}, B_{bi}, and C_{bij} are known, a continuous prediction of O_b in terms of the Wilson coefficients is available.

SMEFT UFO models in `Madgraph` allow for generating separate contributions of the matrix element squared, $|\mathcal{A}_{SMEFT}|^2$ by making use of the syntax that allows separating the different terms that arise from the matrix element squared in Equation 5.1. For instance in `SMEFTsim` [70, 175], `NP^2==0,1,2` allows to separately obtain the distribution of σ_{SM}, σ_{int}, and σ_{BSM} in Equation 5.2 respectively. Being able to separately generate the different contributions containing the information of A_{bi}, B_{bi}, and C_{bij} is crucial to extracting these weights.

For the linear contribution, σ_{int}, the term A_{bi} for a particular Wilson coefficient c_i can be extracted by setting all but c_i to zero and using the squared order syntax `NP^2==1`. For the squared term of the same operators, which contributes to σ_{BSM}, the term B_{bi} for a particular Wilson coefficient, c_i is extracted by setting all but c_i to zero and using the squared order syntax `NP^2==2`. For the cross term, the `NP^2==2` syntax can be used alongside turning on the two relevant coefficients at a time, which then contains a distribution including the C_{bij} contribution alongside B_{bi} and B_{bj} contributions.

In the latest version of `SMEFTsim 3.0` [70], it is furthermore possible to combine the `NP^2` syntax alongside squared order syntax per operators. For instance, the cross term C_{bij} contribution can be directly extracted from the generator by using the `NP^2==2 NPci^2==1 NPcj^2==1`, where `ci, cj` correspond to syntactic names of the Wilson coefficients c_i and c_j, respectively.

The morphing principle [181] generalizes this concept, providing the parametric prediction of Equation 5.4 for a set of independent samples sampled at arbitrary points in the SMEFT parameter space. The morphing method is discussed later in

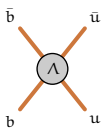

$O_{bu}^{(1)}$

the chapter alongside the C++ implementation within the RooFit package as the RooLagrangianMorphFunc class [4].

5.3 SMEFT parametrization of Higgs boson measurements

The spin-0 Higgs boson is a narrow-width particle, given the large difference between the mass and the decay width, i.e., $m_H \gg \Gamma_H$. In the narrow width approximation, and with vanishing quantum numbers, no information can be transferred between the production and the decay vertex other than the four-momenta $\boldsymbol{p}_H$ of the Higgs boson. The cross-section prediction of Higgs boson production and decay factorizes into the prediction of the cross-section for Higgs boson production $\sigma_{i\to H}$, as a function of its four-momenta, and the branching ratio $\mathcal{B}^{H\to X}$ of the Higgs boson decay, which can be evaluated in its rest frame as the ratio of the partial decay width $\Gamma^{H\to X}$ and the total width of the Higgs boson Γ^H:

$$\sigma^{i\to H\to X}(\boldsymbol{p}_H) \approx \sigma^{i\to H}(\boldsymbol{p}_H)\cdot\mathcal{B}^{H\to X} = \sigma^{i\to H}(\boldsymbol{p}_H)\cdot\frac{\Gamma^{H\to X}}{\Gamma^H}. \tag{5.5}$$

The decay widths $\Gamma^{H\to X}$ and Γ^H, similar to cross-sections, are directly related to the square of the matrix element amplitude, and their SMEFT dependence can be modeled using Equation 5.1. The complete process $\sigma^{i\to H\to X}$ can thus be expressed in terms of individual components $\sigma^{i\to H}$, $\Gamma^{H\to X}$ and Γ^H, each expressed as polynomials of the Wilson coefficients.

To make a cross-section prediction for the signal at the detector level, the smearing of particle-level distributions to reconstruction-level must be explicitly modeled using a confusion matrix ϵ_{ij} that expresses the fraction of events in truth bin j that end up being measured in bin i at the detector level. Then, after adding the background estimate, the prediction for the expected event count in a reconstruction-level bin-i becomes

$$\begin{aligned} N_i^{\text{det.}} &= N_i^{\text{bkg.,det.}} + N_i^{\text{sig.,det.}} && (5.6)\\ &= N_i^{\text{bkg.,det.}} + \sum_j \epsilon_{ij} N_j^{\text{sig.,truth}} && (5.7)\\ &= N_i^{\text{bkg.,det.}} + \sum_j \epsilon_{ij}\frac{1}{\mathcal{L}'}\sigma_j\cdot\mathcal{B}. && (5.8)\end{aligned}$$

Here, $N_i^{det.}$ is the total number of events reconstructed in the detector, $N_i^{\text{bkg.,det.}}$ is the number of reconstructed background events, $\mathcal{L}'$ is the luminosity, σ_j is the Higgs boson production cross-section for truth bin j and $\mathcal{B}$ is the branching ratio

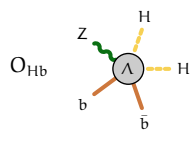

of the Higgs boson decay. In this thesis, the STXS framework is used to study the properties of the Higgs boson.

The dependence of the STXS production cross-section and decay of the Higgs boson in terms of the Wilson coefficients of SMEFT operators is captured by polynomial functions. For each STXS region, a polynomial function is used to express the kinematic dependence of the cross-section on the Wilson parameters. The partial and total decay width also correspond to polynomials in terms of the Wilson coefficients. The origin of the polynomial structure of the cross-sections in terms of the Wilson coefficients is discussed earlier in Section 5.2. The factorized approach to the modeling production and decay separately allows reducing the number of EFT samples required from $O(N_{\text{production}} \times N_{\text{decay}})$ to $O(N_{\text{production}} + N_{\text{decay}})$, where $N_{\text{production}}$ and N_{decay} denote the number of Higgs boson production modes and decay channels for which the parametrization is estimated.

The impact of SMEFT operators on production and decay, therefore, also factorizes and can be derived independently. Thus, the cross-section for a given Higgs boson production process i in the particle-level region k' and for a given decay mode $H \to X$ is

$$(\sigma\times\mathcal{B})^{i,k',H\to X}_{\text{SMEFT}} = \sigma^{i,k'}_{\text{SMEFT}} \times \mathcal{B}^{H\to X}_{\text{SMEFT}} = \left(\sigma^{i,k'}_{\text{SM}} + \sigma^{i,k'}_{\text{int}} + \sigma^{i,k'}_{\text{BSM}}\right) \times \left(\frac{\Gamma^{H\to X}_{\text{SM}} + \Gamma^{H\to X}_{\text{int}} + \Gamma^{H\to X}_{\text{BSM}}}{\Gamma^{H}_{\text{SM}} + \Gamma^{H}_{\text{int}} + \Gamma^{H}_{\text{BSM}}}\right).$$

The factorized SMEFT prediction is calculated with ratios, as in Equation 5.3 to utilize the SM prediction at the highest available order:

$$(\sigma\times\mathcal{B})^{i,k',H\to X}_{\text{SMEFT}} = (\sigma\times\mathcal{B})^{i,k',H\to X}_{\text{SM,(N(N))NLO}} \left(1 + \frac{\sigma^{i,k'}_{\text{int,(N)LO}}}{\sigma^{i,k'}_{\text{SM,(N)LO}}} + \frac{\sigma^{i,k'}_{\text{BSM,(N)LO}}}{\sigma^{i,k'}_{\text{SM,(N)LO}}}\right) \left(\frac{1 + \frac{\Gamma^{H\to X}_{\text{int}}}{\Gamma^{H\to X}_{\text{SM}}} + \frac{\Gamma^{H\to X}_{\text{BSM}}}{\Gamma^{H\to X}_{\text{SM}}}}{1 + \frac{\Gamma^{H}_{\text{int}}}{\Gamma^{H}_{\text{SM}}} + \frac{\Gamma^{H}_{\text{BSM}}}{\Gamma^{H}_{\text{SM}}}}\right), \quad (5.9)$$

where the ratios $\sigma_{\text{int}}/\sigma_{\text{SM}}$ and $\Gamma_{\text{int}}/\Gamma_{\text{SM}}$ have a linear dependence on SMEFT operators and are suppressed by a factor Λ^{-2}, and the ratios $\sigma_{\text{BSM}}/\sigma_{\text{SM}}$ and $\Gamma_{\text{BSM}}/\Gamma_{\text{SM}}$ have a quadratic dependence on SMEFT operators are suppressed by a factor Λ^{-4}. In the analysis, these ratios are parametrized as

$$\frac{\sigma^{i,k'}_{\text{int}}}{\sigma^{i,k'}_{\text{SM}}} = \sum_j A_j^{\sigma_{i,k'}} c_j \qquad \frac{\sigma^{i,k'}_{\text{BSM}}}{\sigma^{i,k'}_{\text{SM}}} = \sum_{j,l\geqslant j} B_{jl}^{\sigma_{i,k'}} c_j c_l \quad (5.10)$$

$$\frac{\Gamma^{H\to X}_{\text{int}}}{\Gamma^{H\to X}_{\text{SM}}} = \sum_j A_j^{\Gamma^{H\to X}} c_j \qquad \frac{\Gamma^{H\to X}_{\text{BSM}}}{\Gamma^{H\to X}_{\text{SM}}} = \sum_{j,l\geqslant j} B_{jl}^{\Gamma^{H\to X}} c_j c_l \quad (5.11)$$

$$\frac{\Gamma^{H}_{\text{int}}}{\Gamma^{H}_{\text{SM}}} = \sum_j A_j^{\Gamma^{H}} c_j \qquad \frac{\Gamma^{H}_{\text{BSM}}}{\Gamma^{H}_{\text{SM}}} = \sum_{j,l\geqslant j} B_{jl}^{\Gamma^{H}} c_j c_l, \quad (5.12)$$

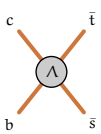

$O^{(8)}_{\text{utbd}}$

with

$$A_j^{\Gamma^H} = \frac{\sum_X \Gamma_{SM}^{H\to X} A_j^{\Gamma^{H\to X}}}{\sum_X \Gamma_{SM}^{H\to X}} \qquad B_{jl}^{\Gamma^H} = \frac{\sum_X \Gamma_{SM}^{H\to X} B_{jl}^{\Gamma^{H\to X}}}{\sum_X \Gamma_{SM}^{H\to X}}. \tag{5.13}$$

In Equation 5.13 all Higgs boson decay modes X with up to four final-state particles are included in the sum. All $A_j^{\sigma_{i,k'}}$, $A_j^{\Gamma^{H\to X}}$, $B_{jl}^{\sigma_{i,k'}}$ and $B_{jl}^{\Gamma^{H\to X}}$ coefficients are constant factors obtained from simulation that express the sensitivity of the process to the operators $\mathcal{O}_j$ and $\mathcal{O}_l$ that correspond to the Wilson coefficients c_j and c_l, where the indices j, l run over all non-negligible operators. The coefficients A_j and B_{jl} are proportional respectively to Λ^{-2} and Λ^{-4}. The values of all SM Higgs branching ratios that enter Equation 5.13 are taken from [88].

In the absence of calculations of dimension-8 operators, the SMEFT expansion is considered valid when the parametrization, including the quadratic terms, approximates the linear parametrization well. Conversely, in case of a difference between the two, missing higher-dimension contributions are expected to have a considerable contribution, and would have to be included to ensure expansion validity. Both such cases are shown in Figure 5.6 where for the $gg \to H, N_{jets} = 0, p_T^H < 10$ region the c_{HG} parametrization agrees between the linear and linear + quadratic case. For the $ZH, p_T^V \geqslant 250$ region, the $c_{Hq}^{(3)}$ parametrization exhibits a difference between the linear and linear + quadratic case. In this thesis, results from two

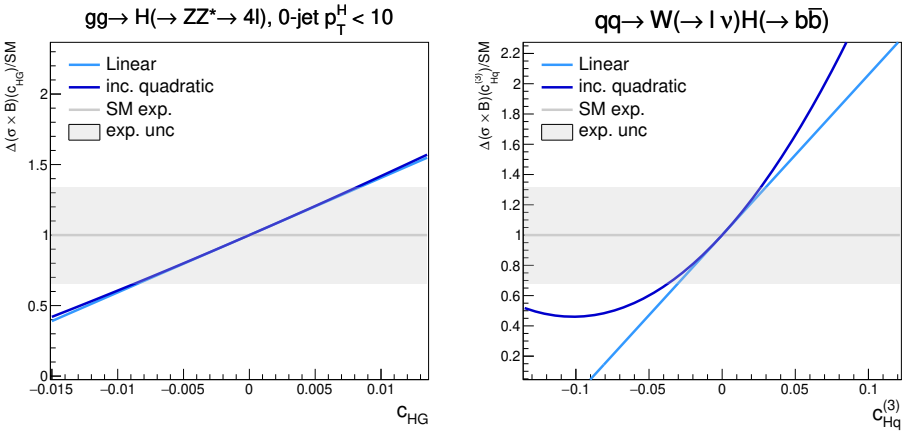

(a) (b)

Figure 5.6: The dependence of the SMEFT modifier for the $gg \to H, N_{jets} = 0, p_T^H < 10$ in $H \to \gamma\gamma$ channel for c_{HG} (left) and the $ZH, p_T^V \geqslant 250$ in $H \to b\bar{b}$ channel for $c_{Hq}^{(3)}$ (right) for both the linear and the linear + quadratic parametrization. The expected SM uncertainty is shown in gray for the two regions.

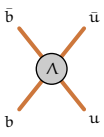

$O_{Qq}^{(1,1)}$

statistical models are constructed for the interpretation of the data,

- *linear* : a linearized variant considering terms suppressed by up to a factor Λ^{-2}.
- *linear and quadratic terms* : Here the quadratic terms of dimension-6 operators entering the production, partial width, and total width are included. Although this is an incomplete parametrization at $O(\Lambda^{-4})$ due to missing contributions from dimension-8 operators, it gives an estimate of the size of the $\mathcal{O}(\Lambda^{-4})$ corrections.

5.3.1 Cross-section calculation with linear terms

In a scenario where Λ^{-4}-suppressed contributions are ignored, the predicted deviation of the cross-section, partial width and total width from their SM values can each be explicitly linearized as a function of the Wilson coefficients $\boldsymbol{c}$. Ignoring all Λ^{-4}-suppressed BSM terms in Equation 5.9, and using the parametrization of Equations 5.10 to 5.12, the expression for the cross-section times branching ratio reduces to

$$\begin{aligned}
(\sigma\times\mathcal{B})^{i,k',H\to X}_{\text{SMEFT}} &= (\sigma\times\mathcal{B})^{i,k',H\to X}_{\text{SM,((N)N)NLO}} \times \left(1+\frac{\sigma^{i,k'}_{\text{int,(N)LO}}}{\sigma^{i,k'}_{\text{SM,(N)LO}}}\right) \times \left(\frac{1+\frac{\Gamma^{H\to X}_{\text{int}}}{\Gamma^{H\to X}_{\text{SM}}}}{1+\frac{\Gamma^{H}_{\text{int}}}{\Gamma^{H}_{\text{SM}}}}\right) \\
&= (\sigma\times\mathcal{B})^{i,k',H\to X}_{\text{SM,((N)N)NLO}} \times \left(1+\sum_j A_j^{\sigma_{i,k'}} c_j\right) \times \left(\frac{1+\sum_j A_j^{\Gamma^{H\to X}} c_j}{1+\sum_j A_j^{\Gamma^{H}} c_j}\right), \\
&= (\sigma\times\mathcal{B})^{i,k',H\to X}_{\text{SM,((N)N)NLO}} \times \left(\frac{1+\sum_j \left(A_j^{\sigma_{i,k'}}+A_j^{\Gamma^{H\to X}}\right) c_j + O\left(\Lambda^{-4}\right)}{1+\sum_j A_j^{\Gamma^{H}} c_j + O\left(\Lambda^{-4}\right)}\right),
\end{aligned} \tag{5.14}$$

where all higher-order terms in the expansion are suppressed by power Λ^{-4} or beyond.

A subsequent Taylor expansion of the width ratio expression of Equation 5.14 and truncation of terms beyond Λ^{-2} would result in a completely linearized expression for $\sigma\times\mathcal{B}$ where,

$$(\sigma\times\mathcal{B})^{i,H\to X}_{\text{SM}+\Lambda^{-2}} =$$

$$(\sigma\times\mathcal{B})^{i,H\to X}_{\text{SM,((N)N)LO}} \times \left(1+\sum_j A_j^{\sigma_i} c_j + \sum_j A_j^{\Gamma^{H\to X}} c_j - \sum_j A_j^{\Gamma^{H}} c_j\right) \tag{5.15}$$

$$= (\sigma\times\mathcal{B})^{i,H\to X}_{\text{SM,((N)N)LO}} \times \left(1+\sum_j \left(A_j^{\sigma_i}+A_j^{\Gamma^{H\to X}}-A_j^{\Gamma^{H}}\right) c_j\right), \tag{5.16}$$

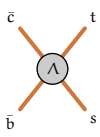

$O^{(1)}_{qQtu}$

where all terms beyond $O(\Lambda^{(-4)})$ are dropped. However, as the parametric dependence of a Wilson coefficient in a branching fraction f is effectively of the form $c/(1+f\cdot c)$, the linearity in c of this expression assumed for small values of c does not hold for large values of c. This effect is particularly pronounced for operators affecting Higgs boson decays with a large branching fraction, e.g., $c_{H\Box}$, c_{bH}, and operators that have a large measured uncertainty that allows large values of c in the error propagation. The parametrization for the $gg \to H, H \to \gamma\gamma$ is shown for $c_{H\Box}$ and c_{tG} in Figure 5.7 where the linearized parametrization is shown to be valid for small values of the Wilson coefficient.

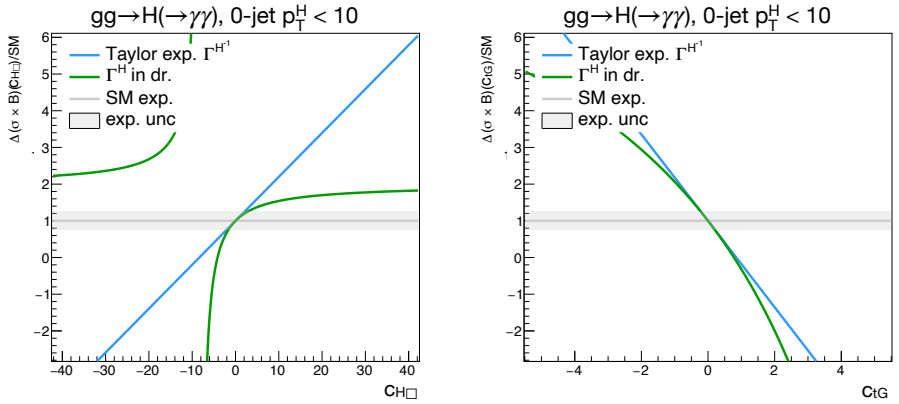

(a) (b)

Figure 5.7: The dependence of the SMEFT modifier for the $gg \to H, N_{jets} = 0, p_T^H < 10$ in $H \to \gamma\gamma$ channel for $c_{H\Box}$ (left) and c_{tG} (right) for both the linear parametrization with (blue) and without (green) the Taylor expansion of the Higgs total width parametrization. The expected SM uncertainty is shown in gray.

For the latest results presented in Chapter 7 the linear parametrization of Equation 5.14 is used whereas the other results in Chapters 6, 8, and 9 use the fully linearized parametrization of Equation 5.16.

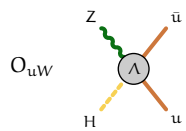

5.3.2 Cross-section calculation with linear and quadratic terms

The SMEFT prediction, including the available terms proportional to Λ^{-4} is:

$$(\sigma\times\mathcal{B})^{i,k',H\to X}_{\text{SMEFT}} = (\sigma\times\mathcal{B})^{i,k',H\to X}_{\text{SM,((N)N)NLO}}\left(1+\sum_j A_j^{\sigma\,i,k'}c_j+\sum_{j,l\geqslant j}B_{jl}^{\sigma\,i,k'}c_jc_l\right)\left(\frac{1+\sum_j A_j^{\Gamma\,H\to X}c_j+\sum_{j,l\geqslant j}B_{jl}^{\Gamma\,H\to X}c_jc_l}{1+\sum_j A_j^{\Gamma\,H}c_j+\sum_{j,l\geqslant j}B_{jl}^{\Gamma\,H}c_jc_l}\right), \tag{5.17}$$

$$= (\sigma\times\mathcal{B})^{i,k',H\to X}_{\text{SM,((N)N)NLO}}\cdot \left(\frac{1+\sum_j\left(A_j^{\sigma\,i,k'}+A_j^{\Gamma\,H\to X}\right)c_j+\sum_{j,l\geqslant j}\left(B_{jl}^{\sigma\,i,k'}+B_{jl}^{\Gamma\,H\to X}+A_j^{\sigma\,i,k'}A_l^{\Gamma\,H\to X}+A_l^{\sigma\,i,k'}A_j^{\Gamma\,H\to X}\right)c_jc_l+O\left(\Lambda^{-6}\right)}{1+\sum_j\left(A_j^{\Gamma\,H}\right)c_j+\sum_{j,l\geqslant j}\left(B_{jl}^{\Gamma\,H}\right)c_jc_l+O\left(\Lambda^{-6}\right)}\right) \tag{5.18}$$

where both numerator and denominator are a second-order Taylor expansion resulting in a linearized expression for terms of order Λ^{-2} and a quadratic expression for terms of order Λ^{-4}. Similar to Equation 5.14, and for the same reason, the width ratio expression in Equation 5.18 is not subjected to a further Taylor expansion.

Additional terms suppressed by a factor Λ^{-4} occur in the general SMEFT expansion of Equation 2.43, *i.e.* the lowest-order cross-section terms generated by dimension-8 operators that involve interference between SM and these operators. As only a subset of Higgs processes have been calculated with dimension-8 operators [182–184], the list of terms suppressed by a factor Λ^{-4} considered is incomplete, and the effect of the missing dimension-8 terms relative to σ_{BSM} is not known in general. However, their effect may be of a magnitude comparable to that of products of two dimension-6 SMEFT operators, as the suppression factor is of the same order. For this reason, SMEFT interpretations are performed both with and without the σ_{BSM} contribution to give a general indication of the sensitivity of the analysis to Λ^{-4} terms.

5.3.3 Assumptions on SM Higgs boson kinematics

With the insertion of the SMEFT cross-section predictions of Equation 5.14 or 5.18 in Equation 5.8 describing the yield N_k, the effect of SMEFT cross-section modifications on the inclusive Higgs boson signal yield for each particle-level region k' is fully taken into account for every reconstruction-level region k. However, the SMEFT operators may also affect other terms of the event yield, such as the efficiency-times-acceptance factors ϵ_{ij} occurring in Equation 5.8.

In both the linear and linear+quadratic SMEFT models, it is assumed that the theoretical systematic uncertainties assigned to the acceptance factors ϵ_{ij}, which are fully taken into account in the SM cross-section prediction, cover the possible acceptance changes induced by SMEFT operators in Higgs boson production through

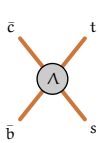

$O^{(8)}_{\text{qu}Qb}$

the full validity range of the SMEFT model. This assumption is motivated by the similarity of reconstruction-level analysis regions to STXS and differential fiducial regions, which are designed to be relatively insensitive to acceptance changes induced by SMEFT operators. In addition, the rather fine binning of the Stage-1.2 STXS regions further reduce the possibility of significant variations of the acceptance factors inside each region. The effect of SMEFT operators on other observables used in the definition of the analysis regions, e.g., through multivariate discriminants, is assumed to be negligible.

The effect of SMEFT operators on Higgs boson decays can strongly affect the acceptance factors ϵ_{ij}^{X}, since decays are not limited to a restricted fiducial phase space in the STXS framework. For 2-body decays, such acceptance effects are generally small. However, the four-body $H \to ZZ^* \to 4\ell$ and $H \to WW^* \to \ell\nu\ell\nu$ decays are significantly impacted by acceptance effects for these decays the impact factors $A_j^{H\to X}$ and $B_{jl}^{H\to X}$ are recalculated, including an approximate implementation of the reconstruction-level requirements at the particle level.

Finally, if the signal yield distribution inside an analysis region deviates from the SM distribution the measured yield may be biased. This effect is expected to be negligible for all regions where the discriminant observable inside the region is the reconstructed invariant mass of the Higgs boson, which is largely unaffected by SMEFT operators. Regions that feature a multivariate discriminant as observable can potentially be more affected by SMEFT-induced shape differences but are only used in regions with low signal yields where it is assumed that any effect induced by signal shape deviations is small compared to the statistical uncertainties.

5.4 Statistical Model

To be able to infer the SMEFT model parameters from an observed dataset, a statistical model that quantifies the probability of all possible observable experimental outcomes must be formulated. The *likelihood function* is constructed to perform statistical inference and is the joint probability of observed data viewed as a function of the parameters of a statistical model. The most common and simplest form of a likelihood function for observed particle physics data is that for a counting experiment in a phase-space region, which is characterized by a Poisson distribution and features one observable - the event count N_{obs} - and one parameter, the expected event count N_{exp}, and is given by

$$\text{Poisson}(N_{obs}|N_{exp}) = \frac{(N_{exp})^{N_{obs}}}{(N_{obs})!} e^{-N_{exp}}. \tag{5.19}$$

In practice, the expected event count N_{exp} is expressed in terms of an expected signal count s and expected background count b, and parameter μ is introduced

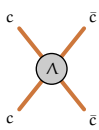

by multiplying the nominal signal count s, so that it expresses deviations from this nominal expectation in a fit to the data, i.e. $N_{exp} = \mu * s + b$. From this basic building block, a probability model for distributions can be constructed simply as the product of a Poisson likelihood for each bin in the measurement:

$$L(\boldsymbol{x}|\boldsymbol{\mu}) = \prod_{i \in \text{bins}} \text{Poisson}(N_i|\mu_i s_i + b_i), \tag{5.20}$$

where $\boldsymbol{x}$ denotes the data, N_i corresponds to the number of events in data in the bin, s_i and b_i correspond to expected signal and background events and $\boldsymbol{\mu} = \{\mu_i\}$ is the set of signal strength of the bins. Systematic uncertainties arise from experimental and theoretical sources and are modeled as nuisance parameters $\boldsymbol{\theta}$ that are incorporated into the likelihood function as

$$L(\boldsymbol{x}|\boldsymbol{\mu}, \boldsymbol{\theta}) = \prod_{i \in \text{bins}} \text{Poisson}(N_i|\mu_i s_i(\theta) + b_i(\theta)) \prod_{j \in \boldsymbol{\theta}} \text{Gauss}(0|\theta_j, 1), \tag{5.21}$$

where each nuisance parameter θ_j represents a source of systematic uncertainty. $s_i(\boldsymbol{\theta})$ and $b_i(\boldsymbol{\theta})$ include response functions that take into account the impact of the systematic sources of uncertainties. In most cases, the response function for a given nuisance parameter (θ), denoted as $\kappa_i(\theta)$, is applied to per-category event yields of signals and backgrounds as

$$\kappa_i(\theta) = \kappa_i^0 (1 + \sigma)^\theta, \tag{5.22}$$

where κ_i^0 is the nominal event yield, and σ is the variation of the event yield caused by the nuisance parameter. If several uncertainties act on the same event yield variable κ_i, several exponential factors are multiplied into κ_i^0. The shape of the response function in practice is always obtained from the study of simulation samples with and without a variation of one of the systematic uncertainties.

In the case where the uncertainty is asymmetric, a similar form is implemented using the `FlexibleInterpVar` class (with the option `icode==4`) of the `HistFactory` package [185, 186]. The asymmetric form is a generalization of Equation 5.22 where the positive uncertainty is used for σ when $\theta > 0$, and the negative uncertainty when $\theta < 0$. It also ensures a smooth transition between the two cases at $\theta = 0$. In some cases when the variation σ is small, the form

$$\kappa_i(\theta) = \kappa_i^0 (1 + \sigma\theta) \tag{5.23}$$

is used instead. The likelihood function is implemented in the ROOT software package using the `RooFit` [187] and `HistFactory` [185] toolkit.

Finally, uncertainties from finite simulation statistics that were used to calculate the nominal values of s_i and b_i are introduced. This procedure nominally intro-

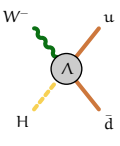

O_{Hud}

duces one additional nuisance parameter, quantifying the Poisson simulation statistics uncertainty, for each estimated s_i or b_i. This approach would result in a large number of additional parameters in a realistic model, so an approximate procedure known as *Beeston-Barlow light* is used in practice, which only models the Poisson uncertainty due to simulation statistics on the sum of all s_i and b_i counts in bin i, either as a Poisson or as Gaussian in cases the statistics are sufficiently large. This *light* procedure introduces only a single nuisance parameter for each bin and is only implemented for bins where simulation statistics are not large compared to the data statistics.

Predictions for SMEFT are introduced in the SM Poisson probability model of Equation 5.21 by replacing the parameters μ_i with the SMEFT cross-section expression divided by $(\sigma \times \mathcal{B})_{SM}$. This substitution explicitly only considers SMEFT modifications to the signal and not to the background, but corresponds to the approach chosen for all analyses covered in this thesis.

5.5 Statistical Inference

From the likelihood function, a variety of statistical inference procedures can be followed to make statements on the SMEFT model parameters. The first of these is the estimate of the parameter values for which the data is the most probable. The Maximum Likelihood Estimator procedure defines the values $\hat{\alpha}$ as those for which the likelihood function $L(\alpha)$ is maximal. In practice, this maximum-finding procedure is performed numerically using the MIGRAD method of the MINUIT2 packages [188], which minimizes the negative logarithm of the likelihood function. The MIGRAD function minimization uses the variable metric method developed by Fletcher, Davidon, and Powell [189, 190].

Uncertainties associated with these parameter point estimates can be quantified in two ways. The first method estimates the variance of the parameter estimate, calculated as the inverse of the curvature of the likelihood at the likelihood maximum expressed as the second derivative, $\partial^2 L(\alpha)/\partial\alpha^2$. In case of multiple parameters, the matrix of all second derivatives, $\{\partial^2 L(\alpha_i, \alpha_j)/\partial\alpha_i\partial\alpha_j\}$, also known as the Hessian Matrix, is inverted into the covariance matrix V_{ij}, expressing the (co)variance of all measurement parameters. Although the variance is well-defined for all sample sizes as the second moment of the parameter distribution, the customary interpretation of variance interval as corresponding to 68% is only calibrated in the asymptotic limit of Gaussian distributions.

For this reason, a second uncertainty estimation procedure is additionally deployed that has a more robust probabilistic calibration. Known as the Neyman construction, this procedure samples all possible experimental outcomes x for each parameter value α and measures in interval x that captures 68% of all possible

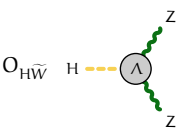

values. The volume in the (x, α) plane that is spanned by these 68% intervals in x for each value of α is known as the confidence belt. The intersection of this confidence belt with an observed value x_{obs} defines an interval in α, that is by construction, calibrated to contain the true value of α in 68% of repeated identical measurements. For complex realistic measurements, where there is far more than a single observable x that characterizes the observed data, a preprocessing step is performed: for each measurement, a *test statistic* $t_\alpha(x)$ is calculated, i.e., a function of the data, that summarized all available information into a single number, the value of $t_\alpha(x)$, which can be used in place of the nominal observable x in the Neyman construction. The Neyman-Pearson lemma states that it is possible to construct such a test statistic without loss of information by choosing a likelihood ratio as a functional form. The test statistic is given by

$$t_\alpha = -2\text{Log}\left(\frac{L(\alpha)}{L(\hat{\alpha})}\right) = -2\text{Log}\Lambda(\alpha), \tag{5.24}$$

where $\Lambda(\alpha)$ is called the profile likelihood ratio. The original Neyman-Pearson likelihood ratio does not account for the existence of nuisance parameters, which are numerous in the likelihood functions considered in this thesis. As the value of the profile likelihood, in principle, depends on the values of the nuisance parameters, a procedure must be introduced to specify their value. The convention at the LHC is to choose their best-fit value in both the numerator and denominator, i.e.,

$$\Lambda(\alpha) = \frac{L(\alpha, \hat{\hat{\theta}}(\alpha))}{L(\hat{\alpha}, \hat{\theta})}, \tag{5.25}$$

where in the numerator, the nuisance parameters correspond to their profiled values $\hat{\hat{\theta}}$, which maximizes the likelihood function of fixed values of the parameters α. In the denominator, both the parameters of interest and nuisance parameters are set to the values $\hat{\alpha}$ and $\hat{\theta}$, respectively, jointly maximizing the likelihood. In the asymptotic regime, where the likelihood is approximately Gaussian, the value of $-2\ln\Lambda(\alpha)$ follows a χ^2 distribution with the number of degrees of freedom (d.o.f) equal to the dimensionality of the vector α.

5.6 Nuisance Parameter Pruning

The likelihood function of Equation 5.21 typically contains numerous (100-1000) nuisance parameters that parametrize systematic uncertainties. As the computation time of the statistical inference techniques described in Section 5.5 scales either linearly or quadratically with the number of parameters, large numbers of model parameters can substantially slow down calculations. In practice, many nuisance parameters for a given likelihood will only contribute marginally to the total

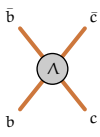

$O_{bu}^{(1)}$

uncertainty of the parameters of interest. They can be eliminated from the function with a minimal loss of accuracy in exchange for a substantial increase in computational performance. The procedure to identify these *weak* nuisance parameters is known as *pruning* and is described below.

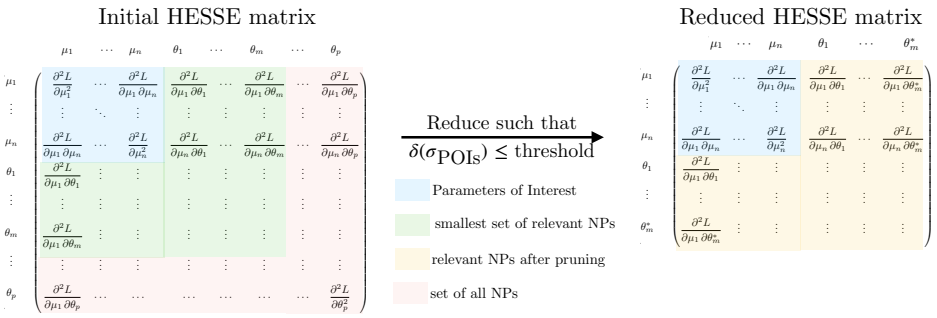

Figure 5.8: Schematic for the pruning procedure, the HESSE matrix is reduced by the aim to identify the largest set of nuisance parameters such that the change in uncertainty of the parameters of interests is less than a threshold.

For the pruning procedure, the full likelihood function is first approximated by its Hessian matrix, i.e., only the curvature exactly corresponding to the measured covariance matrix of the parameters is retained.

The HESSE matrix approximates the full likelihood function as a multivariate Gaussian. A set of nuisance parameters to prune is identified by performing a set of linear algebra operations on the HESSE matrix. A group of nuisance parameters is tested to be prunable by fixing their values and removing their uncertainty contributions to the Hessian matrix. If the collective effect of removing this group reduces the total uncertainty on the POI to less than a threshold amount, typically 1%, the group is determined to be prunable. A sketch of the reduction based on the HESSE matrix is shown in Figure 5.8. The pruning procedure is performed for the expected and the observed dataset separately, as there can be differences in the Hessian for the two cases.

In order to identify the largest set of nuisance parameters that can be pruned, it is necessary to rank each nuisance parameter by order of importance based on its impact on the parameters of interest. The following ranking method is determined to be the most effective metric in identifying the largest group of nuisance parameters based on a threshold and is given by

$$\text{Rank}(\theta_{\text{NP}}) = \max_{i \in \{\text{POIs}\}} \left\{ \left| \frac{\sigma_i^{full} - \sigma_i^{reduced}}{\sigma_i^{full}} \right| \right\}, \tag{5.26}$$

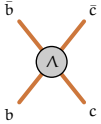

where the σ_i denotes the uncertainty of the i^{th} parameter of interest and the labels *full* and *reduced* denote the cases where the uncertainties are estimated from the full and θ_{NP}-reduced HESSE matrix, respectively. Once the rank is estimated for all nuisance parameters, the second step involves a binary search to identify the largest ranked nuisance parameter such that the group consisting of all the subsequent lower-ranked nuisance parameters does not change the uncertainty of any parameter of interest by more than the threshold.

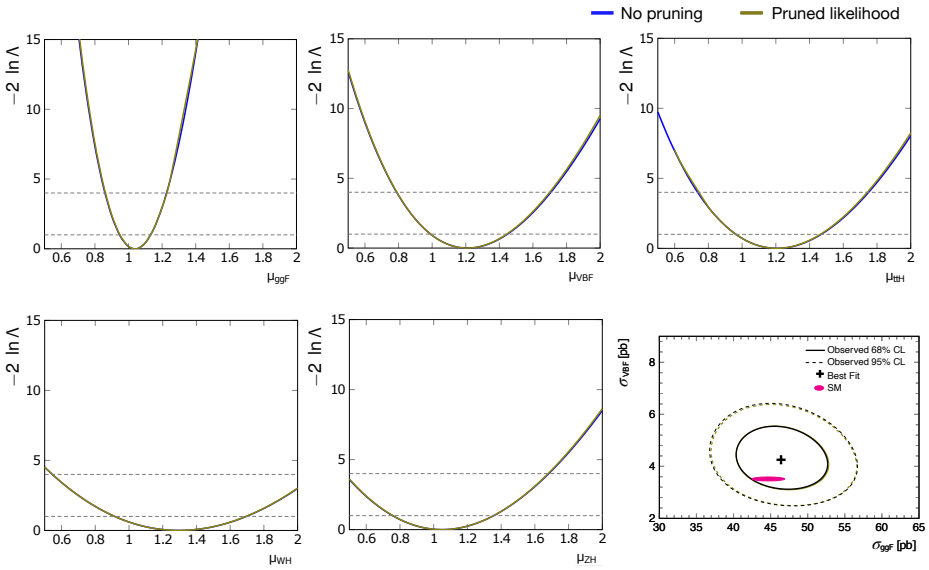

Figure 5.9: A comparison of the 1D profile likelihood scan for the pruned and full likelihood for the five parameters of interest ($\mu_{ggF}, \mu_{VBF}, \mu_{WH}, mu_{ZH}, mu_{ttH}$) and a comparison of the 2D profile likelihood scan for ($\sigma_{ggF}, \sigma_{VBF}$) where σ is the cross-section estimated by $\sigma_i = \sigma_i^{SM} \times \mu_i$.

The closure of the procedure is demonstrated on the combined statistical model of the Higgs boson analyses used to measure the signal strength of Higgs boson production cross-sections $\mu_{ggF}, \mu_{VBF}, \mu_{ttH}, \mu_{WH}, \mu_{ZH}$ based on 80 fb^{-1} of data and containing 1433 nuisance parameters in the statistical model. For a threshold of at most 1% change in the uncertainty of the parameters of interest, 914 nuisance parameters can be pruned, which resulted in a MIGRAD minimization time of 1h37min corresponding to a factor three speedup. The change in uncertainty estimates due to the pruning procedure is tabulated in Table 5.1. In this exam-

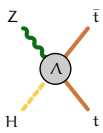

O_{tB}

POI	estimate with no pruning	relative change in central value	relative change in uncertainty
μ_{ggF}	1.0384 ± 0.0922	-0.02%	0.97%
μ_{VBF}	1.210 ± 0.228	0.17%	0.84%
μ_{WH}	1.297 ± 0.389	0.08%	0.24%
μ_{ZH}	1.049 ± 0.299	0.04%	0.42%
μ_{ttH}	1.207 ± 0.252	0.2%	0.9%

Table 5.1: The estimate of uncertainty from HESSE before and after pruning, with a threshold of at most 1% change in the uncertainty of the parameters of interest.

ple, the pruning algorithm terminated the search for the set of prunable nuisance parameters, having reached the maximum allowed change for the uncertainty on μ_{ggF}.

The impact of the pruning is checked with profile likelihood scans, as shown in Figure 5.9, which do not rely on the Hessian approximation used in the pruning and show that the contours obtained with the pruned likelihood function are very close to those obtained with the full likelihood function.

5.7 Effective Lagrangian Morphing

The effective Lagrangian morphing approach [89, 191] provides a method for modeling observable distribution as a function of the EFT parameters. It results in a continuous description of the observable in the parameter space based on the structure of the matrix elements and Monte Carlo templates provided.

The matrix element relation in Equation 5.1 is a linear combination of predicted cross-section components which correspond to phase space integrals which are scaled by the Wilson coefficients. This structure of the equation allows to describe the prediction $\sigma_{i\to f}$ as a polynomial function of the vector of couplings $\boldsymbol{c}$ with the help of individual pre-calculated phase space integrals, i.e., templates generated for some fixed EFT (scenarios A, B, ...). These integrals can be pre-computed at the truth or detector levels, the latter in case the simulation is extended to include the detector. The basis of the phase space integral is mapped to the available predictions $\{A, B, \dots\}$ with the *morphing matrix* M. The elements of the morphing matrix are composed of the coupling polynomial for the different configuration $\{A, B, \dots\}$. The coupling polynomial scales each of the phase space integrals.

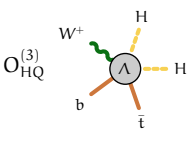

The values of the coefficient c_i for which these templates are generated do not need to follow a rigid grid-like pattern, where individual couplings would be chosen at a value of either 0 or 1.

Some Monte Carlo generators allow to separately generate each of the terms that enter Equation 5.4 as described in Section 5.2. In this case, the individual templates do not correspond to physical scenarios, but constructing the cross-section as a function of the Wilson coefficients is $\sigma(\boldsymbol{c})$ is straightforward. The morphing matrix M, in this case, is fully diagonal,

$$M = \begin{pmatrix} 1_A & & \\ & A_{X,B} & \\ & & \ddots \end{pmatrix}. \tag{5.27}$$

Where the first row in Equation 5.27 corresponds to the SM contribution generated by configuration A, second term to configuration B corresponding to the linear contribution of the cross-section that behaves as c_X as so on. In the general case that MC generators can only provide physically meaningful scenarios and not isolated terms, the morphing matrix can still be constructed from such samples. However, the matrix will acquire non-diagonal elements in that case, and sampled points in the parameter space must be chosen so that the matrix is invertible.

The phase space integrals can be inferred from the provided templates by linear algebra: The total number of predictions of $\sigma_{i\to f}$ at arbitrary coordinates $\boldsymbol{c}_A, \boldsymbol{c}_B, \ldots$ must correspond to the the number of terms in the polynomial. The general morphing matrix M is

$$M = \begin{pmatrix} 1_A & c_{X,A} & \cdots & c^2_{X,A} & \cdots & c_{X,A}c_{Y,A} & \cdots \\ 1_B & c_{X,B} & \cdots & c^2_{X,B} & \cdots & c_{X,B}c_{Y,B} & \cdots \\ \vdots & \vdots & & \vdots & \vdots & & \end{pmatrix}. \tag{5.28}$$

The complete morphing function $\sigma_{i\to f}(\boldsymbol{c})$, which provides a description of the cross-sections for any value of the couplings in terms of the available predictions $\sigma_A, \sigma_B, \ldots$, where σ denotes the cross-section of the kinematic distribution of an observable, is defined as

$$\sigma_{i\to f}(\boldsymbol{c}) = M^{-1} \cdot \begin{pmatrix} \sigma_A \\ \sigma_B \\ \vdots \end{pmatrix}, \tag{5.29}$$

and is calculable as long as the morphing matrix M is invertible. The inverse of morphing matrix allows to calculate the weights in the polynomial dependence

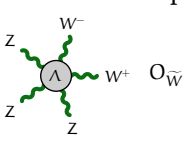

and evaluate the cross-section at any coordinate and the function $\sigma_{i\to f}(\boldsymbol{c})$ is called the *morphing function*. Invertibility on the morphing matrix can always be achieved as the couplings $\boldsymbol{c}$ can be chosen not to be a degenerate set when generating the samples.

The morphing approach is capable of extracting the cross-section components from any sufficiently robust set of pre-computed phase-space integrals for explicitly generated single integrals, corresponding to a fully diagonal morphing matrix, as well as for integrals with mixtures of different contributions as well as any combination.

5.7.1 RooFit implementation

The Effective Lagrangian Morphing methodology is implemented within the `RooFit` library [192]. `RooFit` is an object-oriented language to describe probability models and is widely used in high-energy physics. It is available within the `ROOT` software, which is an open-source data analysis framework used in high-energy physics and other domains. The `RooFit` language allows users to construct probability models of arbitrary complexity by expressing the relation between observables and probability functions as an expression tree of `RooFit` objects by designing all the relevant mathematical concepts as `RooFit` classes. The `RooLagrangianMorphFunc` software that is discussed in the following section is included from `ROOT` release v6.26 onwards.

The `RooLagrangianMorphFunc` class [4] in `RooFit` implements the Effective Lagrangian Morphing method [181] described in Section 5.7. The morphing distribution can be constructed for an arbitrary number of parameters $\boldsymbol{c}$ as long as the required number of non-degenerate samples are provided as input to the morphing function. The morphed distribution provides a continuous description of the observable distribution in the parameter space, as spelled out in Equation 5.29. The `RooLagrangianMorphFunc` implements the morphing as a sum of functions where each of the functions is given by a `RooLinearCombination` object. The `RooLinearCombination` class implements the underlying summation of weight involved for each template as a Kahan sum to reduce the loss of numeric precision that may occur in the repeated addition of a large number of summation terms.

A
`RooLagrangianMorphFunc::Config` object allows to streamline the creation of a morphing function. It can be used to configure the observable name, necessary parameters, coupling structures, and the input templates required to define a morphing function. Once created, the morphing function describes the observable distribution for any coordinate in the parameter space.

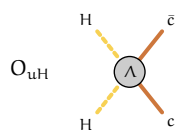

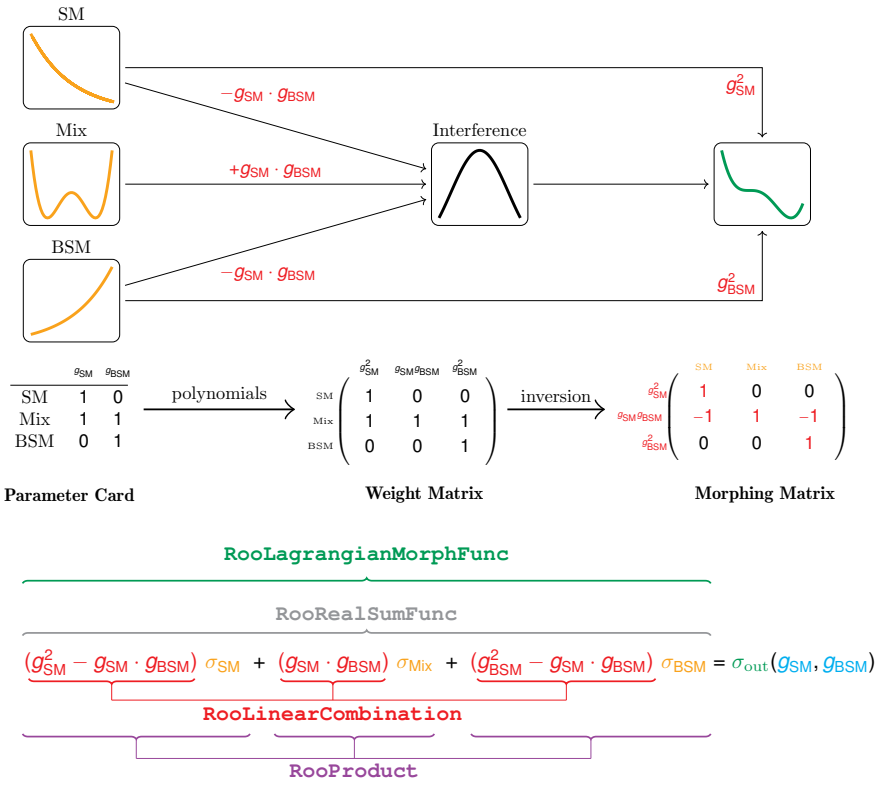

Figure 5.10: Schema showing the design of `RooLagrangianMorphFunc` class in `RooFit` for a simple case involving an effective Lagrangian function with two parameters g_{SM} and g_{BSM}. The cross-section σ_{out} is a distribution of an observable and defined for any (g_{SM}, g_{BSM}) in terms of the input templates of the observable denoted by $\{\sigma_{SM}, \sigma_{Mix}, \sigma_{BSM}\}$. In the above, the observable distributions correspond to $(g_{SM}, g_{BSM}) = \{(1,0), (1,1), (0,1)\}$ respectively. Published in [4].

The user is required to input observable distributions sampled at points in a non-degenerate set of parameter coordinates (corresponding to σ_A, σ_B, ... in Equation 5.29) and the corresponding parameter card, which is used by the class to construct the morphed distribution in terms of the parameters $\boldsymbol{c}$. The input data are expected to be structured in the manner shown in Figure 5.11, where `sample1`, `sample2`, and so on correspond to the different input folders (`TFolder`), and the `histogram_distribution` argument represents the template distribution that is picked up by the morphing function (`TH1`). The `param_cards` (`TH1` with labeled axis) argument contains the truth parameter values for the corresponding sample. The axis label corresponds to the parameter names, and the entry for the corresponding parameter is the truth value. The `flags` object (`TH1` with bin labels) con-

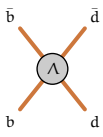

$O^{(1)}_{bd}$

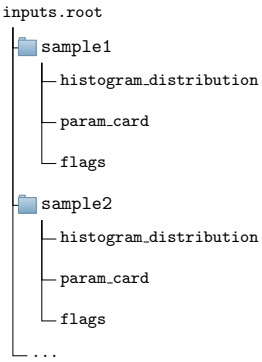

Figure 5.11: Expected structure of input ROOT file provided to the morphing function. Published in [4].

tains the information of powers of Λ^{-2} that is included in the simulated sample. The flags axis is given by {nNP0, nNP1, nNP2, ..} which corresponds to parameters to track the contributions of order Λ^{-2}. The flags label if the simulated samples are solely comprised of the SM contribution {nNP0=1, nNP1=0, nNP2=0}, SM-BSM interference {nNP0=0, nNP1=1, nNP2=0}, BSM-BSM interference {nNP0=0, nNP1=0, nNP2=1}, or a combination of them {nNP0=1, nNP1=1, nNP2=1}.

5.7.2 Usage

The construction of a morphing function is efficient, with the most expensive steps in typical cases being the matrix inversion of the morphing matrix as represented in Equation 5.28 in order to obtain the weight matrix and the I/O of the ROOT file containing the input templates. This inversion needs to be done only once at the initialization phase. Both the linear and quadratic BSM operator terms are considered, hence the number of terms in the polynomial scales as given in Equation 5.30. The dependence of the initialization time of a morphing function and the evaluation time of the morphing function on the number of EFT parameters is shown in Figure 5.12.

The number of required input template distributions depends on the number of terms in the polynomial relation. For n parameters with a single insertion of EFT operators in the Feynman diagram, the total number of samples N that is required to construct the morphing distribution is given by,

$$N = \begin{cases} n+1 & \text{, for linear terms in the BSM operators} \\ \frac{n^2+3n+2}{2} & \text{, for linear \& quadratic BSM operator terms.} \end{cases} \tag{5.30}$$

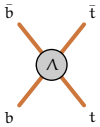

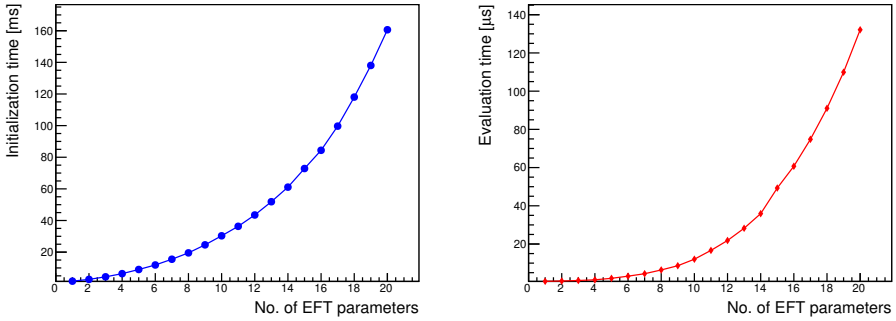

Figure 5.12: The dependence of the CPU time of the morphing as a function of the number of EFT parameters. The initialization time is shown in blue on the left, and the evaluation time is shown on the right. The initialization time estimate corresponds to the median value of the initialization call executed 5000 times. The evaluation time estimate corresponds to the median of 5000 calls to the morphing function evaluated at randomly chosen parameter values. Published in [4].

All input templates and their sampling coordinates in the parameter space must be specified in one transaction to the constructor to construct the C++ object of the morphing function. For ease of use, the `RooLagrangianMorphFunc` object can be configured with a `RooLagrangianMorphFunc::Config`, which can be initialized step-by-step by the user adding one at a time the relevant couplings, input sample names, and the path to the `ROOT` file containing the input templates to the morphing function as shown in the example Listing 1. Alternatively, the morphing function can be constructed through the `RooWorkspace` factory language, as shown in the example in Listing 2 where a named-argument syntax compared to that of other `RooFit` operator classes can be used to structure the input information. The snippets for the example usage of the morphing function with a single and multi-parameter use case are taken from the tutorials available within `ROOT`.

5.7.2.1 Example use case with one morphing parameter

A minimal example of the Lagrangian morphing use case is when one parameter affects one distribution. As an example the $pp \to WH$ with $H \to b\bar{b}$, generated with MadGraph5 [193], and a single insertion of a non-SM operator ($\mathcal{O}_{\text{BSM}}$) $\mathcal{O}_{Hq}^{(3)}$ is chosen from the Warsaw basis [194], using the `SMEFTsim` model [70, 195] where the single insertion of EFT operators per diagram is considered. Three non-degenerate input distributions are required to construct the morphing function for this case. The samples provided as inputs to the morphing are the SM contribution, the interference of the operator with SM, and the squared order contribution of

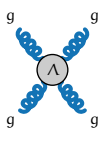

$O_{\widetilde{G}}$

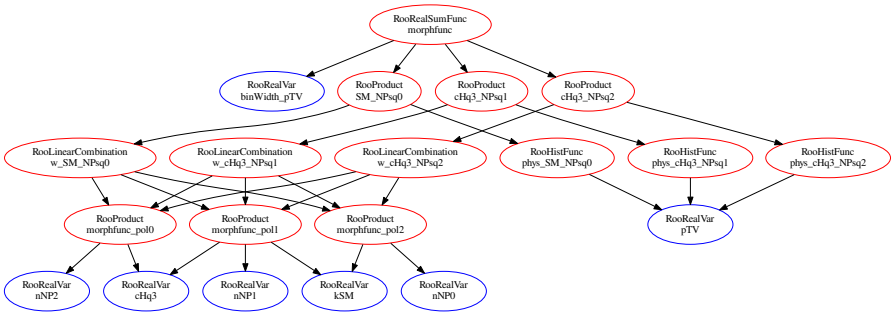

Figure 5.13: Tree structure of dependency graph of the underlying `RooFit` objects in the morphing function used in the 1D example. Published in [4].

the operator for $c_{Hq}^{(3)} = 1.0$ generated using the `NP^2==x` syntax, where x is 0,1, or 2 respectively. The computational graph of the `RooFit` function objects built by the morphing function is shown in Figure 5.13. The input distributions and the predictions computed by the morphing functions are shown in Figure 5.14.

The code snippet to perform this computation using `RooLagrangianMorphFunc` is shown in Listing 1. The corresponding `RooWorkspace` factory interface usage, which can be used as an alternative means to the same end, shown in Listing 2.

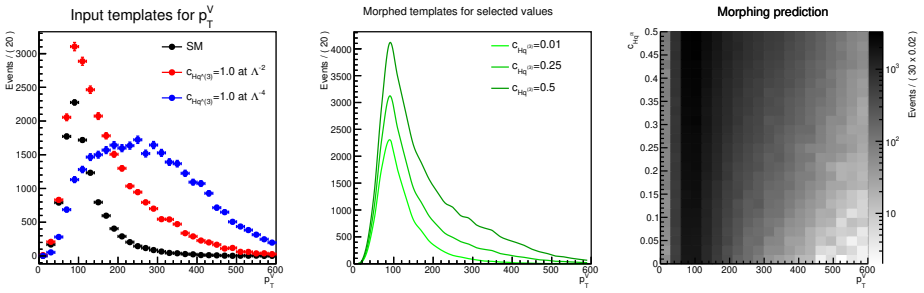

Figure 5.14: example of the Lagrangian morphing for a one-parameter case. The input distributions are shown on the left. The morphing prediction for select parameter values is shown in the center. The continuous description of the morphing function as a function of the parameter is shown on the right. Published in [4].

Multiple parameter use case

The `RooLagrangianMorphFunc` class can be extended to handle arbitrary complexity in parameters and observable distributions simultaneously model multiple 1D distributions. This example uses the same process as Section 5.7.2.1, but now,

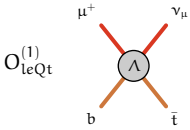

```
// usage of RooLagrangianMorphFunc for simple case
// prepare inputs

// necessary strings for inputs to morphing function
std::string infilename = "inputs/input_histos.root";
std::string obsname = "pTV";
std::vector<std::string> samples = {"SM_NPsq0","cHq3_NPsq1","cHq3_NPsq2"};

// create relevant parameters
RooRealVar cHq3("cHq3","cHq3",0,-10,10);
RooRealVar sm("SM","SM",1);
// Set NewPhysics order of parameter
cHq3.setAttribute("NewPhysics",true);

// Setup config object
RooLagrangianMorphFunc::Config config;
config.couplings.add(cHq3);
config.couplings.add(sm);
config.fileName = infilename.c_str();
config.observableName = obsname.c_str();
config.folderNames = samples;

// Setup morphing function
RooLagrangianMorphFunc morphfunc("morphfunc","morphfunc", config);
```

Listing 1: Setup for a simple, one-dimensional morphing. The RooFit classes shown in the diagram in Figure 5.10 are color-coded here accordingly. Published in [4].

```
//RooLagrangianMorphFunc in the RooWorkspace factory interface
ws.factory("lagrangianmorph::morph(
                    $fileName('inputs/input_histos.root'),
                    $observableName('pTV'),
                    $couplings({cHq3[0,1],SM[1]}),
                    $NewPhysics(cHq3=1),
                    $folders({'SM_NPsq0','cHq3_NPsq1','cHq3_NPsq2'}))");
```

Listing 2: Setup for a simple, one-dimensional morphing using the `RooWorkspace` factory interface. Published in [4].

three different operators are introduced: $\mathcal{O}_{Hq}^{(3)}$, $\mathcal{O}_{Hl}^{(3)}$, and $\mathcal{O}_{HDD}$, with three corresponding Wilson coefficients as parameters: $c_{Hq}^{(3)}$, $c_{Hl}^{(3)}$, and c_{HDD}. Following Equation 5.30, ten input samples are required as input templates for the morphing samples for this example. The ten samples used here as inputs correspond to four classes,

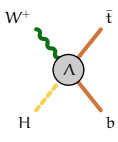

$O_{HQ}^{(3)}$

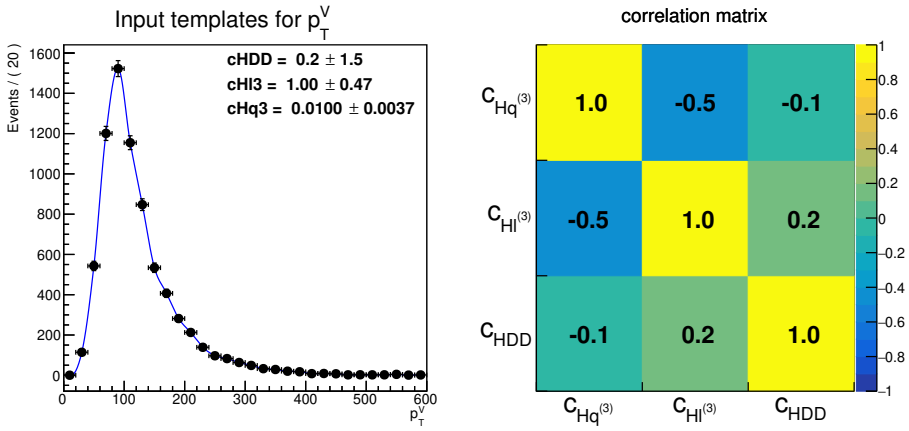

Figure 5.15: example of the Lagrangian morphing for a multi-parameter use case. The figure shows the comparison of a fit to a pseudo dataset generated at $c_{HDD} = 0.2, c_{Hl}^{(3)} = 1.0, c_{Hq}^{(3)} = 0.01$ as well as the correlation matrix. Published in [4].

- SM: the sample corresponding to the SM term in Equation 5.4 generated using `NP^2==0`.
- SM-BSM Interference: three samples linear in c, generated using `NP^2==1` and by setting one of $\{c_{Hq}^{(3)}, c_{Hl}^{(3)}, c_{HDD}\}$ to $c = 1.0$ and the remaining ones to 0.
- BSM Square: three samples quadratic in c, generated using `NP^2==2` and by setting one of $\{c_{Hq}^{(3)}, c_{Hl}^{(3)}, c_{HDD}\}$ to 1 and the remaining ones to 0.
- BSM-BSM Interference: three samples including the contribution of $c_i c_j, c_i^2, c_j^2$ $(i \neq j)$, generated using `NP^2==2` and by setting two of $c_{Hq}^{(3)}, c_{Hl}^{(3)}, c_{HDD}$ to 1 and the remaining ones to 0.

The morphing distribution for an example point in the parameter space is shown in Figure 5.15.

Parametrization scenarios

As discussed in Section 5.3, the parametrization for the cross-section can also be modeled as a ratio of polynomials when modeling the EFT behavior of production and branching ratio separately. The total cross-section in this scenario can be represented with the new `RooRatio` class, which provides the option to build the products and the ratio of individual `RooAbsReal` function objects. To this end, the `RooLagrangianMorphFunc` implementation provides a dedicated `makeRatio` method to construct the ratio of morphing functions as shown in Listing 3. The same con-

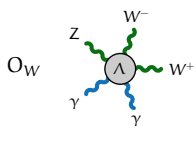

struction can also be achieved with the previously presented morphing functions, which can also be achieved with existing morphing functions. The syntax for that is shown in Listing 4, using the `RooWorkspace` factory interface.

```
// RooRatio to setup up ratio of morphing functions
// morphfunc_prod --> function to model production EFT
// morphfunc_partial_width --> function to model partial width EFT
// morphfunc_total_width --> function to model total width EFT

// Setup numerator and denominator functions
RooArgList nr(morphfunc_prod,morphfunc_partial_width);
RooArgList dr(morphfunc_total_width);

// create ratio
auto ratio = RooLagrangianMorphFunc::makeRatio("ratio","ratio", nr, dr);
```

Listing 3: Usage of the `makeRatio` method to construct a ratio of morphing functions. Published in [4].

```
// RooRatio to setup up ratio of morphing functions
// in RooWorkspace factory interface
ws.factory("Ratio::ratio({morphfunc_prod,morphfunc_partial_width},
                          {morphfunc_total_width});
```

Listing 4: Creation of a ratio of two morphing functions with the `RooWorkspace` factory interface. Published in [4].

Taylor Expansion

The `RooPolyFunc::taylorExpand` method provides the Taylor expansion of any function for a set of parameters with subsequent truncation at either first or second order for improved interpretability of the result. Listings 5 and 6 shows the usage of the truncated Taylor expansion formalism in `C++` and the workspace factory language, respectively.

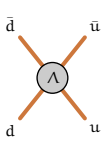

$O_{qd}^{(8)}$

```
// RooRatio to setup up ratio of morphing functions
// in RooWorkspace factory interface
// prodxBR --> RooRatio to model EFT in production & branching ratio
// truncating second-order Taylor expansion of prodxBR w.r.t (par1, par2)
// around 0.0 for both parameters
auto prodxBR_taylor = RooPolyFunc::taylorExpand("prodxBR_taylor",
                                                "prodxBR_taylor",
                        // function to Taylor expand
                                                prodxBR,
                        // parameters to Taylor expand around
                                               RooArgList(par1,par2),
                        // expand around parameter coordinate,
                        // one value of all parameters (0.0)
                        // or vector ({0.0,0.0})
                                                0.0,
                        //truncation order of expansion
                                              2);
```

Listing 5: Usage of the automatic Taylor expansion to obtain a morphing function at quadratic order based on a ratio of cross-sections and branching ratios. Published in [4].

```
// RooRatio to setup up ratio of morphing functions
// in RooWorkspace factory interface
ws.factory("taylorexpand::prodxBR_taylor(prodxBR,{par1,par2},0.0,2);
```

Listing 6: Usage of the automatic Taylor expansion with the `RooWorkspace` factory interface. Published in [4].

O_{lebQ}

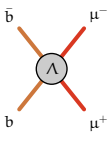

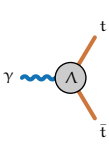

O_{tW}

6

SMEFT Interpretation of $H \to \gamma\gamma$, $H \to 4l$, and $VH, H \to bb$

This chapter presents a combined interpretation of the STXS measurements of the $H \to \gamma\gamma$, $H \to 4l$, and $(VH)H \to bb$ channels in terms of SMEFT parameters. The STXS measurements from these channels provide kinematic information on Higgs boson production in all five major production modes. Additionally, the $H \to \gamma\gamma$ channel provides sensitivity to the inclusive cross-section of the rare production of tH. The analyses are designed to measure the Standard Model Higgs boson production contributing to the different regions defined within the STXS framework.

The statistical combination of the three analyses allows for maximizing the experimental sensitivity of the channels in different kinematic regions of Higgs boson production thus enabling to probe an unprecedented number of parameters in the SMEFT parameter space simultaneously. The allowed deformations to the Standard Model due to New Physics that is decoupled in these kinematic regions are captured by measuring all sensitive SMEFT parameters that affect Higgs boson production and decay.

The SMEFT operators must be constrained simultaneously to ensure that correlations between parameters are captured. A simultaneous constraint is necessary for a consistent interpretation, ensuring that the results can be used further for a global fit with constraints from other experiments or can be interpreted within a UV specific model.

However, given that numerous operators affect the observables, it is not possible to constrain all of them simultaneously. It is necessary to define a subset of sensitive parameters before the combined likelihood fit is performed.

6.1 Input Analyses

The input analyses entering the combination make use of the full Run-2 dataset with an integrated luminosity of 139 fb^{-1} at $\sqrt{s} = 13$ TeV. The references to the input analyses are shown in Table 6.1.

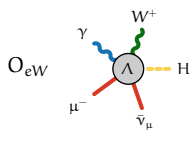

Analysis	Integrated luminosity (fb^{-1})	Reference
$H \to \gamma\gamma$ (ggH,VBF,WH, ZH, $t\bar{t}$H, tH)	139	[109]
$H \to ZZ^* \to 4\ell$ (ggH,VBF,VH, $t\bar{t}$H+tH)	139	[196]
$H \to b\bar{b}$ (WH, ZH)	139	[197]

Table 6.1: The decay channels, targeted production modes, and integrated luminosity used for each input analysis of the combination and the references for the input analyses.

The increase in center-of-mass energy to 13 TeV in Run-2 from 7,8 TeV in Run-1 increased the production cross-section as shown in Figure 2.8 and the corresponding increase in dataset size to 139 fb^{-1} from 25 fb^{-1} vastly improve the number of Higgs bosons produced. Furthermore, advancements in analysis techniques in the individual channel improve the measurement of Higgs boson signal in different kinematic regions. The increase in the number of Higgs bosons between Run-1 and Run-2 is visualized with a side-by-side comparison of an observable distribution from each input channel as shown in Figure 6.1.

6.1.1 $H \to \gamma\gamma$

The STXS analysis of the $H \to \gamma\gamma$ channel is described in detail in [109]. Despite the low branching ratio (0.227%), the $H \to \gamma\gamma$ channel provides a clean environment to study Higgs boson properties thanks to the excellent performance of photon reconstruction and identification, resulting in a clear experimental signature. The signature is a narrow resonance at m_H in the $m_{\gamma\gamma}$ distribution with a width consistent with detector resolution and rising above a smooth background. The background to the Higgs boson signal consists of continuum $\gamma\gamma$ production, γj, and jj production, where jets are misidentified as photons.

The analysis requires two isolated photons such that $p^T_{leading}/m_{\gamma\gamma} > 0.35$ and $p^T_{subleading}/m_{\gamma\gamma} > 0.25$ optimized for the SM Higgs boson mass. The photons are required to have rapidity η in the range $|\eta| < 2.37$ and outside the range $1.37 < |\eta| < 1.52$, which correspond to relevant regions of the EM calorimeters. Jets are required to have $p_T > 25$ GeV and be in the rapidity range of $|y| < 4.4$. Jets with $|\eta| < 2.5$ are tagged for b-hadrons with the DL1R b-tagging algorithm at different working points $\{60\%, 70\%, 77\%, 85\%\}$ to construct a pseudo-continuous b-tagging score.

Muons are selected with $p_T > 10$ GeV, $|\eta| < 2.7$ and are required to satisfy the `MEDIUM` identification requirements, as defined in [201]. Electrons are required

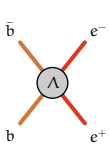

O_{Qe}

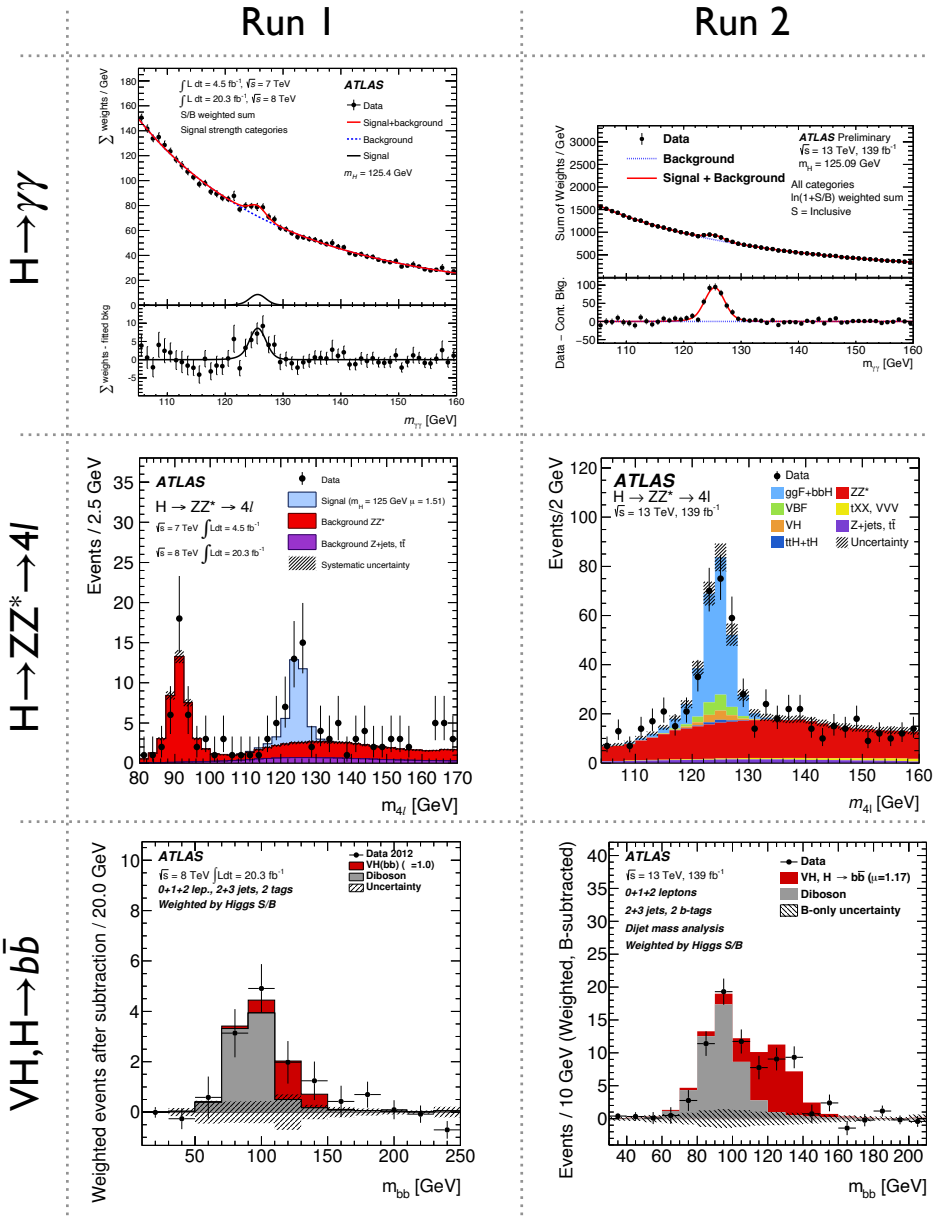

Figure 6.1: The distribution of the $m_{\gamma\gamma}$,m_{4l}, and m_{bb} shown for Run-1(left) [198–200] and Run-2(right) [109, 196, 197].

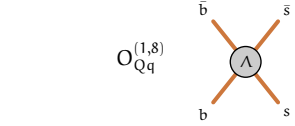

to have $p_T > 10$ GeV, $|\eta| < 2.47$ and are required to satisfy the MEDIUM selection criteria as defined in [202]. The missing transverse momentum is defined as the negative vector sum of the transverse momenta of the selected objects and the remaining transverse momenta of the low-p_T particles associated with the diphoton primary vertex as defined by the procedure in [203]. Top quarks are reconstructed based on a boosted decision tree (BDT) classifier as described in [204].

The analysis is optimized to measure production cross-sections in kinematic regions within the STXS framework. Thus, the reconstructed categories are separated by production modes and kinematic and event properties. The categorization is designed to classify events into mutually exclusive event categories targeting different STXS regions.

The event categorization is based on a two-step classification based on BDTs. First is a multi-class BDT trained to separate signal events in different STXS regions using a simulated dataset of Higgs boson events. This classifier is used to assign events to STXS regions, which also allows the selection of signal events that otherwise would fail a requirement based on detector-level quantities corresponding to the STXS region definition. In each class, events are then classified corresponding to ranges of binary BDT output values, resulting in 88 categories. Subsequently, a binary BDT classifier separates the signal from the background by maximizing the expected significance. This approach increases the purity of the expected signal in the targeted STXS region over the events from the continuum background and Higgs boson events from other STXS regions. The classifier's training is optimized for minimizing uncertainties in different signal regions and decorrelating the STXS regions.

The number of signal events in different categories is determined in a simultaneous fit to data. An analytical probability density function describes the $m_{\gamma\gamma}$ distribution in the different categories. The signal is described by a double-sided Crystal Ball function (DCSB) function over a smoothly falling background chosen from a set of parametric functions. The STXS cross-sections are measured in 27 regions that contain kinematic information in 5 major production modes – ggH,VBF,WH, ZH, $t\bar{t}H$ – and separate the signal produced inclusively in the tH mode.

6.1.2 $H \to ZZ^* \to 4l$

The STXS analysis of $H \to ZZ^* \to 4l$ is presented in detail in [196]. The analysis benefits from a clear experimental signature and a high signal-to-background ratio. The final-state leptons can be reconstructed accurately, allowing to measure kinematic properties of the four-lepton system precisely. The signal is measured in the invariant mass window of 115 GeV $< m_{4l} <$ 130 GeV. The dominant background process is $pp \to ZZ^* \to 4l$ and is constrained using data sidebands measured in a

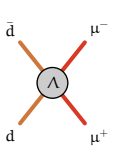

O_{qe}

mass window of 105 GeV $< m_{4l} <$ 115 GeV or 130 GeV $< m_{4l} <$ 160 GeV. For the category involving the associated production of a top quark, the sideband includes the region 160 GeV $\leqslant m_{4l} <$ 350 GeV.

The analysis targets the reconstruction of the Higgs boson produced in the different STXS regions. The Higgs boson decays are classified according to the final state: $4\mu, 4e, 2e2\mu, 2\mu2e$, where two pairs of opposite sign, same flavor leptons are reconstructed. The first pair originates from the on-shell Z boson decay, and the other originates from the off-shell Z boson. The three highest-p_T leptons are required to have $p_T >$ 20 GeV, 15 GeV, and 10 GeV, respectively. The leading lepton pair m_{12} corresponds to the lepton pair with an invariant mass closest to the Z boson mass and is required to satisfy 50 GeV$< m_{12} <$ 106 GeV. The subsequent lepton pair is required to have an invariant mass of $m_{min} < m_{34} <$ 115 GeV. Here, m_{min} is 12 GeV for $m_{4l} <$ 140 GeV and rises linearly to 50 GeV upto $m_{4l} =$ 190 GeV and is 50 GeV for all high m_{4l} values. Muons are selected with $p_T >$ 5 GeV, $|\eta| <$2.7 and are required to satisfy the `LOOSE` identification requirements, as defined in [201]. Muons tagged by the calorimeter are required to have a $p_T >$ 15 GeV. Electrons are required to have $p_T >$ 7 GeV, $|\eta| <$2.47 and are required to satisfy the `LOOSE` selection criteria as defined in [202]. Jets are required to have $p_T >$ 30 GeV and $|\eta| <$ 4.5. Additional leptons are considered for Higgs bosons produced in the $t\bar{t}H$ and VH production modes, where a method based on matrix elements is used to identify the leptons originating from the Higgs boson decay based on the SM tensor structure of the event.

The classification of the Higgs boson signal targeting the different STXS regions is based on neural network (NN) discriminants that distinguish the signal from the various background processes. The discriminant comprises two recurrent neural networks (RNN); one is for the p_T ordered variables of the four-lepton system, and the other is for jet variables. The two RNNs are combined with a feed-forward multilayer perceptron (MLP) that is based on additional event variables. The output of the RNNs and MLP are chained together in another MLP to build the final NN discriminant trained to approximate the probability of an event originating from a given process.

In total, 12 categories are defined to identify the signal in the different STXS regions. The events are categorized into the different kinematic regions sequentially based on the production mode, starting with events classified as ttH, which are further split into categories depending on the decay mode of the W bosons originating from the top decay into leptonic and hadronic categories. Events with additional leptons but not satisfying the jet criteria for $t\bar{t}H$ define the category for VH-lep production, where the associated vector boson decays leptonically. The remaining events are classified according to jet multiplicity into 0-jet, 1-jet, and $\geqslant$ 2-jets regions with further categorization based on the p_T of the four-lepton system. First, events are identified in the 2-jet category and are categorized as

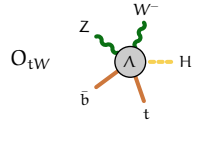

BSM-like if $m_{jj} > 120$ GeV and $p_T^{4l} > 200$ GeV. Next, the 1-jet category is split into four categories defined by $p_T^{4l} < 60$ GeV, 60 GeV $< p_T^{4l} \leqslant 120$ GeV, 120 GeV $< p_T^{4l} \leqslant 200$ GeV, and $p_T^{4l} > 200$ GeV. Finally, the 0-jet category is expected to contain the largest number of events from ggF and is split into three categories based on p_T^{4l} corresponding to $p_T^{4l} < 10$ GeV, 10 GeV $< p_T^{4l} < 200$ GeV, and $p_T^{4l} \geqslant 200$ GeV. This categorization allows measuring cross-sections in 12 bins defined within the STXS framework.

6.1.3 $VH, H \to bb$

The STXS analysis of the $VH, H \to bb$ analysis is presented in detail in [197]. While $H \to b\bar{b}$ is the most abundant decay channel of the Higgs boson with a branching fraction of 58%, the multi-jet background makes it challenging to study the Higgs boson in this channel. The VH production process is the most sensitive production mode for the $H \to b\bar{b}$ decay, as the lepton decay of the associated vector boson helps to trigger efficiently on the signal and allows suppression of the large multi-jet background. The identification of the signal is affected by a large number of dominant background processes of $V+$ heavy flavor jets production, electroweak production of top quarks (single top quark and $t\bar{t}$), and diboson production. The high performance of the b-tagging algorithm is crucial to identifying b-jets and rejecting light and c-jets efficiently.

Muons are selected with $p_T > 7$ GeV, $|\eta| < 2.7$ and are required to satisfy the LOOSE identification requirements, as defined in [201]. For the 1-lepton region, the muons are required to fulfill the MEDIUM quality criterion. Electrons are required to have $p_T > 7$ GeV, $|\eta| < 2.47$ and are required to satisfy the LOOSE selection criteria as defined in [202]. Hadronically decaying τ-leptons are required to have $p_T > 20$ GeV and $|\eta| < 2.5$, outside the transition region in the electromagnetic calorimeters between $1.37 < |\eta| < 1.52$, and satisfy the MEDIUM quality criterion defined in [205]. The τ-leptons are not directly used in the event selection but are used in missing transverse momentum calculation and to avoid double counting the hadronic decay products as other objects. Jets are reconstructed from the energy in topological clusters of calorimeter cells using the anti-k_t algorithm with a radius parameter R=0.4. Jets are required to have $p_T > 20$ GeV in the central region ($|\eta|$) < 2.5 and $p_T > 30$ GeV outside the tracker acceptance corresponding to $(2.5 < |\eta| < 4.5)$. Jets are identified as b-jets using a multivariant discriminant with the selections tuned for the 70% working point.

Events are categorized into different channels based on the number of associated leptons into 0, 1, and 2 lepton channels aimed at the $ZH \to \nu\nu b\bar{b}$, $WH \to l\nu b\bar{b}$, and $ZH \to llb\bar{b}$ processes respectively. Only electrons and muons are considered for the charged leptons. All events are required to have two b-tagged jets, which form the Higgs boson candidate, and at least one b-jet is required with $p_T >$

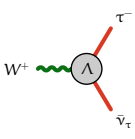

O_{eW}

45 GeV. Events are further split into 2-jet or $\geqslant$ 3-jet categories, where the latter includes events with one or more untagged jets. For the 0- and 1-lepton channels, only one untagged jet is allowed, as the $t\bar{t}$ background is much larger in events with four jets or more. In the 2-lepton channel, any number of untagged jets are accepted in the $\geqslant$ 3-jet category, which increases the signal acceptance in this category by 100%. The analysis focuses on high-p_T^V regions, defined for 150 GeV $< p_T^V <$ 250 GeV and $p_T^V >$ 250 GeV, which allows to better separate the signal from the background since the signal has a harder p_T^V spectrum. Additionally, for the 2 lepton channel, a medium p_T^V region with 75 GeV $< p_T^V <$ 150 GeV is included. Altogether, 14 analysis regions are defined, and each is further split into a signal region and two control regions, resulting in a total of 42 regions. The control regions are enriched in V+heavy flavor jets or $t\bar{t}$ events, respectively, and are used to determine the normalization factors for these backgrounds.

The analysis employs boosted decision trees trained on kinematic event variables of the event to separate signal from background in different categories. Two sets of BDTs are trained to separate VH and VZ production from the background. The first is trained to separate the VH signal process from the backgrounds, and the second is trained to separate the $VZ, Z \to b\bar{b}$ diboson process from the VH signal and other processes and helps to validate the VH analysis. The BDTs are trained in 8 regions by merging some of the 14 analysis regions, in particular, the 150 GeV $< p_T^V <$ 250 GeV and $p_T^V >$ 250 GeV regions in each lepton channel and jet category are merged for the training, as no increase in sensitivity was found when undertaking separate training in the two regions. The output of the BDTs serves as discriminating observables in the signal extraction fit. These p_T^V regions allow to measure the cross-sections in p_T^W (3 regions) for WH-leptonic production and p_T^Z (2 regions) for ZH-leptonic production.

6.2 Combination of STXS measurements

The Higgs boson signal yield in the different production modes is separately parametrized for every contributing Higgs boson production mode in the different decay channels. The likelihood model is described in Section 5.4.

The $H \to b\bar{b}$ (VH), $H \to ZZ^* \to 4\ell$ and $H \to \gamma\gamma$ analysis target STXS regions that are defined in the STXS framework [174] with the most detailed Stage 1.2 version being used. As the analyses do not have the sensitivity to measure the cross-sections of the full STXS granularity, some of these Stage-1.2 categories are merged for some measurements and the corresponding EFT parametrization is performed at this granularity. The mapping of these merged STXS regions to the original STXS Stage 1.2 regions is detailed in Table 6.2. The efficiency and accep-

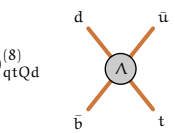

tance factors $\epsilon_k^{i,X}$ are determined using SM predictions for the relative fraction in each fine Stage-1.2 bin. SM uncertainties on these fractions are taken into account.

The corresponding measured signal strengths and their correlations are shown in Figure 6.2 and Figure 6.3, respectively. The cross-sections are measured in 43 bins with 26 bins probed by $H \to \gamma\gamma$, 12 bins from $H \to ZZ^* \to 4\ell$, and five bins from $H \to b\bar{b}$ (VH). The measurements agree with the Standard Model with a p-value (p_{SM}) of 91%. Statistical uncertainties dominate the uncertainties of most of the cross-sections.

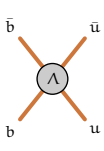

$O_{bd}^{(8)}$

STXS Region Stage-0	STXS Region Stage-1.2	$H\to\gamma\gamma$	$H\to ZZ^*\to 4\ell$	$H\to b\bar{b}$ (VH)
ggH	$N_{jets}=0$, $p_T^H<10$	$N_{jets}=0$, $p_T^H<10$	$N_{jets}=0$, $p_T^H<10$	
	$N_{jets}=0$, $10<p_T^H$	$N_{jets}=0$, $10<p_T^H$	$N_{jets}=0$, $10<p_T^H$	
	$N_{jets}=1$, $p_T^H<60$	$N_{jets}=1$, $p_T^H<60$	$N_{jets}=1$, $p_T^H<60$	
	$N_{jets}=1$, $60<p_T^H<120$	$N_{jets}=1$, $60<p_T^H<120$	$N_{jets}=1$, $60<p_T^H<120$	
	$N_{jets}=1$, $120<p_T^H<200$	$N_{jets}=1$, $120<p_T^H<200$	$N_{jets}=1$, $120<p_T^H<200$	
	$N_{jets}\geqslant 2$, $m_{jj}<350$, $p_T^H<60$	$N_{jets}\geqslant 2$, $m_{jj}<350$, $p_T^H<120$	$N_{jets}\geqslant 2$, $p_T^H\leqslant 200$	
	$N_{jets}\geqslant 2$, $m_{jj}<350$, $60<p_T^H<120$	$N_{jets}\geqslant 2$, $m_{jj}<350$, $p_T^H<120$	$N_{jets}\geqslant 2$, $p_T^H\leqslant 200$	
	$N_{jets}\geqslant 2$, $m_{jj}<350$, $120<p_T^H<200$	$N_{jets}\geqslant 2$, $m_{jj}<350$, $120<p_T^H<200$	$N_{jets}\geqslant 2$, $p_T^H\leqslant 200$	
	$N_{jets}\geqslant 2$, $350<m_{jj}<700$, $p_T^H<200$, $p_T^{Hjj}<25$	$N_{jets}\geqslant 2$, $350<m_{jj}$, $p_T^H<200$	$N_{jets}\geqslant 2$, $p_T^H\leqslant 200$	
	$N_{jets}\geqslant 2$, $350<m_{jj}<700$, $p_T^H<200$, $25<p_T^{Hjj}$	$N_{jets}\geqslant 2$, $350<m_{jj}$, $p_T^H<200$	$N_{jets}\geqslant 2$, $p_T^H\leqslant 200$	
	$N_{jets}\geqslant 2$, $700<m_{jj}$, $p_T^H<200$, $p_T^{Hjj}<25$	$N_{jets}\geqslant 2$, $350<m_{jj}$, $p_T^H<200$	$N_{jets}\geqslant 2$, $p_T^H\leqslant 200$	
	$N_{jets}\geqslant 2$, $700<m_{jj}$, $p_T^H<200$, $25<p_T^{Hjj}$	$N_{jets}\geqslant 2$, $350<m_{jj}$, $p_T^H<200$	$N_{jets}\geqslant 2$, $p_T^H\leqslant 200$	
	$200<p_T^H<300$	$200<p_T^H<300$	$200<p_T^H$	
	$300<p_T^H<450$	$300<p_T^H<450$	$200<p_T^H$	
	$450<p_T^H<650$	$450<p_T^H$	$200<p_T^H$	
	$650<p_T^H$	$450<p_T^H$	$200<p_T^H$	
qq → Hqq "VBF", "qqVH had"	$N_{jets}=0$	$N_{jets}\leqslant 1$		
	$N_{jets}=1$	$N_{jets}\leqslant 1$		
	$N_{jets}\geqslant 2$, $m_{jj}<60$	$N_{jets}\geqslant 2$, $m_{jj}<60 \vee 120<m_{jj}<350$	VBF	
	$N_{jets}\geqslant 2$, $60<m_{jj}<120$	$N_{jets}\geqslant 2$, $60<m_{jj}<120$	$N_{jets}\geqslant 2$, $60<m_{jj}<120$	
	$N_{jets}\geqslant 2$, $120<m_{jj}<350$	$N_{jets}\geqslant 2$, $m_{jj}<60 \vee 120<m_{jj}<350$	VBF	
	$N_{jets}\geqslant 2$, $350<m_{jj}$ $200<p_T^H$	$N_{jets}\geqslant 2$, $350<m_{jj}$, $200<p_T^H$	$N_{jets}\geqslant 2$, $350<m_{jj}$, $200<p_T^H$	
	$N_{jets}\geqslant 2$, $350<m_{jj}<700$, $p_T^H<200$, $p_T^{Hjj}<25$	$N_{jets}\geqslant 2$, $350<m_{jj}<700$, $p_T^H<200$	VBF	
	$N_{jets}\geqslant 2$, $350<m_{jj}<700$, $p_T^H<200$, $25<p_T^{Hjj}$	$N_{jets}\geqslant 2$, $350<m_{jj}<700$, $p_T^H<200$	VBF	
	$N_{jets}\geqslant 2$, $700<m_{jj}$, $p_T^H<200$, $p_T^{Hjj}<25$	$N_{jets}\geqslant 2$, $700<m_{jj}$, $p_T^H<200$	VBF	
	$N_{jets}\geqslant 2$, $700<m_{jj}$, $p_T^H<200$, $25<p_T^{Hjj}$	$N_{jets}\geqslant 2$, $700<m_{jj}$, $p_T^H<200$	VBF	
qq → Hℓν "qqWH lep"	$p_T^V<75$ ($N_{jets}=0$ / $N_{jets}=1$ / $N_{jets}\geqslant 2$)	WH $p_T^V<150$	VH lep	WH $p_T^V<250$
	$75<p_T^V<150$ ($N_{jets}=0$ / $N_{jets}=1$ / $N_{jets}\geqslant 2$)	WH $p_T^V<150$	VH lep	WH $p_T^V<250$
	$150<p_T^V<250$ ($N_{jets}=0$ / $N_{jets}=1$ / $N_{jets}\geqslant 2$)	WH $150<p_T^V$	VH lep	WH $p_T^V<250$
	$250<p_T^V<400$ ($N_{jets}=0$ / $N_{jets}=1$ / $N_{jets}\geqslant 2$)	WH $150<p_T^V$	VH lep	WH $250<p_T^V$
	$400<p_T^V$ ($N_{jets}=0$ / $N_{jets}=1$ / $N_{jets}\geqslant 2$)	WH $150<p_T^V$	VH lep	WH $250<p_T^V$
qq → Hℓℓ "qqZH lep"	$p_T^V<75$ ($N_{jets}=0$ / $N_{jets}=1$ / $N_{jets}\geqslant 2$)	ZH $p_T^V<150$	VH lep	ZH $p_T^V<150$
	$75<p_T^V<150$ ($N_{jets}=0$ / $N_{jets}=1$ / $N_{jets}\geqslant 2$)	ZH $p_T^V<150$	VH lep	ZH $p_T^V<150$
	$150<p_T^V<250$ ($N_{jets}=0$ / $N_{jets}=1$ / $N_{jets}\geqslant 2$)	ZH $150<p_T^V$	VH lep	ZH $150<p_T^V<250$
	$250<p_T^V<400$ ($N_{jets}=0$ / $N_{jets}=1$ / $N_{jets}\geqslant 2$)	ZH $150<p_T^V$	VH lep	ZH $250<p_T^V$
	$400<p_T^V$ ($N_{jets}=0$ / $N_{jets}=1$ / $N_{jets}\geqslant 2$)	ZH $150<p_T^V$	VH lep	ZH $250<p_T^V$
gg → Hℓℓ "ggZH lep"	$p_T^V<75$ ($N_{jets}=0$ / $N_{jets}=1$ / $N_{jets}\geqslant 2$)	ZH $p_T^V<150$	VH lep	ZH $p_T^V<150$
	$75<p_T^V<150$ ($N_{jets}=0$ / $N_{jets}=1$ / $N_{jets}\geqslant 2$)	ZH $p_T^V<150$	VH lep	ZH $p_T^V<150$
	$150<p_T^V<250$ ($N_{jets}=0$ / $N_{jets}=1$ / $N_{jets}\geqslant 2$)	ZH $150<p_T^V$	VH lep	ZH $150<p_T^V<250$
	$250<400$ ($N_{jets}=0$ / $N_{jets}=1$ / $N_{jets}\geqslant 2$)	ZH $150<p_T^V$	VH lep	ZH $250<p_T^V$
	$250<p_T^V$ ($N_{jets}=0$ / $N_{jets}=1$ / $N_{jets}\geqslant 2$)	ZH $150<p_T^V$	VH lep	ZH $250<p_T^V$
ttH	$p_T^H<60$	$p_T^H<60$	t(t)H	
	$60<p_T^H<120$	$60<p_T^H<120$	t(t)H	
	$120<p_T^H<200$	$120<p_T^H<200$	t(t)H	
	$200<p_T^H<300$	$200<p_T^H$	t(t)H	
	$300<p_T^H$	$200<p_T^H$	t(t)H	
	$b\bar{b}H$	merged with ggH		
	tH	tH	t(t)H	

Table 6.2: Definition of Simplified Template Cross Sections at Stage-0 and Stage-1.2 and their mapping to the merged regions used for the EFT reinterpretation analysis. All dimensional quantities are in units of GeV. All bins sharing the same label are merged.

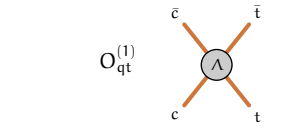

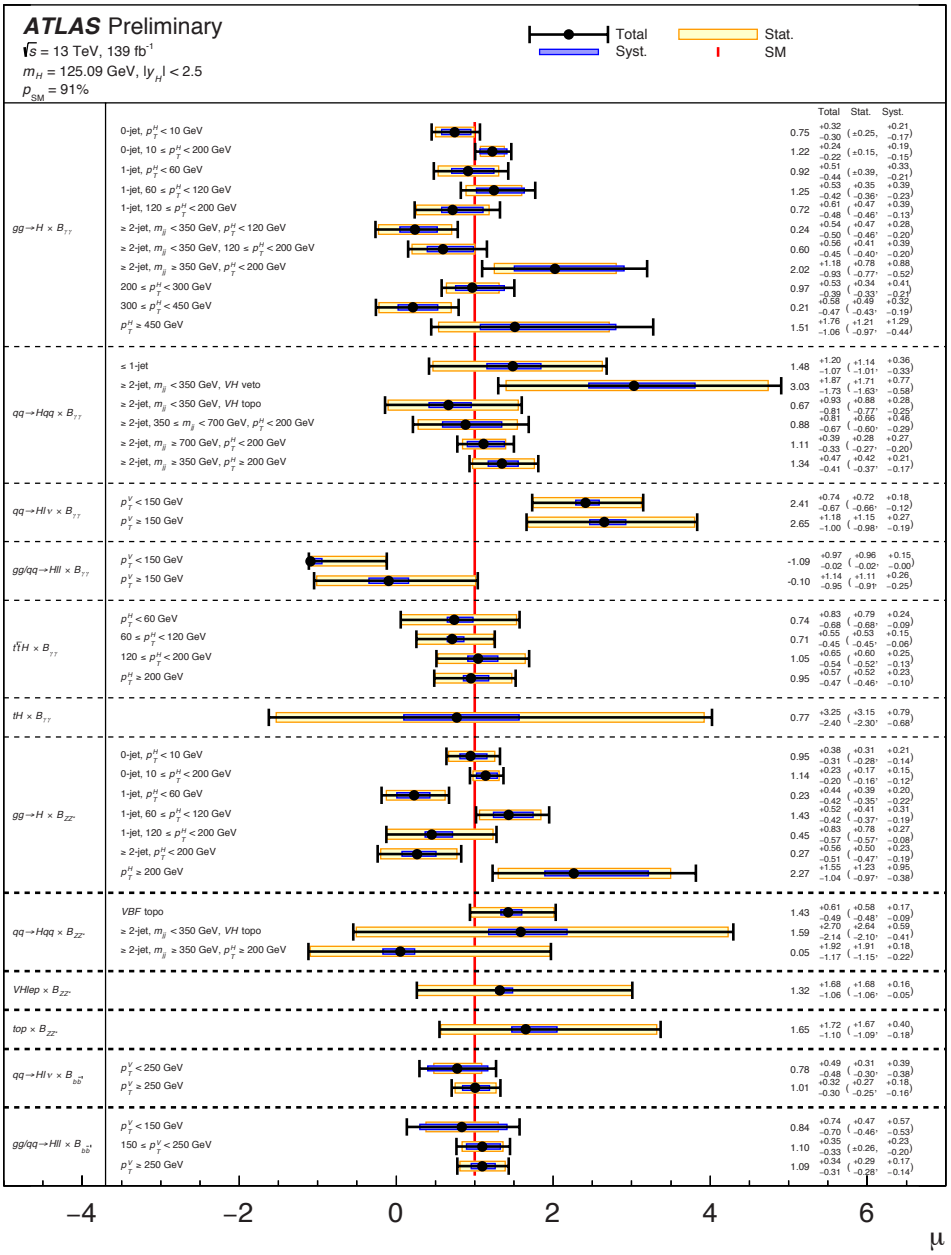

Figure 6.2: Measured signal strength for each STXS category entering the EFT analysis. The corresponding categories are defined in Table 6.2. Input data taken from [206]. The probability to obtain the observed data under the SM hypothesis (p_{SM}) is 91%.

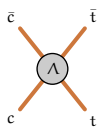

$O_{Qu}^{(1)}$

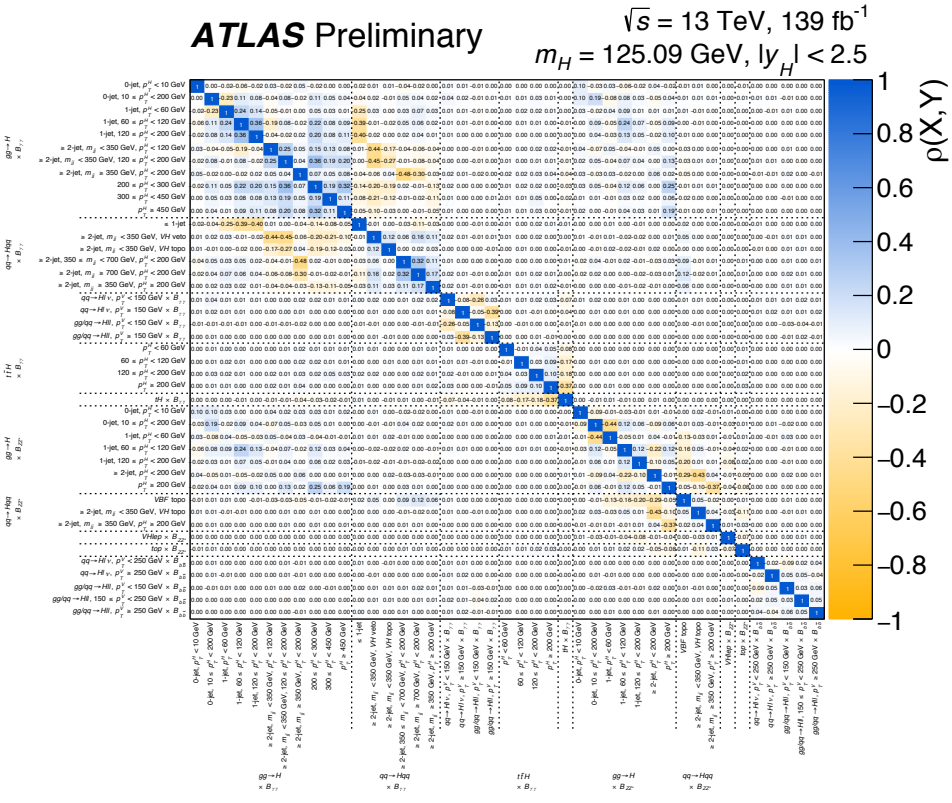

Figure 6.3: Correlation matrix corresponding to the measurements shown in Figure 6.2. Input data taken from [206].

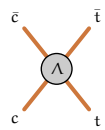

6.3 Impact of SMEFT operators on signal

For this reinterpretation, all the parameters that affect the Higgs boson signal in the production and decay are initially considered. SMEFT simulation for Higgs boson production mode and decay with tree-level SM diagrams is performed with SMEFTsim [195]. For ggH, $gg \to ZH$ and $H \to gg$, cross-sections are calculated at NLO accuracy in QCD with SMEFTatNLO [207] and at NLO accuracy in QED for SMEFT-SM interference terms in $H \to \gamma\gamma$ [208]. The $U(3)^5$ flavor symmetry scenario with the (m_W, m_Z, G_F) scheme is chosen, which corresponds to the maximal symmetry possible for the SMEFT operators in terms of the SM fermion field, as discussed earlier in Section 2.3.3.

All dimension-6 CP-even operators are considered for which at $c_i = 1$ the impact of the operator on any of the STXS categories in Figure 6.2 at $O(\Lambda^{-2})$ exceeds 0.1% with respect to the SM prediction. The operators and the corresponding Wilson coefficients thus selected for this analysis are listed in Table 6.3. The value for the scale of BSM physics (Λ) is set to 1 TeV, where coefficients for alternative values of $\Lambda = X$ can be obtained through a scaling with a simple factor $(X/1\,\text{TeV})^2$. All complex-valued Wilson coefficients, notably c_{uW}, c_{uG}, c_{uB} and c_{uH} in this analysis, are used with $\Im(c_i) = 0$.

In the simulation, kinematic cuts on the minimal jet transverse momentum of $p_T > 20\,\text{GeV}$ are imposed. Furthermore, for the Higgs boson decay, a requirement of $\Delta R > 0.05$ between two jets or two leptons is imposed to avoid divergences in the matrix element calculation. For all events PYTHIA8 [125] is used to simulate parton showering, where the Higgs boson decay is based on the Higgs boson width obtained from Madgraph. A jet-matching procedure is performed to remove jet phase space overlap between the matrix element and the parton shower simulations. The CKKW-l algorithm is used for all tree-level processes, with a matching parameter of 30 GeV, whereas the MLM algorithm [209, 210] is used for loop-induced processes, notably for ggH. The Rivet program [211] with the `HiggsTemplateCrossSections` [212] routine is used to analyze the simulated events, to compute kinematic quantities and to classify the events according to their STXS region.

SMEFT modifications to background processes are not considered in the analysis. For the production of Higgs boson in association with top quark, and top-antitop quark pair $t\bar{t}$, no SMEFT modification is considered for the decay of the top quark.

The systematic uncertainties assigned to the acceptance factors $\epsilon_k^{i,X}$ in Equation 5.8, arising from theory uncertainties are fully taken into account in the SM cross-section prediction, and are assumed to cover the possible acceptance changes induced by SMEFT operators in Higgs boson production through the full validity range of the SMEFT model. The use of this assumption is motivated by the simi-

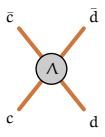

$O^{(8)}_{quqd}$

Wilson coefficient	Operator
$c_{H\Box}$	$(H^\dagger H)\Box(H^\dagger H)$
c_{HD}	$\left(H^\dagger D^\mu H\right)^* \left(H^\dagger D_\mu H\right)$
c_{HG}	$H^\dagger H\, G^A_{\mu\nu} G^{A\mu\nu}$
c_{HB}	$H^\dagger H\, B_{\mu\nu} B^{\mu\nu}$
c_{HW}	$H^\dagger H\, W^I_{\mu\nu} W^{I\mu\nu}$
c_{HWB}	$H^\dagger \tau^I H\, W^I_{\mu\nu} B^{\mu\nu}$
c_{eH}	$(H^\dagger H)(\bar{l}_p e_r H)$
c_{uH}	$(H^\dagger H)(\bar{q}_p u_r \widetilde{H})$
c_{dH}	$(H^\dagger H)(\bar{q}_p d_r \widetilde{H})$
$c^{(1)}_{Hl}$	$(H^\dagger i \overleftrightarrow{D}_\mu H)(\bar{l}_p \gamma^\mu l_r)$
$c^{(3)}_{Hl}$	$(H^\dagger i \overleftrightarrow{D}^I_\mu H)(\bar{l}_p \tau^I \gamma^\mu l_r)$
c_{He}	$(H^\dagger i \overleftrightarrow{D}_\mu H)(\bar{e}_p \gamma^\mu e_r)$
$c^{(1)}_{Hq}$	$(H^\dagger i \overleftrightarrow{D}_\mu H)(\bar{q}_p \gamma^\mu q_r)$
$c^{(3)}_{Hq}$	$(H^\dagger i \overleftrightarrow{D}^I_\mu H)(\bar{q}_p \tau^I \gamma^\mu q_r)$
c_{Hu}	$(H^\dagger i \overleftrightarrow{D}_\mu H)(\bar{u}_p \gamma^\mu u_r)$
c_{Hd}	$(H^\dagger i \overleftrightarrow{D}_\mu H)(\bar{d}_p \gamma^\mu d_r)$
c_{uG}	$(\bar{q}_p \sigma^{\mu\nu} T^A u_r)\widetilde{H}\, G^A_{\mu\nu}$
c_{uW}	$(\bar{q}_p \sigma^{\mu\nu} u_r)\tau^I \widetilde{H}\, W^I_{\mu\nu}$
c_{uB}	$(\bar{q}_p \sigma^{\mu\nu} u_r)\widetilde{H}\, B_{\mu\nu}$
c'_{ll}	$(\bar{l}_p \gamma_\mu l_t)(\bar{l}_r \gamma^\mu l_s)$
$c^{(1)}_{qq}$	$(\bar{q}_p \gamma_\mu q_t)(\bar{q}_r \gamma^\mu q_s)$
$c^{(3)}_{qq}$	$(\bar{q}_p \gamma_\mu \tau^I q_r)(\bar{q}_s \gamma^\mu \tau^I q_t)$
c_{qq}	$(\bar{q}_p \gamma_\mu q_t)(\bar{q}_r \gamma^\mu q_s)$
$c^{(31)}_{qq}$	$(\bar{q}_p \gamma_\mu \tau^I q_t)(\bar{q}_r \gamma^\mu \tau^I q_s)$
c_{uu}	$(\bar{u}_p \gamma_\mu u_r)(\bar{u}_s \gamma^\mu u_t)$
$c^{(1)}_{uu}$	$(\bar{u}_p \gamma_\mu u_t)(\bar{u}_r \gamma^\mu u_s)$
$c^{(1)}_{qu}$	$(\bar{q}_p \gamma_\mu q_t)(\bar{u}_r \gamma^\mu u_s)$
$c^{(8)}_{ud}$	$(\bar{u}_p \gamma_\mu T^A u_r)(\bar{d}_s \gamma^\mu T^A d_t)$
$c^{(8)}_{qu}$	$(\bar{q}_p \gamma_\mu T^A q_r)(\bar{u}_s \gamma^\mu T^A u_t)$
$c^{(8)}_{qd}$	$(\bar{q}_p \gamma_\mu T^A q_r)(\bar{d}_s \gamma^\mu T^A d_t)$
c_W	$\epsilon^{IJK} W^{I\nu}_\mu W^{J\rho}_\nu W^{K\mu}_\rho$
c_G	$f^{ABC} G^{A\nu}_\mu G^{B\rho}_\nu G^{C\mu}_\rho$

Table 6.3: Wilson coefficients c_j and corresponding dimension-6 SMEFT operators $\mathcal{O}_j$ used in this analysis.

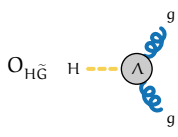

larity of reconstruction-level analysis regions to STXS cross-section regions, which are designed to be relatively insensitive to acceptance changes induced by SMEFT operators. The effect of SMEFT operators on other observables used in the definition of the analysis regions, e.g., through multivariate discriminants, is assumed to be negligible.

6.4 SMEFT parametrization

The parametrization of the Higgs boson signal is described in Section 5.3. For the parametrization including linear terms the fully Taylor expanded version is used, corresponding to Equation 5.16, where the total width is also expanded. This approach is valid only for small deviations from the SM corresponding to a small change in the total width. The impact of the linear scale factors $A_j^{\sigma_i}$ and $(A_j^{\Gamma^{H\to X}} - A_j^{\Gamma^H})$ for the relevant SMEFT operators associated to c_j on the STXS cross-sections and branching fractions is shown in Figure 6.5.

For the quadratic parametrization, the ratio of polynomials is described by Equation 5.17. Figure 6.6 illustrates the relative importance of the quadratic terms by comparing the impact $c_j A_j + c_j^2 B_{jj}$ of variations of coefficients c_j in the various STXS regions and decay rates when including only linear terms A_j (shaded histograms) and when including both the linear and quadratic terms B_{jj} (open histograms).

The relative importance of the quadratic term increases linearly with the considered variation of c_j; hence, the chosen magnitudes of the variations do not only scale the shown impact but also the relative magnitude of the quadratic term. Figure 6.6 shows that the strongest impact of quadratic terms can be expected in the high-p_T regions of VH production for coefficients $c_{Hq}^{(3)}, c_{Hq}^{(1)}, c_{Hd}, c_{Hu}$ and in the tH channel for operator $c_{qq}^{(3)}$. Other regions that are subject to a moderately strong impact of quadratic terms are inclusive ggH production for operators c_{HG} and c_{uG}, and $\Gamma^{H\to\gamma\gamma}$ for c_{HB}, where in the latter case the impact is notably negative.

The effect of SMEFT operators on Higgs boson decays to four particles can strongly affect the acceptance factors ϵ_{ij}^X as discussed in Section 5.3.3.

Generally, an acceptance factor A affects a measured cross-section $\sigma_i^{H\to X}$ as follows,

$$\sigma_i^{H\to X} = \sigma_i \cdot \mathcal{B}_{H\to X} \cdot A \tag{6.1}$$

The dependence of the acceptance A term in Equation 6.1 on Wilson coefficients is estimated by parametrizing the ratio of the yields when the experimental cuts are included ($N_i^{EFT,H\to X,\text{with cuts}}$) with respect to yield the case where no cuts are

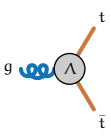

O_{tG}

applied ($N_i^{EFT,H\to X,\text{w.o cuts}}$). Using the general form of the EFT parametrization for the yield as given in Equation 5.9. The acceptance function would take the form of a rational polynomial as follows,

$$A_i^{EFT,H\to X} = \frac{N_i^{EFT,H\to X,\text{with cuts}}}{N_i^{EFT,H\to X,\text{w.o cuts}}} = \frac{\left(N_{SM}\cdot\left(1+\frac{\sigma_{int}}{\sigma_{SM}}+\frac{\sigma_{BSM}}{\sigma_{SM}}\right)\cdot\frac{1+\frac{\Gamma_{int}^{H\to X}}{\Gamma_{SM}^{H\to X}}+\frac{\Gamma_{BSM}^{H\to X}}{\Gamma_{SM}^{H\to X}}}{1+\frac{\Gamma_{int}^{H}}{\Gamma_{SM}^{H}}+\frac{\Gamma_{BSM}^{H}}{\Gamma_{SM}^{H}}}\right)^{\text{with cuts}}}{\left(N_{SM}\cdot\left(1+\frac{\sigma_{int}}{\sigma_{SM}}+\frac{\sigma_{BSM}}{\sigma_{SM}}\right)\cdot\frac{1+\frac{\Gamma_{int}^{H\to X}}{\Gamma_{SM}^{H\to X}}+\frac{\Gamma_{BSM}^{H\to X}}{\Gamma_{SM}^{H\to X}}}{1+\frac{\Gamma_{int}^{H}}{\Gamma_{SM}^{H}}+\frac{\Gamma_{BSM}^{H}}{\Gamma_{SM}^{H}}}\right)^{\text{w.o cuts}}}. \tag{6.2}$$

Acceptance effects significantly impact the $H\to ZZ^*\to 4\ell$ analysis as it is a 4-body decay, and due to the explicit relation of the analysis-level selection to m_{Z^*}, and an acceptance correction factor developed in [196] is used. This acceptance correction is derived only as a function of c_{HW}, c_{HB} and c_{HWB}, as only these are measured in [196]. In principle, a dependence of this correction on $c_{Hl}^{(1)}$ and c_{He} is also expected but is neglected in this analysis as the overall sensitivity to these operators is small. For all other Higgs boson decays, the acceptance effects are neglected as these are all 2-body decays.

The acceptance function from the $H\to 4l$ analysis [196] is modeled as a Lorentzian function of three Wilson coefficients c_{HW}, c_{HWB}, and c_{HB} as

$$\frac{A^{EFT}(c_{HW},c_{HWB},c_{HB})}{A^{SM,LO}} = 0.15+\frac{0.76}{D}, \tag{6.3}$$

where D is given by,

$$\begin{aligned} D = {} & 0.88+2.29(0.005+c_{HB})^2+0.70(-0.12+c_{HWB})^2-1.22c_{HB}c_{HWB} \\ & +0.61(-0.133+c_{HW})^2+0.08c_{HB}c_{HW}-1.21c_{HWB}c_{HW} \\ & +0.05c_{HB}c_{HWB}c_{HW} \end{aligned} \tag{6.4}$$

This function approximates the actual dependence on the Wilson coefficients, which is defined by a ratio of polynomials as given in Equation 6.2. The effect of the acceptance function on the parametrization for $H\to ZZ^*\to 4l$ is shown in Figure 6.4 where there is a considerable difference in the parametrization when the acceptance function is included. The $H\to\gamma\gamma$ channel is expected to have a higher sensitivity to these same SMEFT parameters, therefore the issue of the acceptance from $H\to ZZ^*\to 4l$ is diminished in the combined fit compared to the standalone $H\to ZZ^*\to 4l$ analysis.

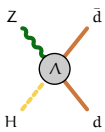

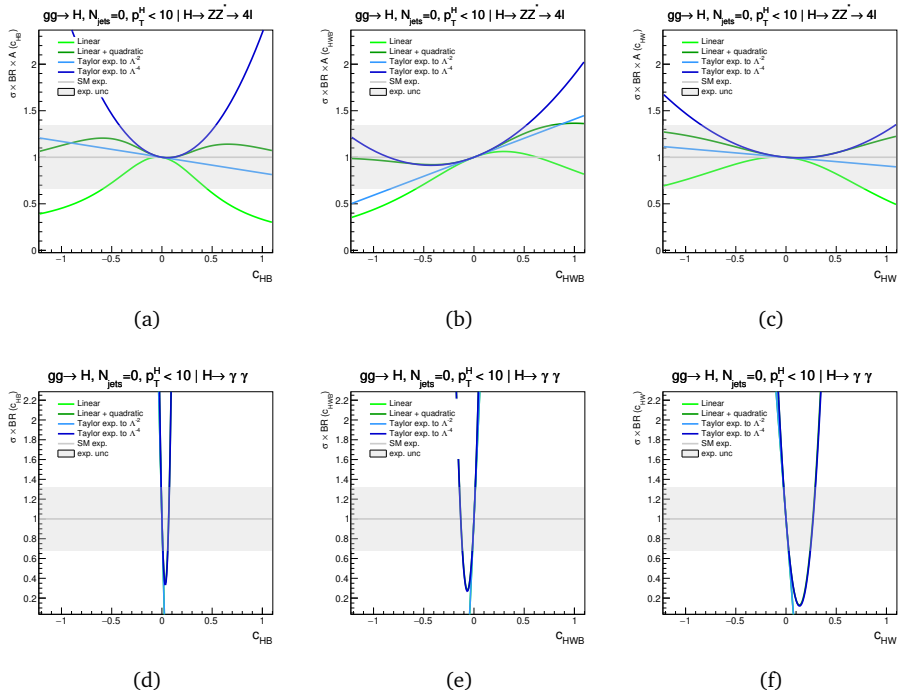

Figure 6.4: Parameterization of the STXS bins ($gg \rightarrow H, N_{jets} = 0, p_T^H < 10$ in the $H \rightarrow ZZ^* \rightarrow 4l$ (top) and the $H \rightarrow \gamma\gamma$ channel (bottom) for the three parameters c_{HB}, c_{HWB}, and c_{HW} where there are considerable changes to the parametrization in the $H \rightarrow ZZ^* \rightarrow 4l$ channel. The corresponding parametrization of the $H \rightarrow \gamma\gamma$ channel is shown for reference exhibiting the linear and linear + quadratic behavior.

6.5 Sensitivity study to determine parameters of interest

All the Wilson coefficients affecting the Higgs boson are shown in Table 6.3 and cannot be measured simultaneously as there is not sufficient information in the ensemble of measurements. As an example, $c_{qq}^{(3,1)}$ and $c_{uu}^{(1)}$ are two parameters of four-fermion operators that primarily affect only the p_T^H spectrum in ttH as shown in Figure 6.5 and have similar shape impact and cannot be distinguished. The impact of this indistinguishable behavior of these parameters leads to a degeneracy in the likelihood within the SMEFT validity range of the parameters. This degeneracy results in the presence of a flat direction in the likelihood that cannot be constrained. Numerical minimizers like `MINUIT` cannot handle such degeneracies.

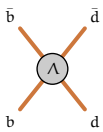

$O_{bq}^{(1)}$

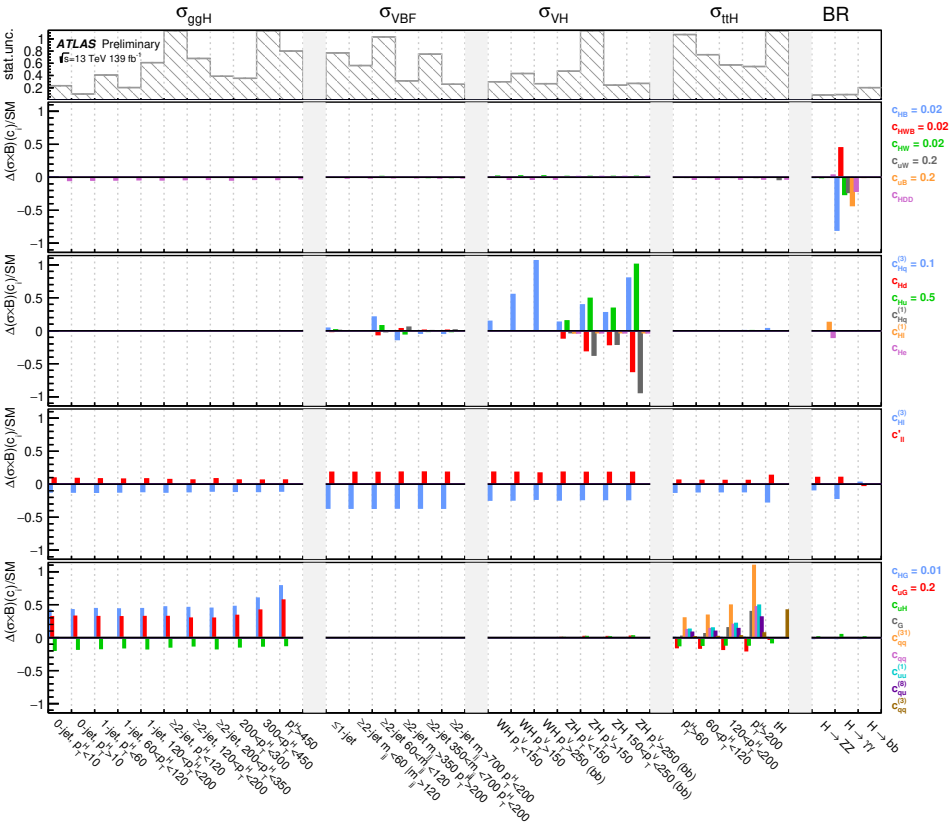

Figure 6.5: Impact of the most relevant SMEFT operators on the STXS regions and decay modes, relative to the SM cross-section, for the SMEFT model with only linear terms. For all coefficients c_j, a unit variation is considered unless specified otherwise in the legend. In order to judge the experimental sensitivity to constrain the operators from the data in the listed STXS regions, the statistical uncertainty on the corresponding regions (σ_{stat}) is shown in the top panel. For columns corresponding to multiple STXS×BR regions, the shown uncertainty reflects the statistical uncertainty on the average, under the assumption of uncorrelated statistical uncertainties. For presentational clarity, the statistical uncertainty of low-precision STXS regions is clipped in the plot.

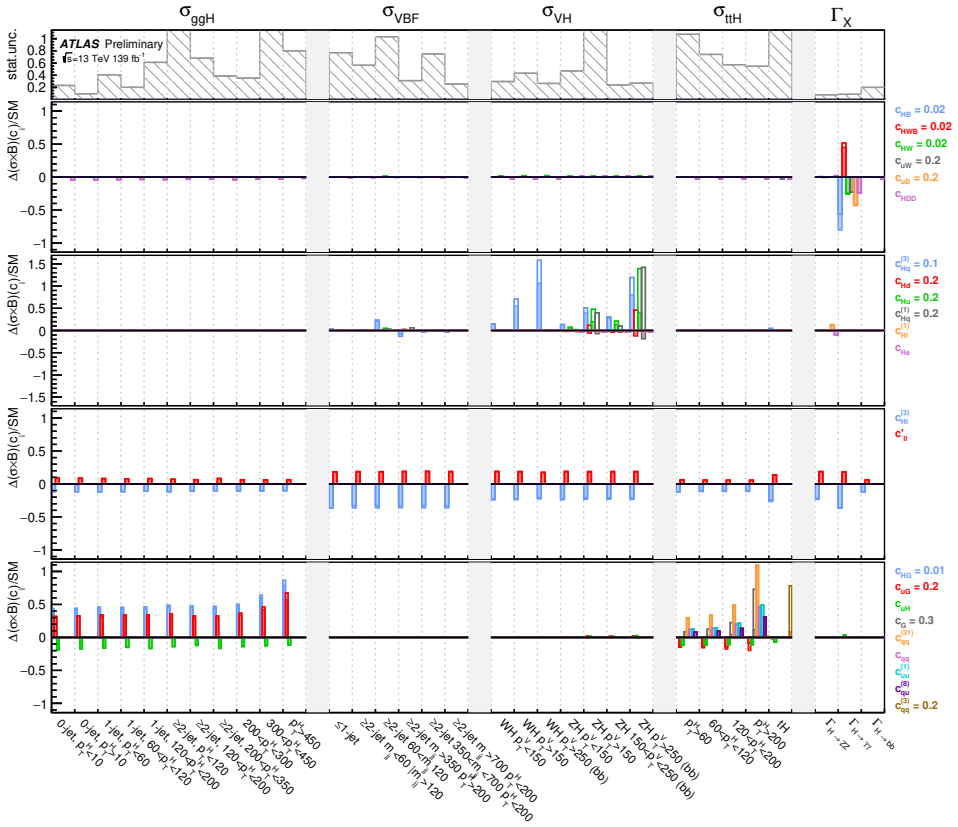

Figure 6.6: Comparison of the impact of the most relevant SMEFT operators on the STXS regions and decay modes, relative to the SM cross-section, for the linearized SMEFT model (shaded histogram) and the linear+quadratic SMEFT model (open histogram). For all coefficients c_j, a unit variation is considered unless specified otherwise in the legend. The variations shown for some c_j differ from those shown in Figure 6.5. In order to judge the experimental sensitivity to constrain the operators from the data in the listed STXS regions, one can refer to the top panel, which displays the statistical uncertainty (σ_{stat}) on the corresponding regions. For columns corresponding to multiple STXS×BR regions, the shown uncertainty reflects the statistical uncertainty on the average under the assumption of uncorrelated statistical uncertainties. For presentational clarity, the statistical uncertainty of low-precision STXS regions is clipped in the plot.

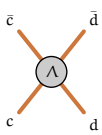

$O^{(1)\prime}_{quqd}$

Hence, it is necessary to predefine a subset of directions that we can expect to constrain well and keep the remaining directions fixed.

The likelihood function, shown as a function of $c_{qq}^{(3,1)}$ and $c_{uu}^{(1)}$ in Figure 6.7, illustrates the existence of a flat direction. A rotation that defines an orthogonal basis in terms of $c'^{[1]} = -0.41c_{qq}^{(3,1)} + 0.91c_{uu}^{(1)}$ and $c'^{[2]} = -0.91c_{qq}^{(3,1)} - 0.41c_{uu}^{(1)}$ allows to separate all flat directions from measurable directions in this example. A subsequent fit to the rotated likelihood function will only consider the first degree of freedom $c'^{[1]}$ as the parameter of the model.

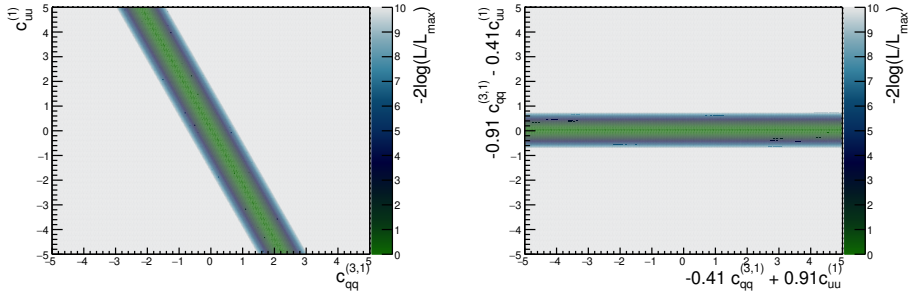

Figure 6.7: Plot of the negative log-likelihood value as a function of $c_{qq}^{(3,1)}$ and $c_{uu}^{(1)}$ (left) and in terms of the rotated directions $-0.41c_{qq}^{(3,1)} + 0.91c_{uu}^{(1)}$ and $-0.91c_{qq}^{(3,1)} - 0.41c_{uu}^{(1)}$ (right).

Following this procedure, a modified basis c'_i is used to separate all flat directions. The modified basis is estimated from the experimental sensitivity, making use of the SM expected covariance matrix V_{STXS} of the STXS measurements. The correlation matrix C_{STXS} corresponding to the V_{STXS} is shown in Figure 6.3. The Fisher information matrix V_{STXS}^{-1} is obtained by numeric inversion and the Fisher information is rotated from the STXS basis $\mu^{i,X}$ to the SMEFT basis c_j using the linear parametrization matrix $P_{(i,X)\to(j)}$ as follows,

$$V_{SMEFT}^{-1} = P_{(i,X)\to(j)}^{T} \, V_{STXS}^{-1} \, P_{(i,X)\to(j)}. \tag{6.5}$$

The rotation matrix $P_{(i,X)\to(j)}$ is based on the linearized SMEFT model of Equation 5.14

$$P_{(i,X)\to(j)} = A_j^{\sigma_i} + A_j^{\Gamma^{H\to X}} - A_j^{\Gamma^{H}}, \tag{6.6}$$

where $A_j^{\sigma_i}$, $A_j^{\Gamma^{H\to X}}$, and $A_j^{\Gamma^{H}}$ are the constant factors obtained from simulation.

The expected Fisher information matrix for the SMEFT parameters in the Warsaw basis is shown in Figure 6.8(a). In the normalized Fisher shown in Figure 6.8(b)

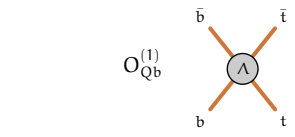

clearly identifies parameters measured by similar experimental information with value ± 1.

6.5.1 Full Eigenvector decomposition

In the limit of Gaussian approximation for the STXS measurements, the matrix V^{-1}_{SMEFT} represents the expected Fisher information matrix of SMEFT parameters. An eigenvalue decomposition of the Fisher information matrix orders the parameters in the SMEFT space by sensitivity and yields the eigenvectors e_i and their corresponding variances obtained from the eigenvalues, $V(e_i) = E_i^{-1}$.

Figure 6.9 lists the eigenvectors and their corresponding eigenvalues obtained from the expected measurements, ranked by eigenvalues. The eigenvectors shown are truncated to eigenvalues $\lambda_i > 0.01$, corresponding to a truncation at an estimated uncertainty of $\sigma_{e_i} < 10$, corresponding to a value well beyond the expected validity range of the c_i of EFTs of $O(1)$.

6.5.2 Principal component analysis within subgroup of operators

While the full eigenvectors shown in Figure 6.9 allow decorrelating the parameter directions fully, it mixes operators with different physics nature, reducing the conceptual clarity of the parameters estimated in the fit. It is desirable to define a basis that maintains the clarity of the physics impact of operators to the extent that this is numerically feasible, at the expense of allowing small to moderate correlations between the parameter estimates.

Based on the ranking of Figure 6.9 and the sensitivity of the STXS regions to the Wilson coefficients in the linearized model, as shown in Figure 6.5, the following behavior is observed:

- Parameter $c^{(3)}_{Hq}$ can be individually well constrained (ev-3). The sensitivity is driven by the WH measurements, in particular $H \to b\bar{b}$ (VH).
- Parameters c_{HG}, c_{uG} and c_{uH} are constrained by ggH and $t\bar{t}H$, while, c_{qq}, $c^{(3)}_{qq}$, $c^{(31)}_{qq}$, $c^{(1)}_{uu}$, $c^{(8)}_{ud}$, $c^{(1)}_{qu}$, $c^{(8)}_{qu}$, and c_G are only constrained from $t\bar{t}H$ (and $c^{(3)}_{qq}$ from tH) and affect the shape of the signal in a similar way. Therefore, only one linear combination (ev-5) of them can be precisely estimated. The most sensitive of these eigenvectors (ev-1,2) is a combination of c_{HG} and c_{uG}, which are the operators constrained strongest from ggH.
- Parameters c_{HW}, c_{HB} and c_{HWB} are primarily constrained from $H \to \gamma\gamma$ decay (ev-1). The direction of ev-1 agrees at the percent level with the predicted direction from the analytical calculation for $H \to \gamma\gamma$ decay width, as well as with the

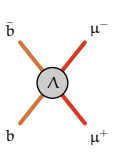

O_{eb}

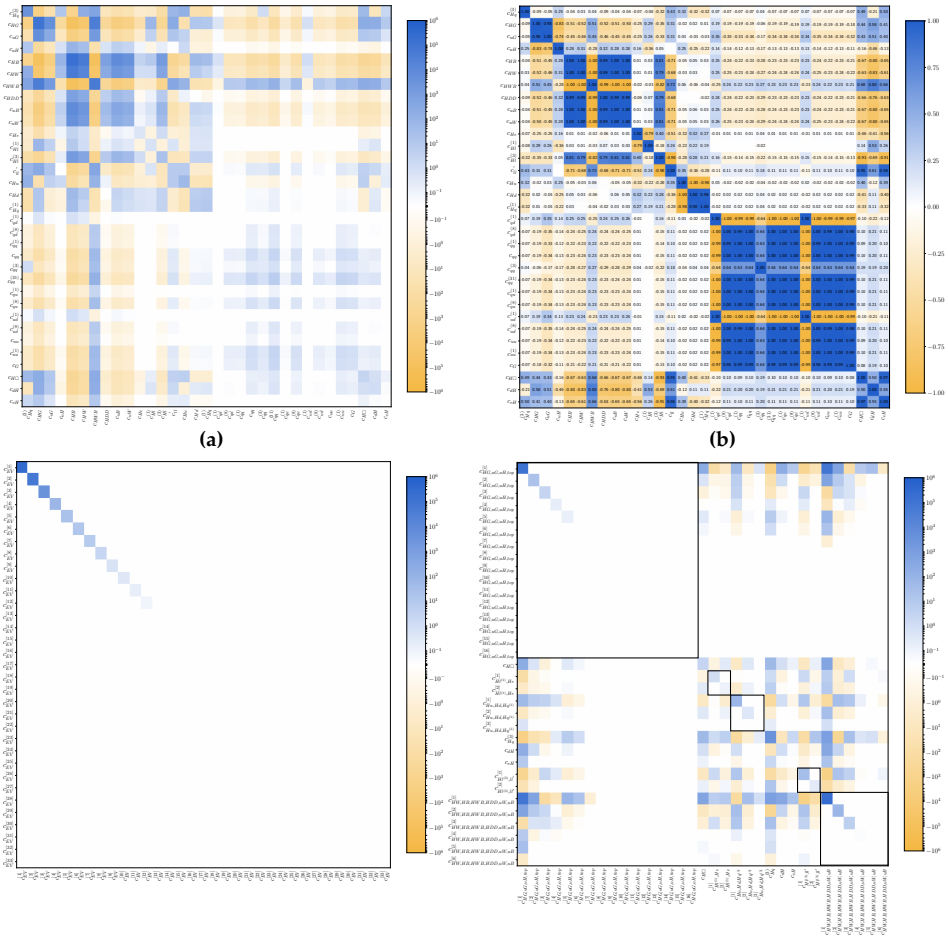

Figure 6.8: Expected Fisher information matrix V^{-1}_{SMEFT} in terms of the SMEFT parameters in the Warsaw basis are shown in (a), the colors represent the value of the Fisher information. The corresponding normalized matrix is shown in (b). The expected Fisher information after rotation to order the basis by information is shown for the full eigenvector basis (c) and the subgroup eigenvector basis (d).

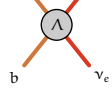

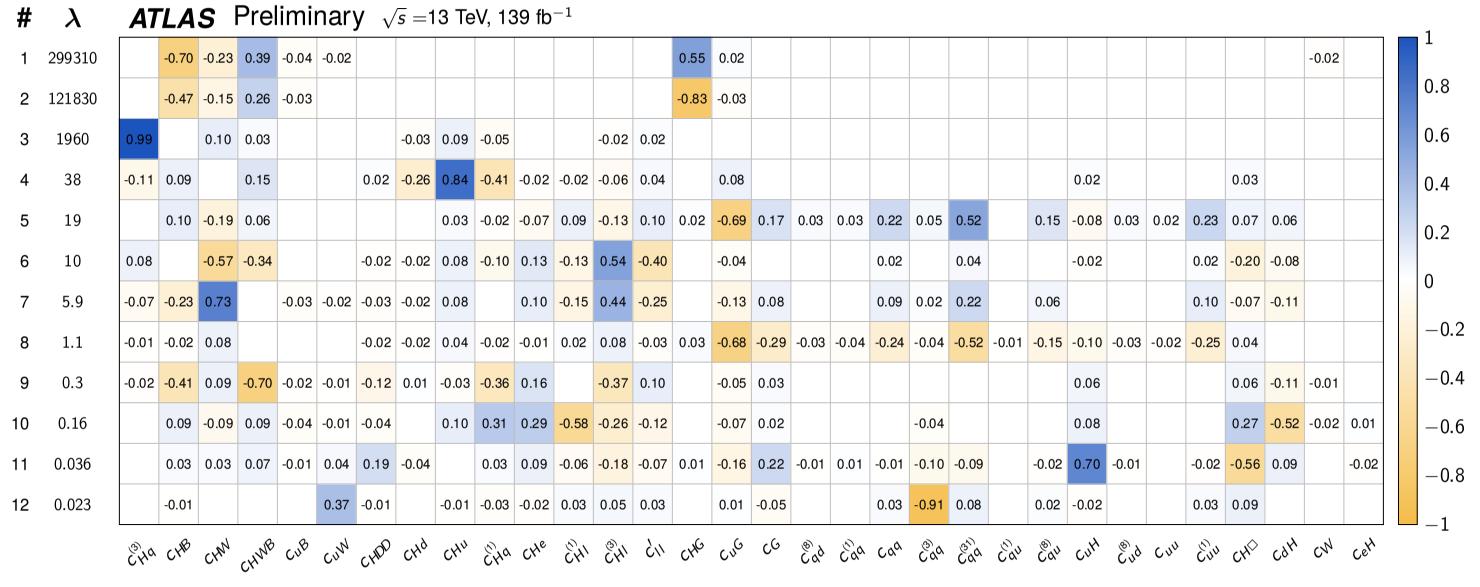

Figure 6.9: Eigenvectors of the inverse EFT covariance matrix obtained from EFT propagation to the covariance matrix V_{STXS} and with a significant (>0.01) eigenvalue λ. This eigenvalue threshold corresponds to an approximate expected uncertainty on that eigenvector of > 10.

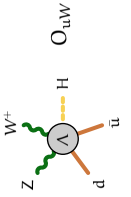

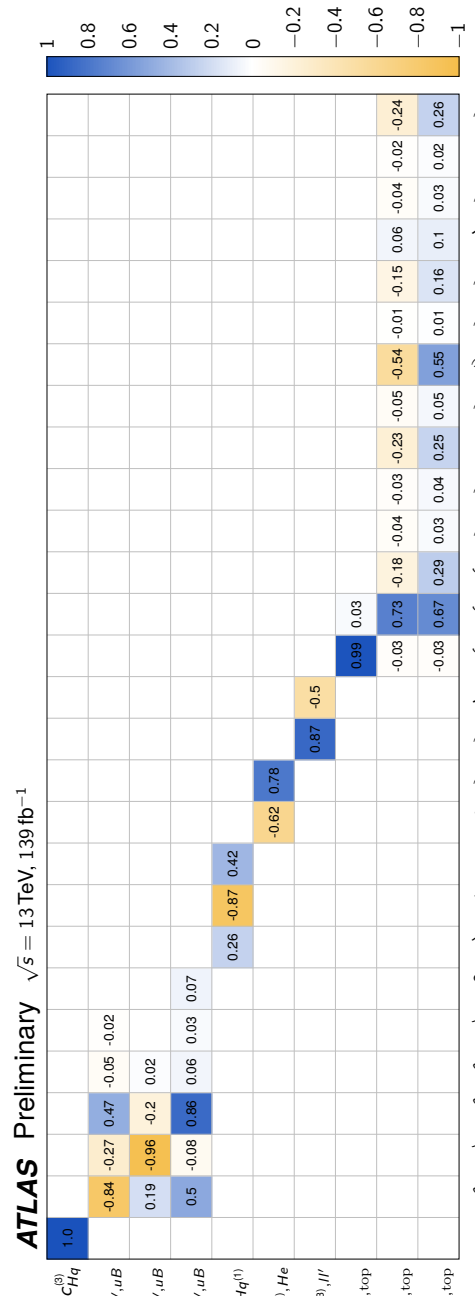

Figure 6.10: Visualization of the rotation matrix from the Warsaw basis c_j to the fit basis c'_j. The indices [i] denote the rank of the direction within the subspace ordered by increasing expected uncertainty.

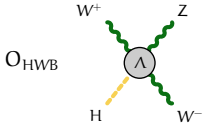

direction defined by the coefficient $C_{\gamma\gamma}$ of the SILH basis. Weaker constraints arise through constraints with VH and VBF production (ev-2,3).

- A notable correlation exists between the weak constraints on $c^{(1)}_{Hl}$, c_{He}, and $c^{(1)}_{Hq}$ (ev-9,10). This correlation has its source in the common measurement of most of these: $H \to b\bar{b}$ (VH). The $c^{(1)}_{Hl}$ and c_{He} parameters also affect the branching ratio of $H \to ZZ^* \to 4l$. The impact of $c^{(1)}_{Hq}$ is similar to c_{Hu} and c_{Hd} are expected to be correlated due to their similar impact on ZH production (ev-4). Based on these observations, $c^{(1)}_{Hl}$ and c_{He} are grouped, and c_{Hu}, c_{Hd} and $c^{(1)}_{Hq}$ are grouped.
- $c^{(3)}_{Hl}$ and c'_{ll} arise from operators that induce a shift to the Fermi constant and appear as constant modifier across production modes as seen in Figure 6.5.

The parameters $c_{H\Box}$, c_{dH}, and c_{eH} act primarily as a global cross-section scale factor. Hence, they are degenerate with a rescaling of all other c_j and are therefore fixed to zero in the fit. Balancing the aims of easy interpretability (each c_j maps to a model parameter, or combinations of c_j that arise in similar processes map to model parameter) and full decorrelation achieving numeric stability, a new eigenvector decomposition in sub-spaces is constructed with guidance from the above observations on the decomposition:

$$
\begin{aligned}
\boldsymbol{c} = {} & \{c^{(3)}_{Hq}\} \cup \\
& \{c_{HG}, c_{uG}, c_{uH}, c^{(1)}_{qq}, c_{qq}, c^{(3)}_{qq}, c^{(31)}_{qq} \\
& c_{uu}, c^{(1)}_{uu}, c^{(8)}_{ud}, c^{(1)}_{qu}, c^{(8)}_{qu}, c^{(8)}_{qd}, c_G\} \cup \\
& \{c_{HW}, c_{HB}, c_{HWB}, c_{HD}, \\
& \\
& c_{uW}, c_{uB}\} \cup \\
& \{c_{Hu}, c_{Hd}, c^{(1)}_{Hq}\} \cup \\
& \{c^{(1)}_{Hl}, c_{He}\} \cup \\
& \{c^{(3)}_{Hl}, c'_{ll}\} \cup
\end{aligned}
\quad \to \quad
\begin{aligned}
\boldsymbol{c'} = {} & \{c^{(3)}_{Hq}\} \cup \\
& \{c^{[1]}_{HG,uG,uH,top}, c^{[2]}_{HG,uG,uH,top}, \\
& c^{[3]}_{HG,uG,uH,top}\} \cup \\
& \{c^{[1]}_{HW,HWB,HDD,uW,uB}, \\
& c^{[2]}_{HW,HWB,HDD,uW,uB}, \\
& c^{[3]}_{HW,HWB,HDD,uW,uB}\} \cup \\
& \{c^{[1]}_{Hu,Hd,Hq^{(1)}}\} \cup \\
& \{c^{[1]}_{Hl^{(1)},He}\} \cup \\
& \{c^{[1]}_{Hl^{(3)},ll'}\}.
\end{aligned}
$$

The definition of the parameters entering the fit from basis c'_j with respect to the Warsaw basis is visualized in Figure 6.10.

While the full eigenvector rotation will fully diagonalize the Fisher information matrix as shown in Figure 6.8b, the subgroup rotation diagonalizes only the direc-

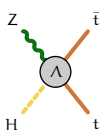

$O^{(1)}_{HQ}$

tions within the subgroup as shown in Figure 6.8d. The non-zero blocks between the parameter groups lead to residual correlations between the parameters.

The impact of variations of c'_j on the STXS cross-sections and Higgs boson branching fractions is shown in Figure 6.11, using the same parameter grouping as was shown in Figure 6.5, and demonstrates clearly that the basis c'_j represents impact variations across regions that are much more orthogonal than the Warsaw basis c_j.

No separate optimization of the parameter basis c'_j is performed for the quadratic SMEFT model of Equation 5.18 as the non-linear effects of this model are expected to vanish for small c_j, thus asymptotically yielding the same rotation matrix as Equation 6.6.

6.5.3 Contribution of individual Higgs measurements to SMEFT parameter measurements

The fit directions chosen are defined by choosing the sensitive directions within the operator subgroup that have a similar physics impact. The information matrix used in this process also provides a way to obtain the relative contribution of measurements to the sensitivity of the particular SMEFT parameter.

The fractional contribution $f_{\mathbf{m}}(c_i)$ of a set of measurement $\mathbf{m}$ to the sensitivity a SMEFT parameter c_i is defined as,

$$f_{\mathbf{m}}(c_i) = \frac{\sigma^{-2}_{\mathbf{m}}(c_i)}{\sum_{k\in\text{meas.}} \sigma^{-2}_{\mathbf{k}}(c_i)} \tag{6.7}$$

where $\sigma^{-2}_{\mathbf{m}}(c_i)$ is the inverse of the estimate for the variance of parameter c_i due to the measurement set $\mathbf{m}$. The estimate of σ^{-2} can be directly obtained by inverting the reduced information matrix, yielding the corresponding value of σ^2. This procedure also accounts for correlations between the parameters. The contribution of the different decay modes is shown in Figure 6.12(b) and for the production modes in Figure 6.12(a).

The leading measurements contributing to the sensitivities of each of the parameters can be understood as follows,

- $c_{HG,uG,uH,top}$: In this operator group the leading direction $c^{[1]}_{HG,uG,uH,top}$ is mainly constrained by the measurement of Higgs boson production in the ggF production mode. The production mode is measured in $H \to \gamma\gamma$ and $H \to 4l$ channel and the relative sensitivity to the ggF production mode in the two channels is shown in the decay-side contribution in Figure 6.12(b). The second direction, $c^{[2]}_{HG,uG,uH,top}$, is dominated by operators that affect the $t\bar{t}H, tH$ production processes and is mainly constrained by the $H \to \gamma\gamma$ channel. The parameter

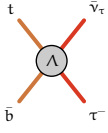

$c^{[3]}_{HG,uG,uH,top}$ consists of operators affecting both ggF and $t\bar{t}H, tH$ production is also primarily measured from the $H \to \gamma\gamma$ channel.

- $c^{[1]}_{Hl^{(1)},He}$: The leading parameter is the only sensitive direction here and is constrained on the decay side by the measurement of the $BR(H \to ZZ)$.
- $c^{[1]}_{Hu,Hd,Hq^{(1)}}$: The leading parameter is constrained by ZH production with the main sensitivity originates from the $VH, H \to bb$ analysis.
- $c_{Hq^{(3)}}$: This operator is constrained by WH production where the main sensitivity originates from the $VH, H \to bb$ analysis.
- $c^{[1]}_{Hl^{(3)},ll'}$: This direction corresponds to a shift in the Fermi constant (ΔG_F), and is a global correction to the production and decay rates.
- $c_{HW,HWB,HDD,uW,uB}$: The leading direction in this group is constrained by the measurement of the $BR(H \to \gamma\gamma)$. The second direction is constrained by a combination of sensitivity from VBF, VH production and $BR(H \to \gamma\gamma)$. The third direction is constrained mostly by ZH measurements.

6.6 Results

In all results presented in this Section, the set of nuisance parameters $\boldsymbol{\theta}$ has been pruned, using an impact ranking technique, from O(1000) down to O(700) nuisance parameters, which has an estimated cumulative impact on the estimated systematic uncertainty on each signal strength parameter of less than 1%.

The results on the parameters using the linearized SMEFT model and including the quadratic terms are shown for observed results in Figure 6.14 and the SM expected constraints in Figure 6.15. All measured parameters are consistent with the SM expectation within their uncertainty. The correlation matrix for the linearized model for observed and expected is provided in Figure 6.13. The subgroup basis directions exhibit correlations due to residual information between the subgroups.

All scanned parameters for the linearized model exhibit Gaussian behavior to a good approximation, except for $c^{[1]}_{Hl^{(1)},He}$, which is affected by the non-linear acceptance correction effects in the $H \to ZZ^* \to 4\ell$ decay channel due to correlations with the parameters c_{HW}, c_{HWB}, and c_{HB} that affect the acceptance parametrization given in Equation 6.3.

The profile likelihood for the model, including quadratic terms, sometimes results in two local minima per parameter, notably for $c^{[1]}_{HW,HB,HWB,HDD,uW,uB}$ and $c^{[3]}_{HG,uG,uH,top}$, and to a lesser extent $c^{(3)}_{Hq}$, and generally result in rather non-Gaussian likelihood scans for that reason. Despite this, constraints obtained from the model, including quadratic terms, are generally tighter than those obtained

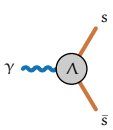

$O^{(3)}_{Hl}$

from the linearized model, suggesting a non-negligible influence of dimension-8 operator terms suppressed by power Λ^{-4}.

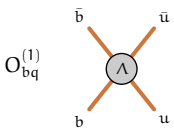

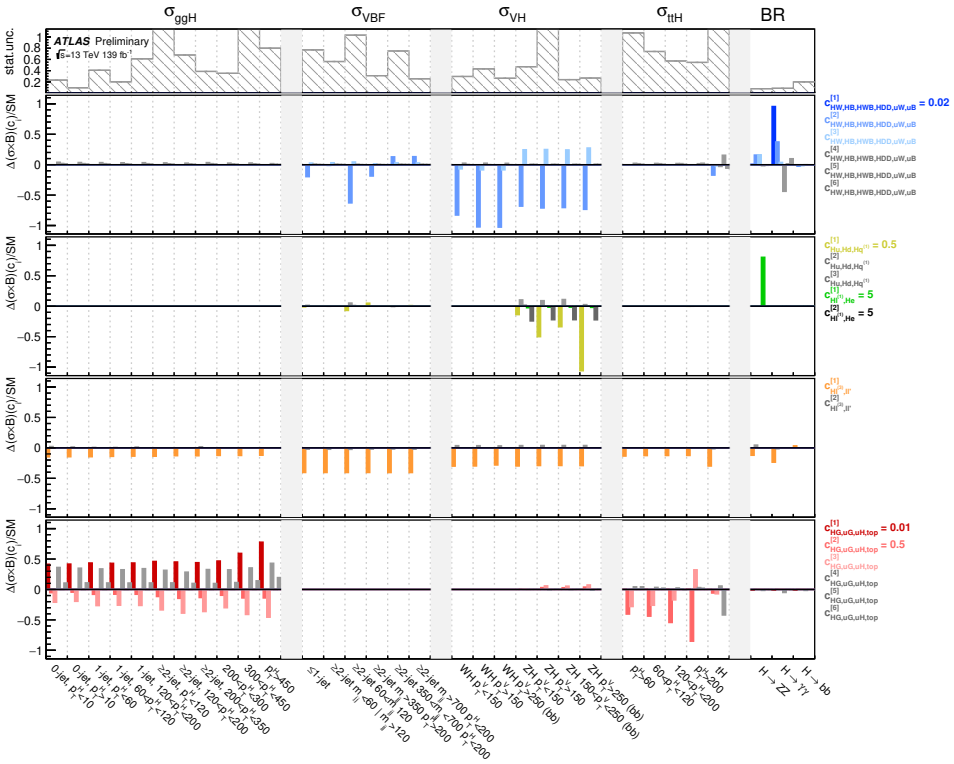

Figure 6.11: Impact of coefficients of the rotated basis c'_j on the STXS regions and decay modes, relative to the SM cross-section, under the assumption of the linearized SMEFT model. For all coefficients c'_j a unit variation is considered unless specified otherwise in the legend. Additional eigenvectors that are not part of the fit basis are shown in gray for completeness. Scales and groupings in this figure are consistent with those in Figure 6.5. To judge the experimental sensitivity to constrain the operators from the data in the listed STXS regions, the statistical uncertainty on the corresponding regions (σ_{stat}) is shown in the top panel. For columns corresponding to multiple STXS×BR regions, the shown uncertainty reflects the statistical uncertainty on the average, under the assumption of uncorrelated statistical uncertainties. For presentational clarity, the statistical uncertainty of low precision STXS regions are clipped in the plot.

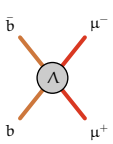

O_{Qe}

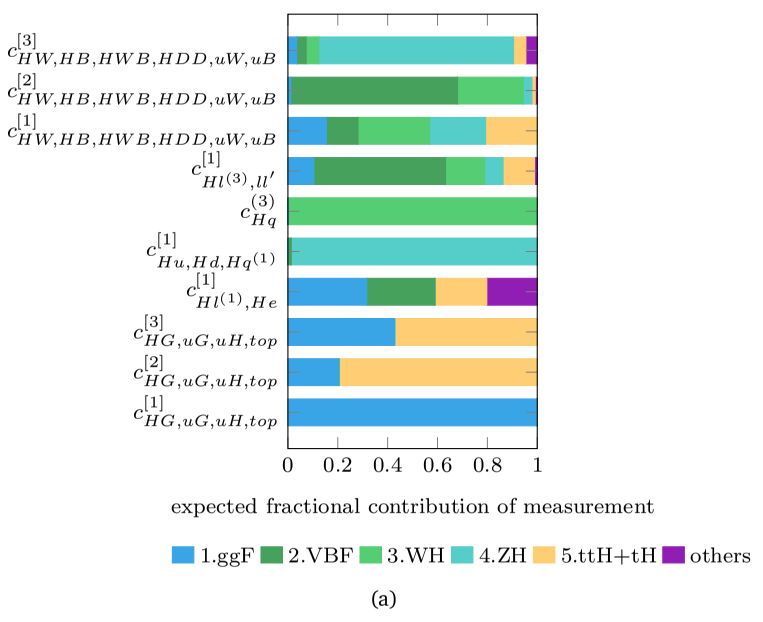

(a)

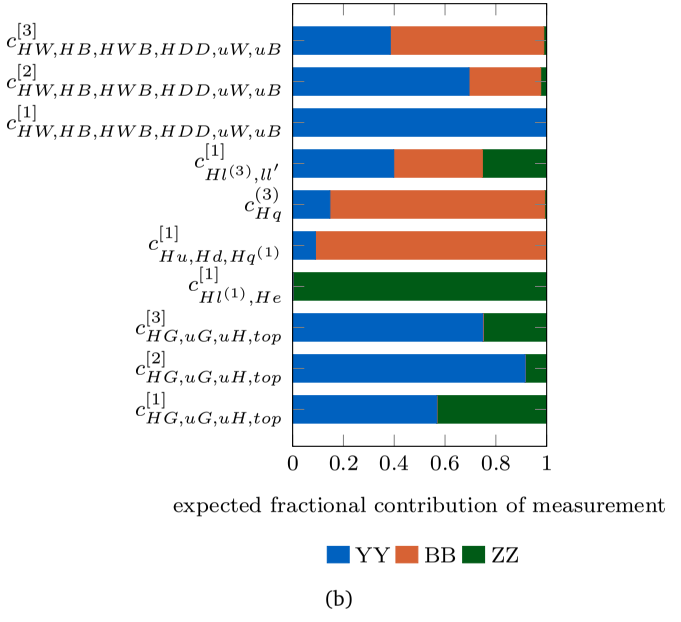

(b)

Figure 6.12: The contribution of the different measurements to the sensitivity of the SMEFT parameters split by production 6.12(a) and decay modes 6.12(b). For the production modes, those bins which are inclusive in the production modes are categorized as inclusive (inc.).

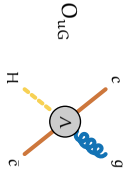

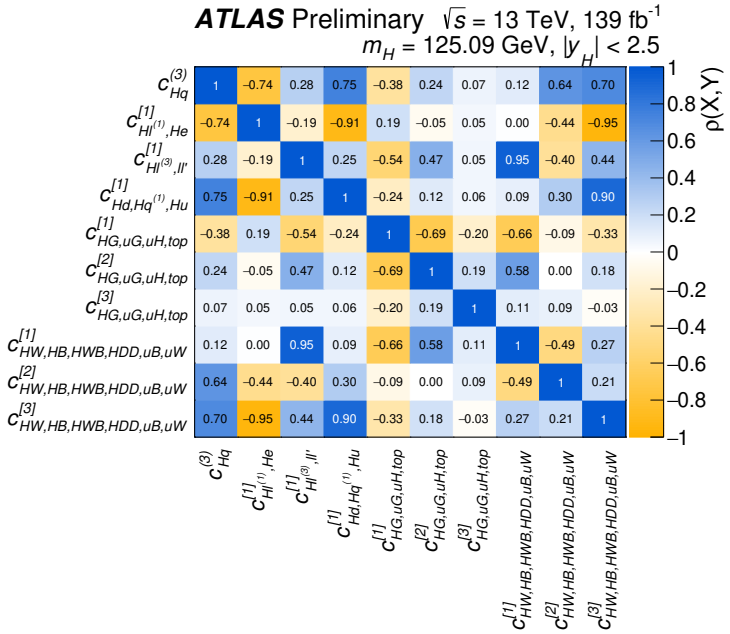

(a)

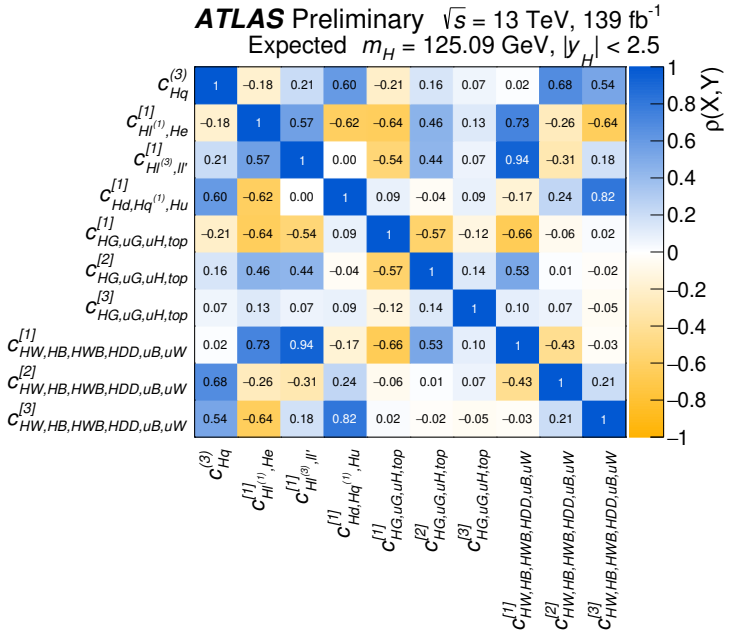

(b)

Figure 6.13: Correlation matrix for the linearized SMEFT model for the observed data (top) and expected (bottom).

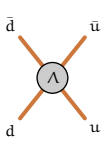

$O_{ud}^{(1)}$

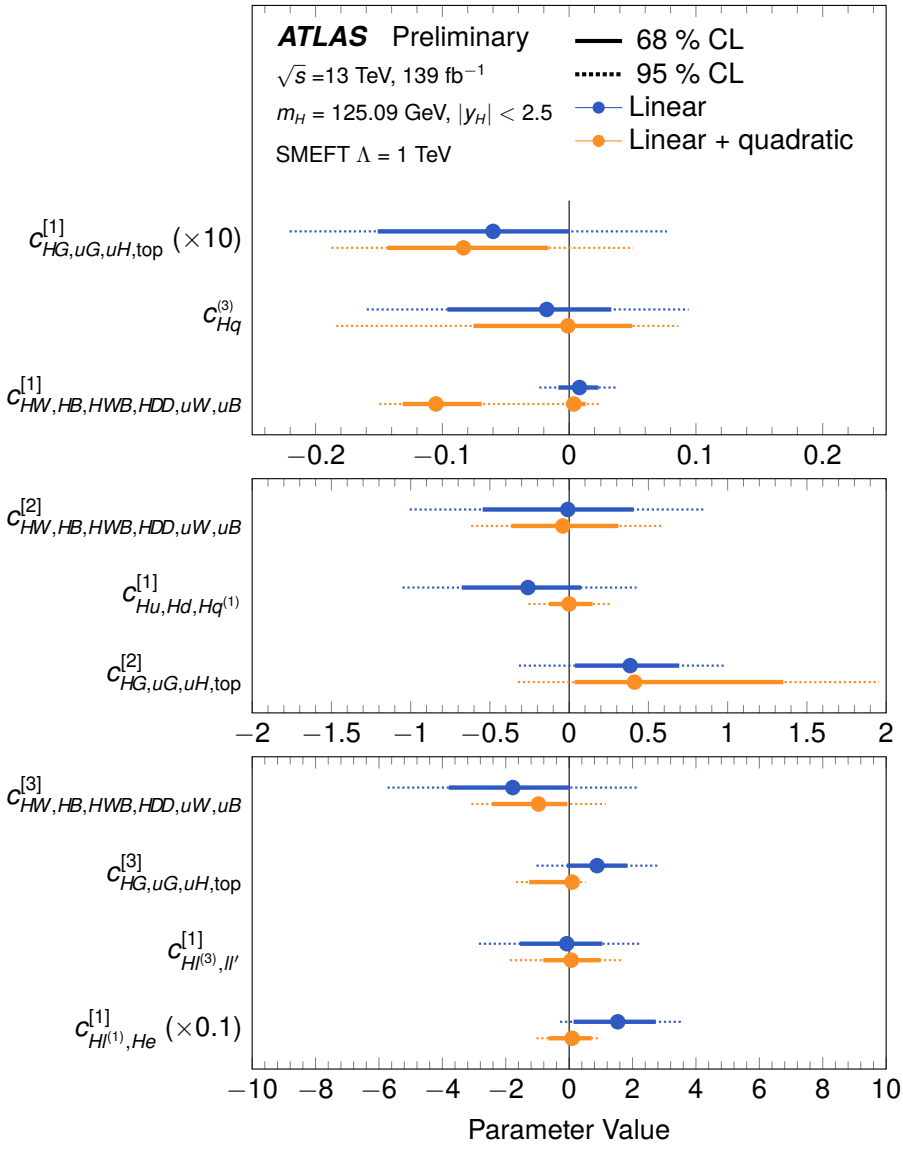

Figure 6.14: Summary of observed measurements of the parameters c_i' with the SMEFT linearized model (blue) and the SMEFT model with additional quadratic terms (orange). The ranges shown correspond to 68% (solid) and 95% (dashed) confidence level intervals, where all other coefficients and all nuisance parameters were profiled. For the model with quadratic terms, two exactly degenerate solutions are found for $c^{[1]}_{HW,HB,HWB,HDD,uW,uB}$, which are both indicated.

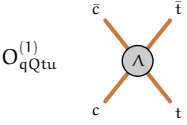

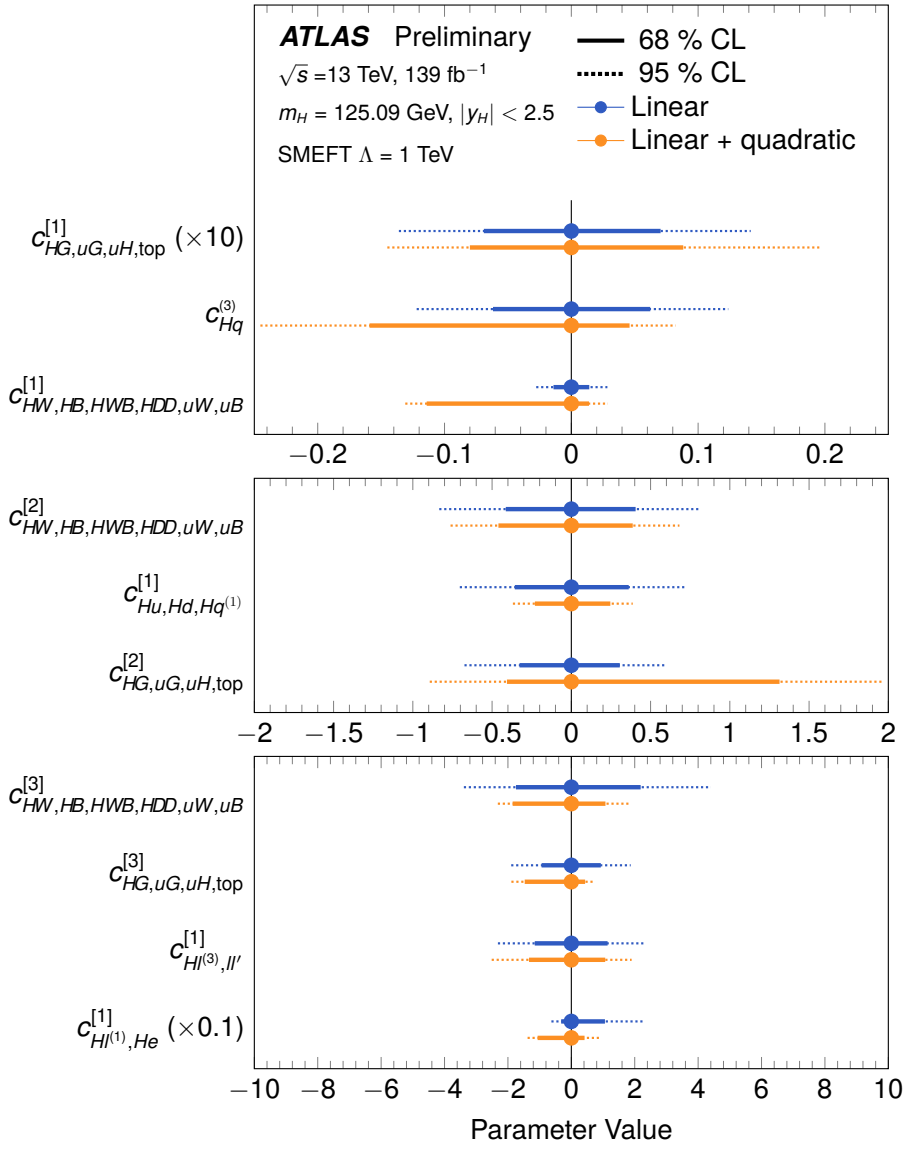

Figure 6.15: Summary of SM expected measurements of the parameters c_i' with the SMEFT linearized model (blue) and the SMEFT model with additional quadratic terms (orange). The ranges shown correspond to 68% (solid) and 95% (dashed) confidence level intervals, where all other coefficients and all nuisance parameters were profiled.

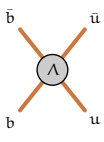

$O^{(8)}_{Quqb}$

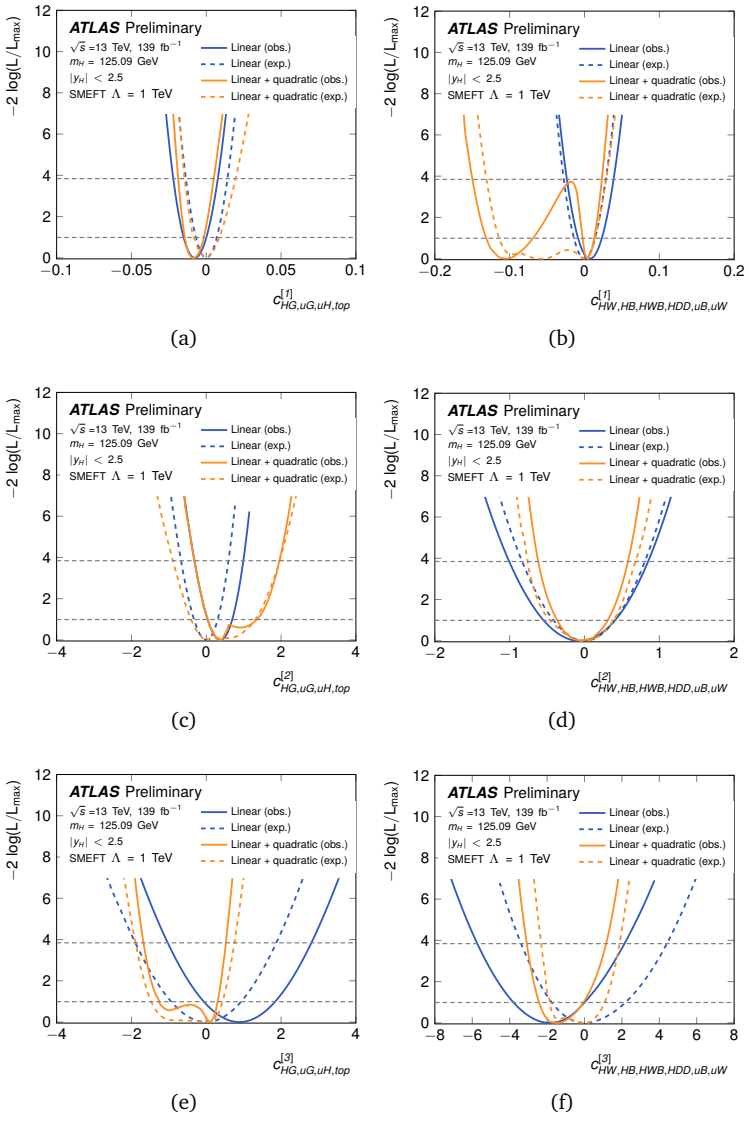

Figure 6.16: Profile likelihood scans of the fitted coefficients c_j' on SM expected and observed data, comparing the SMEFT linearized model (blue) and the SMEFT linear plus quadratic model (orange). The horizontal dashed lines in each plot correspond to the asymptotic threshold values for 68% and 95% confidence intervals. Profile likelihood scans of the linear plus quadratic model can exhibit 2 minima in the scanned parameter, whereas scans of the linearized model can only have one minimum per parameter observed data in (c)).

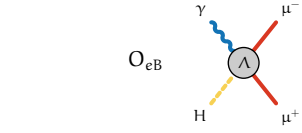

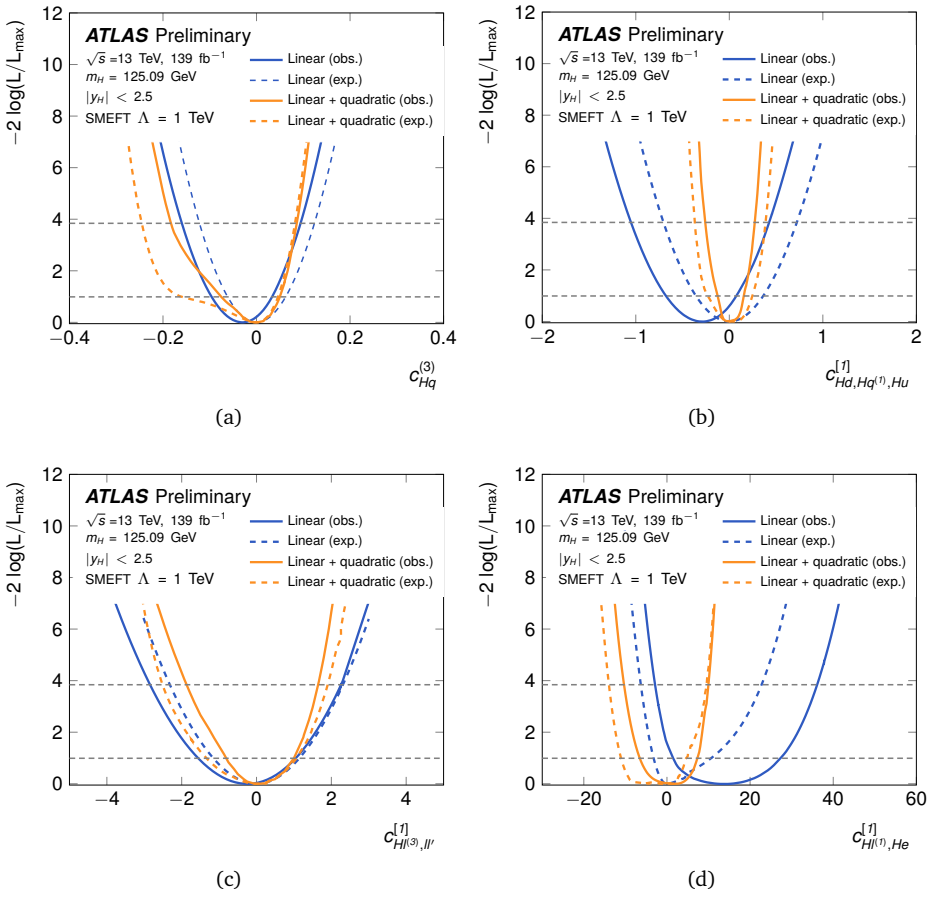

Figure 6.17: Profile likelihood scans of the fitted coefficients c'_j on SM expected and observed data, comparing the SMEFT linearized model (blue) and the SMEFT linear plus quadratic model (orange). The horizontal dashed lines in each plot correspond to the asymptotic threshold values for 68% and 95% confidence intervals. Profile likelihood scans of the linear plus quadratic model can exhibit 2 minima in the scanned parameter, whereas scans of the linearized model can only have one minimum per parameter. Multiple minima in the coefficients c'_j that are profiled in each scan may furthermore result in discontinuities in the profile likelihood.

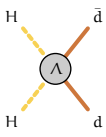

O_{dH}

7

SMEFT Interpretation of ATLAS Run-2 measurements of Higgs boson measurements

Since the discovery of the Higgs boson in 2012, the ATLAS experiment has recorded more than 30 times as many Higgs bosons with respect to the dataset used in the discovery, allowing much more precise measurements and stringent tests of the Standard Model.

This chapter presents the SMEFT interpretation of the combined Higgs boson measurements based on the dataset collected by the ATLAS experiment during Run-2 of the LHC. With respect to the analysis discussed in Chapter 6, several improvements have been implemented. The SMEFT flavor symmetry requirement has been relaxed to account for a dedicated treatment of the top and bottom quark, as well as all lepton families. Additionally, the parametric form of the SMEFT dependence is updated to avoid a Taylor expansion. Finally, many new input channels are included and are described below in Section 7.1. These include both high statistics channels, such as $H \to WW^* \to l\nu l\nu$, and rare searches, such as $H \to \mu\mu$, and allow to extend the sensitivity to SMEFT operators.

7.1 Input Analyses

The results presented in this chapter are updated with additional inputs that cover the five major Higgs boson decay channels and include two rare decay channels. The decay channels measured for the targeted production modes used in each input analysis are summarized in Table 7.1. The new input analyses which have not already been described in Chapter 6 are described further here.

7.1.1 $H \to WW^* \to e\nu\mu\nu$

The $H \to WW^*$ channel has a large branching fraction (21.8%) and benefits from a relatively low background from other SM processes due to having two charged

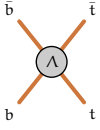

Decay channel	Analysis Production mode	Reference	Binning
$H \to \gamma\gamma$	(ggF, VBF, WH, ZH, $t\bar{t}H$, tH)	[213]	STXS-1.2
$H \to ZZ^*$	($ZZ^* \to 4\ell$: ggF, VBF, $WH + ZH$, $t\bar{t}H + tH$)	[196]	STXS-1.2
$H \to \tau\tau$	(ggF, VBF, $WH + ZH$, $t\bar{t}H + tH$)	[214]	STXS-1.2
$H \to WW^*$	(ggH, VBF)	[215]	STXS-1.2
$H \to b\bar{b}$	(WH, ZH)	[197, 216]	STXS-1.2
	(VBF)	[217]	STXS-1.2
	($t\bar{t}H + tH$)	[218]	STXS-1.2
	(boosted Higgs bosons: inclusive production)	[219]	STXS-1.2
$H \to Z\gamma$	(inclusive production)	[220]	STXS-0*
$H \to \mu\mu$	(ggH + $t\bar{t}H$ + tH, VBF + WH + ZH)	[221]	STXS-0*

Table 7.1: The decay channels (1st column), targeted production modes (2nd column) and integrated luminosity $\mathcal{L}$ (3rd column) of the dataset used for each analysis included in the combined measurements of Higgs boson production and decay rates, couplings and simplified template cross-sections. The references for the input analyses. Note that for analysis targeting the STXS 1.2 framework, the bins measured in the analyses are typically merged in regions where the analysis is not sensitive to perform the kinematic split.

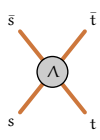

$O_{Qd}^{(8)}$

leptons of the different flavors in the final state. The decay also includes two undetected neutrinos in the final state, which poses a challenge in reconstructing the kinematics of the Higgs boson decay. The STXS analysis of the $H \to WW^* \to e\nu\mu\nu$ is described in [215] in detail.

The analysis requires two opposite-flavor leptons and varying numbers of jets depending on the analysis category. Electron candidates with 15 GeV $< E_T <$ 25 GeV satisfy the `TIGHT` working point. For $E_T >$ 25 GeV, the misidentification backgrounds are less important, so electron candidates satisfying the `MEDIUM` likelihood working point are chosen. For muons, the `TIGHT` working point, as defined in [201], is used.

Jets with $p_T > 20$ GeV and $|\eta| < 4.5$ are selected, with jets with $p_T > 30$ GeV being used for jet counting in the context of event categorization. Furthermore, a jet-vertex-tagger multivariate discriminant selection, which reduces contamination from pile-up, is applied to jets with $20 < p_T < 60$ GeV and $|\eta| < 2.4$, utilizing calorimeter and tracking information to separate hard-scatter jets from pile-up jets. Jets containing b-hadrons (b-jets) are identified using a neural network discriminant satisfying the 85% b-jet tagging efficiency working point.

An important feature to distinguish Higgs boson production from the background is the opening angle between the two leptons, which tends to be small for signal due to the spin-0 nature of the Higgs boson and the chiral structure in the W boson decay. Additionally, the final state may contain additional jets from quarks originating from VBF production or initial-state radiation from quarks or gluons. The analysis is performed separately for different jet categories, i.e. $N_{jet} = 0$, $N_{jet} = 1$, and $N_{jet} \geqslant 2$, and is further categorized for ggF and VBF signal production modes.

To reject background from top-quark production, events containing b-jets with $p_T > 20$ GeV are vetoed in all analysis categories. For the categories targeting the ggF production mode, the di-lepton transverse mass is used as a discriminating observable in the fit. For the $N_{jet} \geqslant 2$ category targeting the VBF production mode, the output of a deep neural network (DNN) trained to identify the VBF topology is used as the discriminating variable in the fit. The analysis combines all signal regions and measures eleven different bins, which correspond to merged bins in the STXS Stage 1.2 framework.

7.1.2 $H \to \tau\tau$

The Higgs boson decay to a $\tau^+\tau^-$ pair has the largest branching fraction (6.3%) for leptonic Higgs boson decays, which allows studying directly the Yukawa interaction as well as the kinematic properties of Higgs boson production. Measurements in this final state are experimentally challenging, as neutrinos in the final state

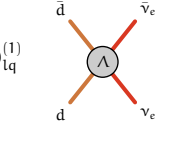

originating from the decay of the τ-leptons significantly degrade the measured Higgs boson four-momentum resolution.

The analysis is described in detail in [214] and targets three di-τ final states: two hadronically decaying τ-leptons ($\tau_{had}\tau_{had}$) ; one leptonically decaying τ-lepton and one hadronically decaying τ-leptons ($\tau_{had}\tau_{lep}$) and two leptonically decaying τ-leptons with different flavors ($\tau_\mu\tau_e$). Additional categories are defined to target Higgs bosons produced in association with objects such as jets, vector bosons, and top anti-top pairs.

The electrons used require the `LOOSE` identification criteria with $p_T > 15$ GeV as well as $|\eta| < 2.47$. In the $\tau_e\tau_\mu$ and $\tau_e\tau_{had}$ channels, the selected electron is additionally required to satisfy the `MEDIUM` identification criteria with the `LOOSE` isolation criteria. Muons with $p_T > 10$ GeV and $|\eta| < 2.5$ satisfying the `LOOSE` identification criteria are used. Finally, in the $\tau_e\tau_\mu$ and $\tau_\mu\tau_{had}$ channels, the selected muons are required to satisfy the `TIGHT` isolation requirement.

Hadronically decaying τ-leptons, denoted by $\tau_{had,vis}$, consists of a neutrino and a set of pions, which is reconstructed using a recurrent neural network to discriminate between jets initiated by quarks or gluons. A separate boosted decision tree discriminant is used to reject electrons that are misidentified. Each $\tau_{had,vis}$ is reconstructed with the anti-k_t algorithm and is required to have $p_T > 10$ GeV and $|\eta| < 2.5$. The $\tau_{had,vis}$ objects are also required to fulfill the `MEDIUM` identification requirement in the signal regions of the $\tau_{lep}\tau_{had}$ and $\tau_{had}\tau_{had}$ categories. Jets are required to fulfill $p_T > 20$ GeV and $|\eta| < 2.5$ are considered. For jets containing b-hadrons, the DL1r b-tagging algorithm is used with the 85% efficiency working point in the $\tau_e\tau_\mu$ and $\tau_{lep}\tau_{had}$ channels and the 70% efficiency working point in the $\tau_{had}\tau_{had}$ channel. The missing transverse momentum $\mathbf{E_T^{miss}}$ is defined as the negative vector sum of the transverse momenta of leptons, $\tau_{had,vis}$ and jets, and the soft-term.

The Higgs boson candidate is formed by the vector momentum sum of the visible τ-lepton decay products and $\mathbf{E_T^{miss}}$. Its invariant mass $m_{\tau\tau}^{MMC}$ is calculated using an advanced likelihood-based technique, the Missing Mass Calculator (MMC) [222], which relies on information about the τ-lepton candidate momenta, the presence of additional jets, $\mathbf{E_T^{miss}}$ and the type of τ-lepton decay. For each channel in the three $\tau^+\tau-$ final states, additional selection criteria are employed to enhance the SM Higgs boson signal and ensure a robust estimate of the invariant mass of the reconstructed $\tau^+\tau^-$ system. The events are further categorized in bins defined to target regions in the STXS framework. The categorization is performed with BDT taggers into the VBF, VH with hadronic-V decays (denoted V(had)H), and tt(0l)H $\rightarrow \tau_{had}\tau_{had}$ categories. The BDT taggers are designed inclusively for all $\tau^+\tau^-$ decay modes and make use of kinematic observables related to jet properties,

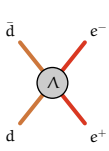

O_{ld}

angular distances, τ properties, reconstructed Higgs observables, and the missing transverse momentum.

High-p_T Higgs candidate events failing to meet the criteria of the VBF, V(had)H or ttH categories, that have high-p_T Higgs candidates are considered for the boosted categories targeting ggF events. Boosted events are required to satisfy $p_T^H > 100$ GeV and are further separated by a p_T^H split at 120, 200, and 300 GeV to match the requirements in the STXS framework. Additionally, events with $p_T^H < 200$ GeV are separated into 1-jet and $\geqslant$ 2-jet categories. The analysis measures cross-sections of nine regions corresponding to bins defined within the STXS framework.

7.1.3 $H \to b\bar{b}$

The Higgs boson decay into $b\bar{b}$ quarks is the most commonly occurring decay of the Higgs boson, with a branching fraction of 58%. However, this jet-only final state is very challenging to identify in the $p\bar{p}$ collisions of the LHC. The analysis of Higgs boson production in $VH, H \to b\bar{b}$ where the two b-jets are resolved separately is introduced in Chapter 6. In the following section, the other analyses from the $H \to b\bar{b}$ final state are described. These analyses are $VH, H \to b\bar{b}$ with boosted topology [216], $t\bar{t}H(H \to b\bar{b})$ [218], $VBF, (H \to b\bar{b})$ [217], and boosted $H \to b\bar{b}$ with a hadronic recoil system [219].

7.1.3.1 VBF, $H \to b\bar{b}$

The final state of the VBF, $H \to b\bar{b}$ process is characterized by two b-jets from the decay of the Higgs boson and two light-quark jets with a large rapidity gap coming from the spectator quarks. The analysis targets events with and without a high p_T forward jet two channels corresponding to the available triggers during data-taking periods.

Jets are reconstructed from calorimeter clusters and tracks that together constitute particle flow objects [223], and which are formed by applying the anti-k_t jet clustering algorithm with a radius parameter of R=0.4 [160, 224]. A multivariate algorithm is used to identify jets containing b-hadrons [225], and the 77% and 85% working points are used.

Photons, electrons, and muons are identified in order to veto events that overlap with other $H \to b\bar{b}$ channels. Muons are additionally used in an embedding procedure to determine the $Z \to b\bar{b}$ background. A tight, cut-based selection is applied to reject hadronic jets where a neutral meson carries most of the jet energy. Electrons are reconstructed based on the `LOOSE` likelihood-based identification criterion supplemented with `LOOSE` isolation requirements [202]. Muons reconstructed are required to satisfy `LOOSE` identification and isolation requirements [201].

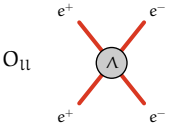

The background consists of events from two processes: non-resonant QCD multijet and $Z \to b\bar{b}$. The $Z \to b\bar{b}$ contribution is constrained directly from data using an embedding process in which $Z \to \mu^-\mu^+$ events are selected in data, the muons are replaced with b-jets from simulation, and the analysis selections are applied to determine the number of selected $Z \to b\bar{b}$ events. The multijet background shape is determined from the data, and the same shape is used in all regions for each channel. Events are divided into regions of varying signal-to-background composition by using an adversarial neural network (ANN). The ANN is trained on signal Monte Carlo (MC) events and data sidebands and defined such that the classifier output score is independent of the invariant mass of the two b-jets ($m_{b\bar{b}}$). Each channel is divided into five regions of varying sensitivity based on the ANN classifier score. The inclusive VBF Higgs boson signal is extracted through a simultaneous fit of the signal and background contributions to $m_{b\bar{b}}$ spectrum in all channels and regions.

7.1.3.2 VH, $H \to b\bar{b}$ (boosted)

The VH, $H \to b\bar{b}$ boosted analysis reconstructs Higgs bosons at large transverse momentum. In the boosted regime, the b-jets originating from the Higgs boson decay are close to each other and cannot be reconstructed separately as two small-R jets, as is done in the VH, $H \to b\bar{b}$ resolved analysis [197]. Instead, the Higgs boson is reconstructed as a single large-radius (large-R) jet with radius parameter R=1.0. The variable used to discriminate the Higgs boson signal from the background is the invariant mass of the large-R jet (m_J). The measurements at high-p_T regions of this analysis have enhanced sensitivity to SMEFT operators. Similar to the resolved analysis, the boosted analysis has separate regions defined by the number of reconstructed leptons corresponding to 0-,1- and 2-lepton channels.

Two types of leptons are defined, corresponding to a baseline lepton selection and a subset known as signal lepton with tighter selections. The low-threshold (7 GeV) baseline leptons are used to define the three main channels requiring exactly zero, one, and two leptons. The latter 1- and 2-lepton channels further require at least one signal lepton, with identification and isolation requirements chosen to optimize the suppression of the multijet background. Signal leptons must have a $p_T > 27$ GeV, except in the 1-lepton muon sub-channel, where a $p_T > 25$ GeV is used. The identification criteria for leptons closely follow the resolved analysis described in Section 6.1.3. Calorimeter jets are reconstructed from topological clusters of calorimeter energy deposits [226] using the anti-k_t algorithm with radius parameter R=1.0 for large-R jets or R = 0.4 for small-R jets [160, 224]. Large-R jets are groomed using a trimming algorithm [227] to improve jet mass resolution and to maintain stability with respect to pile-up by discarding softer components of jets arising from initial-state radiation, pile-up

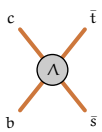

$O^{(1)}_{Quqb}$

interactions, or the underlying event. Large-R jets are required to have $p_T > 250$ GeV, $m_J > 50$ GeV and $|\eta| < 2.0$. Small-R jets are used in building the missing transverse momentum and event categorization and are required to have $p_T > 30$ GeV and $|\eta|<4.5$. Track-jets formed from charged-particle tracks are used to reconstruct a candidate two-body $H \to b\bar{b}$ decay within the large-R jet. Track-jets are built with the anti-k_t algorithm with a p_T-dependent variable radius (VR) parameter from tracks reconstructed in the inner detector with $p_T > 0.5$ GeV and $|\eta| < 2.5$. Only VR track-jets with $p_T > 10$ GeV, $|\eta| < 2.5$ and with at least two constituents are considered. In order to identify track-jets containing b-hadrons, track-jet candidates are tagged with the multivariate b-tagging algorithm [225] configured at the 70% working point.

The dominant background processes after the event selection correspond to the production of V+jets, $t\bar{t}$, single-top, di-bosons, and multijet events with varying compositions in the 0-,1- and 2-lepton channels. All background distributions prior to the fit, except those for multijet, are estimated from samples of simulated events. The multijet distributions are determined using data. In all channels, events are required to contain at least one large-R jet with $p_T > 250$ GeV and $|\eta|<2.0$. Events are further categorized into two associated weak boson transverse momentum (p_T^V) bins with $250 < p_T^V < 400$ GeV and with $p_T^V \geqslant 400$ GeV to improve the discrimination of signal from the background due to their different kinematic behavior. The signal is extracted from a profile likelihood fit to the large-R jet mass, combining several signal and control regions. The cross-section measurements are performed within the simplified template cross-section (STXS) framework and allow measuring four regions corresponding to $250 < p_T^W < 400$ GeV, $400 < p_T^W$ GeV, $250 < p_T^Z < 400$ GeV and $400 < p_T^Z$ GeV.

7.1.3.3 $t\bar{t}H$, $H \to b\bar{b}$

The $t\bar{t}H$ process allows for direct measurement of Higgs boson coupling to top quarks. The $H \to b\bar{b}$ decay allows to reconstruct the kinematic properties of the Higgs boson, which provides information on additional SMEFT operators. The $t\bar{t}H$, $H \to b\bar{b}$ analysis aims to select events with a Higgs boson produced in association with a pair of top-anti-top quarks and decaying into a pair of b-quarks, in which one or both top quarks decay semi-leptonically, producing an electron or a muon. Due to many final-state particles, the main challenges are the low efficiency in reconstructing and identify all of them, the large combinatorial ambiguities when trying to match the observed objects to the decay products of the Higgs boson and the top quarks, and the large background of $t\bar{t}$ + jets process.

Electrons are required to have $p_T > 10$ GeV and $|\eta| < 2.47$ and satisfy the `MEDIUM` likelihood-based identification criterion. Muons are required to have $p_T > 10$ GeV and $|\eta| < 2.5$ and to satisfy the `LOOSE` identification criteria. Jets are identified us-

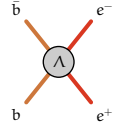

ing the anti-k_t algorithm with a radius parameter of 0.4 for small-R jets and R=1.0 for large-R jets. Jets are required to satisfy $p_T > 25$ GeV and $|\eta| < 2.5$. Jets containing b-hadrons are identified using the multivariate b-tagging algorithm [225]. Four b-tagging working points with efficiencies ranging from 60% to 85% are used for jets with $p_T > 20$ GeV. Hadronically decaying τ-leptons (τ_{had}) are distinguished from jets using their track multiplicity and a multivariate discriminant based on calorimetric shower shapes and tracking information. They are required to have $p_T > 25$ GeV and $|\eta| < 2.5$, and to pass the `MEDIUM` identification working point.

In order to target the $t\bar{t}H(b\bar{b})$ final state, events are categorized into exclusive regions defined by the number of leptons, the number of jets, the number of b-tagged jets at different b-tagging efficiencies (60%, 70%, 77%, or 85%) and the number of boosted Higgs boson candidates. Higgs boson candidates are reconstructed using a DNN in the boosted category. In the resolved category, one set of boosted decision trees (BDT), known as *reconstruction BDT*, is used to associate the reconstructed jets to the final state partons. Another set of BDTs, referred to as *classification BDT*, are then employed to separate signal from background in each of the signal regions. Dedicated control regions are used to constrain the normalization of the backgrounds and the systematic uncertainties when used in a combined fit with the signal regions. The analysis measures the cross-section of five regions of transverse momentum of the Higgs boson, p_T^H, as defined within the STXS framework.

7.1.3.4 boosted all-hadronic, $H \to b\bar{b}$

The boosted all-hadronic $H \to b\bar{b}$ analysis reconstructs Higgs bosons produced at high transverse momentum, where the effect of some SMEFT operators is enhanced. The Higgs boson is reconstructed as a single large-R jet with radius parameter R=1.0, along with a requirement of an energetic hadronic recoil to suppress background. The analysis does not have further criteria to select a specific Higgs boson production mode.

Calorimeter jets are reconstructed from topological clusters of calorimeter energy deposits [226] using the anti-k_t algorithm with radius parameter R=1.0 jets [160, 224]. Track-jets with $p_T > 10$ GeV and $|\eta|<2.5$ are considered to identify the $H \to b\bar{b}$ decay candidate. A multivariate discriminant is used to tag track-jets originating from b-quarks with a 77% efficiency. Muons are required to have $|\eta| < 2.5$, $p_T^\mu > 10$ GeV, and small impact parameter and satisfy the `MEDIUM` quality criterion.

The dominant background is multijet production; the remaining background contributions include hadronically decaying vector bosons produced in association with jets (V+jets) and events with one or two top quarks. Since the invariant mass peaks originating from Higgs and Z boson decays appear on top of a smoothly

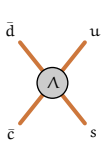

$O_{quqd}^{(8)\prime}$

falling background distribution, the signal is extracted from the reconstructed jet mass distribution. Events are categorized into three exclusive regions, consisting of a signal region used to extract the signal strength, a control region to measure the rate of top quark events, and a validation region to measure the rate of the multijet and V+jets background models. A dedicated $t\bar{t}$ control region is defined to reconstruct $t\bar{t}$ events with one semileptonic decay and one hadronic decay. It provides a highly pure sample of top quark pair events to determine the $t\bar{t}$ yield in conditions similar to the signal region. The discriminating observable in the signal extraction fit is the boosted jet mass m_J. The monotonically decreasing jet mass spectrum of the multijet background is modeled with an exponential function of polynomial expression, using a separate function for each region.

7.1.4 $H \to \mu\mu$

The $H \to \mu\mu$ decay is a promising channel to measure the Higgs boson coupling to second-generation fermions. However, Higgs decay to two muons is a rare process and has a branching fraction of 0.02 %. The analysis is performed in 20 distinct event categories, targeting different Higgs boson production modes ($t\bar{t}H$, VH, ggF, and VBF) with varying signal purity. The analysis is described in detail in [221].

Muon candidates are required to satisfy the `LOOSE` criteria [201] and have $p_T > 6$ GeV and $|\eta| < 2.7$. Additional requirements are imposed on the track parameters to ensure that the muon originates from the primary vertex. Up to one final-state photon candidate per event is included in the $m_{\mu\mu}$ calculation to improve the signal reconstruction, as muons may lose a significant fraction of their energy by final-state radiation denoted FSR. Only photon candidates close to muons ($\Delta R(\gamma, \mu) < 0.2$) are used in the reconstruction. In order to reduce background from pile-up interactions, a variable threshold is imposed on the photon transverse momentum p_T^γ, with the threshold increasing linearly from $p_T^\gamma = 3$ GeV for $\Delta R = 0$ to $p_T^\gamma = 8$ GeV for $\Delta R = 0.2$. Electrons are required to satisfy `MEDIUM` identification criteria, to have $p_T > 7$ GeV and $|\eta| < 2.47$ and to be outside the region of $1.37 < |\eta| < 1.52$. Similarly to muons, electrons are required to be isolated from additional activity measured by ID tracks and the calorimeter energy deposits within $\Delta R < 0.2$ and to be matched to the primary vertex.

Jets are reconstructed from particle flow objects using the anti-k_t algorithm with a radius parameter of $R = 0.4$. Candidate jets must have $|\eta| < 4.5$, and the jet p_T must be larger than 25(30) GeV for $|\eta| < 2.4 (2.4 < |\eta| < 4.5)$. Jets containing b-hadrons with $|\eta| < 2.5$ are identified as b-tagged jets using a multivariate b-tagging algorithm. Two identification working points are used to provide a 60% (85%) efficiency in $t\bar{t}$ events and a rejection factor of 1200 (25) for light-flavor jets, respectively.

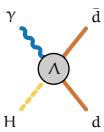

The analysis selects events with two opposite-charge muons and classifies them into 20 exclusive categories based on the event topology and multivariate discriminant scores to increase the signal sensitivity. After event categorization, the signal yield is extracted by a simultaneous fit to the 20 di-muon mass ($m_{\mu\mu}$) distributions in the range 110–160 GeV together with background normalization and shape parameters, exploiting the resonant behavior of the Higgs boson signal.

7.1.5 $H \to Z\gamma$

The rare decay of a Higgs boson to a Z boson and a photon has a branching fraction of (0.16%) and is mediated at leading order by loop diagrams. The Z boson decays into electron or muon pairs can be efficiently triggered and clearly distinguished from background events. Additionally, the $Z(\to ll)\gamma$ ($l = e$ or μ) final state can be reconstructed completely with good invariant mass resolution and relatively small backgrounds. The analysis is described in detail in [220].

Events are required to have at least one photon candidate and at least two same-flavor opposite-charge leptons ($l = e, \mu$) associated with a primary vertex candidate.

Muon candidates are required to satisfy the `MEDIUM` identification criteria, to be within $|\eta| < 2.7$, and have $p_T > 10$ GeV. Electrons are required to satisfy the `LOOSE` identification criteria, be within $|\eta| < 2.47$ and have $p_T > 10$ GeV. Photon candidates are required to satisfy $p_T > 10$ GeV, $|\eta| < 2.37$ and are based on the tight identification criteria. In order to ensure that muon and electron candidates originate from the primary vertex, requirements are imposed on the longitudinal impact parameter. To suppress leptons from heavy-flavor decays, additional requirements are placed on the track fit of muons and electrons. Jets are reconstructed from topological clusters using the anti-k_t parameter of 0.4 and are required to have $p_T > 25$ GeV and $|\eta| < 4.4$.

In order to improve sensitivity to the $H \to Z\gamma$ signal, the selected events are classified into six categories based on lepton flavor and event kinematics. Additionally, a BDT trained to separate the VBF signal events from other Higgs boson production modes and backgrounds is used to define a category of events with at least two jets. A double-sided Crystal Ball function describes the signal in the various categories over a smoothly falling background function chosen from a set of parametric functions. The analysis measures the inclusive signal strength of $H \to Z\gamma$.

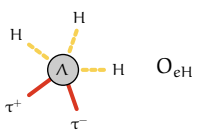

7.2 Simplified Template cross-section measurements per channel

For the interpretations based on the SMEFT framework, measurements of simplified template cross-sections (STXS) of various Higgs boson production processes in the regions of phase space defined within the STXS framework [88, 174, 228, 229] are used.

Analyses of the most sensitive production modes performed with the full Run 2 dataset, labeled *STXS-1.2* in Table 7.1, report measurements of signal yield scale factors in the more fine-grained Stage-1.2 definition of Higgs boson production cross-sections that partitions the Stage-0 regions in particle-level kinematic volumes, such as in a few coarse intervals of Higgs boson transverse momentum (p_T^H). The ensemble of parameters $\mu_{STXS-1.2}^{i,k',X}$ describes deviations in differential distributions, with the level of detail controlled by the number of particle-level regions that are defined.

The precision with which the more fine-grained set of scale factors $\mu_{STXS-1.2}^{i,k',X}$ can be measured depends on the design of the analysis, as well as the amount of available data. As individual analyses provide only limited sensitivity to some of the Stage-1.2 categories with the current dataset, some of these categories are merged with respect to the Stage-1.2 definitions given in [88]. Details of the merged category definitions in each analysis are provided in references [196, 197, 213–219]. The grouping of the production modes for STXS-0* and STXS-1.2 regions is also shown in the second column of Table 7.1.

After merging, a total of 78 signal yield parameters are extracted from the STXS measurements listed in Table 7.1. The kinematic definitions of these 78 STXS signal yield parameters, along with their measured signal strengths (*i.e.* their ratios to the corresponding SM predictions) and uncertainties are shown in Figures 7.1–7.3. While the data underlying the measurements in these figures is the same as that used for the interpretation of the combined Higgs boson measurements shown in [168], the granularity of the STXS model used here is substantially larger, providing additional constraining power for the parameters of the SMEFT interpretation of the data. The χ^2 for the compatibility between the observed values and the SM hypothesis is 50 for 78 degrees of freedom, corresponding to a p-value of 99.4%.

7.3 SMEFT parametrization

The interpretation of the Higgs boson measurements in terms of SMEFT is performed with the top flavor symmetry scheme for EFT operators. The flavor sym-

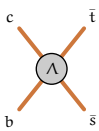

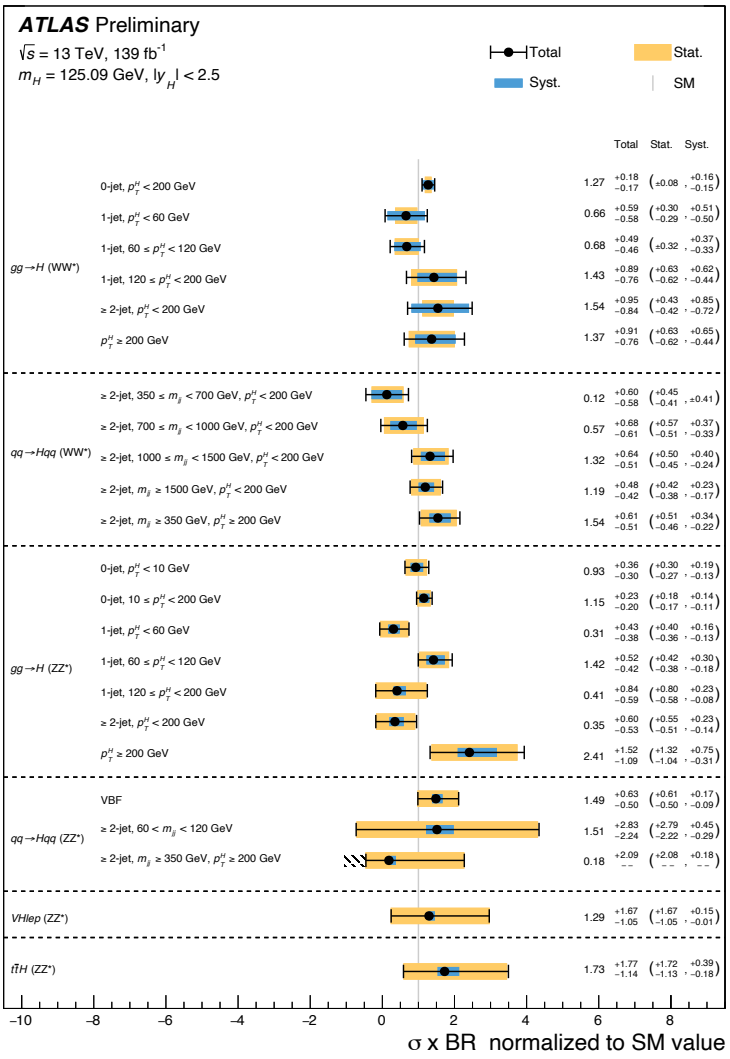

Figure 7.1: Measured signal strength for each of the $H \to WW^*$ and $H \to ZZ^*$ STXS categories included in the combination. In the $H \to ZZ^*$ analysis, VH production events with the vector boson V decaying to leptons are assigned to the VHlep category. In one category, the negative uncertainty is truncated, as indicated by the hatched region, which corresponds to cross-section values for which the total yield prediction in an analysis region is negative. In that case, the negative uncertainty and its breakdown in terms of statistical and systematic components are not reported.

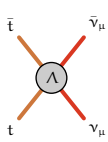

O_{lt}

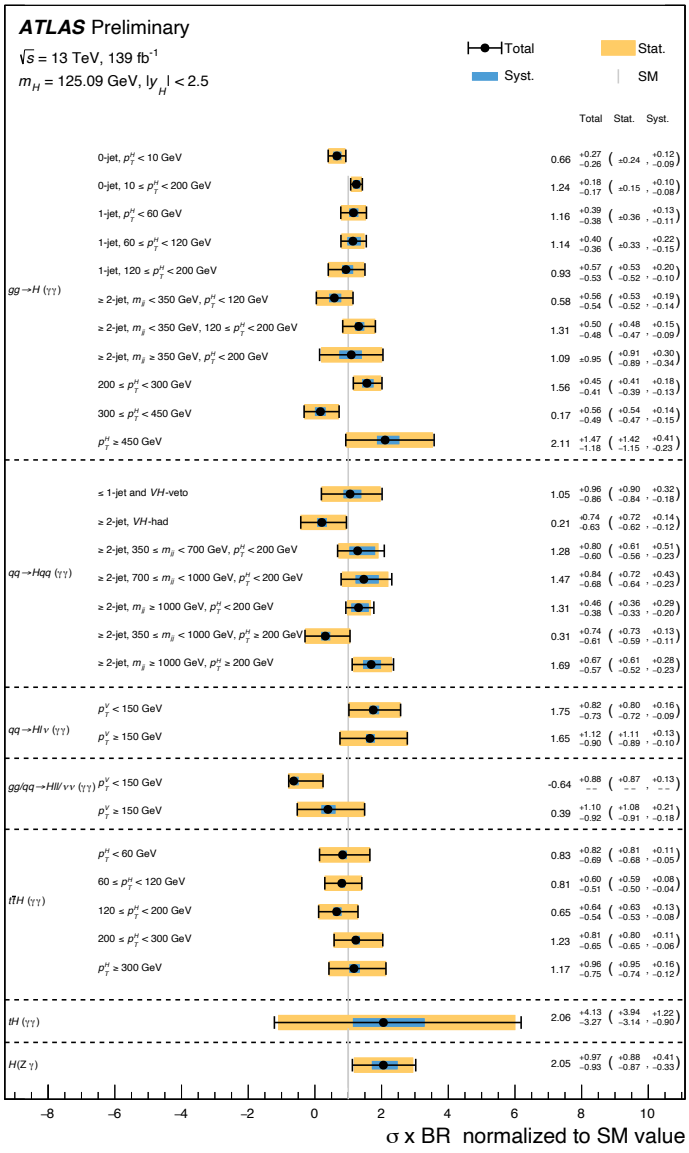

Figure 7.2: Measured signal strength for each of the $H \to \gamma\gamma$ and $H \to Z\gamma$ STXS categories included in the combination. In the $H \to \gamma\gamma$ analysis, events with two or more particle-level jets are assigned to the VH-veto (VH-had) categories if the leading di-jet invariant mass m_{jj} is in the range $m_{jj} < 60$ GeV or $120 \leqslant m_{jj} < 350$ GeV ($60 \leqslant m_{jj} < 120$ GeV). In one category, the uncertainty is truncated, as indicated by the hatched region, which corresponds to cross-section values for which the total yield prediction in an analysis region is negative. In that case, the negative uncertainty and its breakdown in terms of statistical and systematic components are not reported.

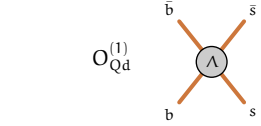

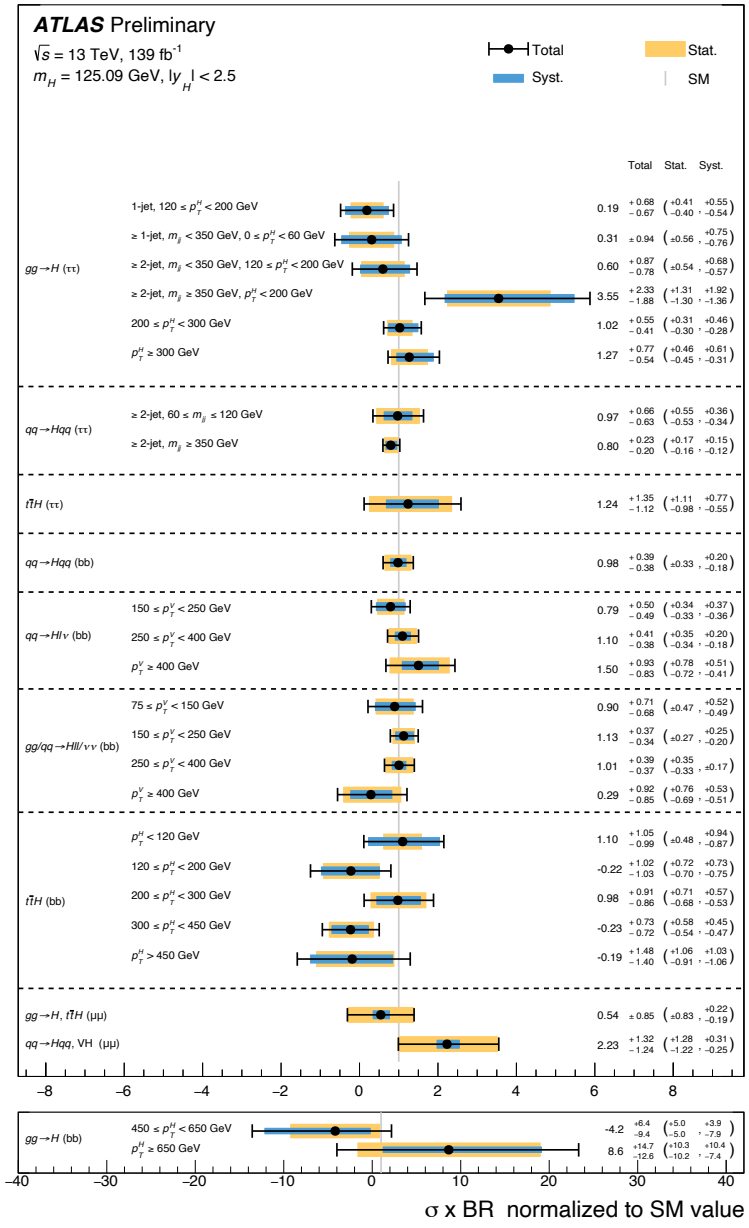

Figure 7.3: Measured signal strength for each of the $H \to \tau\tau$, $b\bar{b}$, and $\mu\mu$ STXS categories implemented.

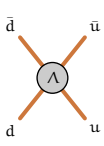

$O^{(8)f}_{quqd}$

metry is discussed earlier in Section 2.3.3. Table 7.2 lists the operators considered in the analysis of STXS data and their corresponding Wilson coefficients c_i. Only CP-even $dimension-6$ operators are listed for which the Λ^{-2}-suppressed contribution to any of the STXS measurements shown in Figures 7.1–7.3 exceeds 0.1% with respect to the SM prediction at $c_i = 1$. A value of $\Lambda = 1\,\text{TeV}$ is assumed, coefficients for alternative values of $\Lambda = X$ can be obtained through a scaling of the results by a factor $(X/1\,\text{TeV})^2$. All Wilson coefficients are assumed to be real.

Figure 7.4 shows the impact of linear and linear+quadratic terms on production and decay rates corresponding to

$$A_j^{\sigma_{i,k'}} \text{ and } \left(\frac{1+A_j^{\Gamma^{H\to X}}}{1+A_j^{\Gamma^H}}-1\right),$$

respectively.

For the linear parametrization, the scenario where the total width is not Taylor expanded is considered as described in Section 5.3.1. The dependence of the signal strength is parametrized as a function of the Wilson coefficients using Equation 5.14 for the linear case and using Equation 5.18 for the case with linear and quadratic terms.

The relative importance of the quadratic term increases linearly with the considered variation of the corresponding Wilson coefficient. Figure 7.4 shows that the quadratic terms have the highest impact in the high-p_T regions of VH production for the coefficients $c_{Hq}^{(3)}, c_{Hq}^{(1)}, c_{Hd}, c_{Hu}$, on high-$p_T$ (inclusive) $t\bar{t}H$ production for the coefficients c_{tG}, $c_{Qq}^{(1,8)}$, $c_{Qq}^{(3,1)}$, $c_{tq}^{(8)}$, $c_{Qu}^{(8)}$, $c_{tu}^{(8)}$, c_G, and in the tH channel for the coefficients $c_{HQ}^{(3)}$ and $c_{Qq}^{(3,1)}$.

The impact of experimental selections can affect the parametrization of the STXS regions as discussed earlier in Chapter 5.3.3. The impact of acceptance effects is evaluated for all operators in Table 7.2 that can affect $\Gamma^{H\to ZZ^*}$ or $\Gamma^{H\to WW^*}$, *i.e.* $c_{H\Box}$, c_{HD}, c_{HW}, c_{HB}, c_{HWB}, $c_{Hl,11}^{(1)}$, $c_{Hl,22}^{(1)}$, $c_{Hl,11}^{(3)}$, $c_{Hl,22}^{(3)}$, $c_{He,11}$, $c_{He,22}$ and $c_{ll,1221}$, and is observed to be non-negligible for four of these, c_{HW}, c_{HB}, c_{HWB}, and $c_{Hl}^{(3)}$. For these, the corresponding recalculated factors $A_j^{H\to X}, B_{jl}^{H\to X} (X = WW^*, ZZ^*)$ with approximate acceptance modeling are used in the STXS SMEFT analysis.

Figure 7.5 illustrates the effect of the c_{HW} operator on the acceptance in the $H \to WW^*$ and $H \to ZZ^*$ decay modes. The acceptance correction is not used in the differential analysis of $H \to ZZ^*$, as none of the three operators analyzed for that measurement are affected. For all other Higgs boson decays, the acceptance effects from SMEFT operators are neglected.

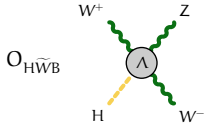

Wilson coefficient	Operator	Wilson coefficient	Operator
c_H	$(H^\dagger H)^3$	$c_{Qq}^{(1,1)}$	$(\bar{Q}\gamma_\mu Q)(\bar{q}\gamma^\mu q)$
$c_{H\Box}$	$(H^\dagger H)\Box(H^\dagger H)$	$c_{Qq}^{(1,8)}$	$(\bar{Q}T^a\gamma_\mu Q)(\bar{q}T^a\gamma^\mu q)$
c_G	$f^{abc}G_\mu^{a\nu}G_\nu^{b\rho}G_\rho^{c\mu}$	$c_{Qq}^{(3,1)}$	$(\bar{Q}\sigma^i\gamma_\mu Q)(\bar{q}\sigma^i\gamma^\mu q)$
c_W	$\epsilon^{ijk}W_\mu^{i\nu}W_\nu^{j\rho}W_\rho^{k\mu}$	$c_{Qq}^{(3,8)}$	$(\bar{Q}\sigma^i T^a\gamma_\mu Q)(\bar{q}\sigma^i T^a\gamma^\mu q)$
c_{HD}	$\left(H^\dagger D^\mu H\right)^*\left(H^\dagger D_\mu H\right)$	$c_{qq}^{(3,1)}$	$(\bar{q}\sigma^i\gamma_\mu q)(\bar{q}\sigma^i\gamma^\mu q)$
c_{HG}	$H^\dagger H\, G_{\mu\nu}^A G^{A\mu\nu}$	$c_{tu}^{(1)}$	$(\bar{t}\gamma_\mu t)(\bar{u}\gamma^\mu u)$
c_{HB}	$H^\dagger H\, B_{\mu\nu}B^{\mu\nu}$	$c_{tu}^{(8)}$	$(\bar{t}T^a\gamma_\mu t)(\bar{u}T^a\gamma^\mu u)$
c_{HW}	$H^\dagger H\, W_{\mu\nu}^I W^{I\mu\nu}$	$c_{td}^{(1)}$	$(\bar{t}\gamma_\mu t)(\bar{d}\gamma^\mu d)$
c_{HWB}	$H^\dagger\tau^I H\, W_{\mu\nu}^I B^{\mu\nu}$	$c_{td}^{(8)}$	$(\bar{t}T^a\gamma_\mu t)(\bar{d}T^a\gamma^\mu d)$
$c_{Hl,11}^{(1)}$	$(H^\dagger i\overleftrightarrow{D}_\mu H)(\bar{l}_1\gamma^\mu l_1)$	$c_{Qu}^{(1)}$	$(\bar{Q}\gamma_\mu Q)(\bar{u}\gamma^\mu u)$
$c_{Hl,22}^{(1)}$	$(H^\dagger i\overleftrightarrow{D}_\mu H)(\bar{l}_2\gamma^\mu l_2)$	$c_{Qu}^{(8)}$	$(\bar{Q}T^a\gamma_\mu Q)(\bar{u}T^a\gamma^\mu u)$
$c_{Hl,33}^{(1)}$	$(H^\dagger i\overleftrightarrow{D}_\mu H)(\bar{l}_3\gamma^\mu l_3)$	$c_{Qd}^{(1)}$	$(\bar{Q}\gamma_\mu Q)(\bar{d}\gamma^\mu d)$
$c_{Hl,11}^{(3)}$	$(H^\dagger i\overleftrightarrow{D}^I_\mu H)(\bar{l}_1\tau^I\gamma^\mu l_1)$	$c_{Qd}^{(8)}$	$(\bar{Q}T^a\gamma_\mu Q)(\bar{d}T^a\gamma^\mu d)$
$c_{Hl,22}^{(3)}$	$(H^\dagger i\overleftrightarrow{D}^I_\mu H)(\bar{l}_2\tau^I\gamma^\mu l_2)$	$c_{tq}^{(1)}$	$(\bar{q}\gamma_\mu q)(\bar{t}\gamma^\mu t)$
$c_{Hl,33}^{(3)}$	$(H^\dagger i\overleftrightarrow{D}^I_\mu H)(\bar{l}_3\tau^I\gamma^\mu l_3)$	$c_{tq}^{(8)}$	$(\bar{q}T^a\gamma_\mu q)(\bar{t}T^a\gamma^\mu t)$
$c_{He,11}$	$(H^\dagger i\overleftrightarrow{D}_\mu H)(\bar{e}_1\gamma^\mu e_1)$	$c_{eH,22}$	$(H^\dagger H)(\bar{l}_2 e_2 H)$
$c_{He,22}$	$(H^\dagger i\overleftrightarrow{D}_\mu H)(\bar{e}_2\gamma^\mu e_2)$	$c_{eH,33}$	$(H^\dagger H)(\bar{l}_3 e_3 H)$
$c_{He,33}$	$(H^\dagger i\overleftrightarrow{D}_\mu H)(\bar{e}_3\gamma^\mu e_3)$	c_{uH}	$(H^\dagger H)(\bar{q}Y_u^\dagger u\tilde{H})$
$c_{Hq}^{(1)}$	$(H^\dagger i\overleftrightarrow{D}_\mu H)(\bar{q}\gamma^\mu q)$	c_{tH}	$(H^\dagger H)(\bar{Q}\tilde{H}t)$
$c_{Hq}^{(3)}$	$(H^\dagger i\overleftrightarrow{D}^I_\mu H)(\bar{q}\tau^I\gamma^\mu q)$	c_{bH}	$(H^\dagger H)(\bar{Q}Hb)$
c_{Hu}	$(H^\dagger i\overleftrightarrow{D}_\mu H)(\bar{u}_p\gamma^\mu u_r)$	c_{tG}	$(\bar{Q}\sigma^{\mu\nu}T^A t)\tilde{H}\, G_{\mu\nu}^A$
c_{Hd}	$(H^\dagger i\overleftrightarrow{D}_\mu H)(\bar{d}_p\gamma^\mu d_r)$	c_{tW}	$(\bar{Q}\sigma^{\mu\nu}t)\tau^I\tilde{H}\, W_{\mu\nu}^I$
$c_{HQ}^{(1)}$	$(H^\dagger i\overleftrightarrow{D}_\mu H)(\bar{Q}\gamma^\mu Q)$	c_{tB}	$(\bar{Q}\sigma^{\mu\nu}t)\tilde{H}\, B_{\mu\nu}$
$c_{HQ}^{(3)}$	$(H^\dagger i\overleftrightarrow{D}^I_\mu H)(\bar{Q}\tau^I\gamma^\mu Q)$	$c_{ll,1221}$	$(\bar{l}_1\gamma_\mu l_2)(\bar{l}_2\gamma^\mu l_1)$
c_{Ht}	$(H^\dagger i\overleftrightarrow{D}_\mu H)(\bar{t}\gamma^\mu t)$		
c_{Hb}	$(H^\dagger i\overleftrightarrow{D}_\mu H)(\bar{b}\gamma^\mu b)$		

Table 7.2: Wilson coefficients $\boldsymbol{c}$ and corresponding $\mathrm{dimension}-6$ SMEFT operators $\mathcal{O}_j$ used in this analysis. The operator and coefficient notation follows the convention of [195].

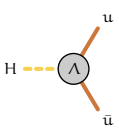

O_{uH}

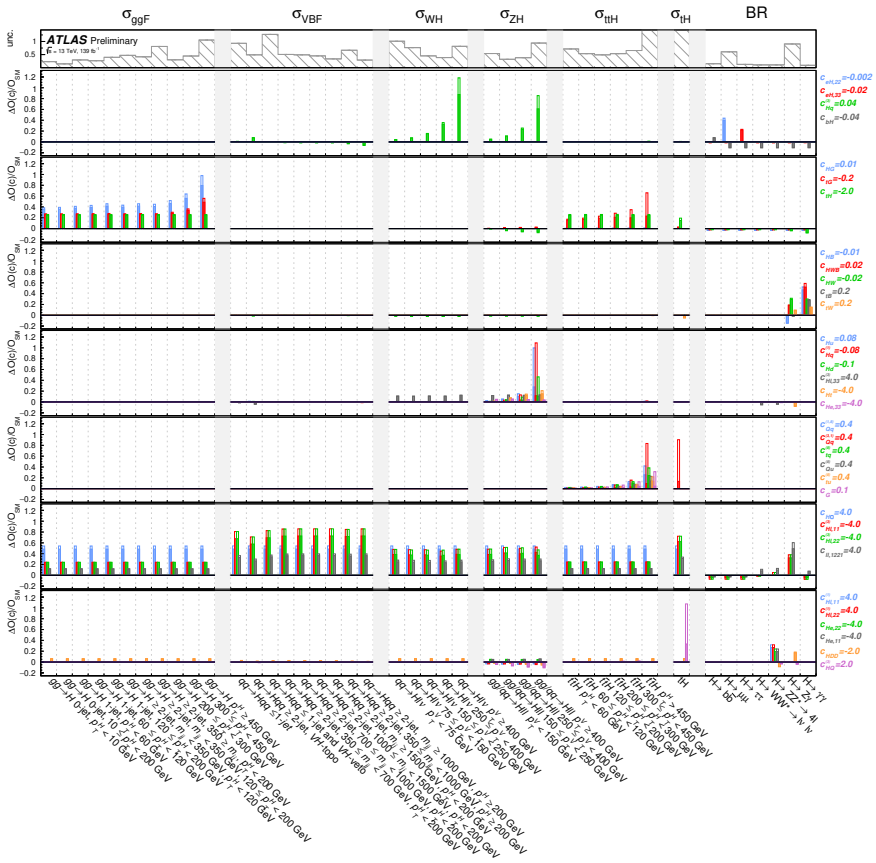

Figure 7.4: Expected impact of the most relevant SMEFT operators on the observables O (cross-sections in STXS-1.2 regions or decay branching ratios), relative to the SM predictions, for the linearized SMEFT model (shaded histogram) and the linear+quadratic SMEFT model (open histogram). The values of the Wilson coefficients, specified in the legend, are chosen to show the distribution of the operator impact in the same range as the typical uncertainty of the measurement. To judge the experimental sensitivity to constrain the operators from the data, the total uncertainty on the measurement of each observable is shown in the top panel. For columns corresponding to multiple measurements of the same observable, the shown uncertainty reflects the uncertainty on the average under the assumption of uncorrelated uncertainties. For presentational clarity, the uncertainty of low-precision measurements is clipped off in the plot.

7.4 Choice of sensitive parameters

A modified basis c' is estimated from data to constrain sensitive directions in the SMEFT parameter space as detailed in Section 6.5. Figure 7.6 lists the eigenvectors

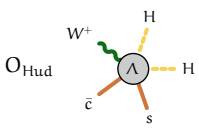

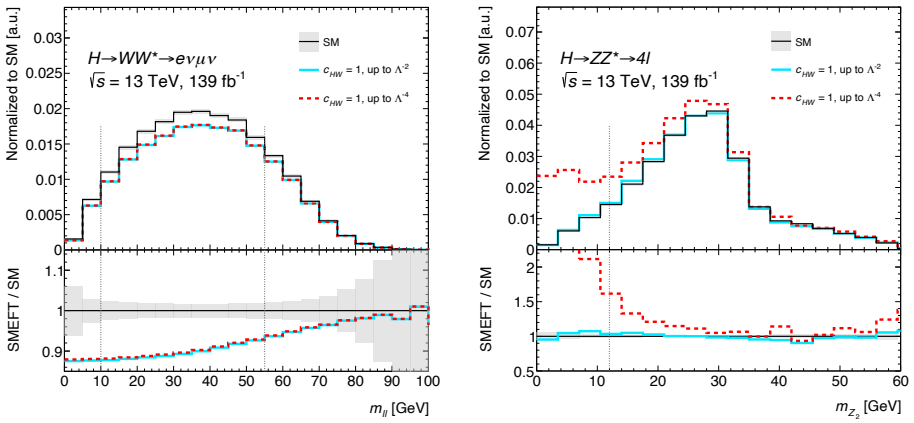

(a) (b)

Figure 7.5: Illustration of the effect of a variation of the SMEFT coefficient c_{HW} on kinematic observables used in the event selection: (a) impact on the dilepton invariant mass in the $H \to WW^* \to e\nu\mu\nu$ analysis, and (b) impact on the invariant mass of the 3rd and 4th p_T-ranked lepton in the $H \to ZZ^* \to 4\ell$ analysis. The vertical dotted lines indicate the selection criteria applied on the corresponding variables by the $H \to WW^*$ analysis ($10 < m_{\ell\ell} < 55$ GeV) and by the $H \to ZZ^*$ analysis ($m_{Z_2} > 12$ GeV). The gray bands show the statistical uncertainty of the SMEFT simulation.

obtained from the expected measurements and accounting for the observed values of nuisance parameters, ranked by eigenvalue and truncated to eigenvalues $\lambda_i \geqslant 0.01$, corresponding to a truncation at an estimated uncertainty of $\sigma(ev^{[i]}) \leqslant 10$, well beyond the validity range of the Wilson coefficients of $\mathcal{O}(1)$.

From the ranking shown in Figure 7.6 and a survey of the sensitivity of the STXS regions to the Wilson coefficients in the linearized model, as shown in Figure 7.4, the following observations are made:

- The coefficients $c_{eH,33}$, $c_{eH,22}$, and c_{bH}, representing the Yukawa coupling modifiers of the $H \to \tau\tau$, $H \to \mu\mu$, and $H \to b\bar{b}$ decays respectively, can be individually measured from the corresponding Higgs channels that enter the combination. There are weak correlations of these operators with other SMEFT operators, primarily for c_{bH}, through their contribution to the total Higgs boson width.
- The coefficient $c_{Hq}^{(3)}$ affects both the WH and ZH production modes with an increasing impact as a function of the transverse momentum p_T^V of the W and Z bosons, and is constrained almost exclusively by the VH, $H \to b\bar{b}$ analysis.

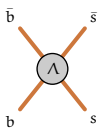

$O_{Qq}^{(3,8)}$

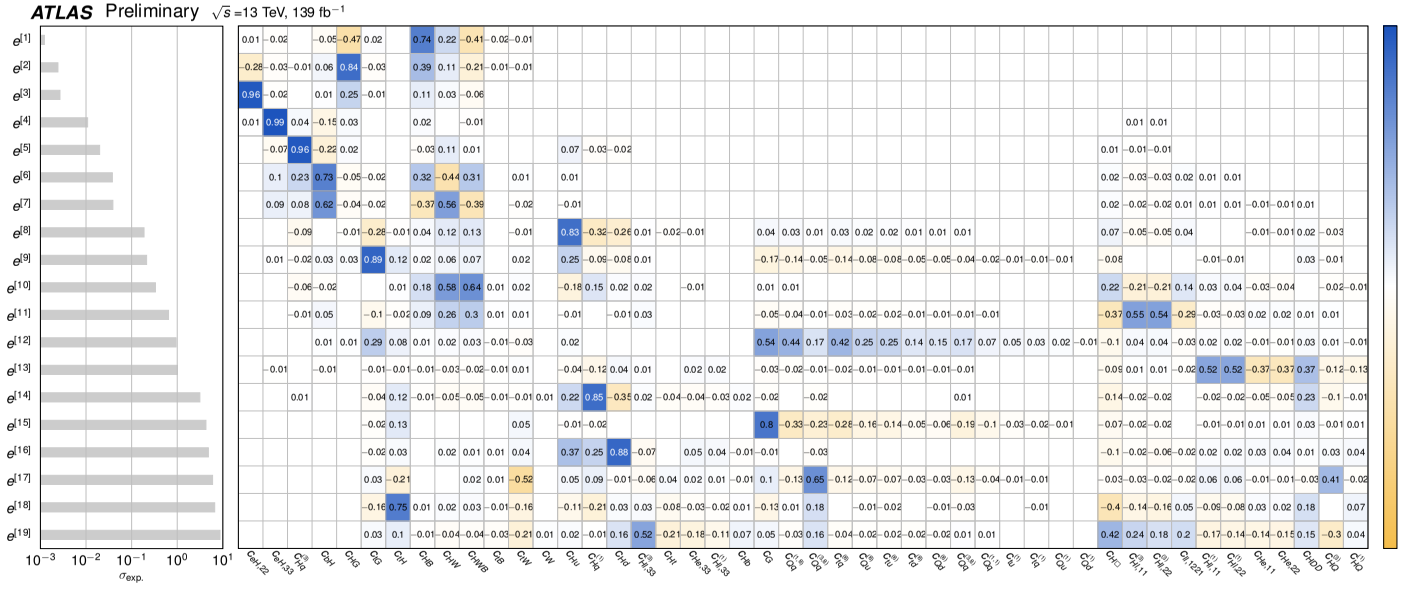

Figure 7.6: Eigenvectors of the inverse EFT covariance matrix obtained by propagating the SMEFT parametrization to the covariance matrix V_{STXS} and requiring a significant ($\geqslant 0.01$) eigenvalue λ. The corresponding expected uncertainty $\sigma_{exp.} = 1/\sqrt{\lambda}$ for each eigenvector is also shown.

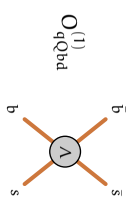

- The coefficients c_{HG}, c_{tG} and c_{tH} are constrained by ggH and $t\bar{t}H$ production. As the uncertainties of the constrained directions span more than two orders of magnitude, it is beneficial to represent them by decorrelated parameters, even though the rotation matrix required to decorrelate them is close to an identity matrix.
- The coefficients c_{HB}, c_{HW}, c_{HWB}, c_{tB} and c_{tW} are constrained in two directions through their impacts on the branching ratios of the $H \to \gamma\gamma$ and $H \to Z\gamma$ decays. There is an additional small impact of these operators on VBF and VH production, mildly constraining a third direction in this parameter group.
- The coefficients c_{Hu}, $c^{(1)}_{Hq}$, c_{Hd}, $c^{(3)}_{Hl,33}$,c_{Ht}, $c_{He,33}$, $c^{(1)}_{Hl,33}$ and c_{Hb} mainly affect the W and Z vertices with third generation fermions, as well as the neutral current interactions with quarks. They are primarily constrained by the VH, $H \to b\bar{b}$ analysis.
- The coefficients of the four-fermion operators involving the top-quark, *i.e.* $c^{(1,8)}_{Qq}$, $c^{(3,1)}_{Qq}$, $c^{(8)}_{tq}$, $c^{(8)}_{Qu}$, $c^{(8)}_{tu}$,$c^{(8)}_{td}$, $c^{(8)}_{Qd}$, $c^{(3,8)}_{Qq}$, $c^{(1,1)}_{Qq}$, $c^{(1)}_{tu}$, $c^{(1)}_{tq}$, $c^{(1)}_{Qu}$, and $c^{(1)}_{Qd}$, as well as the trilinear gluon coupling c_G, affect the $t\bar{t}H$ and tH production modes and are largely degenerate. The p^H_T spectrum measured in the $H \to \gamma\gamma$ and $H \to b\bar{b}$ channels constrains two linear combinations of these 14 coefficients. The separate constraint on tH production in the $H \to \gamma\gamma$ analysis weakly constrains a third direction in this group.
- The coefficients $c_{ll,1221}$, $c^{(3)}_{Hl,11}$, and $c^{(3)}_{Hl,22}$ primarily effectuate a shift in the Fermi constant, resulting in an overall normalization factor across different production modes. The coefficient $c_{H\Box}$ only affects the measurements through a Higgs propagator correction and thus acts similarly as an overall scale factor in the observed cross-sections. Only a single linear combination of these four operators can be constrained from the data.
- The coefficients $c^{(1)}_{Hl,11}$, $c^{(1)}_{Hl,22}$, $c_{He,11}$ and $c_{He,22}$ introduce anomalous HZee and HZμμ vertices and are mainly constrained by the branching ratio of the Higgs boson decay to four leptons (electrons or muons) together with c_{HDD} (responsible for an anomalous HZZ vertex) and $c^{(3)}_{HQ}$, $c^{(1)}_{HQ}$ (leading to HZtt and HZbb couplings that modify the Z boson propagator).

Based on these observations, a new fit basis $\boldsymbol{c'}$ is defined that achieves both fit stability and a reasonable interpretability of the fit parameters. This basis $\boldsymbol{c'}$ is expressed in terms of single Warsaw basis coefficients c_j whenever possible and

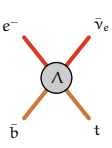

$O^{(1)}_{leQt}$

in terms of linear combinations (denoted with e) of coefficients when necessary:

$$
\begin{aligned}
\boldsymbol{c} = {} & \{c_{eH,22}\} \cup \\
& \{c_{eH,33}\} \cup \\
& \{c^{(3)}_{Hq}\} \cup \\
& \{c_{bH}\} \cup \\
& \{c_{HG}, c_{tG}, c_{tH}\} \cup && \rightarrow \quad \{e^{[1]}_{ggF}, e^{[2]}_{ggF}, e^{[3]}_{ggF}\} \cup \\
& \{c_{HB}, c_{HW}, c_{HWB}, c_{tB}, c_{tW}\} \cup && \rightarrow \quad \{e^{[1]}_{H\gamma\gamma,Z\gamma}, e^{[2]}_{H\gamma\gamma,Z\gamma}, e^{[3]}_{H\gamma\gamma,Z\gamma}\} \cup \\
& \{c_{Hu}, c^{(1)}_{Hq}, c_{Hd}, c^{(3)}_{Hl,33}, \\
& \qquad c_{Ht}, c_{He,33}, c^{(1)}_{Hl,33}, c_{Hb}\} \cup && \rightarrow \quad \{e^{[1]}_{ZH}, e^{[2]}_{ZH}, e^{[3]}_{ZH}, e^{[4]}_{ZH}\} \cup \\
& \{c_G, c^{(1,8)}_{Qq}, c^{(3,1)}_{Qq}, c^{(8)}_{tq}, c^{(8)}_{Qu}, c^{(8)}_{tu}, c^{(8)}_{td}, \\
& \qquad c^{(8)}_{Qd}, c^{(3,8)}_{Qq}, c^{(1,1)}_{Qq}, c^{(1)}_{tu}, c^{(1)}_{tq}, c^{(1)}_{Qu}, c^{(1)}_{Qd}\} \cup && \rightarrow \quad \{e^{[1]}_{ttH}, e^{[2]}_{ttH}, e^{[3]}_{ttH}\} \cup \\
& \{c_{H\Box}, c^{(3)}_{Hl,11}, c^{(3)}_{Hl,22}, c_{ll,1221}\} \cup && \rightarrow \quad \{e^{[1]}_{glob}\} \cup \\
& \{c^{(1)}_{Hl,11}, c^{(1)}_{Hl,22}, c_{He,11}, c_{He,22}, c_{HDD}, c^{(3)}_{HQ}, c^{(1)}_{HQ}\} && \rightarrow \quad \{e^{[1]}_{Hllll}\}.
\end{aligned}
$$

Only subgroup eigenvectors with an expected uncertainty $\leqslant 10$ are retained as model parameters, while the coefficients of the eigenvectors with larger expected uncertainties are fixed to zero in the likelihood function. The subgroup eigenvector directions relative to the Warsaw basis are shown in Figure 7.7. The names of the eigenvectors have been chosen to reflect the production or decay process that dominates the experimental sensitivity of the parameter group, as shown in Figure 7.4, although single parameters within some of the groups sometimes have a dominant sensitivity to another process.

No separate optimization of the parameter basis $\boldsymbol{c}'$ is performed for the quadratic SMEFT model of Equation 5.18 as the non-linear effects of this model are expected to vanish for small c_j, and thus to asymptotically yield the same rotation matrix as Equation 6.6.

The impacts of the variations of the coefficients of the rotated basis $\boldsymbol{c}'$ on the STXS regions and Higgs boson branching ratios are shown in Figure 7.8, with the same parameter grouping as shown in Figure 7.4. The figure clearly demonstrates that the basis $\boldsymbol{c}'$ represents impact variations across regions that are much less correlated than those represented by the Warsaw basis $\boldsymbol{c}$. The magnitude of the parameter variations shown in Figure 7.8 are set to the *expected uncertainty* for each parameter in the linear SMEFT model, thus giving a realistic indication of the magnitude of variations that can be constrained from the data. For completeness, the impact of the quadratic terms for the same values of the parameter basis is overlaid, indicating the relative magnitude of the quadratic terms at the expected sensitivity level of the linear model.

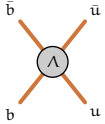

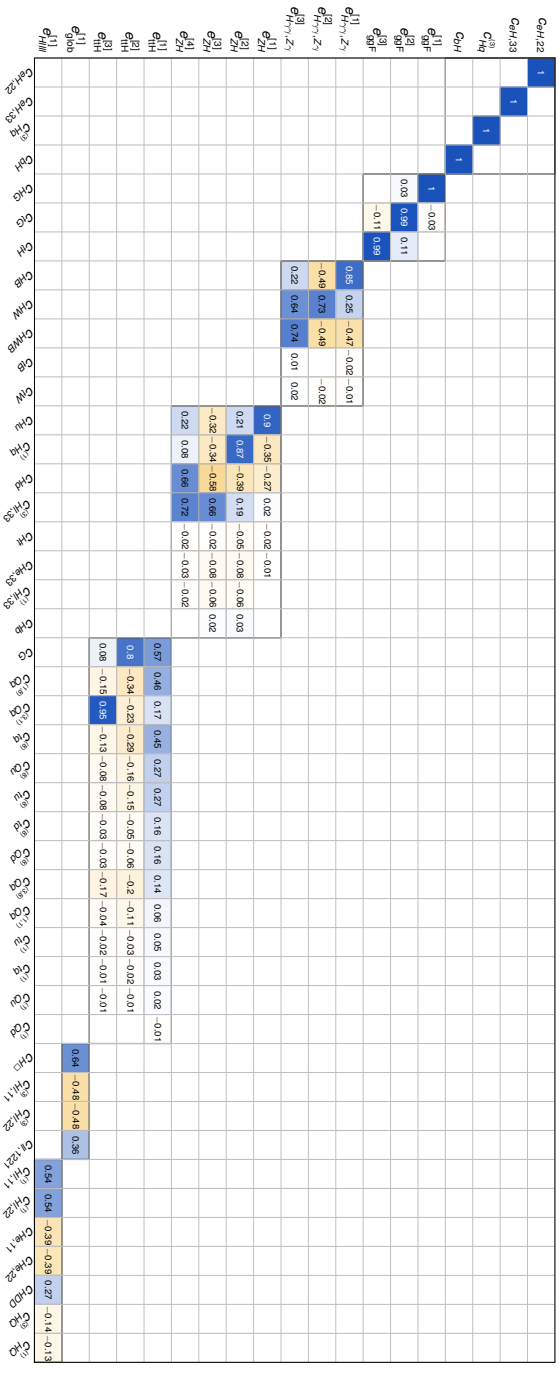

Figure 7.7: Definition of the fit basis coefficients c' in terms of the Warsaw basis coefficients c.

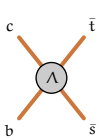

$O^{(1)}_{Qtqd}$

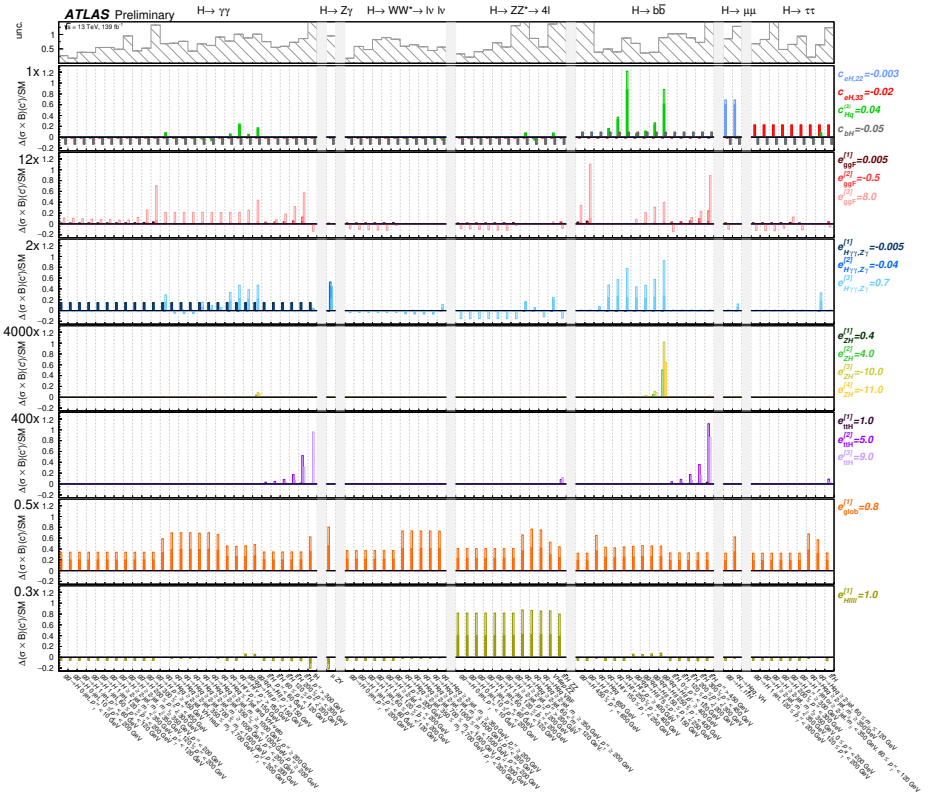

Figure 7.8: Impact of coefficients of the rotated basis $\boldsymbol{c}'$ on the STXS regions, relative to the SM cross-section, under the assumption of the linearized SMEFT model (shaded histogram) and the linear+quadratic SMEFT model (open histogram). For all coefficients, a variation equal to the expected uncertainty when using the linearized model is shown. Groupings in this figure are consistent with those in Figure 7.4, but vertical axis scales differ in order to completely show all quadratic impact terms, which can occasionally be very large. To judge the experimental sensitivity to constrain the operators from the data in the listed STXS regions, the total uncertainty on the corresponding regions is shown in the top panel. For presentational clarity, the uncertainty of low precision STXS regions is clipped off in the plot.

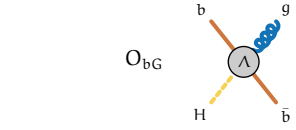

7.5 Results

Linear model Figure 7.9 compares the expected and observed results obtained using the linearized SMEFT model, showing good agreement of the observed data with the SM expectation, corresponding to a p-value of 94.5%. The parameter value ranges shown in the bottom panel correspond to 68% and 95% confidence level (CL) intervals, where all other coefficients and nuisance parameters are profiled. The observed uncertainties are generally about 10% smaller than the expected uncertainties due to the fact that the assumed Higgs boson width, when computed with the observed parameter values, is smaller than its SM expectation value. This effect is mostly driven by a high observed value of c_{bH}, which corresponds to a reduced value of $\Gamma^{H\to b\bar{b}}$. This reduction of the observed linear model uncertainties is comparable to that of the reduced observed uncertainties in the κ model analysis of the same data reported in [168], due to an equivalently low measurement of κ_b.

Figure 7.9 also shows the contributions of each measured Higgs boson decay or production mode to the sensitivity of each measurement of the coefficients of the rotated basis. The contribution of a measurement i to the sensitivity for a coefficient c'_j is determined from the ratio of the Fisher information $\mathcal{I}_i(c'_j)$ of that measurement to the sum of the Fisher information of all contributing components, i.e. $\sum_k \mathcal{I}_k(c'_j)$, where in all cases the Fisher information is estimated as the inverse of the covariance matrix V_{SMEFT}, as defined in Equation 6.5. This breakdown reveals that six parameters are (almost) exclusively measured by a single decay channel: the Yukawa coefficient $c_{He,22}$ by the decay channel $H \to \mu\mu$; the Yukawa coefficient $c_{He,33}$ by the decay mode $H \to \tau\tau$ respectively; the coefficient $c^{(3)}_{Hq}$ by $H \to b\bar{b}$ due to the large sensitivity of this channel to the VH production mode; coefficient $e^{[1]}_{H\gamma\gamma,Z\gamma}$ $H \to \gamma\gamma$ which affects the branching ratio of $H \to \gamma\gamma$; coefficient $e^{[2]}_{H\gamma\gamma,Z\gamma}$ $H \to Z\gamma$ which affects the branching ratio of $H \to Z\gamma$; the coefficient $e^{[1]}_{Hllll}$ by $H \to ZZ^* \to 4l$ which affects the branching ratio of $H \to ZZ^* \to 4l$. Due to its large effect on the Higgs boson width, the measurement of the Yukawa coefficient c_{bH} is not dominated by $H \to b\bar{b}$, but instead constrained by a combination of measured decays. Similarly, five parameters are measured (almost) exclusively by a single production mode: coefficient $e^{[1]}_{ggF}$ by ggH production, $e^{[1]}_{ZH}$ by ZH production, $e^{[1]}_{ttH}$ and $e^{[2]}_{ttH}$ by ttH production at high-p_T and medium-p_T respectively, and $e^{[3]}_{ttH}$ by tH production. No measured coefficient is predominantly sensitive to $H \to WW^*$ decays, or to the VBF or WH production modes, as these processes are affected by coefficients that are also affecting globally, such as $e^{[1]}_{glob}$ or are better constrained by other measurements, such as $e^{[1]}_{H\gamma\gamma,Z\gamma}$ or $e^{[2]}_{H\gamma\gamma,Z\gamma}$ where there is

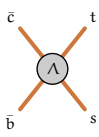

$O^{(1)}_{qtQd}$

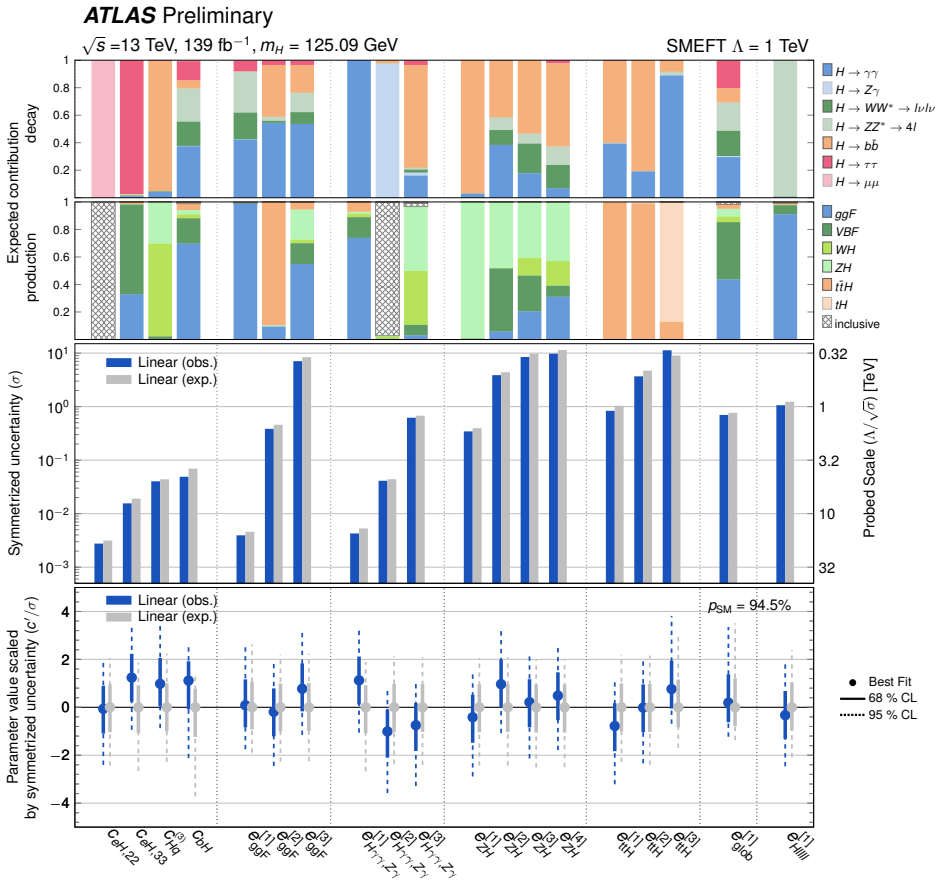

Figure 7.9: Comparison of the expected (gray) and observed (blue) parameters of the rotated basis $\boldsymbol{c}'$ with the SMEFT linearized model, where all other coefficients and nuisance parameters are profiled. The middle panel shows the symmetrized 68% CL uncertainty σ of each parameter measurement (left vertical axis) and the corresponding energy scale $\Lambda/\sqrt{s}$, $\Lambda = 1$ TeV that is probed (right vertical axis). The bottom panel shows the measured parameter value (dot), 68% (solid line), and 95% (dashed line) CL intervals, divided by the symmetrized uncertainty shown in the middle panel. The p-value for the compatibility of the data with the Standard Model expectation (all coefficients vanishing) is 94.5%. The top panel shows the expected breakdown of contributions to the sensitivity of each measurement from the various measured Higgs boson decay and production modes. The production category labeled 'inc' collects final states for which the breakdown into production modes is not available ($H \to \mu\mu$ and $H \to Z\gamma$). The 95% CL interval for $e^{[3]}_{ttH}$ has been truncated at the boundary at which the logarithm of the likelihood function becomes undefined, resulting in a small under coverage.

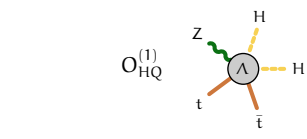

a larger sensitivity to the HWW SMEFT coupling due to the interference with a loop-suppressed SM contribution in $H \to \gamma\gamma$ and $H \to Z\gamma$ respectively.

Analysis of parameter uncertainty sources Figure 7.10 illustrates the relative importance of the various uncertainty components on the coefficients measured in the linearized model, where the top panel shows the relative contributions of the statistical and systematic components, and the bottom panel shows the relative contributions of the experimental, signal theory and background theory contributions to the total systematic uncertainty, where signal theory systematic uncertainties include both total cross-section uncertainties and acceptance uncertainties.

For parameters $c_{He,33}$, $e^{[1]}_{glob}$ and $e^{[1]}_{Hllll}$, the fractional contribution of systematic uncertainties is close to 50%; for parameters $e^{[1]}_{ggF}$, $e^{[2]}_{ggF}$, $e^{[1]}_{ttH}$ and $e^{[2]}_{ttH}$, the fractional contribution of systematic uncertainties is around 40%; the remaining parameters have smaller relative systematic uncertainties. In particular, the uncertainties in the $c_{He,22}$ and $e^{[3]}_{ttH}$ parameters, probed by the measurements of the rare processes of $H \to \mu\mu$ decay and tH production, respectively, are almost completely dominated by the statistical component. The total systematic uncertainty of most parameters is dominated by experimental systematic uncertainties, with the exception of $e^{[1]}_{ggF}$ and $e^{[1]}_{glob}$, where signal theory systematic uncertainties dominate, and $e^{[2]}_{ggF}$, $e^{[1]}_{ttH}$ and $e^{[2]}_{ttH}$, where background theory systematic uncertainties dominate.

The expected and observed correlation matrices are shown in Figure 7.11, and show a reasonably good decorrelation achieved between the fit basis parameters: over half of the off-diagonal elements are smaller than 0.1, and over 85% are smaller than 0.3 in both the observed and expected matrix. A few exceptions stand out, notably the correlation between $e^{[2]}_{ggF}$ and $e^{[1]}_{ttH}$ and between $e^{[3]}_{ggF}$ and $e^{[1]}_{H\gamma\gamma,Z\gamma}$, which are caused by a common sensitivity to $t\bar{t}H$ production and ggH $H \to \gamma\gamma$, respectively.

Quadratic model Figure 7.12 compares the expected and observed results obtained using the SMEFT model including quadratic terms, showing again good agreement of the observed data with the SM expectation, corresponding to a p-value of 98.2%. For most parameters, the observed uncertainty is noticeably smaller than the expected uncertainty. The cause of this discrepancy is related to the appearance of quadratic parameter terms in the cross-section predictions, which cause the likelihood function to generally have multiple minima in each parameter. In the expected result, most close-by minima that are exactly degenerate with the global minimum merge into a single wider uncertainty interval. Conversely, in the observed result, the generally non-zero observed coefficient values lift some of these minima to become local minima, thereby resulting in a narrower

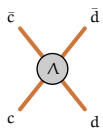

$O^{(8)}_{ud}$

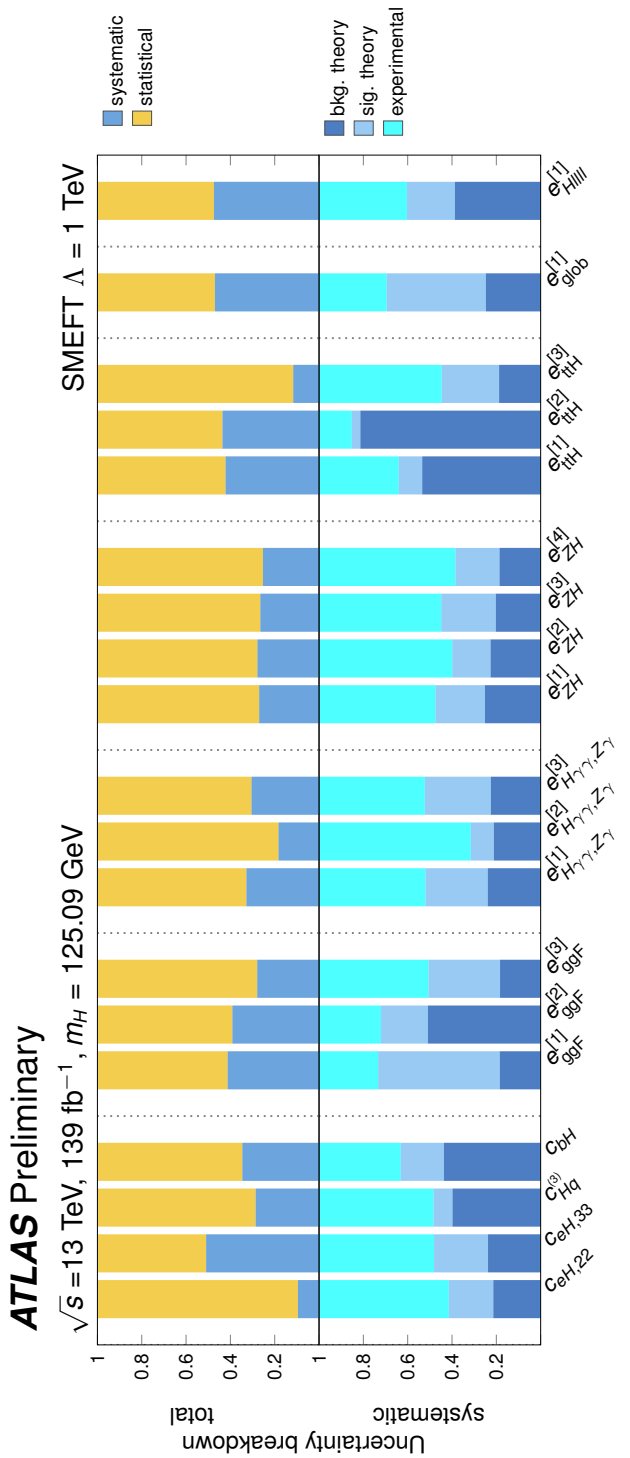

Figure 7.10: Expected fractional contributions of the statistical (orange) and systematic (blue) uncertainties to the total uncertainty on the measurements of the parameters of the rotated basis $\boldsymbol{c}'$ with the SMEFT linearized model (top panel), and the corresponding expected fractional contributions of experimental (cyan), signal theory (light blue) and background theory (dark blue) uncertainties to the total systematic uncertainty (bottom panel).

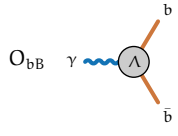

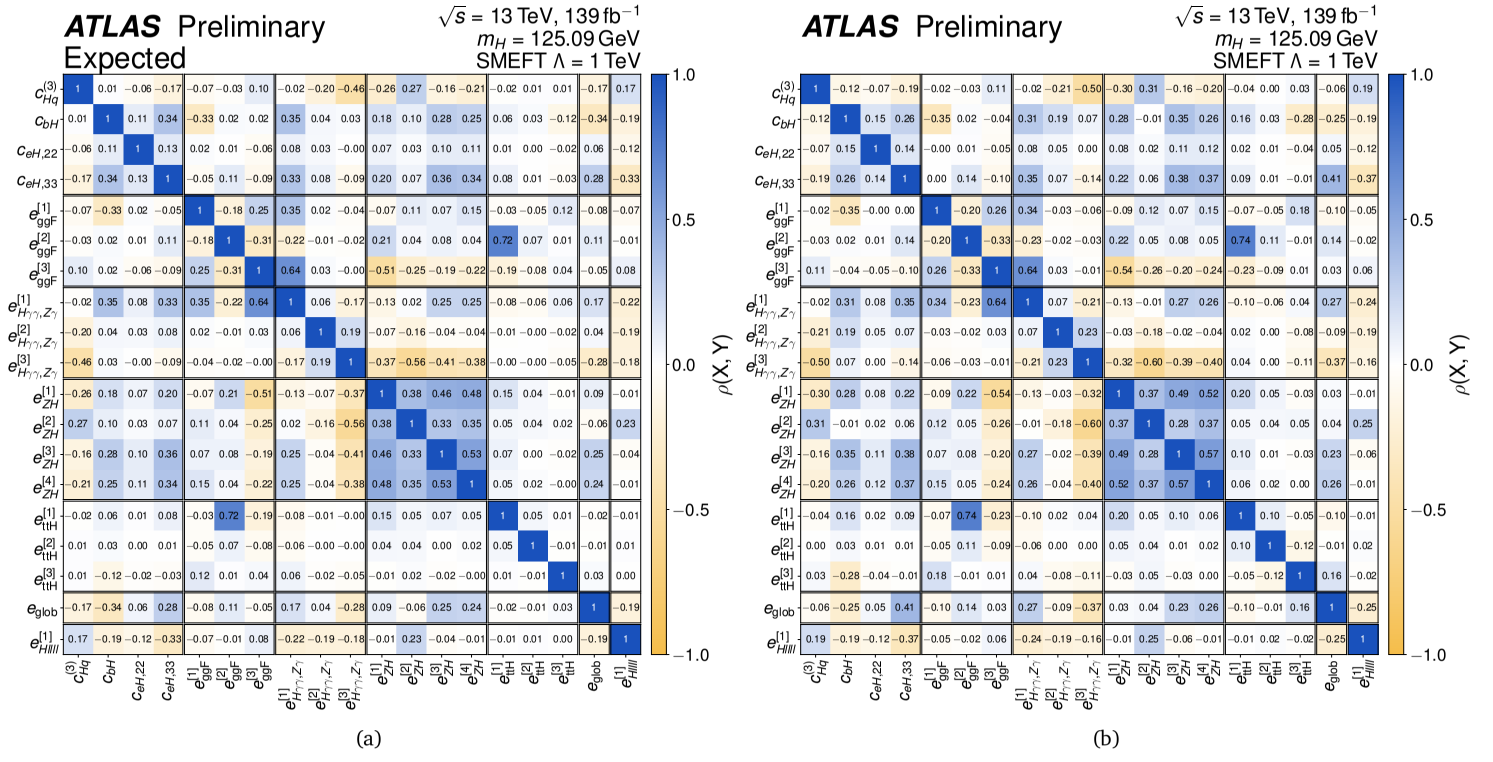

Figure 7.11: The (a) expected and (b) observed correlation matrix for the parameters of the rotated basis $\boldsymbol{c}'$ obtained from a fit to the linearized SMEFT model.

interval around the remaining global minimum. This effect can be clearly seen in more detail in the profile likelihood scans of each parameter, shown in Figures 7.13 and 7.14. Most secondary minima are raised by 1-2 units in $-2\log L$, thus narrowing the 68% confidence intervals, which are based on a unit threshold, but less so the 95% confidence intervals based on a 3.84 unit threshold. For all parameters with multiple solutions, the global minimum in the observed result resolves to the minimum closest to a coefficient value of zero, with the exception of parameter $e^{[1]}_{H\gamma\gamma,Z\gamma}$, where the minimum furthest from zero becomes the global minimum. For the parameter $c_{eH,22}$, there are two exactly degenerate minima. In that case, the minimum closest to that of the interpretation with the linear model is quoted as the best-fit result.

Almost all profile likelihood functions exhibit Gaussian behavior to a good approximation within the 95% CL range of each parameter, although this is masked by the appearance of degenerate solutions. The only exception is the expected profile likelihood for the $e^{[3]}_{ttH}$ parameter in the linearized model, where a boundary occurs at $e^{[3]}_{ttH} = -10$, just before the likelihood threshold of the 95% CL is reached. Here, the yield prediction in the high-p_T region of the $t\bar{t}H$, $H\to\gamma\gamma$ channel becomes negative for very negative values of $e^{[3]}_{ttH}$, rendering the likelihood undefined beyond that point. The 95% CL interval for $e^{[3]}_{ttH}$ shown in Figures 7.9 and 7.15 has been truncated at this boundary, resulting in a small under coverage.

Linear-Quadratic comparison Figure 7.15 compares the results for the linearized model and the model with quadratic terms for the observed data and shows that for several of the coefficients, the constraints from the model with the quadratic terms are significantly stronger than those observed for the linear model. In most cases, the stronger constraints arise from the relatively weak impact of the BSM-SM interference term on the cross-section compared to the quadratic BSM terms in specific production or decay modes.

Figure 7.8 illustrates the impact of both the linear model and the model with quadratic terms, where the impact strength visualized for *both* models corresponds to the expected 68% uncertainty of each fit basis parameter c' under the linear model. Comparatively, larger impacts of the quadratic model at these chosen parameter values identify STXS regions where quadratic terms outweigh the linear terms at the measured scale and thus identify regions that predominantly provide the extra constraining power of the quadratic models. The strongest observed sensitivity enhancements occur in $e^{[3]}_{ggF}$, $e^{[2]}_{ttH}$ and $e^{[3]}_{ttH}$. For coefficient $e^{[3]}_{ggF}$, the quadratic term significantly increases sensitivity in the ggH, ZH and $t\bar{t}H$ production modes as well as in the $H\to\gamma\gamma$ decay mode. For coefficients $e^{[2]}_{ttH}$ and $e^{[3]}_{ttH}$, the quadratic term enhances sensitivity in high-p_T $t\bar{t}H$ production and tH production, respectively. Conversely, for the coefficients $e^{[2]}_{ggF}$ and $e^{[3]}_{H\gamma\gamma,Z\gamma}$, the effect of

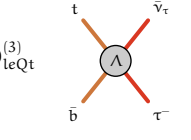

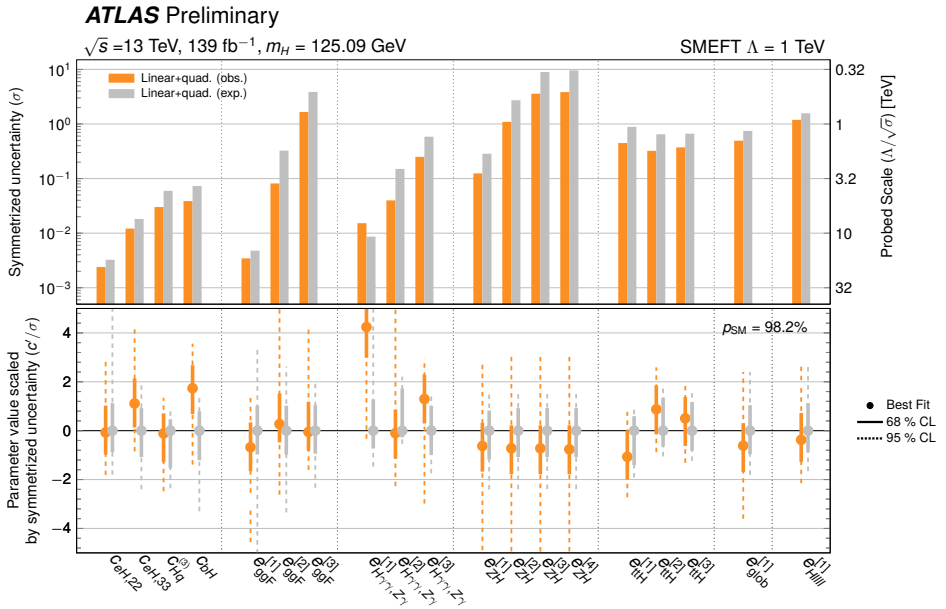

Figure 7.12: Comparison of the expected (gray) and observed (orange) parameters of the rotated basis $\boldsymbol{c}'$ with the SMEFT model with quadratic terms, where all other coefficients and nuisance parameters are profiled. The top panel shows the symmetrized 68% uncertainty σ of each parameter measurement (left vertical axis) and the corresponding energy scale $\Lambda/\sqrt{\sigma}$, $\Lambda = 1$ TeV that is probed (right vertical axis). The bottom panel shows the measured parameter value, 68% (solid) and 95% (dashed) CL intervals, divided by the symmetrized uncertainty shown in the top panel. Some of the observed intervals shown are clipped off. Due to multiple minima, the likelihood curves from which these CL intervals are derived are non-parabolic. For the parameter $c_{eH,22}$, for which there are two degenerate minima in the interpretation of the model including quadratic terms, the point corresponds to the best-fit value that is closest to that of the interpretation with the linear model.

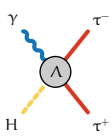

O_{eB}

the increased impacts of the quadratic terms is limited, and the strong reduction in uncertainties is mostly driven by the lifting of degenerate solutions, as visible in the profile likelihood scans in Figure 7.13.

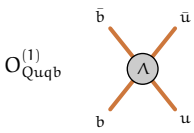

Operators in Warsaw basis: $c_{eH,22}$, $c_{eH,33}$, $c_{Hq}^{(3)}$ and c_{bH}

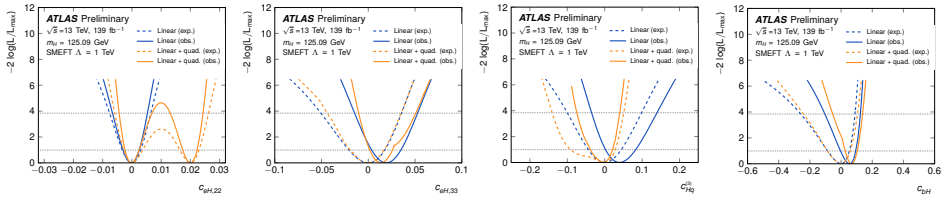

(a) (b) (c) (d)

Eigenvector group ggF

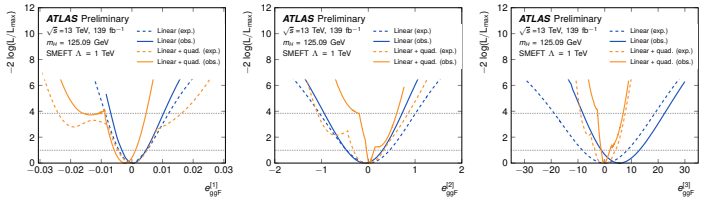

(e) (f) (g)

Eigenvector group $H \to \gamma\gamma, Z\gamma$

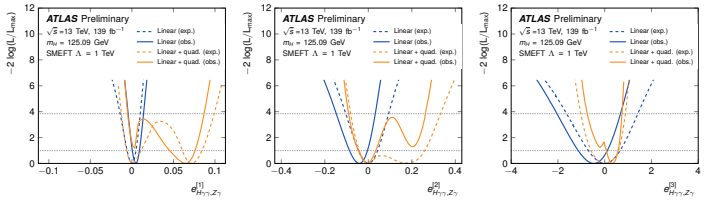

(h) (i) (j)

Eigenvector group ZH

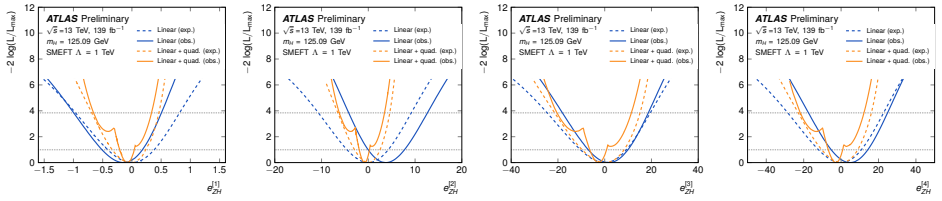

(k) (l) (m) (n)

Figure 7.13: Profile likelihood scans of the fitted coefficients of the rotated basis c' obtained from fits to the SM expectation (dashed lines) and the observed data (solid lines), based on the SMEFT linearized model (blue) and the SMEFT model with quadratic terms (orange). The horizontal dashed lines in each plot correspond to the asymptotic threshold values for 68% and 95% CL intervals. The profile likelihood scans of the SMEFT model with quadratic terms can exhibit two minima in the scanned parameter. In contrast, the scans of the linearized model have one minimum per parameter. Multiple minima in the coefficients that are profiled in each scan may furthermore result in discontinuous derivatives in the profile likelihood (e.g., prominently visible in the observed data in (e) and (l)).

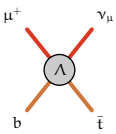

$O_{leQt}^{(1)}$

Eigenvector group *top*

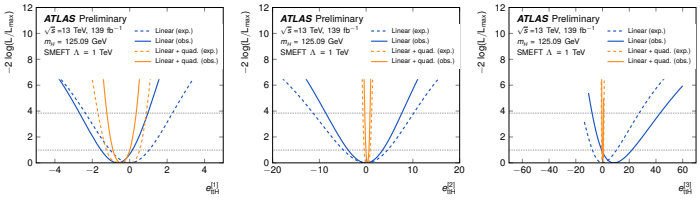

(a) (b) (c)

Eigenvector group *overall normalization*

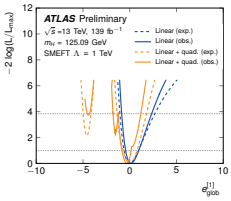

(d)

Eigenvector group $H \to ZZ^*$

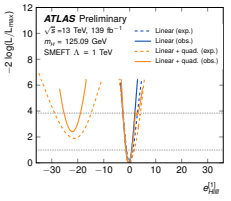

(e)

Figure 7.14: Profile likelihood scans of the fitted coefficients of the rotated basis c' obtained from fits to the SM expected (dashed lines) and to the observed data (solid lines) based on the SMEFT linearized model (blue) and the SMEFT model with quadratic terms (orange). The horizontal dashed lines in each plot correspond to the asymptotic threshold values for 68% and 95% CL intervals. The profile likelihood scans of the SMEFT model with quadratic terms can exhibit two minima in the scanned parameter, whereas the scans of the linearized model can only have one minimum per parameter. Multiple minima in the coefficients that are profiled in each scan may furthermore result in discontinuous derivatives in the profile likelihood (e.g., prominently visible in the observed data in (d)).

$O^{(1)}_{quQb}$

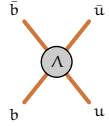

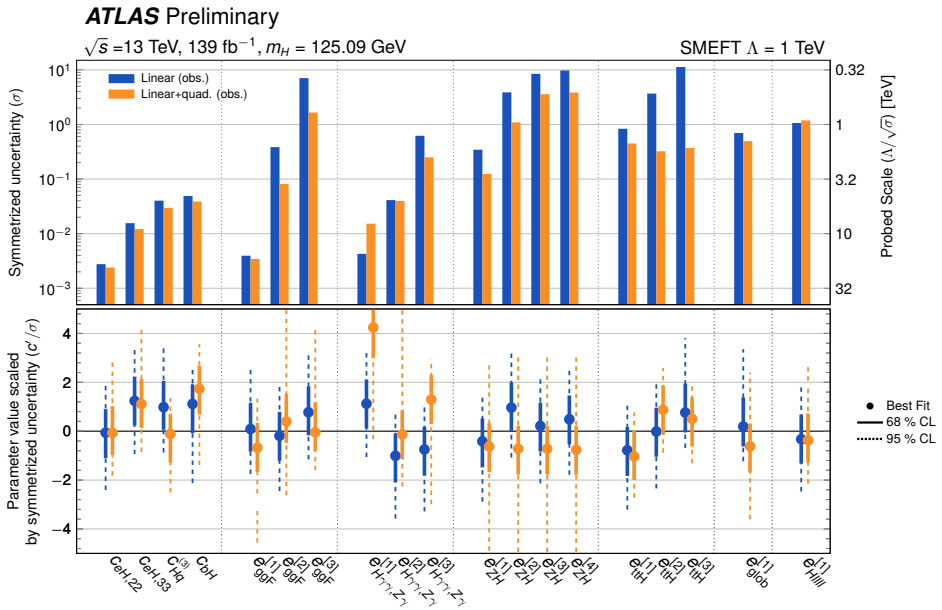

Figure 7.15: Comparison of the observed parameters of the rotated basis $\boldsymbol{c}'$ with the SMEFT linearized model (blue) and the model including quadratic terms (orange), where all other coefficients and nuisance parameters are profiled. The top panel shows the symmetrized 68% CL uncertainty σ of each parameter measurement (left vertical axis) and the corresponding energy scale $\Lambda/\sqrt{s}$, $\Lambda = 1$ TeV that is probed (right vertical axis). The bottom panel shows the measured parameter value, 68% (solid) and 95% (dashed) CL intervals, divided by the symmetrized uncertainty shown in the top panel. Some of the intervals shown for the model with quadratics terms are clipped off. Due to multiple minima, the likelihood curves from which these CL intervals are derived are non-parabolic. The 95% CL interval for $e^{[3]}_{ttH}$ has been truncated at the boundary at which the log-likelihood becomes undefined, resulting in a small undercoverage. For the parameter $c_{eH,22}$, for which there are two degenerate minima in the interpretation with the model, including quadratic terms, the point corresponds to the best-fit value that is closest to that of the interpretation with the linear model.

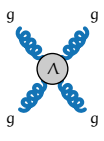

7.6 Post-fit signal strength distribution

In order to understand the role of the measurements in constraining the SMEFT parameter space, the SMEFT constraints can be propagated to the signal strength parameters. This procedure provides the post-fit distribution of the measurement as constrained in SMEFT. This post-fit distribution not only informs which measurements are limiting the current SMEFT constraints but also informs measurements with their current observables that do not bring sufficient information to the SMEFT fit. This information provides a guideline for future measurements to be designed to improve the SMEFT by reducing the uncertainties on the measurements that are limiting the SMEFT fit and choosing alternative observables that can provide better constraints on the SMEFT parameter space.

The projection is based on the parameter estimates $\hat{c}'$ of the observed data. Uncertainties were projected using the corresponding covariance matrix V_{EFT} for $\hat{c}'$ estimators obtained from the data and projected to STXS cross-section space using

$$V_{STXS} = J.V_{EFT}.J^{T}, \tag{7.1}$$

where the Jacobian J is defined as $\partial\mu_i(\boldsymbol{c'})/\partial c_j|_{c'=\hat{c}'}$. The post-fit distribution is shown along with the measured signal strength in Figures 7.16 to 7.18. Bins where the post-fit uncertainty is comparable to the data uncertainty, indicate that those regions are the ones that limit the measurement of the SMEFT parameter space. For the $t\bar{t}H,(b\bar{b})$ process, as shown in Figure 7.18, where the SMEFT impact of the four-fermion operators in the c_{top} group is increasing with increasing p_T^H, the post-fit uncertainty on the bin $p_T^H > 450$ GeV is closest to that of the data uncertainty. Conversely, for regions where the post-fit uncertainty is much smaller than the data uncertainty, the data do not bring a significant constraint in the SMEFT fit. This can be seen in the $gg \to H(bb)$ bins in Figure 7.18, where the differences between the post-fit uncertainty and the measurement uncertainty are large.

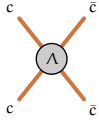

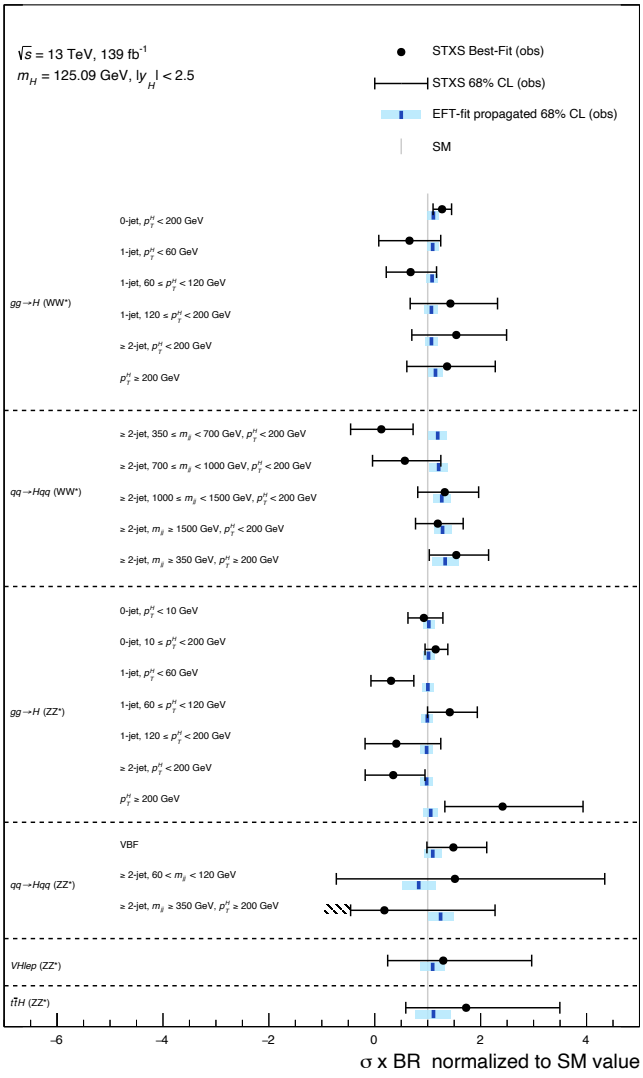

Figure 7.16: Result of SMEFT fit with linear terms projected on input STXS measurements.

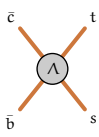

$O^{(1)}_{utbd}$

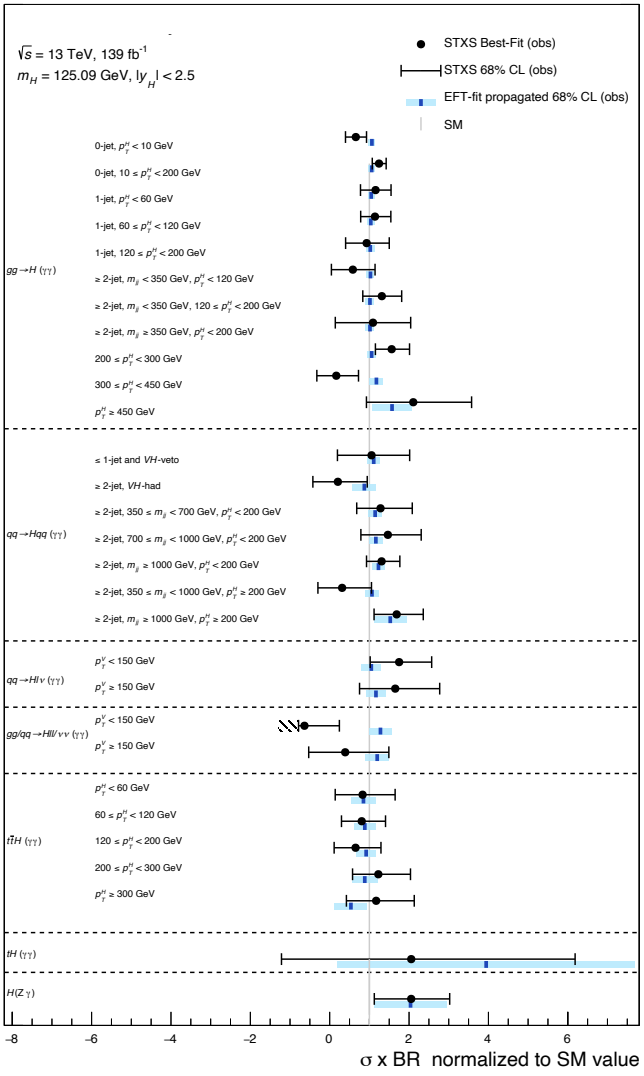

Figure 7.17: Result of SMEFT fit with linear terms projected on input STXS measurements.

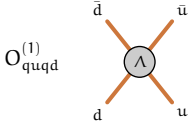

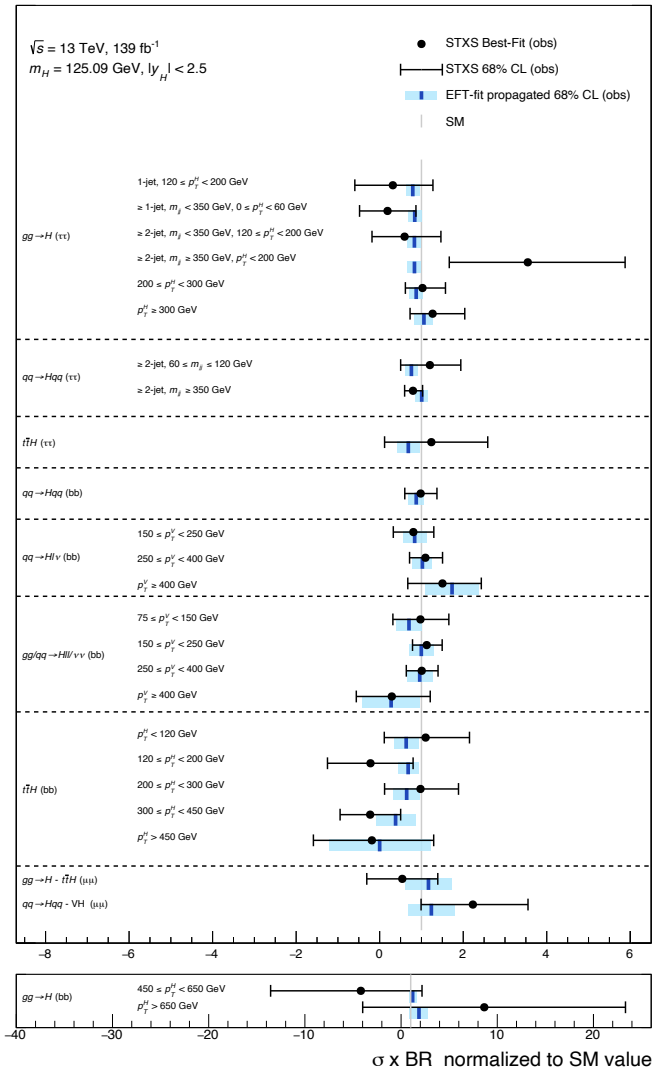

Figure 7.18: Result of SMEFT fit with linear terms projected on input STXS measurements.

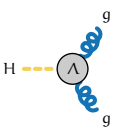

O_{HG}

8

SMEFT Interpretation of $H \to WW^*$ and WW production

8.1 Introduction

One of the strengths of SMEFT is that it can serve as a unifying interpretation framework, allowing for consistent modeling of deviations from the SM across different processes. In this chapter, two different processes are considered, one measuring the Higgs boson production in the $H \to WW^* \to l\nu l\nu$ decay channel and the other that measures the production of WW.

Both measurements are sensitive to numerous dimension-six operators, and a large fraction of those affect both measurements. The combination thus allows to harness the complementarity between the sensitivity of the two processes.

8.2 Data and input measurements

Both the $H \to WW^*$ [230] and the WW measurement [231] are based on 36.1 fb^{-1} of proton-proton collision data collected at $\sqrt{s}$ =13 TeV by the ATLAS experiment at the LHC during the years 2015 and 2016. The $H \to WW^*$ measurement targets Higgs boson production via gluon fusion (ggF) and vector-boson fusion (VBF), and Higgs boson decays through $H \to WW^* \to e^{\pm}\nu_e\mu^{\mp}\nu_\mu$. It is performed in three signal regions, with zero, one, and two jets. Signal candidates are selected by requiring the presence of an isolated $e^{\pm}\mu^{\mp}$ pair, with transverse momentum thresholds of 22 and 15 GeV for the higher-p_T (leading) and lower-p_T (subleading) lepton. Events with jets tagged as containing b-hadrons are rejected to suppress background contributions originating from top-quark production.

The results are extracted in a maximum likelihood fit of two signal-strength parameters that correspond to the overall normalization of the ggF and VBF $H \to WW^*$ production processes relative to that of the SM. For the EFT interpretation, the signal strength modifiers are parametrized in terms of Wilson coefficients.

The WW measurement accepts all production modes and $e^{\pm}\nu\mu^{\mp}\nu$ final states. The event selection suppresses $H \to WW^*$ production by requiring the invariant

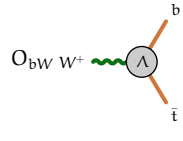

mass of the two charged leptons, $m_{e\mu}$, to be greater than 55 GeV so that the production of two on-shell *W* bosons dominates. A veto on jets with $p_T > 35$ GeV and $|\eta| < 4.5$ is employed in the signal region to suppress backgrounds from top quark production. After subtracting backgrounds, the data is unfolded and fiducial cross-sections are reported for a particle-level phase space that is similar to the reconstruction-level event selection. The unfolded differential cross-section as a function of the highest lepton transverse momentum, $p_T^{\text{lead. lep.}}$, is analyzed here for a SMEFT interpretation, as it is very sensitive to the effects of dimension-six operators that increase in strength with the parton center-of-mass energy. The differential cross-section is measured in 14 bins. The lowest threshold is 27 GeV, and the last bin includes all events with $p_T^{\text{lead. lep.}}$ of 300 GeV or higher. The predicted cross-section in each bin is parametrized in terms of Wilson coefficients.

The signal regions of the two measurements employ orthogonal event selections: $m_{e\mu} > 55$ GeV is required in the *WW* measurement and $m_{e\mu} < 55$ GeV is required in the H → *WW** measurement. However, the latter measurement uses events with $m_{e\mu} > 55$ to estimate the background from on-shell *WW* production, split into two control regions for events with no reconstructed hadronic jets or with exactly one jet. The WW measurement thus overlaps with the 0-jet control region and, despite the jet-veto requirement, also with the 1-jet control region since the H → *WW** and *WW* measurements use different jet object definitions of $p_T^{\text{jet}} > 30$ GeV (H → *WW**) and $p_T^{\text{jet}} > 35$ GeV (*WW*) respectively.

For the combination, the corresponding control region of the H → *WW** analysis is removed, and the signal region of the *WW* measurement is used instead to constrain the *WW* background yield in the H → *WW** signal region.

8.3 Theoretical predictions

8.3.1 Simulation of SM processes

For the interpretation of both analyses, $q\bar{q} \to e^{\pm}\nu\mu^{\mp}\nu$ production is modeled using the SHERPA 2.2.2 [232] generator at NLO accuracy in QCD for up to one additional parton, and LO accuracy for up to three additional parton emissions. The NNPDF3.0NNLO set of parton distribution functions (PDF) is used [122], along with the dedicated set of tuned parton-shower parameters developed by the SHERPA authors. The total $q\bar{q} \to e^{\pm}\nu\mu^{\mp}\nu$ cross-section predicted by this generator configuration is in good agreement with the NNLO cross-section [116, 233–239]. In the phase space of the *WW* analysis, the $gg \to e^{\pm}\nu\mu^{\mp}\nu$ matrix element calculation is based on the OPENLOOPS library [236, 239] that includes off-shell effects and Higgs boson contributions. It incorporates up to one additional parton emission at LO and is matched and merged with the SHERPA parton shower

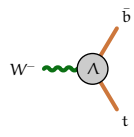

O_{Ht}

based on Catani-Seymour dipole model [240, 241] using the MEPS@NLO prescription [242–245]. The same parton shower and PDFs as for the $q\bar{q} \to e^{\pm}\nu\mu^{\mp}\nu$ sample are employed. The gg-induced process is normalized to its NLO cross section [246].

In the signal region of the $H \to WW^*$ analysis, SM $gg \to WW$ production is simulated with the same setup as used for the WW analysis but excluding s-channel Higgs boson contributions. The Higgs boson signal prediction is obtained in a similar manner as described earlier in Section 2.5.

8.3.2 Simulation of the effect of dimension-six operators

The effect of dimension-six operators on the signal production processes, WW production, as well as ggF and VBF Higgs boson production, is studied at the lowest order of perturbation theory for which the process occurs in the SM similar to the linear parametrization, which is discussed in the previous chapter. A $U(3)^5$ flavor symmetry, which requires operators to be symmetric in the three fermion generations, is assumed, and the m_W, m_Z, G_F input parameter scheme is used.

In total, 24 CP-even operators affect the signal processes of the two measurements. The operators and their corresponding Wilson coefficient are summarized in Table 8.1. All the cross-sections considered here are CP-even observables and hence do not have sensitivity to the interference of CP-odd operators with the Standard Model.

Dedicated samples are generated using MADGRAPH5_aMC@NLO [178] to model linear SMEFT effects caused by the interference of each dimension-six operator with the SM. The effect of dimension-six operators that contribute to $q\bar{q} \to e^{\pm}\nu\mu^{\mp}\nu$ production is simulated at leading order QCD using the SMEFTsim [175] model and MADGRAPH5_aMC@NLO version 2.8.1 [178], interfaced to PYTHIA 8.244 [179], with the A14 tune [247] for parton showering and hadronization. Events with zero or one jet are simulated in MADGRAPH5_aMC@NLO, and the overlap between matrix element partons and parton shower emissions is removed using the CKKW-L merging procedure [248, 249]. In the signal region of the WW analysis, the effect of operators is parametrized differentially in analysis bins. For the $q\bar{q} \to e^{\pm}\nu\mu^{\mp}\nu$ background to the $H \to WW^*$ analysis, the SMEFT variation is assumed to have a flat impact in the analyzed observables with no shape impact and is a good approximation at the particle level.

The vector boson fusion Higgs boson production is also simulated at leading order, using MADGRAPH5_aMC@NLO version 2.6.2 and the SMEFTsim model. The SMEFT effects in ggF $H \to WW^*$ production are simulated with MADGRAPH5_aMC@NLO version 2.7.3 and SMEFTatNLO [177], since the leading contribution to the process is at loop level. The ggF process is generated sepa-

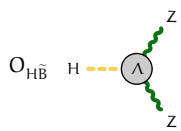

Wilson coefficient and operator		Affected Processes				
$c_i^{(6)}$	$\mathcal{O}_i^{(6)}$	$qq \to e\nu\mu\nu$	$qq \to Hqq$	$gg \to H$	$\Gamma^f_{H\to e\mu\nu\nu}$	Γ^{tot}_H
c_W	$\epsilon^{IJK} W_\mu^{I\nu} W_\nu^{J\rho} W_\rho^{K\mu}$	✓				✓
c_{HW}	$H^\dagger H W^I_{\mu\nu} W^{I\mu\nu}$		✓		✓	✓
c_{HWB}	$(H^\dagger \tau^I H W^I_{\mu\nu} B^{\mu\nu})$	✓	✓			✓
c_{HB}	$H^\dagger H B_{\mu\nu} B^{\mu\nu}$		✓			✓
c_{HDD}	$(H^\dagger D^\mu H)^* (H^\dagger D_\mu H)$	✓	✓	✓	✓	✓
$c_{H\Box}$	$(H^\dagger H)\Box(H^\dagger H)$		✓	✓	✓	✓
c_{HG}	$H^\dagger H G^A_{\mu\nu} G^{A\mu\nu}$			✓		✓
c_{dH}	$(H^\dagger H)(\bar{q}_p d_r H)$					✓
c_{uH}	$(H^\dagger H)(\bar{q}_p u_r H)$			✓		✓
c_{eH}	$(H^\dagger H)(\bar{l}_p e_r H)$					✓
c_{uG}	$(\bar{q}_p \sigma^{\mu\nu} T^A u_r)(\tilde{H} G^A_{\mu\nu})$			✓		✓
c_{uW}	$(\bar{q}_p \sigma^{\mu\nu} u_r)(\tau^I \tilde{H} W^I_{\mu\nu})$					✓
c_{uB}	$(\bar{q}_p \sigma^{\mu\nu} u_r)(\tilde{H} B_{\mu\nu})$					✓
c_{Hd}	$(H^\dagger i\overleftrightarrow{D^I_\mu} H)(\bar{d}\gamma^\mu d)$	✓	✓			
c_{Hu}	$(H^\dagger i\overleftrightarrow{D^I_\mu} H)(\bar{u}\gamma^\mu u)$	✓	✓			
$c^{(1)}_{Hq}$	$(H^\dagger i\overleftrightarrow{D^I_\mu} H)(\bar{q}\gamma^\mu q)$	✓	✓			
$c^{(3)}_{Hq}$	$(H^\dagger i\overleftrightarrow{D^I_\mu} H)(\bar{q}\tau^I\gamma^\mu q)$	✓	✓			✓
$c^{(1)}_{Hl}$	$(H^\dagger i\overleftrightarrow{D^\mu} H)(\bar{l}\gamma^\mu l)$	✓				
$c^{(3)}_{Hl}$	$(H^\dagger i\overleftrightarrow{D^I_\mu} H)(\bar{l}\tau^I\gamma^\mu l)$	✓	✓	✓	✓	✓
$c^{(1)}_{ll}$	$(\overline{l_p}\gamma_\mu l_r)(\overline{l_s}\gamma^\mu l_t)$	✓	✓	✓	✓	✓
c_{ld}	$(\bar{l}_p\gamma_\mu l_r)(\bar{d}_s\gamma^\mu d_t)$	✓				
$c^{(1)}_{lq}$	$(\bar{l}_p\gamma_\mu\ l_r)(\bar{q}_s\gamma^\mu q_t)$	✓				
$c^{(3)}_{lq}$	$(\bar{l}_p\gamma_\mu\tau^I l_r)(\bar{q}_s\gamma^\mu\tau^I q_t)$	✓				
c_{lu}	$(\bar{l}_p\gamma_\mu l_r)(\bar{u}_s\gamma^\mu u_t)$	✓				

Table 8.1: Dimension-six Warsaw basis operators affecting the signals of interest assuming $U(3)^5$ flavor symmetry. The second column shows the operator entering in this coupling. The right columns indicate which measurements are affected by the operator.

rately with zero, one, and two additional partons in the final state, which are then merged with the MLM algorithm [209, 210] which take care of remaining overlaps in the phase space.

The events from the simulation of Higgs boson production are interfaced to PYTHIA 8.230 for parton showering and hadronization. The dependence of the total width of the Higgs boson on Wilson coefficients is computed by simulating Higgs boson decays to all final states. All decays are simulated with SMEFTsim,

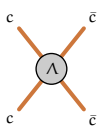

$O^{(1,8)}_{qq}$

barring two cases. The Higgs boson decay into gluons is simulated with SMEFTatNLO to resolve the QCD NLO contributions. For the Higgs boson decay to two photons, an analytically derived parametrization including next-to-leading order electroweak corrections [250] is used for the $H \to \gamma\gamma$ contribution to the total Higgs boson width.

In the phase space of the *WW* analysis, the loop-induced $gg \to \mu^{\pm}e^{\mp}\nu\nu$ process is simulated with SMEFTatNLO for all operators that affect ggF production and Higgs boson decays into $e^{\pm}\nu\mu^{\mp}\nu$. While the addition of this process constitutes only a small correction to *WW* production, the consistent treatment of on-shell and off-shell Higgs boson production is important for the correct modeling of the degeneracies of operators that are involved in ggF production. Operators that do not affect Higgs boson production are not taken into account for $gg \to \mu^{\pm}e^{\mp}\nu\nu$, as the process only constitutes a higher-order QCD correction to *WW* production. Events are generated with MADGRAPH5_aMC@NLO version 2.7.3, interfaced to PYTHIA 8.230, with the A14 tune for parton showering and hadronization. In the signal region of the $H \to WW^*$ analysis, ggF Higgs boson production is simulated separately from the $gg \to \mu^{\pm}e^{\mp}\nu\nu$ background, and the interference of the two processes is negligible. Since $gg \to \mu^{\pm}e^{\mp}\nu\nu$ can be treated as a higher-order correction to *WW* production and is responsible for only 10% of the total WW background, SMEFT effects on the process are neglected in the signal region of the $H \to WW^*$ measurement.

The SMEFT parametrization of the differential cross-section for $pp \to e^{\pm}\nu_e\mu^{\mp}\nu_\mu$ production in the phase space of the *WW* analysis and for the ggF and VBF signal strength times branching ratio into $e^{\pm}\nu\mu^{\mp}\nu$ is summarized in Figure 8.1. For the *WW* analysis, the differential cross-section measured in the *WW* analysis is reported for a fiducial phase space that is defined by requirements that are very similar to the data selection, and SMEFT predictions are evaluated in this phase space. A minor model-dependent extrapolation is needed for the calculation of the measured fiducial cross-section and the result is assumed to remain valid also in the presence of dimension-six operator effects. Similarly, the unfolding of the $p_T^{\text{lead. lep.}}$ distribution is also expected to be mostly model-independent as it mostly corrects for detector effects that do not strongly depend on the precise model used for the hard process. For the $H \to WW^*$ analysis, corrections to the four-body decay parametrization due to analysis sections are estimated separately for the ggF and VBF regions due to the different selections involved. The impact of the selections is less than 10% on the SMEFT impact normalized to the Standard Model. The impact of dimension-six operators on the *WW* background in the $H \to WW^*$ signal region is evaluated after applying selection cuts that correspond to the reconstruction-level event-selection.

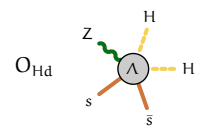

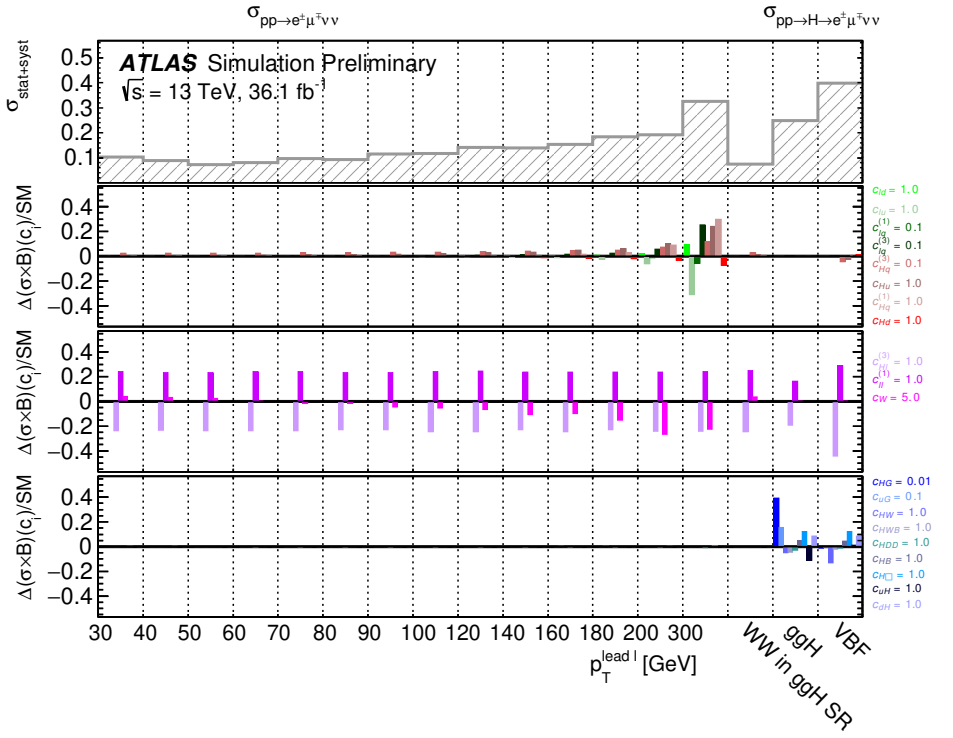

Figure 8.1: The linear impact of the SMEFT operators on the signal strength modifiers of the H → *WW** analysis, the normalization of the *WW* background in the ggF signal region, and the differential cross-section measured in the *WW* analysis, relative to the SM cross-section. In order to illustrate experimental sensitivity to these effects in data, the expected total uncertainty on each modifier is shown in the top panel. $\Lambda = 1$ TeV is assumed, and the values of Wilson coefficients are chosen such that the impact of all operators is of similar size for better visibility.

8.4 Statistical model

This section describes the statistical model used to constrain the SMEFT parameters. The statistical model for the H → *WW** analysis follows the Poissonian likelihood described in Section 5. The statistical model for the unfolded *WW* measurement and its combination with the H → *WW** analysis is explained below.

8.4.1 Statistical model of the *WW* measurement

The probability density function used in the interpretation of the unfolded *WW* measurement is based on a multivariate Gaussian distribution. Experimental and theory uncertainties are modeled with nuisance parameters constrained by Gaus-

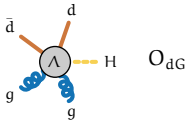

sian distributions that represent auxiliary measurements as well as theoretical expectations.

The prediction of the analyzed $p_T^{\text{lead. lep.}}$ distribution depends on the set of Wilson coefficients $\boldsymbol{c}$, which is listed in Table 8.1, and is also subject to theory systematics, for example, factorization and normalization scale uncertainties, which are parametrized by theory nuisance parameters. For a given theory, nuisance parameter configuration $\boldsymbol{\theta}^{WW}_{\text{theo syst}} = (\theta_1, \ldots, \theta_j, \ldots, \theta_{n^{WW}_{\text{theo syst}}})$, where $n^{WW}_{\text{theo syst}}$ is the number of theory nuisance parameters affecting the signal predictions, the predicted fiducial cross-section in a bin b, x_b^{pred} , of the unfolded $p_T^{\text{lead. lep.}}$ distribution is parametrized as

$$x_b^{\text{pred}}\left(\boldsymbol{c}, \boldsymbol{\theta}^{WW}_{\text{theo syst}}\right) = x_b^{\text{SM}}\left(1 + \sum_i c_i A_{b,i}\right) \times \prod_j^{n^{WW}_{\text{theo syst}}} \left(1 + \theta_j u_{b,j}\right), \tag{8.1}$$

where $u_{b,j}$ is the relative size of the uncertainty j in bin b. Here, it is assumed that the nature and the relative effect of theory uncertainties are the same for linear EFT effects as for the SM, as discussed in Section 9.3.2.

The measured cross-section depends on the model that is used to subtract backgrounds, calculate detector efficiencies, and unfold distributions. Uncertainties of this model can be parametrized with experimental nuisance parameters $\boldsymbol{\theta}^{WW}_{\text{exp syst}} = (\theta_1, \ldots, \theta_j, \ldots, \theta_{n^{WW}_{\text{exp syst}}})$, where $n^{WW}_{\text{exp syst}}$ is the number of experimental nuisance parameters affecting the measurement. The nominal result of the WW measurement corresponds to a model in which all nuisance parameters are set to their nominal values. Alternative results that correspond to 1σ variations of each of the nuisance parameters are also available. This information is used to calculate an alternative measurement result that is a function of the nuisance parameter values:

$$x_b^{\text{meas}}\left(\boldsymbol{\theta}^{WW}_{\text{exp syst}}\right) = x_b \times \prod_j^{n^{WW}_{\text{exp syst}}} \left(1 + \theta_j \nu_{b,j}\right), \tag{8.2}$$

where x_b is the nominal measurement result and $\nu_{b,j}$ is the relative impact of the systematic variation j on the measured cross-section in bin b.

The nominal measured differential cross-section, in $n^{WW}_{\text{bins}} = 14$ bins, is given by $\boldsymbol{x}$. Statistical uncertainties of the unfolded data are correlated and encoded in a covariance matrix C. The likelihood $L^{WW}\left(\boldsymbol{x}|\boldsymbol{c}, \boldsymbol{\theta}^{WW}\right)$, which is modeled as a multivariate Gaussian distribution and is a function of the Wilson coefficients $\boldsymbol{c}$ as

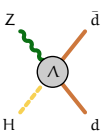

well as the union of experimental and theory nuisance parameters, $\boldsymbol{\theta}^{WW}$, is then given by

$$L(\boldsymbol{x}|\boldsymbol{c},\boldsymbol{\theta}) = \frac{1}{\sqrt{(2\pi)^{n_{\text{bins}}}\det(C)}} \exp\left(-\frac{1}{2}\Delta\boldsymbol{x}^{\intercal}(\boldsymbol{c},\boldsymbol{\theta})\, C^{-1}\Delta\boldsymbol{x}(\boldsymbol{c},\boldsymbol{\theta})\right) \times \prod_{i}^{n_{\text{syst}}} f_i(\theta_i)\,. \tag{8.3}$$

Here n_{syst}^{WW} is the total number of experimental and theory nuisance parameters, f_i correspond to the Gaussian constraints on nuisance parameters while the vector $\Delta\boldsymbol{x}$ represents the difference between measurement and prediction and its components Δx_b are defined as

$$\Delta x_b\left(\boldsymbol{c},\boldsymbol{\theta}^{WW}\right) = x_b^{\text{meas}}\left(\boldsymbol{\theta}^{WW}_{\text{exp syst}}\right) - x_b^{\text{pred}}\left(\boldsymbol{c},\boldsymbol{\theta}^{WW}_{\text{theo syst}}\right). \tag{8.4}$$

8.4.2 Combined statistical model

The likelihood function from the *WW* and H → *WW** measurements are combined to allow a coherent EFT analysis of both measurements. In total, 332 nuisance parameters affect the interpretation of both measurements, while 285 affect only the H → *WW** and 137 only the *WW* measurement.

The *WW* control regions of the H → *WW** measurements overlap with the *WW* analysis phase space, as explained in Section 8.2. For the combination, these are removed, and the overall normalization of the *WW* background in the H → *WW** signal regions is no longer determined from a combined fit of control and signal regions. The *WW* background normalization is instead modeled analogously to the signal parametrization in the *WW* measurement, which is a product of the SM prediction, its uncertainties, and an EFT parametrization, as shown in Equation 8.1. Uncertainties affecting *WW* production are treated as fully correlated between the *WW* and H → *WW** measurements so that inclusion of the *WW* measurement in the fit reduces the uncertainty on the *WW* background yield in the H → *WW** signal region.

8.5 Results

This section presents the results of the combination for the signal strength parameters and the SMEFT parameters.

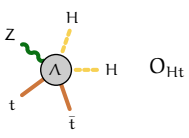

O_{Ht}

8.5.1 Signal strengths measurement

The signal strength of the measurements with respect to the SM in each region, a simultaneous measurement of 16 signal strength parameters is performed. The signal strength parameters correspond to the two signal strength parameters of the Higgs boson production in the gluon-gluon fusion and vector boson fusion from the $H \to WW^*$ analysis and 14 signal strength parameters of the bins of the unfolded $p_T^{lead.lep.}$ of the WW analysis. The results are shown in Figure 8.2 and the corresponding correlation in Figure 8.3.

The central values of the measured $H \to WW^*$ signal strengths differ by less than 2% from the standalone measurement. A 10% degradation of the precision of the ggF signal strength measurement is introduced due to the replacement of the WW control region with the WW measurement while the VBF measurement precision is unaffected.

The WW signal strengths, in bins of $p_T^{\text{lead. lep.}}$, are similar to the ratio of unfolded data to the SM prediction that is presented in the original measurement. Differences in this ratio arise because nuisance parameters that parametrize uncertainties on the measurement or the differential WW cross-section prediction are pulled from their nominal value in the maximum likelihood fit.

8.5.2 Simultaneous Fit to SMEFT parameters

The signal strength measurements are expressed in terms of SMEFT in the linear parametrization scenario described in Section 5.3.1 using Equation 5.16. In order to identify sensitive directions in the SMEFT parameter space, a rotation in the space of Wilson coefficients is performed, as outlined earlier in Section 6.5, to determine a modified basis that consists of sensitive parameters given by linear combinations of the Warsaw basis vectors. Figure 8.4 lists eigenvectors c_j and eigenvalues of the Fisher information matrix. The eigenvalues provide a handle on the expected limits that can be obtained: assuming Gaussian uncertainties, the expected uncertainty for a measurement of an eigenvector is inversely proportional to the square root of the eigenvalue. The first eight directions are shown. They correspond to an eigenvalue of $\lambda \gtrsim 0.01$, which corresponds to an expected uncertainty of less than 10. These eigenvectors, which each probe linear combinations of large numbers of Wilson coefficients, are not directly measured.

In order to improve the interpretability of the measurement, parameter groups that contain Wilson coefficients with a similar physics impact are defined. c_W is treated as its own subgroup, as its physics effect is unique in that it only affects weak boson self-couplings. Coefficients c_{HG}, c_{uG}, and c_{uH} form a group as these operators affect ggF Higgs production. The two coefficients $c^{(1)}_{Hl,33}$ and $c^{(1)}_{ll}$ form a group as

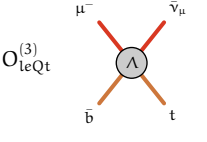

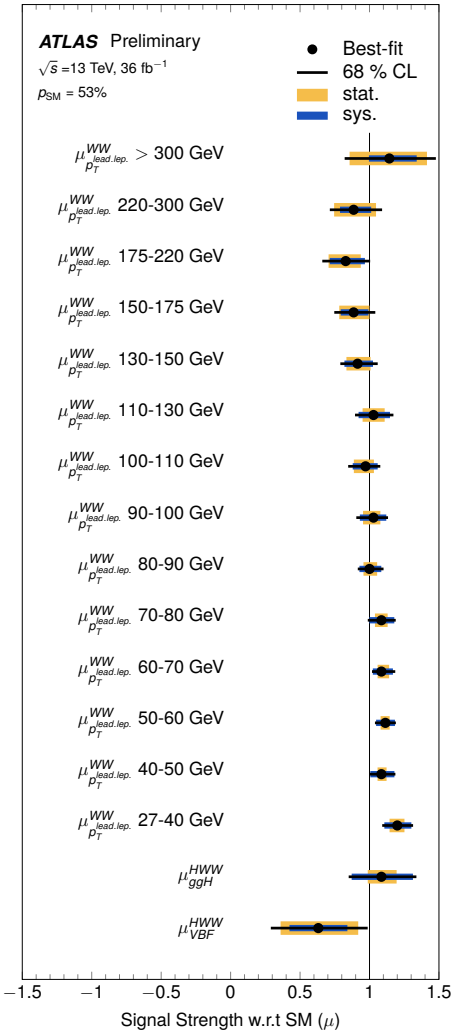

Figure 8.2: Measured signal strengths from the combined fit of signal-strength modifiers in bins of the *WW* analysis and for the two signal-strength modifiers of the H → *WW**analysis. Statistical uncertainties are shown in yellow, and systematic uncertainties in blue bars, and black lines indicate the total uncertainties. The compatibility of the observed data with the SM hypothesis (p_{SM}) is 53%.

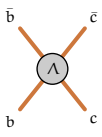

$O_{Qu}^{(1)}$

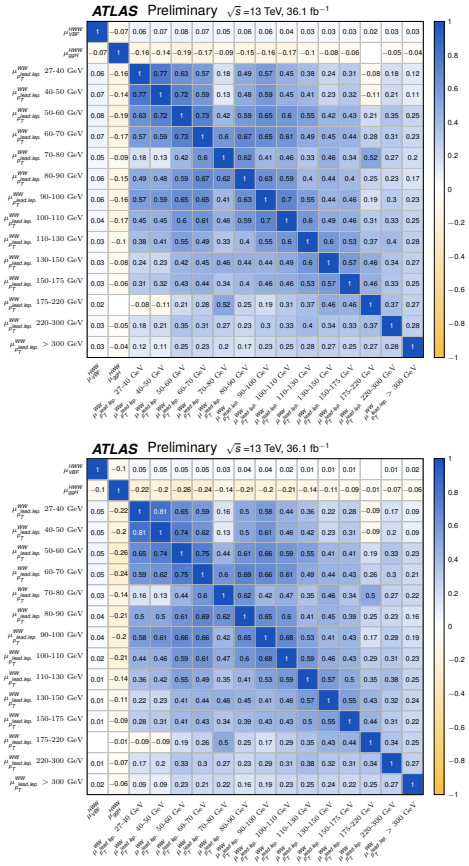

Figure 8.3: Expected (top) and observed (bottom) correlation matrix of the signal strength modifiers of the $H \to WW^*$ analysis and the WW measurement.

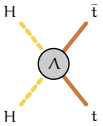

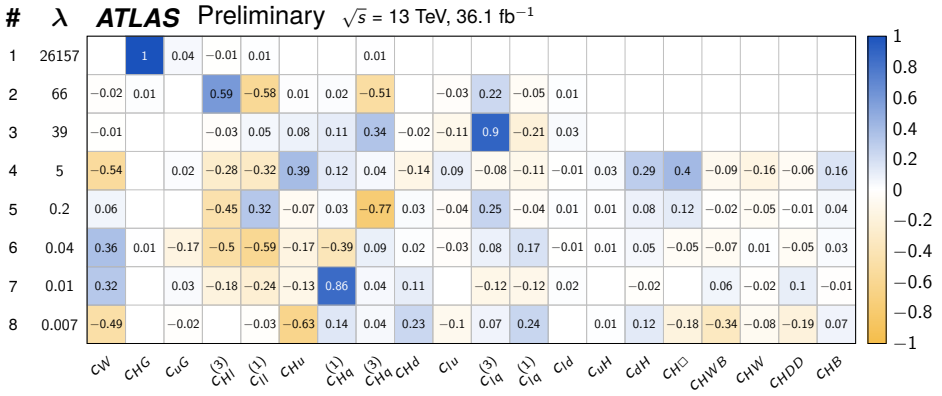

Figure 8.4: The eigenvectors, corresponding eigenvalues, and their components along the Warsaw basis directions. Each line corresponds to an eigenvector, ranked by order of decreasing eigenvalue.

both lead to a shift of the Fermi constant G_F and mainly change the normalization of the observed processes. The coefficients c_{lu}, $c_{lq}^{(3)}$, $c_{lq}^{(1)}$, c_{ld}, c_{Hd}, c_{Hu}, $c_{Hq}^{(1)}$, and $c_{Hq}^{(3)}$ are grouped because their most important effect is the modification of $q\bar{q} \to e^{\pm}\nu\mu^{\mp}\nu$ production at high parton center-of-mass energies. They affect both effective boson-fermion and four-fermion couplings. The next two groups contain c_{HB}, c_{HW}, and c_{HWB}. These parameters affect Higgs boson decays into $e^{\pm}\nu\mu^{\mp}\nu$ and VBF production. The effect of the parameters of the final group, c_{dH}, c_{HD}, and $c_{H\Box}$, is similar for both Higgs-boson production processes.

Eigenvectors of the new grouping that are measured are shown in Figure 8.4 with the impact of variations of the rotated fit parameters c_j on the measured signal strength is shown in Figure 8.6. Eigenvectors that correspond to weakly constrained directions are fixed to zero. These weakly constrained directions are identified by selecting directions that have an uncertainty larger than 10 when considered with the fit directions. Profile-likelihood scans are used to confirm the sensitivity estimate based on the eigenvector analysis.

One of the sensitive directions aligns, by construction, with c_W. The $c^{[1]}_{Hl^{(3)},ll^{(1)}}$ eigenvector changes the normalization of *WW* production and affects the VBF and ggF production rates. The second linear combination of these two coefficients, $c^{[2]}_{Hl^{(3)},ll^{(1)}}$, mainly affects the rate of VBF Higgs boson production while $c^{[1]}_{uG,HG,uH}$ modifies the ggF-production rate.

The main effect of $c^{[1]}_{lu,lq^{(3)},lq^{(1)},ld,Hd,Hu,Hq^{(1)},Hq^{(3)}}$ is a change in the rate of *WW* and VBF Higgs boson production while the remaining operators of that group modify the tail of the $p_T^{\text{lead. lep.}}$ distribution. Only two degrees of freedom can be

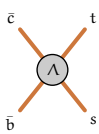

$O^{(8)}_{utbd}$

constrained by the two signal-strength measurements, and these are $c^{[2]}_{Hl^{(3)},ll^{(1)}}$ and $c^{[1]}_{uG,HG,uH}$, following the methodology used for these results.

Constraints on eigenvectors and their correlation are shown in Figure 8.8. All the measurements agree with the SM expectation at the level of one standard deviation. Four parameters can be measured with a precision of better than 1.

The contribution of the $H \to WW^*$ and WW measurements to the constraints on the operators is shown in Figure 8.5. There are four directions that are purely constrained by the WW measurement. The $c^{[1]}_{uG,HG,uH}$ operator that affect gluon-gluon fusion Higgs boson production is purely constrained by the $H \to WW^*$ measurement. There are three directions ($c^{[3]}_{lu,lq^{(3)},lq^{(1)},ld,Hd,Hu,Hq^{(1)},Hq^{(3)}}$, $c^{[1,2]}_{Hl^{(3)},ll^{(1)}}$) which are constrained by both measurements.

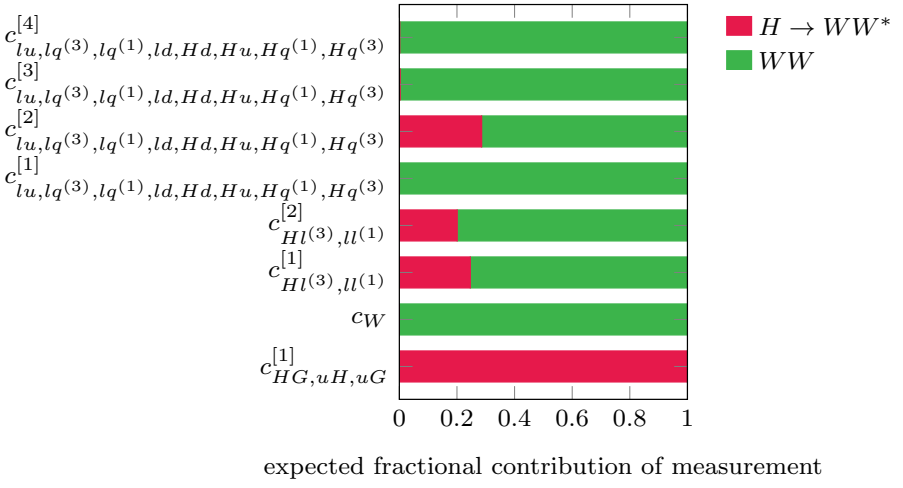

Figure 8.5: The expected fractional contribution of the different the $H \to WW^*$ and WW measurements to the SMEFT parameter sensitivity.

A combination with additional measurements of Higgs-boson production and decay is required to improve constraints and reduce the number of flat directions in the subspace of operators that affect the Higgs sector. The combination with additional measurements of single and multiboson production can help to improve the constraints on the remaining operators and to reduce degeneracies among the parameters that affect boson-fermion and four-fermion couplings.

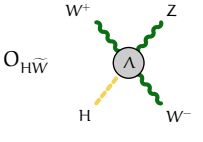

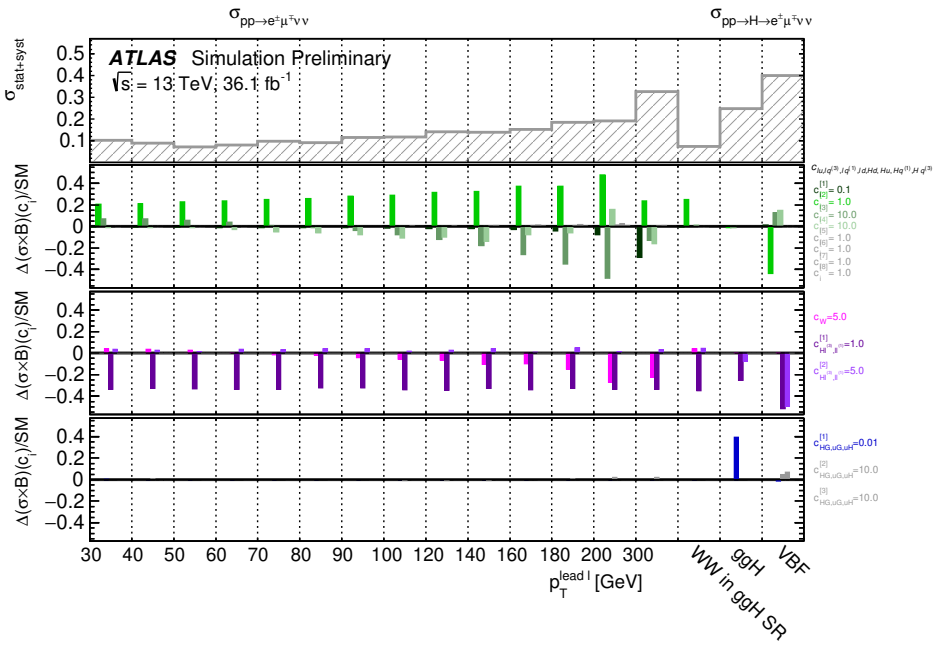

Figure 8.6: Impact of the rotated c_j basis for $\Lambda = 1$ TeV on the signal strength modifiers of the H → *WW**analysis, the normalization of the *WW* background in the ggF signal region, and the differential cross-section measured in the *WW* analysis, relative to the SM cross-section. Operators of the groups that are not included in the fit are shown in gray. In order to illustrate experimental sensitivity to constrain the operators from the data, the total expected uncertainty on the corresponding regions $\sigma_{\text{stat+syst}}$ is shown in the top panel.

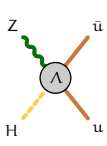

O_{uB}

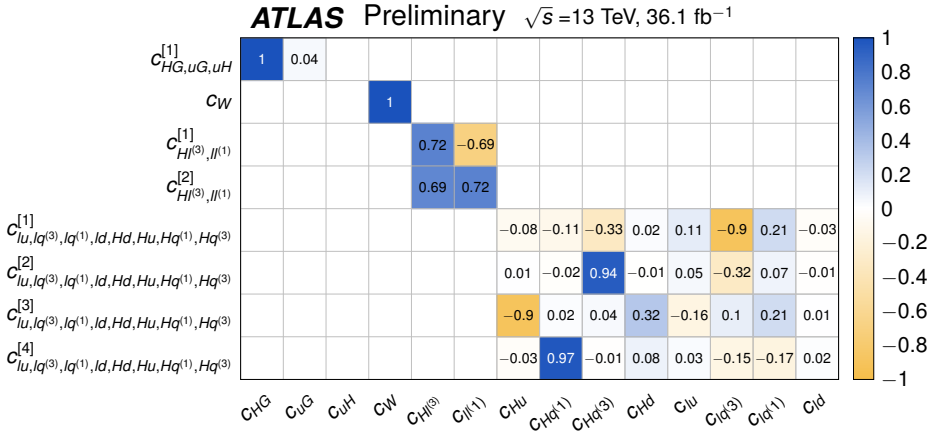

Figure 8.7: Visualization of the eight measured linear combinations of Wilson coefficients. The grid shows the contribution of Warsaw basis vectors to the eigenvectors; each eigenvector corresponds to one line in the above grid. The component of c_{uH} in $c^{[1]}_{HG,uG,uH}$ is small (-0.003) and is not shown for clarity.

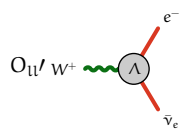

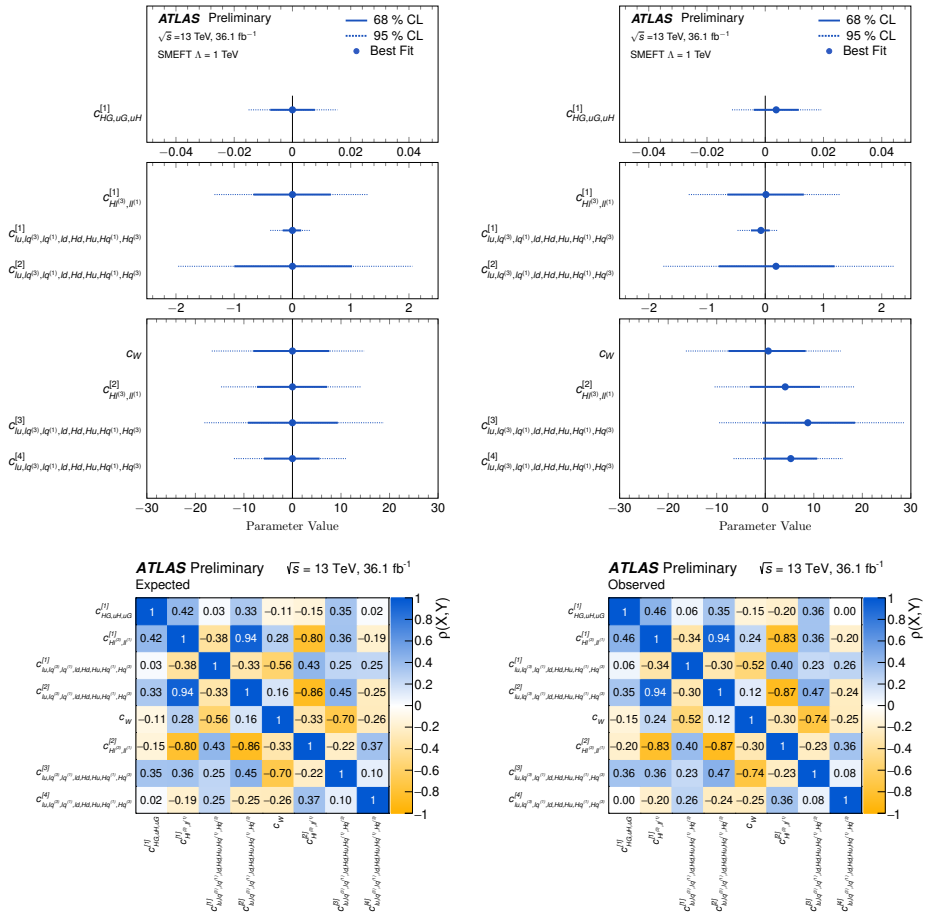

Figure 8.8: Summary of expected (left) and observed (right) measurements in the space of the eigenvectors. In the top figures, the ranges shown correspond to 68% (solid) and 95% (dashed) confidence level intervals, where all other sensitive directions and nuisance parameters were profiled. The corresponding correlations are shown in the bottom figures.

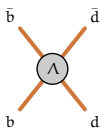

$O_{bd}^{(8)}$

9

Global SMEFT Fit of Higgs and Electroweak measurements from ATLAS data and Electroweak precision observables from LEP and SLC

9.1 Introduction

This chapter describes a global Standard Model Effective Field Theory (SMEFT) interpretation, including measurements from Higgs, electroweak processes, and electroweak precision observables (EWPOs). Combining different processes allows probing consistent deviations in the relevant SMEFT parameters across multiple measurements. SMEFT serves as a universal language that allows looking for deviations in measurements from different experiments and energy scales.

In this chapter, the SMEFT interpretation is performed based on a combination of Higgs measurements within the Simplified Template Cross-Section (STXS) framework, unfolded distributions from the electroweak sector, and EWPOs measured at the Z-pole using LEP and SLC [251]. The measurements with the ATLAS data probe the SMEFT in the high-energy frontier and the LEP observables serve as the precision constraints. The measurements are collectively sensitive to SMEFT operators that affect Higgs boson couplings, weak boson self-couplings, couplings of weak bosons to fermions, and four-fermion couplings.

9.2 Data and input measurements

The ATLAS Higgs boson measurements that are input to the combination are described in Chapter 7 but do not include the rare Higgs boson decay channels. In the following section, the electroweak data from ATLAS and EWPO from LEP and

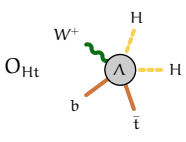

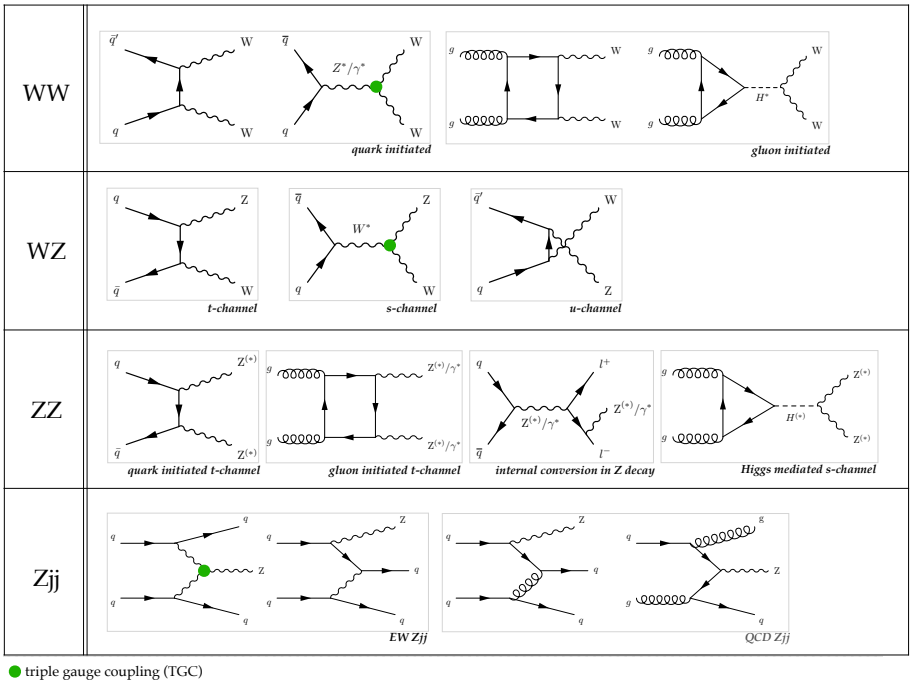

Figure 9.1: The main contributing diagrams for the electroweak production processes. The further decay of unstable particles is not depicted in the diagrams. The Feynman diagrams are adapted from [231, 252–254].

SLD is presented to provide a complete overview of all the input measurements to the combination.

9.2.1 ATLAS measurements for the electroweak processes

Measurements of one-dimensional differential cross-sections of weak boson production and decay are used to constrain the electroweak sector. The measurements are summarized in Table 9.1. The main contributing Feynman diagrams for the electroweak processes are shown in Figure 9.1.

These electroweak measurements include measurement of WW production in the $e^{\pm}\nu\mu^{\mp}\nu$ final state [231], WZ production in the $\ell^{\pm}\nu\ell^{+}\ell^{-}$ final state [255] (where $\ell = e, \mu$), four lepton production [253] (4ℓ, with $4\ell = [\mu^{+}\mu^{-}\mu^{+}\mu^{-}, \mu^{+}\mu^{-}e^{+}e^{-}$, $e^{+}e^{-}e^{+}e^{-}]$, which targets not only ZZ production but also the production of lepton-pairs via virtual photons), and Z boson production in VBF topologies with subsequent Z decays into electron or muon pairs [254]. The corresponding unfolded fiducial cross-section measurements are directly compared to particle-level

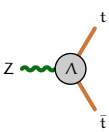

O_{Ht}

Process	Important phase space requirements	Observable	$\mathcal{L}$ [fb^{-1}]	Ref.
$pp \to e^{\pm}\nu_e\mu^{\mp}\nu_\mu$	$m_{\ell\ell} > 55\,\text{GeV}$, $p_T^{\text{jet}} < 35\,\text{GeV}$	$p_T^{\text{lead. lep.}}$	36	[231]
$pp \to \ell^{\pm}\nu\ell^+\ell^-$	$m_{\ell\ell} \in (81, 101)\,\text{GeV}$	m_T^{WZ}	36	[255]
$pp \to \ell^+\ell^-\ell^+\ell^-$	$m_{4\ell} > 180\,\text{GeV}$	m_{Z2}	139	[253]
$pp \to \ell^+\ell^-jj$	$m_{jj} > 1000\,\text{GeV}$, $m_{\ell\ell} \in (81, 101)\,\text{GeV}$	$\Delta\phi_{jj}$	139	[254]

Table 9.1: The LHC electroweak processes entering the combined interpretation, together with the most important phase space requirements in each measurement, the observables used in the reinterpretation, and the integrated luminosity analyzed in the measurement. The signed angle $\Delta\phi_{jj}$ is defined as $\phi_f - \phi_b$, where the two highest transverse-momentum jets f and b are ordered such that $y_f > y_b$.

differential cross-section predictions. The particle-level cross-section prediction in each bin is parametrized as a function of Wilson coefficients.

For each of the four electroweak processes, a differential cross-section measurement as a function of one of the measured observables is chosen as an input. The leading lepton p_T ($p_T^{\text{lead. lep.}}$) and the transverse mass distribution (m_T^{WZ}) are used for the WW and WZ measurements, respectively. The transverse mass is defined as

$$m_T^{WZ} = \sqrt{\left(\sum_{\ell=1}^{3} p_T^{\ell} + E_T^{\text{miss}}\right)^2 - \left[\left(\sum_{\ell=1}^{3} p_x^{\ell} + E_x^{\text{miss}}\right)^2 + \left(\sum_{\ell=1}^{3} p_y^{\ell} + E_y^{\text{miss}}\right)^2\right]}. \tag{9.1}$$

In the $pp \to 4l$ analysis, the invariant mass of the secondary Z boson candidate, (m_{Z_2}), is used. It is the candidate lepton pair with a less compatible mass with the Z boson mass. This observable allows distinguishing between processes involving two or only one on-shell Z boson.

In the analysis of Z boson production in association with two jets, the signed azimuthal angle between the two jets ($\Delta\phi_{jj}$) is used. The $\Delta\phi_{jj}$ variable is defined as $\Delta\phi_{jj} = \phi_f - \phi_b$, where the two highest transverse-momentum jets f and b are ordered such that $y_f > y_b$.

The unfolded data and the comparison to the Standard Model prediction are shown in Figure 9.2.

9.2.2 Electroweak precision observables

Electroweak precision observables (EWPOs) are measurements performed at LEP and SLC at the Z boson peak. The accelerators were designed to operate as Z fac-

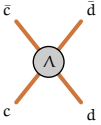

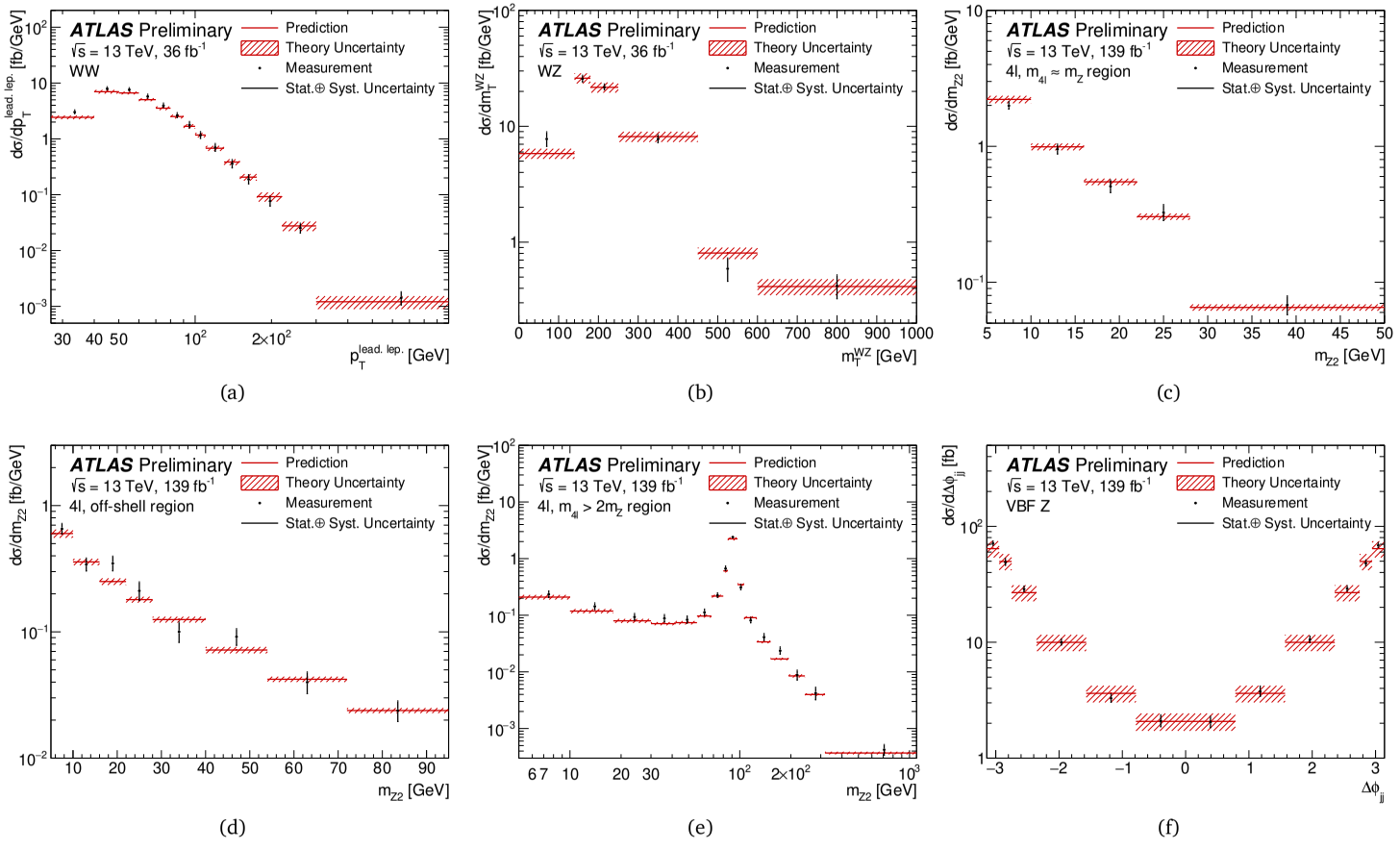

Figure 9.2: Measured differential cross-sections of the electroweak production process, shown in black, compared to the Standard Model in red. From top left to bottom right: the leading lepton transverse momentum in WW production, the WZ transverse mass in WZ production, the invariant mass of the sub-leading lepton pair (pair with invariant mass less compatible with the Z boson mass) in three regions of m_{4l} targeting: Z→4l, off-shell ZZ production, on-shell ZZ pair production, and the signed azimuthal angle between the two jets in Z+jets production. The figures are taken from [256].

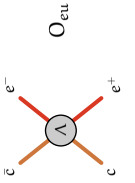

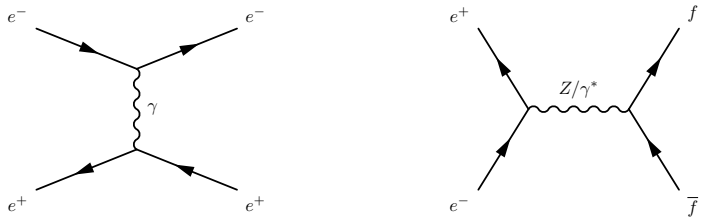

Figure 9.3: The lowest-order Feynman diagrams relevant for LEP-I. The t-channel diagram shown on the left is possible for the e^+e^- final states through the Bhabha scattering process [257] for $e^+e^- \to e^+e^-$. The s-channel diagram of fermion-anti-fermion pairs is shown on the right.

tories by colliding electron and positron beams at center-of-mass energies around the mass of 91 GeV.

The process investigated is the production of fermion anti-fermion pair through the collision of electron and positron ($e^+e^- \to f\bar{f}$), which at the lowest-order proceed through a photon exchange or a Z boson exchange as depicted in Figure 9.3. The Z boson couples to fermions with a mixture of vector and axial couplings. The consequences of this mixture are measurable asymmetries in the angular distributions of the final-state fermions, the dependence of Z production on the helicities of the initial-state electron-positron pair, and the production of polarized decay products of Z bosons.

Asymmetries will manifest themselves through different production rates in the forward and backward hemispheres, defined relative to the orientation of the electron beam, and are quantifiable as

$$A_{FB}^{i} = \frac{N_F^i - N_B^i}{N_F^i + N_B^i}, \tag{9.2}$$

where the index i labels the final-state fermion type, and N_F^i and N_B^i are the number of events in the forward and backward hemispheres, respectively. Here, forward events correspond to the case where the fermion (anti-fermion) is in the direction of the electron beam (positron beam).

Large Electron-Positron Collider

The LEP collider operated from 1989 to 1995 in the LEP-I phase, with electron-positron center-of-mass collision energies around the Z boson resonance mass. During LEP-I, the LEP accelerator operated at seven center-of-mass energy points that are within ± 3 GeV of the Z pole. The four experiments ALEPH [258, 259],

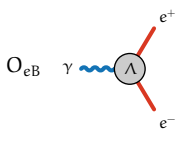

DELPHI [260, 261], L3 [262–265], and OPAL [266–269] collected a dataset containing approximately 17 million Z bosons.

Stanford Linear Collider

The SLC started operation in 1989, and from 1992 the SLD experiment [270–275] accumulated a dataset containing approximately 600 000 Z bosons. Despite the smaller dataset than the LEP experiments, the longitudinal beam polarization at the SLC allowed for complementary and competitive measurements of the Z coupling. Furthermore, the small luminous volume of the interaction point allowed for the reconstruction of heavy flavor hadrons, which improved the selection of events containing b- and c-quarks [251] compared to LEP.

9.2.2.1 Observables chosen for SMEFT interpretation

An experimentally-motivated set of pole parameters is chosen as the measurements from LEP-I to be included in the combination. This reduced set includes cross-sections, partial widths, and total width and corresponds to a highly correlated parameter set. The individual observables are

- the mass of the Z boson - m_Z
- the total width of the Z boson - Γ_Z
- the hadronic cross-section from Z production, σ^0_{had}, defined as

$$\sigma^0_{had} = \frac{12\pi}{m_Z^2}\frac{\Gamma_{ee}\Gamma_{had}}{\Gamma_Z^2}, \tag{9.3}$$

  where Γ_{ee} and Γ_{had} are the partial widths for the decays of the Z boson into electrons and hadrons, respectively.
- the forward-backward asymmetries for leptons, b- and c-quarks ($A^{0,\ell}_{FB}$, $A^{0,b}_{FB}$, $A^{0,c}_{FB}$) as defined in Equation 9.2.
- the ratio of partial decay widths to leptons, b- and c-quarks defined as

$$R^0_i = \frac{\Gamma_{had}}{\Gamma_{ii}}, \tag{9.4}$$

  where Γ_{ii} is the partial width for the Z boson decay into a pair of charged leptons of a given type $i\bar{i}$.

The LEP asymmetries are extracted from a fit to differential cross-section distributions for increased statistical precision. The asymmetry $A^{0,\ell}_{FB}$ is measured in leptonic final states and is corrected for radiative effects, γ exchange, and $\gamma - Z$ inter-

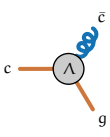

O_{uG}

ference to yield the pole observables. Note that the pole observables are not just the underlying observables but are quantities that involve additional theoretical corrections and are known as *pseudo-observables* and are denoted with the label ^{0}.

The heavy-flavor observables R_b^0, R_c^0, $A_{FB}^{0,b}$, and $A_{FB}^{0,c}$ are determined from a fit involving 14 free parameters to data collected by the four LEP experiments and SLD and are described in [251]. The ratios R_b^0 and R_c^0 are defined as

$$R_q^0 = \frac{\Gamma_{q\,q}}{\Gamma_{had}}, \tag{9.5}$$

where $q = b, c$, while $A_{FB}^{0,b}$ and $A_{FB}^{0,c}$ are defined analogous to $A_{FB}^{0,\ell}$.

Table 9.4 summarizes the measurement results for the eight Z-pole observables included in the combined SMEFT interpretation, together with theoretical SM predictions obtained using the $\{m_W, m_Z, G_F\}$ input parameter scheme (see Section 9.3.3). The precision observables agree very well with the SM expectation, except for $A_{FB}^{0,b}$ and $A_{FB}^{0,c}$, for which deviations of more than three and more than one standard deviation are found, respectively.

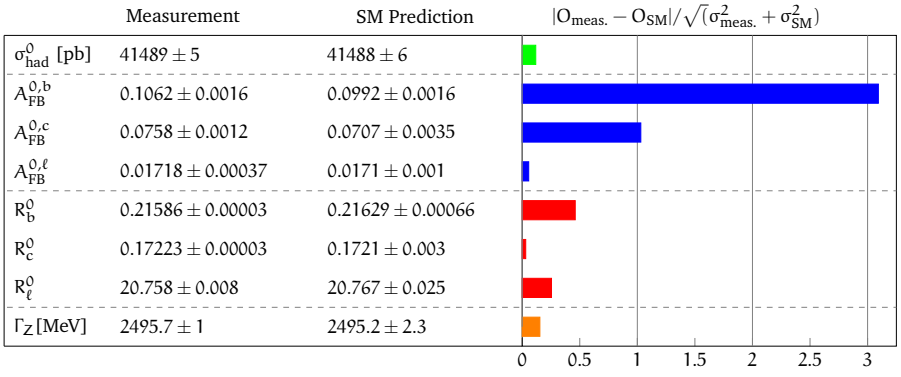

Figure 9.4: Electroweak precision observables included in the analysis. The second column corresponds to the experimental value, the third to the theoretical prediction in the $\{m_W, m_Z, G_F\}$ input parameter scheme, and the fourth is the ratio of the two values.

The combined interpretation of these observables helps to disentangle the impact of SMEFT operators that affect up-type and down-type quarks, the first two quark generations from the third, and couplings to left-handed from couplings to right-handed fermions.

Due to the high measurement precision of lepton collider experiments, the constraints obtained are typically more precise than those of LHC measurements. However, only a limited number of directions in parameter space can be measured.

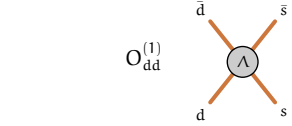

The inclusion of these observables in the global fit simplifies the interpretation of LHC measurements, which are sensitive to a more significant number of operators: the tight EWPO constraints provided on operators affecting weak-boson-fermion couplings allow their impact to be disentangled from the impact of operators affecting only Higgs boson or weak boson self-couplings, which cannot be constrained with Z-pole data.

9.2.3 Overlaps between input datasets

Overlaps in the experimentally reconstructed regions between Higgs boson measurements are studied in [276] and are found to be negligible. Overlaps are also negligible between the four electroweak measurements due to different requirements on the number and flavor of charged leptons in the final state of each measurement.

However, there is some overlap in analyzed events between the datasets for the Higgs boson and electroweak measurements. The inclusive 4ℓ [253] and $H \to 4\ell$ [196] analyses both consider the same four-lepton topologies. The inclusive 4ℓ analysis is performed in various phase-space regions for the four-lepton invariant mass of $m_{4\ell} > 20\,\text{GeV}$, while the signal region of the $H \to 4\ell$, together with the corresponding sideband region used to constrain the continuum 4ℓ background, comprise events with $105\,\text{GeV} < m_{4\ell} < 160\,\text{GeV}$.

An optimal analysis of the Higgs boson mass regions is more important than the relatively weak constraints in SMEFT provided by the low-mass region of the inclusive 4ℓ measurement. Thus, this combined analysis includes the complete $H \to 4\ell$ measurement but excludes analysis regions of the inclusive 4ℓ analysis that targets $m_{4\ell} < 180\,\text{GeV}$.

The overlap of the WW [231] measurement and $H \to WW^*$ [277] analysis in handled as described earlier in Section 8.2.

9.3 Theoretical predictions

The quarks from the first two generations and leptons from all three generations are assumed to be massless, and the four-flavor scheme is used for parton distribution functions. Additionally, the `topU3l` flavor symmetry introduced in Section 2.3.3 is assumed, which imposes a flavor symmetry on the first two quark generations and all three lepton generations.

Only CP-even operators are considered, and Wilson coefficients are assumed to be real-valued. This choice only results in a small loss of information as only the $\Delta\phi_{jj}$ observable studied in the VBF Z measurement [254] is sensitive to CP-odd effects.

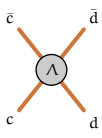

$O_{qd}^{(1)}$

The list of operators and the corresponding Wilson coefficient affecting the processes studied in this note are given in Tables 9.2 and 9.3. The operators are grouped in purely bosonic operators, various operator groups containing both fermion fields and differing numbers of Higgs boson and gauge boson fields, four-lepton operators, four-fermion operators containing both quark and lepton fields, four-fermion operators with only light quarks, and four-fermion operators with both light and heavy quarks.

9.3.1 Simulation of Standard Model processes

This section discusses the simulation of the Standard Model process for the electroweak measurements. The simulation of the Higgs boson processes is described in Section 2.5.

Electroweak processes

The $q\bar{q} \to e^{\pm}\nu\mu^{\mp}\nu$, $q\bar{q} \to \ell^{\pm}\nu\ell^{+}\ell^{-}$, and $q\bar{q} \to \ell^{+}\ell^{-}\ell^{+}\ell^{-}$ production modes in the SM are modeled using the SHERPA2.2.2 [232] generator at the next-to-leading order (NLO) accuracy in the strong coupling for up to one additional parton, and LO accuracy for up to three additional parton emissions. The NNPDF3.0NNLO set of parton distribution functions (PDF) is used [122], along with a set of tuned Parton-shower parameters developed by the SHERPA authors. The calculations are matched and merged with the SHERPA parton shower based on Catani–Seymour dipole factorisation [240, 241], using the MEPS@NLO prescription [242–245]. The OPENLOOPS provided virtual QCD corrections library [236, 239].

NLO electroweak corrections for the above processes [278–281] are applied as a function of $m_{4\ell}$ for $q\bar{q} \to \ell^{+}\ell^{-}\ell^{+}\ell^{-}$ and as a function of the measured observable for $q\bar{q} \to e^{\pm}\nu\mu^{\mp}\nu$ and $q\bar{q} \to \ell^{\pm}\nu\ell^{+}\ell^{-}$.

The gluon-initiated 4ℓ, and $e^{\pm}\nu\mu^{\mp}\nu$ production processes are simulated using SHERPA2.2.2 at LO precision for up to one additional parton emission, with the parton-shower modeling being the same as for the quark-initiated samples. NLO QCD calculations [246, 282, 283] are used to correct the $gg \to \ell^{+}\ell^{-}\ell^{+}\ell^{-}$ cross-section differentially and the $gg \to e^{\pm}\nu\mu^{\mp}\nu$ cross-section with a constant factor. For $gg \to \ell^{+}\ell^{-}\ell^{+}\ell^{-}$, an additional correction factor of 1.2 is taken from the ratio of an NNLO QCD calculation [284, 285] with the NLO prediction.

Electroweak Zjj production is modeled with HERWIG7.1.5 [286, 287] and VBFNLO3.0.0 [288] at NLO QCD. The MMHT2014LO PDF set [289] is used along with the default set of tuned parameters for parton showering, hadronization, and underlying event production. EvtGen is used for the simulation of bottom and charm hadron decays. Strong Zjj production is modeled using the MAD-

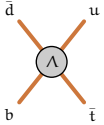

Wilson coefficient and operator		Affected process group		
		LEP/SLD EWPO	ATLAS Higgs	ATLAS EW
$c_{H\Box}$	$(H^\dagger H)\Box(H^\dagger H)$		✓	
c_G	$f^{abc}G^{a\nu}_\mu G^{b\rho}_\nu G^{c\mu}_\rho$		✓	✓
c_W	$\epsilon^{IJK}W^{I\nu}_\mu W^{J\rho}_\nu W^{K\mu}_\rho$		✓	✓
c_{HD}	$\left(H^\dagger D_\mu H\right)^* \left(H^\dagger D_\mu H\right)$		✓	✓
c_{HG}	$H^\dagger H\, G^A_{\mu\nu} G^{A\mu\nu}$		✓	
c_{HB}	$H^\dagger H\, B_{\mu\nu} B^{\mu\nu}$		✓	
c_{HW}	$H^\dagger H\, W^I_{\mu\nu} W^{I\mu\nu}$		✓	
c_{HWB}	$H^\dagger \tau^I H\, W^I_{\mu\nu} B^{\mu\nu}$	✓	✓	✓
c_{eH}	$(H^\dagger H)(\bar{l}_p e_r H)$		✓	
c_{uH}	$(H^\dagger H)(\bar{q} Y^\dagger_u u \widetilde{H})$		✓	
c_{tH}	$(H^\dagger H)(\bar{Q}\widetilde{H} t)$		✓	
c_{bH}	$(H^\dagger H)(\bar{Q} H b)$		✓	
$c^{(1)}_{Hl,11}$	$(H^\dagger i\overleftrightarrow{D}_\mu H)(\bar{l}\gamma^\mu l)$	✓	✓	✓
$c^{(1)}_{Hl,33}$	$(H^\dagger i\overleftrightarrow{D}^I_\mu H)(\bar{l}\tau^I\gamma^\mu l)$	✓	✓	✓
c_{He}	$(H^\dagger i\overleftrightarrow{D}_\mu H)(\bar{e}\gamma^\mu e)$	✓	✓	✓
$c^{(1)}_{Hq}$	$(H^\dagger i\overleftrightarrow{D}_\mu H)(\bar{q}\gamma^\mu q)$	✓	✓	✓
$c^{(3)}_{Hq}$	$(H^\dagger i\overleftrightarrow{D}^I_\mu H)(\bar{q}\tau^I\gamma^\mu q)$	✓	✓	✓
c_{Hu}	$(H^\dagger i\overleftrightarrow{D}_\mu H)(\bar{u}\gamma^\mu u)$	✓	✓	✓
c_{Hd}	$(H^\dagger i\overleftrightarrow{D}_\mu H)(\bar{d}\gamma^\mu d)$	✓	✓	✓
$c^{(1)}_{HQ}$	$(H^\dagger i\overleftrightarrow{D}_\mu H)(\bar{Q}\gamma^\mu Q)$	✓	✓	
$c^{(3)}_{HQ}$	$(H^\dagger i\overleftrightarrow{D}^I_\mu H)(\bar{Q}\tau^I\gamma^\mu Q)$	✓	✓	
c_{Hb}	$(H^\dagger i\overleftrightarrow{D}_\mu H)(\bar{b}\gamma^\mu b)$	✓		
c_{Ht}	$(H^\dagger i\overleftrightarrow{D}_\mu H)(\bar{t}\gamma^\mu t)$	✓	✓	
c_{tG}	$(\bar{Q}\sigma^{\mu\nu}T^A t)\widetilde{H}\, G^A_{\mu\nu}$		✓	
c_{tW}	$(\bar{Q}\sigma^{\mu\nu}t)\tau^I\widetilde{H}\, W^I_{\mu\nu}$		✓	
c_{tB}	$(\bar{Q}\sigma^{\mu\nu}t)\widetilde{H}\, B_{\mu\nu}$		✓	
$c^{(1)}_{ll}$	$(\bar{l}\gamma_\mu l)(\bar{l}\gamma^\mu l)$	✓		✓

Table 9.2: Relevant dimension-6 operators grouped in purely bosonic operators, various operator groups containing both fermion fields and differing numbers of Higgs boson and gauge boson fields, and four-lepton operators.

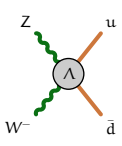

O_{uW}

Wilson coefficient and operator		Affected process group		
		LEP/SLD EWPO	ATLAS Higgs	ATLAS EW
$c_{lq}^{(1)}$	$(\bar{l}\gamma_\mu l)(\bar{q}\gamma^\mu q)$			✓
$c_{lq}^{(3)}$	$(\bar{l}\gamma_\mu \tau^I l)(\bar{q}\gamma^\mu \tau^I q)$			✓
c_{eu}	$(\bar{e}\gamma_\mu e)(\bar{u}\gamma^\mu u)$			✓
c_{ed}	$(\bar{e}\gamma_\mu e)(\bar{d}\gamma^\mu d)$			✓
c_{lu}	$(\bar{l}\gamma_\mu l)(\bar{u}\gamma^\mu u)$			✓
c_{ld}	$(\bar{l}\gamma_\mu l)(\bar{d}\gamma^\mu d)$			✓
c_{qe}	$(\bar{q}\gamma_\mu q)(\bar{e}\gamma^\mu e)$			✓
$c_{qq}^{(1,1)}$	$(\bar{q}\gamma_\mu q)(\bar{q}\gamma^\mu q)$			✓
$c_{qq}^{(1,8)}$	$(\bar{q}T^a\gamma_\mu q)(\bar{q}T^a\gamma^\mu q)$			✓
$c_{qq}^{(3,1)}$	$(\bar{q}\sigma^i\gamma_\mu q)(\bar{q}\sigma^i\gamma^\mu q)$			✓
$c_{qq}^{(3,8)}$	$(\bar{q}\sigma^i T^a\gamma_\mu q)(\bar{q}\sigma^i T^a\gamma^\mu q)$			✓
$c_{uu}^{(1)}$	$(\bar{u}\gamma_\mu u)(\bar{u}\gamma^\mu u)$			✓
$c_{uu}^{(8)}$	$(\bar{u}T^a\gamma_\mu u)(\bar{u}T^a\gamma^\mu u)$			✓
$c_{dd}^{(1)}$	$(\bar{d}\gamma_\mu d)(\bar{d}\gamma^\mu d)$			✓
$c_{dd}^{(8)}$	$(\bar{d}T^a\gamma_\mu d)(\bar{d}T^a\gamma^\mu d)$			✓
$c_{ud}^{(1)}$	$(\bar{u}\gamma_\mu u)(\bar{d}\gamma^\mu d)$			✓
$c_{ud}^{(8)}$	$(\bar{u}T^a\gamma_\mu u)(\bar{d}T^a\gamma^\mu d)$			✓
$c_{qu}^{(1)}$	$(\bar{q}\gamma_\mu q)(\bar{u}\gamma^\mu u)$			✓
$c_{qu}^{(8)}$	$(\bar{q}T^a\gamma_\mu q)(\bar{u}T^a\gamma^\mu u)$			✓
$c_{qd}^{(1)}$	$(\bar{q}\gamma_\mu q)(\bar{d}\gamma^\mu d)$			✓
$c_{qd}^{(8)}$	$(\bar{q}T^a\gamma_\mu q)(\bar{d}T^a\gamma^\mu d)$			✓
$c_{Qq}^{(1,1)}$	$(\bar{Q}\gamma_\mu Q)(\bar{q}\gamma^\mu q)$		✓	
$c_{Qq}^{(1,8)}$	$(\bar{Q}T^a\gamma_\mu Q)(\bar{q}T^a\gamma^\mu q)$		✓	
$c_{Qq}^{(3,1)}$	$(\bar{Q}\sigma^i\gamma_\mu Q)(\bar{q}\sigma^i\gamma^\mu q)$		✓	
$c_{Qq}^{(3,8)}$	$(\bar{Q}\sigma^i T^a\gamma_\mu Q)(\bar{q}\sigma^i T^a\gamma^\mu q)$		✓	
$c_{tu}^{(1)}$	$(\bar{t}\gamma_\mu t)(\bar{u}\gamma^\mu u)$		✓	
$c_{Qu}^{(1)}$	$(\bar{Q}\gamma_\mu Q)(\bar{u}\gamma^\mu u)$		✓	
$c_{Qu}^{(8)}$	$(\bar{Q}T^a\gamma_\mu Q)(\bar{u}T^a\gamma^\mu u)$		✓	
$c_{Qd}^{(1)}$	$(\bar{Q}\gamma_\mu Q)(\bar{d}\gamma^\mu d)$		✓	
$c_{Qd}^{(8)}$	$(\bar{Q}T^a\gamma_\mu Q)(\bar{d}T^a\gamma^\mu d)$		✓	
$c_{tq}^{(1)}$	$(\bar{q}\gamma_\mu q)(\bar{t}\gamma^\mu t)$		✓	
$c_{tq}^{(8)}$	$(\bar{q}T^a\gamma_\mu q)(\bar{t}T^a\gamma^\mu t)$		✓	

Table 9.3: Relevant dimension-6 four-fermion operators.

$O_{qtQd}^{(1)}$

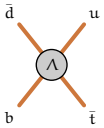

GRAPH5_AMC@NLO [290] event generator and the NNPDF2.3NLO PDF set [291]. The prediction is accurate to NLO in the strong coupling for up to two partons in the final state. Events are interfaced to PYTHIA8.186 for parton showering, hadronization, and underlying-event activity, using the A14 set of tuned parameters [247]. Overlaps between the matrix element and the parton shower are removed using the FxFx prescription [292]. The sample is normalized to a NNLO prediction for inclusive Z-boson production [293].

Additional processes introduce minor contributions to the fiducial phase space of the 4ℓ measurement. These are modeled as described in [253].

9.3.2 Simulation of dimension-six operators effects for LHC processes

Dedicated samples representing SM, linear, and quadratic effects of dimension-six operators, as well as dimension-six cross terms, are generated at leading order using MADGRAPH5_AMC@NLO 2.8.1 [178] (electroweak processes) or MADGRAPH5_AMC@NLO 2.9.3 (Higgs boson production and decay) and the SMEFTsim 3.0 model [175, 176]. Events are interfaced to PYTHIA 8.244 [179] (electroweak processes) or PYTHIA 8.305 (Higgs boson production and decay) to simulate parton shower and hadronization. The decays of bottom and charm hadrons are performed by EVTGEN [294].

For the loop-induced processes $gg \to H$, $gg \to ZH$, and $H \to gg$ calculations are performed with SMEFTatNLO [177], which allows for the calculation of NLO QCD corrections, which is not possible with SMEFTSim. An analytic calculation [208] at NLO accuracy in QED is used to parametrize the $H \to \gamma\gamma$ decay. In both cases, the parametrization is translated to the symmetry assumption introduced in Section 2.3.3.

The effects of dimension-six operators can change the mass and width of intermediate particles, which constitutes an essential correction in cases where intermediate particles are on-shell. These effects are accounted for in the linearized SMEFT expansion where propagator corrections are calculated with SMEFTsim 3.0 using dummy fields, following the methodology described in [176, 295]. Quadratic corrections are expected to be small and are neglected.

Higher-order QCD and electroweak corrections are included, assuming that their relative effect does not change in the presence of dimension-six operators. The differential cross-section predictions in the SMEFT, obtained with MADGRAPH5_AMC@NLO+PYTHIA at leading order (LO) or next-to-leading order (NLO), are scaled in each differential bin by the ratio of the best-known SM particle-level prediction to the LO or NLO SM prediction, respectively.

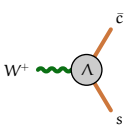

O_{uW}

It is also assumed that the relative effect of theory uncertainties derived for the SM processes remains valid in the presence of dimension-six operators. Details on the precision employed for the SM predictions are given in Section 9.3.1.

The effect of dimension-six operators on background processes is not considered, with two exceptions. For the interpretation of the VBF Z measurement, their effects are simulated for both the targeted electroweak Zjj boson production and for Z boson production with jets produced by the strong interaction, as both processes contribute equally to the signal region. The other exception is the WW production background in the 0-jet $H \to WW^*$ signal region. Here, consistent treatment of the process between the $H \to WW^*$ control region and the WW signal region is essential, as the normalization in both phase spaces is correlated.

Other background processes are either small compared to the signal processes or normalized to the data in kinematically similar control regions.

The linear effect of operators on the observables, including propagator corrections and acceptance corrections are summarized in Figures 9.5 to 9.9.

9.3.3 Predictions for electroweak precision observables

Both SM predictions and SMEFT parametrization of EWPO are derived in [296]. Up-to-date SM predictions are obtained using formulas from [297–300]. A fully flavor-symmetric SMEFT parametrization up to $O(v^2/\Lambda^2)$ is derived in the geoSMEFT [301, 302] formalism. For this work, the parametrization is translated from the $U(3)^5$ to the `topU3l` symmetry.

9.4 Statistical modelling

The same likelihood function described in Chapter 7 is used for the Higgs boson measurements. The WW statistical model described in Chapter 8 is expanded to define the combined electroweak likelihood.

The multivariate Gaussian model in Chapter 8 for the WW likelihood function is also used to interpret the EWPO. The model contains only the Wilson coefficients as parameters and does not contain any nuisance parameters. Both theoretical and experimental uncertainties are included in the covariance matrix of the measurement. The correlation matrix for the electroweak precision observables is taken from [251] and shown in Table 9.10.

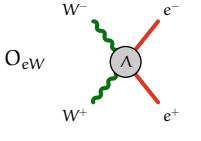

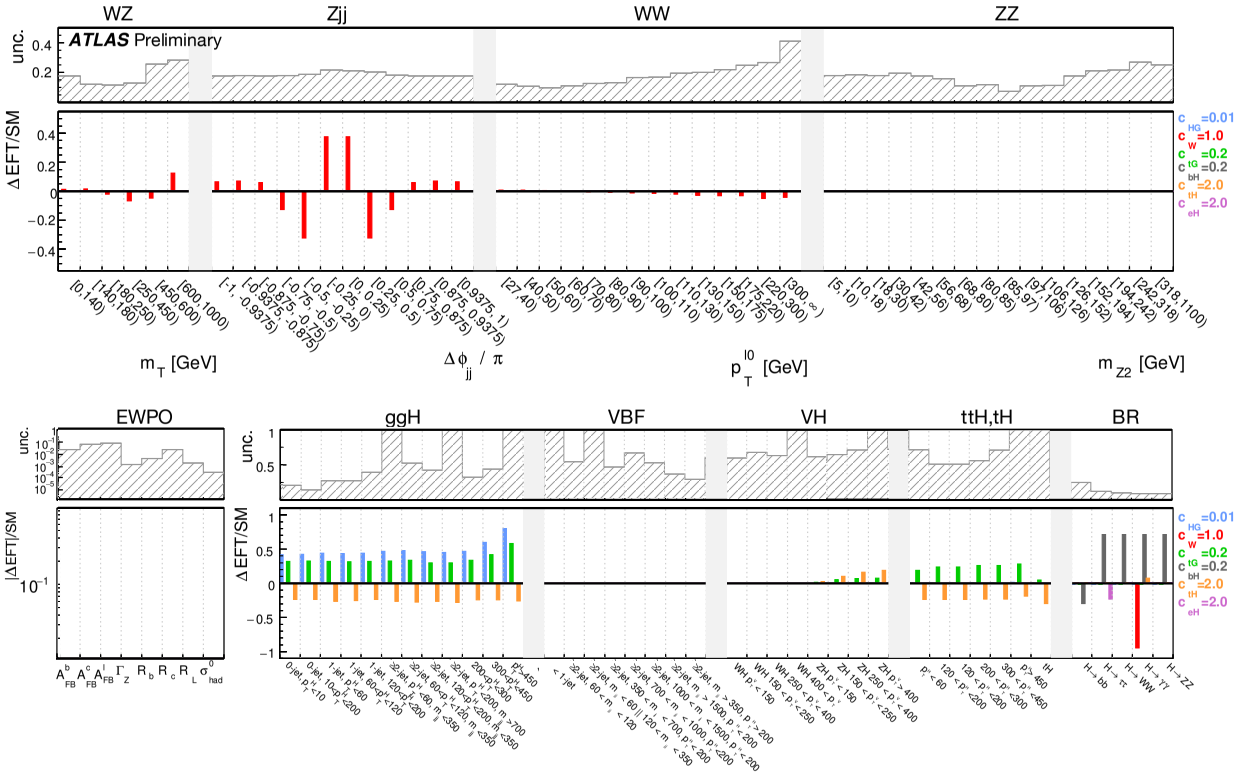

Figure 9.5: Relative impact of linear SMEFT terms with Wilson coefficients c_{HG}, c_W, c_{tG}, c_{bH}, c_{tH}, and c_{eH} on differential cross-sections of electroweak processes, the electroweak precision observables, and on the Higgs STXS cross-sections and branching ratios. The corresponding selected values of Wilson coefficients are shown on the right-hand side of the lower panel. The total relative uncertainty, including statistical, systematic, and theoretical components, on the measurement in the corresponding regions is shown for comparison in the top panel as a shaded area. It shows the sensitivity of each measurement to constrain the coefficients. For presentational clarity, the statistical uncertainty of low-precision STXS regions is clipped.

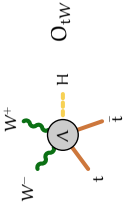

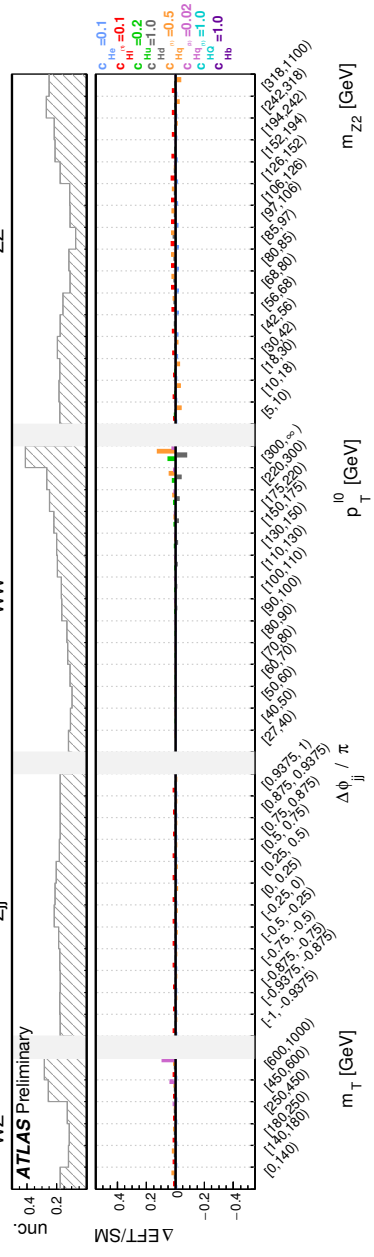

Figure 9.6: Relative impact of linear SMEFT terms with Wilson coefficients c_{He}, $c^{(1)}_{Hl,11}$, c_{Hu}, c_{Hd}, $c^{(1)}_{Hq}$, $c^{(3)}_{Hq}$, $c^{(1)}_{HQ}$, and c_{Hb} on differential cross-sections of electroweak processes, the electroweak precision observables, and on the Higgs STXS cross-sections and branching ratios. The corresponding selected values of Wilson coefficients are shown on the right-hand side of the lower panel. To quantify the sensitivity of each measurement to constrain the coefficients, the total relative uncertainty, including statistical, systematic, and theoretical components, on the measurement in the corresponding regions is shown for comparison in the top panel as a shaded area. For presentational clarity, the statistical uncertainty of low-precision STXS regions is clipped.

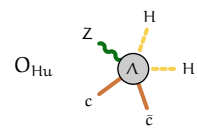

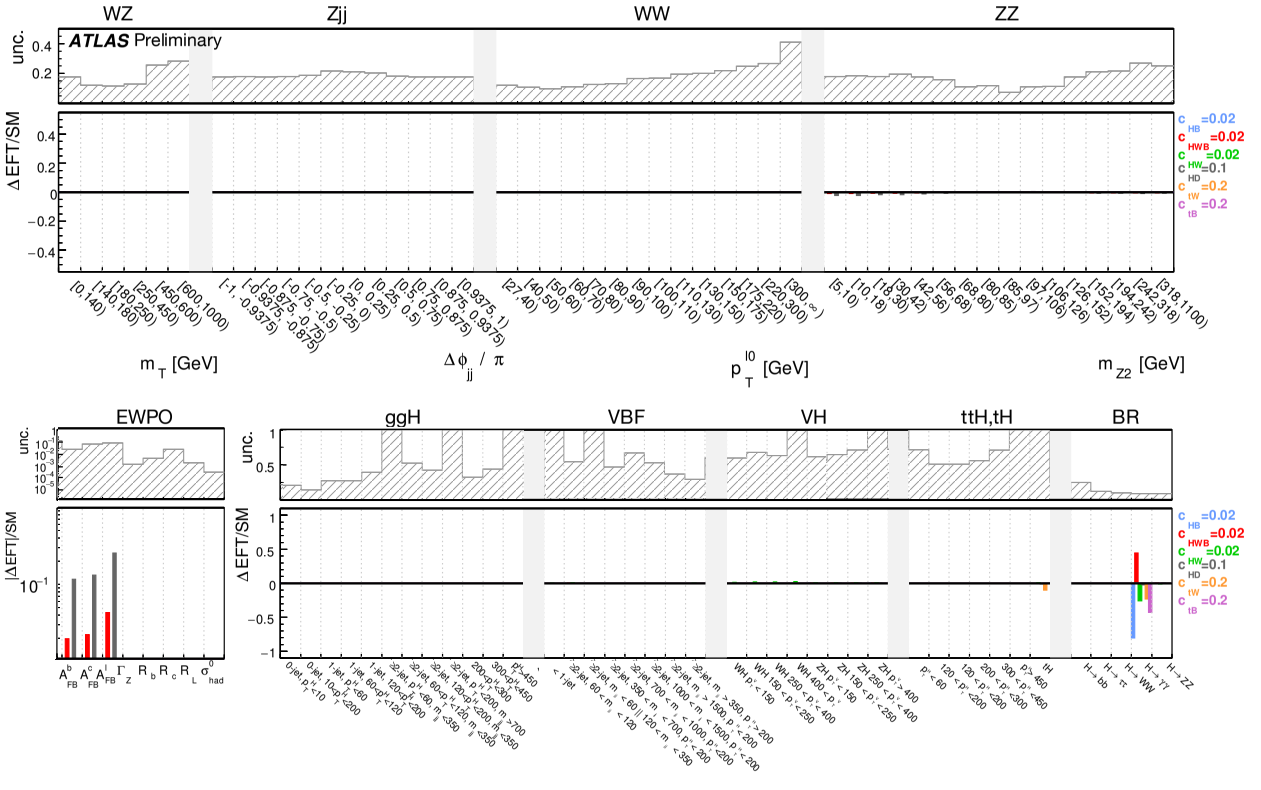

Figure 9.7: Relative impact of linear SMEFT terms with Wilson coefficients c_{HB}, c_{HWB}, c_{HW}, c_{HD}, c_{tW}, and c_{tB} on differential cross-sections of electroweak processes, the electroweak precision observables, and on the Higgs STXS cross-sections and branching ratios. The corresponding selected values of Wilson coefficients are shown on the right-hand side of the lower panel. To quantify the sensitivity of each measurement to constrain the coefficients, the total relative uncertainty, including statistical, systematic, and theoretical components, on the measurement in the corresponding regions is shown for comparison in the top panel as a shaded area. For presentational clarity, the statistical uncertainty of low-precision STXS regions is clipped.

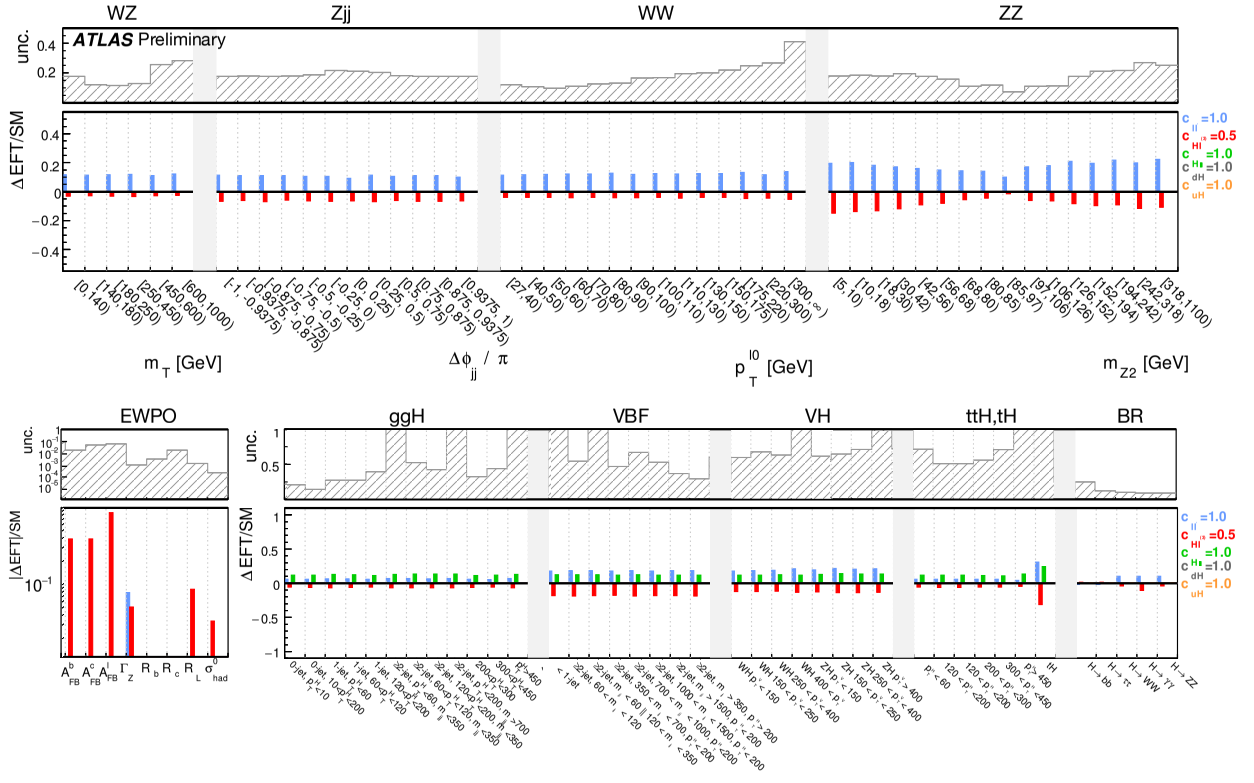

Figure 9.8: Relative impact of linear SMEFT terms with Wilson coefficients $c_{ll}^{(1)}$, $c_{Hl,33}^{(1)}$, $c_{H\Box}$, c_{dH}, and c_{uH} differential cross-sections of electroweak processes, the electroweak precision observables, and on the Higgs STXS cross-sections and branching ratios. The corresponding selected values of Wilson coefficients are shown on the right-hand side of the lower panel. To quantify the sensitivity of each measurement to constrain the coefficients, the total relative uncertainty, including statistical, systematic, and theoretical components, on the measurement in the corresponding regions is shown for comparison in the top panel as a shaded area. For presentational clarity, the statistical uncertainty of low-precision STXS regions is clipped.

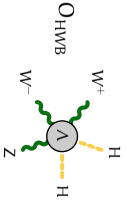

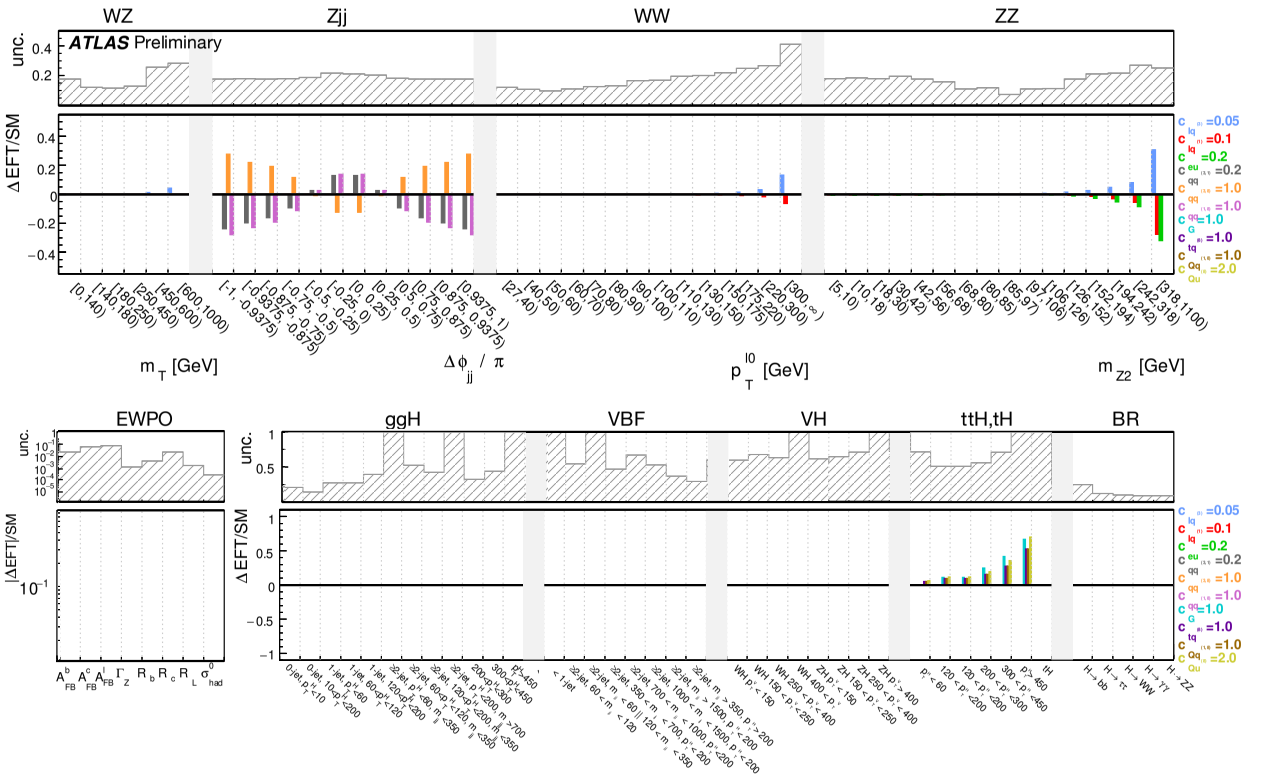

Figure 9.9: Relative impact of linear SMEFT terms with Wilson coefficients $c_{lq}^{(1)}$, $c_{lq}^{(3)}$, $c_{qq}^{(1,8)}$, $c_{qq}^{(3,8)}$, $c_{qq}^{(3,1)}$, $c_{qq}^{(1,1)}$, $c_{Qd}^{(1)}$, $c_{Qd}^{(8)}$, $c_{Qq}^{(1,1)}$, $c_{Qq}^{(1,8)}$, and $c_{Qq}^{(3,1)}$ differential cross-sections of electroweak processes, the electroweak precision observables, and on the Higgs STXS cross-sections and branching ratios. The corresponding selected values of Wilson coefficients are shown on the right-hand side of the lower panel. To quantify the sensitivity of each measurement to constrain the coefficients, the total relative uncertainty, including statistical, systematic, and theoretical components, on the measurement in the corresponding regions, is shown for comparison in the top panel as a shaded area. For presentational clarity, the statistical uncertainty of low-precision STXS regions is clipped.

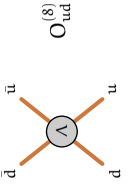

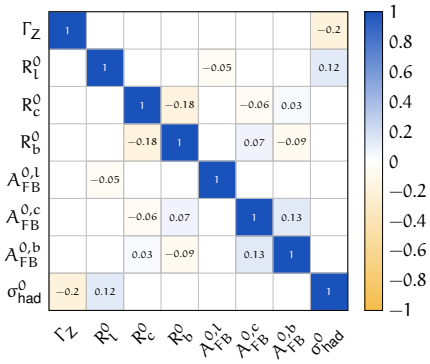

Figure 9.10: Correlation matrix for electroweak precision observables.

9.4.1 Combination of likelihoods

The likelihood for the combination of measurements is the product of measurement likelihoods with the modification that nuisance parameters that describe the same effect in different measurements are described by a common parameter. Only one constraint for each independent nuisance parameter is included in the product. The combined model is implemented in a RooFit workspace [192, 303].

Nuisance parameters that are correlated between Higgs boson and electroweak measurements are listed in Table 9.4. Following the methodology in [206], the luminosity uncertainty is split into three components: one that is correlated across all measurements, one that corresponds to an uncertainty on the integrated luminosity collected in 2015/2016, and one that corresponds to the uncertainty of the 2017/2018 luminosity.

The uncertainty of the pile-up modeling and the pile-up jet suppression efficiency is evaluated with a consistent methodology for all measurements and treated as correlated.

Only some components of the jet energy scale uncertainty can be correlated between the Higgs boson and electroweak measurements, as different versions of the jet energy calibration are used.

WW modeling uncertainties are treated as correlated between the *WW* and $H \to WW^*$ measurements, which allows for the constraint of the modeling uncertainty of the *WW* background to $H \to WW^*$ in combination with the *WW* measurement.

From the primary uncertainty sources affecting the electroweak measurements, only lepton and b-tagging uncertainties are not equated between electroweak and Higgs boson measurements, as different calibrations and schemes to report the uncertainties are used.

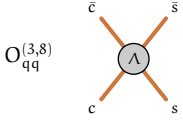

Source of correlated uncertainty	Parameters
Luminosity (common part 2015–2018)	1
Luminosity 2015/2016	1
Luminosity 2017/2018	1
Pile-up modelling	1
Pile-up jet suppression	1
Jet energy scale (pile-up modeling)	3
Jet energy scale η-inter-calibration	1
Jet energy resolution	12
WW modelling (WW and $H \to WW^*$)	2

Table 9.4: Sources of experimental uncertainties that are modeled as correlated between Higgs and electroweak measurements together with the corresponding number of nuisance parameters.

9.5 Results

This section presents fits of ATLAS data and later a combined fit of both the ATLAS data and electroweak precision data from LEP and SLC. The results are obtained using the statistical procedure described in Chapter 5. Finally, a simplified multivariate Gaussian model is introduced that allows for the reproduction of approximate results efficiently inside and outside of the ATLAS collaboration.

The fit to the ATLAS data is performed in both the linear and linear + quadratic scenario. The linear parametrization is carried out with the case where the total width is fully Taylor expanded as expressed in Equation 5.16. For the quadratic case, a fully Taylor expanded version of Equation 5.18 is considered.

9.5.1 Combined interpretation of ATLAS data

This section presents a combined SMEFT interpretation of ATLAS Higgs boson and electroweak measurements. The leading 24 eigenvectors of the principal component analysis are visualized in Figure 9.11. The eigenvectors are ordered by eigenvalues so that $c_{EV}^{[1]}$ represents the direction that can be measured with the highest sensitivity[1]. All eigenvectors with the corresponding expected uncertainty of $\sigma < 5$ are retained. Some Warsaw basis vectors are closely aligned with an eigenvector,

1 A notation that makes no distinction between the eigenvector and the corresponding coefficient is used.

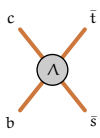

$O_{Quqb}^{(8)}$

for example, $c_{Hq}^{(3)}$ with $c_{EV}^{[3]}$, indicating that an individual measurement in the direction of the Warsaw basis vector is largely uncorrelated to the measurements of other parameters of interest. However, most eigenvectors receive significant contributions from many Warsaw basis vectors, for example, $c_{EV}^{[1]}$ and $c_{EV}^{[2]}$, which predominantly affect $gg \to H$ and $H \to \gamma\gamma$ and $c_{EV}^{[4]}$, which mainly consists of four-fermion operators that impact the tails of diboson production.

In order to obtain a fit basis that is easy to interpret but still numerically stable, the eigenvector analysis is performed using orthogonal subsets of Wilson coefficients. The groups are constructed such that the impact of each group is distinct from the impact of the other groups. At the same time, strong similarities in the impact on observables exist within a given group.

The parameters $c_{Hq}^{(3)}$, c_{bH}, c_W, and c_{eH} can be constrained individually. The three parameters affecting $gg \to H$ (c_{HG}, c_{tG}, and c_{tH}) can also be constrained individually, albeit with a reasonably strong correlation, as loop-induced ZH and $t\bar{t}H$ production offer additional constraining power. Furthermore, eight groups containing multiple operators are constructed.

The groups related to the parameters affecting the Higgs processes are defined with the same motivation described in Chapter 6.5. These includes the following groups of parameters $\{c_{He}, c_{Hl}^{(1)}\}$, $\{c_{Hl}^{(3)}, c_{ll}\}$, $\{c_{Hu}, c_{Hd}, c_{Hq}^{(1)}\}$, and $\{c_{HB}, c_{HW}, c_{HWB}, c_{HD}, c_{tW}, c_{tB}\}$. The other parameters defined here are grouped according to the following considerations:

- c_{uH}, c_{dH}, and $c_{H\Box}$ each have a substantial effect on the overall rate of Higgs boson processes, where $c_{H\Box}$ affects a scaling of the Higgs field and c_{uH} and c_{dH} affect the total width of the Higgs boson due to decays to light up- and down-type quarks, respectively.
- $c_{lq}^{(1)}$, $c_{lq}^{(3)}$, c_{eu}, c_{ed}, c_{lu}, c_{ld}, and c_{qe}, four-fermion operators with two quark and two lepton fields, which have a similar impact in the diboson observables as seen in Figure 9.9.
- $c_{qq}^{(1,1)}$, $c_{qq}^{(1,8)}$, $c_{qq}^{(3,1)}$, $c_{qq}^{(3,8)}$, $c_{uu}^{(1)}$, $c_{uu}^{(8)}$, $c_{dd}^{(1)}$, $c_{dd}^{(8)}$, $c_{ud}^{(1)}$, $c_{ud}^{(8)}$, $c_{qu}^{(1)}$, $c_{qu}^{(8)}$, $c_{qd}^{(1)}$, and $c_{qd}^{(8)}$, four-fermion operators with four light quarks, which are all only relevant for the VBF Z measurement and
- c_G, $c_{Qq}^{(1,1)}$, $c_{Qq}^{(1,8)}$, $c_{Qq}^{(3,1)}$, $c_{Qq}^{(3,8)}$, $c_{tu}^{(1)}$, $c_{Qu}^{(1)}$, $c_{Qu}^{(8)}$, $c_{Qd}^{(1)}$, $c_{Qd}^{(8)}$, $c_{tq}^{(1)}$, and $c_{tq}^{(8)}$, operators mainly affecting $t\bar{t}H$ production, i.e., c_G and the four-quark operators coupling to the top quark.

The resulting eigenvectors are visualized in Figure 9.12. Only eigenvectors with an expected uncertainty of $\sigma < 5$ are retained. The remaining eigenvectors are fixed to zero in the maximum likelihood fit. The removal of these weakly constrained directions allows for the measurement of the remaining coefficients simultaneously.

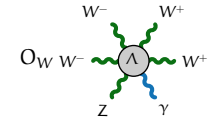

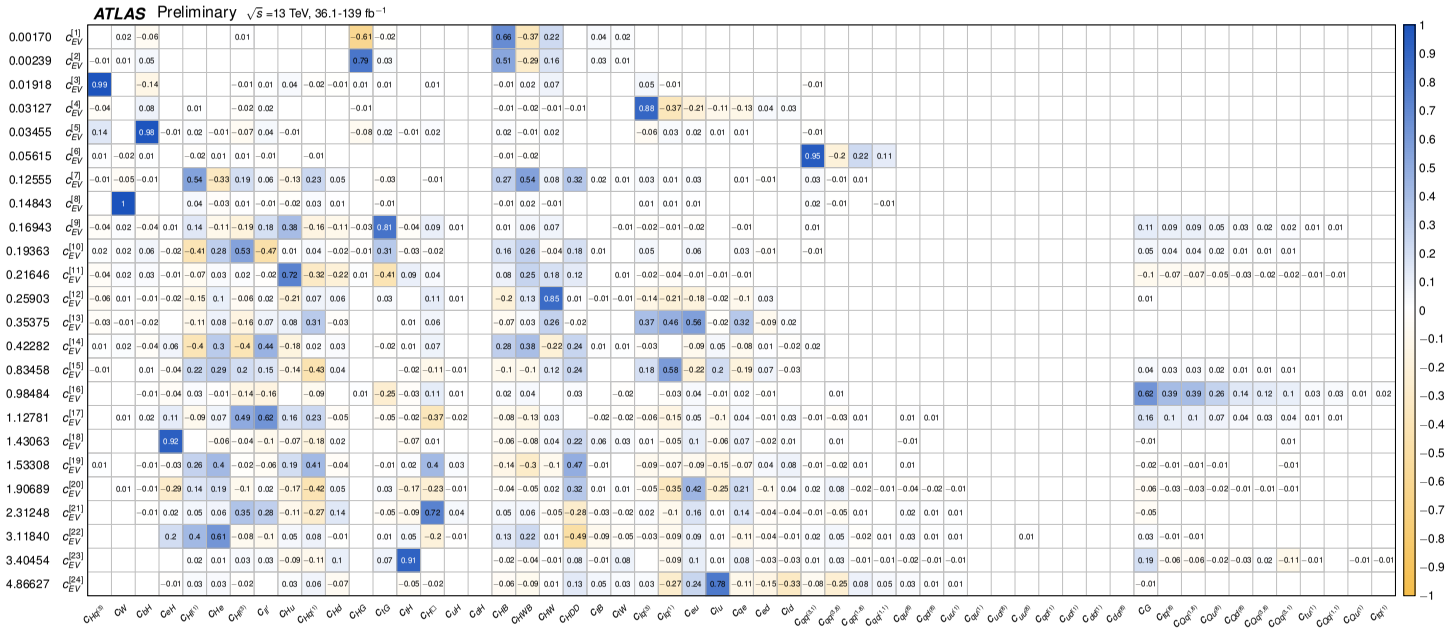

Figure 9.11: Graphical representation of the eigenvectors of the Hesse matrix of the ATLAS-only analysis. Each row corresponds to an eigenvector, and the matrix visualizes the contribution of each Warsaw basis vector to the eigenvector. The components of eigenvectors are rounded to the second decimal place, and their size is also indicated by color code. Empty columns correspond to Wilson coefficients that have little impact on the analyzed measurements and thus contribute to no eigenvector. Eigenvalues are denoted on the left of the plot.

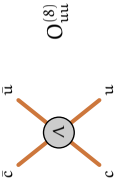

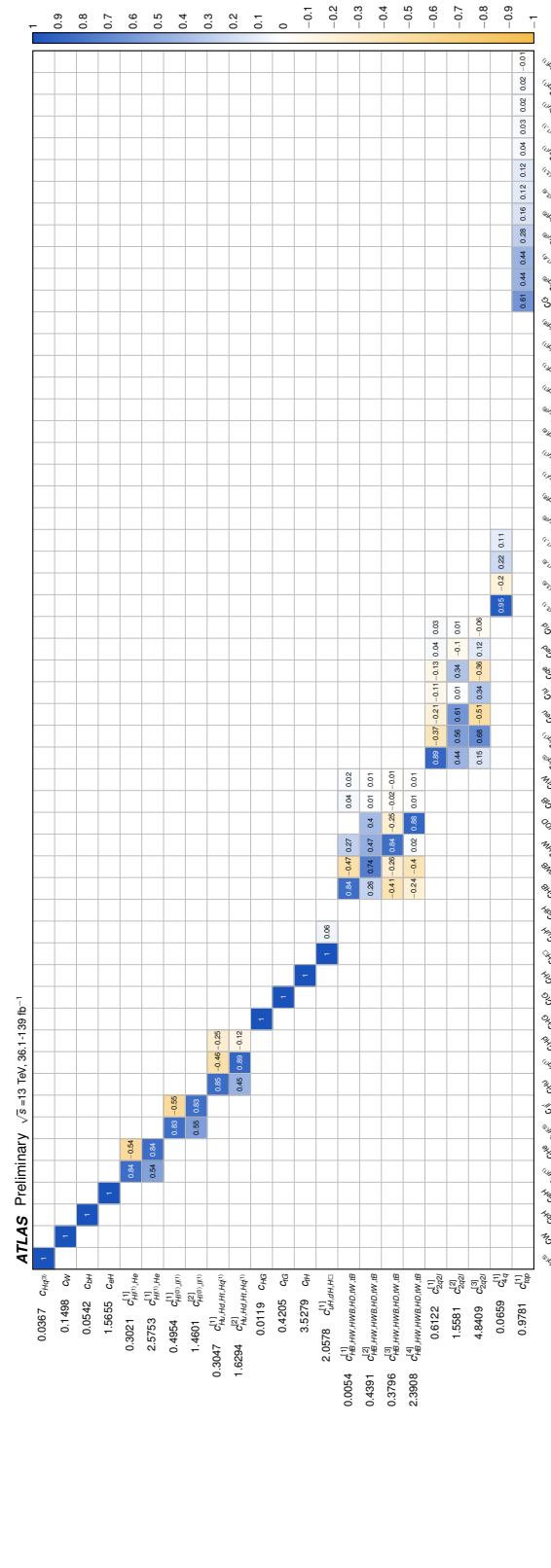

Figure 9.12: Fit basis for the ATLAS-only analysis. Each row corresponds to a fitted linear combination of Warsaw basis vectors. Entries are rounded to the second decimal place, and their size is also indicated by color code. Eigenvalues are denoted on the left of the plot.

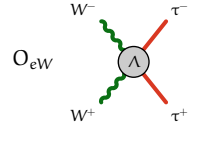

Eigenvector constraints are obtained from profile-likelihood fits, as described in Section 9.4.1. Results based on both the linear and the linear+quadratic models are presented in Figure 9.13. The contribution of Higgs or electroweak (EW) measurements from ATLAS to an eigenvector constraint is estimated using the procedure described in Chapter 6, which is shown on the right-hand side. The correlation of fitted coefficients is shown for the linear model in Figure 9.14.

The most stringent constraints are obtained for $c^{[1]}_{c_{HB},c_{HW},c_{HWB},c_{HD},c_{tW},c_{tB}}$, which modifies the rate of $H \to \gamma\gamma$ decays and c_{HG}, which modifies the $gg \to H$ production rate. These processes are loop-suppressed in the SM but can proceed at the tree level in the SMEFT. Stringent constraints are also obtained for c_{bH}, which impacts the $H \to b\bar{b}$ decay rate. At the same time, the triple-gauge-coupling operator c_W and the leading four-fermion operator eigenvectors are constrained by electroweak measurements (c_W also contributes to $H \to \gamma\gamma$, but this contribution cannot be disentangled from other contributions using Higgs boson measurements only). The tight constraint on $c^{(3)}_{Hq}$ is the result of both diboson and VH measurements, where the latter contribute more strongly, also owing to the larger dataset analyzed compared to the WW and WZ measurements. Constraints in the linear model agree, for all fit directions, with the SM-expectation, at the 95% confidence level.

Results in the quadratic model differ qualitatively from those in the linear model. Constraints on $c^{[1]}_{c_{HB},c_{HW},c_{HWB},c_{HD},c_{tW},c_{tB}}$ and $c^{[1]}_{2q2l}$ are weaker as the introduction of quadratic terms leads to non-linear correlations between parameters. On the other hand, the c_{HG} constraint becomes more stringent as the operators contributing to $gg \to H$ are no longer degenerate. The constraints on $c^{[1]}_{4q}$ and c_W are also stronger due to sizeable quadratic contributions to the VBF Z measurement and WW as well as WZ measurements, respectively. For $c^{(3)}_{Hq}$, the best-fit value is shifted to lower values. For WH, WW, and WZ production – the processes most strongly affected by $c^{(3)}_{Hq}$– this corresponds to a reduction of the cross-section at lower $\hat{s}$ and to an increase at higher $\hat{s}$, which is compatible with the measured deviations from the SM prediction.

For the weakly constrained fit directions in the two lower blocks of Figure 9.13, quadratic contributions are often large due to their quadratic dependence on the Wilson coefficients, and the validity of the obtained constraints in the SMEFT framework is questionable. As in the linear model, all parameters agree with the SM expectation at the 95% confidence level.

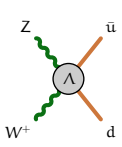

O_{dW}

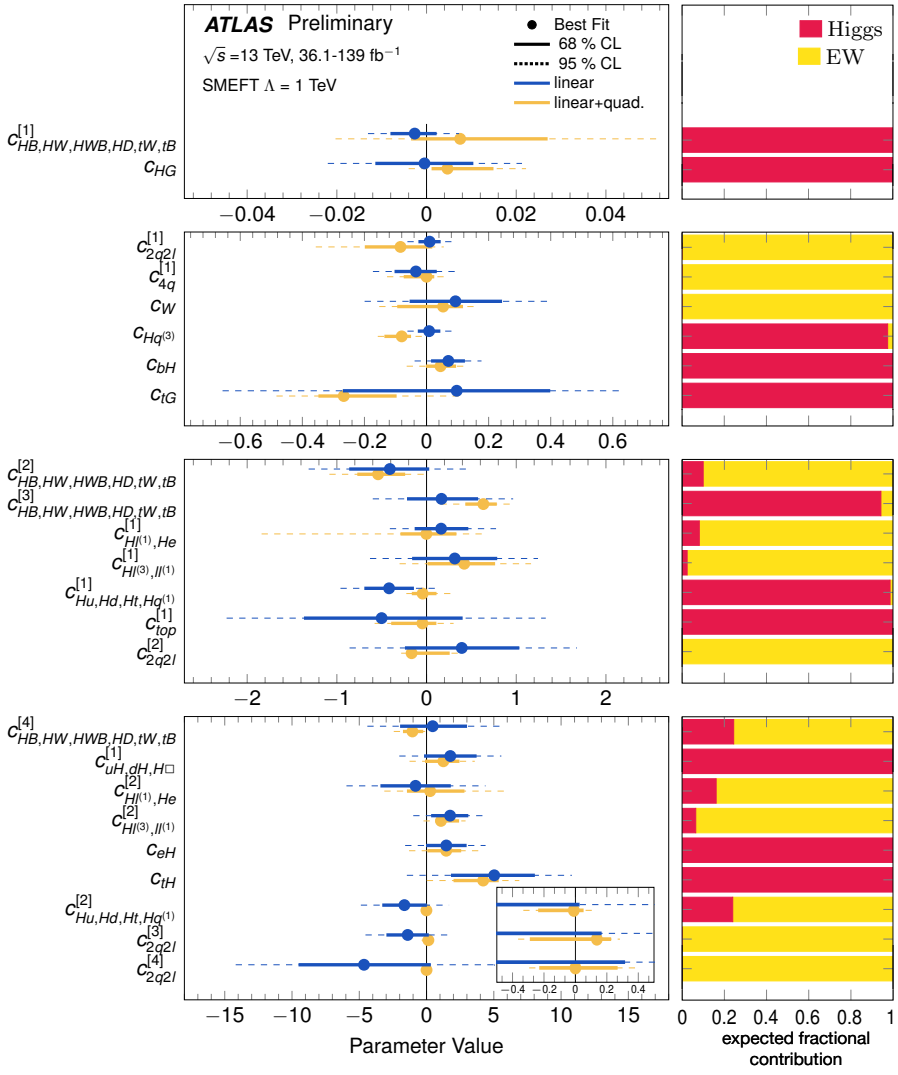

Figure 9.13: Constraints on Wilson coefficients from the combined ATLAS-only analysis, presented in four blocks with different x-axis ranges. The right-hand side panel shows the contribution of each input measurement group to the eigenvector constraint in the Gaussian approximation of the linear model.

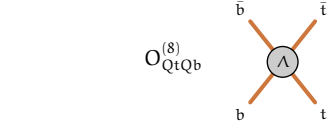

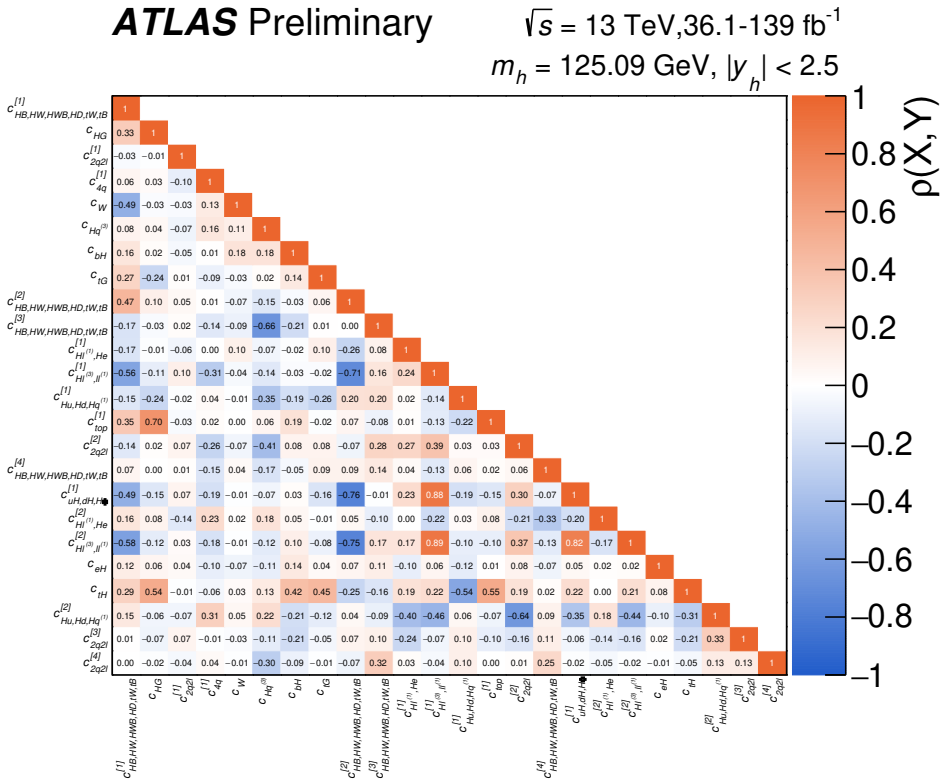

Figure 9.14: correlation of the measurement of the parameters included in the combined maximum likelihood fit of the combined ATLAS-only analysis for the linear model.

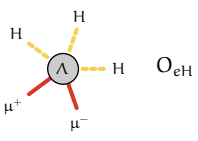

9.5.2 Combined interpretation of ATLAS and electroweak precision data

Including the eight electroweak precision observables (EWPOs) input measurements increases the number of eigenvectors with eigenvalues corresponding to an uncertainty of $\sigma < 5$ from 24 to 28. The eigenvectors are visualized in Figure 9.15. Some Warsaw basis vectors are still closely aligned with a single eigenvector, for example, c_W, which is closely aligned with $c_{EV}^{[13]}$, indicating that an individual measurement is possible. However, the constraints on the Wilson coefficients that affect EWPO are strongly correlated. While, for example, stronger constraints can be obtained on $c_{Hq}^{(3)}$, due to this strong correlation, it can no longer be fitted individually. Instead, a principal component analysis is performed in one large group containing all coefficients affecting EWPO and $H \to \gamma\gamma$. Three other groups identical to those defined in Section 9.5.1 are used and correspond to the two groups of four-fermion operators and the $t\bar{t}H$ operator group. The resulting subgroup eigenvectors are visualized in Figure 9.16.

Constraints obtained from profile-likelihood fits are presented in Figure 9.17, along with the relative contribution of the three measurement groups. Due to the unavailability of a quadratic parametrization of LEP data, no constraints can be derived in the linear+quadratic model. The five most tightly constrained eigenvectors, ($c_{HVV,Vff}^{[1]}$ to $c_{HVV,Vff}^{[4]}$ and c_{HG}) are constrained mainly from a single type of observable σ_{had}^0, $H \to \gamma\gamma$, Γ_Z, the forward-backward asymmetries, and $gg \to H$, respectively. Stringent constraints are furthermore obtained for $c_{2q2l}^{[1]}$, $c_{4q}^{[1]}$, c_W, and c_{bH}– almost identical to the ATLAS-only constraints – and $c_{HVV,Vff}^{[5]}$ to $c_{HVV,Vff}^{[8]}$. These linear combinations are constrained from EWPO measured at LEP and SLC but also receive important contributions from VH and VBF Higgs boson production measurements and the production of weak boson pairs. These contributions of the Higgs and electroweak measurements are expected to become more important for future measurements with larger datasets.

The results of the fits are compatible with the SM expectation of zero for most fitted parameters, except $c_{HVV,Vff}^{[4]}$, whose excess is driven by a well-known discrepancy between $A_{FB}^{0,b}$ and $A_{FB}^{0,c}$ measurements and the SM expectation. The effect of variations of leading eigenvectors of the $c_{HVV,Vff}^{[i]}$, $c_{2q2\ell}^{[i]}$, and $c_{2q2\ell}^{[i]}$ groups on the studied observables is shown in Figures 9.19 and 9.20.

O_{lebQ} 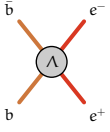

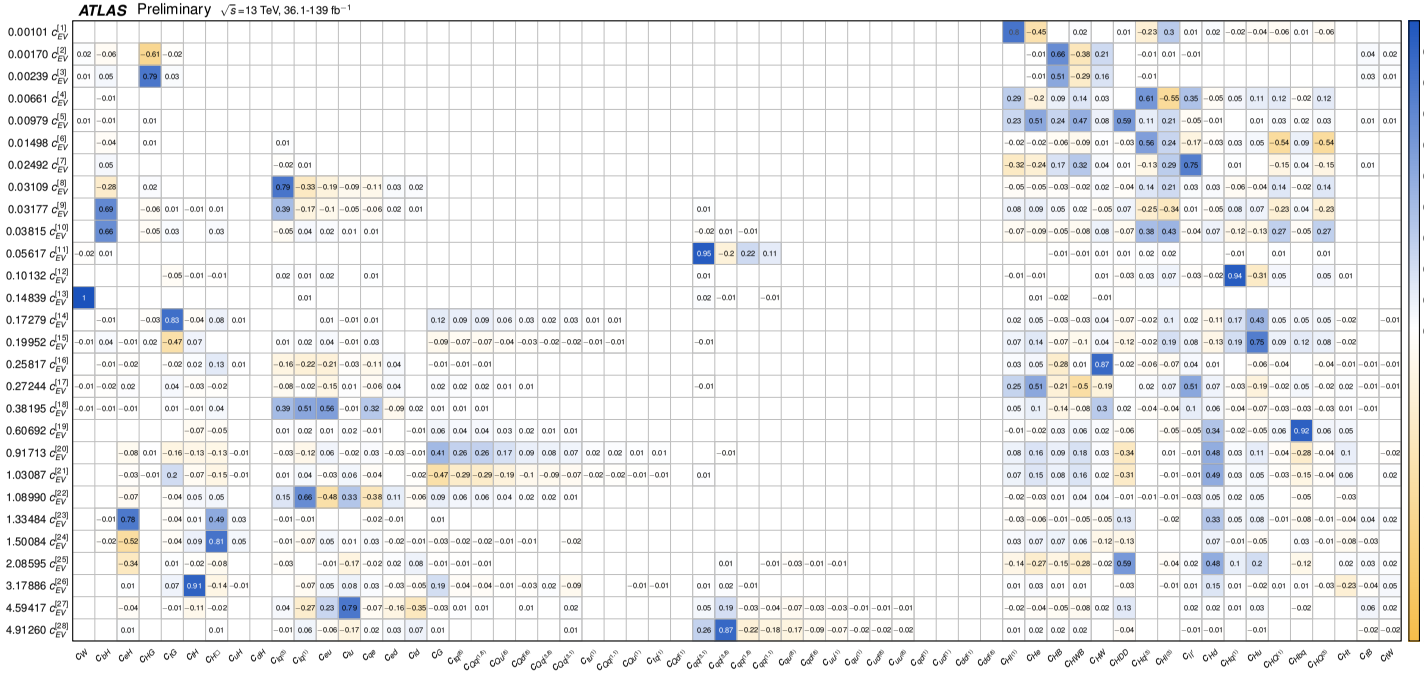

Figure 9.15: Graphical representation of the eigenvectors of the Hesse matrix of the combined LHC+EWPO analysis. Each row corresponds to an eigenvector, and the matrix visualizes the contribution of each Warsaw basis vector to the eigenvector. The components of eigenvectors are rounded to the second decimal place, and their size is also indicated by color code. Empty columns correspond to Wilson coefficients that have little impact on the analyzed measurements and thus contribute to no eigenvector. Eigenvalues are denoted on the left of the plot.

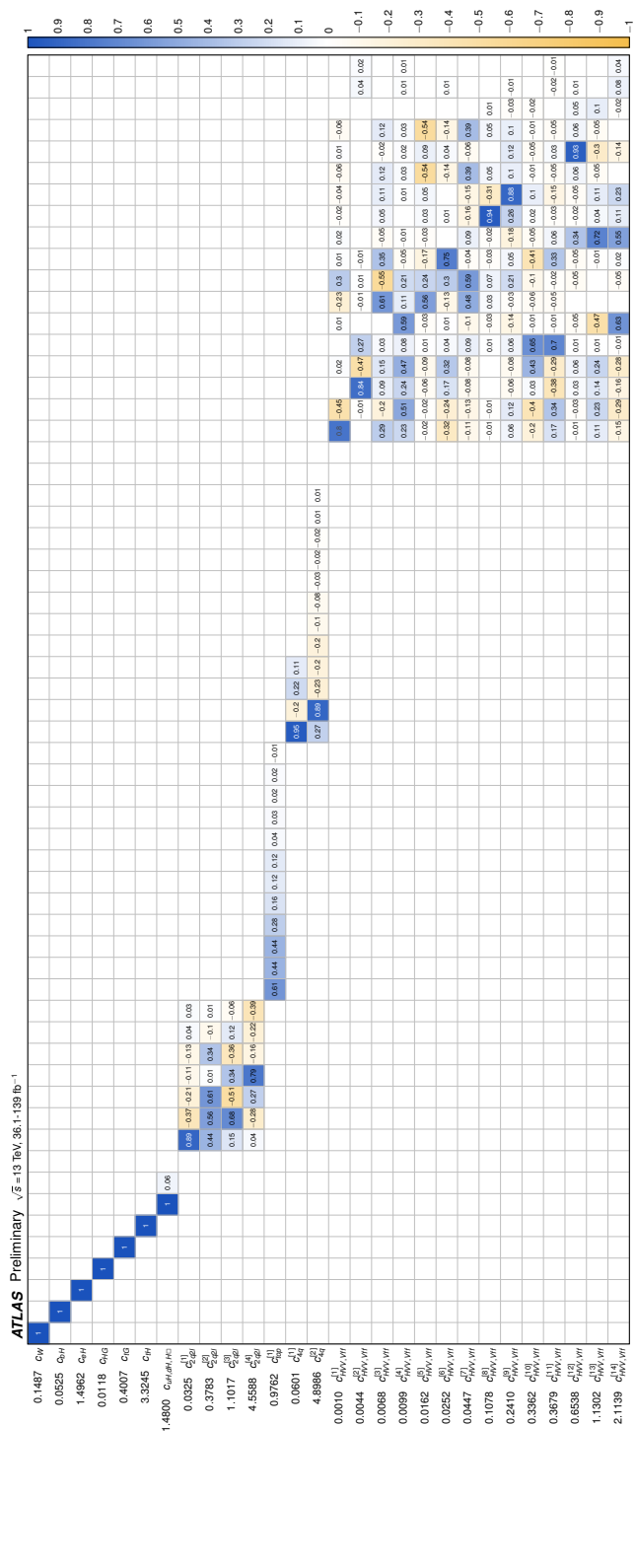

Figure 9.16: Fit basis for the combined LHC+EWPO analysis. Each row corresponds to a fitted linear combination of Warsaw basis vectors. Entries are rounded to the second decimal place, and their value is also indicated by color. Eigenvalues are denoted on the left of the plot.

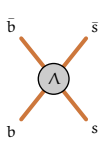

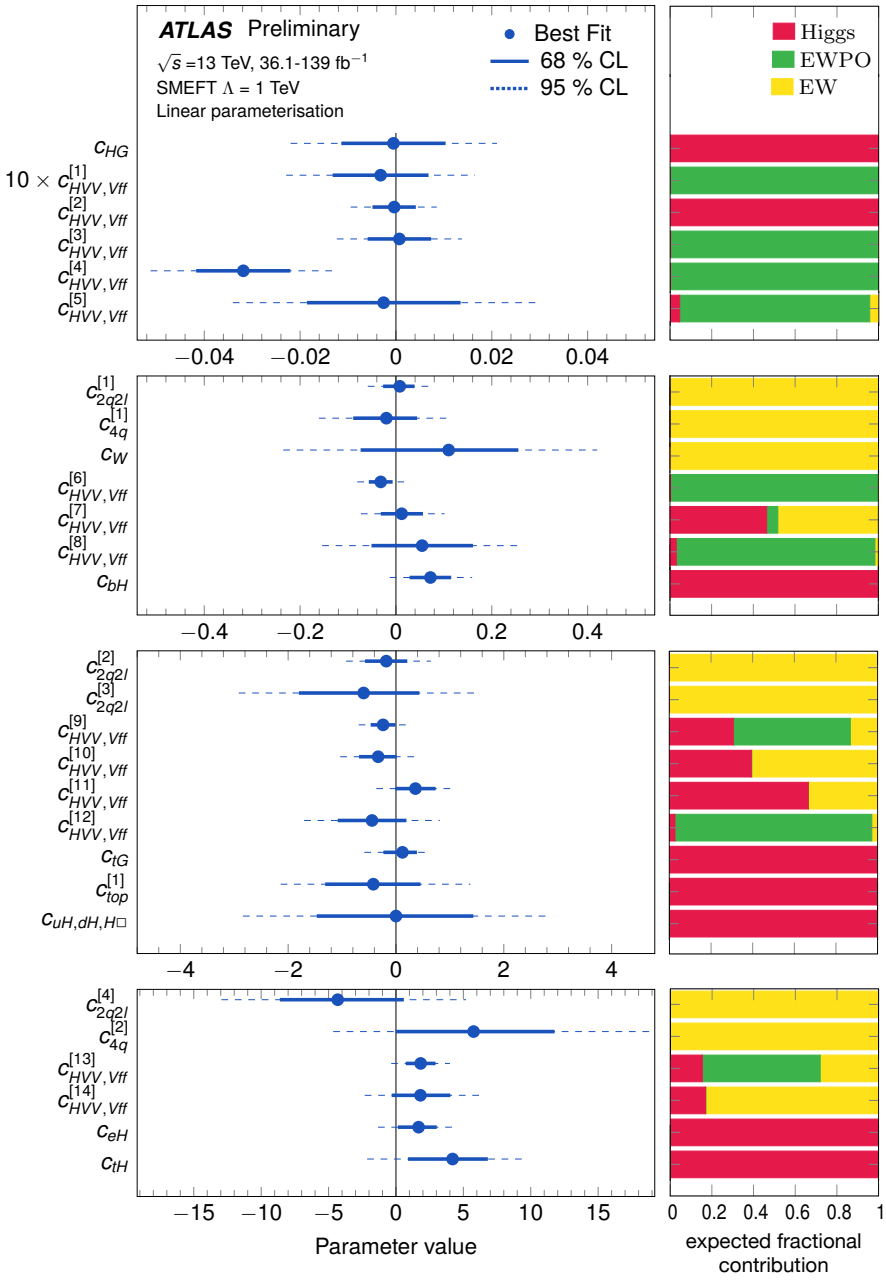

Figure 9.17: Constraints on Wilson coefficients from the combined LHC+EWPO analysis, presented in four blocks with different x-axis ranges. The right-hand side panel shows the contribution of each input measurement group to the eigenvector constraint in the Gaussian approximation.

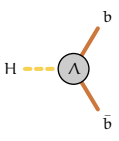

O_{bH}

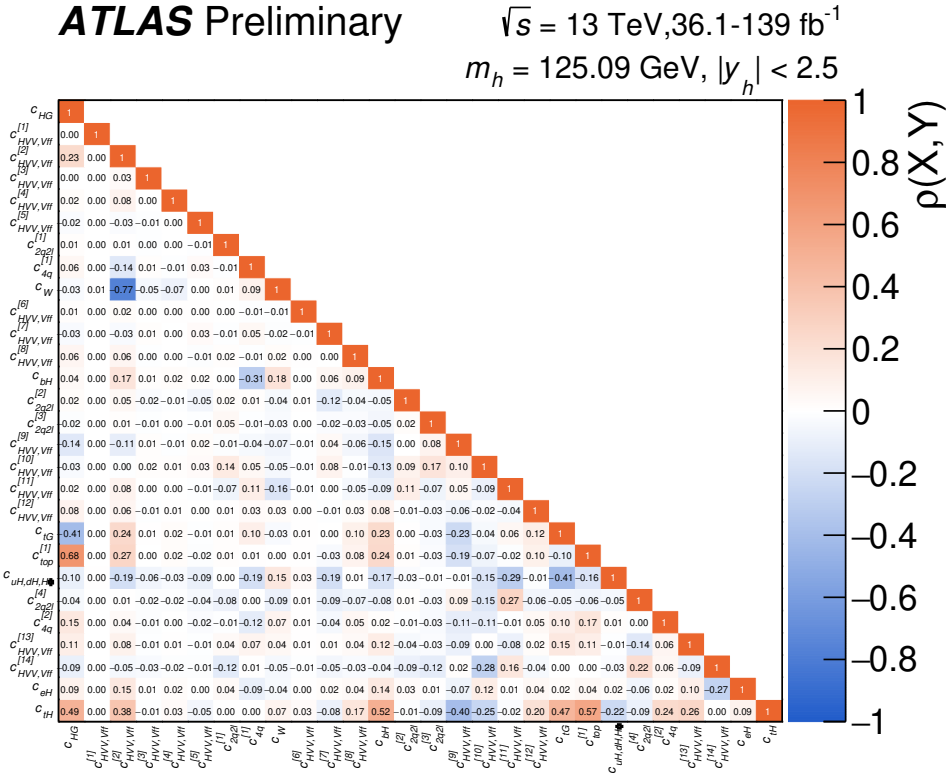

Figure 9.18: correlation of the measurement of the 28 parameters included in the combined maximum likelihood fit of the combined LHC+EWPO interpretation.

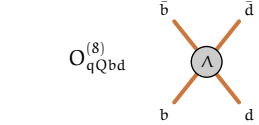

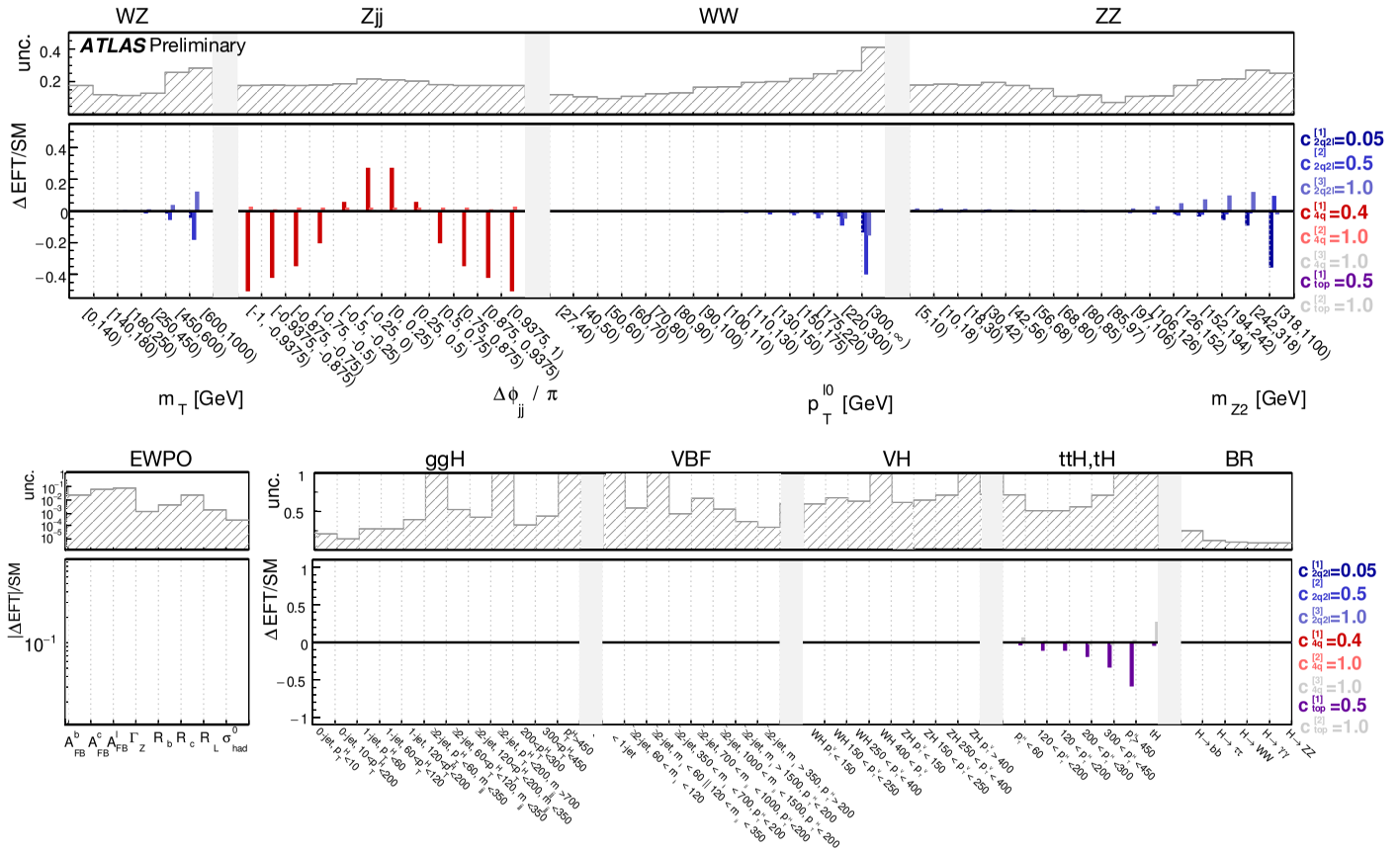

Figure 9.19: Relative impact of the eigenvectors of the four-fermion operators on differential cross-sections of electroweak processes, the electroweak precision observables, and on the Higgs STXS cross-sections and branching ratios. The corresponding selected coefficient values are shown on the right-hand side of the lower panel. Operators that are not sensitive and are fixed in the fit are shown in gray. In order to quantify the sensitivity of each measurement to constrain the coefficients, the total relative uncertainty on measurement in the corresponding regions is shown for comparison in the top panel as a shaded area. For presentational clarity, the statistical uncertainty of low-precision STXS regions is clipped.

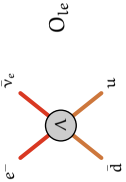

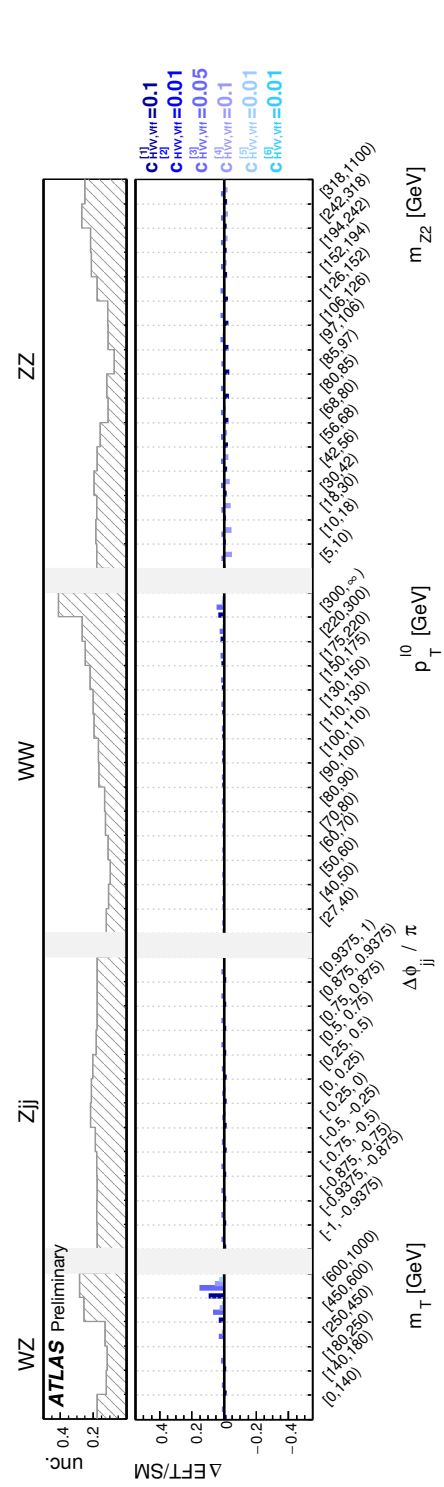

Figure 9.20: Relative impact of the eigenvectors of the HVV, Vff operators on differential cross-sections of electroweak processes, the electroweak precision observables, and the Higgs STXS cross-sections and branching ratios. The corresponding selected coefficient values are shown on the right-hand side of the lower panel. In order to quantify the sensitivity of each measurement to constrain the coefficients, the total relative uncertainty on measurement in the corresponding regions is shown for comparison in the top panel as a shaded area. For presentational clarity, the statistical uncertainty of low-precision STXS regions is clipped.

9.5.3 Simplified Likelihood

This section presents a simplified statistical model of the measurements allowing for the reproduction of the presented fit results with high accuracy. It is based on the model introduced in Equation 9.6, which defines a signal-strength parameter for each EWPO, each electroweak measurement bin, and each STXS region. From the vector of best-fit results, labeled $\hat{\boldsymbol{\mu}}$, and their covariance, V_μ, a Gaussian approximation of the likelihood is constructed:

$$L(\boldsymbol{\mu}) = \frac{1}{\sqrt{(2\pi)^{n_\mu}\det(V_\mu)}} \exp\left(-\frac{1}{2}\Delta\boldsymbol{\mu}^\intercal V_\mu^{-1}\Delta\boldsymbol{\mu}\right), \tag{9.6}$$

where n_μ is the number of signal strength parameters in the multivariate Gaussian and

$$\Delta\boldsymbol{\mu} = \boldsymbol{\mu} - \hat{\boldsymbol{\mu}}\,. \tag{9.7}$$

As a function of the chosen signal strength parameters, the above multivariate Gaussian is a good approximation of the likelihood due to the large underlying dataset. By substituting $\boldsymbol{\mu}$ for the SMEFT parametrization, an approximation of the likelihood used to constrain Wilson coefficients in this note can be obtained. The approximate model is also valid in the linear+quadratic scenario, where the likelihood is non-Gaussian as a function of Wilson coefficients. Profile-likelihood scans of this simplified model result in constraints very similar to the full model, as shown in Figure 9.21.

The simplified model is nuisance parameter-free, as the effect of all uncertainties is encoded in the covariance matrix V_μ, and thus computationally inexpensive. The model can, for example, be used to study alternative EFT scenarios by simply substituting $\boldsymbol{\mu}$ for a modified or alternative parametrization. As the signal strength modifiers describe the measurement in relation to the SM expectation, there is no need to re-evaluate the SM predictions and their uncertainties for such a re-parametrization.

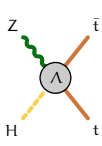

O_{tB}

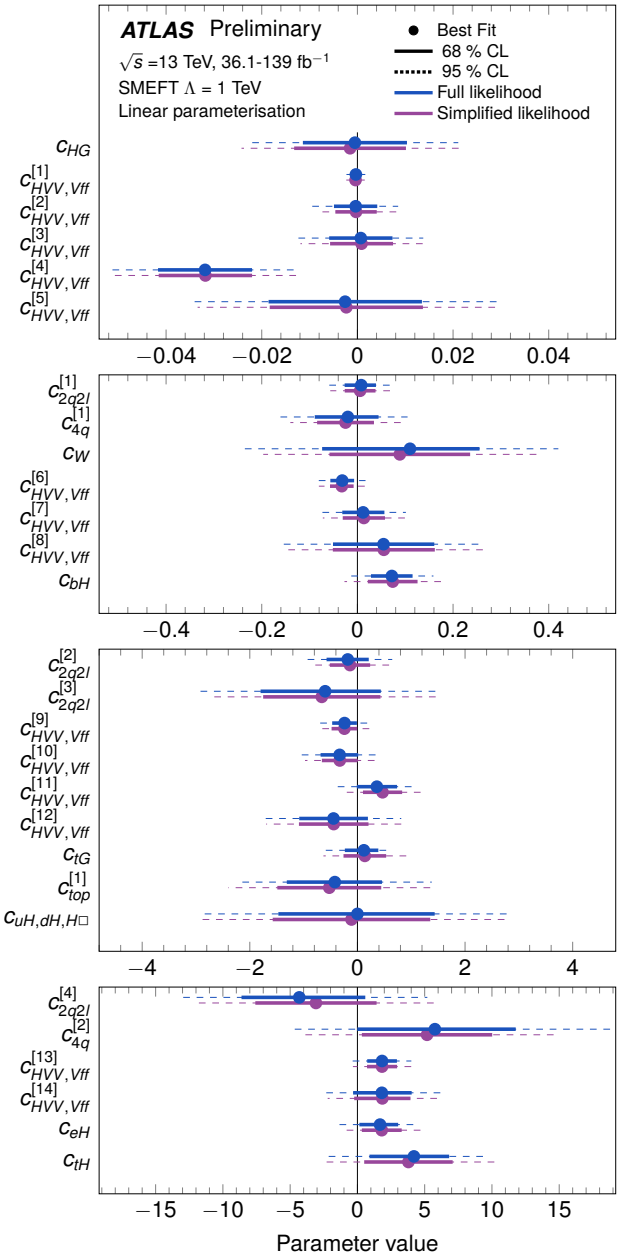

Figure 9.21: comparison of constraints on Wilson coefficients from the combined analysis for the full negative log-likelihood (NLL) and the simplified NLL, using the linearized SMEFT parametrization.

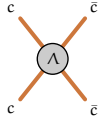

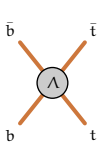

$O^{(1)}_{QtQb}$

10

SMEFT matching for Two Higgs doublet models

In Standard Model Effective Field Theory (SMEFT), deviations from the Standard Model predictions are parametrized by higher-dimensional operators. These operators can serve as a basis for capturing the effects of specific ultraviolet-complete models containing heavy particles that will result in a pattern of deviations in certain SMEFT operators.

The SMEFT UV matching process refers to the process of capturing UV models in SMEFT. By integrating out the heavy particles in a UV model, the matching relation to the SMEFT operators is found. These matching relations help establish the connection between the parameters defining the high-energy UV model and the Wilson coefficients in the low-energy SMEFT.

Deviations in SMEFT operators can be scrutinized to inform the model-building of UV theories. In cases where measurements of UV models have already been performed directly without going through SMEFT, a direct comparison with the SMEFT matching allows us to probe the reliability of assumptions within SMEFT. Given that the SMEFT predictions are available primarily at dimension-6, it is important to test the reliability of the SMEFT matching for known models to check the robustness of SMEFT to capture signatures of UV models.

The two-Higgs-doublet (2HDM) model is a popular extension to the Standard Model allowing for a composite Higgs sector and is introduced in Section 2. The remainder of this chapter will focus on this model, a popular extension of the SM for which both a direct and a SMEFT-based parametrization of Higgs boson production and decays is available, and present a comparison of results obtained through both routes.

10.1 Constraints on two-Higgs-doublet models

For the interpretation of Standard Model Higgs boson measurements in the 2HDM models, the decoupling limit is assumed, where the observed Higgs boson is assumed to be the light Higgs boson, and the other Higgs bosons in 2HDM are much

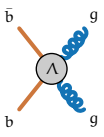

heavier than energy scales typically probed, $m_H \gg v$. This requirement, in turn, implies the *alignment limit*, $|\cos(\beta-\alpha)| \ll 1$, in which the light scalar Higgs boson h has SM-like couplings. The mass of the light Higgs boson m_h is assumed to be close to 125 GeV, while all other Higgs bosons are assumed to be significantly heavier (and their masses are assumed to be degenerate, $m_A \sim m_{H^\pm} \sim m_H \sim M$). Near the alignment limit, i.e., for small $|\cos(\beta-\alpha)|$, the modifications of the tree-level couplings of the h boson with respect to the SM predictions follow the expressions summarized in Table 10.1 [84].

Coupling	Type I	Type II	Lepton-specific	Flipped
u, c, t	$s_{\beta-\alpha} + c_{\beta-\alpha}/\tan\beta$			
d, s, b	$s_{\beta-\alpha} + c_{\beta-\alpha}/\tan\beta$	$s_{\beta-\alpha} - c_{\beta-\alpha} \times \tan\beta$	$s_{\beta-\alpha} + c_{\beta-\alpha}/\tan\beta$	$s_{\beta-\alpha} - c_{\beta-\alpha} \times \tan\beta$
e, μ, τ	$s_{\beta-\alpha} + c_{\beta-\alpha}/\tan\beta$	$s_{\beta-\alpha} - c_{\beta-\alpha} \times \tan\beta$	$s_{\beta-\alpha} - c_{\beta-\alpha} \times \tan\beta$	$s_{\beta-\alpha} + c_{\beta-\alpha}/\tan\beta$
W, Z	$s_{\beta-\alpha}$			
H	$s^3_{\beta-\alpha} + \left(3 - 2\frac{\overline{m}^2}{m_h^2}\right) c^2_{\beta-\alpha} s_{\beta-\alpha} + 2\cot(2\beta)\left(1 - \frac{\overline{m}^2}{m_h^2}\right) c^3_{\beta-\alpha}$			

Table 10.1: Multiplicative factors predicted in the four 2HDM scenarios near the alignment limit, as a function of $\tan\beta$ and $\cos(\beta-\alpha)$, for the Higgs boson couplings to up-type quarks (1st row), down-type quarks (2nd row), charged leptons (3rd row), vector bosons (4th row), and to itself (5th row). The symbol $c_{\beta-\alpha}$ stands for $\cos(\beta-\alpha)$, while $s_{\beta-\alpha}$ stands for $\sin(\beta-\alpha)$. The definition of the parameter $\overline{m}$ is given below.

In addition to the impact of the tree-level coupling modifications, the production and decay rates of the h boson are modified through next-to-leading-order electroweak corrections involving the trilinear hhh coupling λ [304]. In the 2HDM framework, this self-coupling λ is modified with respect to the SM expectation λ_{SM} by a scale factor [305]

$$\kappa_\lambda = \lambda/\lambda_{SM} = \sin^3(\beta-\alpha) + \left(3 - 2\frac{\overline{m}^2}{m_h^2}\right)\cos^2(\beta-\alpha)\sin(\beta-\alpha) + 2\cot\left(2\beta\left(1 - \frac{\overline{m}^2}{m_h^2}\right)\right)\cos^3(\beta-\alpha). \tag{10.1}$$

The parameter $\overline{m}$ is defined by $\overline{m}^2 = \frac{m_{12}^2}{\sin\beta\cos\beta} = m_A^2 + \lambda_5 v^2$, where λ_5 is the coefficient of the $(\Phi_1^\dagger\Phi_2)^2$ term and m_{12} is the coefficient of the $(\Phi_1^\dagger\Phi_2)$ term of the Higgs potential as introduced earlier in Section 2.3.6. Near the alignment limit considered, the value of $\overline{m}$ is close to that of m_A ($\lambda_5 v^2 \ll m_A^2$), and a value $\overline{m} = m_A = 1$ TeV ($\lambda_5 = 0$) is assumed in this section in all scenarios in which the effect of the self-coupling is considered in the calculation of limits on $\cos(\beta-\alpha)$ and $\tan\beta$.

In the following sections, limits on the 2HDM parameters $\cos(\beta-\alpha)$ and $\tan\beta$ are inferred from studies of the ensemble of Higgs boson production and decay rate measurements in two distinct scenarios: first, by using directly the relationship of

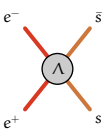

O_{ed}

the Higgs boson coupling strength to other particles in the 2HDM model, and then by using the 2HDM matching relations for the linearized SMEFT statistical model described in Section 7.3.

10.1.1 Constraints based on κ-framework 2HDM coupling strength modifiers

The Higgs boson production-mode cross-sections and decay branching ratios are parametrized in terms of the coupling strength to the other elementary particles in the SM as done in [168]. Within this so-called κ-*framework*, a coupling strength modifier κ_p for a production or decay process via the coupling to a given particle p is defined as $\kappa_p^2 = \sigma_p/\sigma_p^{SM}$ or $\kappa_p^2 = \Gamma_p/\Gamma_p^{SM}$, respectively, where Γ_p is the partial decay width into a pair of particles p. In the 2HDM model considered in this study, the loop-induced processes (gluon-gluon fusion $gg \to H$ and $gg \to ZH$ production, as well as $H \to \gamma\gamma$, $H \to Z\gamma$ and $H \to gg$ decays) are expressed in terms of the strength factors for the couplings to the SM particles inside the loop. It is also assumed that there are no additional contributions of heavy Higgs bosons in the loop. The impact of the trilinear hhh coupling modifier κ_λ on the Higgs boson production and decay rates via NLO electroweak corrections to the LO amplitudes is included in the parametrization. In the likelihood function given in Equation 5.21 the signal strengths are parametrized in terms of the κ-framework and the couples are expressed in terms of $(\cos(\beta-\alpha), \tan\beta)$ using the relations listed in Table 10.1. Confidence regions for $\tan\beta$ and $\cos(\beta-\alpha)$ can thus be inferred from the combined measurements of Higgs boson production and decay rates. The resulting 95% CL contours in the ($\tan\beta$, $\cos(\beta-\alpha)$) plane are shown in Figure 10.1. All models exhibit similar exclusion regions in the ($\tan\beta$, $\cos(\beta-\alpha)$) plane at low values ($\lesssim 1$) of $\tan\beta$, where only a narrow region of $\cos(\beta-\alpha)$ around zero is consistent with the measured values of the Higgs boson production and decay rates. The interval of allowed values of $\cos(\beta-\alpha)$ increases in size with $\tan\beta$, up to a total width of about 0.1–0.2 for $\tan\beta = 1$, depending on the model. For higher values of $\tan\beta$, in the models in which at least one of the coupling strength modifiers is enhanced by a factor $\tan\beta$, i.e., all models except type-I, the allowed range of $\cos(\beta-\alpha)$ around zero shrinks as $\tan\beta$ increases. For the type-I model, the allowed range of $\cos(\beta-\alpha)$ further increases with $\tan\beta$, reaching a width of around 0.5 for $\tan\beta = 10$, but covers regions of the parameter space that deviate significantly from the alignment-limit hypothesis. When the constraint from the trilinear hhh coupling (κ_λ) is included, the width of the 95% CL interval for $\cos(\beta-\alpha)$ at large $\tan\beta$ for the type-I model is reduced by about 50%.

An additional feature of the type-I model result is that in the large $\tan\beta$ region, for positive $\cos(\beta-\alpha)$, the observed exclusion region is significantly larger than the expected one. This derives from the fact that the ATLAS measurement of Higgs

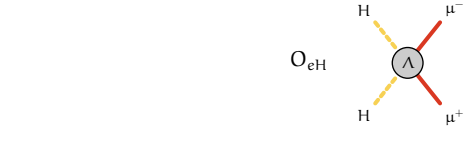

boson production and decay rates favors values of the coupling strength modifiers to b, t quarks and τ leptons smaller than one, and of the couplings to W, Z bosons larger than one ($\kappa_F = 0.95 \pm 0.05$ and $\kappa_V = 1.035 \pm 0.031$ when assuming that all fermions share the same modifier κ_F and that $\kappa_W = \kappa_Z = \kappa_V$ [168]). In this scenario, the model predicts $\sin(\beta - \alpha) = \kappa_V \approx 1$ and $\cos(\beta - \alpha) = \tan\beta(\kappa_F - \sin(\beta - \alpha)) \approx \tan\beta(\kappa_F - 1)$, disfavouring positive values of $\cos(\beta - \alpha)$ for $\kappa_F < 1$.

A second small region of allowed $\tan\beta$ and $\cos(\beta - \alpha)$ values for large $\tan\beta$ and $\cos(\beta - \alpha) \approx 0.2$ is present in type-II, lepton-specific, and flipped models. This corresponds to regions with $\cos(\beta + \alpha) \approx 0$, for which some of the fermion couplings have the same magnitude as in the SM but the opposite sign. In particular, this corresponds to a negative sign of the lepton couplings in the lepton-specific model, of the down-type quark couplings in the flipped model, or both in the type-II model. Since the sign of these couplings is not sufficiently constrained by the current experimental measurements, this region is not excluded. The same region is, however, not allowed in type-I models, in which down-type quarks and leptons coupling strength modifiers have the same sign (and value) as for up-type quarks. In that case, a negative sign of the top-quark coupling strength modifier κ_t is experimentally excluded by the measurement of $H \to \gamma\gamma$ decays, whose branching ratio depends linearly on $\kappa_t \kappa_W$ as a consequence of the interference between W-boson- and top-quark-mediated loop amplitudes.

10.1.2 Constraints using an EFT-based approach

The SMEFT matching of the 2HDM model is valid in the decoupling limit of the 2HDM, where the heavy fields decouple from the light fields. In the decoupling limit, the heavy Higgs bosons can be integrated out, and the matching relations can be obtained by relating the remaining terms in Lagrangian of the 2HDM to SMEFT [306–308]. In the decoupling limit, the masses of the heavy Higgs bosons relate to the scale of New Physics (Λ) as

$$m_A \sim m_{H_0} \sim m_{H^\pm} \equiv M \equiv \Lambda \gg v, m_h \sim v. \tag{10.2}$$

For the 2HDM model, in the exact alignment scenario $\cos(\beta - \alpha) \to 0$, SMEFT operators are not generated at tree level but appear at 1-loop. Away from the alignment limit, tree-level contributions to the Yukawa couplings are generated as well as a correction to the Higgs trilinear coupling. The relevant Wilson coefficients correspond to the Yukawa modifier of the muon, τ-lepton, bottom quark, and top quark given by ($c_{eH,22}, c_{eH,33}, c_{bH}, c_{tH}$) and the Higgs boson self-coupling modifier (c_H). The Wilson coefficients are expressed in terms of $\cos(\beta - \alpha)$ and $\tan\beta$ in Table 10.2.

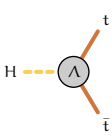

O_{tH}

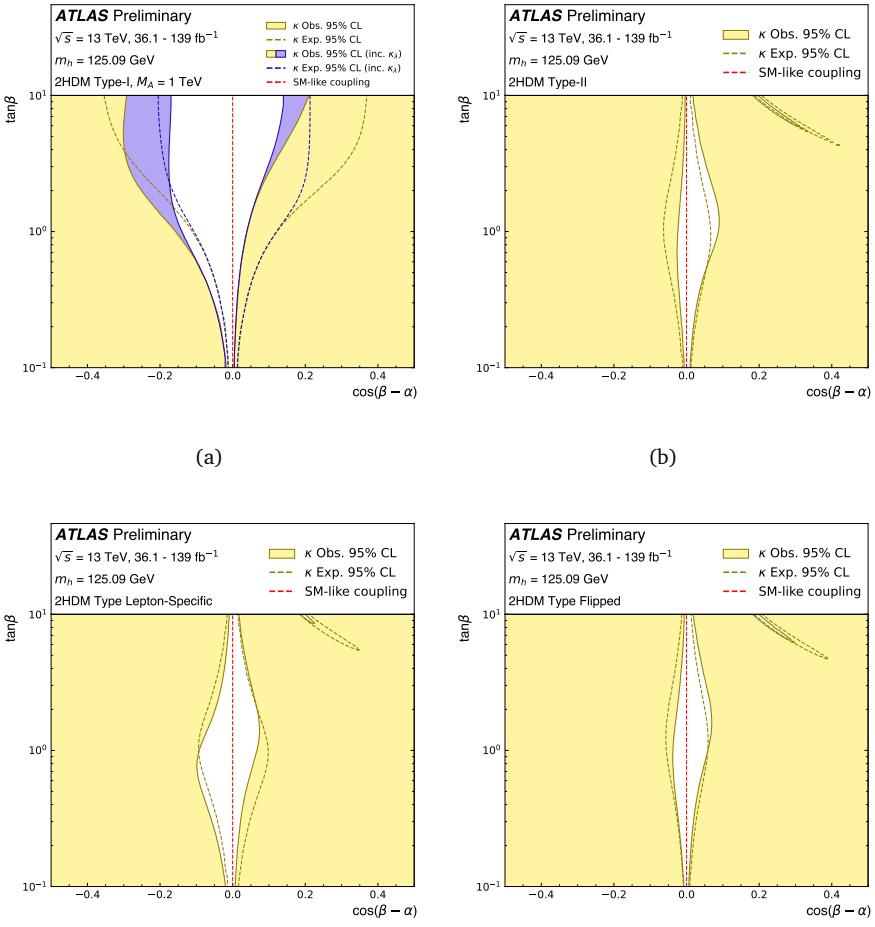

Figure 10.1: Regions of the 2HDM ($\tan\beta$, $\cos(\beta-\alpha)$) parameter plane excluded at 95% CL (light yellow filled regions) in the κ-framework-based approach by the measured rates of Higgs boson production and decays in (a) type I, (b) type II, (c) lepton-specific and (d) flipped models. The dark yellow dashed lines show the borders of the corresponding expected exclusion regions for the SM hypothesis. For type-I models, the observed and expected regions excluded at 95% CL when the κ_λ constraint is considered are also shown (solid and dashed blue lines). Results are derived assuming $|\cos(\beta-\alpha)| \ll 1$, near the alignment limit represented by the red dashed lines, and that the masses of the non-SM-like Higgs bosons are large compared with the SM vev.

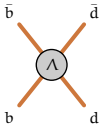

SMEFT parameters	Type I	Type II	Lepton-specific	Flipped
$\frac{v^2}{\Lambda^2}c_{tH}$	$-Y_t c_{\beta-\alpha}/\tan\beta$	$-Y_t c_{\beta-\alpha}/\tan\beta$	$-Y_t c_{\beta-\alpha}/\tan\beta$	$-Y_t c_{\beta-\alpha}/\tan\beta$
$\frac{v^2}{\Lambda^2}c_{bH}$	$-Y_b c_{\beta-\alpha}/\tan\beta$	$Y_b c_{\beta-\alpha}\tan\beta$	$-Y_b c_{\beta-\alpha}/\tan\beta$	$Y_b c_{\beta-\alpha}\tan\beta$
$\frac{v^2}{\Lambda^2}c_{eH,22}$	$-Y_\mu c_{\beta-\alpha}/\tan\beta$	$-Y_\mu c_{\beta-\alpha}\tan\beta$	$Y_\mu c_{\beta-\alpha}\tan\beta$	$-Y_\mu c_{\beta-\alpha}/\tan\beta$
$\frac{v^2}{\Lambda^2}c_{eH,33}$	$-Y_\tau c_{\beta-\alpha}/\tan\beta$	$-Y_\tau c_{\beta-\alpha}\tan\beta$	$Y_\tau c_{\beta-\alpha}\tan\beta$	$-Y_\tau c_{\beta-\alpha}/\tan\beta$
$\frac{v^2}{\Lambda^2}c_H$	$c^2_{\beta-\alpha}M_A^2/v^2$	$c^2_{\beta-\alpha}M_A^2/v^2$	$c^2_{\beta-\alpha}M_A^2/v^2$	$c^2_{\beta-\alpha}M_A^2/v^2$

Table 10.2: The Wilson coefficients at lowest order for SMEFT, modifying the Yukawa couplings c_{tH}, c_{bH}, $c_{eH,33}$, and $c_{eH,22}$ for the top quark, bottom quark, τ, and μ parametrized by $\tan\beta$ and $\cos(\beta-\alpha)$ in the four types of 2HDM where $c_{\beta-\alpha}$ stands for $\cos(\beta-\alpha)$. c_H corresponds to modification to the self-coupling of the Higgs, and M_A corresponds to the mass of the Heavy Higgs bosons in 2HDM. Y_i corresponds to $\sqrt{2}m_i/v$.

In these formulae, computed to first order in $\cos(\beta-\alpha)$, $Y_i = \sqrt{2}m_i/v$ are the SM Higgs boson couplings and the values of η_i depend on the type of model ($\eta_b = -\tan^2\beta$ in type-II and flipped models, as is η_τ in type-II and lepton-specific models; $\eta_{b,\tau,\mu} = 1$ otherwise). The corrections to the HVV vertices are quadratic in $\cos(\beta-\alpha)$ and are captured only by dimension-8 operators. It should be noted that for the EFT to be valid, $\Lambda \gg v$ and therefore $|\cos(\beta-\alpha)| \propto \frac{v^2}{\Lambda^2}$ should be small, close to the alignment limit.

The operator $\mathcal{O}_{\mathcal{H}} = (H^\dagger H)^3$ is also considered in the models under study, with a coefficient that scales with $\cos^2(\beta-\alpha)$ but which can be significantly enhanced if the other scalar states are much heavier than the SM-like Higgs boson. In that case, $\mathcal{O}_{\mathcal{H}}$ is proportional to $(M/v)^2$ [309]:

$$\frac{v^2 c_H}{\Lambda^2} = \cos(\beta-\alpha)^2 \left(\frac{M}{v}\right)^2 .$$

Non-zero values of c_H modify the trilinear hhh coupling λ by a scale factor in 2HDM [310]:

$$\kappa_\lambda = 1 - \frac{v^2 c_H}{\lambda_{SM}\Lambda^2} = 1 - \frac{\cos(\beta-\alpha)^2}{\lambda_{SM}} \left(\frac{M}{v}\right)^2 .$$

In the following, a value of $M = 1$ TeV is assumed for the masses of the heavy scalar particles, and thus $\kappa_\lambda \approx 1 - (11\cos(\beta-\alpha))^2$ for $\Lambda = 1$ TeV. The constraint on κ_λ will affect the Type-I 2HDM interpretation, while exclusion limits for all other types are unaffected. Note that in Equation 10.1.2, the behavior of κ_λ neglected the effects of operators that affect the Higgs boson kinetic term and the Fermi constant, which do not affect the 2HDM model.

Constraints on the values of $\tan\beta$ and $\cos(\beta-\alpha)$ can thus be inferred from those set on c_{bH}, c_{tH}, $c_{eH,33}$, $c_{eH,22}$, and c_H by the SMEFT interpretation of the com-

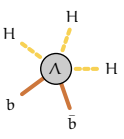

O_{bH}

bined measurement of production and decay rates and STXS. The likelihood model defined in Section 6.6 is used, expressing the Wilson coefficients c_{bH}, c_{tH}, $c_{eH,33}$, $c_{eH,22}$ and c_H in terms of the 2HDM parameters as in Table 10.2 and fixing all the other Wilson coefficients to zero. The results are shown in Figure 10.2.

A comparison between the excluded regions from the two approaches is shown in Figure 10.3.

In the regions where the assumptions used in this study are valid, the excluded regions are very similar in the two approaches. In the type-I model for large values of $\tan\beta$, the EFT-based approach does not exploit constraints from the HVV couplings. The constraints from HVV coupling only enter at dimension-8 in the SMEFT expansion and are not considered here. The SMEFT expansion retains only terms of $\mathcal{O}(\cos(\beta-\alpha))$ in the expansion of κ_λ, leads to looser constraints on $\cos(\beta-\alpha)$ than the κ-framework-based approach, in which $\kappa_V = \sin(\beta-\alpha)$ and the full dependence of κ_λ on $\cos(\beta-\alpha)$ is considered. However, part of the allowed region of parameter space in this case is inconsistent with the alignment limit hypothesis of $|\cos(\beta-\alpha)| \ll 1$.

A significant difference between the $\tan\beta$, $\cos(\beta-\alpha)$ constraints from the approach presented in this section and those obtained using the κ-framework-based approach is the absence here of the second small allowed petal-like region around $\tan\beta \approx 10$, $\cos(\beta-\alpha) \approx 0.2$. This difference follows again from the fact that in the EFT-based approach, only dimension-6 terms are considered in the SMEFT Lagrangian, and a linear expansion of $\sigma \times B$, which does not include terms of second order in the Wilson coefficients, is performed. As a consequence, the region with a flipped coupling sign does not appear. This study shows the capability of SMEFT to capture the main features of the 2HDM model, with the notable exclusion of the couplings to vector bosons and the absence of the petal regions for the linear expansion.

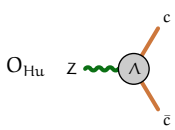

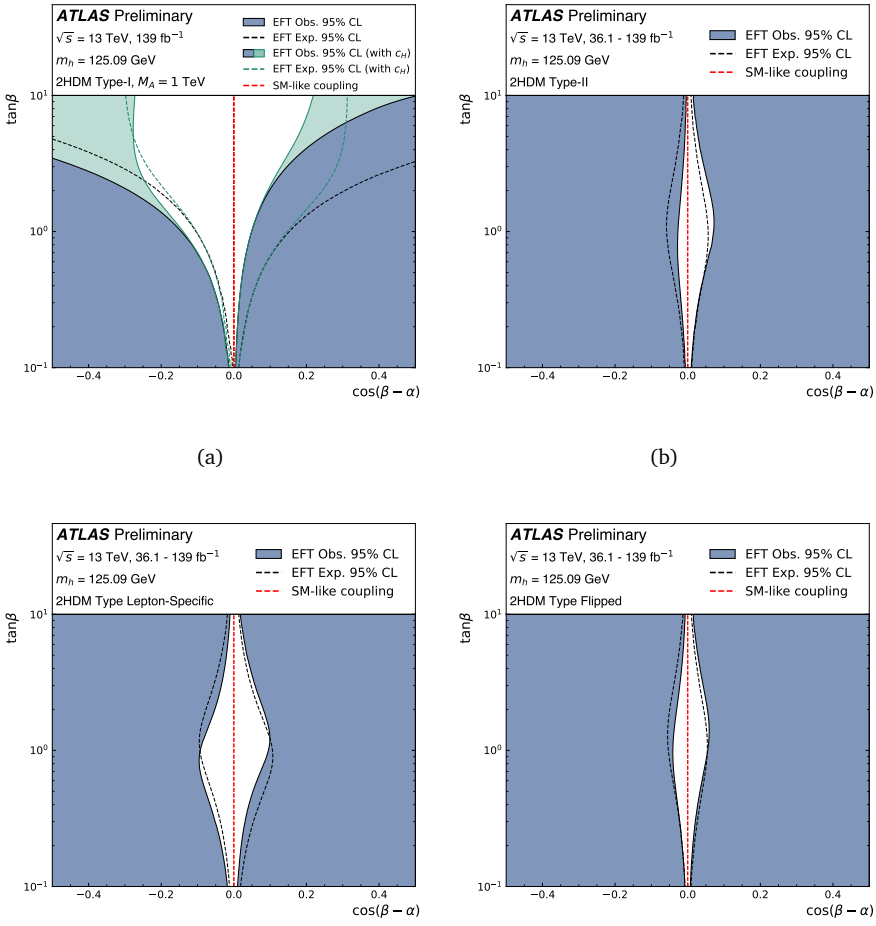

Figure 10.2: Regions of the 2HDM ($\tan\beta$, $\cos(\beta-\alpha)$) parameter plane excluded at 95% CL (blue-filled regions) in the EFT-based approach by the measured rates of Higgs boson production and decays in (a) type-I, (b) type-II, (c) lepton-specific, and (d) flipped models. The dashed black lines show the borders of the corresponding expected exclusion regions for the SM hypothesis. For type-I models, the observed and expected regions excluded at 95% CL when the c_H constraint is considered are also shown (solid and dashed green lines). Results are derived assuming $|\cos(\beta-\alpha)| \ll 1$, near the alignment limit represented by the red dashed lines, and that the masses of the non-SM-like Higgs bosons are large compared with the SM vev.

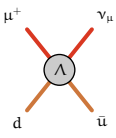

O_{le}

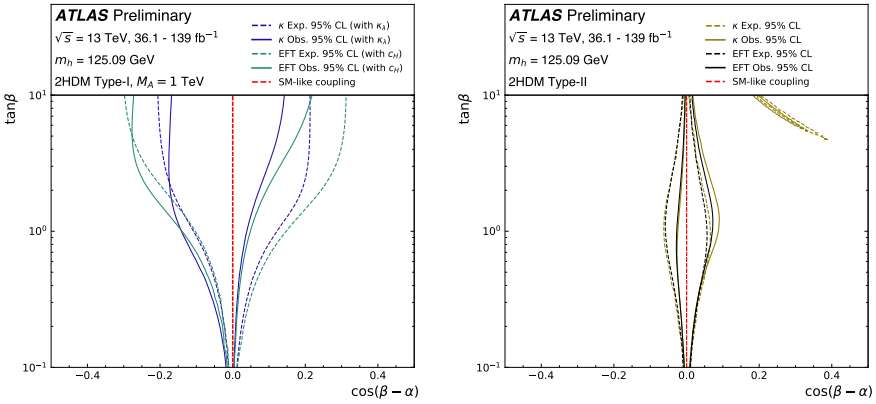

(a) (b)

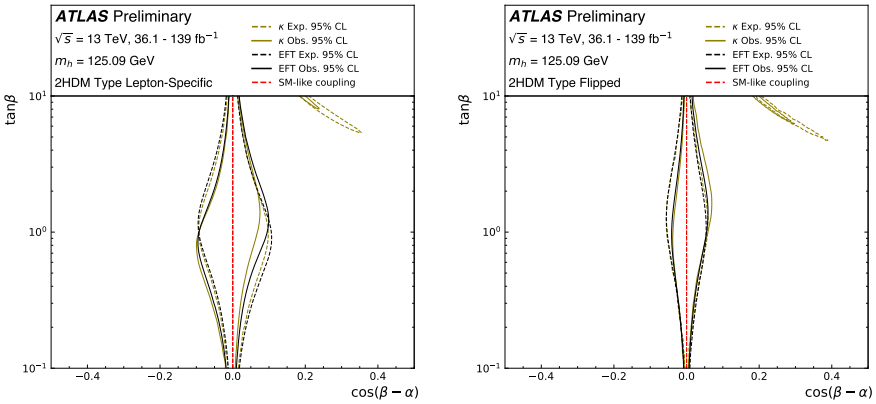

(c) (d)

Figure 10.3: Comparison of the constraints from the approaches based on the κ- and EFT-frameworks in the $(\tan\beta,\ \cos(\beta-\alpha))$ plane in 2HDM. The figures overlay the constraints for the κ- and EFT-frameworks shown in Figure 10.1 and Figure 10.2 respectively for the four types of 2HDM models.

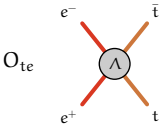

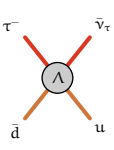

O_{le}

11

Conclusions and Outlook

With the growing dataset at the LHC, the experimental program of Higgs boson physics has grown within a decade from an experimental hunt to an impressive study of its properties in extensive detail. The dataset has enabled precision measurements of the Higgs boson production mode in different kinematic regimes across the five main decay channels ($H \to \gamma\gamma$, $H \to ZZ^* \to 4l$, $H \to WW^* \to l\nu l\nu$,$H \to b\bar{b}$, and $H \to \tau^+\tau^-$). Additionally, the dataset has allowed the search for rare Higgs boson decays such as $H \to \mu^+\mu^-$ and $H \to Z\gamma$.

The SMEFT interpretation of the Higgs boson STXS measurements from $H \to \gamma\gamma$, $H \to ZZ^* \to 4l$, and $VH, H \to b\bar{b}$ provided a first opportunity to constrain the Higgs sector of the SMEFT and resulted in a constraint of ten parameters in the SMEFT. The expanded interpretation of Higgs boson measurements to include the other main decay channels ($H \to \tau^-\tau^+$,$H \to WW^* \to l\nu l\nu$) and rare Higgs boson decay channels ($H \to \mu^+\mu^-$ and $H \to Z\gamma$) increases the number of constrained SMEFT parameters from 10 to 19 in the SMEFT. Although no significant deviation from the Standard Model is observed, these 19 parameters allow excluding scale of new physics varying from ~300 GeV to ~15 TeV, depending on the parameters.

SMEFT effects are not limited to Higgs boson measurements but are also expected to affect measurements of other physics sectors. A SMEFT interpretation of the Higgs boson production measured in the $H \to WW^* \to l\nu l\nu$ channel is combined with the kinematic distribution of the leading-lepton transverse momentum in the production of two W bosons in the $pp \to WW \to l\nu l\nu$ channel. The combined interpretation of these two analyses results in a constraint on eight SMEFT parameters. A combination of the Higgs boson measurements with the electroweak sector measurements from ATLAS, LEP, and SLD shows the utility of the SMEFT as a global framework. The global fit is sensitive to twenty-eight parameters.

While SMEFT has become the standard procedure for interpreting measurements performed at the LHC, no significant deviations from the SM were observed with current data. Many exciting future extensions in both the experimental and theoretical front will need to be addressed in the coming years to ensure that the full potential of the SMEFT is achieved. For example, the SMEFT fits presented in the thesis do not yet consider CP-odd operators, as the observables considered are not sensitive to the interference of CP-odd operators with the Standard Model

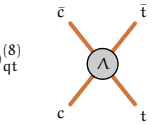

operators. Future measurements of angular observable distributions will provide an opportunity for angular observables to constrain CP-odd operators. Furthermore, the difference in the constraints of the dimension-6 operators with and without quadratic contributions occurring at order Λ^{-4} indicate that the relevance of dimension-8 operators is not negligible and must be accounted for in future fits. This would require developments on the theoretical front to have dimension-8 predictions. For all fits presented in the thesis, the SMEFT parameters are considered primarily for the signal process and not yet for the background processes. In the SMEFT framework, background processes are also affected by operators, so it is necessary to expand the analysis strategy to consider the effects of SMEFT on background processes. Current SMEFT interpretations are performed on measurements that are not specifically optimized for SMEFT operator sensitivity but rather for cross-section measurements. As many SMEFT operators only introduce subtle distortions in differential distributions, this strategy focused on cross-sections can be very suboptimal, and new *ab initio* designs of measurements, based on multivariate classifiers that consider the full kinematic information available in the event, can significantly increase experimental sensitivity. Guidance from global fits can furthermore help the design of new measurements to specifically target the weakly constrained directions in the global parameter space.

The global fit presented in the thesis is limited to the Higgs boson and electroweak sector. The global fit can be expanded to di-boson measurements that utilize the full Run-2 dataset, measurements of on-shell and off-shell Drell–Yan production at the LHC, measurements of top quark production, and additional measurements from the LEP collider. It is helpful to perform these large-scale fits within collaborations with detailed knowledge of the individual measurements. This allows to perform a consistent combination where overlap in measurements is identified and resolved either through orthogonalization of correlation modeling with bootstrap methods, and making combined interpretation models that feature a detailed and robust modeling of correlated systematic uncertainties.

Finally, SMEFT serves as an interface to UV-complete theories, and there have been steady theoretical developments in the matching of SMEFT to UV-complete theories in terms of automated tools [311]. Conversely, information in the SMEFT parameter space can be mined to inform the viability of possible theoretical extensions to the Standard Model.

While the current SMEFT results are primarily dominated by statistical uncertainties, the twenty times larger dataset of the HL-LHC, with 3000 fb^{-1} at the HL-LHC will allow to probe the SMEFT parameter space with unprecedented precision. In the longer-term future, e^+e^- colliders operating as Higgs factories will offer significantly improved measurement of Higgs boson decays are limited by systematic effects at the LHC, such as $H \to b\bar{b}$ and $H \to c\bar{c}$, due to limiting difficulties identifying their signature in a hadronic collider environment. Their additional ability

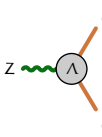

O_{dB}

to precisely constrain the Z boson line shape will further strengthen the global SMEFT program to constrain the electroweak sector of Nature [312].

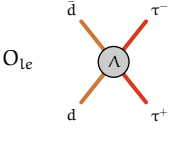

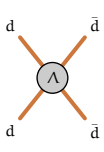

$O^{(1)}_{d\bar{d}}$

Summary

Across civilizations and over thousands of years, humans have been fascinated by the fundamental building blocks of Nature. This fascination has driven a quest to unveil the profound truths that shape the fabric of our reality. The current description of fundamental particles and their interactions is given by the Standard Model of Particle Physics (SM). However, the Standard Model itself is widely regarded as a stepping stone in the quest for a fundamental understanding of Nature. This thesis presents novel interpretations of the data collected by the ATLAS experiment during the Run-2 of the Large Hadron Collider (LHC) at CERN to extend the Standard Model by considering the effects of New Physics present at higher energies than those accessible by the LHC.

Separation of scales: Nature is Effective

An architect does not need to use quantum mechanics to understand the precise nature of how atoms in a material interact to build a bridge. Instead, without worrying about the microscopic details of the material, the architect needs to know the bulk properties of the materials used to build a bridge. How is it possible that the architect can build a bridge without estimating how the atoms constituting the material interact? This simple example illustrates the behavior of separation of scales in the physical world. This separation of scale allows for a process called *decoupling* - where the dynamics occurring at larger distances are decoupled from the underlying dynamics at smaller distances. The *effective principle* states that the dynamics at the relevant length scale can be described without knowing the underlying dynamics at a different scale.

The effective principle is also a powerful way of bettering our understanding of fundamental particle physics. The theory of the Standard Model, with its origins extending back a century, has developed hand-in-hand with the experimental advancements in particle physics. In the study of fundamental particles, accessing higher energies allows the study of physics at smaller distances, where the LHC is the most energetic particle collider to date with a center-of-mass energy of 13 TeV. An important milestone of the LHC is the discovery of the Higgs boson with a mass of 125 GeV in 2012 by the ATLAS and CMS collaborations. The Higgs boson explains the origin of the mass of elementary particles. While it is not known today if other elementary particles exist at higher energies, the effective principle

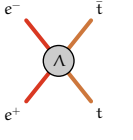

not only allows to understand why the Standard Model behaves so well at the energy scale of the LHC but also provides a way to look for the footprints of these yet-to-be-discovered particles in the ATLAS experiment. Before delving into how to go beyond the Standard Model, let us step back and go before the Standard Model to look at an instance of the effective principle at work in particle physics.

Before the Standard Model: The Fermi theory of weak interactions

In 1933, Enrico Fermi proposed a theory to explain β-decay, which involved the decay of an atomic nucleus into a β-particle (an electron or a positron) and an atom containing the same number of nucleons. Fermi theory prescribes a point-like interaction between the proton (p^+), neutron (n), electron (e^-), and anti-neutrino ($\bar{\nu}_e$), mediated by a coupling with strength G_F known as the Fermi constant. The theory was successful in explaining the experimental properties of nuclear decay rates and the distributions of the kinematic properties for measurements performed at a similar energy scale.

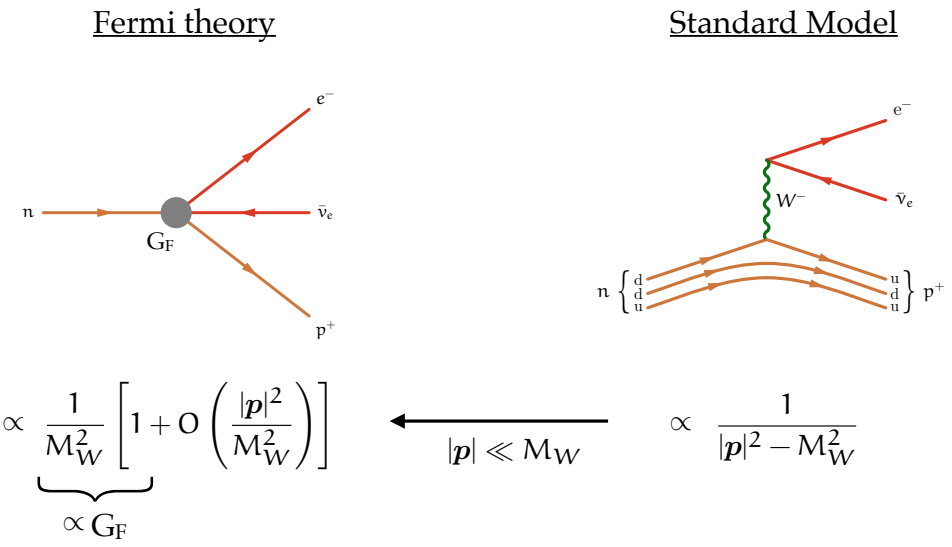

Figure 11.1: Feynman diagram of the neutron β-decay in Fermi theory and the Standard Model. The rate contribution of this process corresponding to the Fermi constant in Fermi theory is the first low-energy approximation of the Standard Model contribution. The Fermi theory is valid when the momentum exchange, $|\boldsymbol{p}|$, is much smaller than the mass of the W boson (M_W).

Today, we know that the β-decay involves the fundamental constituents of the nucleons, the quarks, and it is mediated by the W boson. While Fermi theory ignored

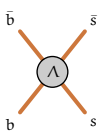

$O_{Qq}^{(3,1)}$

the presence of the W boson, it was still successful in explaining the experimental measurements. The success behind the Fermi theory was because the typical energy exchanged in these processes is much smaller than the W mass and affected the experimental measurements in a feeble manner, much smaller than the experimental precision. The effects sensitive to the more fundamental structure are suppressed by additional powers of $(|\boldsymbol{p}|/m_W) << 1$ and can thus be revealed only when the corrections can be reliably measured. Fifty years later, in 1983, the discovery of the W boson by the UA1 and UA2 collaborations at the CERN Sp$\bar{p}$S collider was a major milestone in unearthing the fundamental structure of the weak interactions. The Feynman diagrams of the process in the Fermi theory and the Standard Model are shown in Figure 11.1. Since the W boson discovery, further discoveries such as the top quark discovery in 1995, the τ-neutrino in 2001, and the Higgs boson in 2012 complete the known constituents of the Standard Model, as shown in Figure 11.2.

An Effective Approach for the Standard Model

The Standard Model provides a unified description of the strong and electroweak interactions. While it explains a wide range of experimental measurements, it is not without limitations. The Standard Model does not explain the origin of dark matter nor the matter-antimatter asymmetry in the universe, to name a few limitations.

It is not unreasonable to expect that the Standard Model is still an accurate description of Nature at even higher energies (smaller distances). Instead, the Standard Model itself can be viewed as a low-energy approximation to a yet-to-be-discovered fundamental theory. The more fundamental theory is expected to contain new heavy particles at a higher energy scale (Λ) that is unknown. The Standard Model can be considered the first term in a low-energy expansion of a more fundamental theory.

The Standard Model in itself does not contain information on the scale of new physics. Why does the Standard Model describe measurements at the LHC reasonably well? The bulk of the measurement rate of a typical Standard Model process typically occurs at the EWSB energy scale (Λ_{EW}). It corresponds to the momentum transfer in the bulk of the kinematic distribution. If the scale of new physics is larger than currently accessible by the LHC, the new physics effects are suppressed by a factor of (Λ_{EW}/Λ). It is, therefore, important to perform measurements that isolate the tails of kinematic distributions, which are enhanced by a factor of E/Λ. This behavior is sketched in Figure 11.3.

The low-energy effects of possible new physics are parametrized in an effective framework known as the Standard Model Effective Field Theory (SMEFT). All pos-

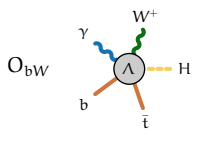

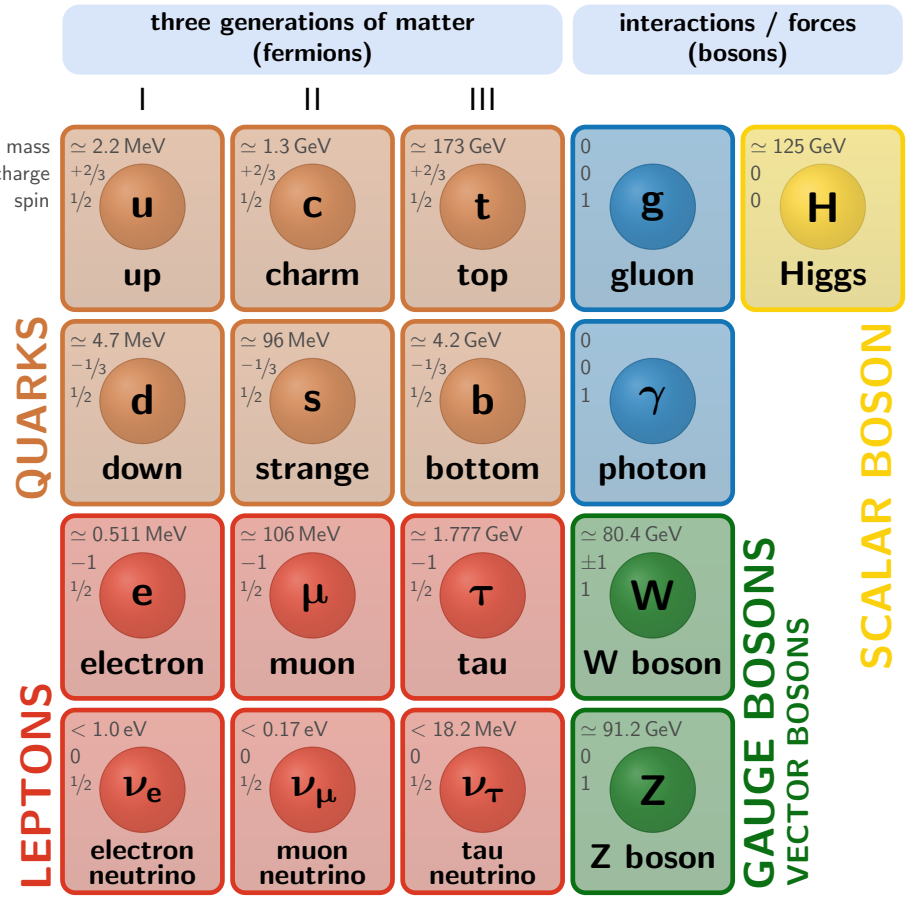

Figure 11.2: Particle content of the Standard Model of particle physics. Figure taken from [16].

sible interactions respecting experimentally well-established symmetries are considered. The new interactions are written as operators that are the footprints of a more fundamental physics manifest at the energy scale Λ. The operators are ordered by their energy dimension (d) and are suppressed accordingly by powers of $\Lambda^{(4-d)}$. The Standard Model does not contain information of Λ. The first leading correction is the lepton flavor violating dimension-5 operator, the Weinberg operator, responsible for giving masses to neutrinos. The small masses of the neutrinos (m_ν) correspond to a high scale of new physics at around 10^{13} GeV for this operator. The next group of operators in SMEFT, at dimension-6, comprises the leading operators that conserve lepton and baryon numbers. Introducing these operators leads instead to subtle deviations from the Standard Model in kinematic

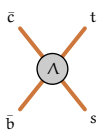

$O^{(1)}_{qQbd}$

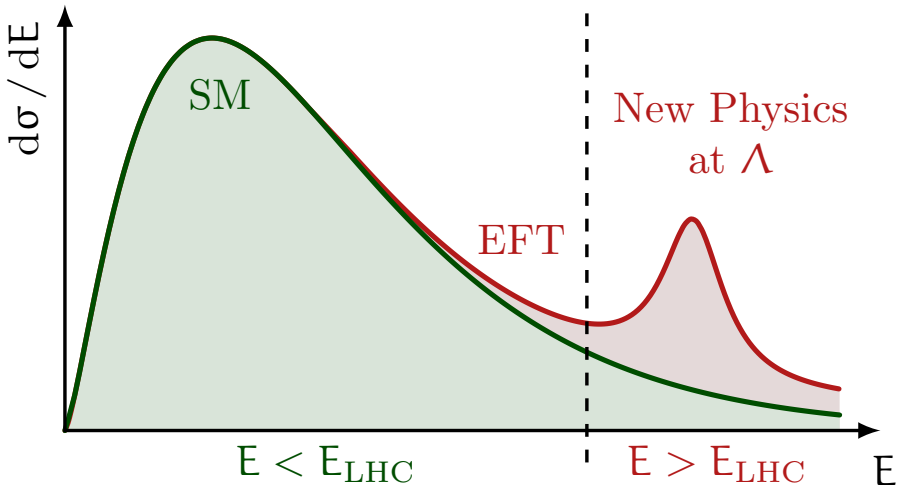

Figure 11.3: An Effective Field Theory (EFT) approach allows to extend the energy reach of the LHC and to look for New Physics that is too heavy to be directly produced at the LHC.

distributions, which indicate the presence of new physics at a higher energy scale, as shown in Figure 11.3.

It is important to note that the effective approach does not make any assumptions about the precise kind of new particles in the more fundamental theory beyond them existing at a very high energy scale. On the contrary, it provides a framework to capture the effects of the new particles from a wide range of possible fundamental theories. In this sense, the effective approach is, in principle, a model-agnostic approach and serves as a basis for capturing potential deviations from the Standard Model.

Constraining the Standard Model Effective Field Theory with the ATLAS experiment

The Standard Model Effective Field Theory (SMEFT) allows to extend the Standard Model by introducing new interactions involving only Standard Model particles that have direct, measurable effects, modifying (differential) cross-sections of one or more observable processes. For example, the process of gluon fusion production of the Higgs boson, with subsequent decay to four leptons, is sensitive to the effects of the operators O_{HG} and O_{He} through the Higgs boson production and decay vertex respectively, in addition to the contributions of multiple other

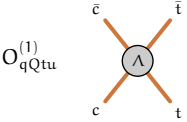

operators. The Feynman diagrams of this example process and their SMEFT contributions are shown in Figure 11.4.

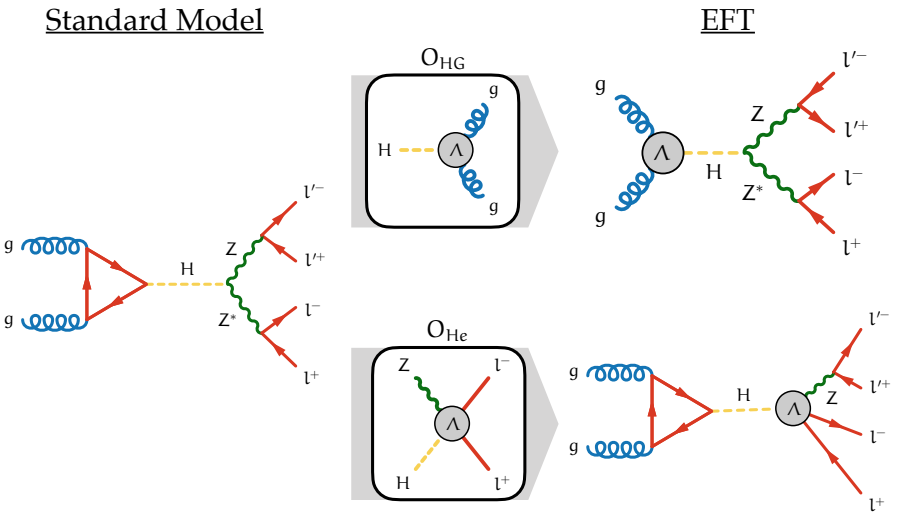

Figure 11.4: Feynman diagrams for the gluon fusion production of the Higgs boson decaying to four leptons showing the Standard Model contribution and the contribution from two operators O_{HG} and O_{He}.

It is important in the study of Higgs physics to choose observables that are sensitive to the effects of the SMEFT operators that can occur in the underlying amplitudes. Since the discovery of the Higgs boson in 2012, the study of the Higgs boson has expanded from an exploratory search to a detailed study of its kinematic properties. The large volume of data collected by the ATLAS experiment during the Run-2 of LHC between 2015-2018 at a center-of-mass energy of 13 TeV allows performing a comprehensive study of SMEFT operators by looking for the presence of their modifications in the observable distributions in the data. Additionally, combining measurements from different Higgs boson decay channels and production modes allows to constrain the effects of the operators by disentangling the effects of the operators affecting the production and decay of the Higgs boson.

Due to the large number of operators, the experimental sensitivity is not sufficient to constrain all possible operators affecting the currently available physics measurements. Thus, a subset of sensitive parameters that are linear combinations of SMEFT parameters is first identified based on the current experimental sensitivity of these measurements. The Run-2 dataset allows to perform a detailed test of the Higgs sector by constraining 19 parameters within the Higgs sector of the SMEFT, as shown in Figure 11.13.

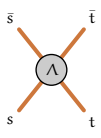

$O_{td}^{(1)}$

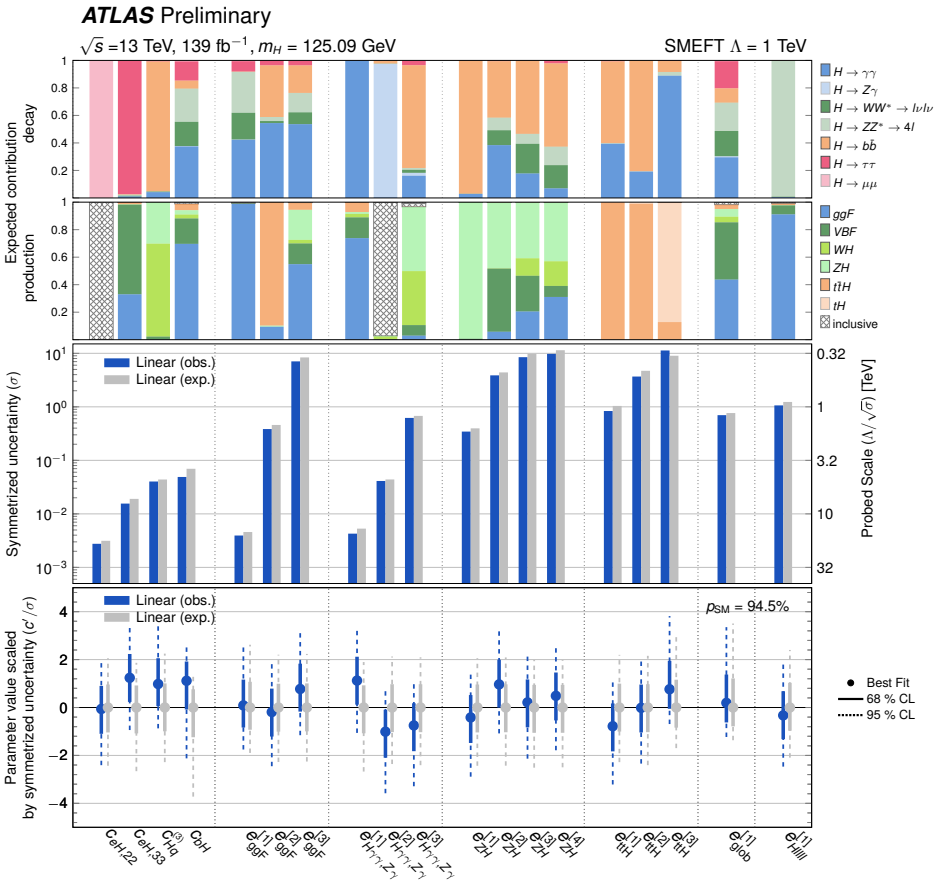

Figure 11.5: Constraints on the 19 sensitive parameters in the Higgs sector of the SMEFT from the ATLAS experiment. The top two rows depict the importance of the corresponding measurement in constraining the parameter. The third row shows the uncertainty of the different parameters and the corresponding energy reach of each parameter. The bottom row shows the deviation of the measured value from zero for each parameter, along with its confidence interval, both scaled with the uncertainty of the parameter.

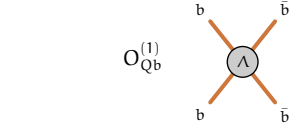

SMEFT effects are not limited to Higgs boson measurements but are expected to also consistently affect measurements of other physics sectors of the Standard Model. The experimental SMEFT program thus requires a global approach where measurements from all available physics sectors are considered. The electroweak (EW) sector of the SMEFT can already be probed with a rich set of measurements, including electroweak processes at the LHC, such as the di-boson production (WW, ZZ, WZ) and Z+jets. These measurements have been performed in the ATLAS experiment and are complemented with precision measurements of the Z boson performed at previous particle colliders, such as the Large Electron-Positron (LEP) collider and Stanford Linear Collider (SLC). Given the crucial role of the Higgs boson in EWSB, Higgs boson measurements are also sensitive to SMEFT operators occurring in the EW sector. The interplay of SMEFT operators across different physics processes is illustrated for operator $O_{Hq}^{(3)}$, which affects Higgs boson production, di-boson production, and Z boson production as shown in Figure 11.14. For consistent statistical treatment, overlap between measurements is identified and resolved through orthogonalization and the construction of combined interpretation models that feature a detailed and robust modeling of correlated systematic uncertainties.

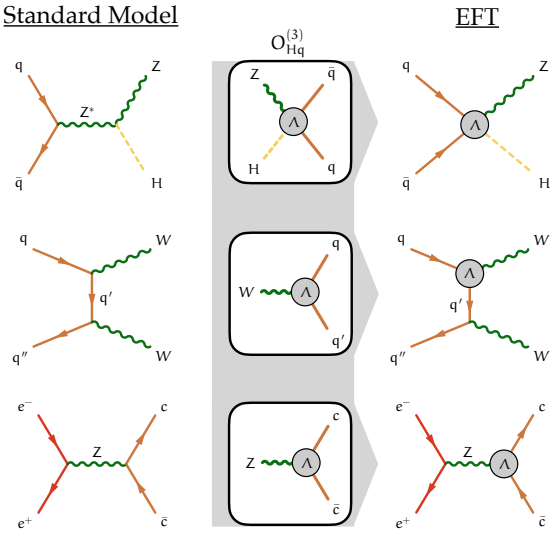

Figure 11.6: Feynman diagrams for the Higgs boson production in association with a weak boson, di-boson (WW) production, and Z boson production, and the EFT modification by operator $O_{Hq}^{(3)}$.

A global fit to the Higgs boson and electroweak measurements from the ATLAS experiment, and the electroweak precision observables from LEP/SLC allows to constrain the effects of 28 SMEFT parameters as shown in Figure 11.15.

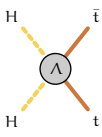

O_{tH}

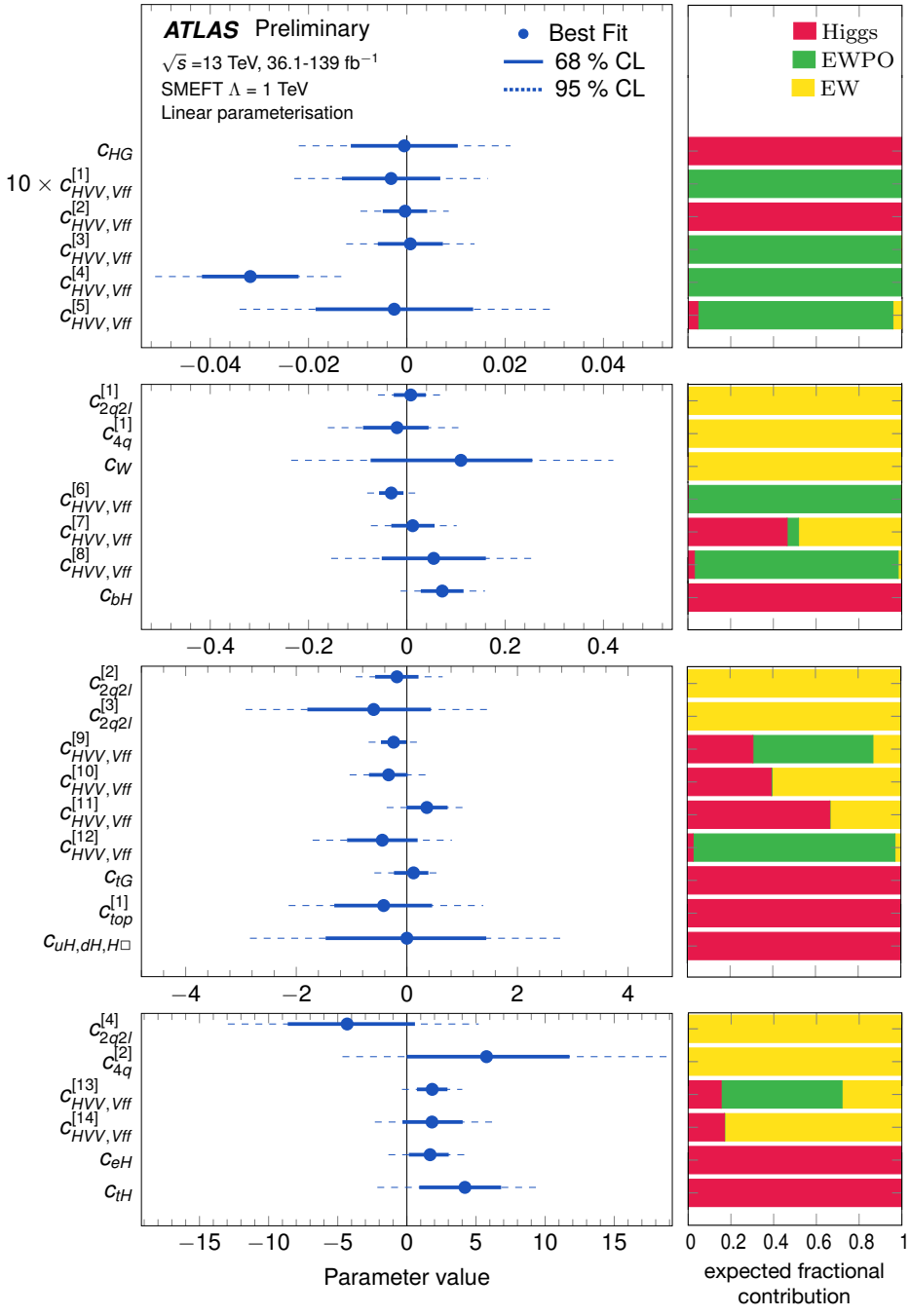

Figure 11.7: Constraints on the 28 sensitive parameters in the global fit. The right column shows the importance of the corresponding measurement in constraining the parameter, where Higgs (red) represents the ATLAS Higgs boson measurements, EW (yellow) denotes the ATLAS electroweak measurements, and EWPO (green) denotes the electroweak precision observables.

$O^{(1)}_{quQb}$

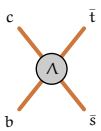

Matching SMEFT to specific models of New Physics

The SMEFT approach also serves as a framework for capturing information of experimental measurements that can be subsequently interpreted as constraints on specific New Physics theories that extend the Standard Model. In this sense, the SMEFT can be regarded as an intermediate language in testing experimental particle physics measurements against specific models of New Physics.

The SMEFT interpretation of the Higgs boson measurements is also used in this thesis to test the accuracy of the SMEFT as an interface to specific UV-complete theories. A popular UV-complete theory is the Two Higgs Doublet Model (2HDM), which extends the Higgs sector of the Standard Model by introducing an additional Higgs doublet field. The extension allows for richer phenomenology compared to the Standard Model, and the model can lead to interesting features such as CP violation, non-minimal Higgs boson spectra, non-universal couplings.

The constraints on 2HDM parameters, obtained from matching to constraints on SMEFT parameters constrained by ATLAS Run-2 Higgs measurements, are shown in Figure 11.16.

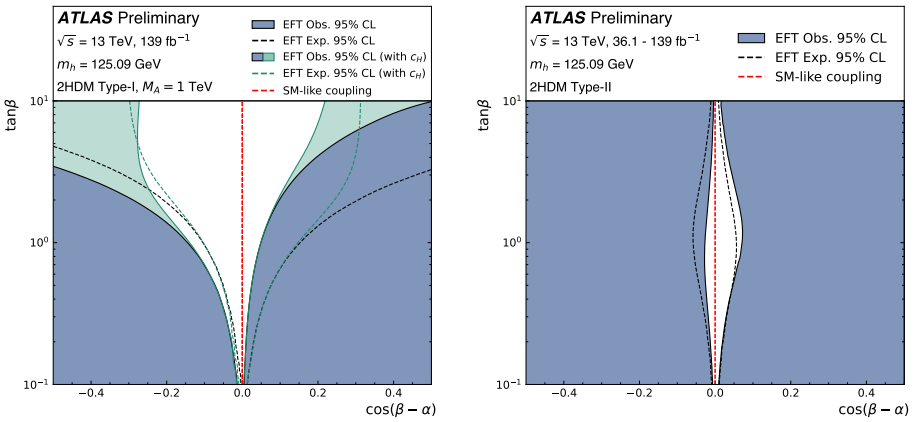

(a) (b)

Figure 11.8: Constraints on the 2HDM parameter plane ($\tan\beta$, $\cos(\beta-\alpha)$) excluded at 95% CL (blue-filled regions) in the matching of SMEFT to the 2HDM. The parameter $\tan\beta$ is the ratio of the vacuum expectation values of the two Higgs doublets, and α is the mixing of the neutral CP-even Higgs bosons. In the 2HDM Type-I case, the green region shows the additional constraint provided by the inclusion of the c_H parameter.

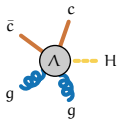

O_{uG}

Some operators will stand the test of time

While it is not known at the time of writing how Nature behaves at a more fundamental scale beyond the Standard Model, the effective principle guarantees that some operators will correspond to the footprints of a more fundamental description of Nature. The current experimental precision of measurements is not yet sufficient to uncover the presence of dimension-6 operators. However, a set of these operators will have a direct connection to a new understanding of how Nature behaves at the smallest distances.

An expanded global fit, including measurements from the top quark sector, flavor physics, and low-energy precision observables, will allow to extend the reach of the SMEFT program and constrain the effects of different SMEFT operators. Looking ahead, the data-rich regime at the LHC will grow rapidly with the high-luminosity LHC program, resulting in a 20x larger dataset than what is currently available today. With this rich dataset and advancement in analysis techniques, it is only a matter of time before the SMEFT allows to tease out subtle deviations from the Standard Model with data if such new physics exists at not too high energy scales. In that case, a select few of the operators depicted in the corners of this thesis will be effectively revealed as footprints of a more fundamental understanding of particle physics beyond the Standard Model.

O_{le}

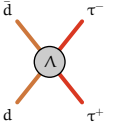

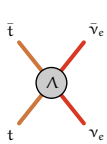

O_{lt}

Samenvatting

Door de eeuwen heen en over duizenden jaren heen zijn mensen gefascineerd geweest door de fundamentele bouwstenen van de natuur. Deze fascinatie heeft geleid tot een zoektocht naar het onthullen van de diepgaande waarheden die de canvas van onze realiteit vormgeven. De huidige beschrijving van fundamentele deeltjes en hun interacties wordt gegeven door de theorie van het Standaardmodel van de deeltjesfysica (SM). Het Standaardmodel zelf wordt echter algemeen beschouwd als een opstapje in de zoektocht naar een fundamenteel begrip van de natuur. Dit manuscript presenteert nieuwe interpretaties van de gegevens verzameld door het ATLAS experiment tijdens Run-2 van de Large Hadron Collider (LHC) bij CERN om het Standaardmodel uit te breiden door rekening te houden met de effecten van nieuwe natuurkunde die aanwezig is bij hogere energieën dan die toegankelijk zijn bij de LHC.

Scheiding van schalen: De Natuur is Effectief

Een architect hoeft geen gebruik te maken van de quantummechanica om de precieze aard te begrijpen van hoe atomen in een materiaal zich gedragen om een brug te bouwen. In plaats daarvan, zonder zich zorgen te maken over de microscopische details van het materiaal, moet de architect de bulk-eigenschappen van de materialen kennen die worden gebruikt om een brug te bouwen. Hoe is het mogelijk dat de architect een brug kan bouwen zonder de schatting te maken van hoe de atomen die het materiaal vormen, interageren? Dit eenvoudige voorbeeld illustreert het gedrag van de scheiding van schalen in de fysieke wereld. Deze scheiding van schalen maakt een proces genaamd ontkoppeling mogelijk - waarbij de dynamica die zich voordoet op grotere afstanden wordt ontkoppeld van de onderliggende dynamica op kleinere afstanden. Het *effectieve principe* stelt dat de dynamica op de relevante lengteschaal kan worden beschreven zonder de onderliggende dynamica op een andere schaal te kennen.

Het effectieve principe is ook een krachtige manier om ons begrip van de fundamentele deeltjesfysica te verbeteren. De theorie van het Standaardmodel, met zijn oorsprong die teruggaat tot een eeuw geleden, heeft zich parallel ontwikkeld met de experimentele vooruitgang in de deeltjesfysica. Bij de studie van fundamentele deeltjes maakt de toegang tot hogere energieën het mogelijk om de dynamica op kleinere afstanden te bestuderen, waarbij de LHC de meest energierijke deelt-

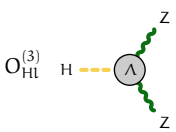

jesversneller is tot op heden, met een zwaartepuntenergie van 13 TeV. Een belangrijke mijlpaal van de LHC is de ontdekking van het higgsboson in 2012 door de ATLAS en CMS experimenten, met een massa van 125 GeV, wat de oorsprong van de massa van elementaire deeltjes verklaart. Hoewel vandaag de dag niet bekend is of andere elementaire deeltjes bestaan op hogere energieën, maakt het effectieve principe niet alleen begrijpelijk waarom het Standaardmodel zich zo goed gedraagt op de energieschaal van de LHC, maar biedt het ook een manier om te zoeken naar de sporen van deze nog te ontdekken deeltjes in het ATLAS experiment. Voordat we ingaan op hoe we voorbij het Standaardmodel kunnen gaan, laten we een stap terug doen en teruggaan naar vóór het Standaardmodel om een voorbeeld te bekijken van het effectieve principe in actie in de deeltjesfysica.

Vóór het Standaardmodel: de Fermi-theorie van zwakke interacties

In 1933 stelde Enrico Fermi een theorie voor om β-verval te verklaren, waarbij het verval van een atoomkern resulteert in een β-deeltje (een elektron of een positron) en een atoom met hetzelfde aantal nucleonen. Fermi-theorie schrijft een puntvormige interactie voor tussen het proton (p^+), neutron (n), elektron (e^-), en anti-neutrino ($\bar{\nu}_e$), bemiddeld door een koppeling met de sterkte G_F, bekend als de Fermi-constante. De theorie slaagde erin de experimentele eigenschappen van nucleaire vervalpercentages en de verdelingen van de kinematische eigenschappen te verklaren voordat metingen uitgevoerd op een vergelijkbare energieschaal.

Vandaag de dag weten we dat het β-verval de fundamentele bestanddelen van de nucleonen, de quarks, betreft en bemiddeld wordt door het W-boson. Hoewel de Fermi-theorie de aanwezigheid van het W-boson negeerde, was deze nog steeds succesvol in het verklaren van de experimentele metingen. Het succes van de Fermi-theorie kwam doordat de typische energie uitgewisseld in deze processen veel kleiner is dan de massa van het W-boson, en het de experimentele metingen op een zwakke manier beïnvloedde, veel kleiner dan de experimentele precisie. De effecten die gevoelig zijn voor de meer fundamentele structuur worden onderdrukt door extra machten van $(|\boldsymbol{p}|/m_W) << 1$ en kunnen dus alleen worden onthuld met een hoge experimentele resolutie. Vijftig jaar later, in 1983, was de ontdekking van het W-boson door de UA1- en UA2-samenwerkingen bij de CERN SpP̄S-collider een belangrijke mijlpaal in het blootleggen van de fundamentele structuur van de zwakke interacties. De feynmandiagrammen van het proces in de Fermi-theorie en het Standaardmodel worden getoond in Figuur 11.9. Sinds de ontdekking van het W-boson zijn er verdere ontdekkingen gedaan, zoals de ontdekking van het topquark in 1995, het τ-neutrino in 2001, en het higgsboson

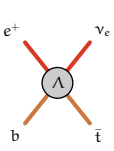

$O^{(1)}_{leQt}$

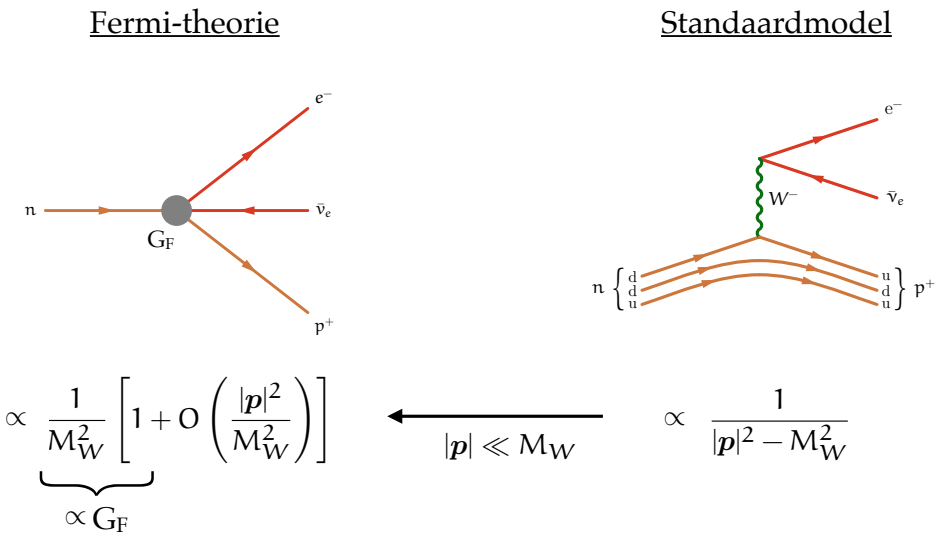

Figure 11.9: Feynmandiagram van het neutron β-verval in de Fermi-theorie en het Standaardmodel. De bijdrage van dit proces overeenkomend met de Fermi-constante in de Fermi-theorie is de eerste lage-energiebenadering van de bijdrage van het Standaardmodel. De Fermi-theorie is geldig wanneer de impulsuitwisseling, $|\boldsymbol{p}|$ veel kleiner is dan de massa van het W-boson (M_W).

in 2012, die het huidige begrip van de deeltjesinhoud van het Standaardmodel completeren, zoals te zien is in Figuur 11.10.

Een Effectieve Benadering voor het Standaardmodel

Het Standaardmodel biedt een verenigde beschrijving van de sterke en elektrozwakke interacties. Hoewel het een breed scala aan experimentele metingen verklaart, heeft het zijn beperkingen. Het Standaardmodel verklaart niet de oorsprong van donkere materie noch de materie-antimaterie-asymmetrie in het universum, om er slechts een paar te noemen.

Het is niet onredelijk om te verwachten dat het Standaardmodel geen nauwkeurige beschrijving van de natuur meer is bij nog hogere energieën (kleinere afstanden). Daarom kan het Standaardmodel zelf worden beschouwd als een benadering op lage energie van een nog te ontdekken fundamentele theorie. Men verwacht dat de meer fundamentele theorie nieuwe zware deeltjes bevat op een hogere energieschaal (Λ) die onbekend is. Het Standaardmodel kan worden beschouwd als het eerste term in een lage-energie-beschrijving van een meer fundamentele theorie.

Het Standaardmodel bevat op zichzelf geen informatie over de schaal van nieuwe natuurkunde. Waarom beschrijft het Standaardmodel metingen bij de LHC redelijk

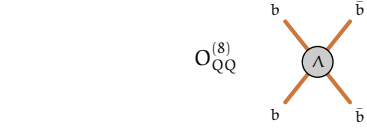

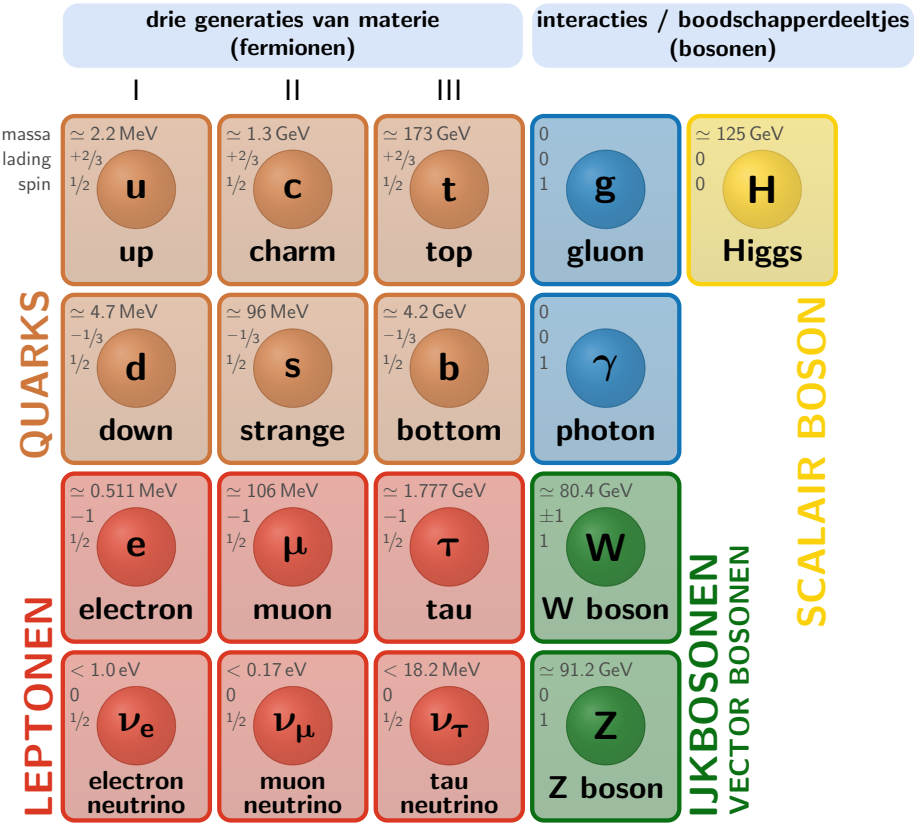

Figure 11.10: De deeltjesinhoud van het Standaardmodel van de deeltjesfysica. Figuur overgenomen van [16].

goed? Het grootste deel van de meetwaarschijnlijkheid van een typisch Standaardmodelproces doet zich typisch voor bij de energieschaal van elektrozwakke symmetriebreking (Λ_{EW}) en komt overeen met de impulsuitwisseling in het grootste deel van de kinematische verdeling. Als de schaal van nieuwe natuurkunde groter is dan momenteel toegankelijk is door de LHC, worden de effecten van nieuwe natuurkunde onderdrukt met een factor (Λ_{EW}/Λ). Het is daarom belangrijk om metingen uit te voeren die de staarten van de kinematische verdelingen isoleren, die worden versterkt met een factor E/Λ. Dit gedrag is geschetst in Figuur 11.11.

De laag-energetische effecten van mogelijke nieuwe natuurkunde worden geparametriseerd in een effectief kader dat bekend staat als de Standaard Model Effectieve Veldentheorie (SMEFT). Alle mogelijke interacties die experimenteel goed gevestigde symmetrieën respecteren, worden meegenomen. De nieuwe interacties worden geschreven als operatoren die de voetafdrukken zijn van een meer funda-

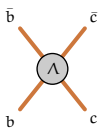

$O_{bq}^{(8)}$

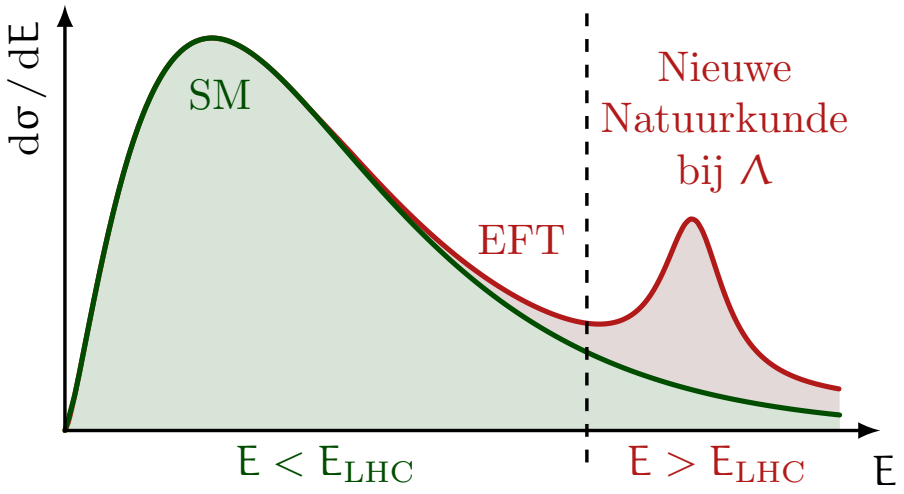

Figure 11.11: Een benadering met Effectieve Veldentheorie (EFT) maakt het mogelijk om het energiebereik van de LHC uit te breiden en op zoek te gaan naar Nieuwe Natuurkunde die te zwaar is om rechtstreeks bij de LHC te worden geproduceerd.

mentele natuurkunde die zich manifesteert op de energieschaal Λ. De operatoren zijn geordend naar hun energiedimensie (d) en worden dienovereenkomstig onderdrukt door machten van $\Lambda^{(4-d)}$. Het Standaardmodel bevat geen informatie over Λ. De eerste leidende correctie is de dimensie-5 operator die leptonflavorverval mogelijk maakt en bestaat uit één operator, de Weinberg-operator, die verantwoordelijk is voor het geven van massa aan neutrino's. De kleine massa's van de neutrino's (m_ν) komen overeen met een hoge schaal van nieuwe natuurkunde rond de 10^{13} GeV voor deze operator. De volgende groep operatoren in SMEFT, op dimensie-6, zijn de leidende operatoren die lepton- en baryonaantal behouden. De introductie van deze operatoren leidt eerder tot subtiele afwijkingen van het Standaardmodel in kinematische verdelingen, die wijzen op de aanwezigheid van nieuwe natuurkunde op een hogere energieschaal, zoals getoond in Figuur 11.3.

Het is belangrijk op te merken dat de effectieve benadering geen aannames maakt over het precieze soort nieuwe deeltjes in de meer fundamentele theorie, behalve dat ze bestaan op een zeer hoge energieschaal. Integendeel, het biedt een kader om de effecten van de nieuwe deeltjes vast te leggen vanuit een breed scala van mogelijke fundamentele theorieën. In dit opzicht is de effectieve benadering in principe een model-agnostische benadering en dient als basis voor het vastleggen van mogelijke afwijkingen van het Standaardmodel.

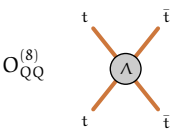

Limieten in Effectieve Veldentheorie van het Standaardmodel met het ATLAS experiment

De Effectieve Veldentheorie van het Standaardmodel (SMEFT) maakt het mogelijk om het Standaardmodel uit te breiden door nieuwe interacties in te voeren die alleen betrekking hebben op de deeltjes van het Standaardmodel en die direct meetbare effecten hebben. Dit resulteert in aanpassingen aan (differentiële) werkzame doorsnedes van één of meer waarneembare processen. Bijvoorbeeld het proces van gluonfusieproductie van het higgsboson, gevolgd door verval tot vier leptonen, is gevoelig voor de effecten van operator O_{HG} en operator O_{He}, via respectievelijk het productie- en vervalvertex, naast de bijdragen van meerdere andere operatoren. De feynmandiagrammen van dit voorbeeldproces en hun SMEFT bijdragen worden getoond in Figuur 11.12.

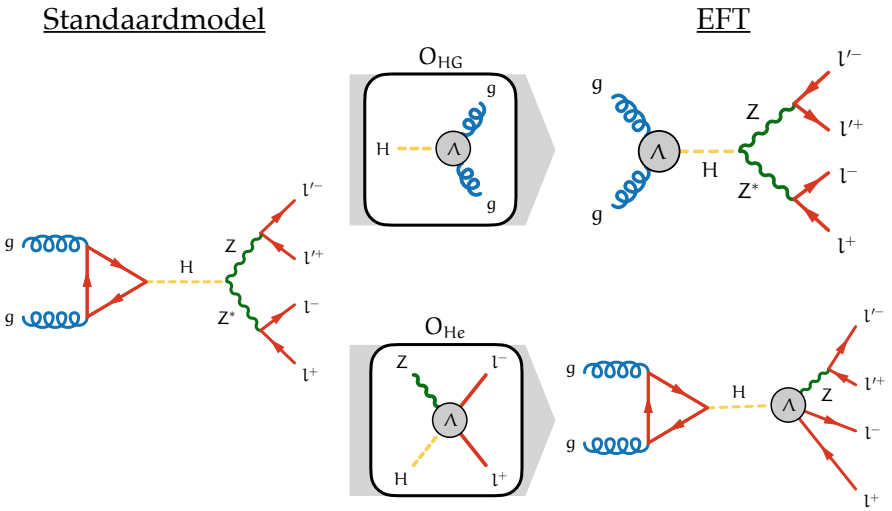

Figure 11.12: Feynmandiagrammen voor de gluonfusieproductie van het higgsbosonverval naar vier leptonen, met de bijdrage van zowel het Standaardmodel als de bijdrage van de operatoren O_{HG} en O_{He}.

Bij de studie van higgsfysica is het belangrijk om observabelen te kiezen die gevoelig zijn voor de effecten van de SMEFT operatoren die zich kunnen voordoen in de onderliggende amplitudes. De grote hoeveelheid gegevens verzameld door het ATLAS experiment tijdens Run-2 van de LHC tussen 2015-2018 bij een zwaartepuntenergie van 13 TeV maakt een uitgebreide studie van SMEFT operatoren mogelijk, door te zoeken naar de aanwezigheid van hun wijzigingen in de waarneembare verdelingen in de gegevens.

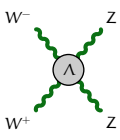

$O_{\widetilde{W}}$

Sinds de ontdekking van het higgsboson in 2012 is de studie van het higgsboson uitgebreid van een verkennende zoektocht naar een gedetailleerde studie van zijn kinematische eigenschappen. Bovendien maakt het combineren van metingen uit verschillende higgsbosonvervalkanalen en productiemodi het mogelijk om de effecten van de operatoren te limiteren door de effecten van de operatoren die van invloed zijn op de productie en het verval van het higgsboson te ontwarren.

Vanwege het grote aantal operatoren is de experimentele gevoeligheid niet voldoende om alle mogelijke operatoren die de momenteel beschikbare fysieke metingen beïnvloeden, te limiteren. Daarom wordt eerst een subset van gevoelige parameters geïdentificeerd, lineaire combinaties van SMEFT parameters, op basis van de huidige experimentele gevoeligheid van deze metingen. De dataset van Run-2 maakt een gedetailleerde test van de higgssector mogelijk door 19 parameters binnen de higgssector van de SMEFT te bepalen, zoals getoond in Figuur 11.13.

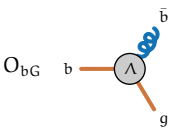

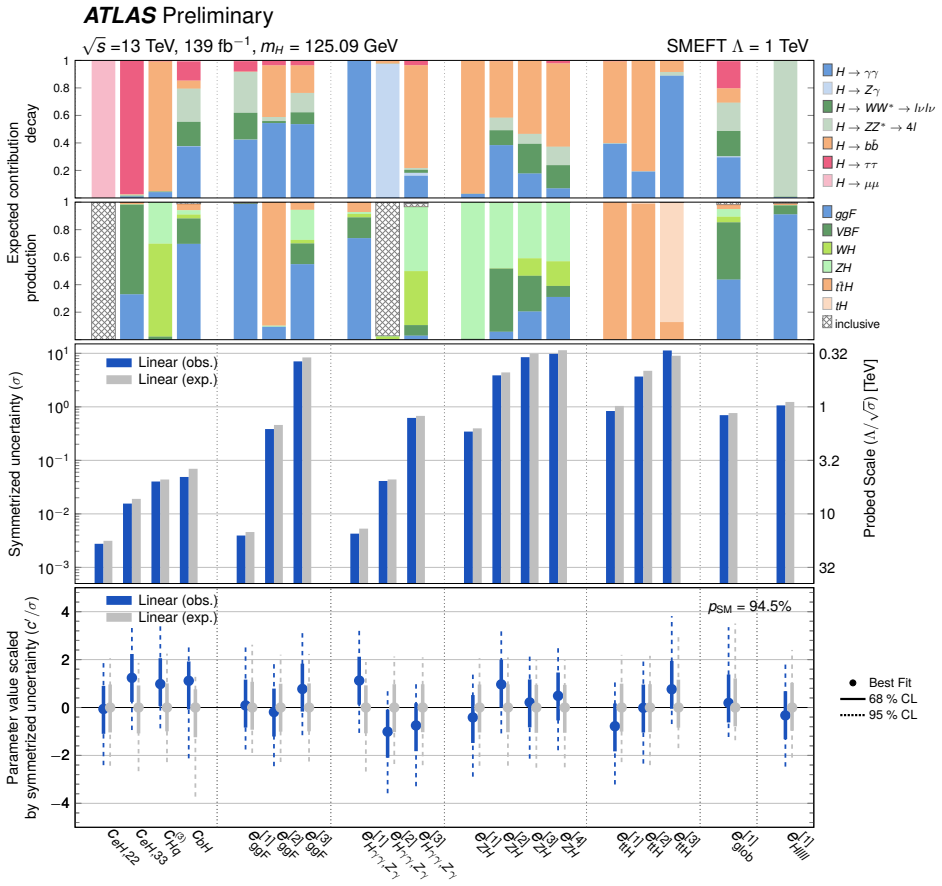

Figure 11.13: Limieten op de 19 gevoelige parameters in de higgssector van de SMEFT van het ATLAS experiment. De bovenste twee rijen tonen de belangrijkheid van de bijbehorende meting bij het beperken van de parameter. De derde rij toont de onzekerheid van de verschillende parameters en het bijbehorende energiebereik van elke parameter. De onderste rij toont de afwijzing ten opzicht van nul van de gemeten waarde van elke parameter, en het bijbehorende betrouwbaarheidsinterval, beide geschaald met de meetonzekerheid.

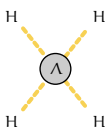

O_{HD}

SMEFT effecten zijn niet beperkt tot metingen van het higgsboson, maar worden ook verwacht consistent invloed te hebben op metingen van andere fysieke sectoren van het Standaardmodel. Het experimentele SMEFT programma vereist daarom een globale aanpak waarbij metingen van alle beschikbare fysieke sectoren worden overwogen. De elektrozwakke (EW) sector van de SMEFT kan al worden onderzocht met een rijke set aan metingen, waaronder elektrozwakke processen bij de LHC, zoals dibosonproductie (WW, ZZ, WZ) en Z+jets. Deze metingen zijn uitgevoerd in het ATLAS experiment en worden aangevuld met precisiemetingen aan het Z-boson uitgevoerd bij eerdere deeltjesversnellers zoals de Large Electron-Positron (LEP) collider en Stanford Linear Collider (SLC). Gezien de cruciale rol van het higgsboson in EWSB, zijn metingen van het higgsboson ook gevoelig voor SMEFT operatoren die voorkomen in de EW-sector. De wisselwerking van SMEFT operatoren tussen verschillende natuurkundige processen wordt geïllustreerd voor operator $O_{Hq}^{(3)}$, die van invloed is op de productie van het higgsboson, di-bosonproductie en Z-bosonproductie, zoals getoond in Figuur 11.14.

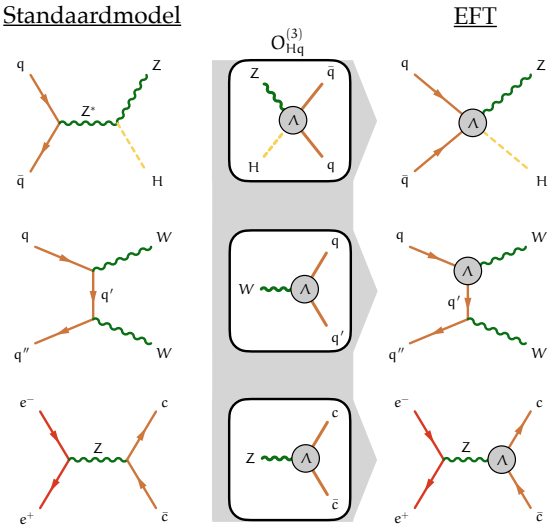

Figure 11.14: feynmandiagrammen voor de productie van het higgsboson in samenhang met een zwak boson, di-boson (WW)-productie en Z-bosonproductie en de EFT-modificatie door operator $O_{Hq}^{(3)}$.

Een globale fit aan de metingen van het higgsboson en de metingen van de elektrozwakke sector van het ATLAS experiment en de elektrozwakke precisieobservaties van LEP/SLC stelt ons in staat om de effecten van 28 SMEFT parameters te beperken, zoals getoond in Figuur 11.15.

$O_{qq}^{(3,8)}$ 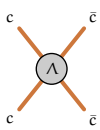

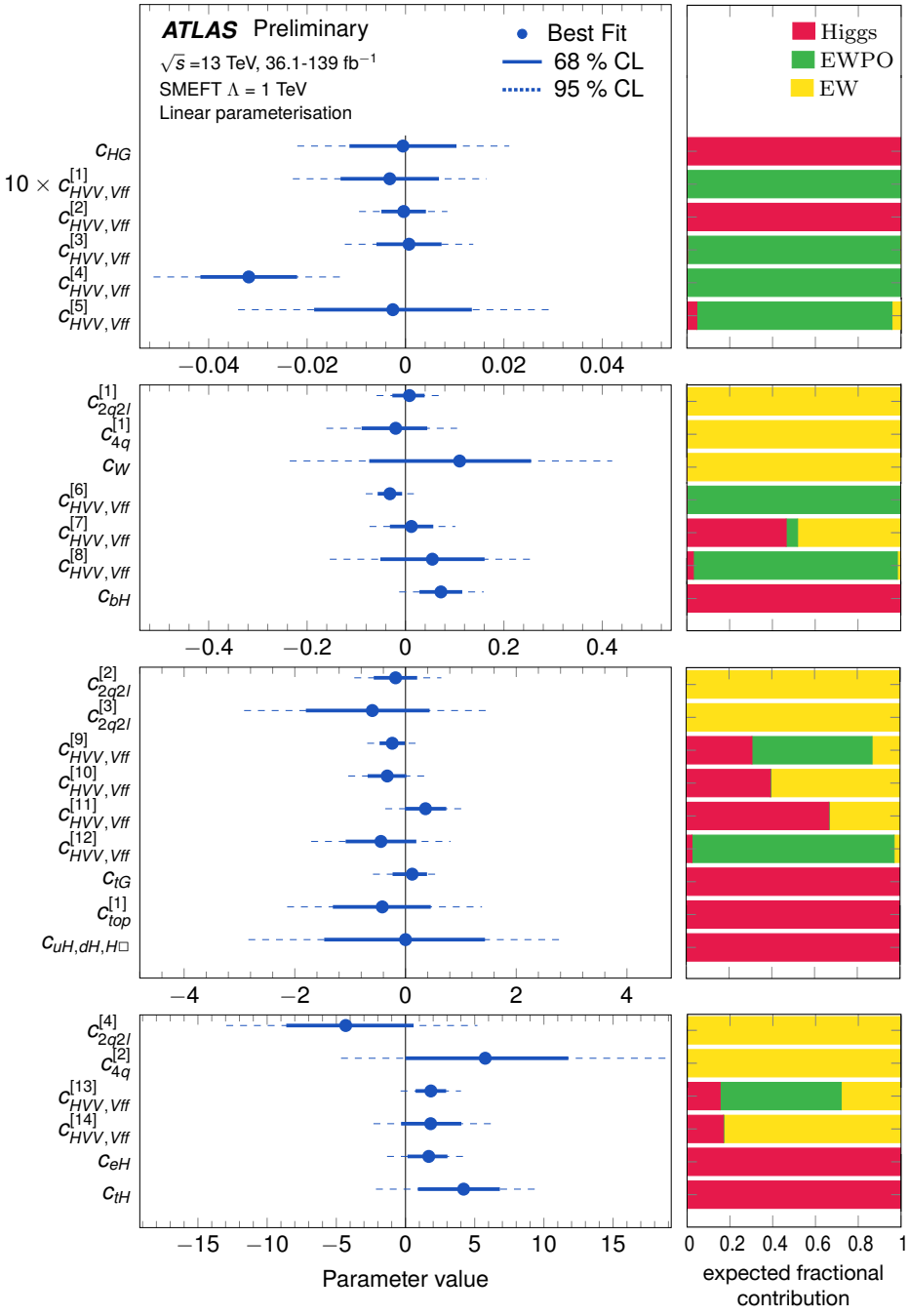

Figure 11.15: Limieten op de 28 gevoelige parameters in de globale fit. De rechterkolom toont het gewicht van de bijbehorende meting bij het limiteren van de parameter, waarbij higgs (rood) de metingen van het higgsboson van ATLAS voorstellen, EW (geel) de ATLAS elektrozwakke metingen voorstellen en EWPO (groen) de elektrozwakke precisieobservaties voorstellen.

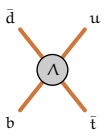

$O^{(8)}_{utbd}$

Afstemming van SMEFT op specifieke modellen van Nieuwe Natuurkunde

De SMEFT benadering dient ook als een kader om informatie vast te leggen van experimentele metingen die vervolgens geïnterpreteerd kunnen worden als beperkingen op specifieke nieuwe natuurkundige theorieën die het Standaardmodel uitbreiden. In deze zin kan de SMEFT worden beschouwd als een tussenliggende taal bij het testen van experimentele deeltjesfysicametingen aan specifieke modellen van Nieuwe Natuurkunde.

De SMEFT interpretatie van metingen van het higgsboson wordt ook gebruikt in dit proefschrift om de nauwkeurigheid van de SMEFT als een *interface* naar specifieke UV-volledige theorieën te testen. Een populaire UV-volledige theorie is het Twee-higgs-doublet (2HDM) model, dat de higgsbosonsector van het Standaardmodel uitbreidt door een extra higgsdoubletveld in te voeren. Deze uitbreiding zorgt voor een rijkere fenomenologie in vergelijking met het Standaardmodel, en het model kan leiden tot interessante kenmerken zoals CP-schending, niet-minimale higgsbosonspectra, niet-universele koppelingen.

De limieten op de parameters van het 2HDM, verkregen uit de overeenkomst met limieten op SMEFT parameters beperkt door ATLAS Run-2 higgsmetingen, worden getoond in Figuur 11.16.

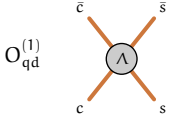

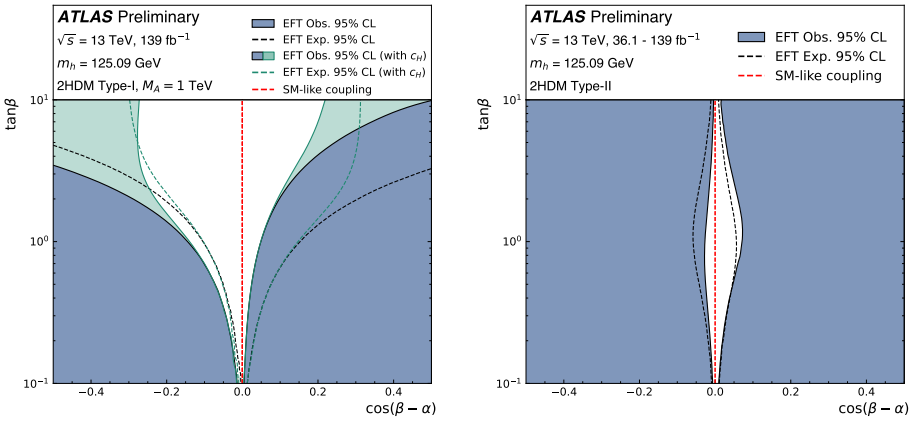

(a) (b)

Figure 11.16: limieten in het parametervlak van het 2HDM ($\tan\beta$, $\cos(\beta-\alpha)$) uitgesloten met 95% betrouwbaarheidsniveau (blauw gevulde gebieden) in de overeenkomst van SMEFT met het 2HDM. De parameter $\tan\beta$ is de verhouding van de vacuümverwachtingswaarden van de twee higgsdoubletten en α is de menging van de neutrale CP-even higgsbosonen. In het geval van het 2HDM Type-I, toont het groene gebied de aanvullende beperking die wordt geboden door de opname van de parameter c_H.

Sommige operatoren zullen de tand des tijds doorstaan

Hoewel het op het moment van schrijven niet bekend is hoe de Natuur zich gedraagt op een meer fundamentele schaal dan het Standaardmodel, garandeert het effectieve principe dat sommige operatoren overeenkomen met de kenmerken van een meer fundamentele beschrijving van de Natuur. De huidige experimentele precisie van metingen is nog niet voldoende om de aanwezigheid van dimensie-6 operatoren bloot te leggen. Echter, een reeks van deze operatoren zal een directe verbinding hebben met een nieuw begrip van hoe de Natuur zich gedraagt op de kleinste afstanden.

Een uitgebreide globale fit, inclusief metingen uit de topquarksector, *flavor*-fysica, en laag-energetische precisieobservaties, zal de reikwijdte van het SMEFT programma vergroten en de effecten van verschillende dimensie-6 operatoren beperken. Vooruitkijkend zal het datarijke regime bij de LHC snel groeien met het high-luminosity LHC-programma, wat resulteert in een dataset die 20 keer groter is dan wat momenteel beschikbaar is. Met deze rijke dataset en de vooruitgang in analysemethoden is het slechts een kwestie van tijd voordat het SMEFT subtiele afwijkingen van het Standaardmodel met data kan onthullen, als dergelijke nieuwe

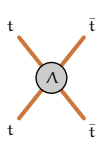

O_{tt}

fysica bestaat op niet al te hoge energieniveaus. In dat geval zullen enkele geselecteerde operatoren, afgebeeld in de hoeken van dit proefschrift, waarschijnlijk effectief worden onthuld als sporen van een dieper begrip van de deeltjesfysica dan het Standaardmodel.

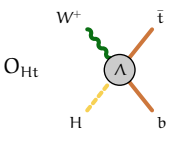

Bibliography

[1] G. Aad et al., *Observation of a new particle in the search for the Standard Model Higgs boson with the ATLAS detector at the LHC*, Phys. Lett. B **716** (2012) 1, arXiv: 1207.7214 [hep-ex] (cit. on p. 1).

[2] S. Chatrchyan et al., *Observation of a New Boson at a Mass of 125 GeV with the CMS Experiment at the LHC*, Phys. Lett. B **716** (2012) 30, arXiv: 1207.7235 [hep-ex] (cit. on p. 1).

[3] I. Brivio and M. Trott, *The Standard Model as an Effective Field Theory*, Phys. Rept. **793** (2019) 1, arXiv: 1706.08945 [hep-ph] (cit. on pp. 2, 25).

[4] R. Balasubramanian, C. Burgard, and W. Verkerke, *Effective Lagrangian Morphing*, (2022), arXiv: 2202.13612 [physics.data-an] (cit. on pp. 3, 91, 105–113).

[5] *Interpretations of the combined measurement of Higgs boson production and decay*, (2020) (cit. on p. 3).

[6] *Interpretations of the ATLAS measurements of Higgs boson production and decay rates and differential cross-sections in* pp *collisions at* $\sqrt{s} = 13$ *TeV*, tech. rep., All figures including auxiliary figures are available at https://atlas.web.cern.ch/Atlas/GROUPS/PHYSICS/CONFNOTES/ATLAS-CONF-2023-052: CERN, 2023, URL: https://cds.cern.ch/record/2870216 (cit. on pp. 3, 4).

[7] *Combined effective field theory interpretation of* $H \to WW^*$ *and WW measurements using ATLAS data*, tech. rep., All figures including auxiliary figures are available at https://atlas.web.cern.ch/Atlas/GROUPS/PHYSICS/PUBNOTES/ATL-PHYS-PUB-2021-010: CERN, 2021, URL: https://cds.cern.ch/record/2758785 (cit. on p. 3).

[8] *Combined effective field theory interpretation of Higgs boson and weak boson production and decay with ATLAS data and electroweak precision observables*, tech. rep., All figures including auxiliary figures are available at https://atlas.web.cern.ch/Atlas/GROUPS/PHYSICS/PUBNOTES/ATL-PHYS-PUB-2022-037: CERN, 2022, URL: https://cds.cern.ch/record/2816369 (cit. on p. 4).

[9] A. Einstein, *Die Grundlage der allgemeinen Relativitätstheorie*, Annalen der Physik **354** (1916) 769 (cit. on pp. 5, 19).

[10] F. Halzen and A. D. Martin, *QUARKS AND LEPTONS: AN INTRODUCTORY COURSE IN MODERN PARTICLE PHYSICS*, 1984, ISBN: 978-0-471-88741-6 (cit. on p. 5).

[11] M. Thomson, *Modern Particle Physics*, Cambridge University Press, 2013 (cit. on p. 5).

[12] D. J. Griffiths, *Introduction to elementary particles; 2nd rev. version*, Physics textbook, New York, NY: Wiley, 2008, URL: https://cds.cern.ch/record/111880 (cit. on p. 5).

[13] M. E. Peskin and D. V. Schroeder, *An Introduction to Quantum Field Theory*, Reading, USA: Addison-Wesley (1995) 842 p, Westview Press, 1995 (cit. on p. 5).

[14] P. A. M. Dirac, *The quantum theory of the electron*, Proc. Roy. Soc. Lond. A **117** (1928) 610 (cit. on p. 6).

[15] E. Majorana, *Teoria simmetrica dell'elettrone e del positrone*, Nuovo Cimento **14** (1937) 171, URL: https://cds.cern.ch/record/107755 (cit. on p. 6).

[16] I. Neutelings, *Standard Model*, 2016, URL: https://tikz.net/sm_particles/ (cit. on pp. 7, 256, 268).

[17] C. N. Yang and R. L. Mills, *Conservation of Isotopic Spin and Isotopic Gauge Invariance*, Phys. Rev. **96** (1 1954) 191, URL: https://link.aps.org/doi/10.1103/PhysRev.96.191 (cit. on p. 6).

[18] E. Noether, *Invariante Variationsprobleme*, Nachr. d. König. Gesellsch. d. Wiss. zu Göttingen, Math-phys. Klasse, Seite 235-157 (1918), eprint: www.physics.ucla.edu/\~\cwp/articles/noether.trans/german/emmy235.html, URL: http://www.physics.ucla.edu/~cwp/articles/noether.trans/german/emmy235.html (cit. on p. 6).

[19] S. Tomonaga, *On a relativistically invariant formulation of the quantum theory of wave fields*, Prog. Theor. Phys. **1** (1946) 27 (cit. on p. 8).

[20] J. S. Schwinger, *Quantum electrodynamics. I A covariant formulation*, Phys. Rev. **74** (1948) 1439, ed. by K. A. Milton (cit. on p. 8).

[21] R. P. Feynman, *Mathematical formulation of the quantum theory of electromagnetic interaction*, Phys. Rev. **80** (1950) 440, ed. by L. M. Brown (cit. on p. 8).

[22] H. D. Politzer, *Reliable Perturbative Results for Strong Interactions?*, Phys. Rev. Lett. **30** (26 1973) 1346, URL: https://link.aps.org/doi/10.1103/PhysRevLett.30.1346 (cit. on p. 8).

[23] D. J. Gross and F. Wilczek, *Ultraviolet Behavior of Non-Abelian Gauge Theories*, Phys. Rev. Lett. **30** (26 1973) 1343, URL: https://link.aps.org/doi/10.1103/PhysRevLett.30.1343 (cit. on p. 8).

[24] P. D. Group, *Review of Particle Physics*, Progress of Theoretical and Experimental Physics **2020** (2020) 083C01, ISSN: 2050-3911, eprint: https://academic.oup.com/ptep/article-pdf/2020/8/083C01/34673722/ptaa104.pdf, URL: https://doi.org/10.1093/ptep/ptaa104 (cit. on p. 10).

[25] P. A. Zyla et al., *Review of Particle Physics*, PTEP **2020** (2020) 083C01 (cit. on p. 11).

[26] W. A. Bardeen, A. J. Buras, D. W. Duke, and T. Muta, *Deep-inelastic scattering beyond the leading order in asymptotically free gauge theories*, Phys. Rev. D **18** (11 1978) 3998, URL: https://link.aps.org/doi/10.1103/PhysRevD.18.3998 (cit. on p. 11).

[27] J. C. Collins and D. E. Soper, *Parton Distribution and Decay Functions*, Nucl. Phys. B **194** (1982) 445 (cit. on p. 11).

[28] R. D. Ball et al., *Parton distributions from high-precision collider data. Parton distributions from high-precision collider data*, Eur. Phys. J. C **77** (2017) 663, arXiv: 1706.00428, URL: https://cds.cern.ch/record/2267455 (cit. on p. 12).

[29] S. Alekhin, *Parton distributions from deep inelastic scattering data*, Phys. Rev. D **68** (2003) 014002, arXiv: hep-ph/0211096 (cit. on p. 12).

[30] S. Alekhin, K. Melnikov, and F. Petriello, *Fixed target Drell-Yan data and NNLO QCD fits of parton distribution functions*, Phys. Rev. D **74** (2006) 054033, arXiv: hep-ph/0606237 (cit. on p. 12).

[31] R. D. Ball et al., *An open-source machine learning framework for global analyses of parton distributions*, Eur. Phys. J. C **81** (2021) 958, arXiv: 2109.02671 [hep-ph] (cit. on p. 12).

[32] Y. L. Dokshitzer, *Calculation of the Structure Functions for Deep Inelastic Scattering and e+ e- Annihilation by Perturbation Theory in Quantum Chromodynamics.*, Sov. Phys. JETP **46** (1977) 641 (cit. on p. 12).

[33] V. N. Gribov and L. N. Lipatov, *e+ e- pair annihilation and deep inelastic e p scattering in perturbation theory*, Sov. J. Nucl. Phys. **15** (1972) 675 (cit. on p. 12).

[34] G. Altarelli and G. Parisi, *Asymptotic freedom in parton language*, Nuclear Physics B **126** (1977) 298, ISSN: 0550-3213, URL: https://www.sciencedirect.com/science/article/pii/0550321377903844 (cit. on p. 12).

[35] S. L. Glashow, *Partial-symmetries of weak interactions*, Nuclear Physics **22** (1961) 579, ISSN: 0029-5582, URL: https://www.sciencedirect.com/science/article/pii/0029558261904692 (cit. on p. 13).

[36] A. Salam, *Weak and Electromagnetic Interactions*, Conf. Proc. C **680519** (1968) 367 (cit. on p. 13).

[37] S. Weinberg, *A Model of Leptons*, Phys. Rev. Lett. **19** (21 1967) 1264, URL: https://link.aps.org/doi/10.1103/PhysRevLett.19.1264 (cit. on p. 13).

[38] E. C. G. Sudarshan and R. e. Marshak, *Chirality invariance and the universal Fermi interaction*, Phys. Rev. **109** (1958) 1860 (cit. on p. 13).

[39] K. Nishijima, *Charge Independence Theory of V Particles**, Progress of Theoretical Physics **13** (1955) 285, ISSN: 0033-068X, eprint: https://academic.oup.com/ptp/article-pdf/13/3/285/5425869/13-3-285.pdf, URL: https://doi.org/10.1143/PTP.13.285 (cit. on p. 14).

[40] M. Gell-Mann, *The interpretation of the new particles as displaced charge multiplets*, Nuovo Cim. **4** (1956) 848 (cit. on p. 14).

[41] P. W. Higgs, *Spontaneous Symmetry Breakdown without Massless Bosons*, Phys. Rev. **145** (4 1966) 1156, URL: https://link.aps.org/doi/10.1103/PhysRev.145.1156 (cit. on p. 14).

[42] P. W. Higgs, *Broken symmetries, massless particles and gauge fields*, Phys. Lett. **12** (1964) 132 (cit. on p. 14).

[43] P. W. Higgs, *Broken Symmetries and the Masses of Gauge Bosons*, Phys. Rev. Lett. **13** (16 1964) 508, URL: https://link.aps.org/doi/10.1103/PhysRevLett.13.508 (cit. on p. 14).

[44] F. Englert and R. Brout,
Broken Symmetry and the Mass of Gauge Vector Mesons,
Phys. Rev. Lett. **13** (9 1964) 321,
URL: https://link.aps.org/doi/10.1103/PhysRevLett.13.321
(cit. on p. 14).

[45] G. S. Guralnik, C. R. Hagen, and T. W. B. Kibble,
Global Conservation Laws and Massless Particles,
Phys. Rev. Lett. **13** (20 1964) 585,
URL: https://link.aps.org/doi/10.1103/PhysRevLett.13.585
(cit. on p. 14).

[46] T. W. B. Kibble, *Symmetry Breaking in Non-Abelian Gauge Theories*,
Phys. Rev. **155** (5 1967) 1554,
URL: https://link.aps.org/doi/10.1103/PhysRev.155.1554
(cit. on p. 14).

[47] P. van Nieuwenhuizen, *Supergravity*, Physics Reports **68** (1981) 189,
ISSN: 0370-1573, URL: https:
//www.sciencedirect.com/science/article/pii/0370157381901575
(cit. on p. 19).

[48] A. Bosma, *The distribution and kinematics of neutral hydrogen in spiral galaxies of various morphological types*,
PhD thesis: University of Groningen, Netherlands, 1978 (cit. on p. 20).

[49] V. C. Rubin, J. Ford W. K., and N. Thonnard,
Rotational properties of 21 SC galaxies with a large range of luminosities and radii, from NGC 4605 (R=4kpc) to UGC 2885 (R=122kpc).,
The Astrophysical Journal **238** (1980) 471 (cit. on p. 20).

[50] P. A. R. Ade et al., *Planck 2015 results. XIII. Cosmological parameters*,
Astron. Astrophys. **594** (2016) A13, arXiv: 1502.01589 [astro-ph.CO]
(cit. on p. 20).

[51] S. Perlmutter and et al,
Measurements of Ω and Λ from 42 high redshift supernovae,
Astrophys. J. **517** (1999) 565, arXiv: astro-ph/9812133 (cit. on p. 20).

[52] A. G. Riess et al., *Observational evidence from supernovae for an accelerating universe and a cosmological constant*,
Astron. J. **116** (1998) 1009, arXiv: astro-ph/9805201 (cit. on p. 20).

[53] J. Martin, *Everything You Always Wanted To Know About The Cosmological Constant Problem (But Were Afraid To Ask)*,
Comptes Rendus Physique **13** (2012) 566,
arXiv: 1205.3365 [astro-ph.CO] (cit. on p. 20).

[54] Y. Fukuda et al., *Evidence for Oscillation of Atmospheric Neutrinos*, Phys. Rev. Lett. **81** (8 1998) 1562, URL: https://link.aps.org/doi/10.1103/PhysRevLett.81.1562 (cit. on p. 20).

[55] Q. R. Ahmad et al., *Measurement of the rate of $\nu_e + d \to p + p + e^-$ interactions produced by ^8B solar neutrinos at the Sudbury Neutrino Observatory*, Phys. Rev. Lett. **87** (2001) 071301, arXiv: nucl-ex/0106015 (cit. on p. 20).

[56] T. Yanagida, *Horizontal Symmetry and Masses of Neutrinos*, Prog. Theor. Phys. **64** (1980) 1103 (cit. on p. 20).

[57] M. B. Gavela, P. Hernandez, J. Orloff, and O. Pene, *Standard model CP violation and baryon asymmetry*, Mod. Phys. Lett. A **9** (1994) 795, arXiv: hep-ph/9312215 (cit. on p. 20).

[58] *Summary Plots for Heavy Particle Searches and Long-lived Particle Searches - March 2023*, tech. rep., All figures including auxiliary figures are available at https://atlas.web.cern.ch/Atlas/GROUPS/PHYSICS/PUBNOTES/ATL-PHYS-PUB-2023-008: CERN, 2023, URL: https://cds.cern.ch/record/2853754 (cit. on p. 22).

[59] T. Appelquist and J. Carazzone, *Infrared singularities and massive fields*, Phys. Rev. D **11** (10 1975) 2856, URL: https://link.aps.org/doi/10.1103/PhysRevD.11.2856 (cit. on p. 21).

[60] E. Fermi, *Tentativo di una teoria dell'emissione dei raggi beta*, Ric. Sci. **4** (1933) 491 (cit. on pp. 21, 30).

[61] C. W. Bauer, S. Fleming, and M. Luke, *Summing Sudakov logarithms in $\overrightarrow{B} \to X_s\gamma$ in effective field theory*, Phys. Rev. D **63** (1 2000) 014006, URL: https://link.aps.org/doi/10.1103/PhysRevD.63.014006 (cit. on p. 21).

[62] C. W. Bauer, S. Fleming, D. Pirjol, and I. W. Stewart, *An effective field theory for collinear and soft gluons: Heavy to light decays*, Phys. Rev. D **63** (11 2001) 114020, URL: https://link.aps.org/doi/10.1103/PhysRevD.63.114020 (cit. on p. 21).

[63] C. W. Bauer and I. W. Stewart,
Invariant operators in collinear effective theory,
Physics Letters B **516** (2001) 134, ISSN: 0370-2693, URL: https://www.sciencedirect.com/science/article/pii/S0370269301009029
(cit. on p. 21).

[64] C. W. Bauer, D. Pirjol, and I. W. Stewart,
Soft-collinear factorization in effective field theory,
Phys. Rev. D **65** (5 2002) 054022,
URL: https://link.aps.org/doi/10.1103/PhysRevD.65.054022
(cit. on p. 21).

[65] C. W. Bauer, D. Pirjol, and I. W. Stewart,
Power counting in the soft-collinear effective theory,
Phys. Rev. D **66** (5 2002) 054005,
URL: https://link.aps.org/doi/10.1103/PhysRevD.66.054005
(cit. on p. 21).

[66] H. Georgi, *An effective field theory for heavy quarks at low energies*,
Physics Letters B **240** (1990) 447, ISSN: 0370-2693, URL: https://www.sciencedirect.com/science/article/pii/037026939091128X
(cit. on p. 21).

[67] S. Weinberg, *Baryon- and Lepton-Nonconserving Processes*,
Phys. Rev. Lett. **43** (21 1979) 1566,
URL: https://link.aps.org/doi/10.1103/PhysRevLett.43.1566
(cit. on p. 24).

[68] B. Henning, X. Lu, T. Melia, and H. Murayama, *2, 84, 30, 993, 560, 15456, 11962, 261485, ...: Higher dimension operators in the SM EFT*,
JHEP **08** (2017) 016, [Erratum: JHEP 09, 019 (2019)],
arXiv: 1512.03433 [hep-ph] (cit. on p. 24).

[69] B. Grzadkowski, M. Iskrzynski, M. Misiak, and J. Rosiek,
Dimension-Six Terms in the Standard Model Lagrangian,
JHEP **10** (2010) 085, arXiv: 1008.4884 [hep-ph] (cit. on pp. 25, 26).

[70] I. Brivio, *SMEFTsim 3.0 — a practical guide*, JHEP **04** (2021) 073,
arXiv: 2012.11343 [hep-ph] (cit. on pp. 25, 26, 29, 90, 108).

[71] R. Alonso, E. E. Jenkins, A. V. Manohar, and M. Trott,
Renormalization Group Evolution of the Standard Model Dimension Six Operators III: Gauge Coupling Dependence and Phenomenology,
JHEP **04** (2014) 159, arXiv: 1312.2014 [hep-ph] (cit. on p. 25).

[72] A. Falkowski, *Lectures on SMEFT*, Eur. Phys. J. C **83** (2023) 656
(cit. on p. 25).

[73] M. E. Peskin and T. Takeuchi,
New constraint on a strongly interacting Higgs sector,
Phys. Rev. Lett. **65** (8 1990) 964,
URL: https://link.aps.org/doi/10.1103/PhysRevLett.65.964
(cit. on p. 27).

[74] J. A. Aguilar-Saavedra et al., *Interpreting top-quark LHC measurements in the standard-model effective field theory*, tech. rep., 2018,
arXiv: 1802.07237, URL: https://cds.cern.ch/record/2305783
(cit. on p. 29).

[75] J. Ellis, M. Madigan, K. Mimasu, V. Sanz, and T. You, *Top, Higgs, Diboson and Electroweak Fit to the Standard Model Effective Field Theory*,
JHEP **04** (2021) 279, arXiv: 2012.02779 [hep-ph] (cit. on p. 31).

[76] J. Kley, T. Theil, E. Venturini, and A. Weiler,
Electric dipole moments at one-loop in the dimension-6 SMEFT,
Eur. Phys. J. C **82** (2022) 926, arXiv: 2109.15085 [hep-ph]
(cit. on p. 30).

[77] J. Brod, J. M. Cornell, D. Skodras, and E. Stamou, *Global constraints on Yukawa operators in the standard model effective theory*,
JHEP **08** (2022) 294, arXiv: 2203.03736 [hep-ph] (cit. on p. 30).

[78] J. Aebischer et al., *Effective field theory interpretation of lepton magnetic and electric dipole moments*, JHEP **07** (2021) 107,
arXiv: 2102.08954 [hep-ph] (cit. on p. 30).

[79] J. Aebischer, A. J. Buras, and J. Kumar, "On the Importance of Rare Kaon Decays: A Snowmass 2021 White Paper", *Snowmass 2021*, 2022,
arXiv: 2203.09524 [hep-ph] (cit. on p. 30).

[80] M. Ciuchini et al.,
Charming penguins and lepton universality violation in $b \to s\ell^+\ell^-$ *decays*,
Eur. Phys. J. C **83** (2023) 64, arXiv: 2110.10126 [hep-ph] (cit. on p. 30).

[81] W. Dekens and P. Stoffer, *Low-energy effective field theory below the electroweak scale: matching at one loop*,
JHEP **10** (2019) 197, [Erratum: JHEP 11, 148 (2022)],
arXiv: 1908.05295 [hep-ph] (cit. on p. 32).

[82] T. D. Lee, *A Theory of Spontaneous T Violation*,
Phys. Rev. D **8** (1973) 1226, [,516(1973)] (cit. on p. 32).

[83] J. F. Gunion and H. E. Haber, *The CP conserving two Higgs doublet model: The Approach to the decoupling limit*, Phys. Rev. D **67** (2003) 075019,
arXiv: hep-ph/0207010 [hep-ph] (cit. on p. 32).

[84] G. Branco et al., *Theory and phenomenology of two-Higgs-doublet models*, Phys. Rept. **516** (2012) 1, arXiv: 1106.0034 [hep-ph] (cit. on pp. 32, 240).

[85] S. L. Glashow and S. Weinberg, *Natural conservation laws for neutral currents*, Phys. Rev. D **15** (7 1977) 1958, URL: https://link.aps.org/doi/10.1103/PhysRevD.15.1958 (cit. on p. 32).

[86] E. A. Paschos, *Diagonal Neutral Currents*, Phys. Rev. D **15** (1977) 1966 (cit. on pp. 32, 33).

[87] S. L. Glashow and S. Weinberg, *Natural Conservation Laws for Neutral Currents*, Phys. Rev. D **15** (1977) 1958 (cit. on p. 33).

[88] D. de Florian et al., *Handbook of LHC Higgs Cross Sections: 4. Deciphering the Nature of the Higgs Sector*, **2/2017** (2016), arXiv: 1610.07922 [hep-ph] (cit. on pp. 34, 40, 41, 85, 87, 93, 159).

[89] LHC Higgs Cross Section Working Group, D. de Florian et al., *Handbook of LHC Higgs Cross Sections: 4. Deciphering the Nature of the Higgs Sector*, (2016), arXiv: 1610.07922 [hep-ph] (cit. on pp. 35, 40, 41, 103).

[90] G. Aad et al., *Measurement of the CP properties of Higgs boson interactions with τ-leptons with the ATLAS detector*, Eur. Phys. J. C **83** (2023) 563, arXiv: 2212.05833 [hep-ex] (cit. on p. 38).

[91] C. Anastasiou, C. Duhr, F. Dulat, F. Herzog, and B. Mistlberger, *Higgs Boson Gluon-Fusion Production in QCD at Three Loops*, Phys. Rev. Lett. **114** (2015) 212001, arXiv: 1503.06056 [hep-ph] (cit. on pp. 40, 41).

[92] C. Anastasiou et al., *High precision determination of the gluon fusion Higgs boson cross-section at the LHC*, JHEP **05** (2016) 058, arXiv: 1602.00695 [hep-ph] (cit. on pp. 40, 41).

[93] S. Actis, G. Passarino, C. Sturm, and S. Uccirati, *NLO electroweak corrections to Higgs boson production at hadron colliders*, Phys. Lett. B **670** (2008) 12, arXiv: 0809.1301 [hep-ph] (cit. on pp. 40, 41).

[94] C. Anastasiou, R. Boughezal, and F. Petriello, *Mixed QCD-electroweak corrections to Higgs boson production in gluon fusion*, JHEP **04** (2009) 003, arXiv: 0811.3458 [hep-ph] (cit. on pp. 40, 41).

[95] M. Ciccolini, A. Denner, and S. Dittmaier,
Strong and Electroweak Corrections to the Production of a Higgs Boson + 2 Jets via Weak Interactions at the Large Hadron Collider,
Phys. Rev. Lett. **99** (2007) 161803, arXiv: 0707.0381 [hep-ph]
(cit. on pp. 40, 41).

[96] M. Ciccolini, A. Denner, and S. Dittmaier, *Electroweak and QCD corrections to Higgs production via vector-boson fusion at the LHC*,
Phys. Rev. D **77** (2008) 013002, arXiv: 0710.4749 [hep-ph]
(cit. on pp. 40, 41).

[97] P. Bolzoni, F. Maltoni, S.-O. Moch, and M. Zaro, *Higgs Boson Production via Vector-Boson Fusion at Next-to-Next-to-Leading Order in QCD*,
Phys. Rev. Lett. **105** (2010) 011801, arXiv: 1003.4451 [hep-ph]
(cit. on pp. 40, 41).

[98] O. Brein, A. Djouadi, and R. Harlander,
NNLO QCD corrections to the Higgs-strahlung processes at hadron colliders,
Phys. Lett. B **579** (2004) 149, arXiv: hep-ph/0307206 [hep-ph]
(cit. on pp. 40, 41).

[99] L. Altenkamp, S. Dittmaier, R. V. Harlander, H. Rzehak, and T. J. E. Zirke, *Gluon-induced Higgs-strahlung at next-to-leading order QCD*,
JHEP **02** (2013) 078, arXiv: 1211.5015 [hep-ph] (cit. on pp. 40, 41).

[100] A. Denner, S. Dittmaier, S. Kallweit, and A. Mück, *Electroweak corrections to Higgs-strahlung off W/Z bosons at the Tevatron and the LHC with HAWK*,
JHEP **03** (2012) 075, arXiv: 1112.5142 [hep-ph] (cit. on pp. 40, 41).

[101] W. Beenakker et al.,
NLO QCD corrections to $t\bar{t}H$ production in hadron collisions,
Nucl. Phys. B **653** (2003) 151, arXiv: hep-ph/0211352 [hep-ph]
(cit. on pp. 40, 41).

[102] S. Dawson, C. Jackson, L. Orr, L. Reina, and D. Wackeroth,
Associated Higgs production with top quarks at the large hadron collider: NLO QCD corrections, Phys. Rev. D **68** (2003) 034022,
arXiv: hep-ph/0305087 [hep-ph] (cit. on pp. 40, 41).

[103] Y. Zhang, W.-G. Ma, R.-Y. Zhang, C. Chen, and L. Guo, *QCD NLO and EW NLO corrections to $t\bar{t}H$ production with top quark decays at hadron collider*,
Phys. Lett. B **738** (2014) 1, arXiv: 1407.1110 [hep-ph]
(cit. on pp. 40, 41).

[104] S. Frixione, V. Hirschi, D. Pagani, H.-S. Shao, and M. Zaro,
Electroweak and QCD corrections to top-pair hadroproduction in association with heavy bosons, JHEP **06** (2015) 184,
arXiv: 1504.03446 [hep-ph] (cit. on p. 40).

[105] S. Dawson, C. Jackson, L. Reina, and D. Wackeroth, *Exclusive Higgs boson production with bottom quarks at hadron colliders*, Phys. Rev. D **69** (7 2004) 074027, arXiv: hep-ph/0311067 [hep-ph] (cit. on p. 40).

[106] S. Dittmaier, M. Krämer, and M. Spira, *Higgs radiation off bottom quarks at the Tevatron and the CERN LHC*, Phys. Rev. D **70** (7 2004) 074010, arXiv: hep-ph/0309204 [hep-ph] (cit. on p. 40).

[107] R. Harlander, M. Krämer, and M. Schumacher, *Bottom-quark associated Higgs-boson production: Reconciling the four- and five-flavour scheme approach*, (2011), arXiv: 1112.3478 [hep-ph] (cit. on p. 40).

[108] F. Demartin, F. Maltoni, K. Mawatari, and M. Zaro, *Higgs production in association with a single top quark at the LHC*, Eur. Phys. J. C **75** (2015) 267, arXiv: 1504.00611 [hep-ph] (cit. on pp. 40, 41).

[109] ATLAS Collaboration, *Measurement of the properties of Higgs boson production at $\sqrt{s} = 13$ TeV in the $H \to \gamma\gamma$ channel using $139\,fb^{-1}$ of pp collision data with the ATLAS experiment*, ATLAS-CONF-2020-026, 2020, URL: https://cds.cern.ch/record/2725727 (cit. on pp. 40, 116, 117).

[110] P. Nason, *A New method for combining NLO QCD with shower Monte Carlo algorithms*, JHEP **11** (2004) 040, arXiv: hep-ph/0409146 (cit. on p. 41).

[111] S. Frixione, P. Nason, and C. Oleari, *Matching NLO QCD computations with parton shower simulations: the POWHEG method*, JHEP **11** (2007) 070, arXiv: 0709.2092 [hep-ph] (cit. on p. 41).

[112] S. Alioli, P. Nason, C. Oleari, and E. Re, *A general framework for implementing NLO calculations in shower Monte Carlo programs: the POWHEG BOX*, JHEP **06** (2010) 043, arXiv: 1002.2581 [hep-ph] (cit. on p. 41).

[113] S. Alioli, P. Nason, C. Oleari, and E. Re, *NLO Higgs boson production via gluon fusion matched with shower in POWHEG*, JHEP **04** (2009) 002, arXiv: 0812.0578 [hep-ph] (cit. on p. 41).

[114] K. Hamilton, P. Nason, E. Re, and G. Zanderighi, *NNLOPS simulation of Higgs boson production*, JHEP **10** (2013) 222, arXiv: 1309.0017 [hep-ph] (cit. on p. 41).

[115] K. Hamilton, P. Nason, and G. Zanderighi, *Finite quark-mass effects in the NNLOPS POWHEG+MiNLO Higgs generator*, JHEP **05** (2015) 140, arXiv: 1501.04637 [hep-ph] (cit. on p. 41).

[116] S. Catani and M. Grazzini,
Next-to-Next-to-Leading-Order Subtraction Formalism in Hadron Collisions and its Application to Higgs-Boson Production at the Large Hadron Collider,
Phys. Rev. Lett. **98** (2007) 222002, arXiv: hep-ph/0703012 [hep-ph]
(cit. on pp. 41, 188).

[117] K. Hamilton, P. Nason, C. Oleari, and G. Zanderighi,
Merging H/W/Z + 0 and 1 jet at NLO with no merging scale: a path to parton shower + NNLO matching, JHEP **05** (2013) 082,
arXiv: 1212.4504 [hep-ph] (cit. on p. 41).

[118] M. Grazzini and H. Sargsyan,
Heavy-quark mass effects in Higgs boson production at the LHC,
JHEP **09** (2013) 129, arXiv: 1306.4581 [hep-ph] (cit. on p. 41).

[119] P. Nason and C. Oleari, *NLO Higgs boson production via vector-boson fusion matched with shower in POWHEG*, JHEP **02** (2010) 037,
arXiv: 0911.5299 [hep-ph] (cit. on p. 41).

[120] K. Hamilton, P. Nason, and G. Zanderighi,
MINLO: multi-scale improved NLO, JHEP **10** (2012) 155,
arXiv: 1206.3572 [hep-ph] (cit. on p. 41).

[121] J. Alwall et al.,
The automated computation of tree-level and next-to-leading order differential cross sections, and their matching to parton shower simulations,
JHEP **07** (2014) 079, arXiv: 1405.0301 [hep-ph] (cit. on p. 41).

[122] R. D. Ball et al., *Parton distributions for the LHC Run II*,
JHEP **04** (2015) 040, arXiv: 1410.8849 [hep-ph]
(cit. on pp. 41, 188, 211).

[123] S. Frixione, V. Hirschi, D. Pagani, H. S. Shao, and M. Zaro, *Weak corrections to Higgs hadroproduction in association with a top-quark pair*,
JHEP **09** (2014) 065, arXiv: 1407.0823 [hep-ph] (cit. on p. 41).

[124] H.-L. Lai et al., *New parton distributions for collider physics*,
Phys. Rev. D **82** (2010) 074024, arXiv: 1007.2241 [hep-ph]
(cit. on p. 41).

[125] T. Sjöstrand, S. Mrenna, and P. Z. Skands,
A brief introduction to PYTHIA 8.1,
Comput. Phys. Commun. **178** (2008) 852, arXiv: 0710.3820 [hep-ph]
(cit. on pp. 41, 126).

[126] ATLAS Collaboration,
Measurement of the Z/γ^* boson transverse momentum distribution in pp collisions at $\sqrt{s} = 7$ TeV with the ATLAS detector, JHEP **09** (2014) 145,
arXiv: 1406.3660 [hep-ex] (cit. on p. 41).

[127] GEANT4 Collaboration, S. Agostinelli, et al., GEANT4 – *a simulation toolkit*, Nucl. Instrum. Meth. A **506** (2003) 250 (cit. on p. 41).

[128] ATLAS Collaboration, *The ATLAS Simulation Infrastructure*, Eur. Phys. J. C **70** (2010) 823, arXiv: 1005.4568 [physics.ins-det] (cit. on p. 41).

[129] A. Martin, W. Stirling, R. Thorne, and G. Watt, *Parton distributions for the LHC*, Eur. Phys. J. C **63** (2009) 189, arXiv: 0901.0002 [hep-ph] (cit. on p. 42).

[130] ATLAS Collaboration, *Summary of ATLAS Pythia 8 tunes*, ATL-PHYS-PUB-2012-003, 2012, URL: https://cds.cern.ch/record/1474107 (cit. on p. 42).

[131] ATLAS Collaboration, *The Pythia 8 A3 tune description of ATLAS minimum bias and inelastic measurements incorporating the Donnachie–Landshoff diffractive model*, ATL-PHYS-PUB-2016-017, 2016, URL: https://cds.cern.ch/record/2206965 (cit. on p. 42).

[132] K. Aamodt et al., *The ALICE experiment at the CERN LHC*, JINST **3** (2008) S08002 (cit. on p. 43).

[133] A. A. Alves Jr. et al., *The LHCb Detector at the LHC*, JINST **3** (2008) S08005 (cit. on p. 43).

[134] S. Chatrchyan et al., *The CMS Experiment at the CERN LHC*, JINST **3** (2008) S08004 (cit. on p. 43).

[135] G. Aad et al., *The ATLAS Experiment at the CERN Large Hadron Collider*, JINST **3** (2008) S08003 (cit. on pp. 43, 46, 49, 51, 53).

[136] *LHC Machine*, JINST **3** (2008) S08001, ed. by L. Evans and P. Bryant (cit. on p. 43).

[137] B. Moser, *The Beauty and the Boost: a Higgs Boson Tale - Measurements of Higgs Boson Production at High Energy in Decays to Bottom Quarks and Their Interpretations with the ATLAS Experiment at the LHC*, Presented 04 Mar 2022, 2021, URL: https://cds.cern.ch/record/2803776 (cit. on p. 44).

[138] I. Neutelings, *CMS coordinate system*, URL: https://tikz.net/axis3d_cms/ (cit. on p. 47).

[139] J. Pequenao and P. Schaffner, "How ATLAS detects particles: diagram of particle paths in the detector", 2013, URL: https://cds.cern.ch/record/1505342 (cit. on p. 48).

[140] *ATLAS approved plots DAQ*, https://twiki.cern.ch/twiki/bin/view/AtlasPublic/ApprovedPlotsDAQ (cit. on p. 55).

[141] *Luminosity determination in* pp *collisions at* $\sqrt{s} = 13$ *TeV using the ATLAS detector at the LHC*, (2022), arXiv: 2212.09379 [hep-ex] (cit. on p. 56).

[142] G. Avoni et al., *The new LUCID-2 detector for luminosity measurement and monitoring in ATLAS*, JINST **13** (2018) P07017, URL: https://cds.cern.ch/record/2633501 (cit. on p. 56).

[143] S. White, *The ATLAS zero degree calorimeter*, Nucl. Instrum. Meth. A **617** (2010) 126, ed. by G. Chiarelli, F. Cervelli, F. Forti, and A. Scribano (cit. on p. 56).

[144] V. C. et al., *The ATLAS Beam Conditions Monitor*, Journal of Instrumentation **3** (2008) P02004, URL: https://dx.doi.org/10.1088/1748-0221/3/02/P02004 (cit. on p. 57).

[145] S. van der Meer, *Calibration of the Effective Beam Height in the ISR*, (1968) (cit. on p. 57).

[146] I. Zurbano Fernandez et al., *High-Luminosity Large Hadron Collider (HL-LHC): Technical design report*, **10/2020** (2020), ed. by I. Béjar Alonso et al. (cit. on p. 57).

[147] *Technical Design Report for the ATLAS Inner Tracker Strip Detector*, (2017) (cit. on pp. 58–60).

[148] *Strain Gage Selection: Criteria, Procedures, Recommendations*, http://www.vishaypg.com/docs/11055/tn505.pdf (cit. on p. 61).

[149] Tektronix, *Overview of Two-Wire and Four-Wire (Kelvin) Resistance Measurements*, click here for link (cit. on p. 63).

[150] Tektronix, *Integra Series Model 2700 Multimeter/ Data Acquisition System*, click here for link, URL: http://www.testequipmenthq.com/datasheets/KEITHLEY-2700-Datasheet.pdf (cit. on p. 63).

[151] M. Aaboud et al., *Performance of the ATLAS Track Reconstruction Algorithms in Dense Environments in LHC Run 2*, Eur. Phys. J. C **77** (2017) 673, arXiv: 1704.07983 [hep-ex] (cit. on p. 70).

[152] T. Cornelissen et al., *The new ATLAS track reconstruction (NEWT)*, J. Phys. Conf. Ser. **119** (2008) 032014, ed. by R. Sobie, R. Tafirout, and J. Thomson (cit. on p. 70).

[153] M. Aaboud et al., *Reconstruction of primary vertices at the ATLAS experiment in Run 1 proton–proton collisions at the LHC*, Eur. Phys. J. C **77** (2017) 332, arXiv: 1611.10235 [physics.ins-det] (cit. on p. 71).

[154] *Vertex Reconstruction Performance of the ATLAS Detector at $\sqrt{s} = 13$ TeV*, tech. rep., All figures including auxiliary figures are available at https://atlas.web.cern.ch/Atlas/GROUPS/PHYSICS/PUBNOTES/ATL-PHYS-PUB-2015-026: CERN, 2015, URL: https://cds.cern.ch/record/2037717 (cit. on p. 71).

[155] M. Aaboud et al., *Electron reconstruction and identification in the ATLAS experiment using the 2015 and 2016 LHC proton-proton collision data at $\sqrt{s} = 13$ TeV*, Eur. Phys. J. C **79** (2019) 639, arXiv: 1902.04655 [physics.ins-det] (cit. on pp. 71, 72).

[156] G. Aad et al., *Electron and photon performance measurements with the ATLAS detector using the 2015–2017 LHC proton-proton collision data*, JINST **14** (2019) P12006, arXiv: 1908.00005 [hep-ex] (cit. on p. 73).

[157] G. Aad et al., *Muon reconstruction and identification efficiency in ATLAS using the full Run 2 pp collision data set at $\sqrt{s} = 13$ TeV*, Eur. Phys. J. C **81** (2021) 578, arXiv: 2012.00578 [hep-ex] (cit. on p. 73).

[158] J. Illingworth and J. Kittler, *A survey of the Hough Transform*, Computer Vision, Graphics, and Image Processing **44** (1988) 87, ISSN: 0734-189X, URL: https://www.sciencedirect.com/science/article/pii/S0734189X88800331 (cit. on p. 73).

[159] M. Cacciari, G. P. Salam, and G. Soyez, *The anti-k_t jet clustering algorithm*, JHEP **04** (2008) 063, arXiv: 0802.1189 [hep-ph] (cit. on p. 75).

[160] M. Cacciari, G. P. Salam, and G. Soyez, *FastJet User Manual*, Eur. Phys. J. C **72** (2012) 1896, arXiv: 1111.6097 [hep-ph] (cit. on pp. 75, 153, 154, 156).

[161] G. Aad et al., *Jet energy scale and resolution measured in proton–proton collisions at $\sqrt{s} = 13$ TeV with the ATLAS detector*, Eur. Phys. J. C **81** (2021) 689, arXiv: 2007.02645 [hep-ex] (cit. on p. 75).

[162] M. Aaboud et al., *In situ calibration of large-radius jet energy and mass in 13 TeV proton–proton collisions with the ATLAS detector*, Eur. Phys. J. C **79** (2019) 135, arXiv: 1807.09477 [hep-ex] (cit. on p. 75).

[163] G. Aad et al., *ATLAS b-jet identification performance and efficiency measurement with $t\bar{t}$ events in pp collisions at $\sqrt{s} = 13$ TeV*, Eur. Phys. J. C **79** (2019) 970, arXiv: 1907.05120 [hep-ex] (cit. on p. 75).

[164] *Measurement of the tau lepton reconstruction and identification performance in the ATLAS experiment using pp collisions at $\sqrt{s} = 13$ TeV*, tech. rep., All figures including auxiliary figures are available at https://atlas.web.cern.ch/Atlas/GROUPS/PHYSICS/CONFNOTES/ATLAS-CONF-2017-029: CERN, 2017, URL: https://cds.cern.ch/record/2261772 (cit. on p. 76).

[165] *E_T^{miss} performance in the ATLAS detector using 2015-2016 LHC p-p collisions*, tech. rep., All figures including auxiliary figures are available at https://atlas.web.cern.ch/Atlas/GROUPS/PHYSICS/CONFNOTES/ATLAS-CONF-2018-023: CERN, 2018, URL: https://cds.cern.ch/record/2625233 (cit. on p. 77).

[166] LHC Higgs Cross Section Working Group, D. de Florian et al., *Handbook of LHC Higgs Cross Sections: 4. Deciphering the Nature of the Higgs Sector*, CERN Yellow Reports: Monographs, 869 pages, 295 figures, 248 tables and 1645 citations. Working Group web page: https://twiki.cern.ch/twiki/bin/view/LHCPhysics/LHCHXSWG, Geneva: CERN, 2016, URL: https://cds.cern.ch/record/2227475 (cit. on p. 80).

[167] LHC Higgs Cross Section Working Group, S. Heinemeyer et al., *Handbook of LHC Higgs Cross Sections: 3. Higgs Properties*, CERN-2013-004, CERN Yellow Reports: Monographs (2013), ed. by S. Heinemeyer, Comments: 404 pages, 139 figures, to be submitted to CERN Report. Working Group web page: https://twiki.cern.ch/twiki/bin/view/LHCPhysics/CrossSections, arXiv: 1307.1347 [hep-ph], URL: https://cds.cern.ch/record/1559921 (cit. on p. 81).

[168] ATLAS Collaboration, *A detailed map of Higgs boson interactions by the ATLAS experiment ten years after the discovery*, Nature **607** (2022) 52, 44 pages in total, author list starting page 27, 7 figures, 1 table, published in Nature. All figures including auxiliary figures are available at http://atlas.web.cern.ch/Atlas/GROUPS/PHYSICS/PAPERS/HIGG-2021-23, arXiv: 2207.00092, URL: https://cds.cern.ch/record/2814946 (cit. on pp. 81, 159, 172, 241, 242).

[169] G. Aad et al., *Measurements of the Higgs boson inclusive and differential fiducial cross sections in the 4ℓ decay channel at $\sqrt{s} = 13$ TeV*,

Eur. Phys. J. C **80** (2020) 942, arXiv: 2004.03969 [hep-ex] (cit. on p. 82).

[170] G. Aad et al., *Measurements of the Higgs boson inclusive and differential fiducial cross-sections in the diphoton decay channel with pp collisions at $\sqrt{s}$ = 13 TeV with the ATLAS detector*, JHEP **08** (2022) 027, arXiv: 2202.00487 [hep-ex] (cit. on pp. 82, 84).

[171] *Measurement of the total and differential Higgs boson production cross-sections at $\sqrt{s} = 13$ TeV with the ATLAS detector by combining the $H \to ZZ^* \to 4\ell$ and $H \to \gamma\gamma$ decay channels*, tech. rep., 23 pages in total, 8 figures, 8 tables, submitted to JHEP. All figures and tables including auxiliary figures and tables are available at https://atlas.web.cern.ch/Atlas/GROUPS/PHYSICS/PAPERS/HIGG-2022-04/: CERN, 2022, arXiv: 2207.08615, URL: https://cds.cern.ch/record/2816107 (cit. on p. 82).

[172] G. Cowan, *Statistical data analysis*, Oxford University Press, USA, 1998 (cit. on p. 83).

[173] M. Delmastro et al., *Simplified Template Cross Sections – Stage 1.1*, tech. rep., 14 pages, 3 figures: CERN, 2019, arXiv: 1906.02754, URL: https://cds.cern.ch/record/2669925 (cit. on p. 84).

[174] N. Berger et al., *Simplified Template Cross Sections - Stage 1.1*, (2019), arXiv: 1906.02754 [hep-ph] (cit. on pp. 85, 121, 159).

[175] I. Brivio, Y. Jiang, and M. Trott, *The SMEFTsim package, theory and tools*, JHEP **12** (2017) 070, arXiv: 1709.06492 [hep-ph] (cit. on pp. 88, 90, 189, 214).

[176] I. Brivio, *SMEFTsim 3.0 — a practical guide*, JHEP **04** (2021) 073, arXiv: 2012.11343 [hep-ph] (cit. on pp. 88, 214).

[177] C. Degrande et al., *Automated one-loop computations in the standard model effective field theory*, Phys. Rev. D **103** (2021) 096024, arXiv: 2008.11743 [hep-ph] (cit. on pp. 88, 189, 214).

[178] J. Alwall, M. Herquet, F. Maltoni, O. Mattelaer, and T. Stelzer, *MadGraph 5: going beyond*, Journal of High Energy Physics **2011** (2011) (cit. on pp. 88, 189, 214).

[179] T. Sjöstrand et al., *An introduction to PYTHIA 8.2*, Comput. Phys. Commun. **191** (2015) 159, arXiv: 1410.3012 [hep-ph] (cit. on pp. 88, 189, 214).

[180] C. Degrande, B. Fuks, K. Mawatari, K. Mimasu, and V. Sanz, *Electroweak Higgs boson production in the standard model effective field theory beyond leading order in QCD*, Eur. Phys. J. **C77** (2017) 262, arXiv: 1609.04833 [hep-ph] (cit. on p. 89).

[181] *A morphing technique for signal modelling in a multidimensional space of coupling parameters*, tech. rep.,
All figures including auxiliary figures are available at https://atlas.web.cern.ch/Atlas/GROUPS/PHYSICS/PUBNOTES/ATL-PHYS-PUB-2015-047: CERN, 2015,
URL: https://cds.cern.ch/record/2066980 (cit. on pp. 90, 105).

[182] T. Corbett, A. Martin, and M. Trott, *Consistent higher order $\sigma(\mathcal{G}\mathcal{G} \to h)$, $\Gamma(h \to \mathcal{G}\mathcal{G})$ and $\Gamma(h \to \gamma\gamma)$ in geoSMEFT*, JHEP **12** (2021) 147,
arXiv: 2107.07470 [hep-ph] (cit. on p. 96).

[183] T. Corbett and A. Martin, *Higgs associated production with a vector decaying to two fermions in the geoSMEFT*, (2023),
arXiv: 2306.00053 [hep-ph] (cit. on p. 96).

[184] A. Martin and M. Trott, *More accurate $\sigma(\mathcal{G}\,\mathcal{G} \to h)$, $\Gamma(h \to \mathcal{G}\,\mathcal{G}, \mathcal{A}\mathcal{A}, \bar{\Psi}\Psi)$ and Higgs width results via the geoSMEFT*, (2023),
arXiv: 2305.05879 [hep-ph] (cit. on p. 96).

[185] K. Cranmer, G. Lewis, L. Moneta, A. Shibata, and W. Verkerke, *HistFactory: A tool for creating statistical models for use with RooFit and RooStats*, CERN-OPEN-2012-016 (2012),
URL: http://cdsweb.cern.ch/record/1456844 (cit. on p. 98).

[186] L. Moneta, K. Cranmer, G. Schott, and W. Verkerke, *The RooStats project, Proceedings of the 13th International Workshop on Advanced Computing and Analysis Techniques in Physics Research. February 22-27, 2010, Jaipur, India. http://acat2010.cern.ch/.*, (2010),
arXiv: 1009.1003 [physics.data-an] (cit. on p. 98).

[187] W. Verkerke and D. P. Kirkby, *The RooFit toolkit for data modeling*,
eConf **C0303241** (2003) MOLT007, ed. by L. Lyons and M. Karagoz,
arXiv: physics/0306116 (cit. on p. 98).

[188] M. Hatlo et al.,
Developments of mathematical software libraries for the LHC experiments,
IEEE Trans. Nucl. Sci. **52** (2005) 2818 (cit. on p. 99).

[189] W. C. Davidon, *Variable Metric Method for Minimization*,
SIAM Journal on Optimization **1** (1991) 1,
eprint: https://doi.org/10.1137/0801001,
URL: https://doi.org/10.1137/0801001 (cit. on p. 99).

[190] R. Fletcher and M. J. D. Powell,
A Rapidly Convergent Descent Method for Minimization,
The Computer Journal **6** (1963) 163, ISSN: 0010-4620,
eprint: https://academic.oup.com/comjnl/article-pdf/6/2/163/1041527/6-2-163.pdf,
URL: https://doi.org/10.1093/comjnl/6.2.163 (cit. on p. 99).

[191] The ATLAS Collaboration, *A morphing technique for signal modelling in a multidimensional space of coupling parameters*, tech. rep. ATL-PHYS-PUB-2015-047, CERN, 2015, CDS: 2066980 (cit. on p. 103).

[192] W. Verkerke and D. P. Kirkby, *The RooFit toolkit for data modeling*, eConf **C0303241** (2003) MOLT007, [,186(2003)], arXiv: physics/0306116 [physics] (cit. on pp. 105, 221).

[193] J. Alwall, M. Herquet, F. Maltoni, O. Mattelaer, and T. Stelzer, *MadGraph 5 : Going Beyond*, JHEP **06** (2011) 128, arXiv: 1106.0522 [hep-ph] (cit. on p. 108).

[194] B. Grzadkowski, M. Iskrzynski, M. Misiak, and J. Rosiek, *Dimension-Six Terms in the Standard Model Lagrangian*, JHEP **10** (2010) 085, arXiv: 1008.4884 [hep-ph] (cit. on p. 108).

[195] I. Brivio, Y. Jiang, and M. Trott, *The SMEFTsim package, theory and tools*, JHEP **12** (2017) 070, arXiv: 1709.06492 [hep-ph] (cit. on pp. 108, 126, 164).

[196] ATLAS Collaboration, *Higgs boson production cross-section measurements and their EFT interpretation in the 4ℓ decay channel at $\sqrt{s} = 13$ TeV with the ATLAS detector*, Eur. Phys. J. C **80** (2020), arXiv: 2004.03447 [hep-ex] (cit. on pp. 116–118, 129, 150, 159, 210).

[197] ATLAS Collaboration, *Measurements of WH and ZH production in the $H \to b\bar{b}$ decay channel in pp collisions at 13 TeV with the ATLAS detector*, Eur. Phys. J. C **81** (2021) 178, arXiv: 2007.02873 [hep-ex] (cit. on pp. 116, 117, 120, 150, 154, 159).

[198] G. Aad et al., *Measurement of Higgs boson production in the diphoton decay channel in pp collisions at center-of-mass energies of 7 and 8 TeV with the ATLAS detector*, Phys. Rev. D **90** (2014) 112015, arXiv: 1408.7084 [hep-ex] (cit. on p. 117).

[199] G. Aad et al., *Measurements of Higgs boson production and couplings in the four-lepton channel in pp collisions at center-of-mass energies of 7 and 8 TeV with the ATLAS detector*, Phys. Rev. D **91** (2015) 012006, arXiv: 1408.5191 [hep-ex] (cit. on p. 117).

[200] G. Aad et al., *Search for the $b\bar{b}$ decay of the Standard Model Higgs boson in associated $(W/Z)H$ production with the ATLAS detector*, JHEP **01** (2015) 069, arXiv: 1409.6212 [hep-ex] (cit. on p. 117).

[201] G. Aad et al., *Muon reconstruction performance of the ATLAS detector in proton–proton collision data at $\sqrt{s}$ =13 TeV*, Eur. Phys. J. C **76** (2016) 292, arXiv: 1603.05598 [hep-ex] (cit. on pp. 116, 119, 120, 151, 153, 157).

[202] G. Aad et al., *Electron and photon performance measurements with the ATLAS detector using the 2015–2017 LHC proton-proton collision data*, JINST **14** (2019) P12006, arXiv: 1908.00005 [hep-ex] (cit. on pp. 118–120, 153).

[203] M. Aaboud et al., *Performance of missing transverse momentum reconstruction with the ATLAS detector using proton-proton collisions at $\sqrt{s} = 13$ TeV*, Eur. Phys. J. C **78** (2018) 903, arXiv: 1802.08168 [hep-ex] (cit. on p. 118).

[204] G. Aad et al., CP *Properties of Higgs Boson Interactions with Top Quarks in the* $t\bar{t}H$ *and* tH *Processes Using* $H \to \gamma\gamma$ *with the ATLAS Detector*, Phys. Rev. Lett. **125** (2020) 061802, arXiv: 2004.04545 [hep-ex] (cit. on p. 118).

[205] M. Hübner, *Measurement of the tau lepton reconstruction and identification performance in the ATLAS experiment using pp collisions at $\sqrt{s} = 13$ TeV*, PoS **LHCP2018** (2018) 024 (cit. on p. 120).

[206] ATLAS Collaboration, *A combination of measurements of Higgs boson production and decay using up to 139 fb^{-1} of proton–proton collision data at $\sqrt{s} = 13$ TeV collected with the ATLAS experiment*, tech. rep. ATLAS-CONF-2020-027, CERN, 2020, URL: https://cds.cern.ch/record/2725733 (cit. on pp. 124, 125, 221).

[207] C. Degrande et al., *Standard Model Effective Theory at Next-to-Leading-Order in QCD*, URL: http://feynrules.irmp.ucl.ac.be/wiki/SMEFTatNLO (cit. on p. 126).

[208] S. Dawson and P. P. Giardino, *Electroweak corrections to Higgs boson decays to $\gamma\gamma$ and W^+W^- in standard model EFT*, Phys. Rev. **D98** (2018) 095005, arXiv: 1807.11504 [hep-ph] (cit. on pp. 126, 214).

[209] M. L. Mangano, M. Moretti, F. Piccinini, and M. Treccani, *Matching matrix elements and shower evolution for top-quark production in hadronic collisions*, JHEP **01** (2007) 013, arXiv: hep-ph/0611129 (cit. on pp. 126, 190).

[210] S. Mrenna and P. Richardson, *Matching matrix elements and parton showers with HERWIG and PYTHIA*, JHEP **05** (2004) 040, arXiv: hep-ph/0312274 (cit. on pp. 126, 190).

[211] A. Buckley et al., *Rivet user manual*, Comput. Phys. Commun. **184** (2013) 2803, arXiv: 1003.0694 [hep-ph] (cit. on p. 126).

[212] LHC Higgs XS WG, URL: https://gitlab.cern.ch/LHCHIGGSXS/LHCHXSWG2/STXS/Classification (cit. on p. 126).

[213] ATLAS Collaboration, *Measurement of the properties of Higgs boson production at $\sqrt{s} = 13$ TeV in the $H \to \gamma\gamma$ channel using 139 fb^{-1} of pp collision data with the ATLAS experiment*, CERN-EP-2022-094 (2022), arXiv: 2207.00348 [hep-ex] (cit. on pp. 150, 159).

[214] ATLAS Collaboration, *Measurements of Higgs boson production cross-sections in the $H \to \tau^+\tau^-$ decay channel in pp collisions at $\sqrt{s} = 13$ TeV with the ATLAS detector*, (2022), arXiv: 2201.08269 [hep-ex] (cit. on pp. 150, 152, 159).

[215] ATLAS Collaboration, *Measurements of Higgs boson production by gluon–gluon fusion and vector-boson fusion using $H \to WW^* \to e\nu\mu\nu$ decays in pp collisions at $\sqrt{s} = 13$ TeV with the ATLAS detector*, CERN-EP-2022-078 (2022), arXiv: 2207.00338 [hep-ex] (cit. on pp. 150, 151, 159).

[216] ATLAS Collaboration, *Measurement of the associated production of a Higgs boson decaying into b-quarks with a vector boson at high transverse momentum in pp collisions at $\sqrt{s} = 13$ TeV with the ATLAS detector*, Submitted to Phys. Lett. B (2020), arXiv: 2008.02508 [hep-ex] (cit. on pp. 150, 153, 159).

[217] ATLAS Collaboration, *Measurements of Higgs bosons decaying to bottom quarks from vector boson fusion production with the ATLAS experiment at $\sqrt{s} = 13$ TeV*, Eur. Phys. J. C **81** (2020) 537, arXiv: 2011.08280 [hep-ex] (cit. on pp. 150, 153, 159).

[218] ATLAS Collaboration, *Measurement of Higgs boson decay into b-quarks in associated production with a top-quark pair in pp collisions at $\sqrt{s} = 13$ TeV with the ATLAS detector*, (2021), arXiv: 2111.06712 [hep-ex] (cit. on pp. 150, 153, 159).

[219] ATLAS Collaboration, *Constraints on Higgs boson production with large transverse momentum using $H \to b\bar{b}$ decays in the ATLAS detector*, (2021), arXiv: 2111.08340 [hep-ex] (cit. on pp. 150, 153, 159).

[220] ATLAS Collaboration, *A search for the $Z\gamma$ decay mode of the Higgs boson in pp collisions at $\sqrt{s} = 13$ TeV with the ATLAS detector*, Phys. Lett. B **809** (2020) 135754, arXiv: 2005.05382 [hep-ex] (cit. on pp. 150, 158).

[221] ATLAS Collaboration, *Search for the dimuon decay of the Standard Model Higgs Boson with the ATLAS Detector*, Submitted to Phys. Lett. B (2020), arXiv: 2007.07830 [hep-ex] (cit. on pp. 150, 157).

[222] A. Elagin, P. Murat, A. Pranko, and A. Safonov, *A New Mass Reconstruction Technique for Resonances Decaying to di-tau*, Nucl. Instrum. Meth. A **654** (2011) 481, arXiv: 1012.4686 [hep-ex] (cit. on p. 152).

[223] ATLAS Collaboration, *Jet reconstruction and performance using particle flow with the ATLAS Detector*, Eur. Phys. J. C **77** (2017) 466, arXiv: 1703.10485 [hep-ex] (cit. on p. 153).

[224] M. Cacciari, G. P. Salam, and G. Soyez, *The anti-k_t jet clustering algorithm*, JHEP **04** (2008) 063, arXiv: 0802.1189 [hep-ph] (cit. on pp. 153, 154, 156).

[225] ATLAS Collaboration, *ATLAS b-jet identification performance and efficiency measurement with $t\bar{t}$ events in pp collisions at $\sqrt{s} = 13$ TeV*, Eur. Phys. J. C **79** (2019) 970, arXiv: 1907.05120 [hep-ex] (cit. on pp. 153, 155, 156).

[226] ATLAS Collaboration, *Topological cell clustering in the ATLAS calorimeters and its performance in LHC Run 1*, Eur. Phys. J. **C77** (2017) 490, arXiv: 1603.02934 [hep-ex] (cit. on pp. 154, 156).

[227] ATLAS Collaboration, *Performance of jet substructure techniques for large-R jets in proton–proton collisions at $\sqrt{s} = 7$ TeV using the ATLAS detector*, JHEP **09** (2013) 076, arXiv: 1306.4945 [hep-ex] (cit. on p. 154).

[228] J. R. Andersen et al., *Les Houches 2015: Physics at TeV Colliders Standard Model Working Group Report*, (2016), arXiv: 1605.04692 [hep-ph] (cit. on p. 159).

[229] S. Amoroso et al., "Les Houches 2019: Physics at TeV Colliders: Standard Model Working Group Report", *11th Les Houches Workshop on Physics at TeV Colliders: PhysTeV Les Houches*, 2020, arXiv: 2003.01700 [hep-ph] (cit. on p. 159).

[230] ATLAS Collaboration, *Measurements of gluon-gluon fusion and vector-boson fusion Higgs boson production cross-sections in the $H \to WW^* \to e\nu\mu\nu$ decay channel in pp collisions at $\sqrt{s} = 13$ TeV with the ATLAS detector*, Phys. Lett. B **789** (2019) 508, arXiv: 1808.09054 [hep-ex] (cit. on p. 187).

[231] ATLAS Collaboration, *Measurement of fiducial and differential W^+W^- production cross-sections at $\sqrt{s} = 13$ TeV with the ATLAS detector*, Eur. Phys. J. C **79** (2019) 884, arXiv: 1905.04242 [hep-ex] (cit. on pp. 187, 204, 205, 210).

[232] E. Bothmann et al., *Event generation with Sherpa 2.2*, SciPost Phys. **7** (2019) 034, arXiv: 1905.09127 [hep-ph] (cit. on pp. 188, 211).

[233] S. Catani, L. Cieri, D. de Florian, G. Ferrera, and M. Grazzini, *Vector boson production at hadron colliders: hard-collinear coefficients at the NNLO*, Eur. Phys. J. C **72** (2012) 2195, arXiv: 1209.0158 [hep-ph] (cit. on p. 188).

[234] T. Gehrmann et al., *W^+W^- Production at Hadron Colliders in Next to Next to Leading Order QCD*, Phys. Rev. Lett. **113** (2014) 212001, arXiv: 1408.5243 [hep-ph] (cit. on p. 188).

[235] T. Gehrmann, A. von Manteuffel, and L. Tancredi, *The two-loop helicity amplitudes for $q\bar{q}' \to V_1V_2 \to 4$ leptons*, JHEP **09** (2015) 128, arXiv: 1503.04812 [hep-ph] (cit. on p. 188).

[236] A. Denner, S. Dittmaier, and L. Hofer, COLLIER*: A fortran-based complex one-loop library in extended regularizations*, Comput. Phys. Commun. **212** (2017) 220, arXiv: 1604.06792 [hep-ph] (cit. on pp. 188, 211).

[237] M. Grazzini, S. Kallweit, S. Pozzorini, D. Rathlev, and M. Wiesemann, *W^+W^- production at the LHC: fiducial cross sections and distributions in NNLO QCD*, JHEP **08** (2016) 140, arXiv: 1605.02716 [hep-ph] (cit. on p. 188).

[238] M. Grazzini, S. Kallweit, and M. Wiesemann, *Fully differential NNLO computations with MATRIX*, Eur. Phys. J. C **78** (2018) 537, arXiv: 1711.06631 [hep-ph] (cit. on p. 188).

[239] F. Cascioli, P. Maierhöfer, and S. Pozzorini, *Scattering Amplitudes with Open Loops*, Phys. Rev. Lett. **108** (2012) 111601, arXiv: 1111.5206 [hep-ph] (cit. on pp. 188, 211).

[240] T. Gleisberg and S. Höche, *Comix, a new matrix element generator*, JHEP **12** (2008) 039, arXiv: 0808.3674 [hep-ph] (cit. on pp. 189, 211).

[241] S. Schumann and F. Krauss, *A Parton shower algorithm based on Catani-Seymour dipole factorisation*, JHEP **03** (2008) 038, arXiv: 0709.1027 [hep-ph] (cit. on pp. 189, 211).

[242] S. Höche, F. Krauss, M. Schönherr, and F. Siegert, *A critical appraisal of NLO+PS matching methods*, JHEP **09** (2012) 049, arXiv: 1111.1220 [hep-ph] (cit. on pp. 189, 211).

[243] S. Höche, F. Krauss, M. Schonherr, and F. Siegert, *QCD matrix elements + parton showers: The NLO case*, JHEP **04** (2013) 027, arXiv: 1207.5030 [hep-ph] (cit. on pp. 189, 211).

[244] S. Catani, F. Krauss, B. R. Webber, and R. Kuhn,
QCD Matrix Elements + Parton Showers, JHEP **11** (2001) 063,
arXiv: hep-ph/0109231 (cit. on pp. 189, 211).

[245] S. Höche, F. Krauss, S. Schumann, and F. Siegert,
QCD matrix elements and truncated showers, JHEP **05** (2009) 053,
arXiv: 0903.1219 [hep-ph] (cit. on pp. 189, 211).

[246] F. Caola, K. Melnikov, R. Röntsch, and L. Tancredi,
QCD corrections to W^+W^- production through gluon fusion,
Phys. Lett. B **754** (2016) 275, arXiv: 1511.08617 [hep-ph]
(cit. on pp. 189, 211).

[247] ATLAS Collaboration, *ATLAS Pythia 8 tunes to 7 TeV data*,
ATL-PHYS-PUB-2014-021, 2014,
URL: https://cds.cern.ch/record/1966419 (cit. on pp. 189, 214).

[248] L. Lönnblad, *Correcting the Colour-Dipole Cascade Model with Fixed Order Matrix Elements*, JHEP **05** (2002) 046, arXiv: hep-ph/0112284
(cit. on p. 189).

[249] L. Lönnblad and S. Prestel,
Matching tree-level matrix elements with interleaved showers,
JHEP **03** (2012) 019, arXiv: 1109.4829 [hep-ph] (cit. on p. 189).

[250] S. Dawson and P. P. Giardino, *Electroweak corrections to Higgs boson decays to $\gamma\gamma$ and W^+W^- in standard model EFT*,
Physical Review D **98** (2018), ISSN: 2470-0029,
URL: http://dx.doi.org/10.1103/PhysRevD.98.095005 (cit. on p. 191).

[251] *Precision electroweak measurements on the Z resonance*,
Physics Reports **427** (2006) 257 (cit. on pp. 203, 208, 209, 215).

[252] ATLAS Collaboration, *Measurement of W±Z production in proton-proton collisions at $\sqrt{s}=7$ TeV with the ATLAS detector*,
The European Physical Journal C **72** (2012) 2173,
URL: https://doi.org/10.1140/epjc/s10052-012-2173-0
(cit. on p. 204).

[253] ATLAS Collaboration,
Measurements of differential cross-sections in four-lepton events in 13 TeV proton–proton collisions with the ATLAS detector, JHEP **07** (2021) 005,
arXiv: 2103.01918 [hep-ex] (cit. on pp. 204, 205, 210, 214).

[254] ATLAS Collaboration,
Differential cross-section measurements for the electroweak production of dijets in association with a Z boson in proton–proton collisions at ATLAS,
Eur. Phys. J. C **81** (2021) 163, arXiv: 2006.15458 [hep-ex]
(cit. on pp. 204, 205, 210).

[255] ATLAS Collaboration,
Measurement of $W^{\pm}Z$ production cross sections and gauge boson polarisation in pp collisions at $\sqrt{s} = 13$ TeV with the ATLAS detector,
Eur. Phys. J. C **79** (2019) 535, arXiv: 1902.05759 [hep-ex]
(cit. on pp. 204, 205).

[256] ATLAS Collaboration, *Combined effective field theory interpretation of differential cross-sections measurements of $WW, WZ, 4\ell$, and Z-plus-two-jets production using ATLAS data*, ATL-PHYS-PUB-2021-022, 2021, URL: https://cds.cern.ch/record/2776648 (cit. on p. 206).

[257] H. J. Bhabha, *The scattering of positrons by electrons with exchange on Dirac's theory of the positron*, Proc. Roy. Soc. Lond. A **154** (1936) 195
(cit. on p. 207).

[258] D. Decamp et al.,
ALEPH: A detector for electron-positron annnihilations at LEP,
Nucl. Instrum. Meth. A **294** (1990) 121, [Erratum: Nucl.Instrum.Meth.A 303, 393 (1991)] (cit. on p. 207).

[259] D. Buskulic et al., *Performance of the ALEPH detector at LEP*,
Nucl. Instrum. Meth. A **360** (1995) 481 (cit. on p. 207).

[260] P. A. Aarnio et al., *The DELPHI detector at LEP*,
Nucl. Instrum. Meth. A **303** (1991) 233 (cit. on p. 208).

[261] P. Abreu et al., *Performance of the DELPHI detector*,
Nucl. Instrum. Meth. A **378** (1996) 57 (cit. on p. 208).

[262] B. Adeva et al., *The Construction of the L3 Experiment*,
Nucl. Instrum. Meth. A **289** (1990) 35 (cit. on p. 208).

[263] M. Acciarri et al., *The L3 silicon microvertex detector*,
Nucl. Instrum. Meth. A **351** (1994) 300 (cit. on p. 208).

[264] M. Chemarin et al., *Test beam results for an upgraded forward tagger of the L3 Experiment at LEP-2*, Nucl. Instrum. Meth. A **349** (1994) 345
(cit. on p. 208).

[265] A. Adam et al., *The Forward muon detector of L3*,
Nucl. Instrum. Meth. A **383** (1996) 342 (cit. on p. 208).

[266] K. Ahmet et al., *The OPAL detector at LEP*,
Nucl. Instrum. Meth. A **305** (1991) 275 (cit. on p. 208).

[267] P. P. Allport et al., *The OPAL silicon microvertex detector*,
Nucl. Instrum. Meth. A **324** (1993) 34 (cit. on p. 208).

[268] P. P. Allport et al.,
The OPAL silicon strip microvertex detector with two coordinate readout,
Nucl. Instrum. Meth. A **346** (1994) 476 (cit. on p. 208).

[269] B. E. Anderson et al.,
The OPAL silicon - tungsten calorimeter front end electronics,
IEEE Trans. Nucl. Sci. **41** (1994) 845 (cit. on p. 208).

[270] M. J. Fero et al., *Performance of the SLD central drift chamber*,
Nucl. Instrum. Meth. A **367** (1995) 111, ed. by W. Bartl, M. Krammer,
G. Neuhofer, M. Regler, and A. Taurok (cit. on p. 208).

[271] D. Axen et al.,
The Lead liquid argon sampling calorimeter of the SLD detector,
Nucl. Instrum. Meth. A **328** (1993) 472 (cit. on p. 208).

[272] K. Abe et al., *Performance of the CRID at SLD*,
Nucl. Instrum. Meth. A **343** (1994) 74, ed. by E. Nappi and T. Ypsilantis
(cit. on p. 208).

[273] S. C. Berridge et al., *First results from the SLD silicon calorimeters*,
IEEE Trans. Nucl. Sci. **39** (1992) 1242, ed. by G. T. Baldwin
(cit. on p. 208).

[274] K. Abe et al., *Design and performance of the SLD vertex detector, a 307 Mpixel tracking system*, Nucl. Instrum. Meth. A **400** (1997) 287
(cit. on p. 208).

[275] A. C. Benvenuti et al., *The Iron Calorimeter and Muon Identifier for Sld*,
Nucl. Instrum. Meth. A **276** (1989) 94 (cit. on p. 208).

[276] ATLAS Collaboration, *Combined measurements of Higgs boson production and decay using up to* $139\,fb^{-1}$ *of proton—proton collision data at* $\sqrt{s} = 13\,TeV$ *collected with the ATLAS experiment*, ATLAS-CONF-2021-053,
2021, URL: https://cds.cern.ch/record/2789544 (cit. on p. 210).

[277] ATLAS Collaboration, *Measurements of gluon fusion and vector-boson-fusion production of the Higgs boson in* $H \to WW^* \to e\nu\mu\nu$ *decays using* pp *collisions at* $\sqrt{s} = 13\,TeV$ *with the ATLAS detector*,
ATLAS-CONF-2021-014, 2021,
URL: https://cds.cern.ch/record/2759651 (cit. on p. 210).

[278] B. Biedermann et al., *Next-to-leading-order electroweak corrections to* $pp \to W^+W^- \to 4$ *leptons at the LHC*, JHEP **06** (2016) 065,
arXiv: 1605.03419 [hep-ph] (cit. on p. 211).

[279] B. Biedermann, A. Denner, S. Dittmaier, L. Hofer, and B. Jager,
Next-to-leading-order electroweak corrections to the production of four charged leptons at the LHC, JHEP **01** (2017) 033,
arXiv: 1611.05338 [hep-ph] (cit. on p. 211).

[280] B. Biedermann, A. Denner, S. Dittmaier, L. Hofer, and B. Jäger, *Electroweak corrections to* $pp \to \mu^+\mu^-e^+e^- + X$ *at the LHC: a Higgs background study*, Phys. Rev. Lett. **116** (2016) 161803, arXiv: 1601.07787 [hep-ph] (cit. on p. 211).

[281] B. Biedermann, A. Denner, and L. Hofer, *Next-to-leading-order electroweak corrections to the production of three charged leptons plus missing energy at the LHC*, JHEP **10** (2017) 043, arXiv: 1708.06938 [hep-ph] (cit. on p. 211).

[282] F. Caola, K. Melnikov, R. Röntsch, and L. Tancredi, *QCD corrections to ZZ production in gluon fusion at the LHC*, Phys. Rev. D **92** (2015) 094028, arXiv: 1509.06734 [hep-ph] (cit. on p. 211).

[283] F. Caola, M. Dowling, K. Melnikov, R. Röntsch, and L. Tancredi, *QCD corrections to vector boson pair production in gluon fusion including interference effects with off-shell Higgs at the LHC*, JHEP **07** (2016) 087, arXiv: 1605.04610 [hep-ph] (cit. on p. 211).

[284] D. de Florian et al., *Handbook of LHC Higgs Cross Sections: 4. Deciphering the Nature of the Higgs Sector*, **2/2017** (2016), arXiv: 1610.07922 [hep-ph] (cit. on p. 211).

[285] G. Passarino, *Higgs CAT*, Eur. Phys. J. C **74** (2014) 2866, arXiv: 1312.2397 [hep-ph] (cit. on p. 211).

[286] M. Bähr, S. Gieseke, M. Gigg, D. Grellscheid, K. Hamilton, et al., *Herwig++ Physics and Manual*, Eur. Phys. J. C **58** (2008) 639, arXiv: 0803.0883 [hep-ph] (cit. on p. 211).

[287] J. Bellm et al., *Herwig 7.0/Herwig++ 3.0 release note*, Eur. Phys. J. C **76** (2016) 196, arXiv: 1512.01178 [hep-ph] (cit. on p. 211).

[288] J. Baglio et al., *VBFNLO: A Parton Level Monte Carlo for Processes with Electroweak Bosons – Manual for Version 2.7.0*, (2011), arXiv: 1107.4038 [hep-ph] (cit. on p. 211).

[289] L. Harland-Lang, A. Martin, P. Motylinski, and R. Thorne, *Parton distributions in the LHC era: MMHT 2014 PDFs*, Eur. Phys. J. C **75** (2015) 204, arXiv: 1412.3989 [hep-ph] (cit. on p. 211).

[290] J. Alwall et al., *The automated computation of tree-level and next-to-leading order differential cross sections, and their matching to parton shower simulations*, JHEP **07** (2014) 079, arXiv: 1405.0301 [hep-ph] (cit. on p. 214).

[291] R. D. Ball et al., *Parton distributions with LHC data*, Nucl. Phys. B **867** (2013) 244, arXiv: 1207.1303 [hep-ph] (cit. on p. 214).

[292] R. Frederix and S. Frixione, *Merging meets matching in MC@NLO*, JHEP **12** (2012) 061, arXiv: 1209.6215 [hep-ph] (cit. on p. 214).

[293] C. Anastasiou, L. Dixon, K. Melnikov, and F. Petriello, *High-precision QCD at hadron colliders: Electroweak gauge boson rapidity distributions at next-to-next-to leading order*, Phys. Rev. D **69** (2004) 094008, arXiv: hep-ph/0312266 (cit. on p. 214).

[294] D. J. Lange, *The EvtGen particle decay simulation package*, Nucl. Instrum. Meth. A **462** (2001) 152 (cit. on p. 214).

[295] G. Brooijmans et al., "Les Houches 2017: Physics at TeV Colliders New Physics Working Group Report", *10th Les Houches Workshop on Physics at TeV Colliders*, 2018, arXiv: 1803.10379 [hep-ph] (cit. on p. 214).

[296] T. Corbett, A. Helset, A. Martin, and M. Trott, *EWPD in the SMEFT to dimension eight*, JHEP **06** (2021) 076, arXiv: 2102.02819 [hep-ph] (cit. on p. 215).

[297] M. Awramik, M. Czakon, and A. Freitas, *Electroweak two-loop corrections to the effective weak mixing angle*, JHEP **11** (2006) 048, arXiv: hep-ph/0608099 (cit. on p. 215).

[298] I. Dubovyk, A. Freitas, J. Gluza, T. Riemann, and J. Usovitsch, *Electroweak pseudo-observables and Z-boson form factors at two-loop accuracy*, JHEP **08** (2019) 113, arXiv: 1906.08815 [hep-ph] (cit. on p. 215).

[299] A. Freitas, *Higher-order electroweak corrections to the partial widths and branching ratios of the Z boson*, JHEP **04** (2014) 070, arXiv: 1401.2447 [hep-ph] (cit. on p. 215).

[300] M. Awramik, M. Czakon, A. Freitas, and G. Weiglein, *Precise prediction for the W boson mass in the standard model*, Phys. Rev. D **69** (2004) 053006, arXiv: hep-ph/0311148 (cit. on p. 215).

[301] A. Helset, A. Martin, and M. Trott, *The Geometric Standard Model Effective Field Theory*, JHEP **03** (2020) 163, arXiv: 2001.01453 [hep-ph] (cit. on p. 215).

[302] C. Hays, A. Helset, A. Martin, and M. Trott, *Exact SMEFT formulation and expansion to* $\mathcal{O}(v^4/\Lambda^4)$, JHEP **11** (2020) 087, arXiv: 2007.00565 [hep-ph] (cit. on p. 215).

[303] L. Moneta, K. Belasco, K. S. Cranmer, S. Kreiss, A. Lazzaro, et al., *The RooStats Project*, PoS **ACAT2010** (2010) 057, arXiv: 1009.1003 [physics.data-an] (cit. on p. 221).

[304] F. Monti et al., *Modelling of the single-Higgs simplified template cross-sections (STXS 1.2) for the determination of the Higgs boson trilinear self-coupling*, tech. rep., 2022, URL: https://cds.cern.ch/record/2803606 (cit. on p. 240).

[305] F. Arco, S. Heinemeyer, and M. J. Herrero, *Exploring sizable triple Higgs couplings in the 2HDM*, Eur. Phys. J. C **80** (2020) 884, arXiv: 2005.10576 [hep-ph] (cit. on p. 240).

[306] M. Gorbahn, J. M. No, and V. Sanz, *Benchmarks for Higgs Effective Theory: Extended Higgs Sectors*, JHEP **10** (2015) 036, arXiv: 1502.07352 [hep-ph] (cit. on p. 242).

[307] J. Brehmer, A. Freitas, D. Lopez-Val, and T. Plehn, *Pushing Higgs Effective Theory to its Limits*, Phys. Rev. D **93** (2016) 075014, arXiv: 1510.03443 [hep-ph] (cit. on p. 242).

[308] H. Bélusca-Maïto, A. Falkowski, D. Fontes, J. C. Romão, and J. P. Silva, *Higgs EFT for 2HDM and beyond*, Eur. Phys. J. C **77** (2017) 176, arXiv: 1611.01112 [hep-ph] (cit. on p. 242).

[309] S. Dawson, S. Homiller, and S. D. Lane, *Putting standard model EFT fits to work*, Phys. Rev. D **102** (2020) 055012, arXiv: 2007.01296 [hep-ph] (cit. on p. 244).

[310] S. Dawson, D. Fontes, S. Homiller, and M. Sullivan, *Role of dimension-eight operators in an EFT for the 2HDM*, Phys. Rev. D **106** (2022) 055012, arXiv: 2205.01561 [hep-ph] (cit. on p. 244).

[311] J. Aebischer et al., "Computing Tools for Effective Field Theories", 2023, arXiv: 2307.08745 [hep-ph] (cit. on p. 250).

[312] J. De Blas, G. Durieux, C. Grojean, J. Gu, and A. Paul, *On the future of Higgs, electroweak and diboson measurements at lepton colliders*, JHEP **12** (2019) 117, arXiv: 1907.04311 [hep-ph] (cit. on p. 251).

Acknowledgments

All the work I have done in this thesis is thanks to the support and collaboration of many people. I feel deep gratitude to have been able to make a livelihood in the past years from pursuing my interest in science, I still pinch myself now and then to make sure I am not dreaming. I cherish that it has also allowed me to build friendships with some amazing people whose paths I would otherwise not have crossed. While I attempt to express my gratitude to you in the following pages, I might have missed you. If that is the case, I ask for your forgiveness. You all mean a lot to me and there is so much that I want to say, however, with great reluctance, I try to remain brief as I am currently writing this on borrowed time. Also, what I feel now when I reflect back goes beyond the capacity of what I can express with language. I try below nonetheless.

I am extremely grateful to Wouter Verkerke and Pamela Ferrari for the opportunity to pursue a Ph.D. and for being my role models. Wouter, you are always there to help regardless of the hour and I admire how you share your vast knowledge and experience, it always feels like talking to a fellow student instead of a *hogeleraar*. I am also amazed at your endless reservoir of energy, I recall a particular time when you were editing the first conference note late at night with Carsten - whilst Carsten and I certainly needed a slow start the next day, you were there early at Nikhef next day to chair the ATLAS group meeting with your contagious enthusiasm. I also admire how you look at things from a different way and this tends to be a much clearer and simpler perspective. Pamela, your motivation, passion, and knowledge are endless and highly infectious. I always come out of our chats feeling energized and inspired. Thanks a lot for your encouragement and advice. I graciously thank Lydia Brenner for providing invaluable comments on the manuscript. Lydia, I would not have managed to get the thesis in good shape without your extensive feedback and constant encouragement. Thanks to you and Vince for being welcoming hosts, I am going to miss playing with Kiki and Max.

I am greatly honored to have Flavia de Almeida Dias, Eric Laenen, Tina Pollmann, Marcel Vreeswijk, Gerhard Raven, Nicolas Berger, and Piet Mulders kindly forming the thesis committee and reviewing the manuscript. A special thanks to Piet for being my C3 member and making sure things were coming along smoothly throughout the Ph.D. Marcel, I am thankful to have worked under your guidance on the ITk at the beginning of my project — I found it a great experience and your

inventive suggestions helped me widen my thought process while searching for solutions.

As someone with no prior experience within the ATLAS collaboration, I am truly grateful to Carsten Burgard for making sure I could get started working smoothly. Your guidance was crucial for making me feel comfortable in such a unique environment. I admire your light-hearted and determined attitude to tackling challenges. The SMEFT work in this thesis kicked off over a productive summer in 2020 working with Saskia Falke and Ana Gomez. I am grateful for your collaboration and for your patience with all kinds of questions, big and small. I am also indebted to have a productive time working with Eleonora Rossi where we achieved many nice results. Eleonora, I remember the first time we started working together for the Higgs 2021 conference note and it felt like we had been collaborating for many years. I am grateful for your support, especially in the challenging period towards the end of the project with the HComb paper effort. I would like to thank Hannes Mildner for a fruitful period working on the global SMEFT fit. Hannes, you always had a German saying for different situations that I always found funny and thoughtful. I am grateful for your support in having the global fit ready in an ambitious timeframe.

ATLAS provided a unique opportunity to work with collaborators from all over the world. I am going to refrain from mentioning names as it will become a large list. I am grateful for all the constructive feedback from the HComb, Higgs, and the global EFT working group which has shaped the trajectory of the work carried out in this thesis, I would like to thank the groups for providing a nice environment to pursue research and their willingness to share their expertise. I warmly cherish feedback from the working group meetings which always provide key insights. Analyses are only as good as the analysis team, and I am happy to have worked with some incredible people over the past years in achieving results typically with ambitious timescales. There are too many people with whom I had a great time working together. I hope you have enjoyed working together as much as I have. We were able to publish the results shown in this thesis on behalf of ATLAS thanks to a thorough but swift review process which was crucial in improving the quality of the work. In this regard, I would like to extend my sincere gratitude to the members of the editorial boards and readers. None of the results could have been shared if not for the excellent work of editors who wrote up our work in a way that it was disseminated concisely and clearly. Given the nature of the topic working in combinations, a lot of my work generously builds on the hard work of many analyzers performing detailed measurements, I am truly grateful for being in such a position. Thank you!

I would like to thank Ilaria Brivio and Mike Trott whose theoretical insights and advice provided an important step in growing my rudimentary SMEFT knowledge. Ilaria, you were super-responsive and gave clear and comprehensive feedback on

any questions that we had for you. Mike, I appreciate your feedback during your STA with ATLAS. I am confident we will work hard to improve the reliability of SMEFT results from ATLAS.

At Nikhef, I had the pleasure of working closely on SMEFT with Bryan, Andrea, and Oliver. *Bryan, mijn hartelijke dank voor de lekker bezig tijd we hebben gehad tijdens de samenwerking aan de HWW+SMWW combinatie. Het was ook een groote plezier aan Tokio ontdekken met Edda en jouw*. Andrea and Oliver, it is great to see you carrying the torch for the SMEFT effort at Nikhef. I look forward to seeing the nice results in the coming period.

I enjoy the vibrant atmosphere at Nikhef, being such a large institute involved in many physics experiments with strong technical departments, I had the pleasure to interact and benefit from the expertise of many people. I would like to graciously thank the secretariat - Joan Berger, Eveline Schram-Post, Wijnanda de Haan, and Eveline Schram for their expedited help in making all matters at Nikhef flawlessly organized. I would also like to thank the HR department consisting of Pieter Van Braam Van Vloten, Ed van Willigen, Linda Berkhout, and Nancy Atmopawiro for their swift support and assistance with all practical matters.

I am indebted to the support of the Stomboot admins at Nikhef. Looking back, I was a complete newbie when it comes to working with an advanced computing infrastructure, and I am grateful for your patience and support. I would to thank Jeff Templon, Dennis van Dok, and David Groep for patiently responding to my queries and gently alerting me when I was doing something silly. I have learned a lot from these interactions and the computing course. Thanks a lot.

Although the pandemic forced me to work from home for a considerable period, I am glad to have had the chance to work at Nikhef alongside a lively and engaging group. I enjoyed the lunch discussions, coffee chats, the table tennis banters, and the dinner contemplations. Thank you for making working at Nikhef enjoyable day-to-day. I would like to warmly thank Alex, Anamika, Andrea A., Andrea V., Ali, Alice, Alessio, Amber, Ann-Kathrin, Ash, Birgit, Broos, Bryan, Clara, Carlo G., Carlo P., Carsten, Dorian, Denys, Diana, Duncan, Dylan, Edwin, Emma, Eveline, Federica, Flavia, Florian, Frank, Geoffrey, Hannah, Hella, Ivo, Jasper, JJ., Jos, Jochem, Jordy, Karel, Kees, Lisanne, Lydia, Liza, Luca, Mengqing, Marc, Marcel, Marion, Marko, Marten, Matouš, Matteo, Michiel, Nicolo, Oliver, Osama, Pamela, Peter K., Peter M., Peter V., Pepijn, Petja, Pim, Polina, Pranati, Robin K., Robin H., Sacha, Saskia, Sil, Stephen, Stefano, Terry, Tommaso, Tim, Tristan, Uraz, Walter, Wouter M., Wouter V., Zef, and Zhuoran. Stephen, thanks for answering all my curiosities related to computing and also helping me set up a beautiful website to understand what SMEFT operators look like. Ivo, thanks for welcoming me into the fray for the cyclotours - I hope to get back into cycling and join you in the future. Matouš, I cherish the discussions during the weekend coffee walks, I hope we get to continue

to do more of them in the future. Alice, thanks for organizing all the nice activities, I hope to go with you to see Kaleo live one day. Birgit, thanks to you and Jasper for hosting some nice Sinterklaas parties. Robin H., thanks for helping me review my job applications and sharing my enthusiasm for ice skating, I hope we will have a few more opportunities to improve our crossover skills. Andrea A., thanks for introducing me to pilates and the stunning cliffs of Langre. Zhuoran, thanks a lot for protecting my books and belongings when I was away at CERN. I am certainly leaving out many nice experiences that I shared with you all, please be assured that I remember and value them. Thanks a lot to all of you for being kind and warm to me.

Beyond the ATLAS group, I had the pleasure of meeting members of the KM3NeT, LHCb, Dark matter, DUNE, Gravitation waves, and Theory groups which always stoked my curiosity and encouraged me to gain a wider perspective of particle physics. I will refrain from mentioning names as I am bound to accidentally miss out on you. I value our discussions and will remember them with fondness.

I would like to thank my teammates from the ARAMEF futsal team - Andreas, Lisanne, Osama, Oliver, Timesh, Zef, Daan, Maksym, Matthias, Matthijs, Matous, Mees, Roberto, and Yashwant - for the fun times playing futsal and for the nice post-match discussions.

Beyond Nikhef, I would also like to share my gratitude to my friends - Anastasiia Skurativska, Matteo Mazzanti, and Natanael Spisak for all the nice summer trips. I look forward to planning our next trip. Nastya, I appreciate your honesty and insights and admire your tenacity. It is always a delight being around you. Matte, thank you for always being open to my suggestions and also for pushing me to pursue things I may have been hesitant about. I had a ton of fun from all the things that we did, whether it was freezing our toes off on the boat going up the Ij or taking a Cargoroo for two for our IKEA trip. Natanael, I always enjoy it when we get together, and, I feel like I have learned so much about genetics and evolution from you and look forward to learning more. A special thanks to Matteo's mum, mama Giovanna, and Nastya's sister, Katya, for enduring me during the Christmas break when I was busy implementing the final comments on the thesis and providing a festive atmosphere with some delicious food.

I would like to convey my deep gratitude to the INSIGHTS ITN program. I would like to thank Glen Cowan for leading this amazing project and the other supervisors for making it a vibrant training network. I cherish the time spent with my fellow ESRs - Artem Golatuviuk, Daria Morozova, Sitong An, Vasyl Hafych, Lukas Layer, Serena Palazzo, Nathan Simpson, Pim Verschuuren, Hevjin Yarar, and Viktor Ananiev where we had engaging discussions on statistics and machine learning during all workshops and schools located in some beautiful places that we all had the chance to attend. I had the chance to do a short stint at KPMG to get a feeling

of working in industry and I thank Jeroen van Leerdam and Sander Klous for being welcoming hosts. I enjoyed working with the data analytics team and had an excellent time with a supportive team. I feel fortunate to have been part of such an enriching experience and hope to catch up with you.

I had the pleasure of making a home away from home with Brian Moser, Ash McDougall, and Marko Stamenkovic during my time in Amsterdam. Brian, I am astounded by the depth of your kindness and how grounded you are as a person, I hope some of it has rubbed off on me. Thanks a lot for your constant support on a whole spectrum of matters ranging from providing shelter when I was in dire straits, the ski masterclass, explaining physics in a simplified way over brunch, to helping with moving when you had a “slight” cough. Ash, you brought light to my time in Amsterdam. It was always a great pleasure to hang out with you whether it was going for a cheeky sunrise ride, skating around the frozen canals and lakes, or the quest for finding the best coffee in Amsterdam (my fellow coffee enthusiasts please try Back to Black, Weteringstraat). I learned a lot about resilience, perseverance, benevolence, and fashion sense from you. Marko, I am amazed at how easily we hit it off from the very beginning. I fondly remember all the nice chats during our jogs, usually clad in our retro sportsuits, where we jumped into a wide range of topics inspired by the latest books or shows that we came across and discussed what we learned from them. Your perfectly round chapattis formed the foundation for many cozy Friday dinners. I’m practicing my chess and hope we can face off soon. I would also like to warmly thank Bouke *Kebou* Jung, Jordan Seneca, Brían Ó Fearraigh, Rasa Muller, and Vladimir Davidovic for being my close Amsterdam compatriots and enriching my time outside work. It was a pleasure hanging out with you and I hope I will have many opportunities to meet you all in the future.

Although many of my friends from before my time in Amsterdam are now spread all over the place, I am fortunate to have had the chance to meet some of them during my Ph.D. whether it was during trips back home to Chennai or in other places. I hope we will manage to plan more things in the future and reconnect.

I dedicate this thesis to all my teachers, whose efforts have greatly benefited me. I would like to specifically thank some kind people who played an important role in my formative years and sparked my interest in pursuing scientific research. From my undergraduate time, I would like to thank C.V. Krishnamurthy for introducing me to the world of research, Marianne Faurobert for guiding me in my first scientific endeavor, James Libby for introducing me to the world of particle physics, and Manuel Schiller for being an endless encouraging supervisor. My skills in particle physics started developing during my master’s studies. In this regard, I would like to thank Javier Castillo Castellanos for his infinite patience and warmth during my first experience with experimental data analysis in particle physics. I would like to thank François Gelis for his lucid explanations on using effective field theory in high-energy physics - it opened my eyes to its pertinence and convinced me

to take on my thesis topic. I would like to express my kindest thanks to Benoît Blossier for his support and advice during my work in lattice QCD. All of your patience and support were crucial in convincing me that I could do research in physics.

I would like to thank my family for their support and encouragement in me to pursue my interests. We are one big family and I am grateful to have so many well-wishers in my aunts, uncles, cousins, and wider family. *Amma* and *baba*, thank you for providing me the freedom to pursue this endeavor. Deepu *dada* and Aarthi *bei*, thanks a lot for your kindness. While I have missed some important moments in our lives during this period, I will strive to be better connected.

Minla *kuttima*, you make me the happiest uncle. You have grown incredibly quickly in the past couple of years since you were born. I affectionately remember holding you for the first time when you were born and now you are already running around calling for your *kaka* which gives me great pleasure. I keenly look forward to all the nice discussions we will have about how the universe works.

I am grateful to all of you for your support and encouragement. I hope to be able to repay your kindness in the future. As this thesis ends so does my time in Amsterdam soon. I am looking forward to meeting you all in the next chapter of my life.